

HARVARD UNIVERSITY
Graduate School of Arts and Sciences



DISSERTATION ACCEPTANCE CERTIFICATE

The undersigned, appointed by the
Department of Physics
have examined a dissertation entitled

Quantum Information Processing and Quantum Simulation with Programmable
Rydberg Atom Arrays

presented by Harry Jay Levine

candidate for the degree of Doctor of Philosophy and hereby
certify that it is worthy of acceptance.

Signature M. Lukin

Typed name: Professor Mikhail Lukin, Chair

Signature M. Greiner

Typed name: Professor Markus Greiner

Signature Ashvin Vishwanath

Typed name: Professor Ashvin Vishwanath

Date: April 19, 2021

Quantum Information Processing and Quantum Simulation with Programmable Rydberg Atom Arrays

A DISSERTATION PRESENTED

BY

HARRY JAY LEVINE

TO

THE DEPARTMENT OF PHYSICS

IN PARTIAL FULFILLMENT OF THE REQUIREMENTS

FOR THE DEGREE OF

DOCTOR OF PHILOSOPHY

IN THE SUBJECT OF

PHYSICS

HARVARD UNIVERSITY
CAMBRIDGE, MASSACHUSETTS

APRIL 2021

©2021 – HARRY JAY LEVINE
ALL RIGHTS RESERVED.

Quantum Information Processing and Quantum Simulation with Programmable Rydberg Atom Arrays

ABSTRACT

A frontier challenge in quantum science and technology is the construction of scalable quantum systems which can operate in regimes beyond classical simulability. Such systems can be used as tools for simulating and exploring complex phenomena in quantum physics; they can also be used to benchmark and test quantum algorithms. Several experimental platforms, based on a variety of quantum mechanical building blocks, are currently being pursued with these goals in mind, with state-of-the-art systems capable of controlling up to around fifty particles.

In this thesis, we present the development of a new platform based on individually controlled neutral atoms. In this approach, hundreds of individual atoms are trapped in an array of optical tweezers, and they are sorted in real-time into programmable geometries in one and two dimensions. After initialization of an array, atom interactions are switched on by coherent excitation to highly excited Rydberg states, resulting in a rich spin Hamiltonian. We experimentally advance several key aspects of this platform, developing new tools for controlling strongly interacting atom arrays and probing novel quantum phases and non-equilibrium dynamics. We additionally utilize Rydberg interactions to entangle atoms, demonstrating high fidelity universal quantum logic gates as well as the preparation of fully entangled Schrödinger cat states. This work highlights the prospects for scalable quantum simulation and quantum information processing beyond the limit of classical computation using neutral atom arrays.

Contents

Title	i
Copyright	ii
Abstract	iii
Table of Contents	iv
Author Contributions	xi
Acknowledgments	xiii
Dedication	xviii

I Introduction 1

1 INTRODUCTION 2
1.1 Background 2
1.2 Neutral atom arrays 5
1.3 Overview of thesis 7

II Experimental Methods 9

2 OPTICAL TWEEZER ARRAYS 10
2.1 Overview of optical tweezer system 10
2.2 Laser system for AOD tweezer arrays 13
2.3 Laser system for SLM tweezer arrays 14
2.4 Laser system for atom cooling and imaging 15
2.5 Atom loading and imaging 17
2.6 Characterizing optical tweezer properties 19
2.6.1 Trap light shifts 19
2.6.2 Trap frequencies 20
2.7 Correcting for optical aberrations 20
2.8 Optical pumping and microwave spectroscopy 22
2.9 Atom temperature and drop-recapture measurements 25

3 RYDBERG ATOMS 27
3.1 Introduction to Rydberg atoms 27
3.2 Two-photon excitation to Rydberg states 29
3.3 Rydberg laser system 32
3.4 Rydberg beam shaping 34
3.5 Protocol for Rydberg experiments 36
3.6 Calibration and alignment of Rydberg lasers 37
3.6.1 Independent calibration of 420 nm laser 38
3.6.2 Independent calibration of 1013 nm laser 40
3.7 Rydberg state detection 41

3.8	Calibration of Rydberg resonance	42
3.9	Measurements of Rydberg interaction energies	44
4	HYPERFINE QUBIT CONTROL	47
4.1	Introduction	47
4.2	Raman transitions are driven by laser amplitude modulation	49
4.3	Dispersive optics for amplitude modulation	53
4.4	Raman laser setup with a chirped Bragg grating	56
4.5	Benchmarking Raman laser system on neutral atom arrays	57
4.6	Coherence properties of hyperfine qubits	59
4.7	Optical pumping into $m_F = 0$ states	61
5	EXPERIMENT CONTROL INFRASTRUCTURE	64
5.1	Image acquisition and analysis	65
5.2	Real-time image analysis and live plotting of data	67
5.3	Atom rearrangement infrastructure	69
5.4	Two-dimensional optical tweezer arrays	71
5.5	Rydberg laser pulse programming	74
5.6	Beam alignment stabilization	76
5.7	Raman laser pulse programming	77
5.8	Remote operation of experiment	79
III	Experimental Results	83
6	ATOM-BY-ATOM ASSEMBLY OF DEFECT-FREE ONE-DIMENSIONAL COLD ATOM ARRAYS	84
6.1	Optical tweezer arrays	85
6.2	Real-time rearrangement of atoms	88
6.3	Repeated rearrangement with an atomic reservoir	90
6.4	Discussion and outlook	91
7	PROBING MANY-BODY DYNAMICS ON A 51-ATOM QUANTUM SIMULATOR	95
7.1	Strongly interacting atom arrays	97
7.2	Programmable quantum simulator	99
7.3	Quantum dynamics across a phase transition	104
7.4	Discussion	107
7.5	Outlook	109
8	QUANTUM KIBBLE-ZUREK MECHANISM AND CRITICAL DYNAMICS	111
8.1	Quantum phase transitions and the quantum Kibble-Zurek mechanism	111
8.2	1D Rydberg Hamiltonian phase diagram	114
8.3	(1+1)D Ising quantum phase transition	115
8.4	Critical scaling beyond Ising transition	118
8.5	Discussion	119
8.6	Outlook	122

9 QUANTUM PHASES OF MATTER ON A 256-ATOM PROGRAMMABLE QUANTUM SIMULATOR	124
9.1 Programmable Rydberg arrays in 2D	126
9.2 Checkerboard phase	127
9.3 (2+1)D Ising quantum phase transition	129
9.4 Phase diagram of the square lattice	131
9.5 Quantum fluctuations in the striated phase	136
9.6 Outlook	137
10 CONTROLLING MANY-BODY DYNAMICS WITH DRIVEN QUANTUM SCARS IN RYDBERG ATOM ARRAYS	139
10.1 Quantum scars in two dimensional Rydberg atom arrays	140
10.2 Decay mechanisms of quantum scars	143
10.3 Robust subharmonic response of driven quantum many-body scars	144
10.4 Discussion	149
10.5 Outlook	151
11 PROBING TOPOLOGICAL SPIN LIQUIDS ON A PROGRAMMABLE QUANTUM SIMULATOR	152
11.1 Introduction	152
11.2 Dimer models in Rydberg atom arrays	153
11.3 Measuring topological string operators	157
11.4 Probing spin liquid properties	161
11.5 Towards a topological qubit	163
11.6 Discussion and outlook	165
12 HIGH-FIDELITY CONTROL AND ENTANGLEMENT OF RYDBERG ATOM QUBITS	168
12.1 Experimental setup	169
12.2 Cavity filtering of high-frequency phase noise on Rydberg lasers	170
12.3 Characterizing Rydberg coherence	173
12.4 Generating entanglement within the Rydberg blockade regime	175
12.5 Characterizing two-particle Bell state	177
12.6 Lifetime of Bell state	178
12.7 Suppressing Doppler dephasing of Bell state	180
12.8 Outlook	180
13 GENERATION AND MANIPULATION OF SCHRÖDINGER CAT STATES IN RYDBERG ATOM ARRAYS	182
13.1 Greenberger–Horne–Zeilinger states	182
13.2 Entanglement protocol	184
13.3 GHZ states with up to 20 atoms	187
13.4 Entanglement distribution	190
13.5 Discussion	191
13.6 Outlook	193

14 PARALLEL IMPLEMENTATION OF HIGH-FIDELITY MULTI-QUBIT GATES WITH NEUTRAL ATOMS	194
14.1 Atom arrays with hyperfine control and Rydberg coupling	195
14.2 A fast, symmetric protocol for the controlled-phase gate	197
14.3 Parallel implementation of CZ gate	200
14.4 Extensions to three-qubit CCZ (and Toffoli) gate	202
14.5 Outlook	204
IV Conclusion	206
15 CONCLUSION	207
15.1 Summary	207
15.2 Extending experimental capabilities	208
15.2.1 System size	208
15.2.2 Rydberg and hyperfine coherence	209
15.2.3 Local addressing	210
15.2.4 Dynamic shuttling of hyperfine qubits	211
15.3 Outlook	211
V Appendices	213
A OPTICAL SETUPS	214
A.1 MOT laser setup	214
A.2 Rydberg laser setup	217
B SUPPLEMENTARY INFORMATION FOR CHAPTER 4	218
B.1 Methods for converting phase modulation to amplitude modulation	218
B.1.1 Filter out carrier component	220
B.1.2 Filter with Mach-Zehnder interferometer	221
B.1.3 Mach-Zehnder modulation	221
B.1.4 Dispersive elements	224
B.2 Dispersive optical elements	225
C SUPPLEMENTARY INFORMATION FOR CHAPTER 6	227
C.1 Experimental Sequence	227
C.1.1 Trap loading	227
C.1.2 Imaging	228
C.1.3 Feedback	229
C.2 Experimental Methods	230
C.2.1 Generating 100 traps	230
C.2.2 Effects of intermodulation	231
C.2.3 Optimizing trap homogeneity	232
C.2.4 Characterizing trap homogeneity	233
C.2.5 Moving traps	234
C.2.6 Lifetimes	235
C.3 Prospects for extensions to 2D arrays	237

C.3.1	Method 1: Row or column deletion and rearrangement	237
C.3.2	Method 2: Row-by-row rearrangement	238
C.3.3	Expected performance and scalability	239
D	SUPPLEMENTARY INFORMATION FOR CHAPTER 7	240
D.1	Trapping setup and experimental sequence	240
D.2	Rydberg lasers setup	242
D.3	Measuring interaction strengths	244
D.4	Timing limits imposed by turning off traps	245
D.5	State detection fidelity	246
D.6	Correcting for finite detection fidelity	246
D.7	Correcting detection infidelity: Many-body ground state preparation	247
D.8	Correcting detection infidelity: Maximum likelihood state reconstruction	248
D.9	Adiabatic pulse optimization	249
D.10	Coherence limitations	250
D.11	Comparison with a classical thermal state	254
D.12	Dynamics after sudden quench: Matrix Product State ansatz	257
D.13	Decay of the oscillations and growth of entanglement after quantum quench	259
D.14	Numerical time evolution via matrix product state algorithm	262
E	SUPPLEMENTARY INFORMATION FOR CHAPTER 8	264
E.1	Rydberg array preparation	264
E.2	Pulse generation	265
E.3	Pulse parameters	266
E.4	Numerical computation of the phase diagram	268
E.5	Correlation length extraction and scaling	272
E.6	\mathbb{Z}_N domain density	274
E.7	Length rescaling of correlation functions	274
E.8	Finite-time scaling	274
E.9	Numerical simulation of Kibble-Zurek dynamics	275
E.10	Chiral clock models	276
F	SUPPLEMENTARY INFORMATION FOR CHAPTER 9	281
F.1	2D atom rearrangement	281
F.2	Rearrangement algorithm	282
F.3	Rearrangement parameters and results	284
F.4	Rydberg laser system	285
F.5	Rydberg pulses	285
F.5.1	Quasi-adiabatic Sweeps	286
F.5.2	Linear sweeps	286
F.6	State detection	287
F.7	Coarse-grained local staggered magnetization	289
F.8	Determination of the quantum critical point	290
F.9	Data collapse for universal scaling	292
F.10	Order parameters for many-body phases	294
F.11	Numerical simulations of the 2D phase diagram	294
F.12	Mean-field wavefunction for the striated phase	295
F.13	Dynamical probe of the striated phase	297

G SUPPLEMENTARY INFORMATION FOR CHAPTER 10	300
G.1 Experimental setup and details	300
G.2 Thermalization mechanisms and fixed-detuning quenches	301
G.2.1 Derivation of effective Hamiltonian	301
G.2.2 Optimal fixed global detuning for suppressing long-range interactions . .	305
G.2.3 Independent measurement of decay mechanisms	306
G.3 Experimental data on enhancement of scars by periodic driving	309
G.3.1 Definition of subharmonic weight	309
G.3.2 Robustness of subharmonic response as a function of system size . . .	310
G.3.3 Signatures of a 4 th subharmonic response	311
G.3.4 Dependence of subharmonic response on the initial state	312
G.3.5 Subharmonic response with square pulse modulation	316
G.3.6 Rationale and robustness for choice of drive parameters Δ_m and Δ_0 .	316
G.4 Theoretical investigations of driven scars	318
G.4.1 Growth of entanglement entropy under drive	318
G.4.2 Stabilization of pure PXP	319
G.4.3 Analysis of pulsed model	320
G.5 Tabulation of system and drive parameters used in Chapter 10	326
G.6 Tabulation of 51-dimensional Hilbert space from Figure 10.3D	327
H SUPPLEMENTARY INFORMATION FOR CHAPTER 11	328
H.1 Experimental system	328
H.2 Basis rotation for X and Z parity loops	330
H.3 Supplemental experimental data	333
H.3.1 Mean Rydberg density and boundary effects	333
H.3.2 Lack of spatial order within spin-liquid phase	334
H.3.3 Phase dependence of quench	335
H.3.4 Z parity measurements with improved state preparation	336
H.3.5 Correlations between parity loops	338
H.3.6 Quasiparticle excitations	339
H.3.7 Additional data for arrays with nontrivial topology	342
H.4 Numerical studies	343
H.4.1 Ground state phase diagram	344
H.4.2 Numerical simulations of dynamical state preparation	346
I SUPPLEMENTARY INFORMATION FOR CHAPTER 12	351
I.1 State initialization	351
I.2 Characterizing state detection fidelity	352
I.3 Rydberg laser alignment onto atoms	353
I.4 Stabilizing the electric field environment with an ultraviolet LED	353
I.5 Single-atom phase gate	354
I.6 Numerical model for single atoms	354
I.7 Definition of $ W\rangle$ state	356
I.8 Extracting off-diagonal matrix elements of density operator	357
I.9 Prospects for near-term improved coherence and readout	359

J SUPPLEMENTARY INFORMATION FOR CHAPTER 13	361
J.1 Experimental setup	361
J.2 Optimal control	362
J.3 Optimal control dynamics	365
J.4 Quantifying detection	368
J.5 Accounting for detection imperfections	370
J.6 Bounding the GHZ state coherence	373
J.7 Parity detection	375
J.8 Staggered field calibration	377
J.9 Measured GHZ fidelities	379
J.10 Experimental imperfections	379
J.11 Ground-state qubit encoding	380
K SUPPLEMENTARY INFORMATION FOR CHAPTER 14	382
K.1 Optical pumping into $ 0\rangle$	383
K.2 Rydberg laser system	383
K.3 Constructing quantum circuits from native single-qubit gates	384
K.3.1 Initializing computational basis states	384
K.3.2 Local $X(\pi/2)$ for CNOT gate	386
K.3.3 Local Hadamard for Toffoli implementation	386
K.4 Design of two-qubit CZ gate	387
K.4.1 Accounting for imperfect blockade	390
K.5 Experimental calibration of CZ gate	391
K.6 Preparation of Bell state using \mathcal{CZ} gate and $\pi/4$ pulse	392
K.7 Implementation of CCZ gate	393
K.8 Echo procedure for CZ and CCZ	396
K.9 State readout through atom loss	396
K.10 Correcting for state preparation and measurement errors	399
K.10.1 Bell state fidelity	400
K.10.2 CNOT truth table	401
K.10.3 Toffoli truth table	401
K.11 Limited tomography of Toffoli gate	403
K.12 Parallel gate implementation in a contiguous array	406
L BESSEL FUNCTION IDENTITIES	407
L.1 Destructive interference of pure phase modulation	407
L.2 Quadratic phase shifts	408
L.3 Even sidebands	410
Bibliography	413

Author Contributions

The following chapters from this thesis were co-authored and previously published:

Chapters 2 through 5 include figures from supplementary materials and slides which were co-authored by several others, including:

Alexander Keesling, Hannes Bernien, Ahmed Omran, Sylvain Schwartz, Tout T. Wang, Giulia Semeghini, Sepehr Ebadi, and Dolev Bluvstein.

Chapter 6 and Appendix C were reproduced from:

Manuel Endres*, Hannes Bernien*, Alexander Keesling*, Harry Levine*, Eric R. An-schuetz, Alexandre Krajenbrink, Crystal Senko, Vladan Vuletić, Markus Greiner, and Mikhail D. Lukin, “Atom-by-atom assembly of defect-free one-dimensional cold atom arrays,” *Science* **354**, 6315 (2016).

Chapter 7 and Appendix D were reproduced from:

Hannes Bernien, Sylvain Schwartz, Alexander Keesling, Harry Levine, Ahmed Omran, Hannes Pichler, Soonwon Choi, Alexander S. Zibrov, Manuel Endres, Markus Greiner, Vladan Vuletić, and Mikhail D. Lukin, “Probing many-body dynamics on a 51-atom quantum simulator,” *Nature* **551**, 579 (2017).

Chapter 8 and Appendix E were reproduced from:

Alexander Keesling, Ahmed Omran, Harry Levine, Hannes Bernien, Hannes Pichler, Soonwon Choi, Rhine Samajdar, Sylvain Schwartz, Pietro Silvi, Subir Sachdev, Peter Zoller, Manuel Endres, Markus Greiner, Vladan Vuletić, and Mikhail D. Lukin, “Quantum Kibble–Zurek mechanism and critical dynamics on a programmable Rydberg simulator,” *Nature* **568**, 207 (2019).

Chapter 9 and Appendix F were reproduced from:

Sepehr Ebadi, Tout T. Wang, Harry Levine, Alexander Keesling, Giulia Semeghini, Ahmed Omran, Dolev Bluvstein, Rhine Samajdar, Hannes Pichler, Wen Wei Ho, Soonwon Choi, Subir Sachdev, Markus Greiner, Vladan Vuletić, and Mikhail D. Lukin, “Quantum Phases of Matter on a 256-Atom Programmable Quantum Simulator,” *arXiv:2012.12281* (2020).

Chapter 10 and Appendix G were reproduced from:

Dolev Bluvstein, Ahmed Omran, Harry Levine, Alexander Keesling, Giulia Semeghini, Sepehr Ebadi, Tout T. Wang, Alexios A. Michailidis, Nishad Maskara, Wen Wei Ho, Soonwon Choi, Maksym Serbyn, Markus Greiner, Vladan Vuletić, and Mikhail D. Lukin, “Controlling quantum many-body dynamics in driven Rydberg atom arrays,” *Science* **371**, 1355 (2021).

Chapter 11 and Appendix H were reproduced from:

Giulia Semeghini, Harry Levine, Alexander Keesling, Sepehr Ebadi, Tout T. Wang, Dolev Bluvstein, Ruben Verresen, Hannes Pichler, Marcin Kalinowski, Rhine Samajdar, Ahmed Omran, Subir Sachdev, Ashvin Vishwanath, Markus Greiner, Vladan Vuletić, and Mikhail D. Lukin, “Probing Topological Spin Liquids on a Programmable Quantum Simulator,” *arXiv:2104.04119* (2021).

Chapter 12 and Appendix I were reproduced from:

Harry Levine, Alexander Keesling, Ahmed Omran, Hannes Bernien, Sylvain Schwartz, Alexander S. Zibrov, Manuel Endres, Markus Greiner, Vladan Vuletić, and Mikhail D. Lukin, “High-Fidelity Control and Entanglement of Rydberg-Atom Qubits,” *Phys. Rev. Lett.* **121**, 123603 (2018).

Chapter 13 and Appendix J were reproduced from:

Ahmed Omran*, Harry Levine*, Alexander Keesling, Giulia Semeghini, Tout T. Wang, Sepehr Ebadi, Hannes Bernien, Alexander S. Zibrov, Hannes Pichler, Soonwon Choi, Jian Cui, Marco Rossignolo, Phila Rembold, Simone Montangero, Tommaso Calarco, Manuel Endres, Markus Greiner, Vladan Vuletić, and Mikhail D. Lukin, “Generation and manipulation of Schrödinger cat states in Rydberg atom arrays,” *Science* **365**, 570 (2019).

Chapter 14 and Appendix K were reproduced from:

Harry Levine, Alexander Keesling, Giulia Semeghini, Ahmed Omran, Tout T. Wang, Sepehr Ebadi, Hannes Bernien, Markus Greiner, Vladan Vuletić, Hannes Pichler, and Mikhail D. Lukin, “Parallel Implementation of High-Fidelity Multiqubit Gates with Neutral Atoms,” *Phys. Rev. Lett.* **123**, 170503 (2019).

*These authors contributed equally to this work.

Acknowledgments

This thesis is the result of an incredible collaborative effort among many amazing scientists with whom I have been so fortunate to work. First and foremost, Misha Lukin has been a fantastic advisor throughout my time in graduate school. His insight into which questions are worth asking has always pointed our team in the right direction. At the same time, he has supported us at each stage in exploring questions we found interesting. Above all, Misha's enthusiasm for collaboration and inclusivity has allowed us to build a team of theorist friends who were absolutely crucial to the success of many of our research projects. The collaborative environment was exemplified also by the co-advising of this project by Markus Greiner and Vladan Vuletić, both of whom offered invaluable support and expertise for solving problems in the lab and planning for the future since the beginning. I want to also thank Ashvin Vishwanath for serving on my thesis committee, and I am grateful we had a chance to collaborate on a recent project regarding quantum spin liquids.

The Atom Array experimental team has been such a pleasure to work with throughout the years. Manuel Endres supervised the initial building of the experiment, and taught me a great deal about atomic physics, and how to do things the right way. Early on, I was building a laser intensity lock and asked him how good the lock should be, and he said just do it *gründlich* (thoroughly). Hannes Bernien went on to establish our working principles to be *gründlich*, *pünktlich* (punctual), and *ausgezeichnet* (excellent). Hannes was an incredible leader and mentor over several years, taught me all kinds of things about various fields of physics and experimental techniques, and famously played great music in lab.

My time in graduate school has been made immeasurably better by working with Alex

Keesling for the last six years. We've had countless great conversations, late nights in the lab, moments of frustration, and moments of excitement. He has consistently pushed me to better understand physics, challenged me when I needed challenging, and made me laugh until I was crying. His hard work, passion, insight, and leadership have made him an incredible lab companion. He has also tolerated my annoying habits like a champion. Hannes, Alex, and I worked very closely to initially build the experiment, and I remember so many fun days, such as when we built a MOT for the first time, and when we were staring at flashing camera images trying to identify our first atoms.

I've been lucky to work in the lab with several other amazing postdocs and graduate students. Sylvain Schwartz did a thorough analysis of Rydberg laser excitation schemes, and built our first generation Rydberg laser system, tucked away in a separate lab space in B22. I also had the pleasure of working for several years with Ahmed Omran, whose technical knowledge in all experimental techniques was amazing to behold. Ahmed loved cats (in particular, Schrödinger cats), and at times there was a great deal of meowing in the lab (more enjoyable than the submarine beeping sounds, at least). Ahmed was also a masterful mine sweeper, and took meticulous lab notes, including such gems as "*This is such a dreadful result I don't even know where to begin.*" - *A.Omran, 2019-02-21*. Tout Wang was a visiting scientist on the experiment for several years, and we had a lot of fun exploring different approaches for improved laser cooling, as well as working collaboratively on many projects over the years. Most recently, I have gotten to work with Giulia Semeghini on several experimental projects, and her focus and diligence played an important role during the lab overhaul when we upgraded to two-dimensional tweezer arrays. Giulia also led the very challenging spin liquid project, taking data on incredible multi-week sprints and coordinating many experimental and theoretical contributors to great success. Giulia was a moderating influence on my childish antics with

Alex, and was always the rational one in the room.

During the latter part of my Ph.D, I also got to work with two fantastic younger graduate students, Sepehr Ebadi and Dolev Bluvstein. Sepehr's love for Fourier optics was infectious and we had great fun playing with spatial light modulators together. Dolev brings boundless energy and enthusiasm, and he was my co-conspirator in preaching the gospel of amplitude modulation and chirped Bragg gratings. I am excited to see what amazing work that Sepehr and Dolev do over the next several years. I also want to acknowledge Alexandre Krajenbrink, Eric Anschuetz, and Kevin Fei for their contributions to several technical aspects of the lab.

We've collaborated with many amazing theorists over the years. A very special thanks to Hannes Pichler and Soonwon Choi, who worked closely with us since the very first Rydberg experiments to make sense of what we were doing. They each have such a deep understanding of physics, as well as an incredible breadth of knowledge of different subfields, allowing them to make connections and translate ideas into language that us experimentalists can understand. Hannes and I also had the opportunity to develop a new quantum gate protocol together (the so-called *Pichler gate*), which was great fun and potentially just the beginning of explorations of new families of quantum gate protocols. I've also greatly enjoyed talking with (and sharing an office with!) Iris Cong, including many great conversations about quantum error correction. Recent work on quantum optimization has involved a large additional group of theorists, including Leo Zhou, Madelyn Cain, and Bea Nash who have been leading the charge in figuring out what kinds of problems will stump classical optimizers. I additionally am grateful to Rhine Samajdar, Wen Wei Ho, Nishad Maskara, and Marcin Kalinowski for many collaborations, and to Ruben Verresen for amazing work on quantum spin liquids, including showing us exactly how to study this exotic type of physics in our lab.

Other members of the Lukin group have been amazing friends and colleagues. I've had

countless great conversations with the atom-cavity lab, including Po Samutpraphoot, Tamara Dordevic, Paloma Ocola, Crystal Senko, and more recently Brandon Grinkemeyer and Ivana Dimitrova. Early in grad school, we would regularly get lunch together and then chat about physics over a coffee afterwards, which was always fun. I also thank the QuEra team, with whom we've had fascinating discussions about all the considerations that go into building a quantum computer using neutral atoms: Nate Gemelke, Shengtao Wang, Alexei Bylinskii, Alex Lukin, Donggyu Kim, Jesse Amato-Grill, and Jinguo Liu. I want to also thank so many people who helped to make the Lukin group and Harvard in general such a welcoming, fun, and stimulating environment: Mihir Bhaskar, David Levonian, Ruffin Evans, Alp Sipahigil, Dominik Wild, Denis Sukachev, Ralf Riedinger, Christian Nguyen, Rivka Bekenstein, Bart Machielse, Erik Knall, Can Knaut, Javier Sanchez-Yamagishi, Gio Scuri, Trond Andersen, Andrey Sushko, Kristine Rezai, Aditya Venkatramani, Elana Urbach, Helena Knowles, Harry Zhou, Leigh Martin, Oksana Makarova, Bo Dwyer, Aaron Kabcenell, Tamara Sumarac, Sona Najafi, Emma Rosenfeld, Emil Khabiboulline, Nathan Leitao, Frankie Fung, DaLi Schaefer, Katherine Van Kirk, Pasha Stroganov, Simon Evered, Tim Guo, and Sasha Zibrov. I also want to thank my friends Andrei Gheorghe and Noah Rubin for being great roommates and friends throughout graduate school.

The Harvard physics department is kept running by an incredible staff. A huge thanks to Sam Dakoulas, Clare Ploucha, Lisa Cacciabuado, Jacob Barandes, Silke Exner, Carol Davis, Adam Ackerman, and to the whole department.

The last year of my Ph.D looked very different than I expected it would, due to the global COVID-19 pandemic. A huge amount of effort went into making it possible to continue working during this year, and I want to thank many members of the Harvard AMO community, particularly Elana Urbach, Sam Dakoulas, and John Doyle, for helping us all to adapt to this

unexpected situation, and to stay safe and productive.

I want to also acknowledge Leo Hollberg and Monika Schleier-Smith who advised me as an undergraduate doing research at Stanford. Monika advised me through some of my very first AMO experiences, such as finding a vapor cell spectroscopy signal and locking my first laser. These experiences were so valuable and completely convinced me that I wanted to pursue AMO. I additionally want to thank Brandon Buscaino, who was both a great friend and also labmate during this time.

Finally, I want to thank my family. My parents Richard and Debby have been an unwavering source of support, always encouraging me to follow my passions. My brother Jacob has always been someone I can turn to for counsel or to chat about anything science or math related, or even just to make sense of the world together. Lastly, I want to thank my partner and fiancée, Katie Chung. Katie and I met right around the time I started at Harvard, so we've gone through this journey together, and I've accompanied her on her amazing journey through medical school. She has made my life so much richer, and reminds me of what really matters. I am so excited to continue our journeys together.

TO MY PARENTS RICHARD AND DEBBY,
MY BROTHER JACOB,
AND MY PARTNER KATIE

Part I

Introduction

1

Introduction

1.1 BACKGROUND

The theory of quantum mechanics underlies modern physics, science, and technology. Since its development one hundred years ago, quantum mechanics has been used to make extraordinary predictions about nature, and experimental verifications of these predictions have rendered quantum mechanics to be among the most successful theories of physics. While quantum theory underpins the modern understanding of the macroscopic world, it also makes counter-intuitive predictions about nature: notions such as quantum superposition and entanglement defy classical intuition [1–3], and are indeed impossible to observe in normal settings. To wit-

ness these phenomena, it is necessary to study nature in exotic regimes: at ultracold temperatures, or in carefully isolated, ultra-high vacuum environments. Pioneering work in the 1980s and 1990s resulted in early measurements showing clear evidence of quantum superposition in single particles, and soon afterwards the controlled entanglement of multiple particles [4–13]. A central modern research frontier is focused on learning how to better control the quantum world using a wide variety of quantum mechanical building blocks, including ultracold atomic gases, individually trapped atoms and ions, electron and nuclear spins confined in solid state systems, individual photons, and superconducting circuits.

While this experimental field is exceptionally challenging due to the demanding requirements of observing quantum effects, it is motivated by a remarkable observation: it is hard to predict how quantum systems will behave. This is exemplified by considering systems composed of quantum bits, which are quantum objects that can exist in two states $|0\rangle$ and $|1\rangle$, or any superposition thereof; this could, for example, describe a single electron spin, which can be oriented in two opposite directions. Quantum mechanically, the state of a single qubit is described by a state vector $|\psi\rangle = \alpha|0\rangle + \beta|1\rangle$, where α and β are complex numbers. In the classical world, one would expect that the state of all qubits in a system could be described in terms of the state of each qubit individually. Indeed, this encompasses the set of quantum states which are so-called *separable*, or non-entangled. Since each qubit is described by two coefficients, a system of N qubits which is separable would be described by $2N$ complex numbers.

But quantum mechanically, the most general description for a system of N qubits is as a superposition of all possible N -qubit states: $|\psi\rangle = \alpha|0000\dots\rangle + \beta|1000\dots\rangle + \gamma|0100\dots\rangle + \delta|1100\dots\rangle + \dots$. This state is described by 2^N coefficients, $\alpha, \beta, \gamma, \delta, \dots$, which means that an enormous amount of information is needed to represent the state of a quantum system with

even just a small number of particles. Even using supercomputers, simply keeping track of the state of quantum systems beyond 50-60 particles is effectively impossible, let alone simulating the evolution of these systems over time.

Since we cannot directly simulate the behavior of quantum systems, how can we learn about them? In 1982, Richard Feynman proposed that the solution is to build toy model quantum systems in the laboratory which can be programmed to mimic the behavior of more complex quantum systems in nature [14]. This idea, termed *quantum simulation*, is based on the notion that these laboratory systems may capture the essential features of various quantum phenomena, but in a highly controlled setting in which the parameters of the system can be widely tuned. Paradigmatic examples include the use of ultracold atoms to simulate the behavior of electrons in condensed matter systems [15] and the study of quantum magnetism using arrays of ions and atoms [16, 17]. In this spirit, quantum simulation enables experimental discoveries about how the rules of quantum mechanics play out in large, complex systems.

The computational challenge of simulating quantum systems motivates another experimental direction: since these systems evolve in ways which we cannot otherwise predict, can we program them such that their evolution results in the answer to some specific computational question? This is the notion of *quantum information processing* or *quantum computing*, whereby classical computational problems are solved by quantum mechanical systems. Central to this field of quantum computing is the question of which types of problems may be solved more efficiently on quantum computers than on classical computers. Several examples of such problems are known, including the factoring of integers (Shor's algorithm [18]) and the search through an unstructured database (Grover's algorithm [19]). In these special examples, the quantum algorithm offers a provable speedup over the best-known classical algorithms. However, there are many other classes of problems, including combinatorial op-

timization and random sampling from probability distributions, for which it is believed that a quantum speedup may be possible, but such a speedup is hard to prove in general. In lieu of mathematical proofs, experimental tests with real laboratory quantum computers will be necessary to evaluate and explore new quantum algorithms. Of special current interest is the question of how quantum algorithms will perform on real, near-term quantum devices with hundreds of qubits but occasional errors – so-called NISQ (noisy intermediate-scale quantum) devices [20].

With these applications towards quantum simulation and quantum information processing in mind, there is an ongoing worldwide race to build quantum systems with upwards of fifty particles, which are beyond the reach of classical simulability. These devices constitute powerful instruments for scientific research, opening the door for studying new physics in exotic regimes; they also serve as valuable testbeds for probing the performance of quantum computation protocols. Recent experiments have claimed to provably surpass the limits of classical simulability for the first time, demonstrating so-called *quantum advantage* [21, 22]. More such experiments will follow in the coming years, using a variety of experimental platforms and studying a wide range of questions.

1.2 NEUTRAL ATOM ARRAYS

Quantum systems based on neutral atoms offer a unique route towards scalable quantum simulation and quantum information processing. In this approach, experiments are conducted in ultra-high vacuum chambers and utilize a well-developed toolbox of lasers, microwaves, and magnetic fields to control atoms. Each experiment begins by laser cooling millions of identical atoms in a magneto-optical trap (MOT). Atoms are then loaded into optical tweezers, which are tightly focused lasers that form trapping potentials at their focal points. Central to the op-

tical tweezer platform is the phenomenon of collisional blockade, which ensures that only one atom is trapped in each tweezer [23]. The accessible system sizes that can be studied using this approach is therefore given by the number of optical tweezers that can be created. Modern systems can produce hundreds or even thousands of tweezers, and simply increasing the available laser power will enable scaling towards even larger arrays.

The optical tweezer platform benefits from rapid experimental cycle times and relative experimental simplicity. However, a major challenge is that the process of loading atoms from the MOT into the optical tweezers is stochastic; after every loading attempt, each tweezer will randomly be filled with a single atom with probability $p \sim 1/2$. To circumvent this problem and create deterministically filled arrays, we developed an atom-by-atom assembly procedure in parallel with two other groups [24–26], whereby we take an image of the initial randomly loaded tweezer array, and then use real-time feedback to move atoms around and prepare a target defect-free geometry. This method is incredibly flexible and allows for initialization of programmable atom arrays in a wide variety of geometries.

After initializing a target atom array, strong and tunable interactions can be introduced by exciting atoms to highly excited atomic states known as *Rydberg states* [27–29]. Rydberg interactions result in a rich quantum spin model that hosts many different quantum phases, each of which emerge from the competition between interactions and coherent driving. These interactions can additionally enable several classes of quantum information and entanglement generation protocols.

The last several years have witnessed remarkable progress in the technical capabilities of neutral atom systems based on tweezer arrays. Hundreds of atoms can now be readily trapped and sorted within such tweezer arrays in two and three spatial dimensions [30–32]. Coherent excitation to Rydberg states and high-fidelity quantum operations have been demonstrated

[33, 34]. Trapping of more exotic species, such as alkaline earth atoms and molecules, additionally offers new opportunities based on more complex atomic structure [35–39, 37]. Optical tweezer arrays constitute a powerful and exciting platform for quantum simulation of a wide variety of quantum spin models and phenomena, as well as for state-of-the-art quantum optimization algorithms with the largest system sizes available in any quantum computing platform.

1.3 OVERVIEW OF THESIS

This thesis is divided into two parts. The first part focuses on the experimental methods which were developed to expand the technical capabilities of tweezer arrays. Chapter 2 describes our approach to generating 1D and 2D arrays of optical tweezers, as well as our apparatus for cooling, imaging, and characterizing trapped atoms. Chapter 3 introduces Rydberg atoms, detailing in particular the newest generation laser system we use for coherent atomic excitation to Rydberg states. Chapter 4 describes hyperfine qubit encoding in neutral atoms, as well as new methods for coherent Raman driving of the hyperfine qubit transition. Chapter 5 describes the experimental control infrastructure, including the real-time feedback procedure for rearranging atoms, automatic calibrations and alignment, and remote operation of the experiment.

The second part of the thesis focuses on experimental results. Chapter 6 describes the deterministic preparation of programmable one-dimensional atom arrays using atom-by-atom assembly. This technique forms the backbone of all experiments in this thesis, as each experimental cycle begins by initializing a pre-programmed target arrangement of atoms. Chapter 7 presents our first experimental results with Rydberg atoms, showing the tunable nature of the Rydberg Hamiltonian and introducing quasi-adiabatic methods for many-body state

control and the exploration of various quantum phases. This chapter additionally highlights a surprising discovery about the dynamical response of the system to a rapid quench, where we observe slow thermalization. This phenomenon has since been extensively studied theoretically and recast in the language of quantum many-body scars. Chapter 8 studies in detail the quantum phase transitions into various phases of the 1D Rydberg Hamiltonian, focusing on the quantum critical properties of these transitions. Chapter 9 shows first results with an upgraded 2D tweezer array, and uses hundreds of atoms to explore quantum phases of the two-dimensional square lattice. Chapter 10 revisits the surprising non-equilibrium dynamics observed in Chapter 7, and shows that an extension of the phenomenon exists in 2D arrays. This chapter additionally presents a surprising twist on many-body scars, showing that these scar trajectories can be further stabilized by periodic driving of the system. Chapter 11 introduces the study of topological quantum phases that emerge when atoms are positioned on the links of the kagome lattice. Topological order in the system is probed using highly nonlocal string operators, enabling for the first time the direct detection of quantum spin liquid ordering. This exotic phase was first theoretically introduced in 1973 by Philip Anderson [40], and has thus far evaded direct detection.

Finally, we turn to entanglement and quantum logic experiments. Chapter 12 describes key improvements in coherent control over Rydberg atoms, and demonstrates a new record in fidelity for Rydberg atom entanglement. Chapter 13 introduces a new protocol for many-body state control, showing creation of a fully entangled Schrödinger cat state with 20 atoms. Chapter 14 combines coherent control over Rydberg atoms with control over the hyperfine qubit transition, and introduces and benchmarks a new protocol for universal multi-qubit gates with neutral atoms.

Part II

Experimental Methods

2

Optical tweezer arrays

2.1 OVERVIEW OF OPTICAL TWEEZER SYSTEM

Optical trapping of neutral atoms is a powerful technique for isolating atomic systems in vacuum, enabling the study of quantum mechanical effects of atomic motion and spin. Based on the AC Stark shift induced by light which is far detuned from atomic transitions, atoms are trapped at local intensity maxima (or minima, depending on the sign of the laser detuning). Optical tweezers utilize this principle by focusing a laser to a micron-scale waist, where individual atoms are trapped at the focus.

Central to the optical tweezer platform is the simple and fast (< 100 ms) procedure for

loading single atoms into the tweezers. This is accomplished by laser cooling thermal atoms in a magneto-optical trap (MOT) which is overlapped with the tweezer array. Tightly focused tweezers operate in a ‘collisional blockade’ regime, in which they load atoms from the MOT but pairs of loaded atoms are ejected due to light-assisted collisions [23]. This mechanism ensures that tweezers are loaded with at most single atoms, but the loading is probabilistic: each trap is loaded with a single atom with probability 50 – 60%.

To prepare deterministic atom arrays, we utilize a real-time feedback procedure, in which the randomly loaded atoms are identified and then rearranged into pre-programmed geometries. Atom rearrangement requires moving atoms in tweezers which can be smoothly steered to minimize heating. Acousto-optic deflectors (AODs) are incredibly effective tools for this application, since they deflect a laser beam by a tunable angle which is controlled by the frequency of a running acoustic wave in the AOD crystal. Dynamic tuning of the acoustic frequency translates into smooth motion of an optical tweezer. Moreover, a multi-frequency acoustic wave creates an array of laser deflections, which after focusing through a microscope objective forms an array of optical tweezers with tunable position and amplitude, all controlled by the acoustic waveform.

Our first generation of experiments utilized a single AOD for the creation of a one-dimensional array of up to 100 dynamically movable optical tweezers. A detailed discussion of the 1D rearrangement procedure is presented in Chapter 6.

The second generation of experiments used a hybrid approach for creating programmable two-dimensional arrays. A spatial light modulator (SLM) was used to imprint a programmable phase hologram on the wavefront of a single laser field, such that after propagating to the focus of a microscope objective, the laser forms a flexible, programmable array of tweezers in 2D. This system, including a higher-power laser source, creates arrays of up to 1000 tweezers.

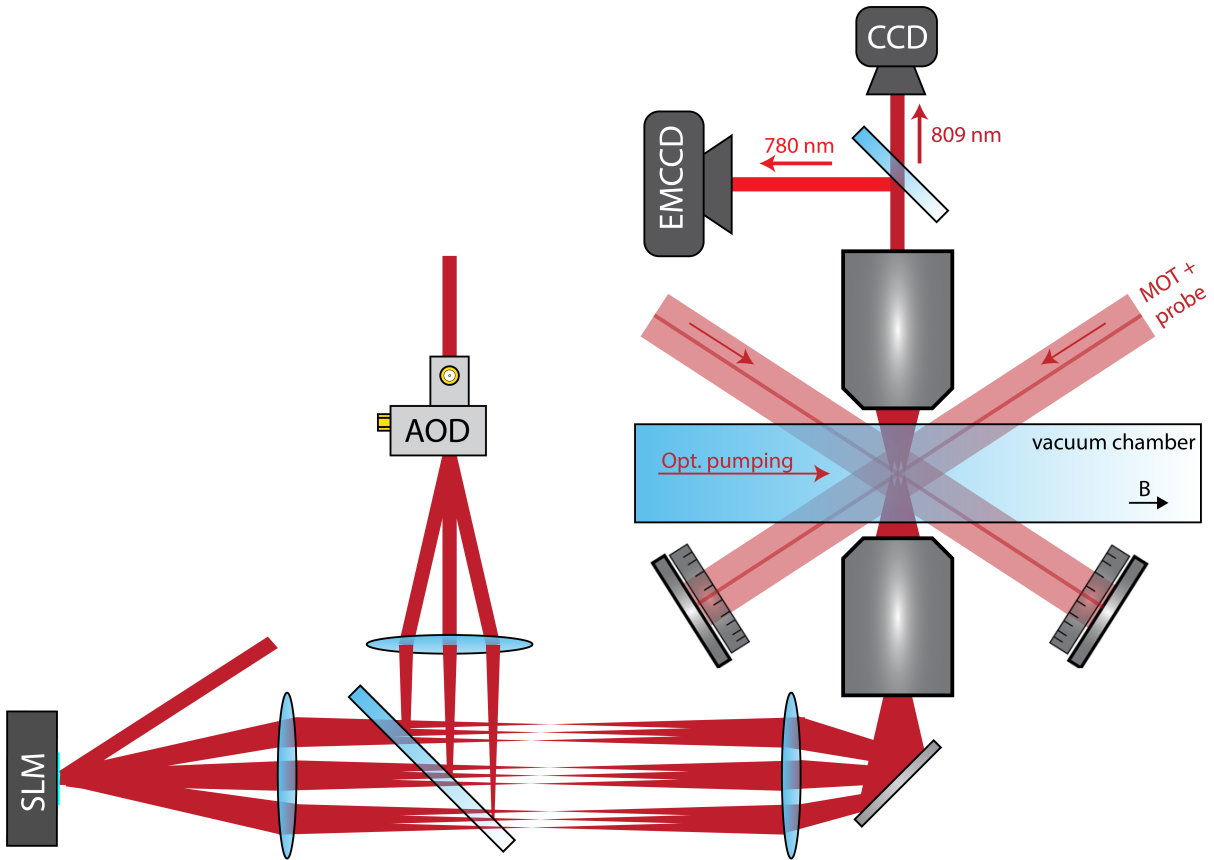


Figure 2.1: Experimental apparatus. Tweezer arrays generated by a spatial light modulator (SLM) and crossed acousto-optic deflectors (AODs) are focused into our vacuum cell through a 0.5 NA microscope objective. Tweezer light and atom fluorescence are collected through a second objective and separated with a dichroic mirror: the 809 nm trap light is imaged on a CCD camera, while the 780 nm atomic fluorescence is collected on an electron-multiplied CCD (EMCCD) camera. The tweezers are loaded from a magneto-optical trap (MOT) which is formed to overlap with the tweezer array, created by three retroreflected MOT beams (diameter of ≈ 1.5 cm). Individual atoms are imaged using a similar set of three retroreflected probe beams (diameter of ≈ 1 mm) to reduce background fluorescence on the EMCCD images. An additional laser aligned to the long axis of the cell is used for optical pumping.

However, the tweezers are static and cannot be dynamically moved. To rearrange atoms in 2D, we therefore use a second set of moving optical tweezers that are steered by a pair of crossed acousto-optical deflectors (AODs) (Fig. 2.1). Details of this 2D setup are presented in Chapter 9 and Appendix F.

2.2 LASER SYSTEM FOR AOD TWEEZER ARRAYS

The laser source for the optical tweezers generated by our acousto-optic deflector system is based on an external-cavity diode laser at ≈ 809 nm which seeds a tapered amplifier (Moglabs, MOA002). The resulting 1.8 W beam is coupled into a single-mode fiber, and passed through three laser clean-up filters (Semrock LL01-808). This results in a 4 mm beam with ≈ 550 mW of power, which is split into an array of beams by an acousto-optic deflector (AOD) (AA Opto-Electronic model DTSX-400-800.850). These beams pass through a 1:1 telescope with 300 mm focal length and are then focused by a 0.5 NA microscope objective (Mitutoyo G Plan Apo 50X, corrected for 3.5 mm glass thickness) into our vacuum chamber to form an array of optical tweezers (Fig. 2.1). These tweezers have a waist of ≈ 900 nm, and contain ≈ 1 mW of optical power, corresponding to a trap depth of ≈ 0.9 mK for ^{87}Rb atoms. The spacing between tweezers is determined by the frequency separation of acoustic frequencies in the AOD. The minimum usable spacing is $\sim 3 \mu\text{m}$, corresponding to 0.5 MHz acoustic frequency separation. For smaller trap spacings, we observe strong atom heating which is due to overlap in the point spread function of adjacent traps, which beats at the difference frequency between optical tweezers (equal to the difference frequency between corresponding acoustic tones). As traps are moved closer, the point spread function overlap increases and the beat frequency decreases, causing an increase in parametric heating of atoms.

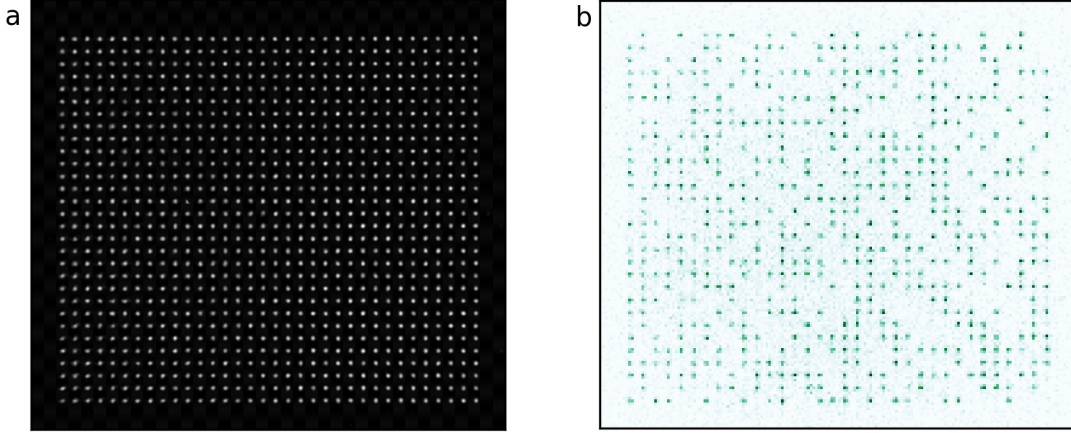


Figure 2.2: Large arrays of optical tweezers. The experimental platform produces optical tweezer arrays with up to ~ 1000 tweezers and $\sim 50\%$ loading probability per tweezer after 100 ms of MOT loading time. **a.** Camera image of an array of 34×30 tweezers (1020 traps), including aberration correction. **b.** Sample image of random loading into this tweezer array, with 543 loaded atoms. Atoms are detected on an EMCCD camera with fluorescence imaging.

2.3 LASER SYSTEM FOR SLM TWEEZER ARRAYS

Our 2D tweezer array is generated by a free-running 810-nm Ti:Sapphire laser (M Squared, 18-W pump). The laser illuminates a phase-control spatial light modulator (Hamamatsu X13138-02), which imprints a computer-generated hologram on the wavefront of the laser field. The phase hologram is calculated using the phase-fixed weighted Gerchberg-Saxton (WGS) algorithm [41] to produce an arbitrary arrangement of tweezer spots after propagating to the focus of the same microscope objective. Using this method, we can create tweezer arrays with roughly 1000 individual tweezers (Fig. 2.2). When calculating the phase hologram, we improve trap homogeneity by pre-compensating for the variation in diffraction efficiency across the tweezer array (roughly given by $\text{sinc}^2(\frac{\pi}{2}(\theta_{\text{trap}}/\theta_{\text{max}}))$ where θ denotes the deflection angle from zeroth order).

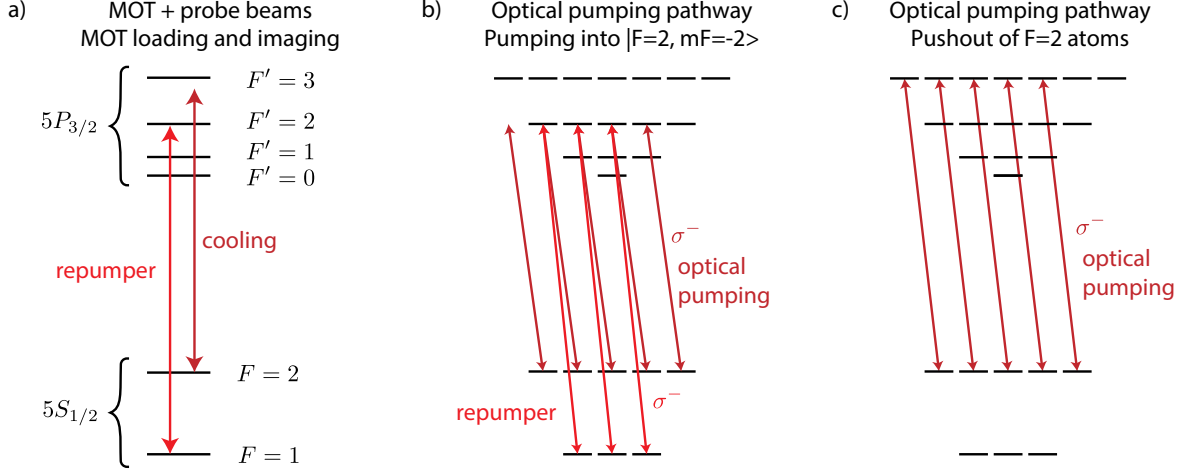


Figure 2.3: Laser transitions for MOT loading, imaging, optical pumping, and pushout. (a) For MOT loading and atom imaging, we use repumper light on the $F = 1 \rightarrow F' = 2$ transition along with cooling light which is red-detuned from $F = 2 \rightarrow F' = 3$. Both laser frequencies are sent through all axes of the MOT beams and probe beams. (b) For optical pumping into $|F = 2, m_F = -2\rangle$, we apply light only on the optical pumping axis, which propagates parallel to the quantization axis and is σ^- polarized. This beam contains both repumper light and optical pumping light on the $F = 2 \rightarrow F' = 2$ transition. (c) For hyperfine state readout, we apply a pushout pulse on the $F = 2 \rightarrow F' = 3$ transition using the optical pumping axis to heat out atoms in the $F = 2$ ground state.

2.4 LASER SYSTEM FOR ATOM COOLING AND IMAGING

We use two laser sources for cooling, imaging, and optical pumping of the ^{87}Rb atoms. Figure 2.3 shows the relevant atomic structure and the driven transitions, and Figure A.1 shows the optical setup used for both lasers. Both lasers are distributed Bragg reflector (DBR) lasers from Photodigm (PH780DBR120TS), tuned to drive transitions on the D2 line from $5S_{1/2}$ to $5P_{3/2}$ with a wavelength of 780 nm. The first laser is the ‘repumper’: this laser is frequency locked using saturated absorption spectroscopy in a Rubidium vapor cell. Specifically, the laser is locked by frequency-modulation spectroscopy to the crossover peak between $F = 1 \rightarrow F' = 1$ and $F = 1 \rightarrow F' = 2$. The repumper laser is then shifted by 78.5 MHz using an acousto-optic modulator (AOM) to become resonant with the $F = 1 \rightarrow F' = 2$ transition. The repumper laser typically remains properly locked for several months at a time without intervention.

The second laser, the ‘cooling’ laser, is offset locked to the repumper laser and tuned to the transitions from $F = 2 \rightarrow F' = 1, 2, 3$. The offset lock uses Vescent phase locking electronics, with a dynamically tunable reference frequency generated from a TimeBase radiofrequency source which is frequency-multiplied by 32. The offset lock frequency can be adjusted from $\sim 5.7 - 7.3$ GHz, covering a wide range including all transitions from $F = 2 \rightarrow F' = 1, 2, 3$. The offset lock stabilizes the frequency of the cooling laser using feedback on the laser diode current, which enables fast frequency jumping over this range in $\lesssim 100 \mu\text{s}$.

The MOT is formed using three intersecting retroreflected beams containing both cooling light and repumper light (Fig. 2.1). One of these beams is perpendicular to the optical table, and the other two are parallel to it (intersecting at an angle of $\approx 120^\circ$ due to the geometric restriction imposed by the high-resolution objectives). The MOT beams are ~ 1.5 cm in diameter, and each carry ≈ 1.5 mW of cooling light and ≈ 0.4 mW of repumping light. The MOT is constructed with the cooling light detuned by 17 MHz from the $F = 2 \rightarrow F' = 3$ transition, with an additional applied magnetic field gradient of 9.7 G/cm. We additionally shine a UV light from a 365 nm LED directly on the glass cell to speed up the MOT loading process [42].

An additional set of probe beams are overlapped with the MOT beams, and also contain cooling and repumper light (with ≈ 50 times less power than the MOT beams). These beams are ~ 1 mm in diameter and are used for polarization gradient cooling and fluorescence imaging of trapped atoms while minimizing background scatter. Despite the reduced background scatter, we still find that scatter from the probe beams on the glass cell can contribute a significant background signal to the EMCCD camera. We use Fourier filtering to reduce this background signal by placing a thin wire in the Fourier plane, one focal length before the final focusing lens onto the EMCCD camera. In this plane, the atom signal is large and collimated, while the background scattered light is focused to a small spot; the wire therefore strongly

suppresses the background signal while minimally reducing atom signal.

An additional optical pathway is used for optical pumping of atoms into $|F = 2, m_F = -2\rangle$ (Fig. 2.1). This optical pumping path, containing both cooling and repumper light, is aligned to the long axis of the glass cell, parallel to the bias magnetic field which defines our quantization axis, and is circularly polarized to drive σ^- transitions. Optical pumping typically takes $20 - 50 \mu\text{s}$, during which the cooling light is tuned to the $F = 2 \rightarrow F' = 2$ transition and repumper light is simultaneously applied, causing population to accumulate in the only dark state $|F = 2, m_F = -2\rangle$ (Fig. 2.3). Polarization impurities in this beam reduce pumping fidelities and cause excess heating by residual photon scattering from the dark state. We optimize polarization by applying a long optical pumping segment of a few milliseconds to make the atoms far more sensitive to the quality of the dark state, and then adjusting the beam polarization while monitoring atom heating. (We note that even for perfect polarization, there will still be off-resonant scattering from the dark state due to off-resonant coupling from $F = 2 \rightarrow F' = 3$; this motivates driving the optical pumping coupling from $F = 2 \rightarrow F' = 2$ around saturation intensity, or alternatively using the more favorable D1 transition at 795 nm for optical pumping.)

2.5 ATOM LOADING AND IMAGING

Optical tweezers are loaded from the MOT in $50 - 100 \text{ ms}$ while the cooling laser is tuned 17 MHz red-detuned from the $F = 2 \rightarrow F' = 3$ transition. Afterwards, the MOT beams are shuttered and the probe beams turn on for polarization gradient cooling-based fluorescence imaging. Images are acquired on an EMCCD camera (Andor iXON3, EM Gain = 300) over 20 ms , during which the cooling laser is set to 30 MHz red-detuned of the bare atom $F = 2 \rightarrow F' = 3$ resonance. Cooling light from the probe beams is scattered by the atoms and collected

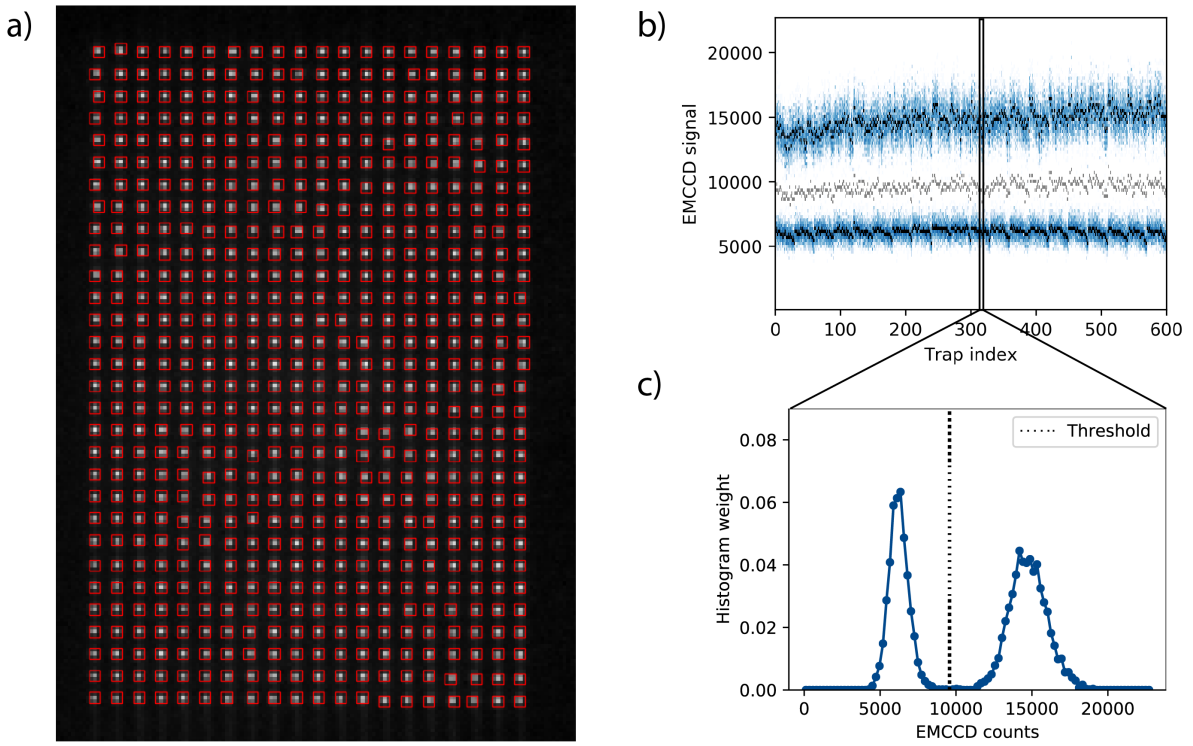


Figure 2.4: Atom loading and imaging characterization. (a) Average of many experimental images showing randomly loaded tweezers. We analyze this image to determine the position of the atom fluorescence signal from each trap, and draw red squares around each trap position to mark the pixels which are binned. (b) We calculate the pixel sum within each red square in each image, and we construct a histogram for the atom signal of each trap. Each histogram is bimodal, with a peak at low counts corresponding to no atom, and a separate peak at high counts corresponding to a single atom. The black markers highlight the fitted center of each mode of the distribution for each trap, and the gray marker shows the chosen threshold. The color scale here is logarithmic to highlight the absence of counts in between the two modes. (c) Sample bimodal distribution from a particular trap.

on the EMCCD, creating an image of the atoms in the array.

The collected photon statistics for each trap forms a bimodal distribution, corresponding to the presence of 0 or 1 atom (Fig. 2.4). We fit the statistics for each tweezer to the sum of two Poisson distributions, and set a threshold in between the two modes. Imaging infidelity due to finite overlap of the Poisson distributions is at the 10^{-6} level; however, in practice, the dominant error mechanism is a $\sim 0.2\%$ probability of atom loss during imaging due to the ~ 10 second vacuum limited lifetime. Repeated imaging of the same atoms with a 50 ms gap between images shows a retention probability of 99 – 99.5%.

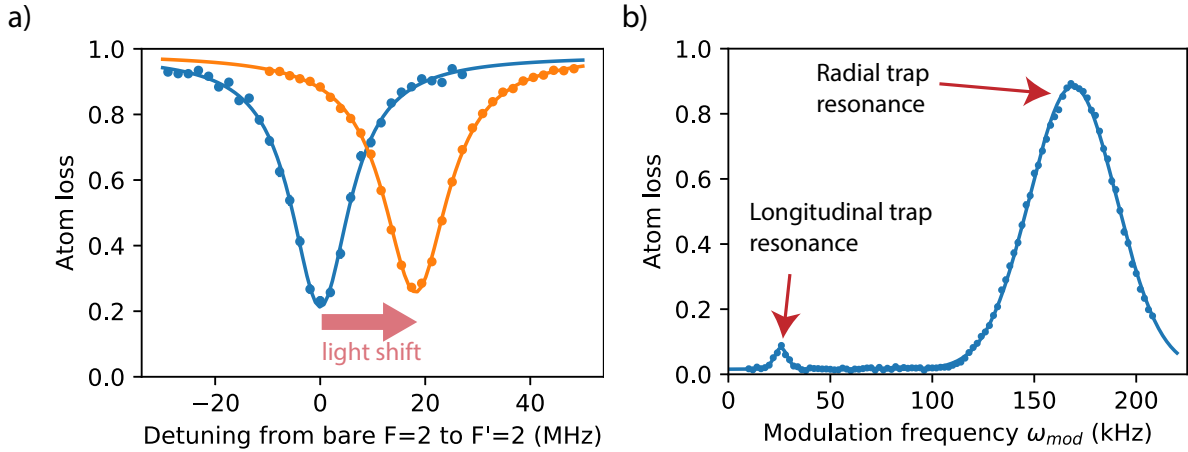


Figure 2.5: Measurement of optical tweezer light shifts and trap frequencies. (a) We coarse pump atoms into the $F = 2$ ground state, and then apply a short laser pulse near the D2 transition from $F = 2 \rightarrow F' = 2$. When this pulse is resonant, it depumps atoms into the $F = 1$ ground state, which is detected by a subsequent pulse which pushes out $F = 2$ atoms. Performing this measurement while the traps are turned off (blue curve) and then again with the traps on (orange curve) gives a direct measurement of the tweezer light shift on the $F = 2 \rightarrow F' = 2$ transition. (b) We measure trap frequencies by applying weak modulation of the trap intensity for several milliseconds at various modulation frequencies. We observe parametric heating when the modulation frequency is twice the trap vibrational frequency. For this measurement, the longitudinal trap frequency is 13 kHz and the radial trap frequency is 85 kHz.

When loading is optimized, we observe 55 – 60% loading probability across the entire array for 50 ms of MOT loading time. However, we sometimes observe lower loading in certain parts of the array, which can typically be corrected by adjusting the magnetic offset fields during MOT loading to better center the MOT on the tweezer array.

2.6 CHARACTERIZING OPTICAL TWEEZER PROPERTIES

2.6.1 TRAP LIGHT SHIFTS

We measure optical tweezer light shifts on the transition from $|5S_{1/2}, F = 2\rangle \rightarrow |5P_{3/2}, F' = 2\rangle$. To measure this resonance, we initialize all atoms in the $F = 2$ ground state manifold by applying the repumper laser. We then apply a 1 μ s laser pulse coupling atoms from $F = 2 \rightarrow F' = 2$ at a variable detuning. Since the excited $F' = 2$ state can decay into the $F = 1$ ground state, scattering on this transition results in depumping into $F = 1$. Finally, we apply

a resonant pulse on the $F = 2 \rightarrow F' = 3$ transition to push out the remaining $F = 2$ atoms.

We perform this measurement both while keeping the traps on during the depumping pulse, and also while briefly turning off the traps during the pulse (Fig. 2.5a). Comparing the two measured resonances gives the differential light shift between the $5S_{1/2}$ ground state and the $5P_{3/2}$ excited state induced by the tweezers, which we measure to be ~ 20 MHz for our typical tweezer powers.

2.6.2 TRAP FREQUENCIES

We measure the optical tweezer trap frequencies by modulating the tweezer intensity at variable frequency ω_{mod} . This trap modulation results in parametric heating when the modulation frequency matches twice the trap frequency. We apply weak modulation over several milliseconds, and find a resonance at 26 kHz corresponding to the longitudinal heating and a resonance at 170 kHz corresponding to radial heating, averaged across a two-dimensional array of 600 tweezers (Fig. 2.5b). From this measurement, we extract an average longitudinal trap frequency of 13 kHz and an average radial trap frequency of 85 kHz.

2.7 CORRECTING FOR OPTICAL ABERRATIONS

For two-dimensional optical tweezer arrays created using a spatial light modulator (SLM), we additionally use the phase control of the SLM to correct for optical aberrations in the system (Fig. 2.6). Aberrations reduce the peak intensity of focal spots (characterized by the Strehl ratio), and correspondingly reduce the light shift of our tweezers on the atoms. In the SLM plane, aberrations can be understood as errors in the phase of the wavefront. This phase error across the wavefront can be decomposed into orthogonal functions known as Zernike polynomials, each of which characterize a particular aberration in the system, such as primary spherical

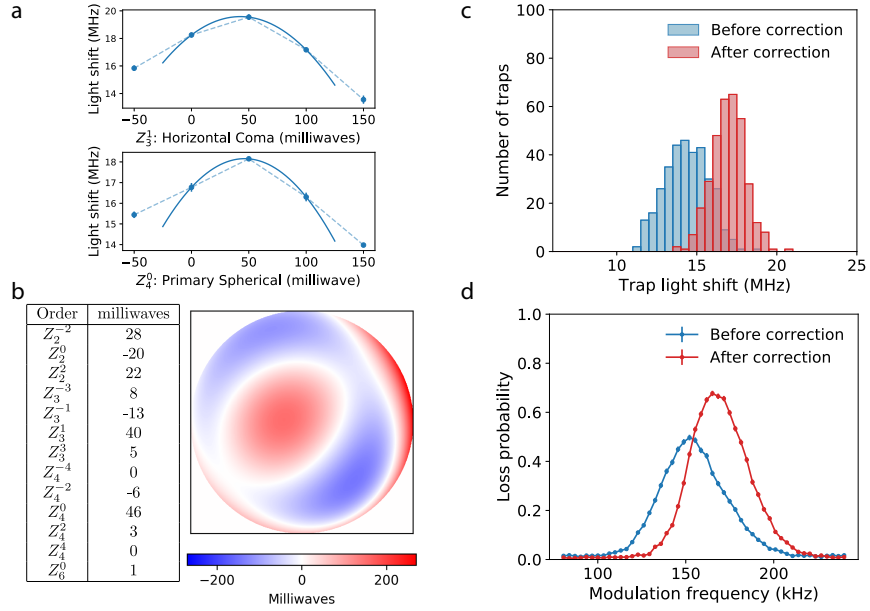


Figure 2.6: Correcting for aberrations in the SLM tweezer array. The aberration correction procedure utilizes the orthogonality of Zernike polynomials and the fact that correcting aberrations increases tweezer light shifts on the atoms. To independently measure and correct each aberration type, Zernike polynomials are added with variable amplitude to the SLM phase hologram, with values optimized to maximize tweezer light shifts. **a.** Two common aberration types: horizontal coma (upper) and primary spherical (lower), for which ~ 50 milliwaves compensation on each reduces aberrations and results in higher-depth traps. **b.** Correcting for aberrations associated with the thirteen lowest order Zernike polynomials. The sum of all polynomials with their associated coefficients gives the total aberrated phase profile in the optical system, which is now corrected (total RMS aberration of ~ 70 milliwaves). **c.** Trap depths across a 26×13 trap array before and after correction for aberrations. Aberration correction results in tighter focusing (higher trap light shift) and improved homogeneity. Trap depths are measured by probing the light shift of each trap on the $|5S_{1/2}, F=2\rangle \rightarrow |5P_{3/2}, F'=2\rangle$ transition. **d.** Aberration correction also results in higher and more homogeneous trap frequencies across the array. Trap frequencies are measured by modulating tweezer depths at variable frequencies, resulting in parametric heating and atom loss when the modulation frequency is twice the radial trap frequency. The measurement after correction for aberrations shows a narrower spectrum and higher trap frequencies (averaged over the whole array).

aberration or horizontal coma. We correct for these effects by adding Zernike polynomials with optimized amplitudes to our SLM phase hologram. We optimize each polynomial amplitude by measuring tweezer light shifts as a function of the correction amplitude (Fig. 2.6a).

Using this method, we compensate for 70 milliwaves of aberrations with the phase correction shown in Fig. 2.6b. We observe an increase of 18% in our trap light shifts (Fig. 2.6c), and measure a corresponding reduction in the spread of trap frequencies across the array (Fig. 2.6d). Aberration correction additionally allows us to place tweezers closer together, reaching a minimum separation of $3 \mu\text{m}$.

2.8 OPTICAL PUMPING AND MICROWAVE SPECTROSCOPY

After optically pumping atoms into particular hyperfine states, we use microwave spectroscopy to characterize the resulting population distribution over the $|F, m_F\rangle$ levels of $5S_{1/2}$. The microwave field is linearly polarized and perpendicular to our applied magnetic field, so it couples all six σ^+ and σ^- spin transitions, of which there are only four distinct resonance frequencies (depicted in Fig. 2.7a). To perform microwave spectroscopy, we apply a fixed length microwave pulse ($20 \mu\text{s}$) at variable frequency, followed by a push-out of $F = 2$ atoms.

We measure microwave spectroscopy in two configurations: first, we apply repumper only on the $F = 1 \rightarrow F' = 2$ transition to coarse pump atoms into all m_F levels within $F = 2$. In this configuration, we observe a microwave resonance for all transitions (Fig. 2.7b, upper panel). If we instead apply both repumper and σ^- optical pumping light on the $F = 2 \rightarrow F' = 2$ transition, then we polarize the atoms in $|F = 2, m_F = -2\rangle$. Here, microwave spectroscopy shows only a single peak at the lowest transition frequency (Fig. 2.7b, lower panel). We estimate an optical pumping fidelity of $\gtrsim 0.998$.

For atoms trapped in optical tweezers, the coherence properties of magnetically sensitive

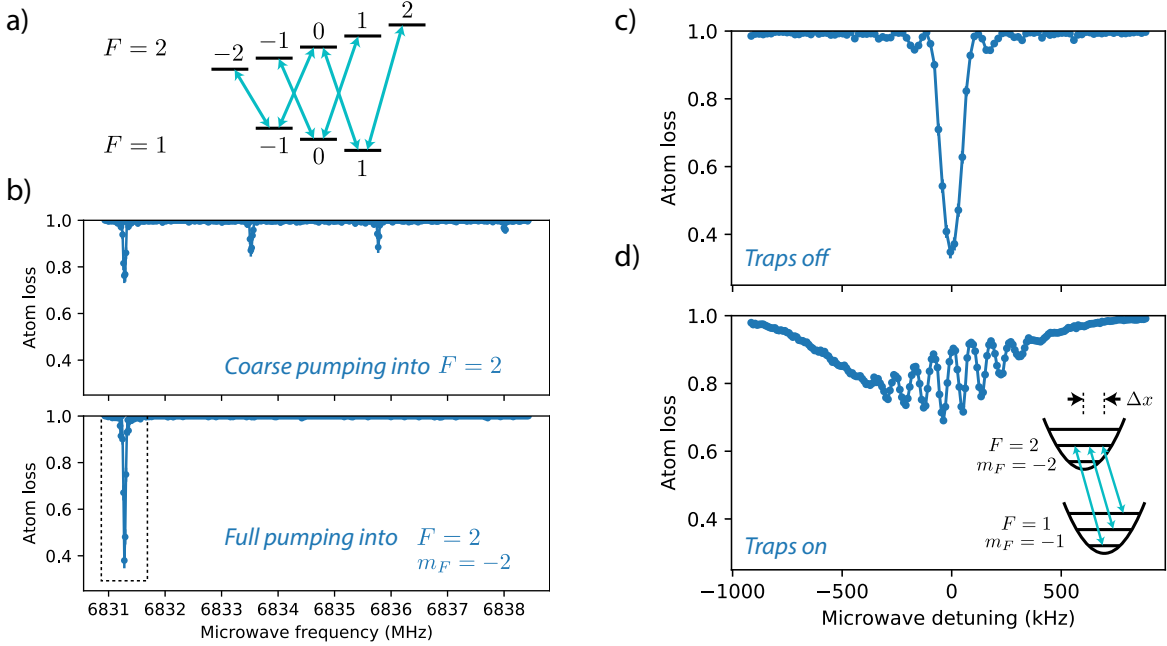


Figure 2.7: Microwave spectroscopy. (a) We apply global microwaves which are linearly polarized and drive σ^+ and σ^- spin transitions in the $5S_{1/2}$ ground state. (b) We apply a $20\ \mu s$ microwave pulse at variable frequency, during which the tweezers are turned off. Afterwards, an $F = 2$ pushout pulse is applied. For experiments in which we coarse pump into all m_F levels within $F = 2$, we observe four resonances, corresponding to all possible σ^+ and σ^- transitions (upper panel). (There are three additional π transitions which we do not observe here.) For experiments in which we apply full pumping into $|F = 2, m_F = -2\rangle$, we observe only one peak corresponding to the stretch microwave transition. (c) Zooming into the stretch microwave peak, we observe a clean sinc functional form for the spectroscopy signal when the microwave pulse is applied while the traps are turned off. (d) In the presence of the traps, the trapping potential for the $|F = 2, m_F = -2\rangle$ state is displaced from the trapping potential for $|F = 1, m_F = -1\rangle$ due to polarization breakdown near the focus of the tweezer which results in vector light shift gradients. The displaced trapping potential results in a nonzero wave function overlap between the n -th vibrational level for $|F = 2, m_F = -2\rangle$ and other $n' \neq n$ levels for $|F = 1, m_F = -1\rangle$. This results in a modified microwave spectrum which shows motional sidebands separated by the radial trap frequency. The red sidebands are more cleanly resolved than the blue sidebands, likely due to anharmonicity in the traps. This measurement is taken with a reduced microwave Rabi frequency to better resolve the sideband spectrum.

hyperfine transitions (ie., not the $m_F = 0 \rightarrow m_F = 0$ clock transition) are strongly suppressed due to spin-motion coupling [43]. This coupling emerges from the breakdown of the paraxial approximation near the focus of the tweezers, which produces a spatially varying effective elliptical polarization on either side of the focus, despite the traps being linearly polarized [43]. Circularly polarized light induces vector light shifts, which act as a fictitious magnetic field – and since the polarization varies across the focus, the result is an effective magnetic field *gradient*. This gradient produces an m_F -state-dependent displacement of the optical tweezer minimum (denoted in Fig. 2.7c as Δx displacement between the trapping potential for $|F = 2, m_F = -2\rangle$ and $|F = 1, m_F = -1\rangle$).

The spin-motion coupling is cleanly demonstrated by comparing spectroscopy of the stretch microwave transition in traps and out of traps. With the traps turned off for the duration of the microwave pulse (order 20 μs), the spectroscopy response is a standard sinc function, indicating coherent driving (Fig. 2.7c). With the traps on, however, we observe a resonance broadened by distinct motional sidebands spaced by the radial trap frequency (Fig. 2.7d). Normally, one expects to see motional sidebands only when the coupling field carries momentum, such as in a Raman coupling with counter-propagating lasers. However, the state-dependent tweezer potential results in sizable wavefunction overlap between vibrational level n for the first spin state and n' for the second state, allowing direct microwave coupling of these $n \rightarrow n'$ transitions [44]. This effect is particularly strong in our tweezer array due to the relatively close-detuned tweezer wavelength (809 nm), which increases the strength of vector light shifts [43]. We thus observe many motional sidebands, some of which correspond to changing the vibrational level by several quanta at once (ie., $n \rightarrow n - 4$).

Spin-motion coupling can be a useful tool for microwave-only sideband cooling and motional control [44]. Brief attempts in our experiment showed limited success, but not enough

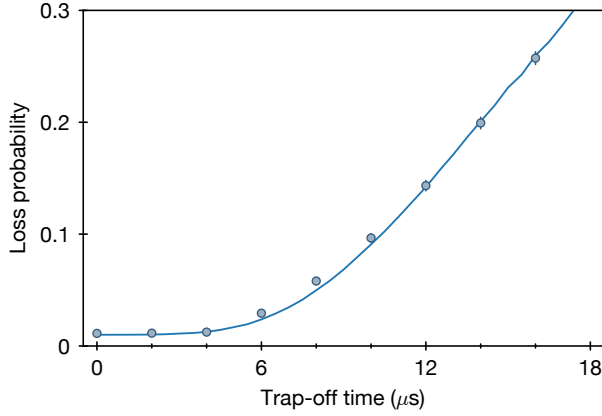


Figure 2.8: Drop-recapture curve. Measurements of atom loss probability as a function of trap-off time. For short times of up to $4\ \mu\text{s}$, the loss is dominated by finite trap lifetime (1% plateau). At larger trap-off times, the atomic motion away from the tweezer introduces additional losses. The solid line is a Monte Carlo simulation for a temperature of $11.8\ \mu\text{K}$.

to incorporate into any primary experiments in this thesis. In practice, spin-motion coupling serves to broaden and complicate the microwave resonances. In most cases where microwave spectroscopy is used to measure light shifts or as a diagnostic, we perform such measurements out of traps to avoid this effect altogether, at the cost of a reduction in signal contrast due to atoms not being recaptured when the tweezers are turned back on. Other approaches to suppress spin-motion coupling by applying a strong orthogonal bias magnetic field are also possible [43].

2.9 ATOM TEMPERATURE AND DROP-RECAPTURE MEASUREMENTS

Atoms are loaded into the optical tweezers and cooled using polarization gradient cooling. The resulting atom temperatures are characterized using drop-recapture measurements (Fig. 2.8). We compare these experimental measurements with Monte-Carlo simulations of atoms in free flight to evaluate atom temperatures.

The measured drop-recapture curves depend on the tweezer depth from which we release the atoms. In particular, if we perform this measurement with our normal tweezer depths that

are used for loading and imaging, then we observe temperatures around $30 \mu\text{K}$. However, by ramping the trap power down prior to drop-recapture, we observe lower temperatures, which can be understood as an “adiabatic cooling” that results from the populations of each vibrational level remaining fixed during the ramp [45]. Of course, this holds only as long as the trap depths are not lowered too dramatically, otherwise vibrational states will become no longer bound, and atoms will be lost in the process. For experiments throughout this thesis, we ramp trap depths to $\sim 1/4$ their initial value prior to drop-recapture measurements and Rydberg experiments, and estimate a temperature of $\sim 12 \mu\text{K}$ in this configuration (Fig. 2.8).

3

Rydberg atoms

3.1 INTRODUCTION TO RYDBERG ATOMS

While Chapter 2 reviewed the optical tweezer platform for programmable atom arrays, a key ingredient is missing for using these atom arrays to study many-body physics: *interactions*. At the micrometer lengthscales separating optical tweezers, atoms in their ground electronic states have negligible van der Waals interactions, and unlike optical lattice experiments, there is no atom tunneling between tweezers. Fortunately, neutral atoms offer a remarkable way to *switch on* strong interactions, through the coherent excitation to Rydberg states.

Rydberg states are highly-excited atomic states, with principal quantum number $n \gg 1$.

The properties of atomic states scale dramatically with principal quantum number*, as described in e.g. Refs. [27–29]. For the work in this thesis, of utmost importance is the strong van der Waals interactions which arise between two atoms which are both excited to the same Rydberg state. The interaction energy is given by $V(R) = C_6/R^6$, where R is the interatomic distance and the coefficient C_6 scales with an incredible power law $C_6 \propto n^{11}$. For commonly used Rydberg states with principal quantum number $50 < n < 100$, the interaction energies are of scale megahertz or even gigahertz for atoms which are separated by several microns. This is perfectly suited to optical tweezer arrays, and establishes a timescale on which interactions play a strong role.

Also important is the lifetime of Rydberg states. While typical atomic excited states have short lifetimes (i.e., ~ 26 ns for $5P_{3/2}$), the radiative lifetime of Rydberg states scales as n^3 , resulting in long lifetimes of hundreds of microseconds or even milliseconds for large n . Other decay mechanisms, however, can emerge for Rydberg states: in particular, the dipole matrix element between neighboring Rydberg states also grows with principal quantum number ($\propto n^2$), and thermal blackbody radiation can stimulate transitions between these nearby levels. The blackbody-limited lifetime scales as n^2 , becoming the dominant lifetime limitation for high Rydberg states.

Finally, the dipole matrix element between the atomic ground state and a dipole-coupled Rydberg state scales as $n^{-3/2}$, reducing for large n due to the decreasing overlap between the tightly bound ground state wavefunction and the weakly bound Rydberg wavefunction. This gives a practical consideration: while higher Rydberg states have longer lifetimes and stronger interactions, the laser excitation coupling is weaker, which can pose its own limitation. (An-

More accurately, the scaling is with respect to a modified principal quantum number n^ which accounts for screening effects of inner electrons; this is the so-called quantum defect theory, which takes $n^* = n - \delta$. For Rydberg S states (angular momentum $L = 0$) of rubidium, $\delta \approx 3.13$ [46].

other limitation: the strong interaction between Rydberg states is closely tied to large polarizability, which scales as n^7 – this can result in unwanted sensitivity to stray electric fields at large n .)

With these scaling considerations in mind, we work with the Rydberg state $|70S_{1/2}, m_J = -1/2\rangle$ throughout this thesis. The C_6 coefficient for this state is $C_6 = 2\pi \times 874 \text{ GHz } \mu\text{m}^6$, which gives an interaction of $2\pi \times 1.2 \text{ GHz}$ at 3 micron separation, or $2\pi \times 0.9 \text{ MHz}$ at 10 micron separation [47]. The radiative lifetime of this Rydberg state is $410 \mu\text{s}$, while room temperature blackbody radiation reduces the lifetime to $147 \mu\text{s}$ [48].

3.2 TWO-PHOTON EXCITATION TO RYDBERG STATES

Optical excitation from an atomic ground state to a target Rydberg state is a key ingredient in Rydberg experiments. Several schemes have been used, with various advantages and disadvantages. The simplest is direct laser excitation with a single-photon transition. Due to dipole selection rules, this couples ground S states to Rydberg P states. The wavelength for these transitions is in the ultraviolet (i.e., the single-photon wavelength for ^{87}Rb is 297 nm). Ultraviolet lasers pose serious experimental challenges, due to material degradation, unavailability of optical fibers and low-loss optics, and more. Additionally, Rydberg P states have more structure, anisotropy, and sensitivity to external perturbations than Rydberg S states, making them more challenging for coherent manipulation [49].

Alternatively, two-photon laser excitation can be used to couple ground S states to Rydberg S states through an intermediate P state. For rubidium, there are two natural choices for the intermediate state: $5P_{3/2}$ or $6P_{3/2}$. For the $5P$ intermediate state, the first excitation step is at wavelength 780 nm and the second step is at 480 nm, whereas for the $6P$ intermediate state, the two wavelengths are 420 nm and 1013 nm. In comparing the two approaches, a

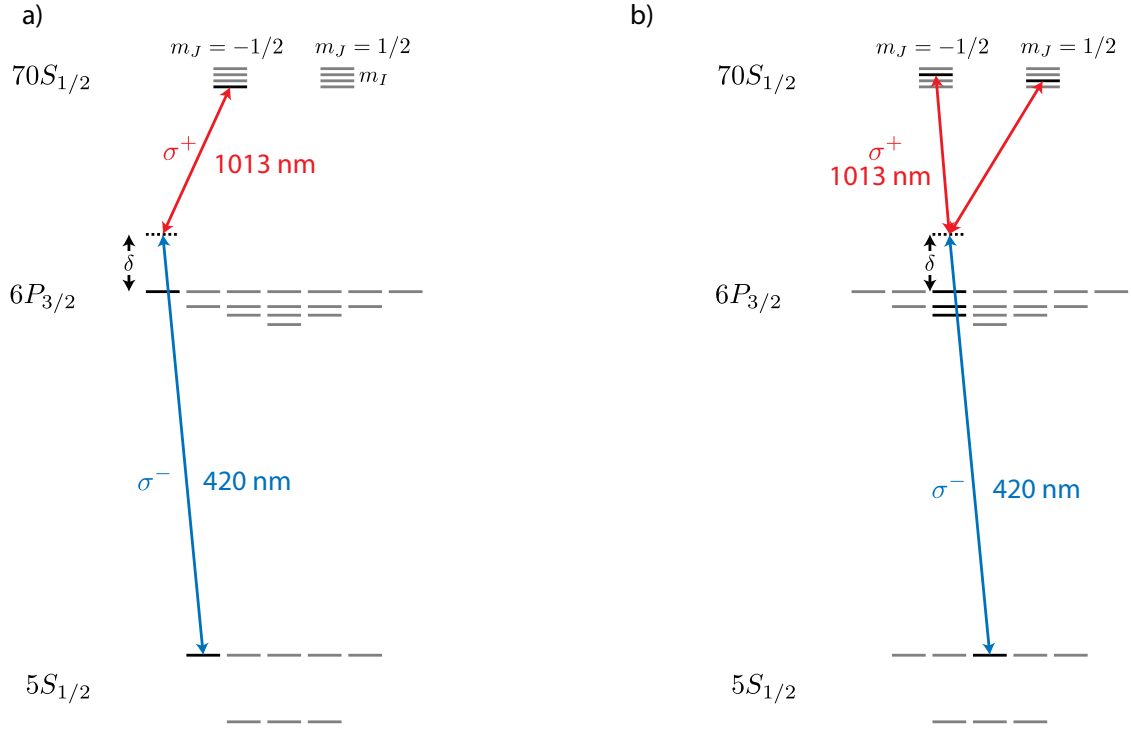


Figure 3.1: Two-photon excitation scheme. (a) Starting from $|5S_{1/2}, F = 2, m_F = -2\rangle$, the σ^- 420 nm laser couples to the intermediate state $|6P_{3/2}, F = 3, m_F = -3\rangle$. The final σ^+ 1013 nm laser couples to the target Rydberg state $|70S_{1/2}, m_J = -1/2, m_I = -3/2\rangle$. (b) Starting from $|5S_{1/2}, F = 2, m_F = 0\rangle$, the 420 nm laser couples to the intermediate states $|6P_{3/2}, F = 1, 2, 3, m_F = -1\rrangle$. The 1013 nm laser then couples these states both to $|70S_{1/2}, m_J = -1/2, m_I = +1/2\rangle$ and $|70S_{1/2}, m_J = +1/2, m_I = -1/2\rangle$. The two-photon Rabi frequency from $m_F = 0$ to $m_J = -1/2$ is a factor of $\sqrt{2}$ smaller than the stretch configuration in (a). The Rabi frequency from $m_F = 0$ to $m_J = +1/2$ is an additional factor of 3 smaller.

central consideration is how to achieve high single-photon Rabi frequencies on each leg of the transition, which is optimal for minimizing intermediate state scattering relative to the two-photon Rabi frequency. In the experiments in this thesis, we use the $6P$ intermediate state due to the higher availability of optical power at the upper transition from the intermediate state to the Rydberg state, since this transition has a significantly smaller dipole matrix element and thus requires more optical power to drive with equivalent strength.

In this thesis, two different ^{87}Rb ground state levels are coupled to the Rydberg state $70S_{1/2}$. The first, which is used for all quantum simulation experiments, is the ground state $|g\rangle = |5S_{1/2}, F = 2, m_F = -2\rangle$. As shown in Fig. 3.1a, the 420 nm laser is applied with σ^- polarization, and couples to a single intermediate state $|6P_{3/2}, F = 3, m_F = -3\rangle$. The 1013 nm laser is applied with σ^+ polarization, and couples the intermediate state to the Rydberg state $|70S_{1/2}, m_J = -1/2, m_I = -3/2\rangle$. Note that when labeling Rydberg states, the good quantum numbers are m_J and m_I , rather than F and m_F ; this is because the hyperfine interaction is very weak in Rydberg states (~ 100 kHz for $70S$ [46]), and therefore even at small Gauss-scale magnetic fields, the level structure is in the Paschen-Back regime [50]. For this “stretch” excitation scheme, the F, m_F labeling is equivalent to the m_J, m_I description, since all individual angular momentum components are maximal: the ground state is $|F = 2, m_F = -2\rangle = |m_J = -1/2, m_I = -3/2\rangle$, the intermediate state is $|F = 3, m_F = -3\rangle = |m_J = -3/2, m_I = -3/2\rangle$, and the Rydberg state is $|F = 2, m_F = -2\rangle = |m_J = -1/2, m_I = -3/2\rangle$. Moreover, we note that the m_J and m_I projections in the Rydberg state are the same as in the initial ground state. This transition is therefore magnetic-field insensitive.

The second excitation scheme (shown in Fig. 3.1b) uses the ground state $|g\rangle = |5S_{1/2}, F = 2, m_F = 0\rangle$ and the same $\sigma^- \rightarrow \sigma^+$ polarization scheme. Here, several intermediate states are coupled: $|6P_{3/2}, F = 1, 2, 3, m_F = -1\rangle$. Unlike in the previous scheme, the upper tran-

sition couples to both $m_J = -1/2$ and $m_J = 1/2$ within the Rydberg manifold. This can be understood by recalling the selection rule that $\Delta m_J = +1$ for a σ^+ dipole transition. Since m_J is not a good quantum number for the intermediate states; these states, which have $m_F = -1$, include components of $|m_J = -3/2, m_I = 1/2\rangle, |m_J = -1/2, m_I = -1/2\rangle$, and $|m_J = 1/2, m_I = -3/2\rangle$, and therefore can couple through $\Delta m_J = +1$ transitions to both $m_J = -1/2$ and $m_J = +1/2$. Another way to view this scheme is that the ground state level $|g\rangle = |F = 2, m_F = 0\rangle = \frac{1}{\sqrt{2}}(|m_J = -1/2, m_I = +1/2\rangle + |m_J = 1/2, m_I = -1/2\rangle)$. The two-photon excitation with $\sigma^- \rightarrow \sigma^+$ polarization must induce a total angular momentum change of $\Delta m_J = 0$ and $\Delta m_I = 0$ (for large intermediate state detuning relative to the intermediate state hyperfine structure). The two components of the ground state therefore couple to the corresponding angular momentum states within the Rydberg manifold: $|m_J = -1/2, m_I = +1/2\rangle$ and $|m_J = +1/2, m_I = -1/2\rangle$. For coherent excitation, this scheme requires a sufficient magnetic field to frequency-resolve the excitation to one particular Rydberg state. We use the $m_J = -1/2$ Rydberg state due to larger dipole matrix elements for the chosen polarizations (Fig. 3.1 and caption).

3.3 RYDBERG LASER SYSTEM

In all Rydberg experiments in this thesis, we couple the atomic $5S_{1/2}$ ground state to the $70S_{1/2}$ Rydberg state through the intermediate $6P_{3/2}$ state. The transition from ground to intermediate state is driven by a blue 420 nm laser, and the transition from the intermediate to the Rydberg state is driven by an infrared 1013 nm laser. The single-photon Rabi frequency of each coupling is labeled Ω_{420} and Ω_{1013} , respectively. The lasers are detuned from the intermediate state by detuning $\delta \gg \Omega_{420}, \Omega_{1013}$ (Fig. 3.1), such that the dynamics are reduced to an effective two-level system between the ground and Rydberg states which is driven by

two-photon Rabi frequency $\Omega = \Omega_{420}\Omega_{1013}/2\delta$. The 420 and 1013 beams are applied counter-propagating to one another along the axis of the array. An external magnetic field is additionally applied on this axis (Fig. 2.1), and the beams are circularly polarized to drive σ^- and σ^+ transitions, respectively.

Several generations of Rydberg laser systems have been used for the experiments in this thesis. While details of the system used for each experiment are described in the corresponding appendices, this section will describe the newest version of the laser system. An annotated picture of the Rydberg laser locking setup is shown in Fig. A.2.

The 420 nm laser is a frequency-doubled Ti:Sapphire laser (M Squared, 15-W pump). We stabilize the laser frequency by locking the fundamental (840 nm) to an ultra-low expansion (ULE) reference cavity (notched cylinder design from Stable Laser Systems, free spectral range 1.5 GHz), with finesse $\mathcal{F} = 30,000$ at 840 nm. The fundamental light is phase modulated by a high-frequency fiber modulator to generate tunable sidebands on the locking pathway; the lock is applied to one of these sidebands to enable a tunable offset from the cavity resonance.

The 1013-nm laser source is an external-cavity diode laser (Toptica DL Pro), which is locked to the same reference cavity ($\mathcal{F} = 50,000$ at 1013 nm). To suppress high-frequency phase noise from this diode laser, we use the transmitted light through the cavity, which is filtered by the narrow cavity transmission spectrum (30 kHz linewidth) (see Chapter 12). This filtered light is used to injection lock another laser diode (Toptica, LD-1020-0400-2), whose output is subsequently amplified to 10 W by a fiber amplifier (Azur Light Systems). We note that unlike the 420 nm laser which can be locked at any tunable offset relative to a cavity resonance, the 1013 nm must be locked directly on resonance, since we only use the transmitted light through the cavity. This gives a rigid 1.5 GHz spacing of accessible lock-points; additional tunability is achieved using AOMs for frequency shifting.

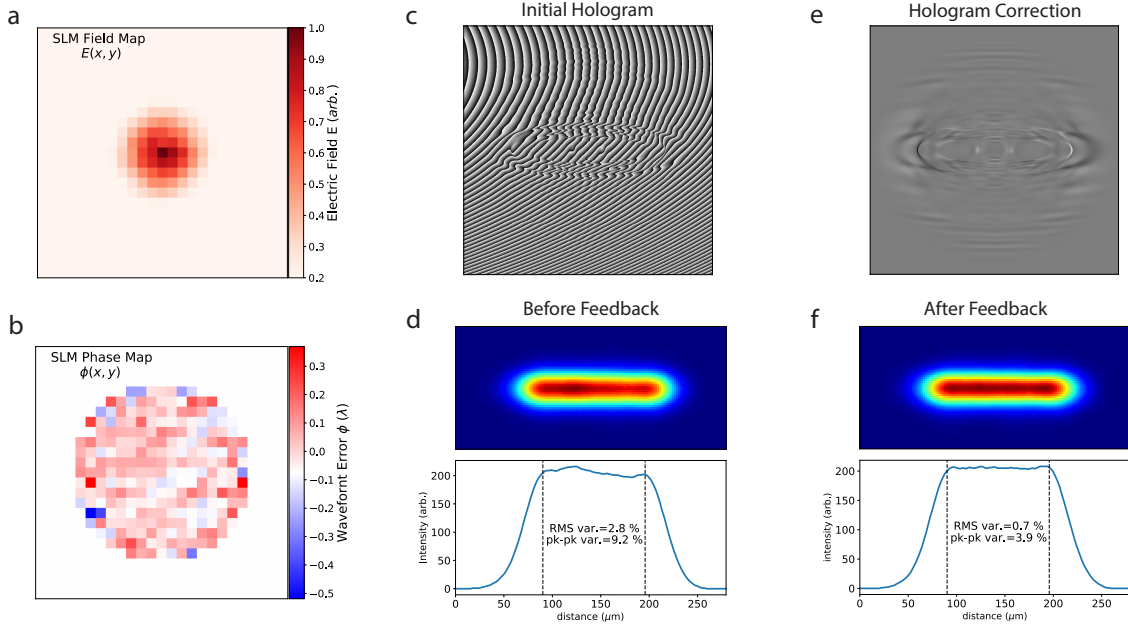


Figure 3.2: Generating homogeneous Rydberg beams. **a)** Measured Gaussian-beam illumination on the SLM for shaping the 420-nm Rydberg beam. A Gaussian fit to this data is used as an input for the hologram optimization algorithm. **b)** Corrected and measured wavefront error through our optical system, showing a reduction of aberrations to $\lambda/100$. **c)** Computer-generated hologram for creating the 420-nm top-hat beam. **d)** Measured light intensity of the 420-nm top-hat beam (top), and the cross section along where atoms are positioned (bottom). Vertical lines denote the $105\text{-}\mu\text{m}$ region where the beam should be flat. **e)** Using the measured top-hat intensity, a phase correction is calculated for adding to the initial hologram. **f)** Resulting top-hat beam after feedback shows significantly improved homogeneity.

3.4 RYDBERG BEAM SHAPING

For experiments with one-dimensional atom arrays, the Rydberg lasers are Gaussian beams which are focused along the array axis to globally illuminate the atoms. For two-dimensional arrays, the beams are shaped into one-dimensional top-hats (light sheets) to illuminate the plane of the atoms (Fig. 3.2). This beam shaping is accomplished by placing a phase spatial light modulator (SLM) in the Fourier plane (e.g., one focal length before the final lens which focuses the light onto the atoms). Ideally, we would like to produce a beam on the atoms which has a top-hat intensity profile, and also a flat phase profile such that it propagates cleanly across the array. However, phase-only control in the Fourier plane cannot give arbitrary phase and amplitude control in the image plane.

The resolution to this issue is that we target a particular phase and amplitude profile only in the region of the image plane where the atoms are located, and we relax our constraints elsewhere in the image plane. While ideally the field amplitude would be zero outside of the top-hat, this constraint relaxation results in a substantial portion of light deflected into other parts of the image plane, i.e., outside of the top-hat mode. Indeed, there is a necessary compromise between optimizing the efficiency of the hologram (i.e., what fraction of the light is projected in the top-hat mode) and optimizing the homogeneity of the top-hat itself.

We generate the holograms using the conjugate gradient minimization algorithm [51]. The resulting top-hat beams have a flat width of $105 \mu\text{m}$ and a perpendicular Gaussian width of $25 \mu\text{m}$. The conversion efficiencies into the top-hat modes are 30% for the 420 nm laser and 38% for the 1013 nm laser.

Since holographic beam shaping relies on the intricate interplay of different high spatial frequency components in the light field, it is extremely sensitive to optical aberrations. We correct for all aberrations up to the window of our vacuum chamber by measuring the amplitude and phase of the electric field as it propagates through the optical beam path (Fig. 3.2a,b) [52]. We do so by picking off a small portion of the Rydberg beam and observing it on a camera with small pixel size and with sensor cover removed for high-fidelity beam characterization (Imaging Source DMM 27UP031-ML). In this way, we reduce the wavefront error in our beam down to $\lambda/100$, and also use the measured field profile as the starting guess in our hologram generation algorithm (Fig. 3.2a,b). Furthermore, by imaging the top-hat beams we also correct for remaining inhomogeneities by updating the target field profile in our optimization algorithm (Fig. 3.2e,f). Due to aberrations and imperfections of the vacuum windows, we observe slightly larger intensity variations on the atoms than expected ($\sim 3\%$ RMS, $\sim 10\%$ peak-to-peak).

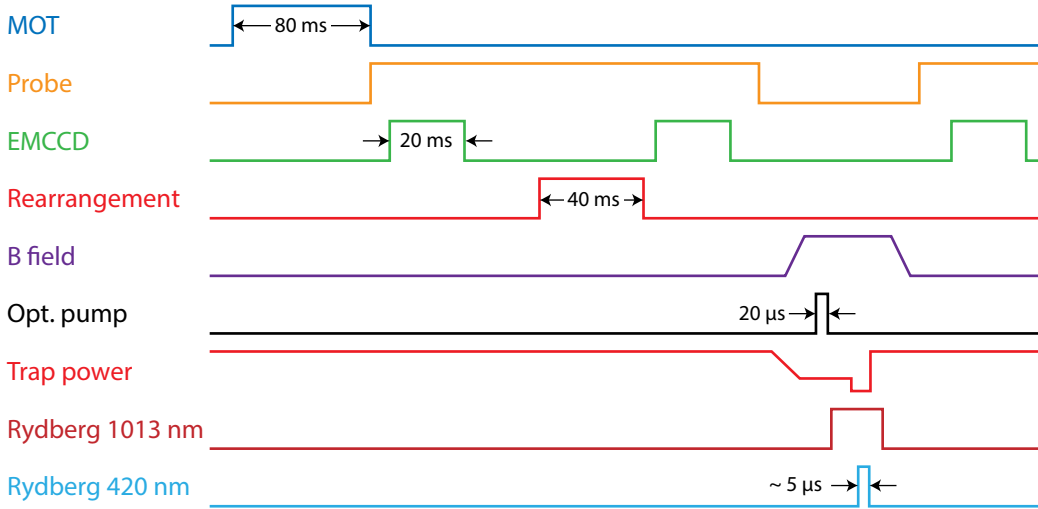


Figure 3.3: Experimental protocol. The experiment begins by loading a MOT, and then turning on probe beams and acquiring a first EMCCD image to show the randomly loaded tweezer array. The image is processed and atoms are rearranged into a target pattern, and then subsequently imaged a second time to verify that atoms are properly arranged. Afterwards, probe beams are turned off, the trap depth ramps down to $\sim 1/4$ the initial value, and the magnetic field is turned on to define a quantization axis. Optical pumping is applied to prepare atoms in $|F = 2, m_F = -2\rangle$. The 1013 nm Rydberg laser turns on first, and then the 420 nm is pulsed according to the desired Rydberg Hamiltonian evolution. The tweezers are briefly turned off during the Rydberg pulse, and then turned back on at high power to push out Rydberg atoms. (Alternatively, tweezers can be turned back on at low power and a microwave pulse can be applied to increase Rydberg detection fidelity.) The magnetic field is turned off, and a final image is taken for readout.

Using this beam shaping approach to homogeneously illuminate the atom array with both Rydberg lasers, we achieve single-photon Rabi frequencies of up to $\Omega_{420} = 2\pi \times 360$ MHz and $\Omega_{1013} = 2\pi \times 50$ MHz. Typical intermediate state detuning is $\delta = 2\pi \times 1$ GHz, resulting in two-photon Rabi frequencies of several megahertz. The specific operating parameters used in each experiment are available in the associated appendices.

3.5 PROTOCOL FOR RYDBERG EXPERIMENTS

The protocol for Rydberg experiments is shown in Fig. 3.3. The traps are loaded from a magneto-optical trap (MOT), with single atom loading probabilities of ~ 0.6 . A fluorescence image of the array is taken, and then atoms are rearranged into pre-programmed positions. Following

the rearrangement procedure, another image of the array is taken such that we can postselect on instances in which the prepared configuration is defect-free. After taking the second image, we apply a magnetic field of ~ 1.5 G along the axis of the array, and then we optically pump all atoms into the target initial state (i.e., $|F = 2, m_F = -2\rangle$) using a σ^- -polarized beam, see Section 2.8). We then turn off the traps and pulse the Rydberg lasers on a timescale of a few microseconds. In most cases, the 1013 nm laser turns on first, followed by the carefully shaped pulse of the 420 nm laser, and then the 1013 nm turns off. This is because the 420 nm laser is focused through a double-pass AOM for amplitude, frequency, and phase control with a fast rise time of ~ 10 ns, while the 1013 nm has a slower AOM rise time (we do not focus the 1013 nm as tightly through its AOM, since we instead optimize for AOM deflection efficiency).

After the Rydberg pulse, we turn the traps back on to recapture the atoms that are in the ground state $|g\rangle$ while pushing away the atoms in the Rydberg state $|r\rangle$, and finally take a third image. Because of their long lifetime, most of the Rydberg atoms escape from the trapping region before they decay back to the ground state. This provides a convenient way to detect them as missing atoms on the third image (see Section 3.7 for more details). The entire experimental sequence, from MOT formation to the third image, takes ~ 300 ms. For some experiments, we perform two rounds of rearrangement to improve the target array preparation fidelity; in this case, we take four images per sequence rather than three, and the experimental cycle time is ~ 400 ms.

3.6 CALIBRATION AND ALIGNMENT OF RYDBERG LASERS

Both the 420 nm laser and the 1013 nm laser need to be properly aligned on the atoms for a Rydberg signal to be visible. While the two-photon Rydberg signal can be used for calibration and alignment of each laser, this signal depends on both systems working properly, and

requires using sparse arrays of isolated atoms. For this reason, we prefer to use independent protocols to measure the intensity of each laser separately on the atoms by studying the light shifts on atomic ground states. These signals are measured and integrated with automatic beam alignment procedures to maximize each laser's intensity on the atoms. This process is described in Section 5.6.

3.6.1 INDEPENDENT CALIBRATION OF 420 NM LASER

To measure and calibrate the effect of the 420 nm laser on the atoms, we measure the differential light shift induced by this laser on the microwave transition from $|F = 2, m_F = -2\rangle$ to $|F = 1, m_F = -1\rangle$ (Fig. 3.4a). For Rydberg excitation, the 420 nm laser is tuned around 1 GHz blue-detuned from the 6P intermediate state. This leads to a strong MHz-scale differential shift on these two ground state hyperfine levels which are separated by 6.8 GHz. We can measure this light shift directly by measuring the microwave resonance with and without the blue laser applied (Fig. 3.4b). However, in this approach, the 420 nm laser remains on for the duration of the microwave pulse ($20 \mu\text{s}$), leading to non-negligible off-resonant scattering and broadening of the microwave resonance. This necessitates working at relatively low blue power to avoid significant broadening. Alternatively, we can measure the light shift on this transition using a Ramsey sequence, in which the blue laser pulse is applied briefly in between the two Ramsey microwave $\pi/2$ pulses (Fig. 3.4c,d). The Ramsey fringe frequency gives a direct measurement of the differential light shift, which is proportional to 420 nm laser intensity on the atoms. Moreover, by taking enough statistics to analyze each tweezer position independently, we can assess homogeneity across the array. For two-dimensional arrays, the blue laser illuminates the atoms from the side, so we characterize the light shift on each row in the system (i.e., Fig. 3.4e).

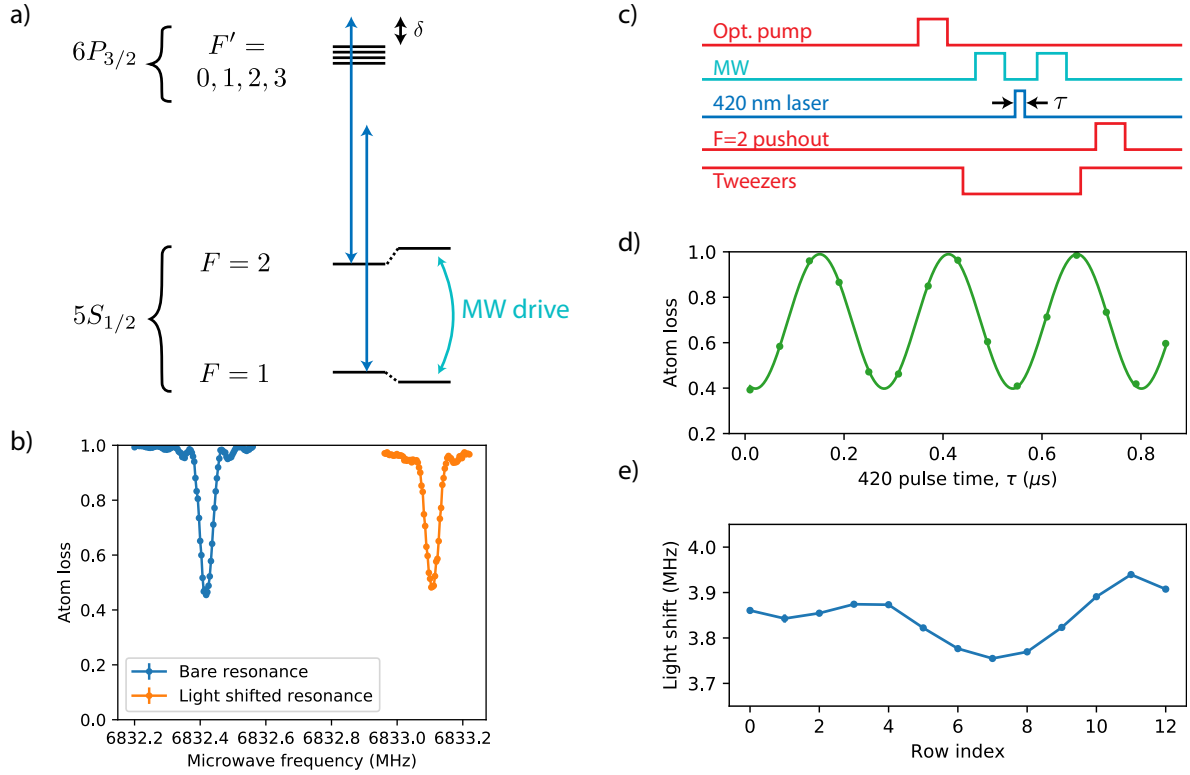


Figure 3.4: 420 nm light shift measurement. (a) We calibrate and align the 420 nm laser by measuring its differential light shift on the hyperfine ground state levels. In particular, since this laser is detuned close to the transition from $F = 2 \rightarrow 6P_{3/2}$, it exerts a strong light shift on the $F = 2$ ground states and a weaker shift in the opposite direction on the $F = 1$ ground states. (b) We measure the stretch microwave resonance (from $|F = 2, m_F = -2\rangle$ to $|F = 1, m_F = -1\rangle$) with and without the 420 nm laser and observe a megahertz-scale shift which is proportional to the intensity on the atoms. This is measured with the tweezers turned off, and the 420 nm power is reduced to avoid scattering that would occur over the long timescale of the microwave pulse. (c) Our standard approach is to measure the differential light shift in a Ramsey sequence, where the 420 nm is pulsed only briefly (for time τ) in between two microwave $\pi/2$ pulses. (d) Sample Ramsey oscillation on the stretch transition. (e) When using a top-hat 420 nm beam to address two-dimensional arrays, we analyze the light shift on each row of the system to characterize homogeneity, given by the flatness of the top-hat.

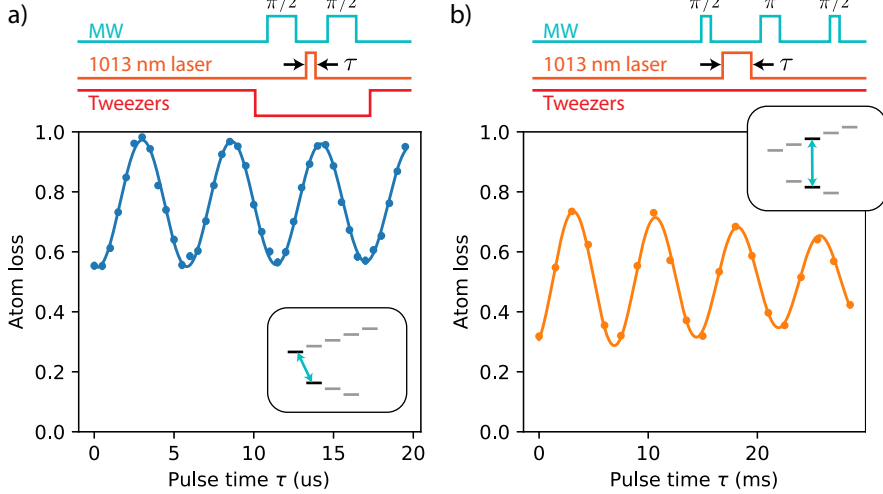


Figure 3.5: 1013 nm light shift measurement. We calibrate and align the 1013 nm laser by measuring its differential light shift on the hyperfine ground states. (a) The light shift on the stretch microwave transition ($|F = 2, m_F = -2\rangle$ to $|F = 1, m_F = -1\rangle$) is measured in a Ramsey sequence while traps are turned off. This light shift is dominated by vector light shifts from the 1013 nm due to its σ^+ polarization. (b) The light shift on the clock transition ($|F = 2, m_F = 0\rangle$ to $|F = 1, m_F = 0\rangle$) is the differential scalar shift and is of scale 100 Hz. We measure this using a spin-echo procedure over much longer timescales, while the tweezers remain on. The reduced contrast is from decoherence in spin-echo over 30 ms.

3.6.2 INDEPENDENT CALIBRATION OF 1013 NM LASER

While the high power 1013 nm laser induces a strong MHz-scale shift on the ground state levels, the *differential* light shift on the various ground states is much smaller due to the large detuning of 1013 nm from the D1 and D2 optical transitions at 795 nm and 780 nm. In this regime, the differential *scalar* light shifts between the $F = 1$ and $F = 2$ ground states is of order 100 Hz, while the differential *vector* light shifts on the stretch microwave transition is of order 100 kHz (for σ^\pm polarized light).

The stretch microwave transition is probed while optical tweezers are turned off to preserve coherence between the $|F = 2, m_F = -2\rangle$ and $|F = 1, m_F = -1\rangle$ spin states (see Section 2.8). This causes background loss of atoms which reduces the contrast of Ramsey fringes. For our highest 1013 nm laser intensities used in one-dimensional array experiments, the differential vector light shift on the stretch microwave transition is large enough to measure in standard

Ramsey-type experiments with reasonable trap-off times of 20-30 μs (Fig. 3.5a). For lower laser intensity, longer trap-off times are required, making this approach unfavorable.

Alternatively, the 1013 nm light shift can be measured on the clock transition from $|F = 1, m_F = 0\rangle$ to $|F = 2, m_F = 0\rangle$ while the tweezers remain on (Fig. 3.5b). Although the differential scalar light shift is much smaller, the coherence can be probed on much longer timescales while the atoms remain trapped. In this approach, we apply a spin-echo procedure with a 30 ms gap between each of the two $\pi/2$ pulses and the middle π pulse, and we turn on the 1013 nm for a variable duration during the first gap. The optical tweezer trap depths are reduced during this coherent evolution to $\sim 1/4$ the depths used for loading, which extends the coherence time and improves the contrast of the Ramsey fringes (see Chapter 4).

3.7 RYDBERG STATE DETECTION

Each atom is identified as being in $|g\rangle$ (or $|r\rangle$) at the end of the Rydberg pulse by whether it is (or is not) present in the third fluorescence image. Detection infidelity arises from accidental loss of atoms in $|g\rangle$ or accidental recapture of atoms in $|r\rangle$. For an atom in state $|g\rangle$, detection fidelity is set by the finite trap lifetime and motion away from the tweezer while the traps are off (i.e., as in Section 2.9). To quantify this error, we perform our normal experimental sequence while disabling only the 420 nm laser pulse. This keeps all atoms in state $|g\rangle$, and we measure the baseline loss probability. The precise fidelity depends on atom temperature, trap lifetime, and the parameters of the tweezer turn-off procedure during the Rydberg pulse, but is typically around 99%.

For an atom in state $|r\rangle$, the optical tweezer yields an anti-trapping potential, but there is a finite probability that the atom will decay back to the ground state and be recaptured by the tweezer before it can escape the trapping region [53]. This recapture probability can be

reduced by increasing the optical tweezer depth when recapturing atoms, as this more strongly pushes Rydberg atoms away from the tweezer. Typical estimation of Rydberg detection fidelity is done by measuring Rabi oscillations between $|g\rangle$ and $|r\rangle$ and extracting the amplitude of the oscillation. This simple approach assumes perfect initialization in $|g\rangle$ as well as perfect Rabi driving. A more careful analysis of Rydberg detection fidelity can be performed by varying the trap depth during recapture, as described in Section J.4, where the extracted detection fidelity was found to be 0.9773(42).

For two-dimensional arrays created with a spatial light modulator (SLM), the tweezer push-out approach is less effective because atoms which drift away from their initial traps can still be recaptured in a large 3D trapping structure created by out-of-plane interference of tweezers. Following an approach similar to Ref. [34], we increase the Rydberg detection fidelity using a strong microwave (MW) pulse to enhance the loss of atoms in $|r\rangle$ while leaving atoms in $|g\rangle$ unaffected. This approach is described in Section F.6 of Appendix F.

3.8 CALIBRATION OF RYDBERG RESONANCE

We calibrate the Rydberg resonance at the beginning of each batch of experimental runs, typically at least once per day. To find resonance, we prepare arrays of isolated atoms, with separations of at least 16 microns between atoms. The Rydberg laser detuning is controlled using the acousto-optic modulator (AOM) on the 420 nm laser pathway. We measure Rabi oscillations on the isolated atoms at various frequency offsets, from which we extract the generalized Rabi frequency as a function of detuning (Fig. 3.6a). The center of the fitted generalized Rabi frequency curve gives the Rydberg resonance condition, including all light shifts from the Rydberg lasers. We then measure Rabi oscillations on resonance to extract the two-photon Rabi frequency (Fig. 3.6b).

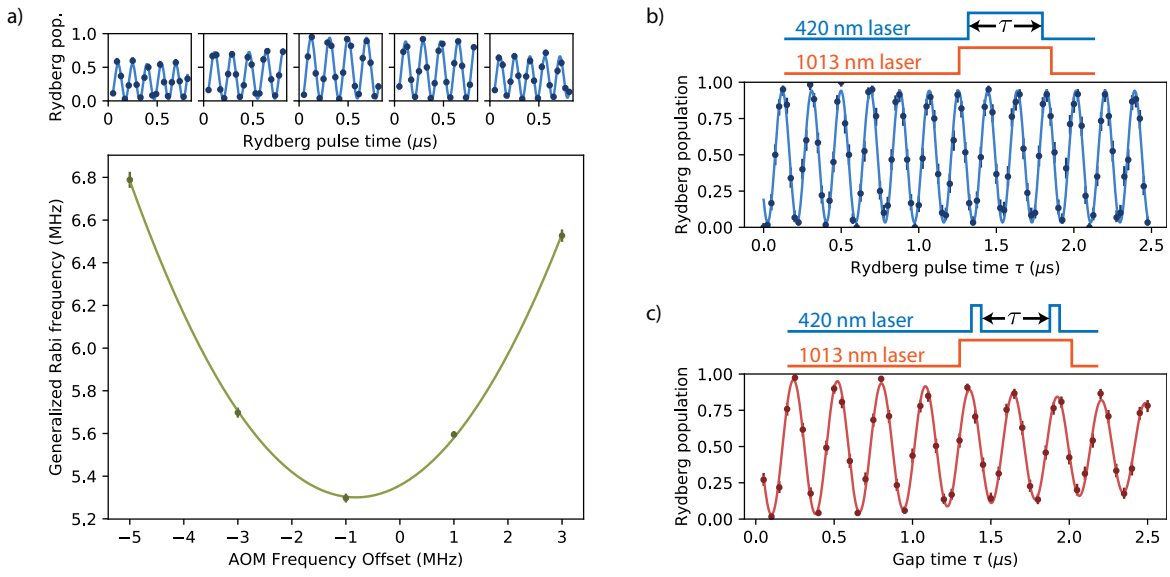


Figure 3.6: Calibration of Rydberg parameters. (a) We calibrate the Rydberg resonance by performing Rabi oscillations at several laser detunings around where we expect to find resonance (upper panel). The frequency of these oscillations is given by $\sqrt{\Omega^2 + \Delta^2}$, so fitting the measured frequencies to this functional form directly gives the resonance frequency. (b) After finding the resonance, we measure resonant Rabi oscillations to extract the Rabi frequency. (c) We measure the 420 nm laser light shift on the Rydberg transition by performing a Ramsey measurement, where during the gap the 420 nm laser is off. This is used to properly compensate for the 420 nm light shift in measurements where the laser intensity is dynamically changed. This Ramsey measurement is ultimately limited in coherence by Doppler fluctuations on the Rydberg transition to $\sim 5 \mu\text{s}$ for our atom temperatures, and may be additionally reduced by fluctuating laser intensities (or, for high Rydberg states, fluctuating electric fields).

While these calibrations are sufficient to drive resonant Rabi oscillations, in many experiments we vary the two-photon Rabi frequency Ω by dynamically changing the 420 nm laser power during the pulse. As the 420 nm power changes, the light shift on the atoms change. We correct for this by compensating for this changing light shift with the AOM frequency. To properly compensate, we first measure the total light shift induced by the 420 nm laser on the Rydberg transition at maximum power by performing a Ramsey sequence (Fig. 3.6c). During the gap time (with the 420 nm laser off), the atomic resonance is shifted due to the “missing” 420 nm light shift, and this results in phase accumulation. This measured value is then incorporated into the pulse programming for subsequent experiments (see Section 5.5).

3.9 MEASUREMENTS OF RYDBERG INTERACTION ENERGIES

Interactions between Rydberg atoms play a central role in many-body experiments throughout this thesis. These interactions take the form of an energy shift for pairs of atoms that are simultaneously excited. When this interaction shift V is larger than the strength of the excitation coupling, excitation to doubly excited states $|rr\rangle$ is suppressed; this is known as the *Rydberg blockade*, and is discussed extensively throughout this thesis, particularly in Chapters 7 and 12. The Rydberg blockade effect is generally insensitive to the particular strength of the interaction, as long as $V \gg \Omega$. Specifically, the first order corrections to the blockade involve AC Stark shifts due to off-resonant coupling to the blockaded states, of order Ω^2/V .

While many experiments are not sensitive to the exact interaction strength, it is helpful to calibrate these interaction energies, especially to account for many-body systems wherein long-range interactions are weaker and may be more comparable to Ω . We utilize a simple scheme to measure pairwise interaction energies: first, we reduce the Rabi frequency Ω until we can cleanly measure blockaded Rabi oscillations (i.e., as in Fig. 7.1 of Chapter 7). In this regime,

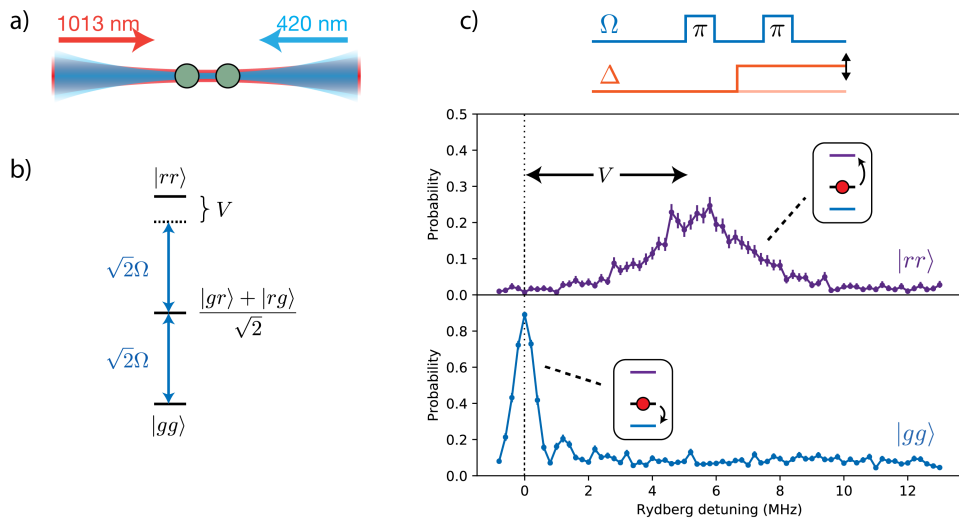


Figure 3.7: Rydberg interaction spectroscopy. (a) We measure Rydberg interactions between pairs of atoms which are globally coupled to the Rydberg state. (b) The collective driving couples the ground state $|gg\rangle$ to the symmetrically excited state $|W\rangle = (|gr\rangle + |rg\rangle)/\sqrt{2}$ with enhanced Rabi frequency $\sqrt{2}\Omega$. Similarly, the intermediate state is coupled to the doubly excited state $|rr\rangle$, which is shifted by the Rydberg interaction energy V . The Rydberg blockade regime is defined by $V \gg \Omega$, and results in effective two-level system dynamics between $|gg\rangle$ and $|W\rangle$. (c) We measure V in the blockade regime by applying a resonant π pulse (at the enhanced Rabi frequency $\sqrt{2}\Omega$ to prepare the state $|W\rangle$). We then apply a second π pulse at variable frequency, and monitor the probability of observing either $|rr\rangle$ (upper plot) or $|gg\rangle$ (lower plot). If the second pulse is also on resonance, we observe a peak in the population of $|gg\rangle$. At a separate resonance frequency shifted by V , we observe a peak in the population of $|rr\rangle$. This double-excitation peak is broadened by fluctuations in the interaction energy V .

after initializing two atoms in $|gg\rangle$, they are coupled by global Rydberg driving to the symmetric excited state $|W\rangle = \frac{1}{\sqrt{2}}(|gr\rangle + |rg\rangle)$, and the further coupling to the doubly excited state $|rr\rangle$ is far off-resonant since $V \gg \Omega$ (Fig. 3.7b). We apply a calibrated π pulse at the bare atom resonance to prepare $|W\rangle$. We then apply a second pulse at a variable detuning. If the second pulse is also applied on bare atom resonance, we de-excite $|W\rangle$ and primarily observe $|gg\rangle$ (Fig. 3.7c, lower panel). However, for a detuning $\Delta = V$, we find a second resonance where we primarily observe double-excitation to $|rr\rangle$ (Fig. 3.7c, upper panel). We note that the double-excitation resonance is significantly broader than the de-excitation resonance; we attribute this to fluctuations in the interaction energy due to thermal fluctuations in atom positions.

4

Hyperfine qubit control

4.1 INTRODUCTION

Trapped neutral atoms and atomic ions offer among the most pristine quantum coherence properties of any platforms for quantum science. In such systems, quantum bits can be encoded in pairs of atomic levels which are defined in hyperfine ground state manifolds or on narrow optical transitions from a single ground state to a metastable excited state. Hyperfine encoded qubits are particularly attractive due to their transition frequencies in the several gigahertz range – for ^{87}Rb in particular, the hyperfine splitting is 6.8346826 GHz [50]. These transitions can be readily driven by microwave fields, as demonstrated in Section 2.8.

In practice, microwave driving of cold atoms is limited to $20 - 50$ kHz Rabi frequencies, and microwaves cannot be used to address individual atoms. An alternate approach based on two-photon stimulated Raman transitions is in many cases favorable, enabling high megahertz-scale Rabi frequencies [54, 55] as well as the opportunity for local addressing of individual qubits separated by micrometer lengthscales.

A variety of experimental approaches have been used to drive stimulated Raman transitions of hyperfine qubits. The canonical formulation of Raman driving uses two phase-locked lasers, with a frequency difference equal to the hyperfine splitting. Alternatively, mode-locked frequency comb lasers have been used in trapped ion systems, wherein pairs of frequency components combine to drive Raman transitions [56–58]. In both cases, the frequency offsets must be actively stabilized to the hyperfine frequency. Another approach is based on phase modulation of a single laser to produce low-noise sidebands at the hyperfine frequency. This approach, while experimentally convenient, necessitates additional interferometric filtering to reduce destructive interference between sideband pairs, requiring both active stabilization as well as loss of optical power.

In this chapter, we demonstrate a new method for Raman driving based on phase modulation followed by reflection from a highly dispersive optical element. The dispersive element, a chirped Bragg grating (CBG), changes the relative phases of the phase-modulated sidebands, converting destructive interference to constructive interference. Moreover, we show that this constructive interference, and Raman driving in general, can be understood as being driven by laser amplitude modulation at the hyperfine frequency. In this framework, we show that the dispersive approach offers high efficiency conversion from phase modulation to amplitude modulation, enables scaling to high optical power, and is passively stable.

Finally, we benchmark the performance of our amplitude modulated laser system on an ar-

ray of ~ 300 neutral ^{87}Rb atomic qubits trapped in optical tweezers. We show high-fidelity hyperfine control across all atoms with global driving, and use this system to measure several coherence metrics in the neutral atom array. These results demonstrate that this robust approach to Raman driving enables scalable optical control of hyperfine qubits, with future opportunities to integrate into local optical addressing technologies in both neutral atom and trapped ion systems.

4.2 RAMAN TRANSITIONS ARE DRIVEN BY LASER AMPLITUDE MODULATION

We begin by analyzing stimulated Raman transitions for a general drive field which couples both hyperfine qubit states to an excited state (Fig. 4.1a). We will assume the drive field has some bandwidth that is comparable to or larger than the hyperfine frequency ω_q , but small compared to the detuning Δ from the intermediate excited state. While the canonical approach to evaluating the Raman Rabi frequency in this setup is to consider each pair of frequency components in the drive field with frequency difference ω_q , we will highlight that an equivalent interpretation is to consider only the amplitude modulation of the laser field, as would be measured on a photodetector, without considering its electric field spectrum. This interpretation simplifies our understanding of Raman laser systems, and offers a simple way to compare various approaches.

We consider first a three-level Λ system (Fig. 4.1a), with two ground levels $|0\rangle$ and $|1\rangle$ each coupled to a mutual excited state $|2\rangle$. We take both couplings to be driven by the same general laser field with single-photon Rabi frequency $\Omega(t)$. This system is described by the following Hamiltonian, given in the rotating frame for the excited state $|2\rangle$:

$$H = \hbar\omega_q|1\rangle\langle 1| + \hbar\Delta|2\rangle\langle 2| - \frac{\hbar\Omega(t)}{2}(|2\rangle\langle 0| + |2\rangle\langle 1|) + h.c \quad (4.1)$$

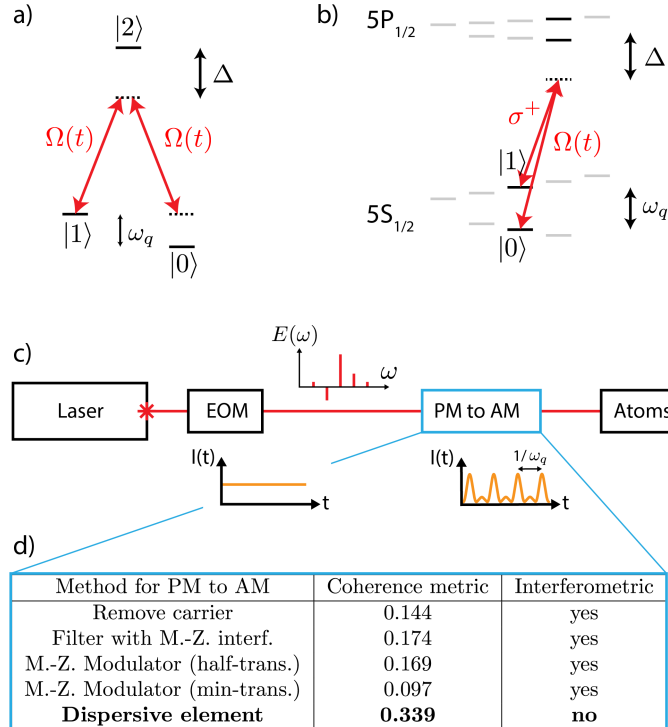


Figure 4.1: Amplitude modulation for driving Raman transitions. (a) Stimulated Raman transitions in a Λ -type 3-level system. Adiabatic elimination of the excited state results in an effective Raman coupling between ground states $|0\rangle$ and $|1\rangle$. (b) Level structure for ^{87}Rb , showing Raman driving of the clock transition from $|0\rangle = |F = 1, m_F = 0\rangle$ to $|1\rangle = |F = 2, m_F = 0\rangle$. This transition is driven by a time-dependent σ^+ polarized field $\Omega(t)$, which is far detuned by Δ from the excited state (but not far detuned relative to the splitting between the $5P_{1/2}$ and $5P_{3/2}$ excited states). (c) Several approaches for Raman driving, including the dispersive approach presented here, operate by converting phase modulation to amplitude modulation at the qubit frequency, which resonantly drives the Raman transition. (d) Comparison of methods for converting phase modulation to amplitude modulation. The coherence metric (described in Appendix B) is highest for the dispersive approach, which is also passively stable since it does not rely on interferometric filtering.

If the intermediate detuning Δ is large compared to $\Omega(t)$ and its bandwidth, we can adiabatically eliminate the excited state, resulting in an effective two-level Hamiltonian for states $|0\rangle$ and $|1\rangle$:

$$H_{\text{TLS}} = \hbar\omega_q|1\rangle\langle 1| - \frac{\hbar\Omega_{\text{TLS}}(t)}{2}|1\rangle\langle 0| + h.c \quad (4.2)$$

with an effective coupling

$$\Omega_{\text{TLS}}(t) = \frac{|\Omega(t)|^2}{2\Delta} \quad (4.3)$$

We highlight here that the Hamiltonian in eq. (4.2) describes a two-level system (TLS) with splitting ω_q and time-dependent coupling $\Omega_{\text{TLS}} \propto |\Omega(t)|^2$. From this, it is apparent that the *intensity* of the laser field produces an effective field which couples the two qubit states; amplitude modulation of the laser field at the qubit frequency therefore drives the qubit transition, akin to resonant driving of a spin transition directly using the rapidly oscillating magnetic fields of microwave radiation. Interestingly, we note that in real atoms (i.e., level structure for ^{87}Rb as shown in Fig. 4.1b), the “effective field” which is proportional to the laser intensity is the *fictitious magnetic field* associated with vector light shifts [59]. Specifically, an off-resonant laser field induces vector light shifts which act as a fictitious magnetic field given by $\mathbf{B}^{\text{fict}} \propto \text{Im}[\boldsymbol{\epsilon}^* \times \boldsymbol{\epsilon}]$, where $\boldsymbol{\epsilon}$ is the polarization vector of the laser field [60, 43]. For circularly polarized light, i.e., $\boldsymbol{\epsilon}_+ = \hat{\mathbf{x}} + i\hat{\mathbf{y}}$, the resulting fictitious field is oriented along the $\hat{\mathbf{z}}$ axis, which off-resonant laser, therefore, introduces an effective magnetic field along the $\hat{\mathbf{z}}$ axis, which couples π -polarized spin transitions – and thus laser amplitude modulation is equivalent to π -polarized microwave radiation.

The connection between this interpretation and standard formulations summing over pairs of frequency components is clearly illustrated by considering a field with regularly spaced fre-

quency components, described by $\Omega(t) = \Omega_0 \sum_n a_n e^{in\omega t}$ with normalized component amplitudes such that $\sum_n |a_n|^2 = 1$. For such a field, the intensity modulates at all harmonics of the sideband spacing according to the sum of amplitude pairs:

$$|\Omega(t)|^2 = |\Omega_0|^2 \sum_{n,m} a_n^* a_m e^{i(m-n)\omega t} \quad (4.4)$$

$$= |\Omega_0|^2 \sum_k e^{ik\omega t} \left[\sum_n a_n^* a_{n+k} \right] \quad (4.5)$$

where in the second line the summation indices are changed from n, m to n, k with $k = m - n$. The intensity modulation at the qubit frequency, driven by the term $e^{i\omega_q t}$ (corresponding to $k = 1$ if the component spacing is $\omega = \omega_q$) is given by the usual expression [56] for combined Raman Rabi frequency with many contributing pairs of components:

$$\Omega_{\text{eff}} = \frac{|\Omega_0|^2}{2\Delta} \sum_n a_n^* a_{n+1} \quad (4.6)$$

Importantly, for a field with a fixed amount of total power (characterized by $|\Omega_0|^2$), the amount of amplitude modulation is determined by how the power is distributed among frequency components, and their relative phases. We encapsulate this in the amplitude modulation efficiency, $\eta^{AM} = |\sum_n a_n^* a_{n+1}|$. Laser fields with a higher amplitude modulation efficiency have a higher ratio of Raman Rabi frequency (given by amplitude modulation) to optical scattering (given by the average optical power). Amplitude modulation efficiency is bounded above by $\eta^{AM} < 1$, where this bound is approached as the power is distributed among more and more sidebands, as in mode-locked frequency comb lasers. On the other hand, the canonical formulation with power split into two frequency components has efficiency $\eta^{AM} = 1/2$. This offers a convenient metric for comparing various approaches for producing Raman laser

systems, as detailed in Appendix B.

4.3 DISPERSIVE OPTICS FOR AMPLITUDE MODULATION

While laser amplitude modulation is necessary for Raman driving, the most accessible form of high-frequency laser modulation is *phase modulation* using electro-optics. Sinusoidal phase modulation produces frequency sidebands according to the Jacobi-Anger expansion:

$$\Omega(t) = \Omega_0 e^{i\beta \sin \omega t} = \Omega_0 \sum_{n=-\infty}^{\infty} J_n(\beta) e^{in\omega t} \quad (4.7)$$

where J_n is the Bessel function of the first kind, β is the *modulation depth*, and ω is the modulation frequency. Since the laser intensity is constant ($|\Omega(t)|^2 = |\Omega_0|^2$), a phase modulated laser cannot resonantly drive qubits. This can be seen also as destructive interference between pairs of adjacent sidebands: $\sum_{n=-\infty}^{\infty} J_n(\beta)^* J_{n+1}(\beta) = 0$ (see Section L.1 for a more explicit proof).

There are several methods for modifying the sideband spectrum of a phase modulated laser to produce amplitude modulation. These methods are primarily interferometric in nature, since they act selectively on frequency components with only gigahertz scale separation. For example, one approach is to use a Fabry-Perot cavity to filter out the carrier ($n = 0$) spectral component [54]. Another method is to use a Mach-Zehnder interferometer to filter out all odd-order sidebands. Yet another approach is a Mach-Zehnder intensity modulator [33], in which the phase modulation occurs in one arm of an interferometer. These approaches are necessarily inefficient, in that they discard some portion of the laser light by filtering out components, and they are sensitive to path length fluctuations on wavelength scales. (Some fiber-based versions of these systems can be more robust, but they are limited to low optical power.) The

performance of these approaches is compared in Fig. 4.1d and Table B.1.

Rather than filtering out specific spectral components, we consider here an approach to change the relative phases of these spectral components using dispersive optics. We consider in particular a dispersive element which has a nonzero group-delay dispersion (GDD), defined as $\text{GDD} = \frac{\partial^2 \varphi}{\partial \omega^2}$. This element imparts a phase shift to frequency components which is *quadratic* in their frequency; that is, it produces a modified electric field of the form

$$\Omega(t) = \Omega_0 \sum_{n=-\infty}^{\infty} J_n(\beta) e^{in\omega t} e^{i\alpha n^2} \quad (4.8)$$

where $\alpha = \text{GDD} \cdot \omega^2/2$ describes the phase curvature as a function of sideband index. The resulting amplitude modulation efficiency depends simply on the phase modulation depth β and the dispersion curvature α according to a remarkable Bessel function identity (see Section L.2):

$$\eta^{AM} = |J_1(2\beta \sin \alpha)| \quad (4.9)$$

For an optimal $\beta \sin \alpha = 0.92$ rad, the efficiency is maximized at $J_1(2\beta \sin \alpha) = 0.582$, surpassing the efficiency of the standard bichromatic drive ($\eta^{AM} = 1/2$). However, in practice, electro-optic phase modulation depth is limited to $\beta \lesssim \pi$, requiring $\alpha \gtrsim \pi/4$ to achieve reasonable efficiency; this corresponds to an enormously large dispersion of $\text{GDD} \gtrsim 8.5 \times 10^8 \text{ fs}^2$. For comparison, dispersion in a typical optical fiber is $4 \times 10^4 \text{ fs}^2/\text{meter}$. Even ultra-high dispersion chirped Bragg mirrors (mirrors with gradually varying Bragg layer thickness) offer only up to 1300 fs^2 from a single reflection (see Appendix B for further discussion).

Recently, new optical elements based on *volumetric* Bragg gratings have enabled a new level of frequency selectivity and dispersion control [61]. These crystals have a weak modulation in

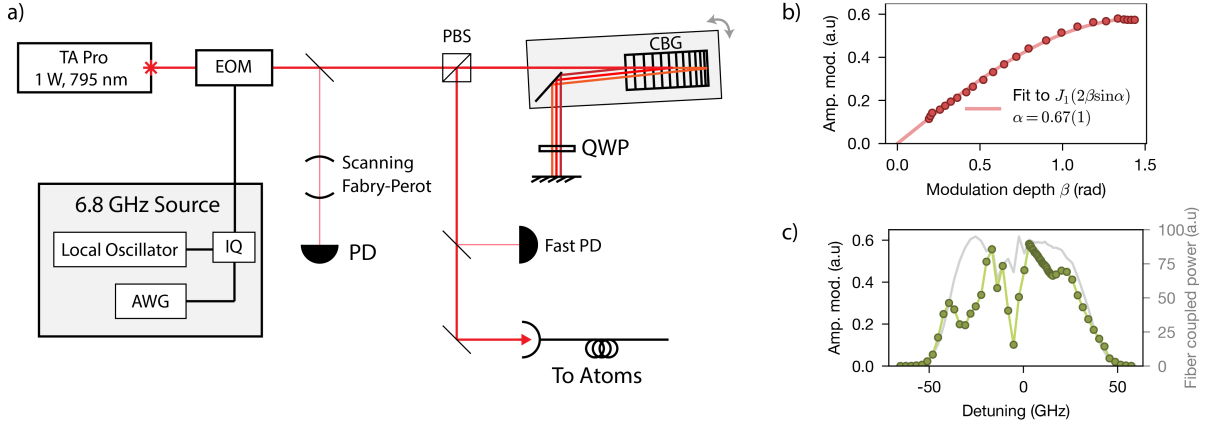


Figure 4.2: Raman laser system using a chirped Bragg grating. (a) Optical setup. The chirped Bragg grating (CBG) and the first mirror afterwards (in the shaded gray region) are mounted on a single rotation mount. Spectral components separate after first reflection from the CBG, but recombine after the second reflection. A scanning Fabry-Perot cavity measures the sideband spectrum, and a fast photodetector measures the amplitude modulation. (b) The amplitude modulation depends on both the dispersion of the CBG as well as the phase modulation depth (see main text). We observe the expected Bessel function relation, and can extract the dispersion coefficient. (c) As we scan the laser frequency across the CBG bandwidth, we see effects associated with the nonuniform dispersion within the CBG bandwidth. While more uniform CBGs can be used, the current device can be angle tuned to park at the peak, and is still sufficiently passively stable even with a free-running laser.

their refractive index over a lengthscale of ~ 1 cm. Devices for which the index modulation wavelength changes as a function of depth have highly dispersive properties. We use a chirped volumetric Bragg grating with $GDD = 4 \times 10^8 \text{ fs}^2$ (OptiGrate, CBG-795-95). Reflecting twice from the grating doubles the dispersive effect; this allows us to reach an optimal amplitude modulation efficiency with an easily accessible phase modulation depth $\beta \sim 1.3 \text{ rad}$. Moreover, the dispersive element does not waste optical power by filtering out components, and it is passively stable: ultimately, it serves as an element which passively converts phase modulation to amplitude modulation, so the effective Raman coupling field (phase, amplitude, and frequency) is inherited from the microwave source of the phase modulator.

4.4 RAMAN LASER SETUP WITH A CHIRPED BRAGG GRATING

Our Raman laser system (shown in Fig. 4.2a) is sourced from a tapered amplifier system which outputs up to 1.5 W of fiber-coupled optical power at 795 nm (Toptica TA Pro). This light is phase modulated by a free-space resonant electro-optic modulator (EOM) from Qubig. The EOM is driven by a 6.8 GHz microwave source, which consists of a local oscillator (Stanford Research Systems, SG384) that is IQ-modulated by an arbitrary waveform generator (Spectrum Instrumentation) to achieve arbitrary frequency, phase, and amplitude control of the phase modulation signal. The laser is then reflected twice from a chirped Bragg grating to convert phase modulation to amplitude modulation, and the output is gated by an acousto-optic modulator (AOM) and coupled into a single-mode fiber. The phase modulation depth β is measured by a pickoff onto a scanning Fabry-Perot cavity, and the resulting amplitude modulation is characterized on a fast photodetector.

The operational bandwidth of the CBG is 50 GHz; angle tuning of the CBG around the 3° target angle of incidence allows shifting of this bandwidth relative to the laser frequency. While the CBG nominally has a uniform dispersion within its bandwidth, we find that in practice the dispersion oscillates within its finite bandwidth; for this reason, it is helpful to have fine control of the incident angle and to monitor the resulting amplitude modulation while tuning the angle.

Proper retroreflection of the light following the first reflection from the CBG is important to ensure that subsequent alignments remain correct while tuning the CBG angle. This is made more challenging by the fact that the different spectral components of laser light penetrate different depths within the CBG and therefore spatially separate; we want these components to properly recombine after retroreflection and the second pass through the CBG.

Our approach is to mount both the CBG and the following mirror on the same rotation stage, where the entrance facet of the CBG is at the origin of the rotation stage. The final retro-reflection mirror is aligned once and then fixed in place.

After optimizing the CBG angle to maximize amplitude modulation, we experimentally measure the dependence of amplitude modulation on the phase modulation depth to confirm the expected Bessel function relationship from eq. (4.9) and extract the dispersion coefficient (Fig. 4.2b). Finally, at full modulation depth, we measure the amplitude modulation as we scan the laser frequency across the bandwidth of the CBG to assess sensitivity to drifts of the free-running laser (Fig. 4.2c).

4.5 BENCHMARKING RAMAN LASER SYSTEM ON NEUTRAL ATOM ARRAYS

We test our high-power Raman laser system on neutral ^{87}Rb atoms which are randomly loaded within an array of 600 optical tweezers in two dimensions, arranged in a $100\text{-}\mu\text{m} \times 200\text{-}\mu\text{m}$ rectangle (Fig. 4.3a). The optical tweezers are linearly polarized and have a wavelength of 809 nm. Atoms are imaged on an electron-multiplied CCD (EMCCD) camera to detect their loaded positions, and their final states are read out by a second fluorescence image after pushing out atoms in $F = 2$ by cycling photons on the D_2 transition $F = 2 \rightarrow F' = 3$. During loading and imaging, the tweezers have a trap depth of 14 MHz. During Raman driving, the trap depths are lowered to 4 MHz and an 8.5-G magnetic field is applied.

The Raman laser illuminates the atom plane from the side and is cylindrically focused onto the atoms, resulting in an elliptical beam with waists of $40\text{ }\mu\text{m}$ and $560\text{ }\mu\text{m}$ on the thin axis and the tall axis, respectively, with a total average optical power of 150 mW on the atoms. The large vertical extent ensures homogeneity across the atom plane without more complicated beam-shaping techniques. The laser is σ^+ polarized and tuned 100 GHz blue-detuned

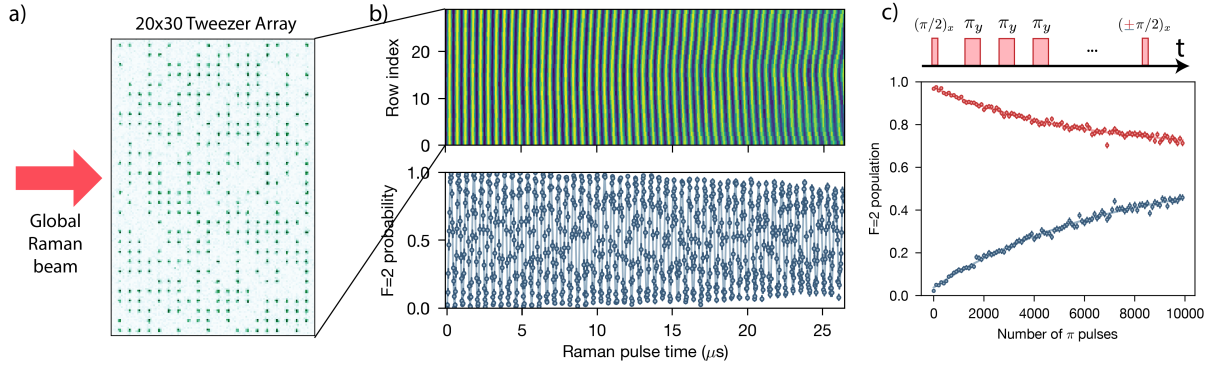


Figure 4.3: Raman driving of ^{87}Rb atoms in an optical tweezer array. (a) Sample fluorescence image of ~ 300 atoms individually loaded into a 20×30 optical tweezer array. The Raman laser globally illuminates the array. (b) Rabi oscillations, averaged over each row individually (upper panel) or over just the middle four rows (lower panel). The measured Rabi frequency is $2\pi \times 1.95$ MHz. The decay is caused primarily by inhomogeneous averaging across the system. (c) We use a CPMG pulse train to measure how many pulses we can apply before scattering from the Raman laser causes T_1 -type decay. We compare two measurements in which the final $\pi/2$ pulse is applied along $+x$ (red) or $-x$ (blue), and find that these curves converge with a $1/e$ fit of $7852(76)$ pulses. This gives a scattering-limited π pulse fidelity of $0.999873(1)$.

of the 795-nm transition to the $5P_{1/2}$ excited state. By tuning the EOM drive frequency, the Raman laser can resonantly drive π -polarized spin transitions in the ground state hyperfine manifold. We use Raman-assisted optical pumping to prepare atoms in $|0\rangle = |F = 1, m_F = 0\rangle$ (see Section 4.6). Subsequently, the EOM drive frequency is tuned to the clock resonance, and atoms are coupled from $|0\rangle$ to $|1\rangle = |F = 2, m_F = 0\rangle$.

We globally drive the qubit array and measure Rabi oscillations across the array. We analyze Rabi oscillations individually for each row (Fig. 4.3b, upper panel), as well as averaged over the middle four rows (Fig. 4.3b, lower panel), where we find an average $\Omega_{\text{eff}} = 2\pi \times 1.95275(8)$ MHz. Rabi oscillations decay due to inhomogeneity across the array and small ($\lesssim 1\%$) power fluctuations.

For Raman driving of hyperfine qubits, there is a fundamental tradeoff between Raman Rabi frequency ($\propto \Omega^2/2\Delta$) and incoherent scattering processes ($\propto \Gamma [\Omega^2/4\Delta^2]$). For a given target Rabi frequency, higher optical power enables working at a larger intermediate detuning, increasing the ratio of Rabi frequency to scattering rate (proportional to the coherence

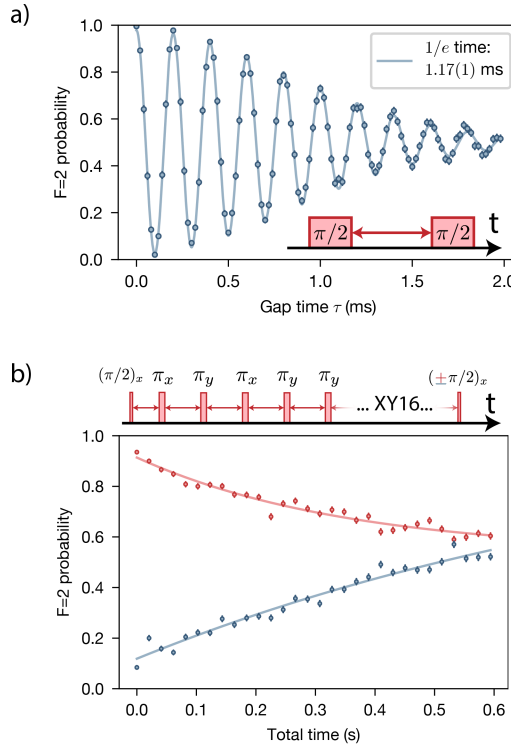


Figure 4.4: Idle coherence of atoms in optical tweezers. (a) Ramsey measurement, taken with a 5 kHz detuning between pulses. The atoms occupy several vibrational levels within the tweezers which have different average differential light shifts on the qubit transition, resulting in dephasing. (b) Dynamical decoupling sequence using XY16-256, with a total of 256 π pulses. The final $\pi/2$ pulse is applied about $+x$ (red) or $-x$ (blue). These two curves converge with a fitted $T_2 = 303(13)$ ms.

metric tabulated in Fig. 4.1c). To evaluate this coherence limitation for our high-power system, we apply a $(\pi/2)_x$ pulse followed by a train of π_y pulses (Fig. 4.3c); this so-called CPMG sequence [62] is robust to pulse miscalibrations that limit our observed Rabi coherence time. By varying the total number of π_y pulses, we observe a T_1 -type decay from scattering, with a characteristic $1/e$ scale of 7852 ± 76 pulses. This decay constant sets a lower bound on our scattering-limited π pulse fidelity of $0.999873(1)$.

4.6 COHERENCE PROPERTIES OF HYPERFINE QUBITS

We additionally use this system to characterize the idle coherence properties of the neutral atoms in optical tweezers. We first benchmark the coherence in tweezers by measuring a Ram-

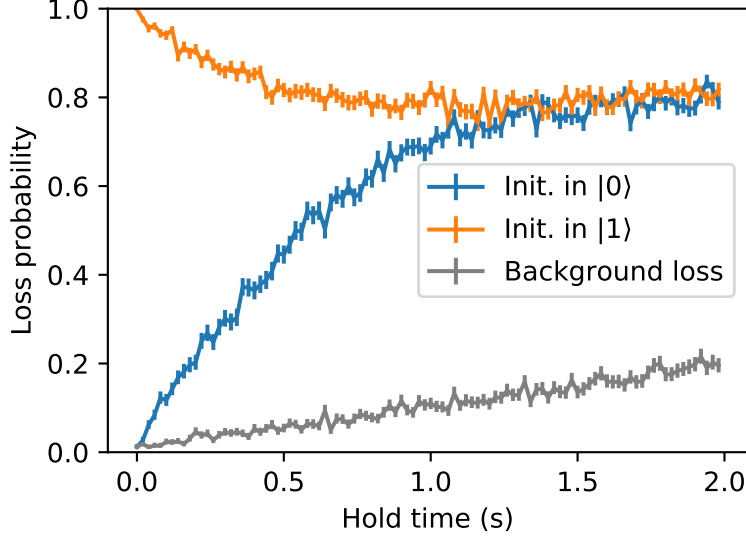


Figure 4.5: T_1 measurement. We initialize atoms in either $|0\rangle = |F = 1, m_F = 0\rangle$ or $|1\rangle = |F = 2, m_F = 0\rangle$ (blue and orange curves, respectively), and hold the atoms in the optical tweezers for a variable time before pushing out the $F = 2$ population. These two curves converge with a fitted $1/e$ time of $0.45(1)$ s. The tweezer depths are ramped down to ~ 4 MHz during the hold time. We additionally turn off the $F = 2$ pushout to measure the background loss probability (gray), which is consistent with a 10 s vacuum-limited lifetime.

sey $T_2^* = 1.17(1)$ ms, limited by the finite atomic temperature and small differential light shifts in the tweezers (Fig. 4.4a). By applying a train of π pulses, we dynamically decouple the atomic qubits from noise sources such as the tweezer differential light shifts and extend the coherence time to $T_2 = 303(13)$ ms, showing second-timescale coherence across hundreds of qubits (Fig. 4.4b). The π pulses are applied according to the XY16-256 pulse sequence (256 total π pulses), which is robust against pulse imperfections for generic initial superposition states.

This T_2 coherence time is partially limited by off-resonant scattering from the optical tweezers. Interestingly, however, this coherence time is actually *longer* than would be expected given the calculated rate of off-resonant scattering in the tweezer, ≈ 17 Hz – and this is because not all scattering events cause qubit decoherence [63, 64]. In particular, for far-detuned optical tweezers, the dominant scattering mechanism, so-called Rayleigh scattering, does not change the spin state after the scattering event, and affects both qubit states approximately

equally – and thus a single scattering event does not collapse the qubit state. Another scattering mechanism is Raman scattering, which describes photon scattering events that do change the spin state and thus cause decoherence. With our 809 nm tweezers, we estimate a Rayleigh scattering rate of 14.7 Hz, while the Raman scattering rate is only 2.1 Hz. Raman scattering induces T_1 -type decay out of the qubit states, which we measure to be consistent with this scattering timescale (Fig. 4.5). Notably, for tweezers which are far detuned relative to the excited state fine structure splitting, the Raman scattering rate scales very favorably as Ω^2/Δ^4 , despite the total scattering rate scaling as Ω^2/Δ^2 [65].

Since state-of-the-art Rydberg-based entangling operations are sub-microsecond timescale, and Raman-based single-qubit rotations are also microsecond timescale, this coherence time is sufficiently long for tens or hundreds of thousands of qubit operations before idle coherence properties become limiting. Moreover, this coherence time should support new approaches for quantum algorithms based on dynamically reconfigurable neutral atom arrays, all while preserving coherence.

4.7 OPTICAL PUMPING INTO $m_F = 0$ STATES

Optical pumping into $m_F = 0$ states is traditionally accomplished by applying π -polarized optical pumping light on an $F \rightarrow F' = F$ optical transition, along with repumper light from other ground state hyperfine levels. This approach utilizes the special selection rule which forbids dipole transitions with $\Delta F = 0, m_F = 0, m'_F = 0$. The $|F, m_F = 0\rangle$ state is thus a dark state to the optical pumping light, and accumulates population. This approach is challenging because imperfection in the π polarization, which can come both from misalignment of the beam propagation relative to the quantization axis or due to polarization impurity, reduces the quality of the $m_F = 0$ dark state.

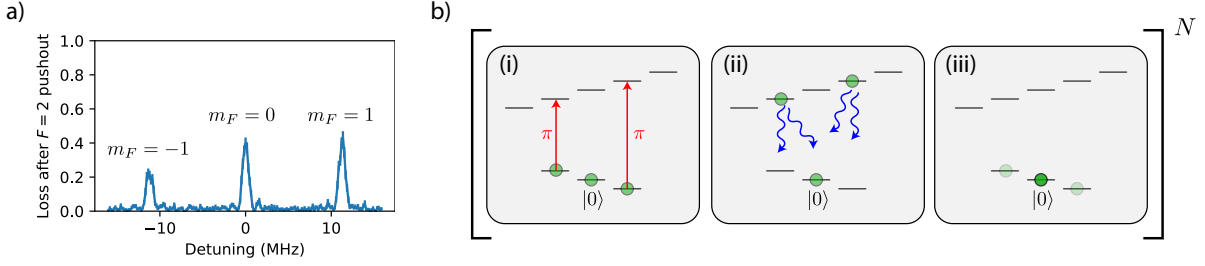


Figure 4.6: Raman laser spectroscopy and optical pumping. a) The Raman laser drives two-photon transitions within the $5S_{1/2}$ ground state, and couples π spin transitions from $|F = 1, m_F\rangle$ to $|F = 2, m_F\rangle$. After depumping all atoms into $F = 1$, we apply a Raman pulse at variable detuning to find resonances for the three π transitions. These measurements are taken with an 8.5 G magnetic field. b) Raman-assisted optical pumping. (i) We begin by coarse pumping into all three sublevels of $F = 1$, and apply a Raman π -pulse to excite from $|F = 1, m_F = -1\rangle$ to $|F = 2, m_F = -1\rangle$ and from $|F = 1, m_F = +1\rangle$ to $|F = 2, m_F = +1\rangle$. (ii) We then coarse pump back from $F = 2$ to $F = 1$. (iii) The net effect is to transfer some population from $|F = 1, m_F = \pm 1\rangle$ to $|F = 1, m_F = 0\rangle$. We repeat this cycle $N = 70$ times and achieve a net population of 99.3(1)% in $|0\rangle = |F = 1, m_F = 0\rangle$.

We instead use an active Raman-assisted optical pumping scheme to prepare atoms in $|0\rangle = |5S_{1/2}, F = 1, m_F = 0\rangle$. We apply a bias magnetic field of several Gauss (8.5 G for experiments in Chapter 14), and make use of the Raman laser which drives effective π polarized spin transitions within the ground state hyperfine manifold (Fig. 4.1b and Fig. 4.6a). As illustrated in Fig. 4.6b, we begin by coarse pumping of atoms into all m_F states within the $|5S_{1/2}, F = 1\rangle$ manifold by shining resonant light on the $|5S_{1/2}, F = 2\rangle$ to $|5P_{3/2}, F' = 2\rangle$ transition. We then apply a Raman π pulse at a detuning that drives population from $|F = 1, m_F = -1\rangle$ to $|F = 2, m_F = -1\rangle$, and a second pulse to drive population from $|F = 1, m_F = +1\rangle$ to $|F = 2, m_F = +1\rangle$ (Fig. 4.6a). The process then repeats by again coarse pumping any population that was transferred to $F = 2$ back into the $F = 1$ manifold. The net effect of one cycle is to transfer a portion of the population in $|F = 1, m_F = \pm 1\rangle$ into $|F = 1, m_F = 0\rangle$. We repeat this cycle 70 times over a duration of 300 μ s to achieve a $|0\rangle$ preparation fidelity of 99.3(1)%.

This protocol does not require the π pulses on the $m_F = \pm 1$ states to be perfect; the higher the transfer probability, the faster the convergence into $m_F = 0$. However, as discussed in

Section 2.8, these transitions for $m_F = \pm 1$ are coupled to the atomic motion. For low Rabi frequencies such as those typical with microwave driving (~ 20 kHz), this decoherence strongly suppresses the population transfer, and we therefore observe only limited optical pumping fidelity of $\sim 90\%$ when using microwaves to apply these transitions. However, for larger Rabi frequencies such as those achieved with Raman driving ($\gtrsim 150$ kHz), we can observe a few coherent oscillations on these transitions, and have $\gtrsim 95\%$ population transfer for a single π pulse.

5

Experiment control infrastructure

Our experimental control infrastructure consists of a variety of modular tools for controlling all the equipment in the lab. At the core is an Adwin processor (ADwin-Pro II), which implements precise timing control for 16 analog outputs and 32 digital outputs. This system controls laser detunings and powers, magnetic field coils, acousto-optic modulators (AOMs), laser shutters, microwave TTL switches, etc. The software for programming the sequence of voltages and TTL settings for these outputs was developed by Peter Schauss and Stefan Kuhr at the Max Planck Institute for Quantum Optics. Separate home-built software modules perform real-time image analysis and atom rearrangement, stabilize laser beam alignments, calibrate laser pulse parameters, and more. In this chapter, we detail key aspects of these modules, and

then describe adaptations to the system to enable remote operation of the machine.

5.1 IMAGE ACQUISITION AND ANALYSIS

All experimental sequences consist of a large number of cycles, each of which produces the same number of atom fluorescence images (usually at least two images per cycle). After the sequence is complete, analysis of the acquired images begins by evaluating the sum of the first image from each cycle. While individual images show random loading of the tweezers, the combined image displays atom signal from every optical tweezer in the system. This combined image is therefore used to determine the position of the atom fluorescence signal from each tweezer on the Andor EMCCD sensor. For all experiments described in this thesis, the signal from each tweezer is evaluated by summing the pixel values in a small 3x3 bin centered at its position on the sensor. More advanced techniques, such as deconvolution against the expected atom point spread function, could further improve the signal to noise.

The signal for each tweezer in the first image per cycle forms a bimodal distribution, where low values correspond to an empty tweezer and larger values correspond to a single loaded atom (Fig. 2.4). A threshold is assigned in between the two modes for each tweezer in the array. Comparing the analyzed signal from each tweezer in all acquired images to these determined thresholds results in a binary array describing whether each tweezer was loaded or empty in each image of the sequence; this forms the basis for all subsequent analysis. Additionally, the determined atom positions and signal thresholds can be saved in a configuration file to be used for subsequent real-time analysis of images.

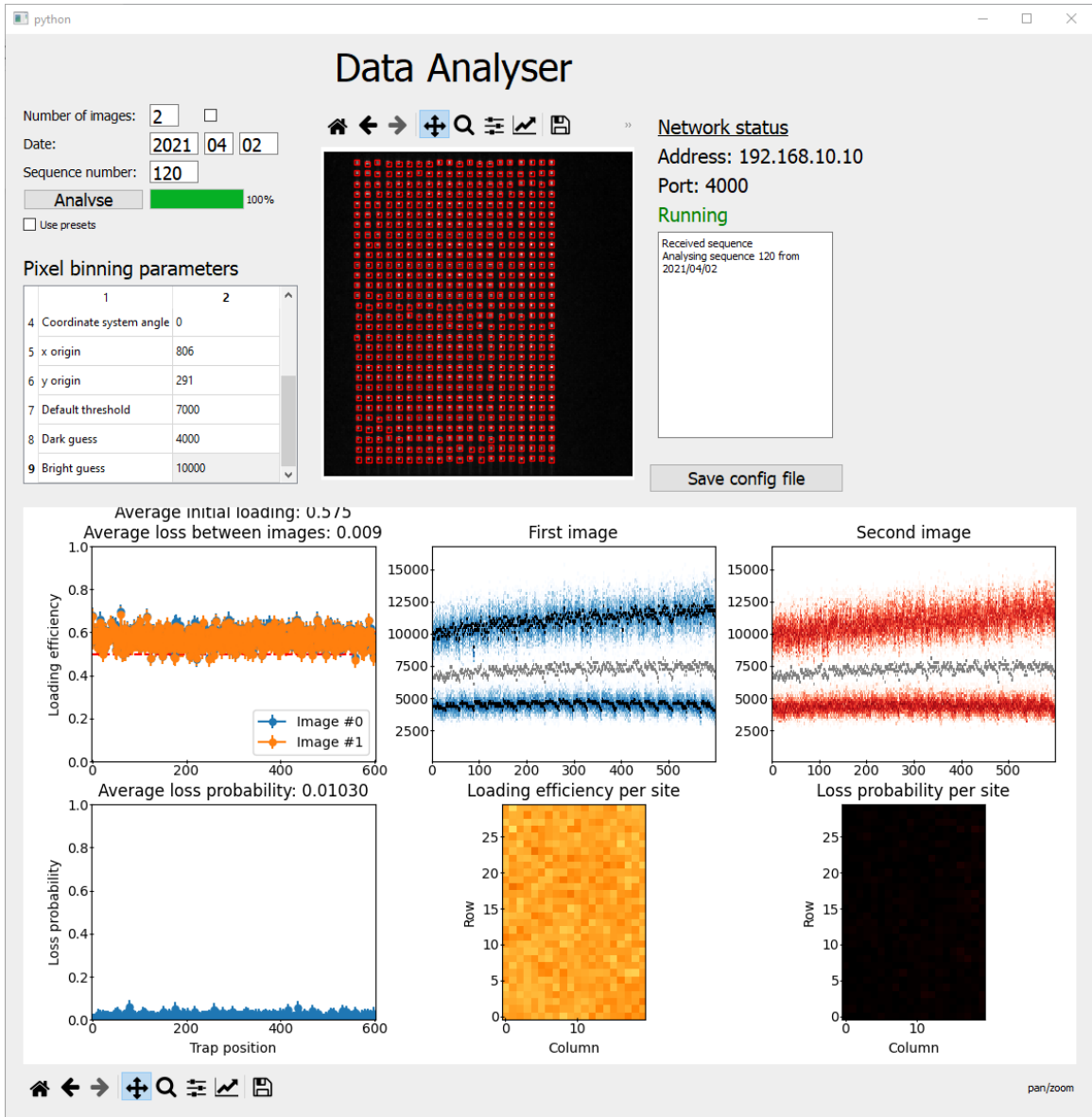


Figure 5.1: Initial analysis of images. *Upper panel:* Each sequence is automatically analyzed after completion. Trap positions are converted into EMCCD pixel coordinates and locally optimized to encompass as much atom signal as possible (red squares in the middle panel). *Lower panel:* Atom signal histograms for each trap are shown in the upper middle and upper right plot; black markers highlight the fitted peaks of the '0 atom' and '1 atom' distributions; gray markers indicate the assigned thresholds. We count the number of repetitions in which the atom signal is above the threshold to measure the average site occupation probability (upper left panel). We typically observe 50-60% loading in the first image. In this example, we simply re-image the same atoms, and plot the loss probability from the first to the second image (lower left). The lower right two panels show average occupation in the first image, and average loss probability per site, reshaped according to the array geometry.

5.2 REAL-TIME IMAGE ANALYSIS AND LIVE PLOTTING OF DATA

The atom array platform utilizes real-time rearrangement of atoms based on an acquired fluorescence image which reveals which optical tweezers are loaded with single atoms and which tweezers are empty. Prior to performing experiments with rearrangement, an imaging calibration measurement is first run with ~ 100 cycles, in which atoms are simply loaded and imaged. This sequence is used to produce the calibration file describing the center pixel and threshold for each tweezer.

Images are acquired and processed in real-time with a C++ program, using the Andor software development kit (SDK). This program periodically checks if a new image has been acquired by the Andor hardware; if so, and if this image is meant to be used for feedback, it is analyzed using the prepared calibration file. Pixels corresponding to each tweezer are binned and compared to their respective thresholds. The resulting list of binary values are sent over the local network to a separate program which handles atom rearrangement (described in the next section). While the image processing time is fast (< 1 ms), the main delay in this chain is the acquisition of the image data from the camera, which takes 10-30 ms depending on the camera region of interest. Other approaches for fast data acquisition from the camera (i.e., Camera Link) could reduce the latency of this image processing [66].

After the acquired images have been analyzed and reported (if being used for feedback), they are displayed in visualization software which shows the most recently acquired images as well as simple statistics of the loaded atoms (Fig. 5.2). This real-time tracking of data acquisition is helpful in verifying that sequences are running correctly; additionally, parameters of the experiment can be tweaked while tracking atom signals in real-time.

The first statistic tracks the number of loaded atoms in the first image of each experimental

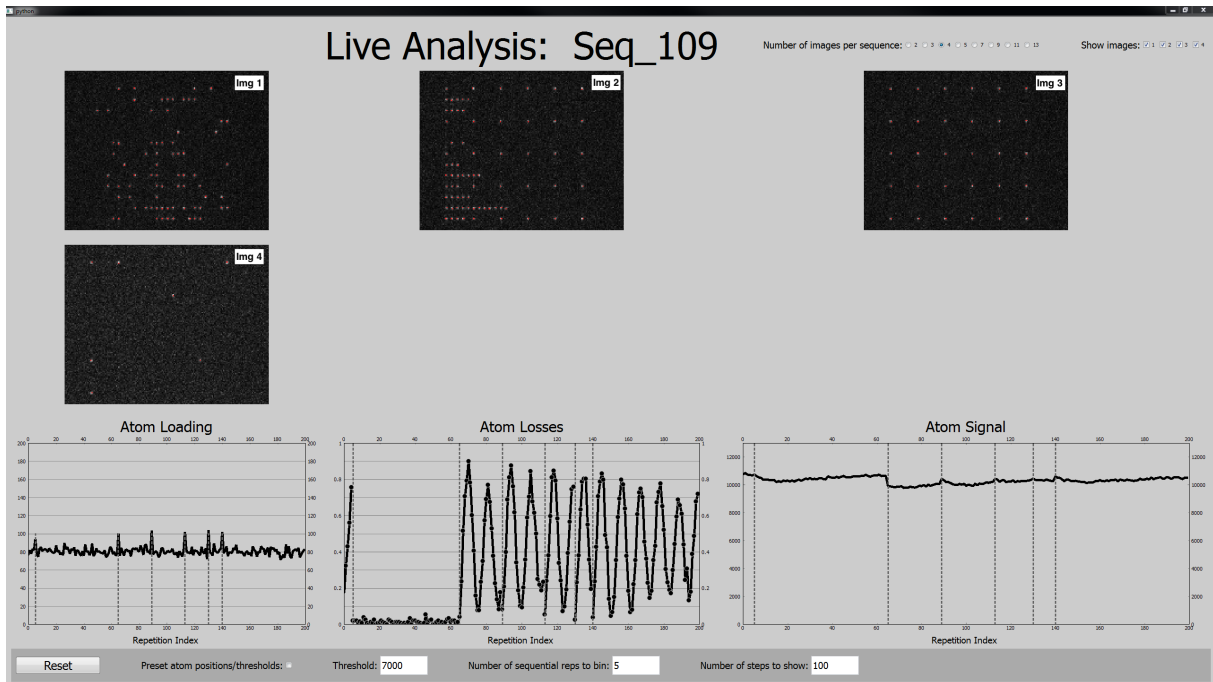


Figure 5.2: Live analysis. Images are displayed in real-time as they are acquired. Here, we show an example snapshot from a sequence with four images per repetition. The first image shows a randomly loaded array. The second shows the same atoms after doing an initial sorting. The third image shows atoms after a second round of sorting, preparing an array of isolated atoms. The fourth image shows the remaining atoms after a Rydberg laser pulse which drives Rabi oscillations. Basic analysis, including loading, losses, and atom signal are plotted as a function of time to verify that the experiment is working properly, and in some cases to align optics based on the real-time analysis.

cycle. It is often useful to monitor loading while adjusting MOT loading parameters, such as loading duration and magnetic field offsets.

The second statistic tracks the probability of atoms being lost between two sequential images of each cycle. Since atom loss is the primary readout mechanism in both Rydberg experiments and hyperfine qubit experiments, this atom loss signal gives early insight into the data quality before the sequence is finished. For example, Rabi oscillations are traced out visually as they are acquired. Live monitoring of atom loss can also be integrated with alignment of laser systems or optics; for example, the polarization of our optical pumping laser is fine-tuned by cycling a sequence in which imperfect polarization results in excess heating and atom loss, and then tweaking half-wave plates and quarter-wave plates while monitoring atom loss.

The last statistic that is reported live is the average brightness of the atoms. This is a useful signal when optimizing the focus of the objectives.

5.3 ATOM REARRANGEMENT INFRASTRUCTURE

Atom rearrangement is handled by a C++ program which generates real-time AOD waveforms. The waveforms are composed of one or more frequency components, each of which are within the AOD bandwidth (75 MHz to 125 MHz) and correspond to an individual deflection from the AOD. The waveforms are generated in the time-domain to keep careful track of the amplitude, frequency, and phase of each component. Control of each component, and in particular the relative phases, is crucial due to considerations of intermodulations produced from nonlinearities in the AOD and amplifier (see Section C.2). Additionally, phase continuity of each frequency component in the waveform is important to avoid flicker in the output beams, including while frequencies are being dynamically changed to steer the optical tweezers.

Our one-dimensional tweezer array used Software Defined Radio (SDR) (Ettus Research,

model USRP X310, daughterboard UBX 160) to generate waveforms. The rearrangement software generated the time-domain waveforms and streamed them to the SDR, which performs digital-analog conversion, low-pass filtering, and subsequent analog IQ upconversion by a frequency of $\omega_{\text{up}} = 74$ MHz. As a result, each frequency component was calculated in the shifted band of 0 to 50 MHz. This is convenient since it enables the waveform to be sampled at a lower sampling rate, speeding up calculations and easing the requirements on connection speed between the computer and SDR. We sampled these waveforms at 100 MHz, whereas $\gtrsim 250$ MHz sampling rate is necessary to directly synthesize a 100 MHz waveform. For our hardware setup, 100 MHz sampling rate was roughly the maximum that we could sustain by streaming. We found that optical tweezers generated using the SDR caused excess heating on atoms as compared with standard high-quality microwave sources (Appendix C).

For experiments with two-dimensional tweezer arrays, we use two crossed AODs, one of which controls horizontal beam positions and the other controlling vertical positions. To generate waveforms for both AODs, we use a dual-channel arbitrary waveform generator (AWG) (M4i.6631-x8 by Spectrum), operated in first-in first-out (FIFO) streaming mode. This PCI Express interface enables higher streaming rates, so we directly synthesize the waveforms in the 75 MHz - 125 MHz band, with a sampling rate of 333 MHz.

Since the waveforms for rearrangement are generated in real-time, any delay that comes from the computation of the waveform translates to a slowdown of the experimental cycle time, as well as a decrease in rearrangement fidelity (due to the background-limited lifetime of atoms in tweezers). We therefore take care to optimize the calculation of waveforms. Towards this end, we precompute as much as possible prior to any real-time processing. Typically, this includes precomputing static frequency components at each frequency that we may want to generate, and also time-dependent frequency chirped waveforms corresponding to in-

dividual tweezer trajectories. For real-time summation, we utilize Advanced Vector Extensions 2 (AVX2) which offers a modest speed boost over straightforward addition of each sample separately. As sections of the rearrangement waveform are completed, they are streamed to the AODs while later trajectories are still being calculated.

For experimental sequences with rearrangement of two-dimensional arrays, the primary bottlenecks are image acquisition time (typically 20 ms), the time it takes for the image processing software to receive the image from the camera hardware (up to \sim 30 ms), and the actual atom sorting time (20-40 ms, depending on system size). While these times are mainly limited by hardware and optics, additional software delays are the latency of the FIFO stream (\sim 10 ms for the Spectrum AWG at 333 MHz sampling rate), as well as delays from waiting for calculations of the rearrangement waveforms to finish (\sim 10 ms). While these software delays do not currently pose a major limitation, future experimental upgrades to the camera hardware and optics could be used to receive and process camera images with a significantly lower latency [66], and other hardware-based approaches could be used to more quickly synthesize and combine AOD waveforms.

5.4 TWO-DIMENSIONAL OPTICAL TWEEZER ARRAYS

Our two-dimensional optical tweezer arrays are generated using a phase spatial light modulator (SLM) from Hamamatsu (X13138-02). The SLM is connected to a lab computer using a DVI interface, and is controlled as if it were an external monitor. The phase hologram is displayed using the Python PyQt interface in a window which is made full screen on the SLM (with the toolbar and window border hidden).

We program our target optical tweezer arrays by defining an underlying grid structure, with a specified number of rows and columns and corresponding row spacing and column spacing

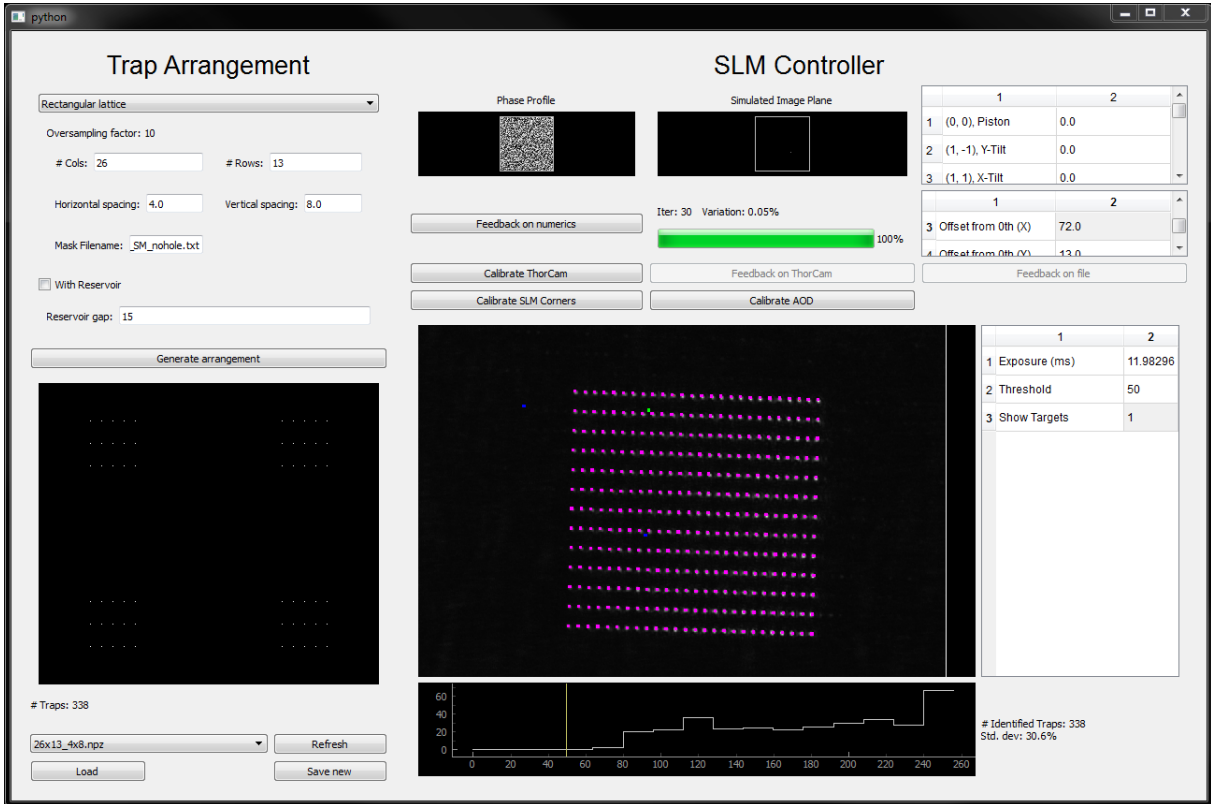


Figure 5.3: Spatial light modulator control software. The control software for our two-dimensional tweezer array SLM includes several methods for defining target arrays of tweezers. Weighted Gerchberg-Saxton (WGS) is performed to produce phase holograms, and Zernike polynomials are added to these holograms to correct for optical aberrations in the system. The produced tweezer array is characterized on a CCD camera, with a calibrated mapping between tweezer positions in SLM coordinates and pixel positions on the camera (predicted tweezer positions marked in pink). This camera also serves as a position reference to align AOD tweezers onto SLM tweezers.

(Fig. 5.3). The target trap array is selected as an arbitrary subset of traps from this underlying grid. These target positions are used to define a target intensity profile in the atom plane, which is used in the phase-fixed weighted Gerchberg-Saxton (WGS) algorithm to generate the phase hologram [41].

In the standard WGS algorithm, the Fourier plane is sampled according to the pixel dimensions of the SLM, and the image plane is calculated by the discrete Fourier transform of the Fourier plane. This defines an effective resolution in the image plane: if we perform WGS with a particular target trap position, or with the closest neighboring target position, what is the distance between these two spots in the atom plane? This is termed the ‘diffraction unit’, and is our experimental unit for defining trap positions. However, the diffraction unit is not the fundamental resolution limit of the SLM: in particular, adding small gradients to the phase hologram can produce displacements in the image plane which are smaller than the diffraction unit.

To achieve sub-diffraction unit positioning with WGS, we sample the Fourier plane in an enlarged region around the SLM. We assume that the input Gaussian beam is still confined to the central SLM region of the Fourier plane, but this enlarged Fourier plane results in an image plane with finer resolution. We typically use a 10x enlarged Fourier plane, enabling trap positioning with 0.1 diffraction-unit resolution. In our optical SLM setup, the diffraction unit is $0.844 \mu\text{m}$.

When calculating the phase hologram, we improve trap homogeneity by pre-compensating for the variation in diffraction efficiency across the tweezer array (roughly given by $\eta(\theta) = \text{sinc}^2(\frac{\pi}{2}(\theta_{\text{trap}}/\theta_{\text{max}}))$ where θ denotes the deflection angle from zeroth order). This compensation is incorporated by setting the WGS target intensities in the image plane to $1/\eta(\theta)$. We additionally add Zernike polynomials to the WGS-generated phase hologram to correct for

aberrations in the optical system (see Section 2.7).

The SLM optical tweezer array is measured on a monitor CCD camera. While we have at times performed additional homogenization of the trap array based on CCD-measured intensities, we find that this is not typically necessary, and indeed this requires eliminating systematic variation on the CCD sensor that comes from etalon effects or inhomogeneous pixels.

5.5 RYDBERG LASER PULSE PROGRAMMING

Many Rydberg experiments are based on many-body evolution under a time-dependent ground-Rydberg coupling $\Omega(t)$, with time-dependent detuning $\Delta(t)$. To implement these programmable pulses, we modulate the 420 nm laser using a double-pass AOM configuration. The AOM is driven by an arbitrary waveform generator (M4i.6631-x8 by Spectrum). The AWG control software contains implementations of common Rydberg pulse profiles, such as square pulses, adiabatic sweeps, and various quench protocols; these pulse types can be established by network commands defining the functional form, along with the key parameter values.

Importantly, this control software accounts for multiple calibration parameters when generating waveforms. For example, the 420 nm laser induces a light shift on the Rydberg transition which can be large (of scale $2\pi \times 5$ MHz). While the pulse intensity changes, this light shift changes, modifying the detuning profile. We therefore correct the frequency profile as a function of the pulse intensity to compensate this shift. Similarly, laser detuning profiles are calculated relative to the most recently calibrated resonance frequency, and amplitude profiles are calibrated relative to the most recently measured Rabi frequency. Finally, the double-pass AOM response to changing amplitudes and frequency is nonlinear, so we measure this response and apply a feed-forward correction to obtain the target output intensity. We note here that even close to resonance, we typically suppress the AOM power, to allow us to main-

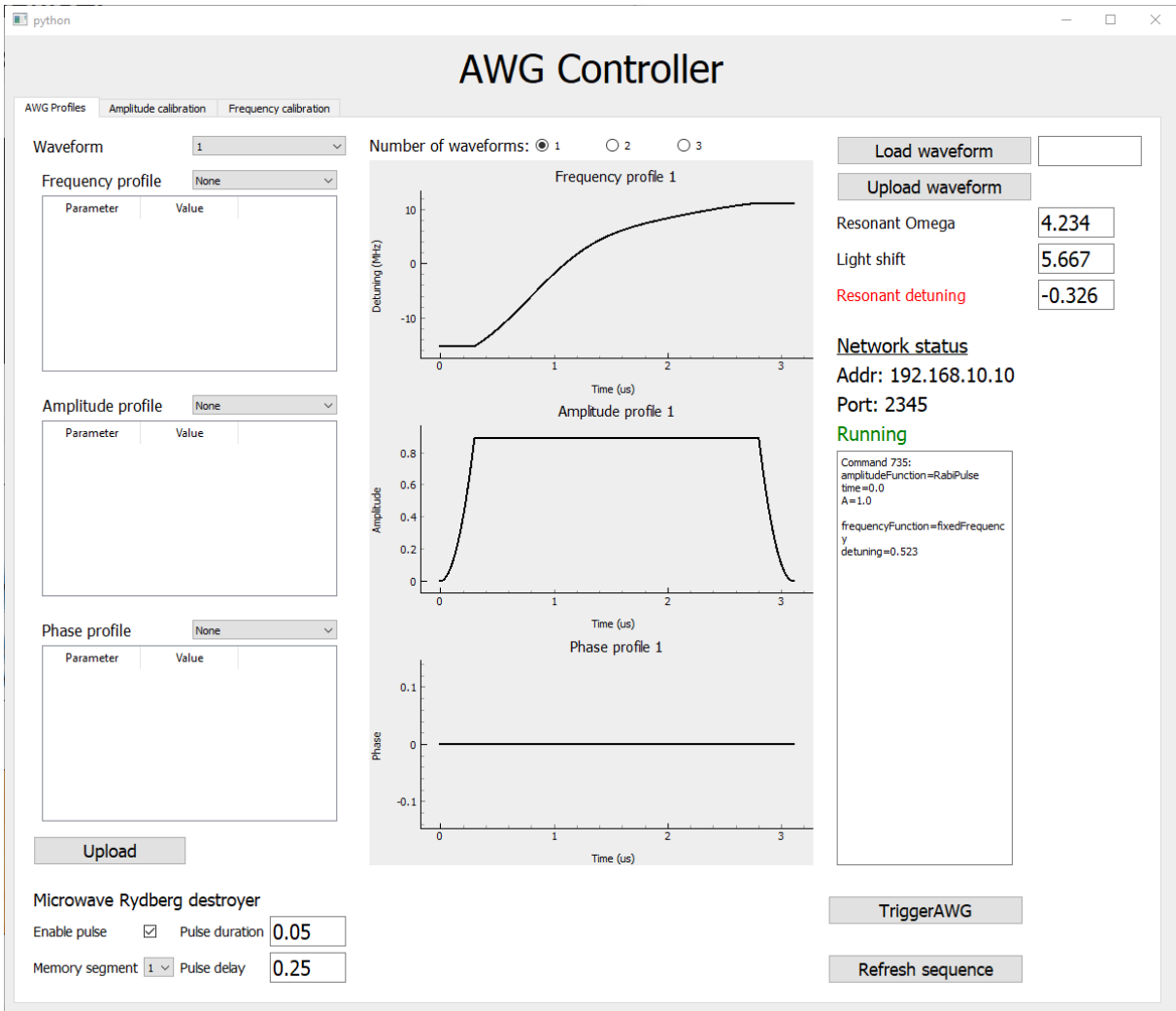


Figure 5.4: Rydberg AWG control. We implement programmable Rydberg laser pulses by modulating the amplitude, frequency, and phase of the 420 nm laser using a double-pass AOM. The AOM is driven by an amplified waveform from an AWG which is controlled using this interface. The target pulse profile is described using a variety of flexible waveform functional forms, and displayed here. To implement this target profile, we feed-forward to correct for several effects, including the changing AOM deflection efficiency as we change frequency, the nonlinear AOM response to RF power, as well as the change in light shift on the atoms when we change the 420 nm laser power.

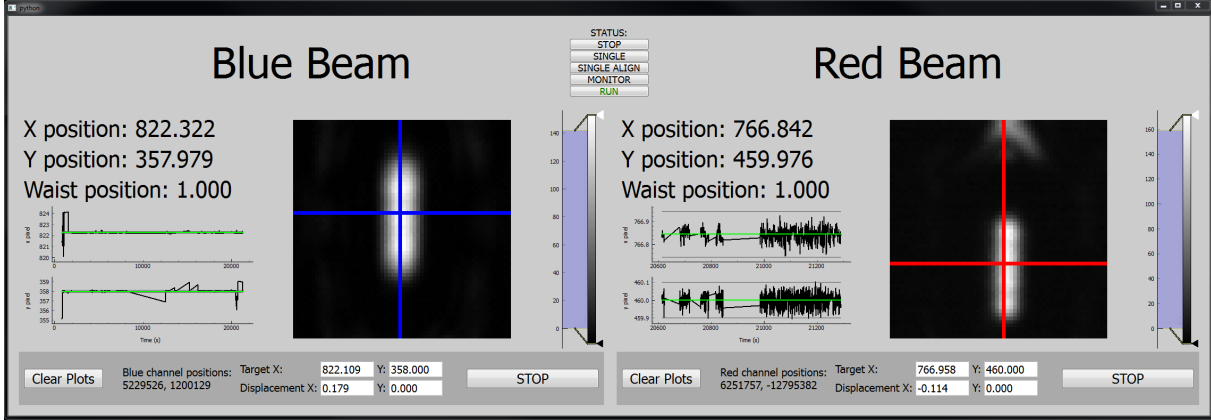


Figure 5.5: Rydberg beam alignment. Small portions of the 420 nm and 1013 nm Rydberg lasers are picked off and focused onto monitor cameras, which mark the beam positions relative to the plane of the atoms. The beams are steered to target pixel positions by actuating on motor-controlled mirrors in the optical pathways. This alignment occurs continuously while the experiment is idle, and once every several minutes during long experimental sequences.

tain constant power as we ramp the frequency across a large portion of the AOM bandwidth. These steps ensure that the experimentally applied pulse is a faithful representation of the desired profile.

5.6 BEAM ALIGNMENT STABILIZATION

Proper alignment of both Rydberg lasers onto the atoms is crucial to keep stable Rabi frequencies and stable light shifts. Since both lasers have long optical pathways (and final focusing lenses with $f = 25$ cm for the 1013 nm and $f = 40$ cm for the 420 nm), these laser alignments drift with small thermal changes of the experimental apparatus. To minimize sensitivity to such drifts, we perform intermittent feedback to keep both lasers aligned. Both lasers have piezoelectric inertia “slip-stick” motor-controlled mirrors placed one focal length before their focusing lenses, so computer control of these mirrors allows for control over beam positions in the plane of the atoms.

The beam alignment protocol uses CCD cameras (Thorlabs) which serve as position references for the atoms. A beam alignment software package (Fig. 5.5) extracts the beam posi-

tions on the CCD cameras, and can steer the beams to arbitrary chosen positions using the motor-controlled mirrors. Extraction of the beam position on the CCD sensor is done by Gaussian fitting for simple Gaussian beams. For ‘top-hat’ beams used for two-dimensional Rydberg experiments, we isolate the pixels which correspond to the main section of the top hat (excluding light which is deflected to the outside of the top-hat) and evaluate the centroid of those pixels.

The first calibration step, which is performed at least once per day, is to identify the location on the CCD camera that corresponds to optimal alignment onto the atoms. This is done by systematically displacing the beam to several different positions, and at each position measuring the intensity on the atoms (see Section 3.6). We fit these measurements, along with their corresponding positions on the CCD, to extract the optimal position. This procedure takes 5 minutes. For the next several hours or until the next day, we keep the beam aligned onto this position on the camera. This alignment is actively performed while the experiment is idle. While long sequences are running, periodic breaks are inserted to realign the lasers every ~ 10 minutes.

5.7 RAMAN LASER PULSE PROGRAMMING

The Raman laser used in hyperfine qubit experiments is controlled by an electro-optic phase modulator (EOM) which is driven at or near the hyperfine qubit frequency of 6.835 GHz. The phase modulation is converted to amplitude modulation using passive optics or interferometry (Chapter 4), which then serves as the effective drive field for the qubit. Dynamic control over the phase modulation signal therefore translates into dynamic control over the effective qubit drive field.

The EOM is driven by an amplified, frequency-doubled microwave source (Stanford Re-

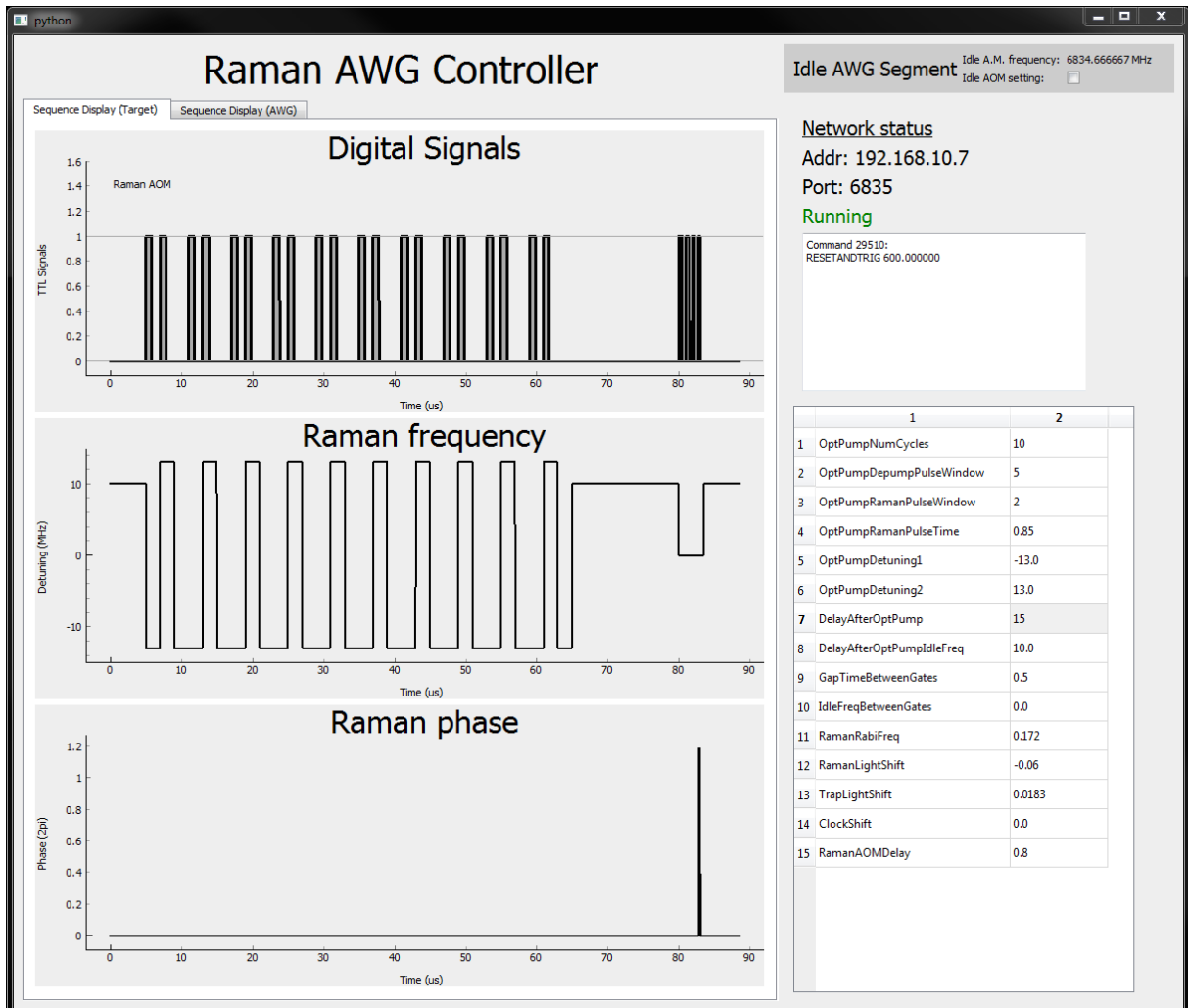


Figure 5.6: Raman laser control. The Raman laser is controlled by an AWG which modulates the EOM phase modulation signal, and also generates TTL signals to turn on and off the AOM which gates the laser. The AWG waveform is constructed based on many parameters, detailing both the timing and frequencies needed for optical pumping (left section of waveform), as well as the parameters for the target pulse sequence (right section of waveform).

search Systems, SG384). The SRS is IQ modulated, and the I and Q ports are controlled by two channels of an arbitrary waveform generator (AWG) from Spectrum Instrumentation. The IQ modulation is driven in single-sideband generation mode, where the Q port is always $\pi/2$ out of phase with the I port. The AWG output is programmed according to a time-dependent waveform which enables arbitrary frequency, phase, and amplitude control of the microwave source (Fig. 5.6). The AWG also outputs a TTL signal which gates an AOM to turn on/off the Raman laser, synchronously with the phase modulation signal.

Several parameters are calibrated and incorporated automatically into the AWG waveform. Firstly, the Raman laser induces a light shift on the atoms, which must be accounted for as the laser turns on and off. More subtly, the AOM which gates the Raman laser has a $\sim 1 \mu\text{s}$ propagation delay, which results in an offset between the timing of the EOM drive and the AOM pulsing. We measure the propagation delay, and automatically shift the timing of the AOM TTL signal to pre-compensate for the offset.

Raman pulse sequences are constructed using simple instructions which encode arbitrary qubit rotations; i.e., $\text{R}[\phi, \tau, \Delta]$ implements a pulse with relative phase ϕ , for duration τ , with a detuning Δ . Longer pulse sequences are constructed from such building blocks, and are transmitted over the local network.

5.8 REMOTE OPERATION OF EXPERIMENT

The experimental apparatus was constructed to be operated in-person. However, due to the COVID-19 pandemic, in-person access to lab was significantly restricted starting in March 2020. We transitioned as much experiment control as possible to be remotely operable, and most experiments performed since early 2020 have been conducted remotely.

The adaptations to remote operation have centered on remote control of the Rydberg laser

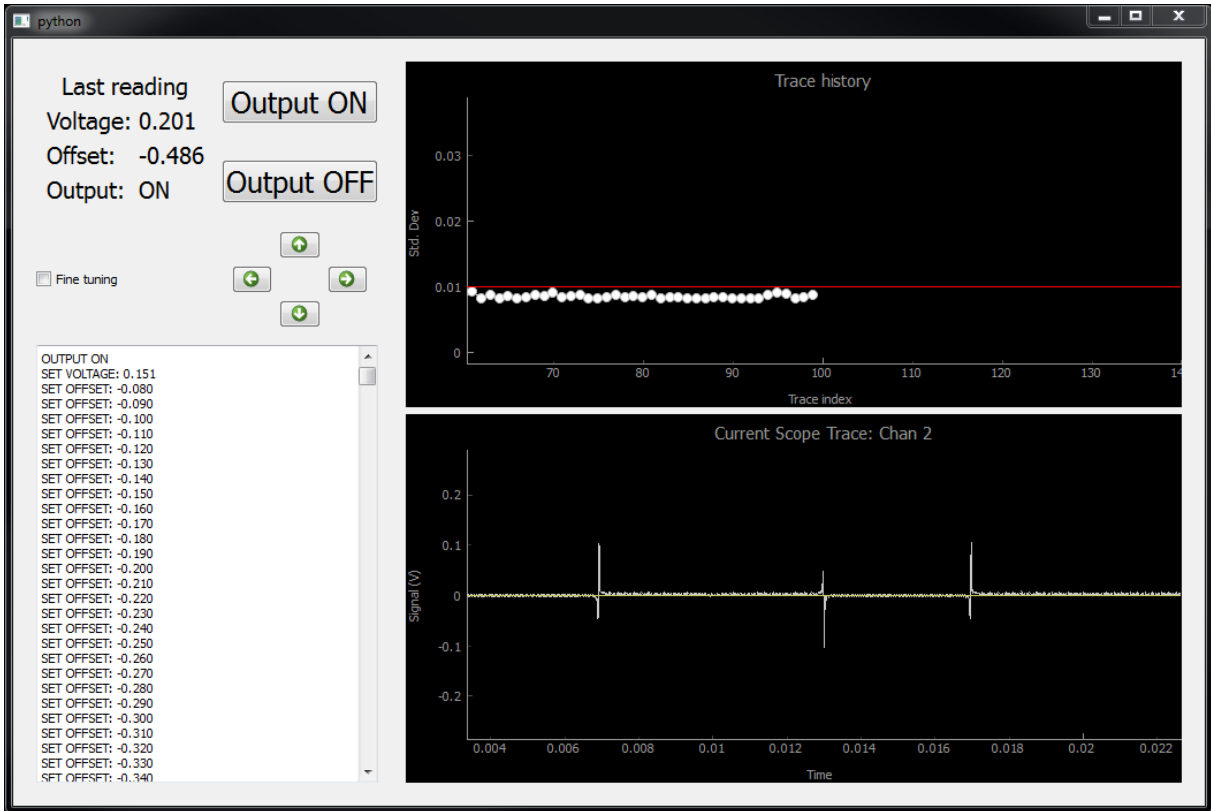


Figure 5.7: Remote laser locking. The 420 nm laser lock is one of the main instabilities in the lab, and requires periodic re-locking. When the lock is disabled, the laser frequency is ramped across the cavity resonance and the Pound Drever Hall (PDH) error signal is measured. The ramp is controlled by a computer-controlled frequency synthesizer, and is tuned to center the error signal and then zoom in, after which the lock is re-engaged. The noise on the error signal is monitored over time to automatically detect when the lock breaks.

systems. Both Rydberg laser locks utilize Vescent electronics (D2-125), which has a manual flip-switch for engaging the lock. To adapt to remote re-locking, we keep the lock switch engaged and use a TTL signal to remotely override and disable the lock when needed. With the lock disabled, an external signal (generated by a Rigol DG1022) can be output to ramp across the lock point. The error signal is tracked on an oscilloscope (Rigol DS1054Z), which is connected to the lab local network. A software module reads the oscilloscope traces and adjusts the ramp signal to center on the target lock point (Fig. 5.7). Using this tool, a remote user controlling the lab computers can relock the Rydberg lasers in around one minute. This infrastructure is currently implemented only for the 420 nm laser system, since the 1013 nm laser remains locked on several week timescales.

The 1013 nm source laser (Toptica DL Pro), which is locked to the ultra-low expansion reference cavity, is used to injection lock another laser diode. The injection locked laser diode is driven by a Thorlabs current controller (LDC205C), which allows for external modulation of the drive current. This external modulation signal is generated by a Rigol voltage supply (DP831), which is connected to the lab local network and is remotely controllable. This allows remote users to tune the laser diode current, which is necessary to periodically adjust to keep the injection lock in the center of the locking window.

The 1013 nm injection locked diode is used to seed a high-power fiber amplifier (ALS-IR-1015-10-A-SP by Azur Light Systems). The fiber amplifier output is tunable with an external modulation input, and similarly to the injection lock, we use a computer-controlled power supply (Rigol DP831) to program the output power setpoint.

While much of the equipment can be connected to the local lab network for computer control or monitoring, several important instruments cannot be connected to the network. We therefore installed several web cameras around the lab (Swann 12-camera 1080p DVR Surveil-

lance System), which are used to check if laser frequency and power locks are stable, to monitor water chillers, vacuum ion pump gauge, and other equipment interfaces. While the cameras natively offer computer monitoring, we use an additional camera screen capture (Elgato Game Capture HD60 S+) to view the images with reduced latency.

Part III

Experimental Results

6

Atom-by-atom assembly of defect-free one-dimensional cold atom arrays

The detection and manipulation of individual quantum particles, such as atoms or photons, is now routinely performed in many quantum physics experiments [67, 68]; however, retaining the same control in large-scale systems remains an outstanding challenge. For example, major efforts are currently aimed at scaling up ion-trap and superconducting platforms, where high-fidelity quantum computing operations have been demonstrated in registers consisting of several qubits [69, 70]. In contrast, ultracold quantum gases composed of neutral atoms offer inherently large system sizes. However, arbitrary single atom control is highly demand-

ing and its realization is further limited by the slow evaporative cooling process necessary to reach quantum degeneracy. Only in recent years has individual particle detection [71, 72] and basic single-spin control [73] been demonstrated in low entropy optical lattice systems. Here we demonstrate atom-by-atom assembly of large defect-free 1D arrays of cold neutral atoms [74, 75].

We use optical microtraps to directly extract individual atoms from a laser-cooled cloud [23, 76, 77] and employ recently demonstrated trapping techniques [78–81] and single-atom position control [82–84, 26] to create desired atomic configurations. Central to our approach is the use of single-atom detection and real-time feedback [82, 26] to eliminate the entropy associated with the probabilistic trap loading [23] (currently limited to ninety percent loading probability even with advanced techniques [85–87]). Related to the fundamental concept of “Maxwell’s demon” [74, 75], this method allows us to rapidly create large defect-free arrays, and when supplemented with appropriate atom-atom interactions [80, 81, 88, 27, 89, 29, 90–92] provides a potential platform for scalable experiments with individually controlled neutral atoms.

6.1 OPTICAL TWEEZER ARRAYS

The experimental protocol is illustrated in Fig. 6.1A. An array of 100 tightly focused optical tweezers is loaded from a laser-cooled cloud. The collisional blockade effect ensures that each individual tweezer is either empty or occupied by a single atom [23]. A first high-resolution image yields single-atom resolved information about the trap occupation, which we use to identify empty traps and to switch them off. The remaining occupied traps are rearranged into a regular, defect-free array and we detect the final atom configuration with a second high-resolution image. Our implementation relies on fast, real-time control of the tweezer positions

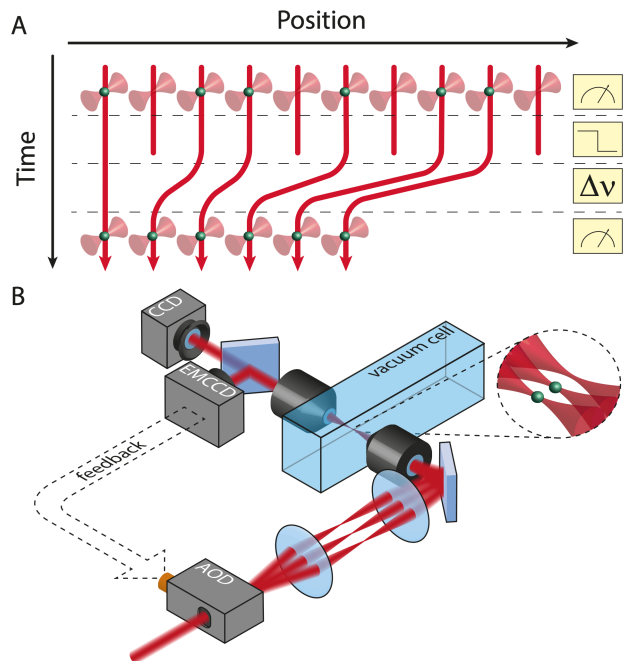


Figure 6.1: Protocol for creating defect-free arrays. (A) A first image identifies optical microtraps loaded with a single atom, and empty traps are turned off. The loaded traps are moved to fill in the empty sites and a second image verifies the success of the operation. (B) The trap array is produced by an acousto-optic deflector (AOD) and imaged with a 1:1 telescope onto a 0.5 NA microscope objective, which creates an array of tightly focused optical tweezers in a vacuum chamber. An identical microscope objective is aligned to image the same focal plane. A dichroic mirror allows us to view the trap light on a charge-coupled-device camera (CCD) while simultaneously detecting the atoms via fluorescence imaging on an electron-multiplied-CCD camera (EMCCD). The rearrangement protocol is realized through fast feedback onto the multi-tone radio-frequency (RF) field driving the AOD.

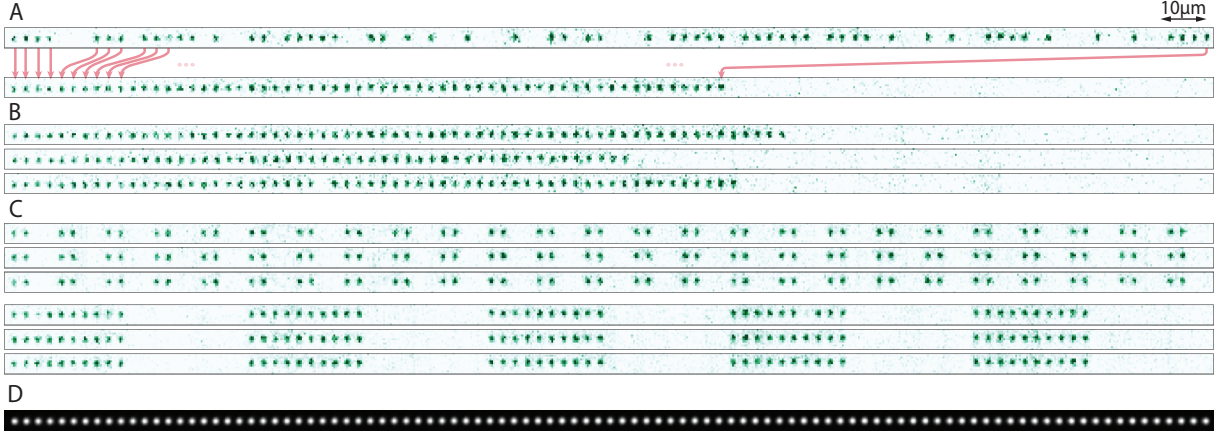


Figure 6.2: Assembly of regular atom arrays. (A) Single-shot, single-atom resolved fluorescence images recorded with the EMCCD before (top) and after (bottom) rearrangement. Defects are identified and the loaded traps are rearranged according to the protocol in Fig. 6.1, indicated by arrows for a few selected atoms. (B) Two instances of successfully rearranged arrays (first two pictures), and one instance (last picture) where a defect is visible after rearrangement. (C) The final arrangement of atoms is flexible, and we generate, e.g., clusters of two (top) or ten (bottom) atoms. Non-periodic arrangements and adjustable lattice spacings are also possible. (D) High-resolution CCD image of trap array. Our default configuration for loading atoms consists of an array of 100 tweezers with a spacing of 0.49 MHz between the RF-tones, corresponding to a real-space distance of 2.6 μm between the focused beams (Appendix C).

(Fig. 6.1B), which we achieve by employing an acousto-optic deflector (AOD) that we drive with a multi-tone radio-frequency (RF) signal.

This generates an array of deflected beams, each controlled by its own RF-tone [80, 81]. The resulting beam array is then focused into our vacuum chamber and forms an array of optical tweezers, each with a Gaussian waist of ≈ 900 nm, a wavelength of 809 nm, and a trap depth of $U/k_B \approx 0.9$ mK (k_B , Boltzmann constant) that is homogeneous across the array within 2% (Appendix C). The tweezer array is loaded from a laser-cooled cloud of Rubidium-87 atoms in a magneto-optical trap (MOT). After the loading procedure, we let the MOT cloud disperse and we detect the occupation of the tweezers with fluorescence imaging. Fast, single-shot, single-atom resolved detection with 20 ms exposure is enabled by a sub-Doppler laser-cooling configuration that remains active during the remainder of the sequence (Fig. 6.2A-C, and Chapter 2). Our fluorescence count statistics show that individual traps are either empty or occupied by a single atom [23], and we find probabilistically filled arrays with an

average single atom loading probability of $p \approx 0.6$ (see Fig. 6.2A and 6.3A).

6.2 REAL-TIME REARRANGEMENT OF ATOMS

The central part of our scheme involves the rearrangement procedure for assembling defect-free arrays (see Fig. 6.1A). In the first step, unoccupied traps are switched off by setting the corresponding RF-amplitudes to zero. In a second step, all occupied tweezers are moved to the left until they stack up with the original spacing of 2.6 m. This movement is generated by sweeping the RF-tones to change the deflection angles of the AOD and lasts 3 ms (Appendix C). Finally, we detect the resulting atom configuration with a second high-resolution image. These steps implement a reduction of entropy via measurement and feedback. The effect is immediately visible in the images shown in Fig. 6.2A,B. The initial filling of our array is probabilistic, whereas the rearranged configurations show highly ordered atom arrays. Our approach also allows us to construct flexible atomic patterns (Fig. 6.2C).

The rearrangement procedure creates defect-free arrays with high fidelity. This can be quantified by considering the improvement of single atom occupation probabilities (Fig. 6.3A) and the success probabilities, p_N , for creating defect-free arrays of length N (Fig. 6.3B). The single atom occupation probability in the left-most forty traps increases from ≈ 0.6 before rearrangement to 0.988(3) after rearrangement, demonstrating our ability for high-fidelity single-atom preparation. Furthermore, the success probabilities for creating defect-free arrays show an exponential improvement. Prior to rearrangement, the probability of finding a defect-free array of length N is exponentially suppressed with $p_N = p^N$ where $p \approx 0.6$ (blue circles, Fig. 6.3B). After rearrangement, we find success probabilities as high as $p_{30} = 0.75(1)$ and $p_{50} = 0.53(1)$ (red circles, Fig. 6.3B).

The same exponential improvement is observed by considering the average wait time for

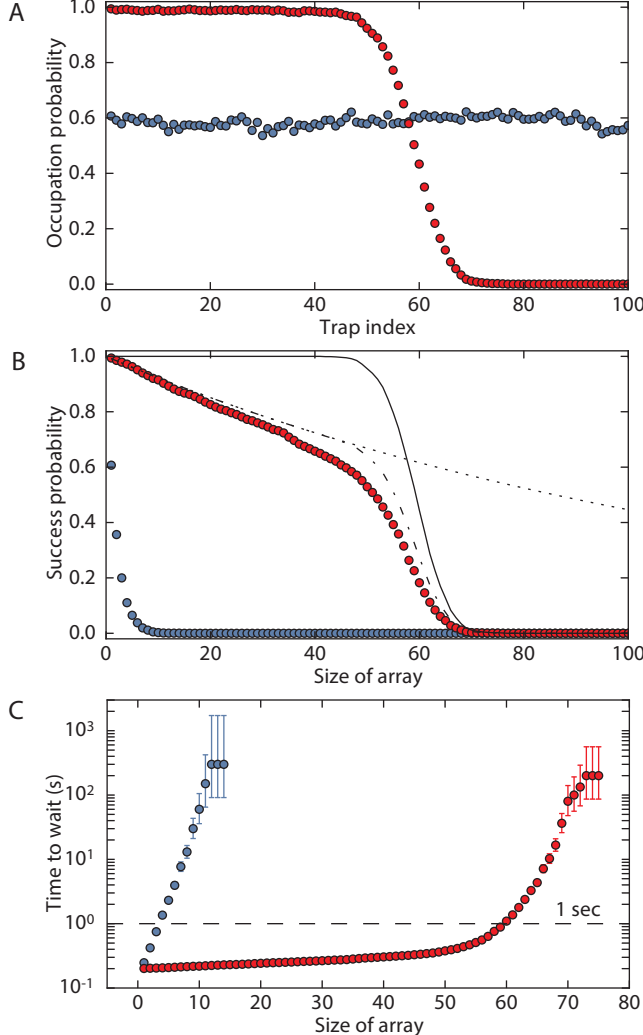


Figure 6.3: Quantifying the rearrangement performance. (A) The initial loading (blue circles) results in an occupation probability of ≈ 0.6 for each trap in the array. After rearrangement (red circles), close to unity filling is reached on the left side of the array. (B) In the initial image, the probability of finding a defect-free length- N array (starting from the leftmost trap) falls off exponentially with N (blue circles). Following the rearrangement of all loaded traps to form the largest possible array, we demonstrate strongly enhanced success probabilities at producing defect-free arrays (red circles). Theory curves show limits set by the total initial atom number (solid line), the background limited lifetime of $\tau = 6.2$ s (dashed line) and the product of both (dashed dotted line) (Appendix C). (C) Expected amount of time to wait on average to produce a defect-free array of a given size taking into account the experimental cycle time of 200 ms (150 ms without rearrangement). Without rearrangement, the wait time grows exponentially (blue circles). Employing the rearrangement procedure, we can produce arrays of length 50 in less than 400 ms (red circles). All error bars denote 68% confidence intervals, which are smaller than the marker size in (A) and (B).

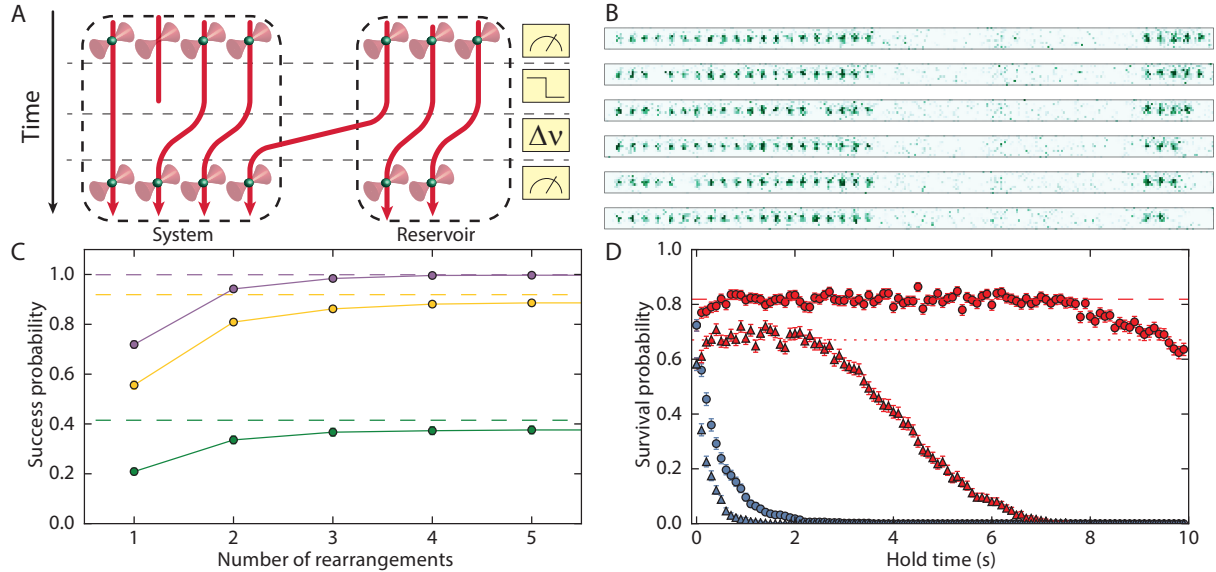


Figure 6.4: Creating and maintaining regular arrays using an atomic reservoir. (A) For a given target array size, surplus atoms are kept in a reservoir and used for repetitive reloading of the array. (B) A 20 atom target array with a reservoir of atoms on the right. Defects occasionally develop in the target array and are replaced by atoms in the reservoir. The reservoir depletes as it is used to fill in defects. (C) By performing repeated rearrangements (once every 50 ms) the probability to successfully produce a defect-free array in any of these attempts increases and approaches the limit set by the number of initially loaded atoms (dashed lines). We show data for targeting 40 (purple), 50 (yellow), and 60 (green) atom arrays. Solid lines are guides to the eye. (D) Probing for defects and filling them once every 100 ms from the reservoir extends the lifetime of a defect-free array. Shown is the success probability of maintaining arrays of 20 (circles) and 40 (triangles) atoms with (red) and without (blue) replenishing atoms from the reservoir. With replenishing, the probability to maintain a defect-free array remains at a fixed plateau for as long as we have surplus atoms in the reservoir. The initial plateau value is set by the probability that no atoms in the array are lost in 100 ms (calculated value for 10 s single atom lifetime shown as the dotted line). All error bars denote 68% confidence intervals, which are smaller than the marker size in (C).

producing defect-free arrays, given by T/p_N , where $T = 200$ ms is the cycling time of our experiment (see Fig. 6.3B). For example, we are able to generate defect-free arrays of 50 atoms with an average wait time of less than 400 ms (red circles, Fig. 6.3C).

6.3 REPEATED REARRANGEMENT WITH AN ATOMIC RESERVOIR

The success probabilities can be further enhanced through multiple repetitions of the rearrangement protocol. Figure 6.4 illustrates the procedure in which we target an atomic array of fixed length and create a reservoir from surplus atoms in a separate zone. After the initial arrangement of atoms into the target and reservoir zones, we periodically take images to

identify defects in the target array and pull atoms from the reservoir to fill in these defects.

This enhances our initial success probabilities at producing defect-free arrays within one MOT-loading cycle to nearly the ideal limit (Fig. 6.4C).

Finally, a similar procedure can be used for correcting errors associated with atomic loss. This becomes a significant limitation for large arrays because for a given lifetime of an individual atom in the trap τ , the corresponding lifetime of the N atom array scales as τ/N . To counter this loss, we repeatedly detect the array occupation after longer time intervals and replenish lost atoms from the reservoir. This procedure leads to exponentially enhanced lifetimes of our arrays (Fig. 6.4D).

6.4 DISCUSSION AND OUTLOOK

These results demonstrate the ability to generate and control large, defect-free arrays at a fast repetition rate. The success probabilities are limited by two factors: the initial number of loaded atoms and losses during rearrangement. For example, the average total atom number in our array is 59 ± 5 (Appendix C), which results in the cutoff in the success probability in Fig. 6.3B starting from $N \approx 50$ (solid line). For shorter arrays, the fidelity is mostly limited by losses during rearrangement. These losses are dominated by our finite vacuum-limited lifetime, which varies from $\tau \approx 6$ s to $\tau \approx 12$ s (depending on the setting of our atomic dispenser source), and are only minimally increased by the movement of the atoms (Appendix C). The single atom occupation probability is correspondingly reduced by a factor $\exp(-t_r/\tau)$, where $t_r = 50$ ms is the time for the whole rearrangement procedure (Appendix C). This results in the success probabilities of creating length- N arrays scaling as $\exp(-t_r N/\tau)$, which dominates the slope for $N \sim 50$ in Fig. 6.3B (dashed line). Currently, we reach vacuum limited lifetimes only with sub-Doppler cooling applied throughout the sequence. However, the lifetime with-

out cooling could be improved, for example, by using a different trapping laser and trapping wavelength (Appendix C).

The size of the final arrays can be considerably increased by implementing a number of realistic experimental improvements. For example, the initial loading probability could be enhanced to 0.9 [85–87] and the vacuum limited lifetime could be improved to $\tau \approx 60$ s in an upgraded vacuum chamber. Increasing the number of traps in the current configuration is difficult because of the AOD bandwidth of ≈ 50 MHz and strong parametric heating introduced when the frequency spacing of neighboring traps approaches ≈ 450 kHz (Appendix C). However, implementing two-dimensional (2d) arrays could provide a path towards realizing thousands of traps, ultimately limited by the availability of laser power and the field of view of high-resolution objectives. Such 2d configurations could be realized by either directly using a 2d-AOD or by creating a static 2d lattice of traps (using spatial light modulators [79] or optical lattices [77]) and sorting atoms with an independent AOD (Chapter 9 and Appendix C). With increased loading efficiencies [85–87], realistic estimates for the rearrangement time t_r in such 2d arrays indicate that the robust creation of defect-free arrays of hundreds of atoms is feasible (Appendix C). Finally, the repetitive interrogation techniques, in combination with periodic reservoir reloading from a cold atom source (such as a MOT), could be used to maintain arrays indefinitely.

Atom-by-atom assembly of defect-free arrays forms a scalable platform with unique possibilities. It combines features that are typically associated with ion trapping experiments, such as single-qubit addressability [93, 94] and fast cycling times, with the flexible optical trapping of neutral atoms in a scalable fashion. Furthermore, in contrast to solid-state platforms, such atomic arrays are highly homogeneous (Appendix C) and mostly decoupled from their environment. The homogeneity of our array should also allow for cooling of the atomic motion via

simultaneous sideband cooling in all tweezers at once [95, 43].

These features provide an excellent starting point for multi-qubit experiments, studies of quantum many body effects and for exploring future applications. The required interactions between the atoms can be engineered using several approaches. Even without sideband cooling, exciting the atoms into high-lying Rydberg states would introduce strong dipole interactions that can be used for fast entangling gates [88, 27, 29]. The parallelism afforded by our flexible atom rearrangement enables efficient diagnostics of such Rydberg-mediated entanglement. These interactions may also enable approaches to quantum simulations that involve both coherent coupling and engineered dissipation [89, 29], as well as large-scale entangled quantum states for applications in precision measurements [96].

An alternative approach to engineering interactions involves the integration of atom arrays with nanophotonic platforms as demonstrated previously [90, 91]. These enable photon-mediated interactions that can be employed to couple the atoms within a local multi-qubit register or for efficient communication between the registers using a modular quantum network architecture [69]. Finally, our platform could enable new bottom-up approaches to studying quantum many-body physics in Hubbard models [80, 81, 92], where atomic Mott insulators with fixed atom number and complex spin patterns could be directly assembled. This requires atom temperatures close to the ground state, coherent tunneling between the traps, and sizable on-site interactions. With side-band cooling, ground state fractions in excess of 90% have already been demonstrated [95, 43], and can likely be improved via additional optical trapping along the longitudinal tweezer axes, which would also increase on-site interaction strengths. Coherent tunneling of Rb atoms between similarly sized tweezers has been observed before by reducing the tweezer distance [80, 81]. The parametric heating, currently limiting the minimal distance between our traps, could be reduced by working with shallower traps, as

needed for tunneling, and by employing fewer traps to increase the frequency separation between neighboring traps. Eventually, this approach could be applied to create ultracold quantum matter composed of exotic atomic species or complex molecules [97, 98] that are difficult to cool evaporatively.

7

Probing many-body dynamics on a 51-atom quantum simulator

The realization of fully controlled, coherent many-body quantum systems is an outstanding challenge in modern science and engineering. As quantum simulators, they can provide unique insights into strongly correlated quantum systems and the role of quantum entanglement [15], and enable realizations and studies of new states of matter, even away from equilibrium. These systems also form the basis for the realization of quantum information processors [99]. While basic building blocks of such processors have been demonstrated in systems of a few coupled qubits [69, 70, 100], the current challenge is to increase the number of coherent

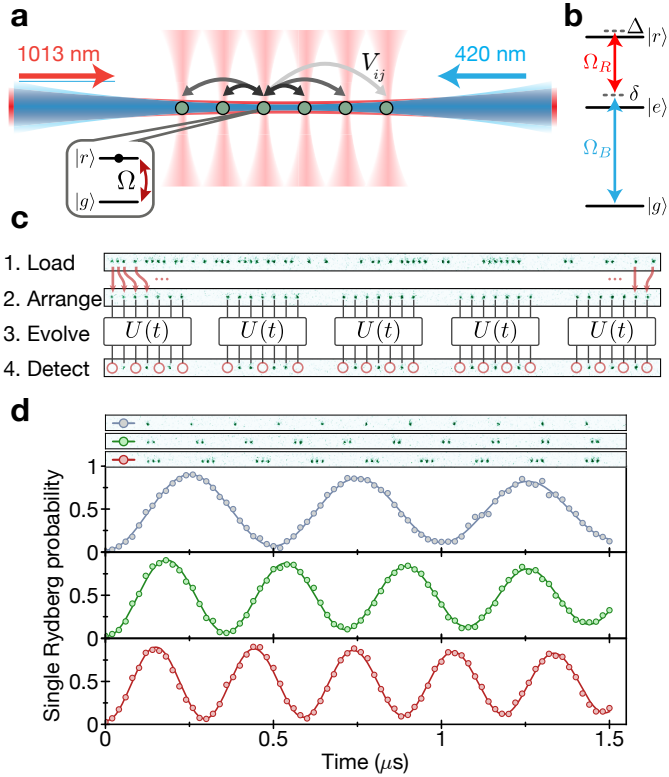


Figure 7.1: Experimental platform. **a**, Individual ^{87}Rb atoms are trapped using optical tweezers and arranged into defect-free arrays. Coherent interactions V_{ij} between the atoms are enabled by exciting them to a Rydberg state, with strength Ω and detuning Δ . **b**, A two photon process is used to couple the ground state $|g\rangle = |5S_{1/2}, F = 2, m_F = -2\rangle$ to the Rydberg state $|r\rangle = |70S_{1/2}, J = 1/2, m_J = -1/2\rangle$ via an intermediate state $|e\rangle = |6P_{3/2}, F = 3, m_F = -3\rangle$ using circularly polarized 420 nm and 1013 nm lasers (typically $\delta \sim 2\pi \times 560\text{MHz} \gg \Omega_B, \Omega_R \sim 2\pi \times 60, 36\text{ MHz}$). **c**, The experimental protocol consists of loading the atoms into a tweezer array (1) and rearranging them into a preprogrammed configuration (2). After this, the system evolves under $U(t)$ with tunable parameters $\Delta(t), \Omega(t), V_{ij}$. This can be implemented in parallel on several non-interacting sub-systems (3). We then detect the final state by fluorescence imaging (4). **d**, For resonant driving ($\Delta = 0$), isolated atoms (blue points) display Rabi oscillations between $|g\rangle$ and $|r\rangle$. Arranging the atoms into fully blockaded clusters of $N = 2$ (green) and $N = 3$ (red) atoms results in only one excitation being shared between the atoms in the cluster, while the Rabi frequency is enhanced by \sqrt{N} . The probability to detect more than one excitation in the cluster is $\leq 5\%$. Error bars indicate 68% confidence intervals (CI) and are smaller than the marker size.

ently coupled qubits to potentially perform tasks that are beyond the reach of modern classical machines.

A number of physical platforms are currently being explored to reach these challenging goals. Systems composed of about 10-20 individually controlled atomic ions have been used to create entangled states and explore quantum simulations of Ising spin models [101, 102]. Similarly sized systems of programmable superconducting qubits have been recently implemented [103]. Quantum simulations have been carried out in larger ensembles of over 100 trapped ions without individual readout [104]. Strongly interacting quantum dynamics have been explored using optical lattice simulators [105]. These systems are already addressing computationally difficult problems in quantum dynamics [106] and the fermionic Hubbard model [107]. Larger-scale Ising-like machines have been realized in superconducting [108] and optical [109] systems but these realizations lack either coherence or quantum nonlinearity that are essential for achieving full quantum speedup.

7.1 STRONGLY INTERACTING ATOM ARRAYS

A promising avenue for realizing strongly interacting quantum matter involves coherent coupling of neutral atoms to highly excited Rydberg states [88, 89] (Fig. 7.1a). This results in repulsive van der Waals interactions ($V_{ij} = C/R_{ij}^6, C > 0$) between Rydberg atom pairs at a distance R_{ij} [88]. Such interactions have recently been used for realizing quantum gates [110–112], implementing strong photon-photon interactions [113] and studying quantum many-body physics of Ising spin systems in optical lattices [114–116] and in probabilistically loaded dipole trap arrays [117]. Our approach combines such strong, controllable interactions with atom-by-atom assembly of cold neutral ^{87}Rb atom arrays [25, 24, 26]. The quantum dynam-

ics of this system is governed by the Hamiltonian

$$\frac{\mathcal{H}}{\hbar} = \sum_i \frac{\Omega_i}{2} \sigma_x^i - \sum_i \Delta_i n_i + \sum_{i < j} V_{ij} n_i n_j, \quad (7.1)$$

where Δ_i are the detunings of the driving lasers from the Rydberg state (Fig. 7.1b), $\sigma_x^i = |g_i\rangle\langle r_i| + |r_i\rangle\langle g_i|$ describes the coupling between the ground state $|g\rangle$ and the Rydberg state $|r\rangle$ of an atom at position i , driven at Rabi frequency Ω_i , and $n_i = |r_i\rangle\langle r_i|$. Here, we focus on homogeneous coherent coupling ($|\Omega_i| = \Omega, \Delta_i = \Delta$), controlled by changing laser intensities and detunings in time. The interaction strength V_{ij} is tuned by either varying the distance between the atoms or coupling them to a different Rydberg state.

The experimental protocol that we implement is depicted in Fig. 7.1c (see also D.1). First, atoms are loaded from a magneto-optical trap into a tweezer array created by an acousto-optic deflector (AOD). We then use a measurement and feedback procedure that eliminates the entropy associated with the probabilistic trap loading and results in the rapid production of defect-free arrays with over 50 laser cooled atoms as described previously [24]. These atoms are prepared in a preprogrammed spatial configuration in a well-defined internal ground state $|g\rangle$ (Appendix D). We then turn off the traps and let the system evolve under the unitary time evolution $U(\Omega, \Delta, t)$, which is realized by coupling the atoms to the Rydberg state $|r\rangle = |70S_{1/2}\rangle$ with laser light along the array axis (Fig. 7.1a). The final states of individual atoms are detected by turning the traps back on, and imaging the recaptured ground state atoms via atomic fluorescence, while the anti-trapped Rydberg atoms are ejected. The atomic motion in the absence of traps limits the time window for exploring coherent dynamics. For a typical sequence duration $\sim 1 \mu\text{s}$ used in this work, the resulting atom loss probability is below 1% (see 2.8 of Chapter 2).

The strong, coherent interactions between Rydberg atoms provide an effective coherent constraint that prevents simultaneous excitation of nearby atoms into Rydberg states. This is the essence of the so-called Rydberg blockade [88], demonstrated in Fig. 7.1d. When two atoms are sufficiently close so that their Rydberg-Rydberg interactions V_{ij} exceed the effective Rabi frequency Ω , then multiple Rydberg excitations are suppressed. This defines the Rydberg blockade radius, R_b , for which $V_{ij} = \Omega$ ($R_b = 9 \mu\text{m}$ for $|r\rangle = |70S_{1/2}\rangle$ and $\Omega = 2\pi \times 2 \text{ MHz}$ as used here). In the case of resonant driving of atoms separated by $a = 23 \mu\text{m}$, we observe Rabi oscillations associated with non-interacting atoms (blue curve on Fig. 7.1d). However, the dynamics change significantly as we bring multiple atoms close to each other ($a = 2.87 \mu\text{m} < R_b$). In this case, we observe Rabi oscillations between the ground state and a collective W-state with exactly one excitation $\sim \sum_i \Omega_i |g_1 \dots r_i \dots g_N\rangle$ with the characteristic \sqrt{N} -scaling of the collective Rabi frequency [118, 119, 117]. These observations allow us to quantify the coherence properties of our system (see Appendix D for details and Fig. D.2). In particular, the contrast of Rabi oscillations in Fig. 7.1d is mostly limited by the state detection fidelity (93% for $|r\rangle$ and $\sim 98\%$ for $|g\rangle$, see Chapter 3 and Appendix D). The individual Rabi frequencies are controlled to better than 3% across the array, while the coherence time is ultimately limited by the small probability of spontaneous emission from the intermediate state $|e\rangle$ during the laser pulse (scattering rate $0.022/\mu\text{s}$, Appendix D).

7.2 PROGRAMMABLE QUANTUM SIMULATOR

In the case of homogeneous coherent coupling considered here, Hamiltonian (1) closely resembles the paradigmatic Ising model for effective spin-1/2 particles with variable interaction range. Its ground state exhibits a rich variety of many-body phases that break distinct spatial symmetries (Fig. 7.2a). Specifically, at large, negative values of Δ/Ω , its ground state

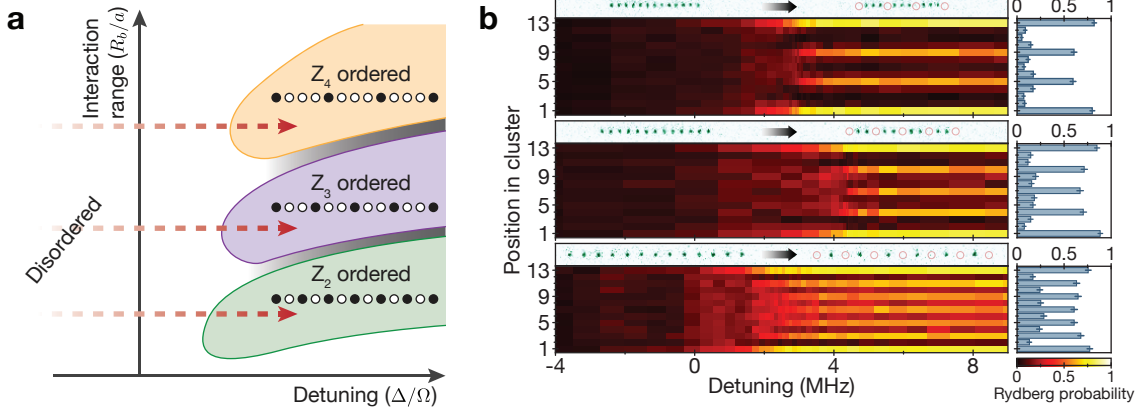


Figure 7.2: Phase diagram and buildup of crystalline phases. **a**, The schematic ground-state phase diagram of Hamiltonian (7.1) displays phases with various broken symmetries depending on the interaction range R_b/a (R_b blockade radius, a trap spacing) and detuning Δ (see main text). Shaded areas indicate potential incommensurate phases (diagram adapted from [120]). Shown is the experimentally accessible region with further details to be found in [120–122]. **b**, The buildup of Rydberg crystals on a 13 atom array is observed by slowly changing the laser parameters as indicated by the red arrows in a (see also Fig. 7.3a). The bottom panel shows a configuration where the atoms are $a = 5.74 \mu\text{m}$ apart which results in a nearest neighbor interaction of $V_{i,i+1} = 2\pi \times 24 \text{ MHz}$ and leads to a Z_2 order where every other atom is excited to the Rydberg state $|r\rangle$. The right bar plot displays the final, position-dependent Rydberg probability (error bars denote 68% CI). The configuration in the middle panel ($a = 3.57 \mu\text{m}$, $V_{i,i+1} = 2\pi \times 414.3 \text{ MHz}$) results in Z_3 order and the top panel ($a = 2.87 \mu\text{m}$, $V_{i,i+1} = 2\pi \times 1536 \text{ MHz}$) in a Z_4 ordered phase. For each configuration, we show a single-shot fluorescence image before (left) and after (right) the pulse. Red circles highlight missing atoms, which are attributed to Rydberg excitations.

corresponds to all atoms in the state $|g\rangle$, corresponding to paramagnetic or disordered phase.

As Δ/Ω is increased towards large positive values, the number of atoms in $|r\rangle$ rises and interactions between them become significant. This gives rise to spatially ordered phases where Rydberg atoms are regularly arranged across the array, resulting in ‘Rydberg crystals’ with different spatial symmetries [120, 123], as illustrated in Fig. 7.2a. The origin of these correlated states can be understood intuitively by first considering the situation when $V_{i,i+1} \gg \Delta \gg \Omega \gg V_{i,i+2}$, i.e. blockade for neighboring atoms but negligible interaction between next-nearest neighbors. In this case, the ground state corresponds to a Rydberg crystal breaking Z_2 translational symmetry that is analogous to antiferromagnetic order in magnetic systems. Moreover, by tuning the parameters such that $V_{i,i+1}, V_{i,i+2} \gg \Delta \gg \Omega \gg V_{i,i+3}$ and $V_{i,i+1}, V_{i,i+2}, V_{i,i+3} \gg \Delta \gg \Omega \gg V_{i,i+4}$, we obtain arrays with broken Z_3 and Z_4 symmetries, respectively (Fig. 7.2).

To prepare the system in these phases, we dynamically control the detuning $\Delta(t)$ of the driving lasers to adiabatically transform the ground state of the Hamiltonian from a product state of all atoms in $|g\rangle$ into crystalline states [123, 115]. In contrast to prior work where Rydberg crystals are prepared via a sequence of avoided crossings [123, 115, 124], the operation at a finite Ω and well-defined atom separation allows us to directly move across a single phase transition into the desired phase [122].

In the experiment, we first prepare all atoms in state $|g\rangle = |5S_{1/2}, F = 2, m_F = -2\rangle$ by optical pumping. We then switch on the laser fields and sweep the two-photon detuning from negative to positive values using a functional form shown in Fig. 7.3a. Fig. 7.2b displays the resulting single atom trajectories in a group of 13 atoms for three different interaction strengths as we vary the detuning Δ . In each of these instances, we observe a clear transition from the initial state $|g_1, \dots, g_{13}\rangle$ to an ordered state of different broken symmetry. The

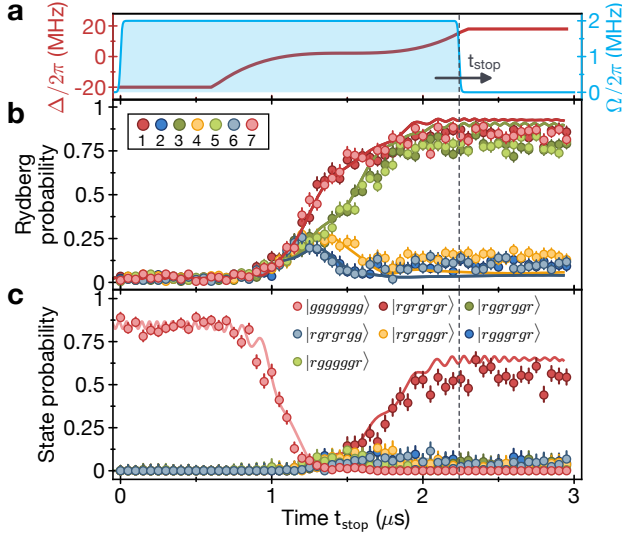


Figure 7.3: Comparison with a fully coherent simulation. **a**, The laser driving consists of a square shaped pulse $\Omega(t)$ with a detuning $\Delta(t)$ that is chirped from negative to positive values. **b**, Time evolution of Rydberg excitation probability for each atom in a $N = 7$ atom cluster (colored points), obtained by varying the duration of laser excitation pulse $\Omega(t)$. The corresponding curves are theoretical single atom trajectories obtained by an exact simulation of quantum dynamics with (7.1), the functional form of $\Delta(t)$ and $\Omega(t)$ used in the experiment, and finite detection fidelity. **c**, Evolution of the seven most probable many-body states. The target state is reached with 54(4)% probability (77(6)% when corrected for finite detection fidelity). Error bars denote 68% CI.

distance between the atoms determines the interaction strength which leads to different crystalline orders for a given final detuning. To achieve a Z_2 order, we arrange the atoms with a spacing of $5.74 \mu\text{m}$, which results in a measured nearest neighbor interaction (see D.3) of $V_{i,i+1} = 2\pi \times 24 \text{ MHz} \gg \Omega = 2\pi \times 2 \text{ MHz}$, while the next-nearest neighbor interaction is small ($2\pi \times 0.38 \text{ MHz}$). This results in a buildup of antiferromagnetic order where every other trap site is occupied by a Rydberg atom (Z_2 order). By reducing the spacing between the atoms to $3.57 \mu\text{m}$ and $2.87 \mu\text{m}$, Z_3 - and Z_4 - orders are respectively observed (Fig. 7.2b).

We benchmark the performance of the quantum simulator by comparing the measured Z_2 order buildup with theoretical predictions for a $N = 7$ atom system, obtained via exact numerical simulations. As shown in Fig. 7.3, this fully coherent simulation without free parameters yields excellent agreement with the observed data when the finite detection fidelity is

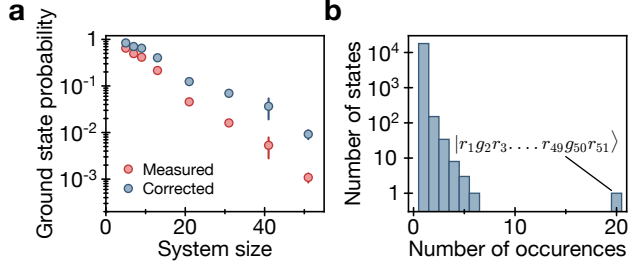


Figure 7.4: Scaling behavior. **a**, Preparation fidelity of the crystalline ground state as a function of cluster size. The red dots are the measured values and the blue dots are corrected for finite detection fidelity (Appendix D). Error bars denote 68% CI. **b**, Number of observed many-body states per number of occurrences out of 18439 experimental realizations in a 51-atom cluster. The most occurring state is the ground state of the many-body Hamiltonian.

accounted for. The evolution of the many-body states in Fig. 7.3c shows that we measure the perfect antiferromagnetic state with 54(4)% probability. When corrected for the known detection infidelity, we find that the desired many-body state is reached with a probability of $p = 77(6)\%$.

To investigate how the preparation fidelity depends on system size, we perform detuning sweeps on arrays of various sizes (Fig. 7.4a). We find that the probability of observing the system in the many-body ground state at the end of the sweep decreases as the system size is increased. However, even at system sizes as large as 51 atoms, the perfectly ordered crystalline many-body state is obtained with $p = 0.11(2)\%$ ($p = 0.9(2)\%$ when corrected for detection fidelity). These probabilities compare favorably with those measured previously for smaller systems [102, 125] (see also D.5) and are remarkably large in view of the exponentially large 2^{51} -dimensional Hilbert space of the system. Furthermore, we find that the state with perfect Z_2 order is by far the most commonly observed many-body state (Fig. 7.4b). The observations of perfectly ordered states resulting from the dynamical evolution across the phase transition indicate that a substantial degree of quantum coherence is preserved in our 51 atom system over the entire evolution time.

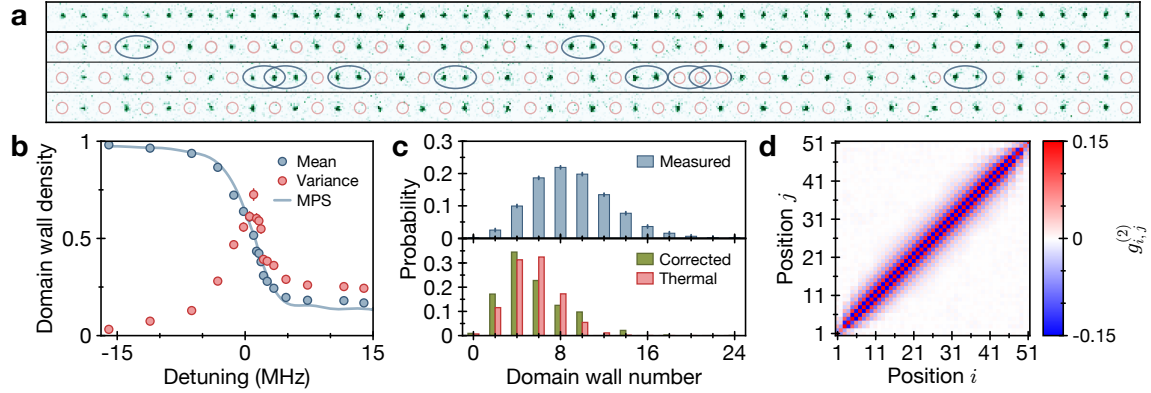


Figure 7.5: Quantifying Z_2 order in a $N = 51$ atom array after slow detuning sweep. **a**, Single-shot fluorescence images of a 51 atom array before applying the adiabatic pulse (top row) and after the pulse (bottom three rows correspond to three separate instances). Red circles mark missing atoms, which are attributed to Rydberg excitations. Domain walls are identified as either two neighboring atoms in the same state or a ground state atom at the edge of the array (Appendix D), and are indicated with ellipses. Long Z_2 ordered chains between domain walls can be observed. **b**, Blue points show the mean of the domain wall density as a function of detuning during the sweep. Error bars show the standard error of the mean, and are smaller than the marker size. The red points are the corresponding variances, where the error bars represent one standard deviation. The onset of the phase transition is witnessed by a decrease in the domain wall density and a peak in the variance (see main text for details). Each point is obtained from ~ 1000 realizations. The solid blue curve is a fully coherent MPS simulation without free parameters (bond dimension $D = 256$), taking measurement fidelities into account. **c**, Domain wall number distribution for $\Delta = 2\pi \times 14$ MHz, obtained from 18439 experimental realizations (blue bars, top plot). Error bars indicate 68% CI. Owing to the boundary conditions, only even numbers of domain walls can appear (Appendix D). Green bars in the bottom plot show the distribution obtained by correcting for finite detection fidelity using a maximum likelihood method (Appendix D), which results in an average number of 5.4 domain walls. Red bars show the distribution of a thermal state with the same mean domain wall density (Appendix D). **d**, Measured correlation function (7.2) in the Z_2 phase.

7.3 QUANTUM DYNAMICS ACROSS A PHASE TRANSITION

We next present a detailed study of the transition into the Z_2 phase in an array of 51 atoms, which allows us to minimize edge effects and study properties of the bulk. We first focus on analyzing the atomic states resulting from a slow sweep of the laser detuning across the resonance, as described in the previous section (Fig. 7.5). In single instances of the experiment, after such a slowly changing laser pulse, we observe long ordered chains where the atomic states alternate between Rydberg and ground state. These ordered domains can be separated by domain walls that consist of two neighboring atoms in the same electronic state (Fig. 7.5a) [126].

We note that these features cannot be observed in the average excitation probability of the bulk (see D.9a).

The domain wall density can be used to quantify the transition from the disordered phase into the ordered Z_2 phase as a function of detuning Δ . As the system enters the Z_2 phase, ordered domains grow in size, leading to a substantial reduction in the domain wall density (blue points in Fig. 7.5b). Consistent with expectations for an Ising-type second-order quantum phase transition [126], we observe domains of fluctuating lengths close to the transition point between the two phases, which is reflected by a pronounced peak in the variance of the density of domain walls. Consistent with predictions from finite-size scaling analysis [120, 121], this peak is shifted towards positive values of Δ/Ω . The measured position of the peak is $\Delta \simeq 0.5\Omega$. The observed domain wall density is in excellent agreement with fully coherent simulations of the quantum dynamics based on 51-atom matrix product states (MPS, blue line); however, these simulations underestimate the variance at the phase transition (see D.9b).

At the end of the sweep, deep in the Z_2 phase ($\Delta/\Omega \gg 1$) we can neglect Ω such that the Hamiltonian (7.1) becomes essentially classical. In this regime, the measured domain wall number distribution allows us to directly infer the statistics of excitations created when crossing the phase transition. From 18439 experimental realizations we obtain the distribution depicted in Fig. 7.5c with an average of 9.01(2) domain walls. From a maximum-likelihood estimation we obtain the distribution corrected for detection fidelity (see D.4), which corresponds to a state that has on average 5.4 domain walls. These domain walls are most likely created due to non-adiabatic transitions from the ground state when crossing the phase transition [127], where the energy gap depends on the system size (scaling of $\sim 1/N$) [121]. In addition, the preparation fidelity is also limited by spontaneous emission during the laser pulse (an average number of 1.1 photons is scattered per μs for the entire array, see Appendix D).

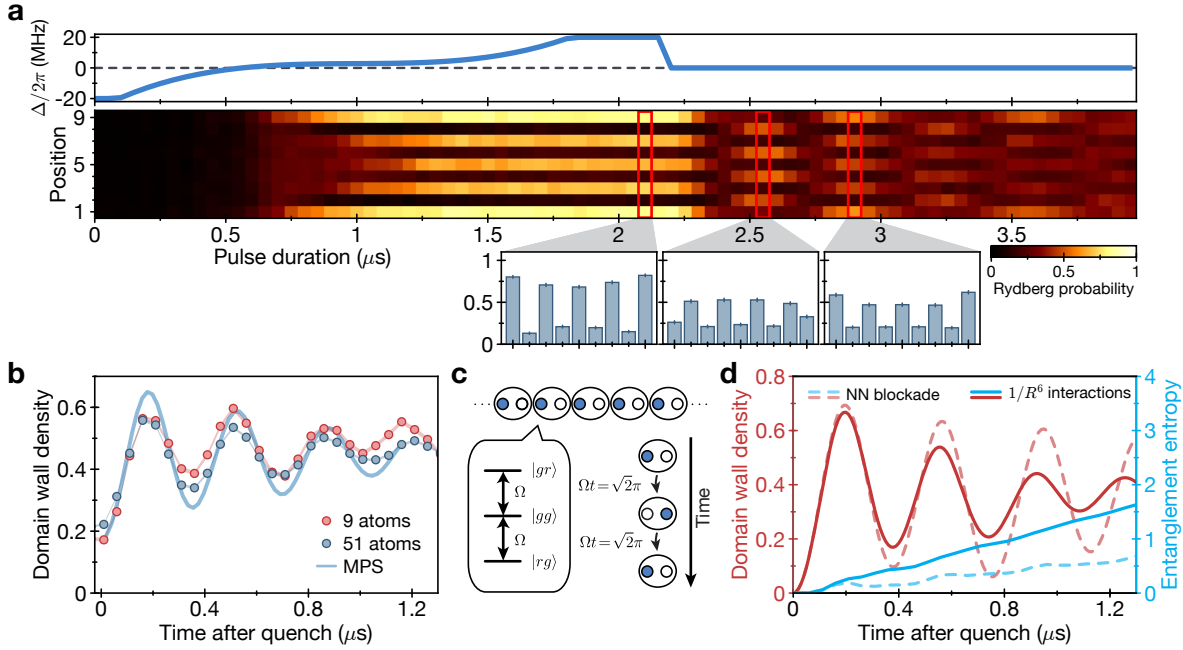


Figure 7.6: Emergent oscillations in many-body dynamics after sudden quench. **a**, Schematic sequence (top, showing $\Delta(t)$) involves adiabatic preparation and then a sudden quench to single-atom resonance. The heat map shows the single atom trajectories for a 9 atom cluster. We observe that the initial (left inset) crystal with a Rydberg excitation at every odd trap site collapses after the quench and a crystal with an excitation at every even site builds up (middle inset). At a later time the initial crystal revives with a frequency of $\Omega/1.38(1)$ (right inset). Error bars denote 68% CI. **b**, Density of domain walls after the quench. The dynamics decay slowly on a timescale of $0.88 \mu\text{s}$. Shaded region represents the standard error of the mean. Solid blue line is a fully coherent MPS simulation with bond dimension $D = 256$, taking into account measurement fidelity. **c**, Toy model of non-interacting dimers (see main text). **d**, Numerical calculations of the dynamics after a quench starting from an ideal 25 atom crystal, obtained from exact diagonalization. Domain wall density as a function of time (red), and growth of entanglement entropy of the half chain (13 atoms) (blue). Dashed lines take into account only nearest neighbor blockade constraint. Solid lines correspond to the full $1/R^6$ interaction potential.

To further characterize the created Z_2 ordered state, we evaluate the correlation function

$$g_{ij}^{(2)} = \langle n_i n_j \rangle - \langle n_i \rangle \langle n_j \rangle \quad (7.2)$$

where the average $\langle \dots \rangle$ is taken over experimental repetitions. We find that the correlations decay exponentially over distance with a decay length of $\xi = 3.03(6)$ sites (see Fig. 7.5d and Appendix D). We note that this length does not fully characterize the system as discussed below (see also D.6).

Finally, Fig. 7.6 demonstrates that our approach also enables the study of coherent dynamics of many-body systems far from equilibrium. Specifically, we focus on the quench dynamics of Rydberg crystals initially prepared deep in the Z_2 ordered phase, as we suddenly change the detuning $\Delta(t)$ to the single-atom resonance $\Delta = 0$ (Fig. 7.6a). After such a quench, we observe oscillations of many-body states between the initial crystal and a complementary crystal where each internal atomic state is inverted (Fig. 7.6a). We find that these oscillations are remarkably robust, persisting over several periods with a frequency that is largely independent of the system size. This is confirmed by measuring the dynamics of the domain wall density, signaling the appearance and disappearance of the crystalline states, shown in Fig. 7.6b for arrays of 9 and 51 atoms. We find that the initial crystal repeatedly revives with a period that is slower by a factor of 1.38(1) compared to the Rabi oscillation period for independent, non-interacting atoms.

7.4 DISCUSSION

Several important features of these experimental observations should be noted. First of all, our Z_2 ordered state cannot be characterized by a simple thermal ensemble. More specifically, if an effective temperature is estimated based on the experimentally determined, corrected domain wall density of 0.1, the corresponding thermal ensemble predicts a correlation length $\xi_{\text{th}} = 4.48(3)$, which is significantly longer than the measured value $\xi = 3.03(6)$ (Appendix D). Such a discrepancy is also reflected in distinct probability distributions for the number of domain walls (Fig. 7.5c). These observations suggest that the system does not thermalize within the timescale of the Z_2 state preparation.

Even more striking is the coherent and persistent oscillation of the crystalline order after the quantum quench. With respect to the quenched Hamiltonian ($\Delta = 0$), the energy density

of our Z_2 ordered state corresponds to that of an infinite-temperature ensemble within the manifold constrained by Rydberg blockade. Also, our Hamiltonian does not have any explicit conserved quantities other than total energy. Nevertheless, the oscillations persist well beyond the natural timescale of local relaxation $\sim 1/\Omega$ as well as the fastest timescale, $1/V_{i,i+1}$.

To understand these observations, we consider a simplified model where the effect of long-range interactions is neglected, and nearest-neighbor interactions are replaced by hard constraints on neighboring excitations of Rydberg states [120]. In this limit, the qualitative behavior of the quench dynamics can be understood in terms of dimerized spins (Fig. 7.6c); owing to the blockade constraint, each dimer forms an effective spin-1 system with three states $|rg\rangle$, $|gg\rangle$, and $|gr\rangle$, where the resonant drive “rotates” the three states over the period $\sqrt{2}(2\pi/\Omega)$, close to that observed experimentally. While this qualitative picture does not take into account the strong interactions (constraints) between neighboring dimers, it can be extended by considering a minimal variational ansatz for the many-body wave function based on matrix product states that respect all blockade constraints (Appendix D). Using the time-dependent variational principle, we derive analytical equations of motion and obtain a crystalline-order oscillation with frequency $\sim \Omega/1.51$ (see D.7), which is within 10% of the experimental observations. These considerations are supported by various numerical simulations. Indeed, the exact numerics predict that this simplified model exhibits crystal oscillations with the observed frequency, while the entanglement entropy grows at a rate much smaller than Ω , indicating that the oscillation persists over many cycles (Fig. 7.6d and Appendix D). The addition of long-range interactions leads to a faster decay of the oscillations, with a timescale that is determined by $\sim 1/V_{i,i+2}$, in good agreement with experimental observations (Fig. 7.6b), while the entanglement entropy also grows on this time scale (Fig. 7.6d, see also D.8).

Thus, our observations and analysis indicate that the decay of crystal oscillation is governed by weak next-nearest-neighbor interactions. This relatively slow thermalization is rather unexpected, since our Hamiltonian, with or without long-range interactions, is far from any known integrable systems [120], and features neither strong disorder nor explicitly conserved quantities [128]. Instead, our observations are likely associated with constrained dynamics due to Rydberg blockade and large separations of timescales $V_{i,i+1} \gg \Omega \gg V_{i,i+2}$ [129] that result in an effective Hilbert space dimension determined by the golden ratio $\sim (1+\sqrt{5})^N/2^N$ [130, 131]. The evolution within such a constrained Hilbert space gives rise to the so-called quantum dimer models, that are known to possess non-trivial dynamics [132]. While these considerations provide important insights into the origin of robust emergent dynamics, we emphasize that our results challenge conventional theoretical concepts and warrant further studies.

7.5 OUTLOOK

Our observations demonstrate that Rydberg excitation of neutral atom arrays constitutes an exceptionally promising platform for studying quantum dynamics and quantum simulations in large systems. Our method can be extended and improved in a number of ways. Individual qubit rotations around the z -axis can be implemented using light shifts associated with trap light, while a second AOD can be used for individual control of coherent rotations around other directions. Further improvement in coherence and controllability can be obtained by encoding qubits into hyperfine sublevels of the electronic ground state and using state-selective Rydberg excitation [116]. Implementing two-dimensional (2d) arrays could provide a path towards realizing thousands of traps. Such 2d configurations could be realized by directly using a 2d-AOD or by creating a static 2d lattice of traps and sorting atoms with an independent AOD, as demonstrated recently [25]. With increased loading efficiencies [86], the robust cre-

ation and control of arrays composed of hundreds of atoms is feasible.

While our current observations already allow us to gain unique insights into the physics associated with transitions into ordered phases and to explore novel many-body phenomena in quantum dynamics, they can be directly extended along several directions [89]. These include studies of various aspects of many-body coherence and entanglement in large arrays [133], investigation of quantum critical dynamics and tests of the quantum Kibble-Zurek hypothesis [127], and the exploration of stable non-equilibrium phases of matter [134]. Further extension may allow for studies of the interplay between long-range interactions and disorder, quantum scrambling [135], topological states in spin systems [136], dynamics of Fibonacci anyons [130, 131], and investigation of chiral clock models associated with transitions into exotic Z_3 and Z_4 states [137]. Finally, we note that our approach is well suited for the realization and testing of quantum optimization algorithms [138, 139] with system sizes that cannot be simulated by modern classical machines.

8

Quantum Kibble-Zurek mechanism and critical dynamics

8.1 QUANTUM PHASE TRANSITIONS AND THE QUANTUM KIBBLE-ZUREK MECHANISM

Quantum phase transitions (QPTs) involve transformations between different states of matter that are driven by quantum fluctuations [126]. These fluctuations play a dominant role in the quantum critical region surrounding the transition point, where the dynamics are governed by the universal properties associated with the QPT. While time-dependent phenomena associated with classical, thermally driven phase transitions have been extensively studied in

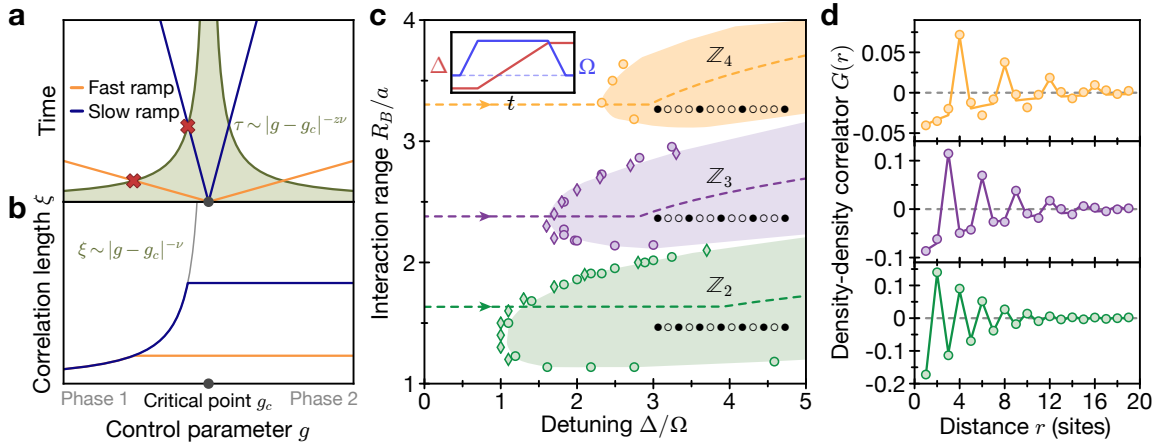


Figure 8.1: Quantum Kibble-Zurek mechanism (QKZM) and phase diagram. **a**, Illustration of the QKZM. As the control parameter approaches its critical value, the response time, τ , given by the inverse energy gap of the system, diverges. When the temporal distance to the critical point becomes equal to the response time, as marked by red crosses, the correlation length, **b**, stops growing due to nonadiabatic excitations. **c**, Numerically calculated ground-state phase diagram. Circles (diamonds) denote numerically obtained points along the phase boundaries calculated using (infinite-size) Density-Matrix Renormalization Group techniques (see Appendix E). The shaded regions are a guide to the eye. Dashed lines show the experimental trajectories across the phase transitions determined by the pulse diagram shown as an inset. **d**, Measured (circles) density-density Rydberg correlations with fits to the expected ordered pattern (solid lines) consistent with \mathbb{Z}_4 - (orange), \mathbb{Z}_3 - (purple) and \mathbb{Z}_2 -ordered (green) states. Error bars denote the standard error of the mean (s.e.m.) and are smaller than the marker size.

systems ranging from the early universe to Bose Einstein Condensates [140–143], understanding critical real-time dynamics in isolated, non-equilibrium quantum systems is an outstanding challenge [144]. Here, we use a Rydberg atom quantum simulator with programmable interactions to study the quantum critical dynamics associated with several distinct QPTs. By studying the growth of spatial correlations while crossing the QPT, we experimentally verify the quantum Kibble-Zurek mechanism (QKZM) [145, 127, 146] for an Ising-type QPT, explore scaling universality, and observe corrections beyond QKZM predictions. This approach is subsequently used to measure the critical exponents associated with chiral clock models [147, 148], providing new insights into exotic systems that have not been understood previously, and opening the door for precision studies of critical phenomena, simulations of lattice gauge theories [149, 89] and applications to quantum optimization [150, 151].

The celebrated Kibble-Zurek mechanism [140, 141] describes nonequilibrium dynamics and the formation of topological defects in a second-order phase transition driven by thermal fluctuations, and has been experimentally verified in a wide variety of physical systems [142, 143]. Recently, the concepts underlying the Kibble-Zurek description have been extended to the quantum regime [145, 127, 146]. Here, the typical size of the correlated regions, ξ , after a dynamical sweep across the QPT scales as a power-law of the sweep rate, s , with an exponent, μ , determined entirely by the QPT's universality class. Specifically, QKZM postulates that when the time scale over which the Hamiltonian changes becomes faster than the characteristic response time, τ , determined by the inverse of the energy gap between the ground and excited states, nonadiabatic excitations prevent the continued growth of correlated regions (Figs. 8.1a,b). The resulting scaling exponent, $\mu = \nu/(1 + \nu z)$, is determined by a combination of the critical exponent ν , that characterizes the divergent correlation length, and the dynamical critical exponent z , that characterizes the relative scaling of space and time close to the critical point [126]. While QKZM has many important implications, e.g. in quantum information science [150], its experimental verification is challenging due to the coupling of many-body systems to the environment [151]. Recently, experimental control over isolated quantum systems enabled the observation of scaling behavior across quantum phase transitions described by mean-field theories [152, 153]. While important aspects of QPTs have already been explored in strongly correlated systems [154], experimental observation of quantum critical phenomena beyond mean-field in real-time dynamics remains an outstanding challenge [155, 156, 151].

8.2 1D RYDBERG HAMILTONIAN PHASE DIAGRAM

We probe quantum criticality using a reconfigurable 1D array of ^{87}Rb atoms with programmable interactions [157]. In our system, 51 atoms in the electronic ground state $|g\rangle$, evenly separated by a controllable distance, are homogeneously coupled to the excited Rydberg state $|r\rangle$, in which they experience van der Waals interactions with a strength that decays as $V(r) \propto 1/r^6$, where r is the interatomic distance. This system is described by the many-body Hamiltonian,

$$\frac{\mathcal{H}}{\hbar} = \frac{\Omega}{2} \sum_i (|g_i\rangle \langle r_i| + |r_i\rangle \langle g_i|) - \Delta \sum_i n_i + \sum_{i < j} V_{ij} n_i n_j, \quad (8.1)$$

where $n_i = |r_i\rangle \langle r_i|$ is the projector onto the Rydberg state at site i , Δ and Ω are the detuning and Rabi frequency of the coherent laser coupling between $|g\rangle$ and $|r\rangle$, and V_{ij} is the interaction strength between atoms in the Rydberg state at sites i and j . For negative values of Δ , the many-body ground state corresponds to a state in which all atoms are in the electronic ground state $|g\rangle$, up to quantum fluctuations, and belongs to a so-called “disordered” phase with no broken spatial symmetry. For $\Delta > 0$, several spatially ordered phases arise from the competition between the detuning term, which favors a large Rydberg fraction, and the Rydberg blockade, which prohibits simultaneous excitation of atoms separated by a distance smaller than the blockade radius, R_B , defined via $V(R_B) \equiv \Omega$. As illustrated in Fig. 8.1c,d, we probe different QPTs into states breaking various symmetries by choosing the interatomic spacing, and sweeping the control parameter, Δ , across the phase boundary.

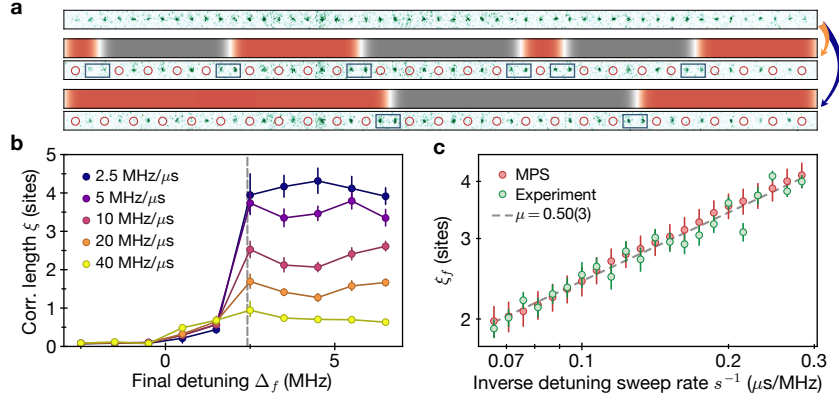


Figure 8.2: Quantum Kibble-Zurek mechanism for a quantum phase transition (QPT) into the \mathbb{Z}_2 -ordered phase. **a**, Single-shot images of the atom array before and after a fast (orange arrow) and a slow (blue arrow) sweep across the phase transition, showing larger average sizes of correlated domains for the slower sweep. Green spots (open circles) represent atoms in $|g\rangle$ ($|r\rangle$). Blue rectangles mark the position of domain walls, and the red and gray colored regions above highlight the extent of the correlated domains. **b**, Correlation length growth and saturation as the system crosses the QPT at different rates. The gray dashed line indicates the critical detuning. **c**, Dependence of correlation length on inverse sweep rate across the phase transition with experimentally measured (green) and matrix product state-simulated results (red). The length is extracted from fitting the modulus of the correlation data to an exponential decay. Error bars denote fit uncertainty. The dashed line indicates a power-law fit with a scaling exponent $\mu = 0.50(3)$ for the experiment.

8.3 (1+1)D ISING QUANTUM PHASE TRANSITION

We first focus on the QPT into the antiferromagnetic phase with broken \mathbb{Z}_2 symmetry, which is known to belong to the Ising universality class [126]. Using an interatomic spacing, a , such that $R_B/a \sim 1.69$, we create an array of 51 atoms in the electronic ground state, and slowly turn on Ω at $\Delta < 0$, adiabatically preparing the system in the ground state of the disordered phase. The detuning is then increased at a constant rate, s , up to a final value Δ_f , at which point Ω is slowly turned off (see inset of Fig. 8.1c), and the state of every atom is measured. We examine the dynamical development of correlations between the atoms, characterized by the Rydberg density-density correlation function:

$$G(r) = \sum_i (\langle n_i n_{i+r} \rangle - \langle n_i \rangle \langle n_{i+r} \rangle) / N_r, \quad (8.2)$$

where the normalization N_r is the number of pairs of sites separated by distance r . By fitting an exponential decay to the modulus of the correlation function, we extract the correlation length. The experimental results show growth of the correlation length as the detuning approaches the critical point, followed by saturation once the detuning is swept past the critical point into the ordered phase (Fig. 8.2b). From the individual images, it is apparent that, while for fast sweeps the ordered domains are frequently interrupted by defects (domain walls), for slow ramps, significantly longer domains are observed (Fig. 8.2a). A systematic analysis of the final correlation lengths after crossing into the ordered phase shows that a power-law scaling model $\xi(s) = \xi_0(s_0/s)^\mu$ with $\mu = 0.50(3)$ accurately describes our measurements (Fig. 8.2c). These results are consistent with numerical simulations (red points) of the coherent evolution of the system using Matrix Product States (MPS).

The QPT into the \mathbb{Z}_2 -ordered phase is in the Ising universality class [126], with critical exponents in 1D of $z = 1$, $\nu = 1$, and consequently, $\mu_{\text{ISING}} = 0.5$. Our observations are consistent with these quantitative predictions, and are quite distinct from those associated with a mean-field Ising transition, described by $z = 1$, $\nu = 1/2$, and yielding $\mu_{\text{MF}} = 1/3$ [126, 152]. These results offer the first experimental verification of the quantum Kibble-Zurek mechanism in an isolated quantum system that defies a mean-field description.

A key concept associated with critical phenomena is that of universality, which is manifested by the collapse of correlations to a universal form when rescaled according to the corresponding critical exponents [126]. Such a signature is a strong test of an underlying universal scaling law, and in connection with the QKZM, should appear upon rescaling lengths by $(s/s_0)^\mu$ [158]. Fig. 8.3a shows that the rescaled correlations for $R_B/a \sim 1.81$ indeed collapse onto two smooth branches, which in turn collapse on top of each other when the correlations are rectified as $(-1)^r G(r)$ (inset in Fig. 8.3a), according to the \mathbb{Z}_2 order parameter.

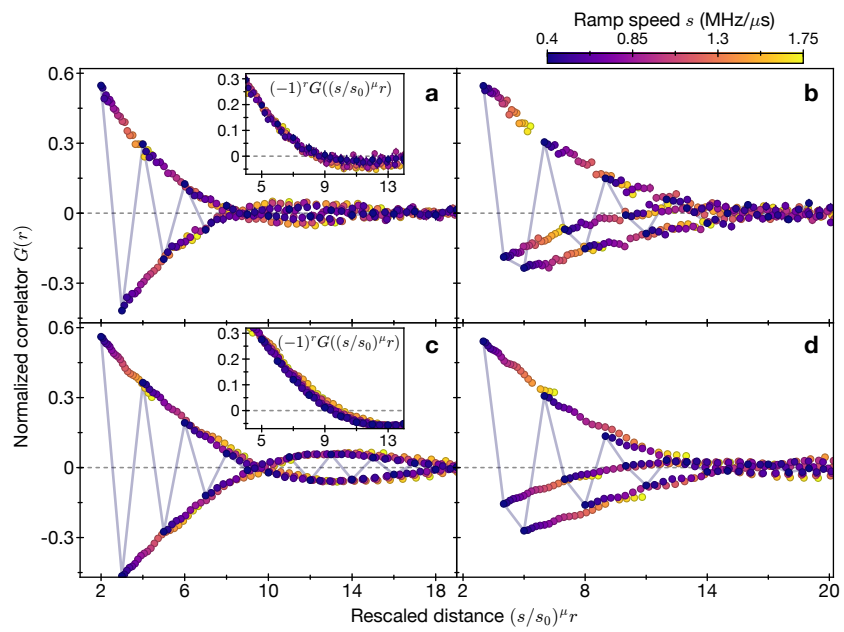


Figure 8.3: Universality of spatial correlations. Collapse of the measured (a) and numerically calculated (c) correlations in the \mathbb{Z}_2 -ordered phase with distances rescaled according to the extracted scaling exponents. The blue line connects the points of the correlation function corresponding to the slowest sweep rate. The insets show the staggered rescaled correlations. The negative values of the correlation function indicate nontrivial correlations between domain walls. Collapse of the measured (b) and numerically calculated (d) correlations in the \mathbb{Z}_3 -ordered phase highlighting the energetic difference of the different types of defects, as shown by the distinguishability of the two negative branches, i.e., a deviation from a period-3 density wave. All error bars indicate the s.e.m.

While the quantum Kibble-Zurek mechanism is a coarse-grained description predicting the mean density of defects, the shape of the correlation function gives further access to microscopic details of the system. Detailed inspection of the rescaled correlation functions reveals nontrivial deviations from a simple exponential decay. In particular, the correlations in Fig. 8.3a become negative for a range of distances, which implies complex dynamics in the formation and spreading of defects. The observed corrections to simple QKZM predictions are consistent with recent theoretical analyses [158, 159] and are in good agreement with numerical simulations using MPS (Fig. 8.3c). Finally, applying the universal rescaling to the correlation growth shown in Fig. 8.2b allows us to independently estimate the values of critical exponents (Fig. E.7), showing that our results are consistent with $z = \nu = 1$ associated with the Ising QPT.

8.4 CRITICAL SCALING BEYOND ISING TRANSITION

Having established the validity of the QKZM, as well as its limitations, for a QPT in the Ising universality class, we now explore transitions into more complex \mathbb{Z}_N -ordered phases, where Rydberg excitations are evenly separated by $N > 2$ sites (see Fig. 8.1c). The correlation functions at smaller interatomic spacings after slow detuning sweeps reflect the spatial ordering of the \mathbb{Z}_3 - and \mathbb{Z}_4 -ordered phases (Fig. 8.1d). In addition, we determine the probability of finding two Rydberg excitations separated by N -sites, for each value of N and R_B (Fig. 8.4b). Combining these measurements with the numerically obtained critical points (see Fig. 8.1c), we experimentally identify approximate boundaries for the regions consistent with the \mathbb{Z}_2 -, \mathbb{Z}_3 -, and \mathbb{Z}_4 -ordered phases in Fig. 8.4b. Within these regions, the dominant type of order is the one associated with the corresponding phase, while the second most prevalent type of order arises from the lowest-energy (most probable) defects. In particular, we observe that in the

\mathbb{Z}_3 -ordered phase, the most-likely defect changes from \mathbb{Z}_2 -like for smaller values of R_B/a , to \mathbb{Z}_4 -like as R_B/a increases.

We test for a power-law scaling behavior of the correlation length growth as a function of ramp speed at different interaction strengths in Fig. 8.4c. To consistently compare the results for all interaction strengths, we fit the correlation function to an exponentially decaying density wave with a period set by the underlying order (as opposed to the modulus of the correlation function used in Fig. 8.2c). The scaling is extracted through a power-law fit to the resulting correlation lengths. In parameter regimes far away from regions of competing order, we observe three stable plateaus for the regions consistent with \mathbb{Z}_2 , \mathbb{Z}_3 , and \mathbb{Z}_4 order, respectively. For interaction strengths where there is a strong competition between different types of order, we do not observe the formation of long-range correlations (pale points in Fig. 8.4c). In these cases, the detuning sweeps either do not fully cross the phase boundary into the ordered phases (see Appendix E) or potentially enter theoretically predicted incommensurate phases [148, 120].

8.5 DISCUSSION

To understand these observations, we compare them to finite-size scaling analyses of ground-state properties [160–162], as well as MPS-based numerical simulations of our experimental protocol for the full Hamiltonian (8.1). For the transitions into the \mathbb{Z}_2 -ordered phase, some of the extracted values of μ are slightly larger than the expected exponent from the Ising model $\mu_{\text{Ising}} = 0.5$. We attribute these deviations, to a combination of the long-ranged interactions, finite-size and/or time effects, and systematic effects related to the inversion of the alternating pattern (Fig. 8.3a,c, see also Appendix E).

Quantum phase transitions associated with the breaking of a \mathbb{Z}_3 symmetry are more com-

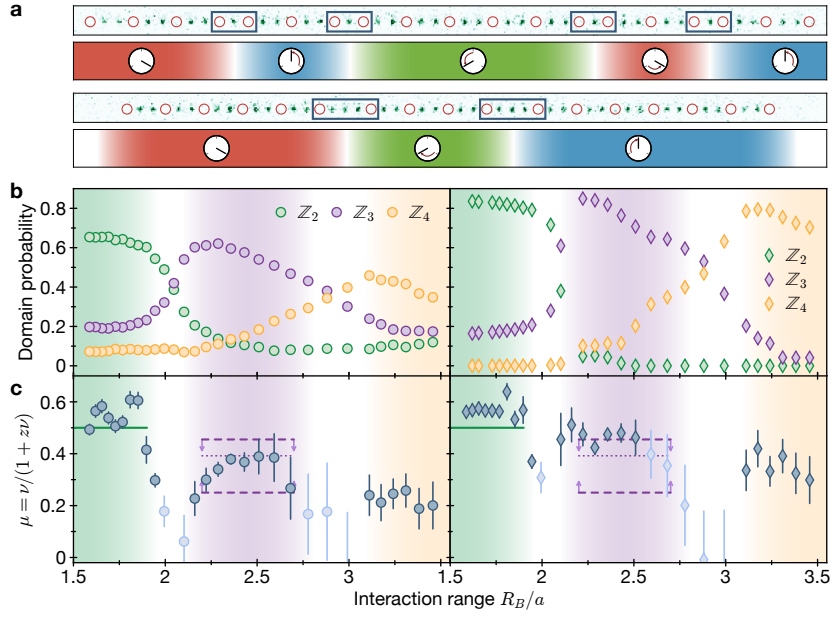


Figure 8.4: Power-law scaling for different interactions. **a**, Experimental realization of the chiral clock model [160]. The top row shows a single fluorescence image of a state in the \mathbb{Z}_3 -symmetry broken phase ($R_B/a \sim 2.16$), with four \mathbb{Z}_2 -type defects displacing the Rydberg atoms in one direction (counter-clockwise chirality). The bottom rows display a system with stronger interactions ($R_B/a \sim 2.43$), where \mathbb{Z}_4 -type defects are favored, and the Rydberg atoms are displaced in the opposite direction (clockwise chirality). The colored regions highlight the extent of the correlated domains, labeled by clock orientations in connection to the chiral clock model. **b**, Fraction of the final state consistent with the different \mathbb{Z}_N -ordered states observed in the experiment (left, circles) and in numerical simulations (right, diamonds). Within the \mathbb{Z}_3 -ordered region, the most dominant type of defect changes from \mathbb{Z}_2 - to \mathbb{Z}_4 -type as the interaction range increases. The higher contrast in the calculated domain probabilities in Fig. 8.4b is due to finite detection fidelity, which does not affect the extracted value of μ . **c**, Scaling exponent, μ , as a function of R_B/a obtained from experimental data (left, circles), and matrix product state simulations (right, diamonds). Pale blue points indicate instances where the measured correlation lengths do not grow beyond the size of R_B/a . Shaded areas indicate the regions consistent with \mathbb{Z}_2 - (green), \mathbb{Z}_3 - (purple), and \mathbb{Z}_4 -ordered (orange) phases. The solid green line corresponds to μ_{ISING} , the purple dashed lines represent the upper [160], and lower [161] bounds of μ_{CCM} , while the purple dotted line is the value of μ_{CCM} obtained from the best numerical estimates of z [160] and ν [162]. Error bars represent the 68% confidence interval (b), and uncertainty of the power-law fit (c), which is dominated by systematic effects in the extraction of individual correlation lengths.

plex due to competition between the different types of defects that can be formed. In our system, the defects correspond to two different types of domain walls, where the distance between neighboring Rydberg excitations is 2 sites and 4 sites (see Fig. 8.4a). For the experimentally accessible parameter regimes, the different associated excitation energies lead, in general, to an asymmetry between these defects (see also Fig. 8.4b). Correspondingly, the \mathbb{Z}_3 -symmetry breaking is believed to be in the universality class of the 3-state *chiral* clock model (CCM) (Fig. 8.4a, Appendix E, and [160]).

The exact nature of such phase transitions has been a subject of intense theoretical research for the past three decades [147, 148, 163, 160–162]. Only very recently, numerical studies of equilibrium scaling properties [160–162] provided evidence for a direct transition [162] along some paths across the phase boundary, where the expected range of values of the scaling exponent is $\mu < 0.45$ [160], and $\mu > 0.25$ [161]. Our experimental results are consistent with a direct CCM phase transition over a range of interaction strengths with $\mu \sim 0.38$, in agreement with the theoretical value obtained by combining the results of the most extensive numerical finite-size scaling studies [160, 162] (dashed line in Fig. 8.4c). Further evidence for a direct chiral QPT is provided by the universal scaling behavior into the \mathbb{Z}_3 -ordered phase (see Fig. 8.3b,d).

The transition into the \mathbb{Z}_4 -ordered phase is even more involved. At present, complete understanding of this transition is lacking, in particular due to the potential presence of an intermediate gapless incommensurate phase [148, 163]. Our experimental results in this region are reasonably consistent with power-law scaling with $\mu \sim 0.25$. While recent theoretical work shows that QKZM scaling may still hold on quenching through a gapless phase, albeit with a modified (system-specific) power-law exponent [164], detailed theoretical understanding of our experimentally observed exponents in the \mathbb{Z}_4 regime requires further studies.

Detailed comparison of our experimental results across all phases to the numerical simulation of the Hamiltonian dynamics using MPS are presented in Figure 8.4. While qualitatively similar, they display clear discrepancies. Most significant is a systematic offset in the extracted values of μ between experiment, finite-size scaling analysis and time-dependent MPS simulations. While it can be potentially attributed to experimental imperfections and subtle differences between the experimental system and the model used for the numerical simulations (see Appendix E), the disagreement of MPS with both experimental results and finite-size scaling analyses of equilibrium properties highlights the difficulty in approximately modeling complex nonequilibrium dynamics of many-body systems.

8.6 OUTLOOK

Our observations demonstrate a novel approach for probing quantum critical phenomena and provide new insights into the physics of exotic QPTs that do not lend themselves to simple theoretical analyses. Increasing the system size, improving atomic coherence properties, and exploring wider parameter regimes may allow for more precise probing of exotic QPTs into both ordered and incommensurate phases [148, 120, 160, 162] in various models. In particular, the present approach is well suited for simulations of lattice gauge theories [89]. Whereas the system studied here is formally equivalent to a quantum link model on a ladder [165], two- and three-dimensional systems, realized using novel trapping techniques [30, 166], can be used to simulate a wide variety of non-trivial lattice gauge models [149]. Finally, the methods demonstrated in this work can be used to effectively encode and explore solutions to computationally difficult combinatorial optimization problems such as finding the Maximum Independent Set [167]. Detailed understanding of quantum dynamics in such systems might have direct applications for exploring quantum speedup in both adiabatic and dynamical quantum

optimization algorithms [150].

9

Quantum Phases of Matter on a 256-Atom Programmable Quantum Simulator

Recent breakthroughs have demonstrated the potential of programmable quantum systems, with system sizes reaching around fifty trapped ions [168–170] or superconducting qubits [171, 172, 21], for simulations and computation. Correlation measurements with over seventy photons have been used to perform boson sampling [22], while optical lattices with hundreds of atoms are being used to explore Hubbard models [173, 174, 107]. Larger-scale Ising spin systems have been realized using superconducting elements [175], but they lack the coherence essential for probing quantum matter.

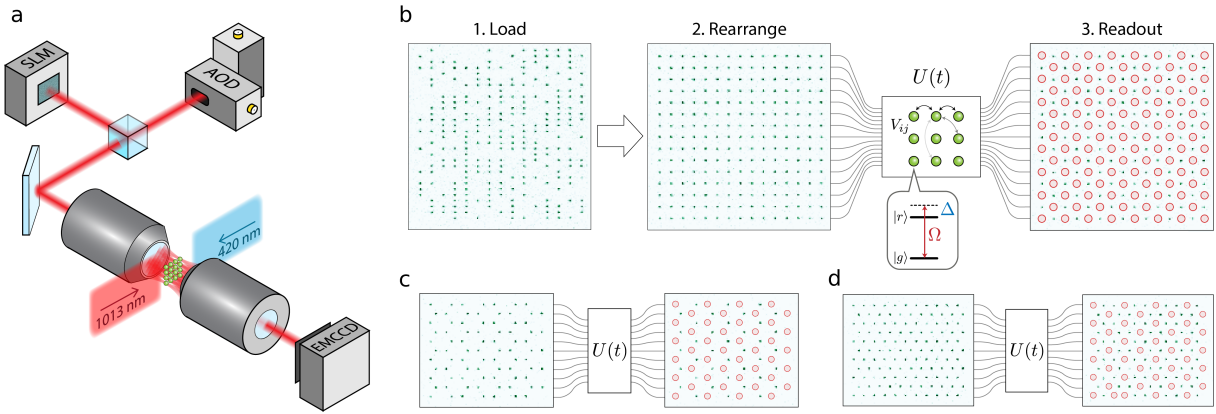


Figure 9.1: Programmable two-dimensional arrays of strongly-interacting Rydberg atoms. **a.** Atoms are loaded into a 2D array of optical tweezer traps and rearranged into defect-free patterns by a second set of moving tweezers. Lasers at 420 nm and 1013 nm drive a coherent two-photon transition in each atom between ground state $|g\rangle = |5S_{1/2}, F=2, m_F=-2\rangle$ and Rydberg state $|r\rangle = |70S_{1/2}, m_j=-1/2, m_I=-3/2\rangle$. **b.** Fluorescence image of initial random loading of atoms, followed by rearrangement to a defect-free 15×15 (225 atoms) square array. After this initialization, the atoms evolve coherently under laser excitation with Rabi frequency $\Omega(t)$ and detuning $\Delta(t)$, and long-range interactions V_{ij} . Finally, the state of each atom is read out, with atoms excited to $|r\rangle$ detected as loss and marked with red circles. Shown on the far right is an example measurement following quasi-adiabatic evolution into the checkerboard phase. **c, d.** Similar evolution on honeycomb and triangular lattices result in analogous ordered phases of Rydberg excitations with filling 1/2 and 1/3, respectively.

Neutral atom arrays have recently emerged as a promising platform for realizing programmable quantum systems [17, 117, 157]. Based on individually trapped and detected cold atoms in optical tweezers with strong interactions between Rydberg states [176], atom arrays have been utilized to explore quantum dynamics in one- and two-dimensional systems [157, 177–181], to create high-fidelity [35] and large-scale [182] entanglement, to perform parallel quantum logic operations [34, 33], and to realize optical atomic clocks [183, 36]. While large numbers of atoms have been trapped [36] and rearranged in two and three dimensions [184, 166, 32, 30], coherent manipulation of programmable, strongly interacting systems with more than a hundred individual particles remains an outstanding challenge. Here, we realize a programmable quantum simulator using arrays of up to 256 neutral atoms with tunable interactions, demonstrating several novel quantum phases and quantitatively probing the associated phase transitions.

9.1 PROGRAMMABLE RYDBERG ARRAYS IN 2D

Our experiments are carried out on the second generation of an experimental platform described previously [157]. The new apparatus uses a spatial light modulator (SLM) to form a large, two-dimensional (2D) array of optical tweezers in a vacuum cell (Fig. 9.1a and Chapter 2). This static tweezer array is loaded with individual ^{87}Rb atoms from a magneto-optical trap (MOT), with a uniform loading probability of 50–60% across up to 1000 tweezers. We rearrange the initially loaded atoms into programmable, defect-free patterns using a second set of moving optical tweezers that are steered by a pair of crossed acousto-optical deflectors (AODs) to arbitrary positions in 2D (Fig. 9.1a) [25]. Our parallel rearrangement protocol (see Appendix F) enables rearrangement into a wide variety of geometries including square, honeycomb, and triangular lattices (left panels in Fig. 9.1b-d). The procedure takes a total time of 50–100 ms for arrays of up to a few hundred atoms and results in filling fractions exceeding 99%.

Qubits are encoded in the electronic ground state $|g\rangle$ and the highly-excited $n = 70$ Rydberg state $|r\rangle$ of each atom. We illuminate the entire array from opposite sides with two counter-propagating laser beams at 420 and 1013 nm, shaped into light sheets (see Chapter 3), to coherently couple $|g\rangle$ to $|r\rangle$ via a two-photon transition (Fig. 9.1a).

The resulting many-body dynamics $U(t)$ are governed by a combination of the laser excitation and long-range van der Waals interactions between Rydberg states ($V_{ij} = V_0/|\mathbf{x}_i - \mathbf{x}_j|^6$), described by the Hamiltonian

$$\frac{H}{\hbar} = \frac{\Omega}{2} \sum_i (|g_i\rangle\langle r_i| + |r_i\rangle\langle g_i|) - \Delta \sum_i n_i + \sum_{i < j} V_{ij} n_i n_j \quad (9.1)$$

where \hbar is the Planck's constant, $n_i = |r_i\rangle\langle r_i|$, and Ω and Δ are the two-photon Rabi fre-

quency and detuning, respectively. After evolution under the Hamiltonian (9.1), the state of each atomic qubit is read out by fluorescence imaging that detects only atoms in $|g\rangle$, while atoms in $|r\rangle$ are detected as loss. Detection fidelities exceed 99% for both states (see Appendix F).

The Rydberg blockade mechanism [88, 185] is central to understanding the programmable dynamics driven by the Hamiltonian (9.1). It originates from the long-range interactions between Rydberg states, providing an effective constraint that prevents simultaneous excitation of atoms within a blockade radius $R_b \equiv (V_0/\Omega)^{1/6}$. We control the effective blockade range R_b/a by programming the lattice spacing a for the atom array. Using these control tools, we explore quantum evolution resulting in a wide variety of quantum phases.

9.2 CHECKERBOARD PHASE

The smallest value of R_b/a that results in an ordered phase for the quantum many-body ground state of the system corresponds to $R_b/a \approx 1$, where only one out of every pair of nearest-neighbor atoms can be excited to $|r\rangle$. On a square array, this constraint leads to a \mathbb{Z}_2 -symmetry-broken *checkerboard* phase with an antiferromagnetic (AF) ground state. To realize such a state, we initialize the array at $R_b/a = 1.15$ ($a = 6.7 \mu\text{m}$, $\Omega = 2\pi \times 4.3 \text{ MHz}$) with all atoms in $|g\rangle$. We then dynamically sweep the detuning Δ from negative to positive values while keeping the Rabi frequency Ω fixed to bring the system quasi-adiabatically into the checkerboard phase (Fig. 9.1b and Fig. 9.2a). A similar approach can be used to create analogous ordered phases on other lattice geometries (Fig. 9.1c, d).

We quantify the strength of antiferromagnetic correlations in the checkerboard phase over many experimental repetitions using the connected density-density correlator $G^{(2)}(k, l) = \frac{1}{N_{(k,l)}} \sum_{i,j} (\langle n_i n_j \rangle - \langle n_i \rangle \langle n_j \rangle)$, where the sum is over all pairs of atoms (i, j) separated by

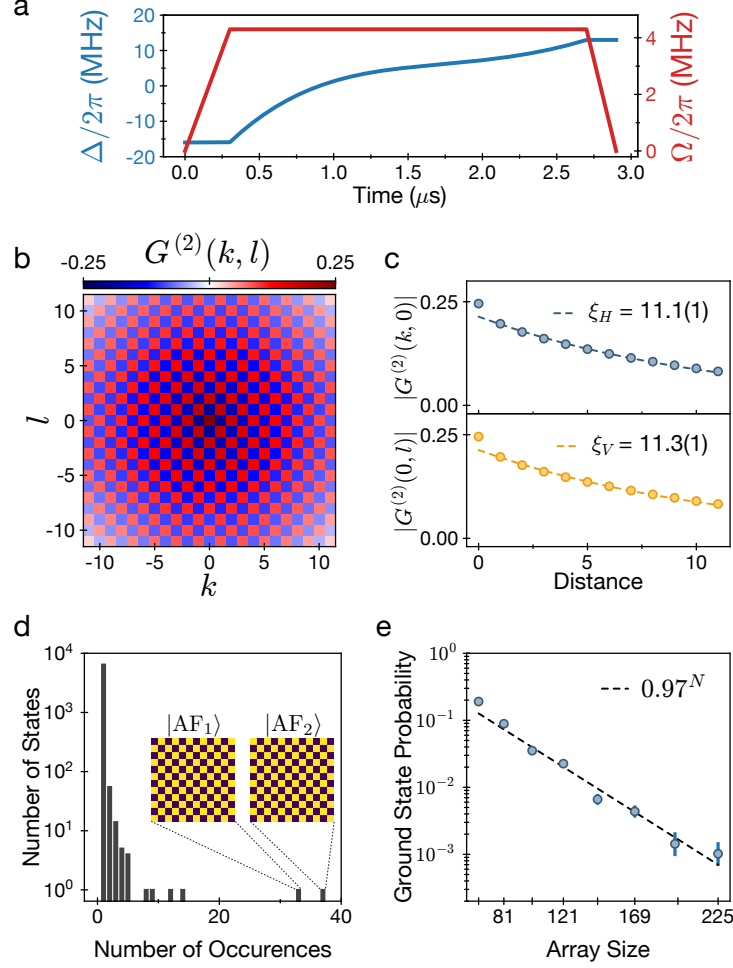


Figure 9.2: Benchmarking of quantum simulator using checkerboard ordering. **a.** A quasi-adiabatic detuning sweep $\Delta(t)$ at constant Rabi frequency Ω is used to prepare the checkerboard ground state with high fidelity. **b.** Two-site correlation function $G^{(2)}(k, l)$, averaged over all pairs of atoms on a 12×12 array, showing near-perfect alternating correlations throughout the entire system. **c.** Exponential fits of rectified horizontal and vertical correlations are used to extract correlation lengths in the corresponding directions ξ_H and ξ_V . **d.** Histogram of many-body state occurrence frequency after 6767 repetitions of the experiment on a 12×12 array. The two most frequently occurring microstates correspond to the two perfect checkerboard orderings, and the next four most common ones are those with a single defect in one of the corners of the array. **e.** Probability of finding a perfect checkerboard ground state as a function of array size. The slightly higher probabilities in odd \times odd systems is due to commensurate edges on opposing sides of the array. All data in this figure are conditioned on defect-free rearrangement of the array.

the same relative lattice displacement $\mathbf{x} = (k, l)$ sites, normalized by the number of such pairs $N_{(k,l)}$. Our measurement of $G^{(2)}(k, l)$ on a 12×12 system (Fig. 9.2b) yields horizontal and vertical correlation lengths of $\xi_H = 11.1(1)$ and $\xi_V = 11.3(1)$ respectively (Fig. 9.2c), showing long-range correlations across the entire 144 atom array. These exceed the values reported previously for two-dimensional systems [177, 178] by nearly an order of magnitude.

Single-site readout also allows us to study individual many-body states of our system (Fig. 9.2d). Out of 6767 repetitions on a 12×12 array, the two perfectly ordered states $|\text{AF}_1\rangle$ and $|\text{AF}_2\rangle$ are by far the most frequently observed microstates, with near-equal probabilities between the two. We benchmark our state preparation by measuring the probability of observing perfect checkerboard ordering as a function of system size (Fig. 9.2e). We find empirically that the probability scales with the number of atoms according to an exponential 0.97^N , offering a benchmark that includes all experimental imperfections such as finite detection fidelity, non-adiabatic state preparation, spontaneous emission, and residual quantum fluctuations in the ordered state (see Appendix F). Remarkably, even for a system size as large as 15×15 (225 atoms), we still observe the perfect antiferromagnetic ground state with probability $0.10^{+5}_{-4}\%$ within the exponentially large Hilbert space of dimension $2^{225} \approx 10^{68}$.

9.3 (2+1)D ISING QUANTUM PHASE TRANSITION

We now describe quantitative studies of the quantum phase transition into the checkerboard phase. Quantum phase transitions fall into universality classes characterized by critical exponents that determine *universal* behavior near the quantum critical point, independent of the microscopic details of the Hamiltonian [126]. The transition into the checkerboard phase is expected to be in the paradigmatic—but never previously observed—quantum Ising universality class in (2+1) dimensions [186] (with expected dynamical critical exponent $z = 1$ and

correlation length critical exponent $\nu = 0.629$.

To explore universal scaling across this phase transition for a large system, we study the dynamical build-up of correlations associated with the quantum Kibble-Zurek mechanism [127, 181] on a 16×16 (256 atoms) array, at fixed $R_b/a = 1.15$. We start at a large negative detuning with all atoms in $|g\rangle$ and linearly increase Δ/Ω , stopping at various points to measure the growth of correlations across the phase transition (Fig. 9.3a,b). Slower sweep rates $s = d\Delta/dt$ result in longer correlation lengths ξ , as expected (Fig. 9.3c).

The quantum Kibble-Zurek mechanism predicts a universal scaling relationship between the control parameter Δ and the correlation length ξ . Specifically, when both Δ and ξ are rescaled with the sweep rate s (relative to a reference rate s_0)

$$\tilde{\xi} = \xi(s/s_0)^\mu \quad (9.2)$$

$$\tilde{\Delta} = (\Delta - \Delta_c)(s/s_0)^\kappa \quad (9.3)$$

with exponents $\mu \equiv \nu/(1+z\nu)$ and $\kappa \equiv -1/(1+z\nu)$, then universality implies that the rescaled $\tilde{\xi}$ vs. $\tilde{\Delta}$ collapses onto a single curve [181] for any sweep rate s . Taking $z = 1$ to be fixed (as expected for a Lorentz-invariant theory), we extract ν for our system by finding the value that optimizes this universal collapse.

In order to obtain ν , we first independently determine the position of the critical point Δ_c , which corresponds to the peak of the susceptibility $\chi = -\partial^2\langle H \rangle / \partial \Delta^2$ and is associated with a vanishing gap [126]. For adiabatic evolution under the Hamiltonian (9.1), the susceptibility χ is related to the mean Rydberg excitation density $\langle n \rangle$ by $\chi = \partial \langle n \rangle / \partial \Delta$ according to the Hellman-Feynman theorem. We measure $\langle n \rangle$ vs. Δ along a slow linear sweep to remain as adiabatic as possible. We take the numerical derivative of the fitted data to obtain χ , finding

its peak to be at $\Delta_c/\Omega = 1.12(4)$ (see Appendix F).

Having identified the position of the critical point, we now extract the value of ν that optimizes data collapse (inset of Fig. 9.3d and Appendix F). The resulting $\nu = 0.62(4)$ rescales the experimental data to clearly fall on a single universal curve (Fig. 9.3d). This measurement is in good agreement with the predicted $\nu = 0.629$ for the quantum Ising universality class in (2+1) dimensions[186], and distinct from both the mean-field value[126] of $\nu = 1/2$ and the previously verified value in (1+1) dimensions [181] of $\nu = 1$. Despite imperfections associated with non-adiabatic state preparation and decoherence in our system, this demonstration of universal scaling highlights opportunities for quantitative studies of quantum critical phenomena on our platform.

9.4 PHASE DIAGRAM OF THE SQUARE LATTICE

A rich variety of new phases have been recently predicted for the square lattice when Rydberg blockade is extended beyond nearest neighbors [186]. To map this phase diagram experimentally, we use the Fourier transform of single-shot measurement outcomes $\mathcal{F}(\mathbf{k}) = \left| \sum_i \exp(i\mathbf{k} \cdot \mathbf{x}_i/a) n_i / \sqrt{N} \right|$, which characterizes long-range order in our system. For instance, the checkerboard phase shows a prominent peak at $\mathbf{k} = (\pi, \pi)$, corresponding to the canonical antiferromagnetic order parameter: the staggered magnetization (Fig. 9.4a). We construct order parameters for all observed phases using the symmetrized Fourier transform $\tilde{\mathcal{F}}(k_1, k_2) = \langle \mathcal{F}(k_1, k_2) + \mathcal{F}(k_2, k_1) \rangle / 2$, averaged over experimental repetitions, which takes into account the reflection symmetry in our system (see Appendix F).

When interaction strengths are increased such that next-nearest (diagonal) neighbor excitations are suppressed by Rydberg interactions ($R_b/a \gtrsim \sqrt{2}$), translational symmetry along the diagonal directions is also broken, leading to the appearance of a new *striated* phase (Fig. 9.4b).

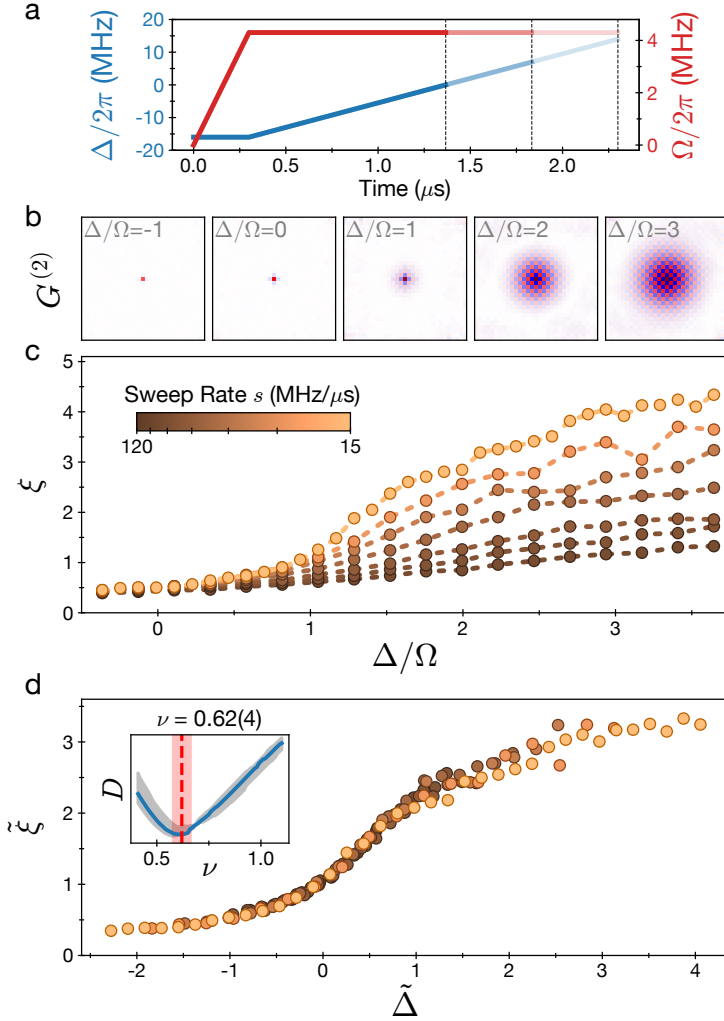


Figure 9.3: Observation of the (2+1)D Ising quantum phase transition on a 16×16 array. **a.** The transition into the checkerboard phase is explored using a linear detuning sweep $\Delta(t)$ at constant Ω . The resulting checkerboard ordering is measured at various endpoints. **b.** Example of growing correlations $G^{(2)}$ with increasing Δ/Ω along a linear sweep with sweep rate $s = 15$ MHz/ μ s. **c.** Growth of correlation length ξ for s spanning an order of magnitude from 15 MHz/ μ s to 120 MHz/ μ s. ξ used here measures correlations between the coarse-grained local staggered magnetization (see Appendix F). **d.** For an optimized value of the critical exponent ν , all curves collapse onto a single universal curve when rescaled relative to the quantum critical point Δ_c . Inset: distance D between all pairs of rescaled curves as a function of ν (see Appendix F). The minimum at $\nu = 0.62(4)$ (red dashed line) yields the experimental value for the critical exponent (red and gray shaded regions indicate uncertainties).

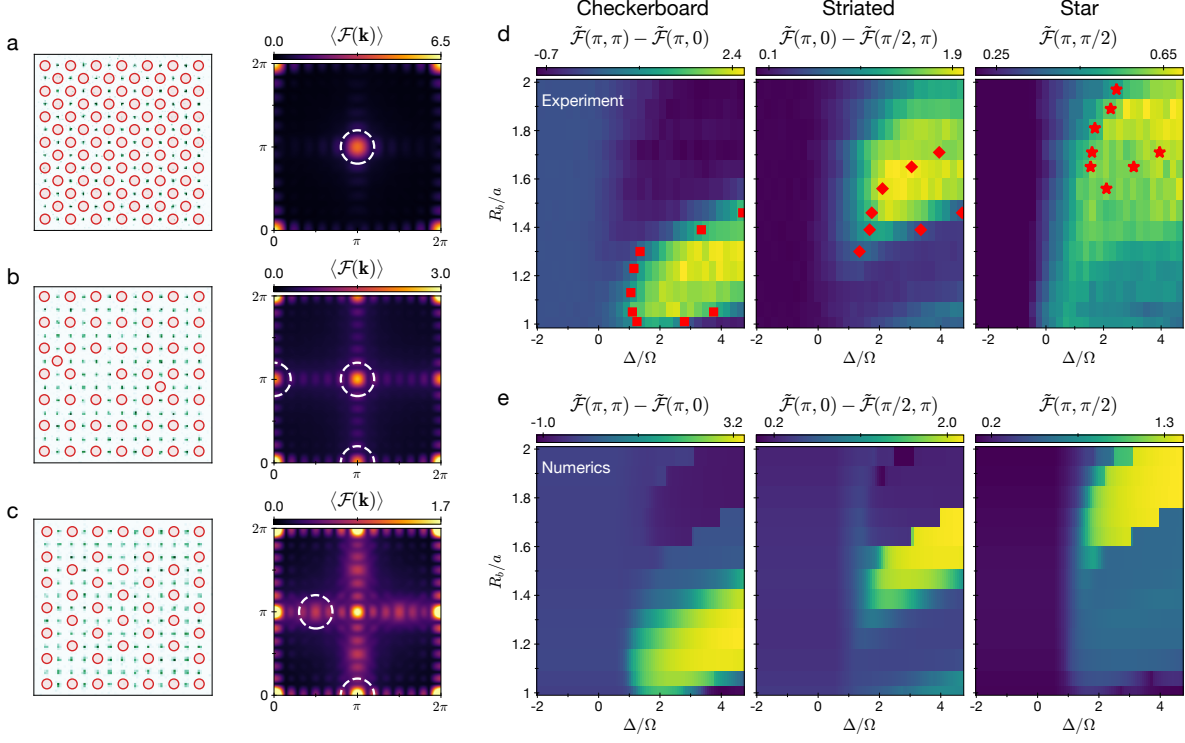


Figure 9.4: Phase diagram of the two-dimensional square lattice. **a.** Example fluorescence image of atoms in the checkerboard phase and the corresponding Fourier transform averaged over many experimental repetitions $\langle \mathcal{F}(\mathbf{k}) \rangle$, highlighting the peak at (π, π) (circled). **b.** Image of atoms in the striated phase and the corresponding $\langle \mathcal{F}(\mathbf{k}) \rangle$ highlighting peaks at $(0, \pi)$, $(\pi, 0)$ and (π, π) (circled). **c.** Image of atoms in the star phase with corresponding Fourier peaks at $(\pi/2, \pi)$ and $(\pi, 0)$ (circled), as well as at symmetric partners $(\pi, \pi/2)$ and $(\pi, 0)$. **d.** The experimental phase diagram is constructed by measuring order parameters for each of the three phases for different values of the tunable blockade range R_b/a and detuning Δ/Ω . Red markers indicate the numerically calculated phase boundaries (see Appendix F). **e.** The order parameters evaluated numerically using DMRG for a 9×9 array (see Appendix F).

In this phase, Rydberg excitations are mostly located two sites apart and hence appear both on alternating rows and alternating columns. This ordering is immediately apparent through the observation of prominent peaks at $\mathbf{k} = (0, \pi)$, $(\pi, 0)$, and (π, π) in the Fourier domain. As discussed and demonstrated below, quantum fluctuations, appearing as defects on single shot images (Fig. 9.4b), play a key role in stabilizing this phase.

At even larger values of $R_b/a \gtrsim 1.7$, the *star* phase emerges, with Rydberg excitations placed every four sites along one direction and every two sites in the perpendicular direction. There are two possible orientations for the ordering of this phase, so Fourier peaks are ob-

served at $\mathbf{k} = (\pi, 0)$ and $(\pi/2, \pi)$, as well as at their symmetric partners $(0, \pi)$ and $(\pi, \pi/2)$ (Fig. 9.4c). In the thermodynamic limit, the star ordering corresponds to the lowest-energy classical configuration of Rydberg excitations on a square array with a density of $1/4$.

We now systematically explore the phase diagram on 13×13 (169 atoms) arrays, with dimensions chosen to be simultaneously commensurate with checkerboard, striated, and star orderings (see Appendix F). For each value of the blockade range R_b/a , we linearly sweep Δ (similar to Fig. 9.3a but with a ramp-down time of 200 ns), stopping at evenly spaced endpoints to raster the full phase diagram. For every endpoint, we extract the order parameter corresponding to each many-body phase, and plot them separately to show their prominence in different regions of the phase diagram (Fig. 9.4d).

We compare our observations with numerical simulations of the phase diagram using the density-matrix renormalization group (DMRG) on a smaller 9×9 array with open boundary conditions (Fig. 9.4e and red markers in Fig. 9.4d). We find excellent agreement in the extent of the checkerboard phase. For the striated and star phases, we also find good similarity between experiment and theory, although due to their larger unit cells and the existence of many degenerate configurations, these two phases are more sensitive to both edge effects and experimental imperfections. We emphasize that the numerical simulations evaluate the order parameter for the exact ground state of the system at each point, while the experiment quasi-adiabatically prepares these states via a dynamical process. These results establish the potential of programmable quantum simulators with tunable, long-range interactions for studying large quantum many-body systems that are challenging to access with state-of-the-art computational tools [187].

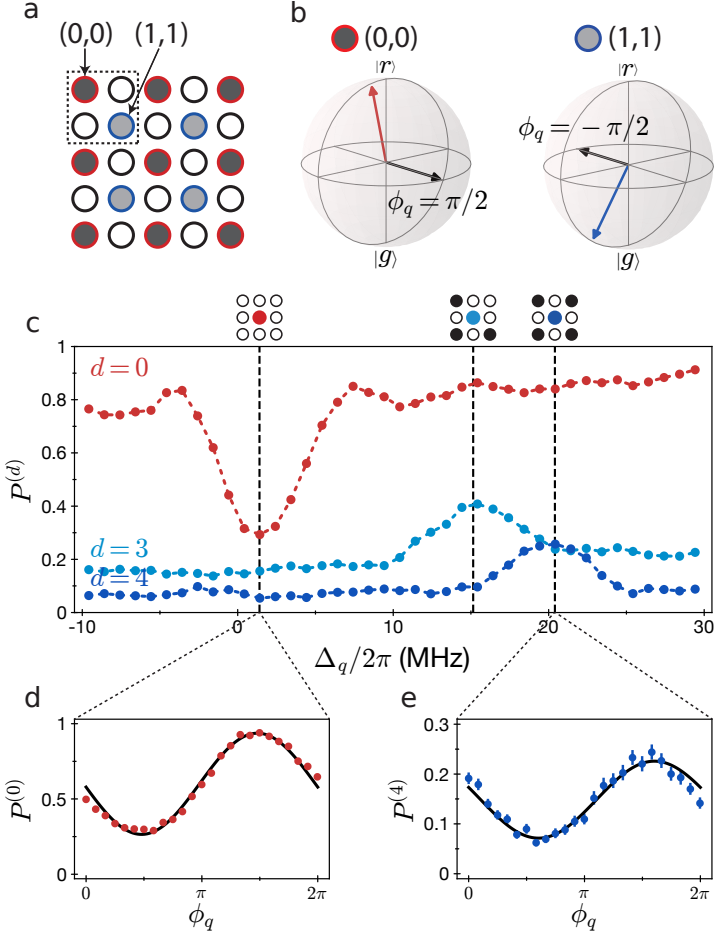


Figure 9.5: Probing correlations and coherence in the striated phase via quench dynamics. **a.** Unit cell of striated ordering (dashed box) with $(0,0)$ and $(1,1)$ sublattices outlined in red and blue, respectively. The fill shade on each site reflects the mean Rydberg excitation. **b.** The variational states for the $(0,0)$ and $(1,1)$ sublattices are illustrated on the Bloch sphere (see Appendix F). The black arrow illustrates the phase ϕ_q of Ω during the quench. **c.** Probability $P^{(d)}$ of an excitation, conditioned on observing no nearest-neighbor excitations, and zero (red), three (light blue), or four (dark blue) diagonal next-nearest neighbor excitations. $P^{(0)}$ is plotted for $\phi_q = \pi/2$, showing resonant de-excitation of the $(0,0)$ sublattice near the bare-atom resonance (leftmost vertical line). $P^{(3)}$ and $P^{(4)}$ are plotted for $\phi_q = -\pi/2$, showing excitation peaks for the $(1,1)$ sublattice at interaction shifts corresponding to 3 or 4 diagonal neighbors (two rightmost vertical lines). **d, e.** $P^{(0)}$ and $P^{(4)}$ vary with quench phase ϕ_q at their corresponding resonances ($\Delta_q/2\pi = 1.4$ and 20.4 MHz, respectively), demonstrating coherence on both the $(0,0)$ and $(1,1)$ sublattices. Solid line fits are used to extract Bloch vector components.

9.5 QUANTUM FLUCTUATIONS IN THE STRIATED PHASE

We now explore the nature of the striated phase. In contrast to the checkerboard and star phases, which can be understood from a dense-packing argument [186], this phase has no counterpart in the classical limit ($\Omega \rightarrow 0$) (see Appendix F). Striated ordering allows the atoms to lower their energy by partially aligning with the transverse field, favoring this phase at finite Ω . This can be seen by considering the 2×2 unit cell, within which one site has a large Rydberg excitation probability (designated the (0,0) sublattice) (Fig. 9.5a). Excitations on its nearest-neighbor (0,1) and (1,0) sublattices are suppressed due to strong Rydberg blockade. The remaining atoms on the (1,1) sublattice have no nearest neighbors in the Rydberg state and experience a much weaker interaction from four next-nearest (diagonal) neighbors on the (0,0) sublattice, thus allowing the (1,1) atoms to lower their energy by forming a coherent superposition between ground and Rydberg states (Fig. 9.5b).

We experimentally study quantum fluctuations in this phase by observing the response of the system to short quenches (with quench times $t_q < 1/\Omega_q$). The dependence on the detuning Δ_q and laser phase ϕ_q of the quench contains information about local correlations and coherence, which allows us to characterize the quantum states on the different sublattices. The quench resonance for each site depends on the state of its nearest and next-nearest neighbors. Due to the large difference between the interaction energies on the (0,0) and (1,1) sublattices, when one sublattice is resonantly driven, the other is effectively frozen.

The nature of the striated phase is revealed using nine-particle operators to measure the state of an atom, conditioned on its local environment. Specifically, we evaluate the conditional Rydberg density $P^{(d)}$, defined as the excitation probability of an atom if all nearest neighbors are in $|g\rangle$, and exactly d next-nearest (diagonal) neighbors are in $|r\rangle$ (see Appendix F).

For $d = 0$, we observe a dip in $P^{(0)}$ near the bare atom resonance (Fig. 9.5c), corresponding to resonant de-excitation of the (0,0) sublattice. Meanwhile, $P^{(3)}$ and $P^{(4)}$ have two separate peaks that correspond to resonant excitation of the (1,1) sublattice with $d = 3$ and $d = 4$ next-nearest neighbor excitations, respectively (Fig. 9.5c). Remarkably, we find that the quench response of both the (0,0) and (1,1) sublattices depends on the phase ϕ_q of the driving field during the quench (Fig. 9.5d,e). The measured visibilities, together with a simple mean-field model (see Appendix F), enable the estimation of unknown Bloch vector components on the two sublattices, yielding $\langle \sigma_x \rangle = -0.82(6)$, $\langle \sigma_y \rangle = 0.25(2)$ for the (0,0) sublattice, and $\langle \sigma_x \rangle = -0.45(4)$, $\langle \sigma_y \rangle = 0.09(1)$ for the (1,1) sublattice. We emphasize that accurate characterization requires the use of more sophisticated variational wavefunctions (based on e.g. tensor networks) and warrants further investigation. This approach can also be extended through techniques such as shadow tomography [188].

9.6 OUTLOOK

These experiments demonstrate that two-dimensional Rydberg atom arrays constitute a powerful platform for programmable quantum simulations with hundreds of qubits. We expect that system size, quantum control fidelity, and degree of programmability can all be increased considerably via technical improvements. In particular, array sizes and rearrangement fidelities, along with atomic state readout, are currently limited by collisions with background gas particles, and can be improved with an upgraded vacuum system [35] and increased photon collection efficiency. Quantum coherence can be enhanced using higher-power Rydberg lasers and by encoding qubits in hyperfine ground states [33, 176]. Tweezers with different atomic [38, 35, 36] and molecular [37, 39] species can provide additional features and lead to novel applications in both quantum simulations and metrology. Finally, rapidly switchable local

control beams can be used to perform universal qubit operations in parallel across the system.

Our experiments realize several new quantum phases and provide unprecedented insights into quantum phase transitions in two-dimensional systems. These studies can be extended along several directions, including the exploration of non-equilibrium entanglement dynamics via rapid quenches across quantum phase transitions [189–191], the investigation of topological quantum states of matter on frustrated lattices [192, 193], the simulation of lattice gauge theories [194, 195], and the study of broader classes of spin models using hyperfine encoding [89]. Quantum information processing can also be explored with hardware-efficient methods for multi-qubit operations [33] and protocols for quantum error correction and fault tolerant control [196]. Finally, our approach is well suited for efficient implementation of novel algorithms for quantum optimization [197, 198] and sampling [199], enabling experimental tests of their performance with system sizes exceeding several hundred qubits.

10

Controlling many-body dynamics with driven quantum scars in Rydberg atom arrays

Dynamics of complex, strongly interacting many-body systems have broad implications in quantum science and engineering, ranging from understanding fundamental phenomena such as the nature of quantum gravity [200] to realizing robust quantum information systems [21, 22]. In these many-body systems, dynamics typically lead to a rapid growth of quantum entanglement and a chaotic spreading of the wave function throughout an exponentially large Hilbert space, a phenomenon associated with quantum thermalization [201–203]. Recent advances in the controlled manipulation of isolated, programmable many-body systems have

enabled detailed studies of non-equilibrium states in strongly interacting quantum matter [204, 205, 203], in regimes inaccessible to numerical simulations on classical machines. Identifying non-trivial states for which dynamics can be stabilized or steered by external controls is a central question explored in these studies. For instance, it has been shown that strong disorder, leading to many-body localization (MBL), allows systems to suppress entanglement growth and retain memory of their initial state for long times [206]. Another striking example involves quantum many-body scars, which manifest as special initial states that avoid rapid thermalization within an otherwise chaotic system [207, 157, 189]. Further, periodic driving in strongly interacting systems can give rise to exotic non-equilibrium phases of matter, such as the discrete time crystal (DTC) which spontaneously breaks the discrete time-translation symmetry of the underlying drive [208, 209].

In this Report, we investigate stability, thermalization, and control of quantum many-body scars in systems ranging from 3 to 200 strongly interacting qubits with varying geometry [157, 31]. We discover that entanglement dynamics associated with such scarring trajectories can be stabilized via parametric driving, resulting in an emergent phenomenon akin to discrete time-crystalline order. We show this phenomenon can be harnessed to steer entanglement dynamics in complex many-body systems.

10.1 QUANTUM SCARS IN TWO DIMENSIONAL RYDBERG ATOM ARRAYS

In our experiments, neutral ^{87}Rb atoms are trapped in optical tweezers and arranged into arbitrary two-dimensional patterns generated by a spatial light modulator [117, 31]. This programmable system allows us to explore quantum dynamics in systems ranging from chains and square lattices to exotic decorated lattices, with sizes up to 200 atoms. All atoms are initialized in an electronic ground state $|g\rangle$ and coupled to a Rydberg state $|r\rangle$ by a two-photon

optical transition with an effective Rabi frequency $\Omega(t)$ and detuning $\Delta(t)$, as depicted schematically in Fig. 10.1A. When excited into Rydberg states, atoms interact via a strong, repulsive van der Waals interaction $V \sim 1/d^6$, where d is the inter-atomic separation, resulting in the many-body Hamiltonian [157],

$$\frac{H}{\hbar} = \frac{\Omega(t)}{2} \sum_i \sigma_i^x - \Delta(t) \sum_i n_i + \sum_{i < j} V_{ij} n_i n_j \quad (10.1)$$

where \hbar is the reduced Planck constant, $n_i = |r_i\rangle\langle r_i|$ is the projector onto the Rydberg state at site i and $\sigma_i^x = |g_i\rangle\langle r_i| + |r_i\rangle\langle g_i|$ flips the atomic state. We choose lattice spacings where the nearest-neighbor (NN) interaction $V_0 > \Omega$ results in the Rydberg blockade [88, 210, 117], preventing adjacent atoms from simultaneously occupying $|r\rangle$. For large negative detunings, the many-body ground state is $|gggg\dots\rangle$, and at large positive detunings on bipartite lattices the ground state is antiferromagnetic, of the form $|rgrg\dots\rangle$. Starting with all atoms in $|g\rangle$, adiabatically increasing Δ from large negative values to large positive values thus prepares antiferromagnetic initial states $|\text{AF}\rangle$ [123, 115, 157]; we choose array configurations (e.g. odd numbers of atoms) such that one of the two classical orderings, $|\text{AF}_1\rangle$, is energetically preferred.

To explore quantum scarring in two-dimensional systems, we prepare $|\text{AF}_1\rangle$ on an 85-atom honeycomb lattice, and then suddenly quench at fixed Ω to a small positive detuning (Fig. 10.1B). The system quickly evolves from $|\text{AF}_1\rangle$ into a disordered, vast superposition of many-body states as expected from a thermalizing system, but then strikingly the opposite order $|\text{AF}_2\rangle$ emerges at a later time [189]. Through the same process the system evolves back to $|\text{AF}_1\rangle$, consistent with previous observations of quantum scars in one-dimensional chains [157, 189]. These scarring dynamics can be seen in the evolution of sublattice A and B populations as a function of quench duration (Fig. 10.1C), where disordered configurations arise when the sub-

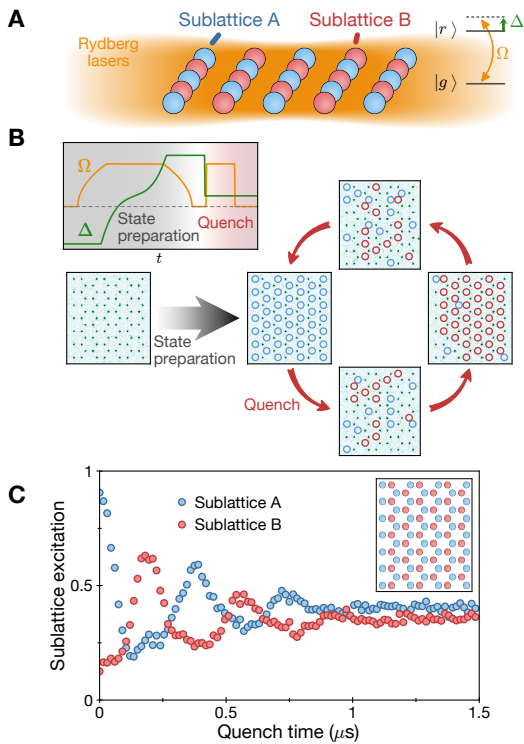


Figure 10.1: Experimental investigations of quantum many-body scars. **(A)** Two-dimensional atom array subject to global Rydberg lasers with Rabi frequency Ω and detuning Δ . **(B)** A quasi-adiabatic ramp of Δ and Ω prepares an antiferromagnetic state $|\text{AF}_1\rangle$ with sublattice A excited, and a detuning quench launches non-equilibrium dynamics. Atoms in $|g\rangle$ are imaged in optical tweezers via fluorescence while atoms in $|r\rangle$ (empty circles) are expelled and detected as atom loss. **(C)** The Rydberg population on sublattices A and B undergo periodic oscillations (Inset: geometry used here).

lattice populations are approximately equal. These observations are surprising in a strongly interacting system: the fact that the atoms entangle and disentangle periodically while traversing through the complicated Hilbert space (as shown theoretically [211]) indicates a special dynamical behavior as well as a form of ergodicity breaking [189, 211]. This scarring behavior is captured by the so-called ‘PXP’ model of perfect nearest-neighbor blockade, in which V_0 is infinite and interactions beyond nearest-neighbor are zero: $H_{\text{PXP}} = (\Omega/2) \sum_i P_{i-1} \sigma_i^x P_{i+1}$ with $P_i = |g_i\rangle \langle g_i|$ [131, 189, 211–213].

We observe this oscillatory behavior in a wide variety of bipartite lattices, shown in Fig. 10.2A (we do not observe scarring on the non-bipartite lattices we measure). As an example, we plot the difference between the sublattice A and B populations $\langle n \rangle_A - \langle n \rangle_B$ for a 49-atom square and a 54-atom decorated honeycomb [214], with Rabi frequency $\Omega/2\pi = 4.2$ MHz and interaction strength $V_0/2\pi = 9.1$ MHz. We note a marked difference in the lifetime of periodic revivals for these two different lattices. Quantitatively, we find that dynamics of $\langle n \rangle_A - \langle n \rangle_B$ are well-described by a damped cosine, $y_0 + C \cos(\tilde{\Omega}t) \exp(-t/\tau)$, with oscillation frequency $\tilde{\Omega}$, decay time τ , offset y_0 , and contrast C . While $\tilde{\Omega} \approx 0.6 \Omega$ on both the square and decorated honeycomb lattices, the fitted τ for these two different configurations are $0.22(1) \mu\text{s}$ and $0.50(1) \mu\text{s}$, respectively.

10.2 DECAY MECHANISMS OF QUANTUM SCARS

To understand this geometry dependence, we consider an empirical model for the decay rate of many-body scars (see Appendix G), parametrized as follows:

$$\frac{1}{\tau} = \alpha \left(\frac{1}{2\pi} \sum_{\text{NN}} \frac{\Omega^2}{4V_0} \right) + \beta \left(\frac{1}{2\pi} \sum_{\text{NNN}} V_{ij} \right) + \frac{1}{\tau_0} \quad (10.2)$$

where the first two terms capture deviations of the Rydberg Hamiltonian from the idealized PXP model, due to second-order virtual coupling to states violating blockade and next-nearest-neighbor (NNN) interactions, respectively (Appendix G); α, β, τ_0 are phenomenological values. In Fig. 10.2B we plot the measured $1/\tau$ as a function of the first and second terms in Eq. (10.2) for all geometries shown in Fig. 10.2A and varied interaction strengths V_0 . We find that the decay rates fit well to a plane with slopes $\alpha = 0.72(12)$ and $\beta = 0.58(5)$ and offset $1/\tau_0 = 0.4(2)$ MHz. Note that $1/\tau_0 \ll 1/\tau$, i.e., we find that the decay of scars is dominated by imperfect blockade and long-range interactions. The observation that long-range fields contribute to decay also motivates quenching to small positive $\Delta_q = \Delta_{q,\text{opt}} = 1/2 \sum_{i,j>\text{NN}} V_{ij}$, which enhances scarring by cancelling the static, mean-field contribution from the long-range interactions (Appendix G), and is implemented for all geometries throughout this work. These results also suggest an intrinsic limit to the scar lifetime, coming from the trade-off between imperfect blockade ($\propto 1/V_0$) and long-range interactions ($\propto V_0$). E.g., with $\Omega/2\pi = 4.2$ MHz, for a one-dimensional chain at an optimal $V_0/2\pi \approx 19$ MHz we estimate a maximum lifetime $\tau_{\max} \approx 0.9 \mu\text{s}$, or instead $\tau_{\max} \approx 0.4 \mu\text{s}$ for a honeycomb lattice.

10.3 ROBUST SUBHARMONIC RESPONSE OF DRIVEN QUANTUM MANY-BODY SCARS

We next investigate the effect of parametric driving on many-body scars. To this end, we implement quenches to a time-dependent detuning $\Delta_q(t) = \Delta_0 + \Delta_m \cos(\omega_m t)$, as illustrated in Figure 10.3A, and explore a non-perturbative regime of $\Delta_m, \Delta_0, \omega_m \sim \Omega$. Remarkably, in Fig. 10.3B we find that such a quench results in a five-fold increase of scar lifetime compared to the fixed-detuning case, for properly chosen drive parameters (modulation frequency $\omega_m = 1.24 \Omega$, offset $\Delta_0 = 0.85 \Omega$, and amplitude $\Delta_m = 0.98 \Omega$ for this 9-atom chain). Further, we find the drive changes the oscillation frequency $\tilde{\Omega}$ to $\omega_m/2$, apparent in the synchronous

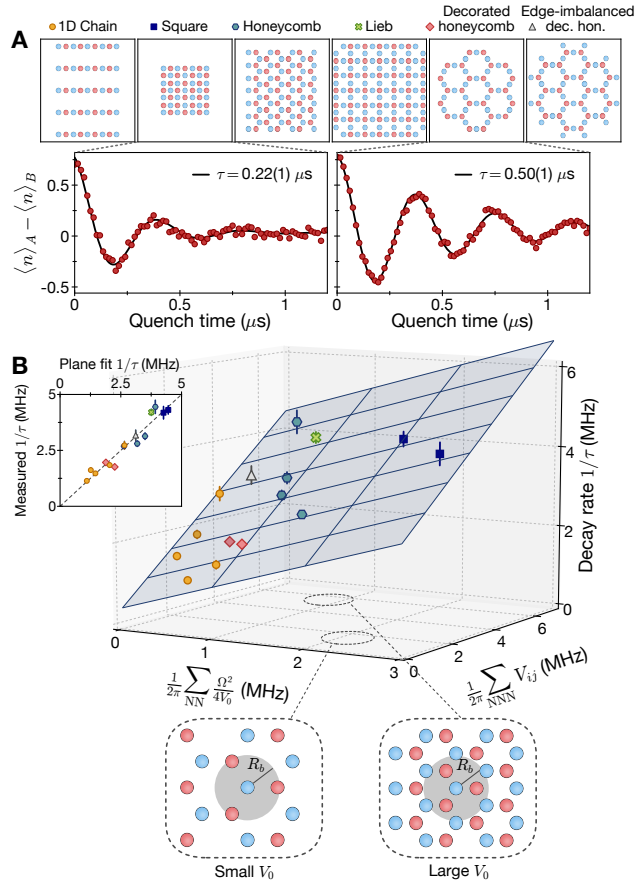


Figure 10.2: Universal empirical description of scar lifetime. **(A)** Different geometries used in this study. The lifetime τ of the sublattice excitation difference depends strongly on the geometry. **(B)** As a function of coupling to blockade-violating states ($\propto \Omega^2/V_0$) and next-nearest-neighbor (NNN) interactions, the scar decay rate $1/\tau$ displays a bilinear dependence (Inset: cross-section of the plane). Schematics depict regimes where the two different decay processes dominate.

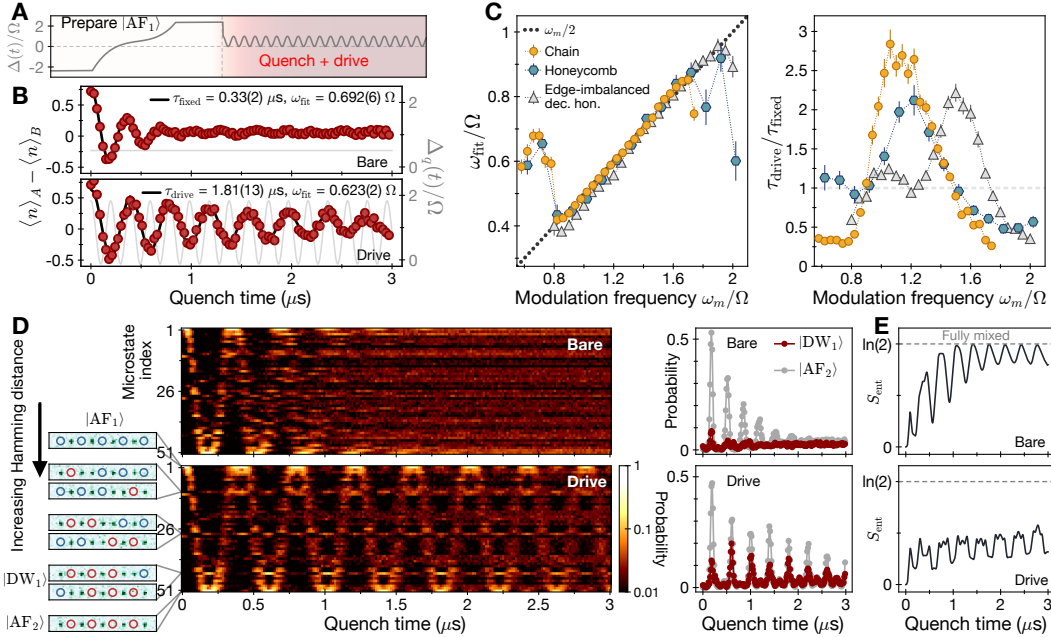


Figure 10.3: Emergent subharmonic locking and stabilization. **(A)** Pulse sequence showing state preparation and quench with $\Delta_q(t)$. **(B)** Scar dynamics on a chain during quench to fixed optimal detuning (bare) with lifetime τ_{fixed} , and time-dependent detuning (drive) with modulation frequency $\omega_m = 1.24 \Omega$ and lifetime τ_{drive} . The drive increases the scar lifetime and changes its frequency to $\omega_m/2$. **(C)** Scar lifetime and response frequency as a function of ω_m , showing a lifetime increase and subharmonic locking. **(D)** Dynamics of the entire Hilbert space measured with experimental snapshots (0.5 million total bit strings). The microstates of the constrained Hilbert space are ordered by $n_A - n_B$, or equivalently by Hamming distance from $|\text{AF}_1\rangle$ (Appendix G). Right subplots highlight $|\text{AF}_2\rangle$ and a state with a domain wall $|\text{DW}_1\rangle$. **(E)** Reduced density matrix of a single atom in a chain (numerics) shows that driving reduces the growth of entanglement entropy S_{ent} .

revival of $\langle n \rangle_A - \langle n \rangle_B$ every two drive periods of $\Delta_q(t)$.

Figure 10.3C shows the scar lifetime and oscillation frequency as a function of modulation frequency ω_m , for a 9-atom chain (with different V_0 than Fig. 10.3A), a 41-atom honeycomb, and a 66-atom edge-imbalanced decorated honeycomb (tabulation of system and drive parameters in Appendix G). For all three lattices, a robust subharmonic locking of the scar frequency is observed at $\omega_m/2$ over a wide range of ω_m , accompanied by a marked increase in the scar lifetime. We note that significant lifetime enhancements are found even when $\Delta_m, \Delta_0 \gg \sum_{\text{NNN}} V_{ij}$, and even in numerics for the idealized PXP model (Appendix G), indicating that the physical origin of the enhancement is not simply a mean-field-interaction cancellation akin to fixed $\Delta_{q,\text{opt}}$.

To gain insight into the origin of the subharmonic stabilization, Figure 10.3D shows the experimentally observed distribution of microscopic many-body states across the entire Hilbert space of the 9-atom chain, as a function of quench time. For the fixed detuning quench, oscillations between $|\text{AF}_1\rangle$ and $|\text{AF}_2\rangle$ product states are observed, before the quantum state spreads and thermalizes to a near-uniform distribution across the many-body states [201, 202]. Notably, parametric driving not only delays thermalization, but also alters the actual trajectory being stabilized: the driven case also shows periodic, synchronous occupation of several other many-body states, seemingly dominated by those with near-maximal excitation number (indicated in the left panel of Fig. 10.3D). This suggests that, rather than enhancing oscillations between the $|\text{AF}\rangle$ states, the parametric driving actually stabilizes the scar dynamics to oscillations between entangled superpositions composed of various product states. Figure 10.3E further illustrates the change in trajectory with numerical simulations of the local entanglement entropy, revealing that driving stabilizes the periodic entangling and disentangling of an atom with the rest of the system.

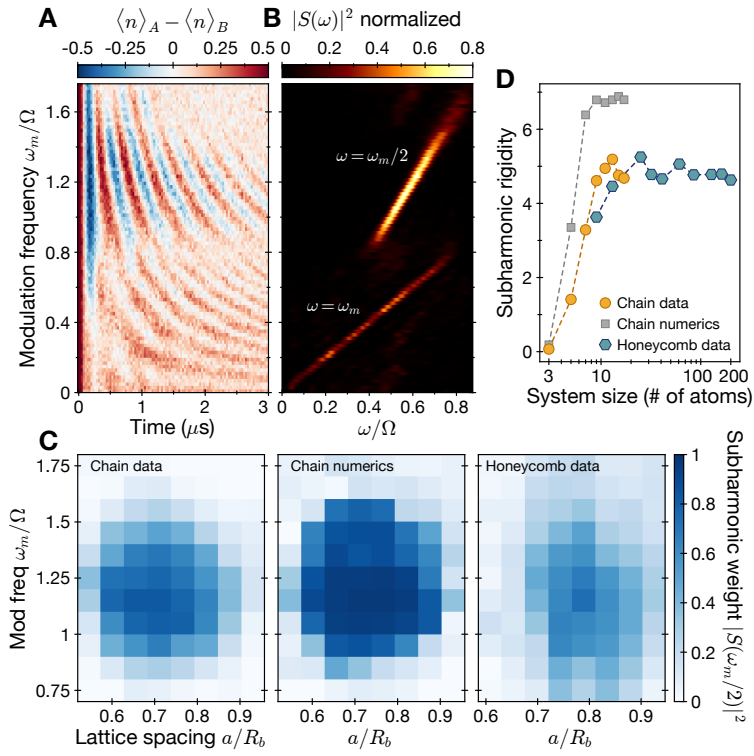


Figure 10.4: Robustness of the subharmonic response. **(A)** Dynamics of sublattice population difference after quench, as a function of modulation frequency. **(B)** Fourier transform intensity $|S(\omega)|^2$ of data in (a), showing a harmonic locking for $\omega_m < 0.8 \Omega$ and a subharmonic locking for $\omega_m > 0.8 \Omega$. **(C)** Phase diagram of the subharmonic response $|S(\omega = \omega_m/2)|^2$ in chain data (left), chain numerics (middle) from perfectly initialized $|\text{AF}_1\rangle$ without experimental imperfections, and honeycomb data (right). **(D)** Increase of subharmonic rigidity (see text) with increasing system size.

We observe this emergent subharmonic stabilization for a wide range of system and drive parameters. Figs. 4A and 4B show the time dynamics of $\langle n \rangle_A - \langle n \rangle_B$ and the normalized intensity of its associated Fourier transform $|S(\omega)|^2$ as a function of the drive frequency for a 9-atom chain. A response is observed at $\omega = \omega_m$ for $\omega_m < 0.8 \Omega$, before suddenly transitioning into a subharmonic response $\omega = \omega_m/2$ for $\omega_m > 0.8 \Omega$. For different drive parameters a weak 4th subharmonic response at $\omega = \omega_m/4$ is also observed (Appendix G). To quantify the robustness of the observed response, we evaluate the subharmonic weight, $|S(\omega = \omega_m/2)|^2$, which encapsulates both the $\omega_m/2$ response and enhanced lifetime [215, 216]. Fig. 10.4C shows the corresponding results for a 9-atom chain and a 41-atom honeycomb as a function of the modulation frequency ω_m and the lattice spacing a (in units of the blockade radius R_b defined by $V(R_b) = \Omega$). A wide plateau in the subharmonic weight is clearly observed for both lattices, as a function of both modulation frequency and interaction strength (range $0.6 - 0.9 a/R_b$ corresponds to $V_0/2\pi \approx 8 - 80$ MHz). To quantify the many-body nature of this stable region [209], we define the subharmonic rigidity, which evaluates the robustness of the subharmonic response over a range of modulation frequencies and is defined as $\sum_{\omega_m} |S_{\omega_m}(\omega = \omega_m/2)|^2$ for $\omega_m = 0.75, 0.85, \dots, 1.75 \Omega$. Figure 10.4D plots subharmonic rigidity vs system size for both a chain and a honeycomb lattice, increasing with system size until saturating at roughly 13 atoms, and appearing stable for the honeycomb lattice even to 200 atoms.

10.4 DISCUSSION

We now turn to a discussion of these experimental observations. The emergent subharmonic response and its rigidity is strongly reminiscent of those associated with discrete time-crystalline order [208, 209, 215–217]. Yet, there are clear distinctions. Specifically, this behavior is observed only for antiferromagnetic initial states, while other initial states such as $|ggg\dots\rangle$ ther-

malize and do not show subharmonic responses (Appendix G). This significant state dependence distinguishes these observations from conventional MBL or prethermal time crystals [218], where subharmonic responses are not tied to special initial states. Moreover, it is striking that our drive, whose frequency is resonant with local energy scales, enhances quantum scarring and ergodicity breaking instead of rapidly injecting energy into the system, as would generally be expected in many-body systems [219].

To gain intuition into the origin of our experimental observations, we consider a toy, pulsed driving model with Floquet unitary $U_F(\theta, \tau) = e^{-i\theta \sum_i n_i} e^{-iH_{\text{PXP}}\tau}$, where θ arises from an infinitesimal, strong detuning pulse. Due to the particle-hole symmetry of the PXP Hamiltonian, for $\theta = \pi$ the time evolution $e^{-iH_{\text{PXP}}\tau}$ during one pulse is cancelled by the time evolution $e^{iH_{\text{PXP}}\tau}$ in a subsequent pulse, generating an effective many-body echo and subharmonic response (Appendix G). Interestingly, for small deviations from perfect π rotations, $\theta = \pi + \varepsilon$, revivals vanish for generic initial states but persist robustly for an initial $|\text{AF}\rangle$ state (Appendix G). This behavior can be understood as follows. Due to the scarring character of the antiferromagnetic initial states, the PXP evolution approximately realizes an effective π -pulse from $|\text{AF}_1\rangle$ to $|\text{AF}_2\rangle$, but results in ergodic spreading for other initial states. Accordingly, for $\theta = \pi + \varepsilon$, evolution still approximates a many-body echo for the scarred $|\text{AF}\rangle$ but does not reverse the chaotic evolution of generic initial states. Finally, the additional $\varepsilon \sum_i n_i$ in fact serves as a “stabilizing Hamiltonian” by creating an effective gap between the $|\text{AF}\rangle$ states (which have maximal atomic excitations $n_{\max} = \sum_i n_i$) from the rest of the spectrum. In practice, the $|\text{AF}\rangle$ states will be dressed by other states with near-maximal atomic excitations, consistent with Fig. 10.3D showing stabilized oscillations between two superpositions of states with largest $\sum_i n_i$. Although the above arguments utilize pulses, neglect large NNN interactions, and do not explicitly explain the observations in imbalanced lattices (Fig. 10.3C),

this analysis already offers useful insight and warrants further study.

10.5 OUTLOOK

These considerations indicate that the observed subharmonic stabilization of many-body scars in large-scale quantum systems constitutes a new physical phenomenon that can be used for steering quantum entanglement dynamics in complex systems. While these observations challenge conventional understandings of quantum thermalization, the exact nature and conditions for these phenomena and their relationship to dynamical phases of matter such as the DTC warrant further theoretical and experimental investigation. In particular, it would be interesting to explore if many-body states with larger degrees of entanglement could also be stabilized by driving. Such studies could be extended to systems with more complex geometry, control, and topology: ranging from other initial states [220], non-bipartite arrays [117], and utilizing hyperfine qubits [33], to implementing these techniques in other controllable many-body systems. This phenomenon opens the door to tantalizing possibilities for robust creation and control of complex entangled states in the exponentially large Hilbert spaces of many-body systems, with intriguing potential applications in areas such as quantum metrology [221] and quantum information science [200, 21, 22, 101].

11

Probing Topological Spin Liquids on a Programmable Quantum Simulator

11.1 INTRODUCTION

Motivated by visionary theoretical work carried out over the past five decades, a broad search is currently underway to identify signatures of quantum spin liquids (QSL) in novel materials [222, 223]. Moreover, inspired by the intriguing predictions of quantum information theory [224], techniques to engineer such systems for topological protection of quantum information are being actively explored [225]. Systems with frustration [226] caused by the lattice

geometry or long-range interactions constitute a promising avenue in the search for QSLs. In particular, such systems can be used to implement a class of so-called dimer models [227–231], which are among the most promising candidates to host quantum spin liquid states. However, realizing and probing such states is challenging since they are often surrounded by other competing phases. Moreover, in contrast to topological systems involving time-reversal symmetry breaking, such as in the fractional quantum Hall effect [232], these states cannot be easily probed via, e.g., quantized conductance or edge states. Instead, to diagnose spin liquid phases, it is essential to access nonlocal observables, such as topological string operators [222, 223]. While some indications of QSL phases in correlated materials have been previously reported [233, 234], thus far, these exotic states of matter have evaded direct experimental detection.

Programmable quantum simulators are well suited for the controlled exploration of these strongly correlated quantum phases [173, 89, 235–238, 180]. In particular, recent work showed that various phases of quantum dimer models can be efficiently implemented using Rydberg atom arrays [192] and that a dimer spin liquid state of the toric code type could be potentially created in a specific frustrated lattice [193]. We note that toric code states have been dynamically created in small systems using quantum circuits [239, 240]. However, some of the key properties, such as topological robustness, are challenging to realize in such systems. Spin liquids have also been explored using quantum annealers, but the lack of quantum coherence in these systems has precluded the observation of non-classical features [241].

11.2 DIMER MODELS IN RYDBERG ATOM ARRAYS

The key idea of our approach is based on a correspondence [193] between Rydberg atoms placed on the links of a kagome lattice (or equivalently the *sites* of a ruby lattice), as shown in Fig. 11.1A, and dimer models on the kagome lattice [229, 231]. The Rydberg excitations can

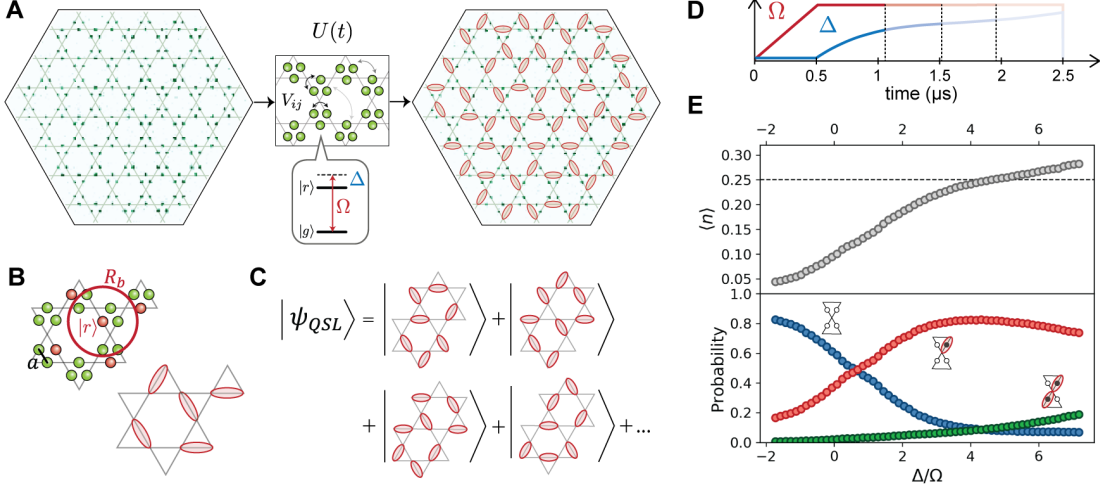


Figure 11.1: Dimer model in Rydberg atoms arrays. (A) Fluorescence image of 219 atoms arranged on the links of a kagome lattice. The atoms, initially in the ground state $|g\rangle$, evolve according to the many-body dynamics $U(t)$. The final state of the atoms is determined via fluorescence imaging of ground state atoms. Rydberg atoms are marked with red dimers on the bonds of the kagome lattice. (B) We adjust the blockade radius to $R_b/a = 2.4$, by choosing $\Omega = 2\pi \times 1.4$ MHz and $a = 3.9 \mu\text{m}$, such that all six nearest neighbors of an atom in $|r\rangle$ are within the blockade radius R_b . A state consistent with the Rydberg blockade at maximal filling can then be viewed as a dimer covering of the kagome lattice, where each vertex is touched by exactly one dimer. (C) The quantum spin liquid state corresponds to a coherent superposition of exponentially many dimer coverings. (D) Detuning $\Delta(t)$ and Rabi frequency $\Omega(t)$ used for quasi-adiabatic state preparation. (E) (Top) Average density of Rydberg excitations $\langle n \rangle$ in the bulk of the system, excluding the outer three layers (Appendix H). (Bottom) Probabilities of empty vertices in the bulk (monomers), vertices attached to a single dimer, or to double dimers (weakly violating blockade). After $\Delta/\Omega \sim 3$, the system reaches $\sim 1/4$ filling, where most vertices are attached to a single dimer, consistent with an approximate dimer phase.

be viewed as “dimer bonds” connecting the two adjacent vertices of the lattice (Fig. 11.1B).

Due to the Rydberg blockade [27], strong and properly tuned interactions constrain the density of excitations such that each vertex is touched by a maximum of one dimer. At $1/4$ filling, each vertex is touched by exactly one dimer, resulting in a perfect dimer covering of the lattice. Smaller filling fractions result in a finite density of vertices with no proximal dimers, which are referred to as *monomers*. A quantum spin liquid can emerge within this dimer-monomer model close to $1/4$ filling [193], and can be viewed as a coherent superposition of exponentially many degenerate dimer coverings with a small admixture of monomers [231] (Fig. 11.1C). This corresponds to the resonating valence bond (RVB) state [40, 227], predicted long ago but so far still unobserved in any experimental system.

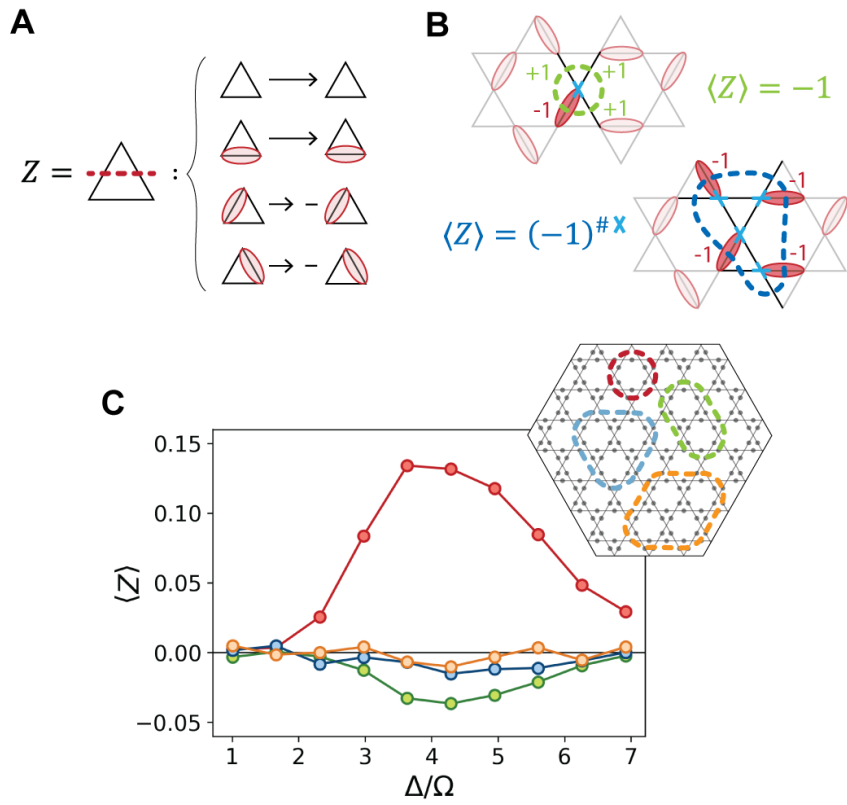


Figure 11.2: Detecting a dimer phase via diagonal string operator. (A) The Z string operator measures the parity of dimers along a string. (B) A perfect dimer covering always has exactly one dimer touching each vertex of the array, so that $\langle Z \rangle = -1$ around a single vertex and $\langle Z \rangle = (-1)^{\# \text{enclosed vertices}}$ for larger loops. (C) Z parity measurements following the quasi-adiabatic sweep of Fig. 11.1D, with the addition of a 200 ns ramp-down of Ω at the end to optimize preparation. At different endpoints of the sweep and for different loop sizes (inset), we measure a finite $\langle Z \rangle$, consistent with an approximate dimer phase.

To create and study such states experimentally, we utilize two-dimensional arrays of 219 ^{87}Rb atoms individually trapped in optical tweezers [31, 242] and positioned on the links of a kagome lattice, as shown in Fig. 11.1A. The atoms are initialized in an electronic ground state $|g\rangle$ and coupled to a Rydberg state $|r\rangle$ via a two-photon optical transition with Rabi frequency Ω . The atoms in the Rydberg state $|r\rangle$ interact via a strong van der Waals potential $V = V_0/d^6$, with d the interatomic distance. This strong interaction prevents the simultaneous excitation of two atoms within a blockade radius $R_b = (V_0/\Omega)^{1/6}$ [27]. We adjust the lattice spacing a and the Rabi frequency Ω such that, for each atom in $|r\rangle$, its six nearest neighbors are all within the blockade radius (Fig. 11.1B), resulting in a maximum filling fraction of 1/4. The resulting dynamics corresponds to unitary evolution $U(t)$ governed by the Hamiltonian

$$\frac{H}{\hbar} = \frac{\Omega(t)}{2} \sum_i \sigma_i^x - \Delta(t) \sum_i n_i + \sum_{i < j} V_{ij} n_i n_j \quad (11.1)$$

where \hbar is the reduced Planck constant, $n_i = |r_i\rangle\langle r_i|$ is the Rydberg state occupation at site i , $\sigma_i^x = |g_i\rangle\langle r_i| + |r_i\rangle\langle g_i|$ and $\Delta(t)$ is the time-dependent two-photon detuning. After the evolution, the state is analyzed by projective readout of ground state atoms (Fig. 11.1A, right panel) [31].

To explore many-body phases in this system, we utilize quasi-adiabatic evolution, in which we slowly turn on the Rydberg coupling Ω and subsequently change the detuning Δ from negative to positive values using a cubic frequency sweep over about 2 μs (Fig. 11.1D). We stop the cubic sweep at different endpoints and first measure the density of Rydberg excitations $\langle n \rangle$. Away from the array boundaries (which result in edge effects permeating just two layers into the bulk), we observe that the average density of Rydberg atoms is uniform across the array (see Fig. H.3 and Appendix H). Focusing on the bulk density, we find that for $\Delta/\Omega \gtrsim 3$,

the system reaches the desired filling fraction $\langle n \rangle \sim 1/4$ (Fig. 11.1E, top panel). The resulting state does not have any obvious spatial order (Fig. 11.1A) and appears as a different configuration of Rydberg atoms in each experimental repetition (see Fig. H.4 and Appendix H). From the single-shot images, we evaluate the probability for each vertex of the kagome lattice to be attached to: one dimer (as in a perfect dimer covering), zero dimers (i.e. a monomer), or two dimers (representing weak blockade violations). Around $\Delta/\Omega \sim 4$ we observe an approximate plateau where $\sim 80\%$ of the vertices are connected to a single dimer (Fig. 11.1E), indicating an approximate dimer covering.

11.3 MEASURING TOPOLOGICAL STRING OPERATORS

A defining property of a phase with topological order is that it cannot be probed locally. Hence, to investigate the possible presence of a QSL state, it is essential to measure topological string operators, analogous to those used in the toric code model [224]. For the present model, there are two such string operators, the first of which characterizes the effective dimer description, while the second probes quantum coherence between dimer states [193]. We first focus on the diagonal operator $Z = \prod_{i \in S} \sigma_i^z$, with $\sigma_i^z = 1 - 2n_i$, that measures the parity of Rydberg atoms along a string S perpendicular to the bonds of the kagome lattice (Fig. 11.2A). For the smallest closed Z loop, which encloses a single vertex of the kagome lattice, $\langle Z \rangle = -1$ for any perfect dimer covering. Larger loops can be decomposed into a product of small loops around all the enclosed vertices, resulting in $\langle Z \rangle = (-1)^{\# \text{ enclosed vertices}}$ (Fig. 11.2B). Note that the presence of monomers or double-dimers reduces the effective contribution of each vertex, resulting in a reduced $\langle Z \rangle$.

To measure $\langle Z \rangle$ for different loops (Fig. 11.2C), we evaluate the string observables directly from single-shot images, averaging over many experimental repetitions and over all loops of

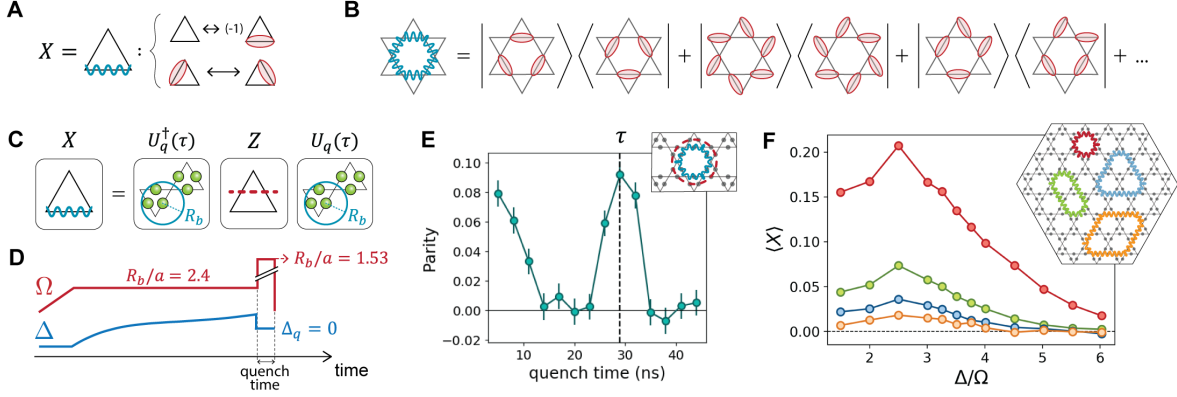


Figure 11.3: Probing coherence between dimer states via off-diagonal string operator. (A) Definition of X string operator on a single triangle of the kagome lattice. (B) On any closed loop, the X operator maps any dimer covering into another valid dimer covering, such that $\langle X \rangle$ measures the coherence between pairs of dimer configurations. (C) The X operator is measured by evolving the initial state under Hamiltonian (eq. (11.1)) with $\Delta = 0$ and reduced blockade radius to encompass only atoms within each individual triangle, implementing a basis rotation that maps X into Z . (D) In the experiment, after the state preparation, we set the laser detuning to $\Delta_q = 0$ and we increase Ω to $2\pi \times 20$ MHz to reach $R_b/a = 1.53$. (E) By measuring the Z parity on the dual string (red) of a target X loop (blue) after a variable quench time, we identify the time τ for which the mapping in (C) is implemented. (F) We measure $\langle X \rangle$ for different final detunings of the cubic sweep and for different loop sizes (inset), and find that the prepared state has long-range coherence that extends over a large fraction of the array (Appendix H).

the same shape in the bulk of the lattice (Appendix H). In the range of detunings where $\langle n \rangle \sim 1/4$, we clearly observe the emergence of a finite $\langle Z \rangle$ for all loops, with the sign matching the parity of enclosed vertices, as expected for dimer states (Fig. 11.2B). The measured values are generally $|\langle Z \rangle| < 1$ and decrease with the loop size, suggesting the presence of a finite density of defects, as discussed below. Nevertheless, these observations indicate that the state we prepare is consistent with an approximate dimer phase.

We next explore quantum coherence properties of the prepared state. To this end, we consider the off-diagonal X operator, which acts on strings along the bonds of the kagome lattice. It is defined in Fig. 11.3A by its action on a single triangle [193]. Applying X on any closed string maps a dimer covering to another valid dimer covering (see e.g. Fig. 11.3B for a loop around a single hexagon). A finite expectation value for X therefore implies that the state contains a coherent superposition of one or more pairs of dimer states coupled by that specific

loop, a prerequisite for a *quantum* spin liquid. The measurement of X can be implemented by performing a collective basis rotation [193] illustrated in Fig. 11.3C. This rotation is implemented by time-evolution under the Rydberg Hamiltonian (eq. (11.1)) with $\Delta = 0$ and reduced blockade radius $R_b/a = 1.53$, such that only the atoms within the same triangle are subject to the Rydberg blockade constraint. Under these conditions, it is sufficient to consider the evolution of individual triangles separately, where each triangle can be described as a 4-level system ($\triangle, \triangle, \triangle, \triangle$). Within this subspace, after a time $\tau = 4\pi/(3\Omega\sqrt{3})$, the collective 3-atom dynamics realizes a unitary U_q which implements the basis rotation that transforms an X string into a dual Z string (Appendix H).

Experimentally, the basis rotation is implemented following the state preparation by quenching the laser detuning to $\Delta_q = 0$ and increasing the laser intensity by a factor of ~ 200 to reduce the blockade radius to $R_b/a = 1.53$ (Fig. 11.3D and Appendix H). We calibrate τ by preparing the state at $\Delta/\Omega = 4$ and evolving under the quench Hamiltonian for a variable time. We measure the parity of a Z string that is dual to a target X loop, and observe a sharp revival of the parity signal at $\tau \sim 30$ ns (Fig. 11.3E) [193]. Fixing the quench time τ , we measure $\langle X \rangle$ for different values of the detuning Δ at the end of the cubic sweep (Fig. 11.3F) and observe a finite X parity signal for loops that extend over a large fraction of the array. We emphasize that, in light of experimental imperfections (Appendix H), the observation of finite parities for string observables of up to 28 atoms within μs -long experiments is rather remarkable. These observations clearly indicate the presence of long-range coherence in the prepared state.

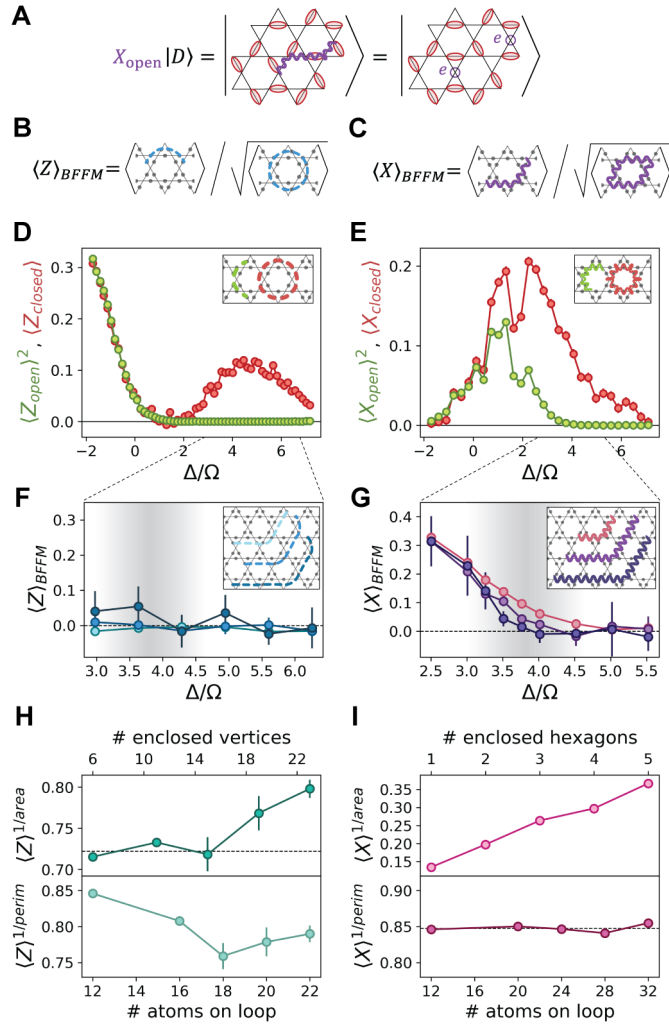


Figure 11.4: String order parameters and quasiparticle excitations. (A) An open string operator X_{open} acting on a dimer state $|D\rangle$ creates two monomers (e-anyons) at its endpoints (see Fig. H.9 for m -anyons). (B,C) Definition of the string order parameters $\langle Z \rangle_{\text{BFFM}}$ and $\langle X \rangle_{\text{BFFM}}$. (D) Comparison between $\langle Z_{\text{closed}} \rangle$ and $\langle Z_{\text{open}} \rangle^2$ measured on the strings shown in the inset. The expectation value shown for the open string is squared to account for the different length of the strings. (E) Analogous comparison for X . (F,G) Zooming in on the range with finite closed loop parities we measure the BFFM order parameters for different open strings (insets). We find that $\langle Z \rangle_{\text{BFFM}}$ is consistent with zero on the entire range of Δ , while $\langle X \rangle_{\text{BFFM}}$ vanishes for $\Delta/\Omega \gtrsim 3.3$, allowing us to identify a range of detunings consistent with the onset of a QSL phase (shaded area). (H) Rescaled parities $\langle Z \rangle^{1/\text{area}}$ and $\langle Z \rangle^{1/\text{perim}}$ evaluated for $\Delta/\Omega = 3.6$, where area and perimeter are defined as the number of vertices enclosed by the loop and the number of atoms on the loop, respectively. For small loops, Z scales with an area law, while it deviates from this behavior for larger loops, converging towards a perimeter law. (I) $\langle X \rangle^{1/\text{area}}$ (the area, in this case, is the number of enclosed hexagons) and $\langle X \rangle^{1/\text{perim}}$ evaluated for $\Delta/\Omega = 3.5$, indicating an excellent agreement with a perimeter-law scaling.

11.4 PROBING SPIN LIQUID PROPERTIES

The study of closed string operators shows that we prepare an approximate dimer phase with quantum coherence between dimer coverings. While these closed loops are indicative of topological order, it is important to compare their properties to those of open strings to distinguish topological effects from trivial ordering—the former being sensitive to the topology of the loop [243–245]. This comparison is shown in Fig. 11.4D,E, indicating several distinct regimes. For small Δ , we find that both Z and X loop parities factorize into the product of the parities on the half-loop open strings—in particular, the finite $\langle Z \rangle$ is a trivial result of the low density of Rydberg excitations. In contrast, loop parities no longer factorize in the dimer phase ($3 \lesssim \Delta/\Omega \lesssim 5$). Instead, the expectation values for both open string operators vanish in the dimer phase, indicating the nontrivial nature of the correlations measured by the closed loops (see also Appendix H). More specifically, topological ordering in the dimer-monomer model can break down either due to a high density of monomers, corresponding to the trivial disordered phase at small Δ/Ω , or due to the lack of long-range resonances, corresponding to a valence bond solid (VBS) [193]. Open Z and X strings distinguish the target QSL phase from these proximal phases: when normalized according to the definition from Bricmont, Frölich, Fredenhagen and Marcu [243, 244] (BFFM) (Fig. 11.4B,C), these open strings can be considered as order parameters for the QSL. In particular, open Z strings have a finite expectation value when the dimers form an ordered spatial arrangement, as in the VBS phase. At the same time, open X strings create pairs of monomers at their endpoints (Fig. 11.4A), so a finite $\langle X \rangle$ can be achieved in the trivial phase where there is a high density of monomers. Therefore, the QSL can be identified as the unique phase where both order parameters vanish for long strings [193].

Figures 11.4F,G show the measured values of these order parameters. We find that $\langle Z \rangle_{\text{BFFM}}$ is compatible with zero on the entire range of Δ/Ω where we observed a finite Z parity on closed loops, indicating the absence of a VBS phase (Fig. 11.4F), consistent with our analysis of density-density correlations (Fig. H.5 and Appendix H). At the same time, $\langle X \rangle_{\text{BFFM}}$ converges towards zero on the longest strings for $\Delta/\Omega \gtrsim 3.3$ (Fig. 11.4G), indicating a transition out of the disordered phase. By combining these two measurements with the regions of non-vanishing parity for the closed Z and X loops (Figs. 11.2,11.3), we conclude that for $3.3 \lesssim \Delta/\Omega \lesssim 4.5$ our results constitute a direct detection of the onset of a quantum spin liquid phase (shaded area in Fig. 11.4F,G).

The measurements of the closed loop operators in Fig. 11.2,11.3 show that $|\langle Z \rangle|, |\langle X \rangle| < 1$ and that the amplitude of the signal decreases with the loop size, which results from a finite density of quasiparticle excitations. Specifically, defects in the dimer covering such as monomers and double-dimers can be interpreted as *electric* (e) anyons in the language of lattice gauge theory [193]. Since the presence of a defect inside a closed loop changes the sign of Z , the parity on the loop is reduced according to the number of enclosed e -anyons as $|\langle Z \rangle| = | \langle (-1)^{\# \text{enclosed } e\text{-anyons}} \rangle |$. The average number of defects inside a loop is expected to scale with the number of enclosed vertices, i.e. with the *area* of the loop, and indeed we observe an approximate *area-law* scaling of $|\langle Z \rangle|$ for small loop sizes (Fig. 11.4H). However, for larger loops we notice a deviation towards a *perimeter-law* scaling, which can emerge if pairs of anyons are correlated over a characteristic length scale smaller than the loop size (see Appendix H for a discussion of the expected scaling). Pairs of correlated anyons which are both inside the loop do not change its parity since their contributions cancel out; they only affect $\langle Z \rangle$ when they sit across the loop, leading to a scaling with the length of the perimeter. These pairs can be viewed as resulting from the application of X string operators to a dimer cover-

ing (Fig. 11.4A), originating, e.g., from virtual excitations in the dimer-monomer model (Appendix H) or from errors due to state preparation and detection. Note that state preparation with larger Rabi frequency (improved adiabaticity) results in larger Z parity signals and reduced e -anyon density (see Fig. H.7).

A second type of quasiparticle excitation that could arise in this model is the so-called *magnetic* (m) anyon. Analogous to e -anyons which live at the endpoints of open X strings (Fig. 11.4A), m -anyons are created by open Z strings and they correspond to phase errors between dimer coverings (Fig. H.9 and Appendix H). These excitations cannot be directly identified from individual snapshots, but they are detected by the measurement of closed X loop operators. The remarkable perimeter law scaling observed in Fig. 11.4I indicates that m -anyons only appear in pairs with short correlation lengths (Appendix H). These observations highlight the prospects for using topological string operators to detect and probe quasiparticle excitations in the system.

11.5 TOWARDS A TOPOLOGICAL QUBIT

To further explore the topological properties of the spin liquid state, we create an atom array with a small hole by removing three atoms on a central triangle, which creates an effective inner boundary (Fig. 11.5). This results in two distinct topological sectors for the dimer coverings, where states belonging to different sectors can be transformed into each other only via large X loops which enclose the hole, constituting a highly nonlocal process (involving at least a 16-atom resonance) (Fig. H.11). We define the logical states $|0_L\rangle$ and $|1_L\rangle$ as the superpositions of all dimer coverings from the topological sectors 0 and 1, respectively. One can define [193] the logical operator σ_L^z as proportional to any Z_L string operator that connects the hole with the outer boundary, since these have a well-defined eigenvalue ± 1 for all dimer states

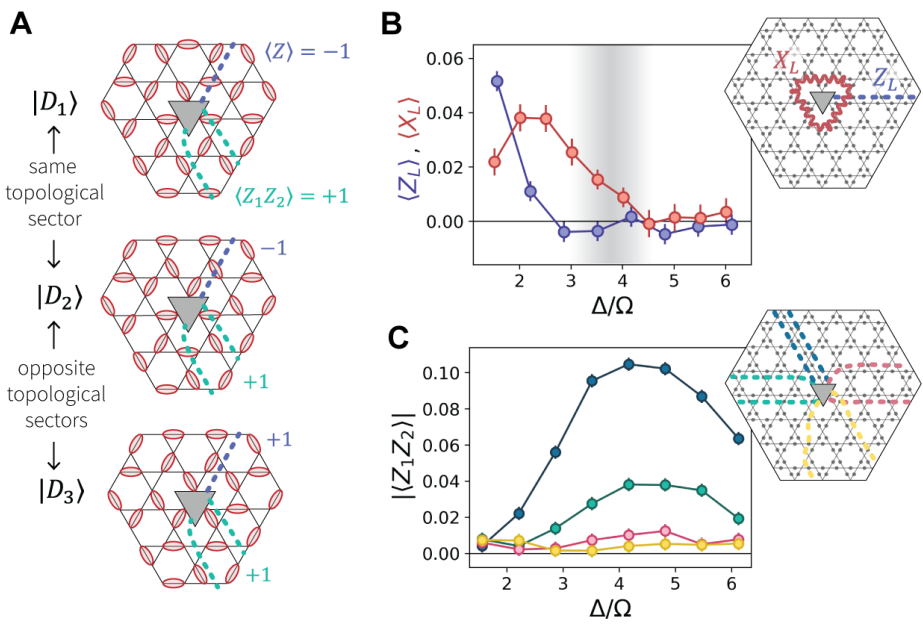


Figure 11.5: Topological properties in array with a hole. (A) A lattice with nontrivial topology is obtained by removing three atoms at the center to create a small hole. The dimer states can be divided into two distinct topological sectors 0 and 1. Z strings connecting the hole to the boundary always have a well-defined expectation value within each sector and opposite sign between the two sectors, while the correlations between two such strings Z_1Z_2 are identical for both sectors. (B) Measured expectation values for the operators Z_L and X_L defined in the inset, indicate that in the QSL region (shaded area) we prepare a superposition state of the two topological sectors ($\langle Z_L \rangle = 0$) with a finite overlap with the $|+\rangle$ state ($\langle X_L \rangle > 0$). (C) Finite expectation values for the correlations between pairs of hole-to-boundary Z strings (inset), consistent with (A).

in the same sector but opposite for the two sectors. The logical σ_L^x is instead proportional to X_L , which is any X loop around the hole. This operator anticommutes with Z_L and has eigenstates $|+\rangle \sim (|0_L\rangle + |1_L\rangle)/\sqrt{2}$ and $|-\rangle \sim (|0_L\rangle - |1_L\rangle)/\sqrt{2}$.

We measure Z_L and X_L on the strings defined in the inset of Fig. 11.5B, following the same quasi-adiabatic preparation as in Fig. 11.1D. We find that in the range of Δ/Ω associated with the onset of a QSL phase, $\langle Z_L \rangle = 0$, and $\langle X_L \rangle > 0$, indicating that the system is in a superposition of the two topological sectors, with a finite overlap with the $|+\rangle$ state (Fig. 11.5B). To further support this conclusion, we evaluate correlations $\langle Z_1 Z_2 \rangle$ between hole-to-boundary strings, which are expected to have the same expectation values for both topological sectors (Fig. 11.5A). In agreement with this prediction, we find that the correlations between different pairs of strings have finite expectation values, with amplitudes decreasing with the distance between the strings (Fig. 11.5C) due to imperfect state preparation. These measurements represent the first steps towards initialization and measurement of a topological qubit.

11.6 DISCUSSION AND OUTLOOK

Noting that it is not possible to classically simulate quantum dynamics for the full experimental system, we compare our results with several theoretical approaches. We first note that our observations qualitatively disagree with the ground state phase diagram obtained from density-matrix-renormalization-group (DMRG) [246, 247] simulations on infinitely-long cylinders. For the largest accessible system sizes, including van der Waals interactions only up to intermediate distances ($\sim 4a$), we find a \mathbb{Z}_2 spin liquid in the ground state. However, unlike in deformed lattices [193], longer-range couplings destabilize the spin liquid in the ground state of the Hamiltonian (eq. (11.1)) on the specific ruby lattice used in the experiment, leading to a direct first-order transition from the disordered phase to the VBS phase (Appendix H). In

contrast, we experimentally observe the onset of the QSL phase in a relatively large parameter range, while no signatures of a VBS phase are detected.

To develop additional insight, we perform time-dependent DMRG calculations [246, 248, 247] simulating the same state preparation protocol as in the experiment on an infinitely-long cylinder with a seven-atom-long circumference (Appendix H). The results of these simulations are in good qualitative agreement with our experimental observations (see Fig. H.17). Specifically, similar to the results in Fig. 11.4, we find that the region $\Delta/\Omega \sim 3.54.5$ hosts nonzero signals for closed Z and X loops which cannot be factorized into open strings, a characteristic fingerprint of spin liquid correlations. In addition, exact diagonalization studies of a simplified blockade model reveal how the dynamical state preparation creates an approximate equal-weight and equal-phase superposition of many dimer states, instead of the VBS ground state (Appendix H). We conclude that quasi-adiabatic state preparation occurring over a few microseconds is insensitive to longer-range couplings and generates states that retain the QSL character (Appendix H). While this phenomenon deserves further theoretical studies, these considerations point towards the creation of a novel *metastable* state with key characteristic properties of a quantum spin liquid.

Our experiments offer unprecedented insights into elusive topological quantum matter, and open up a number of new directions in which these studies can be extended, including: improving the robustness of the QSL by using modified lattice geometries and boundaries [192, 193], as well as optimizing the state preparation to minimize quasiparticle excitations; understanding and mitigating environmental effects associated, e.g., with dephasing and spontaneous emission (Appendix H); optimizing string operator measurements using quasi-local transformations [249], potentially with the help of quantum algorithms [250]. At the same time, hardware-efficient techniques for robust manipulation and braiding of topological qubits

can be explored. Furthermore, methods for anyon trapping and annealing can be investigated, with eventual applications towards fault-tolerant quantum information processing [251]. With improved programmability and control, a broader class of topological quantum matter and lattice gauge theories can be efficiently implemented [194, 252], opening the door to their detailed exploration under controlled experimental conditions, and providing a novel route for the design of quantum materials that can supplement exactly solvable models [224, 253] and classical numerical methods [246, 247].

12

High-fidelity control and entanglement of Rydberg atom qubits

Neutral atoms are attractive building blocks for large-scale quantum systems. They can be well isolated from the environment, enabling long-lived quantum memories. Initialization, control, and read-out of their internal and motional states is accomplished by resonance methods developed over the past four decades [254]. Recent experiments demonstrated that arrays with a large number of identical atoms can be rapidly assembled while maintaining single-atom optical control [25, 24, 26]. These bottom-up approaches are complementary to the methods involving optical lattices loaded with ultracold atoms prepared via evaporative cooling [173],

and generally result in atom separations of several micrometers. In order to utilize these arrays for quantum simulation and quantum information processing, it is necessary to introduce controllable interactions between the atoms. This can be achieved by coherent coupling to highly excited Rydberg states, which exhibit strong, long-range interactions [29]. Over the past decade, this approach has emerged as a powerful platform for many applications, including fast multi-qubit quantum gates [88, 112, 110, 111, 255–257], quantum simulations of Ising-type spin models with up to 250 spins [115, 117, 258, 157, 177–179], and the study of collective behavior in mesoscopic ensembles [259, 260, 118, 261, 262]. Despite these impressive demonstrations, experimental progress to date has been limited by short coherence times and relatively low gate fidelities associated with such Rydberg excitations [112]. This imperfect coherence limits the quality of quantum simulations, and especially dims the prospects for neutral atom quantum information processing. The limited coherence becomes apparent even at the level of single isolated atomic qubits [53].

This Letter reports the experimental realization of high-fidelity quantum control of Rydberg atom qubits. We show that by reducing laser phase noise, a significant improvement in the coherence properties of individual qubits can be achieved, consistent with recent theoretical analysis [53]. We further demonstrate that this high-fidelity control extends to the multi-particle case by preparing a two-atom entangled state with a fidelity exceeding 0.97(3). Finally, we extend the lifetime of the prepared Bell state with a novel two-atom dynamical decoupling protocol.

12.1 EXPERIMENTAL SETUP

Our experimental setup has been described in detail previously [24, 157]. We deterministically prepare individual cold Rubidium-87 atoms in optical tweezers at programmable positions in

one dimension. The atoms are initialized in a Zeeman sublevel $|g\rangle = |5S_{1/2}, F = 2, m_F = -2\rangle$ of the ground state via optical pumping in a 1.5 G magnetic field (Chapter 2 and Appendix I). We then rapidly switch off the tweezer potentials, and apply a laser field to couple the atoms to the Rydberg state $|r\rangle = |70S, J = 1/2, m_J = -1/2\rangle$. After the laser pulse of typical duration 3-8 μ s, we restore the tweezer potentials. Atoms that are in the ground state are recaptured by the tweezers, whereas those left in the Rydberg state are pushed away by the tweezer beams [53]. This simple detection method has Rydberg state detection fidelity $f_r = 0.96(1)$ and ground state detection fidelity f_g ranging from 0.955(5) to 0.990(2), depending on the trap-off time (Chapter 3 and Appendix I).

In our experiments, the Rydberg states are excited via a two-photon transition. A 420 nm laser is blue detuned by Δ from the transition from $|g\rangle$ to $|e\rangle = |6P_{3/2}, F = 3, m_F = -3\rangle$. A second laser field at 1013 nm couples $|e\rangle$ to $|r\rangle$. The two lasers are polarized to drive σ^- and σ^+ transitions, respectively, such that only a single intermediate sublevel and Rydberg state can be coupled, avoiding the population of additional levels and associated dephasing (see Fig. 12.1(a)).

12.2 CAVITY FILTERING OF HIGH-FREQUENCY PHASE NOISE ON RYDBERG LASERS

The two lasers (external-cavity diode lasers from MogLabs) are frequency stabilized by a Pound-Drever-Hall (PDH) lock to an ultra-low expansion reference cavity (StableLasers). The PDH lock strongly suppresses laser noise at frequencies below the effective bandwidth of the lock, resulting in narrow linewidths of < 1 kHz, as estimated from in-loop noise. However, noise above the lock bandwidth cannot be suppressed, and can be amplified at high locking gain. This results in broad peaks in phase noise around $\sim 2\pi \times 1$ MHz (see inset of Fig. 12.1(b)). This high-frequency phase noise has been reported as a known coherence lim-

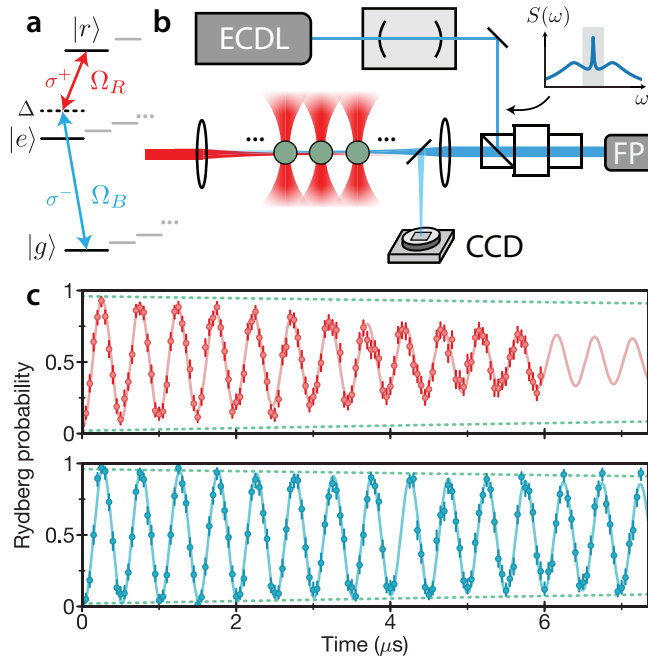


Figure 12.1: Experimental setup and single-atom Rabi oscillations. (a) The ground state $|g\rangle = |5S_{1/2}, F = 2, m_F = -2\rangle$ is coupled to $|r\rangle = |70S, J = 1/2, m_J = -1/2\rangle$ via the intermediate state $|e\rangle = |6P_{3/2}, F = 3, m_F = -3\rangle$. (b) The lasers are locked to a reference cavity whose narrow transmission window (shaded region in inset) suppresses high-frequency phase noise. This transmitted light is used to injection lock a Fabry-Perot (FP) laser diode. The laser diode output is focused onto the array of atoms trapped in optical tweezers, with a small pickoff onto a reference CCD camera used for alignment. (c) Resonant two-photon coupling induces Rabi oscillations between $|g\rangle$ and $|r\rangle$. The upper plot is a typical measurement from the previous setup used in [157]. The lower plot shows typical results with the new setup, with a fitted coherence time of $27(4)\mu\text{s}$. Each data point is calculated from 50-100 repeated measurements of two identically-coupled atoms separated by $23 \mu\text{m}$ such that they are effectively non-interacting. In all figures, error bars mark 68% confidence intervals, solid lines are fits to experimental data, and dotted lines indicate the expected contrast from the numerical model.

itation in Rydberg experiments [53] and experiments with trapped ions [263, 264], and has also been studied in the context of atomic clocks [265]. To suppress this phase noise, we follow the approach of [266, 267, 263, 264] in which the reference cavity is used as a spectral filter. In particular, the transmission function of the cavity is a Lorentzian with a full-width at half maximum of $\Gamma \sim 2\pi \times 500$ kHz (corresponding to a finesse of $F \sim 3000$). When the laser is locked, its narrow linewidth carrier component is transmitted through the cavity, whereas the power spectral density $2\pi \times 1$ MHz away from the carrier is suppressed by a factor of $\gtrsim 16$ (estimated using the cavity linewidth). To amplify the transmitted light at both 420 and 1013 nm, we split the two colors and use each beam to injection lock a separate laser diode (1013 nm from Toptica, 420 nm from TopGaN), which inherits the same spectral properties. This amplifies the spectrally pure transmitted light to 5 mW of 420 nm and 50 mW of 1013 nm light. While the 420 nm power is sufficient to drive the blue transition directly, the 1013 nm is further amplified by a tapered amplifier (MogLabs).

We focus both lasers onto the atom array in a counter-propagating configuration to minimize Doppler shifts due to finite atomic temperature. The 420 (1013) nm laser is focused to a waist of 20 (30) μm . We achieve single-photon Rabi frequencies of $\Omega_B \simeq 2\pi \times 54$ MHz ($\Omega_R \simeq 2\pi \times 40$ MHz). At our intermediate detuning of $\Delta \simeq 2\pi \times 540$ MHz, this leads to a two-photon Rabi frequency of $\Omega = \Omega_B \Omega_R / (2\Delta) \simeq 2\pi \times 2$ MHz. Each beam is power-stabilized to $< 1\%$ by an acousto-optic modulator that is also used for fast (~ 20 ns) switching. We use a sample-and-hold method to pause the intensity lock during the Rydberg pulses to avoid introducing additional intensity noise. To minimize sensitivity to pointing fluctuations, we ensure well-centered alignment onto the atoms using a reference camera (depicted in Fig. 12.1(b)) and an automatic beam alignment procedure (Chapter 5 and Appendix I).

12.3 CHARACTERIZING RYDBERG COHERENCE

With these technical improvements in place, we measure long-lived Rabi oscillations with a $1/e$ lifetime of $\tau = 27(4) \mu\text{s}$, to be compared with a typical $\lesssim 7 \mu\text{s}$ lifetime in previous experiments [157] (see Fig. 12.1(c)). Importantly, we observe excellent agreement between these new measurements and a simple numerical model for our single-atom system, indicated by dotted lines in all figures. The numerical model has no free parameters and accounts only for the effects of random Doppler shifts, off-resonant scattering from the intermediate state, the Rydberg state lifetime, and finite detection fidelity (Appendix I). In the case of resonant Rabi oscillations, the primary limitation is off-resonant scattering.

Next, we characterize the coherence of single atoms and demonstrate single-qubit control. To begin, we experimentally measure the lifetime of the Rydberg state in Fig. 12.2(a). The measured $T_1 = T_{r \rightarrow g} = 51(6) \mu\text{s}$ is consistent with the $146 \mu\text{s}$ Rydberg state lifetime [48] when combined with the $\sim 80 \mu\text{s}$ timescale for off-resonant scattering of the 1013 nm laser from $|e\rangle$. A Ramsey experiment shows Gaussian decay that is well-explained by thermal Doppler shifts (see Fig. 12.2(b)). At $10 \mu\text{K}$, the random atomic velocity in each shot of the experiment appears as a random detuning δ^D from a Gaussian distribution of width $2\pi \times 43.5 \text{ kHz}$, resulting in dephasing as $|\psi\rangle \rightarrow \frac{1}{\sqrt{2}}(|g\rangle + e^{i\delta^D t}|r\rangle)$. However, since the random Doppler shift is constant over the duration of each pulse sequence, its effect can be eliminated via a spin-echo sequence (orange in Fig. 12.2(b)). Note that the spin-echo measurements display some small deviations from the numerical simulations, indicating the presence of an additional dephasing channel. Assuming an exponential decay, we measure a fitted $T_2 = 32(6) \mu\text{s}$ and extract a pure dephasing time $T_\phi = (1/T_2 - 1/(2T_{r \rightarrow g}))^{-1} = 47(13) \mu\text{s}$. We hypothesize that this dephasing may result from residual laser phase noise.

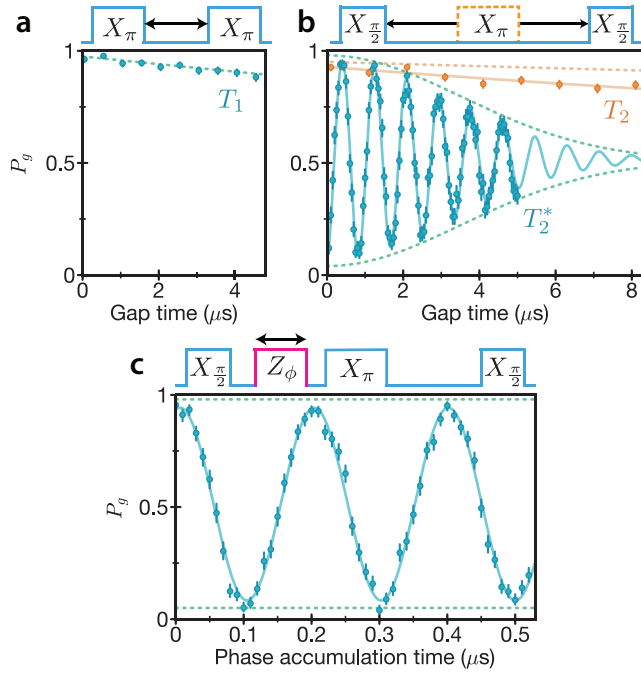


Figure 12.2: Characterization of single-atom coherence and phase control. (a) The lifetime of $|r\rangle$ is measured by exciting from $|g\rangle$ to $|r\rangle$ with a π -pulse, and then de-exciting after a variable delay. The probability to end in $|g\rangle$ (denoted P_g) decays with an extracted lifetime of $T_1 = 51(6)$ μs (fitted to an exponential decay model with no offset). (b) A Ramsey experiment (blue) shows Gaussian decay with a $1/e$ lifetime of $T_2^* = 4.5(1)$ μs , limited by thermal Doppler shifts. Inserting an additional π -pulse (orange) between the $\pi/2$ -pulses cancels the effect of the Doppler shifts and results in a substantially longer coherence lifetime of $T_2 = 32(6)$ μs (fitted to an exponential decay model with an offset of 0.5). (c) A single-atom phase gate is implemented by applying an independent 809 nm laser which induces a light shift $\delta = 2\pi \times 5$ MHz on the ground state for time t , resulting in an accumulated dynamical phase $\phi = \delta t$. The gate is embedded in a spin-echo sequence to cancel Doppler shifts. In each measurement shown here, the 1013 nm laser remains on for the entire pulse sequence, while the 420 nm laser is pulsed according to the sequence shown above each plot. Each data point is calculated from 200 – 500 repeated measurements with a single atom per realization.

Finally, we demonstrate a single-atom phase gate by applying an independent focused laser that shifts the energy of the ground state $|g\rangle$ (see Fig. 12.2(c)) (Appendix I). By controlling the duration of the applied laser pulse, we impart a controlled dynamical phase on $|g\rangle$ relative to $|r\rangle$. The contrast of the resulting phase gate (embedded in a spin-echo sequence) is close to the limit imposed by detection and spin-echo fidelity.

12.4 GENERATING ENTANGLEMENT WITHIN THE RYDBERG BLOCKADE REGIME

We next turn to two-atom control. To this end, we position two atoms at a separation of $5.7 \mu\text{m}$, at which the Rydberg-Rydberg interaction is $U/\hbar = 2\pi \times 30 \text{ MHz} \gg \Omega = 2\pi \times 2 \text{ MHz}$. In this so-called Rydberg blockade regime, the laser field globally couples both atoms from $|gg\rangle$ to the symmetric* state $|W\rangle = \frac{1}{\sqrt{2}}(|gr\rangle + |rg\rangle)$ at an enhanced Rabi frequency of $\sqrt{2}\Omega$ (see Fig. 12.3(a)). The measured probabilities for the states $|gg\rangle$, $|gr\rangle$, $|rg\rangle$, and $|rr\rangle$ (denoted by P_{gg} , P_{gr} , P_{rg} , and P_{rr} , respectively) show that indeed no population enters the doubly-excited state ($P_{rr} < 0.02$, consistent with only detection error). Instead, there are oscillations between the manifold of zero excitations and the manifold of one excitation with a fitted frequency of $2\pi \times 2.83 \text{ MHz} \approx \sqrt{2}\Omega$ (see Fig. 12.3(b)).

These collective Rabi oscillations can be used to directly prepare the maximally entangled Bell state $|W\rangle$ by applying a π -pulse at the enhanced Rabi frequency (denoted by X_π^W). To determine the fidelity of this experimentally prepared entangled state, given by $\mathcal{F} = \langle W|\rho|W\rangle$, we express it in terms of diagonal and off-diagonal matrix elements of the density operator ρ :

$$\mathcal{F} = \frac{1}{2}(\rho_{gr,gr} + \rho_{rg,rg}) + \frac{1}{2}(\rho_{gr,rg} + \rho_{rg,gr}) \quad (12.1)$$

*Here the excited states $|r\rangle$ are defined in the rotating frame to incorporate the spatial phase factors e^{ikx} , as discussed in Appendix I.

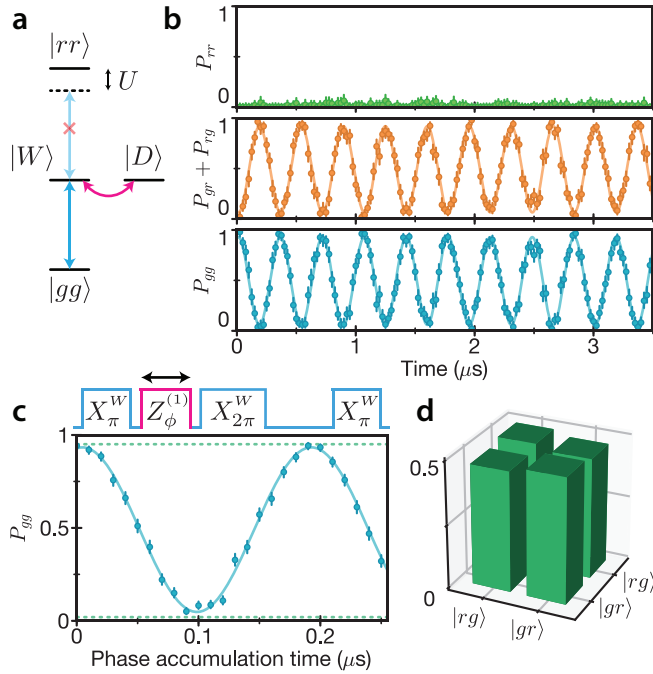


Figure 12.3: Coherent control and entanglement generation with two atoms. (a) The level structure for two nearby atoms features a doubly excited state $|rr\rangle$ which is shifted by the interaction energy $U \gg \hbar\Omega$. In this Rydberg blockade regime, the laser field only couples $|gg\rangle$ to $|W\rangle$. The symmetric and antisymmetric states $|W\rangle, |D\rangle = \frac{1}{\sqrt{2}}(|gr\rangle \pm |rg\rangle)$ can be coupled by a local phase gate on one atom (pink arrow). (b) After driving both atoms on resonance for variable time, we measure the probability of the resulting two-atom states. Population oscillates from $|gg\rangle$ to $|W\rangle$ at the enhanced Rabi frequency $\sqrt{2}\Omega$. (c) We measure the entanglement fidelity of the two atoms after a resonant π -pulse in the blockade regime. A local phase gate $Z_\phi^{(1)}$ rotates $|W\rangle$ into $|D\rangle$, which is detected by a subsequent π -pulse. The fitted contrast $0.88(2)$ measures the off-diagonal density matrix elements. The phase gate is implemented by an off-resonant laser focused onto one atom, with a crosstalk of $< 2\%$ (Appendix I). The measurement is embedded in a spin-echo sequence to cancel dephasing from thermal Doppler shifts. (d) The four components of the density matrix correspond to an entangled state with fidelity $\mathcal{F} = 0.97(3)$ (corrected for detection error). Each data point in (b) and (c) is calculated from ~ 50 and ~ 250 repeated measurements, respectively, with a single atom pair per realization. Dotted lines in (c) mark the limits of detection fidelity.

where $\rho_{\alpha\beta\gamma\delta} = \langle\alpha\beta|\rho|\gamma\delta\rangle$ for $\alpha, \beta, \gamma, \delta \in \{g, r\}$. The diagonal elements can be directly measured by applying a π -pulse and then measuring the populations. The results closely match those of a perfect $|W\rangle$ state after accounting for state detection errors, with $\rho_{gr,gr} + \rho_{rg,rg} = 0.94(1)$, relative to a maximum possible value of 0.95(1).

12.5 CHARACTERIZING TWO-PARTICLE BELL STATE

To measure the off-diagonal elements of the density matrix, we make use of the single-atom phase gate $Z_\phi^{(1)}$ demonstrated in Fig. 12.2(c), which introduces a variable phase on one atom (as demonstrated in [268]). Specifically, a local beam adds a light shift δ to $|gr\rangle$ but not to $|rg\rangle$, such that $|W\rangle \rightarrow \frac{1}{\sqrt{2}}(e^{i\delta t}|gr\rangle + |rg\rangle)$.

This phase accumulation rotates $|W\rangle$ into the orthogonal dark state $|D\rangle = \frac{1}{\sqrt{2}}(|gr\rangle - |rg\rangle)$ according to:

$$|W\rangle \rightarrow \cos(\delta t/2)|W\rangle + i \sin(\delta t/2)|D\rangle \quad (12.2)$$

Since $|D\rangle$ is uncoupled by the laser field, a subsequent π -pulse maps only the population of $|W\rangle$ back to $|gg\rangle$. The probability of the system to end in $|gg\rangle$ therefore depends on the phase accumulation time as $P_{gg}(t) = A \cos^2(\delta t/2)$. Here, the amplitude of the oscillation A precisely measures the off-diagonal matrix elements $\rho_{gr,rg} = \rho_{rg,gr}$ (see Appendix I for derivation). Note that in order to mitigate sensitivity to random Doppler shifts, we embed this entire sequence in a spin-echo protocol (see Fig. 12.3(c)). The resulting contrast is $A = 0.88(2) = 2\rho_{gr,rg} = 2\rho_{rg,gr}$. Combining these values with the diagonal matrix elements, we have directly measured entanglement fidelity of $\mathcal{F} = 0.91(2)$. The maximum measurable fidelity given our state detection error rates would be 0.94(2), so after correcting for imperfect detection, we find that the entangled Bell state was created with fidelity of $\mathcal{F} = 0.97(3)$. We note that this fidelity

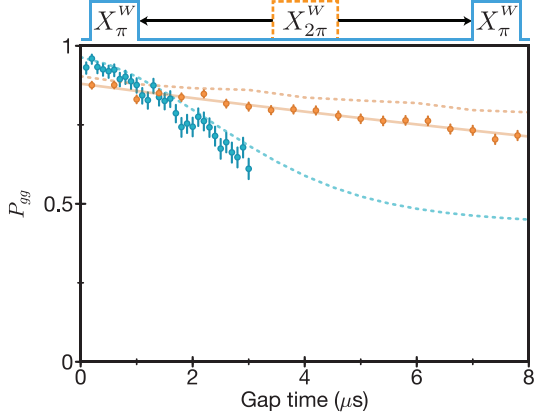


Figure 12.4: Extension of entangled-state lifetime via dynamical decoupling. We measure the lifetime of $|W\rangle$ by exciting $|gg\rangle$ to $|W\rangle$ and then de-exciting after a variable time (blue). The lifetime is limited by dephasing from random Doppler shifts. Inserting an additional 2π -pulse (orange) in the blockade regime swaps the populations of $|gr\rangle$ and $|rg\rangle$ to refocus the random phase accumulation, extending the lifetime to $\sim 36 \mu\text{s}$ (fitted to an exponential decay with no offset, shown as the solid orange line). The initial offset in each curve is set by the ground state detection fidelity associated with the given trap-off time. All data points are calculated from 30-100 repeated measurements, averaged over nine independent identically-coupled atom pairs per realization.

includes errors introduced during the pulses that follow the initial π -pulse, and therefore constitutes a lower bound on the true fidelity.

12.6 LIFETIME OF BELL STATE

Finally, we explore the lifetime of the entangled state by exciting $|W\rangle$ with a π -pulse and then de-exciting after a variable delay (see Fig. 12.4). The decay in contrast is in good agreement with numerical predictions associated with random Doppler shifts. In particular, the two components $|gr\rangle$ and $|rg\rangle$ of the $|W\rangle$ state dephase as $|W\rangle \rightarrow \frac{1}{\sqrt{2}}(e^{i\delta_2^D t}|gr\rangle + e^{i\delta_1^D t}|rg\rangle)$, where δ_i^D is the two-photon Doppler shift on atom i .

We extend the lifetime of the two-atom entangled state with a many-body echo sequence. After the $|W\rangle$ state has evolved for time T , we apply a 2π -pulse to the two-atom system. In the Rydberg blockade regime, such a pulse swaps the populations of $|gr\rangle$ and $|rg\rangle$. After again evolving for time T , the total accumulated Doppler shifts are the same for each

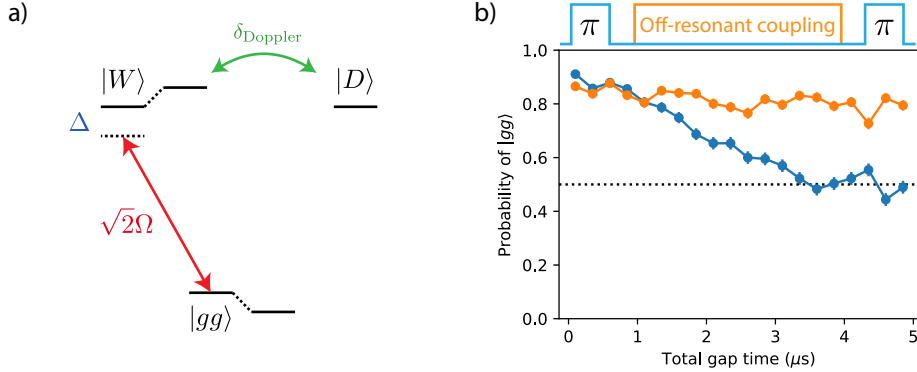


Figure 12.5: Suppressing Doppler dephasing of Bell state. (a) Doppler shifts due to finite atomic temperature are a dominant source of dephasing of the $|W\rangle$ state, leading to a random coupling δ_{Doppler} from $|W\rangle$ to $|D\rangle$ given by the difference in Doppler shifts for the two atoms. By applying the Rydberg laser in an off-resonant configuration, detuned by Δ , the states $|gg\rangle$ and $|W\rangle$ are shifted in energy by $\Omega^2/2\Delta$ due to the AC Stark effect. When this light shift is larger than the rate of Doppler dephasing, $\Omega^2/2\Delta > \delta_{\text{Doppler}}$, the dephasing mechanism is off-resonance and therefore suppressed. (b) We measure the $|W\rangle$ state lifetime similarly to in Fig. 12.4, with and without the presence of the off-resonant Rydberg laser. We observe that the presence of the off-resonant coupling indeed suppresses dephasing and leads to an increased lifetime.

part of the two-atom wavefunction, and therefore do not affect the final $|W\rangle$ state fidelity.

Indeed, Figure 12.4 shows that its lifetime is extended far beyond the Doppler-limited de-

decay to $T_2^W = 36(2)$ μs . As in the single atom case, we extract a pure dephasing timescale

$$T_\phi^W = (1/T_2^W - 1/T_{r \rightarrow g})^{-1} > 100 \text{ } \mu\text{s}.$$

Remarkably, the Bell state dephasing time $T_\phi^W > 100 \text{ } \mu\text{s}$ is significantly longer than the single atom dephasing time $T_\phi = 47(13)$ μs . This can be understood by noting that the states $|gr\rangle$ and $|rg\rangle$ form a decoherence-free subspace that is insensitive to global perturbations such as laser phase and intensity fluctuations that couple identically to both atoms [269, 270]. In contrast, a single atom in a superposition $|\psi\rangle = \frac{1}{\sqrt{2}}(|g\rangle + |r\rangle)$ is sensitive to both the laser phase and the laser intensity. These measurements provide further indications that laser noise is not completely eliminated in our experiment.

12.7 SUPPRESSING DOPPLER DEPHASING OF BELL STATE

The simple dynamics of the blockaded two-atom system enable simple echo protocols to eliminate the effect of Doppler dephasing. However, more general approaches that do not rely on echo pulses are also possible, and may be applicable in more complex systems. Here, we consider a method to suppress Doppler dephasing of the Bell state $|W\rangle$ by application of the Rydberg laser in an off-resonant configuration.

Doppler dephasing results from a random coupling between $|W\rangle$ and $|D\rangle$, with rate given by the difference in Doppler shifts for the two atoms. In each experimental cycle, this can be regarded as a static, coherent coupling, but with random amplitude. In the absence of laser fields, $|W\rangle$ and $|D\rangle$ are degenerate, so random Doppler coupling leads to large population transfer out of $|W\rangle$ on the timescale set by the Doppler shifts. However, in the presence of the Rydberg laser which is far off-resonance, the state $|W\rangle$ shifts due to the AC Stark effect, and $|D\rangle$ is unshifted because it is uncoupled by the laser field. The population transfer from $|W\rangle$ to $|D\rangle$ is now suppressed as long as the dephasing rate is smaller than the AC Stark shift of $|W\rangle$ (Fig. 12.5a). Indeed, we observe that this protocol substantially extends the Bell state lifetime (Fig. 12.5b).

12.8 OUTLOOK

Our measurements establish Rydberg atom qubits as a competitive platform for high-fidelity quantum simulation and computation. The techniques demonstrated in this Letter are of immediate importance to ongoing experiments using neutral atom arrays. Furthermore, the demonstrated fidelities can be further improved by increasing laser intensities and operating at larger detunings from the intermediate state, thereby reducing the deleterious effect of off-

resonant scattering (Appendix I), or by using a direct single-photon transition. In addition, sideband cooling of atoms in tweezers [95, 43] can dramatically decrease the magnitude of Doppler shifts, while low-noise laser sources such as Titanium-Sapphire lasers or diode lasers filtered by higher-finesse cavities will further eliminate errors caused by phase noise. Advanced control techniques, such as laser pulse shaping, can also be utilized to reach higher fidelities [271]. Finally, state detection fidelities can be improved by mapping Rydberg states to separate ground state levels, which will additionally enable long-term storage of the prepared entangled states.

13

Generation and manipulation of Schrödinger cat states in Rydberg atom arrays

13.1 GREENBERGER–HORNE–ZEILINGER STATES

GHZ states constitute an important class of entangled many-body states [272]. On the one hand, such states provide an important resource for applications ranging from quantum metrology [273] to quantum error correction [274]. On the other hand, these states are among the most fragile many-body states, since a single error on any one of the N qubits collapses the superposition resulting in a statistical mixture. Remarkably, despite their highly entangled

nature, GHZ states can be characterized by just two diagonal and two off-diagonal terms in the N -particle density matrix. In contrast to quantifying the degree of general entangled states in many-body systems, which is extremely challenging [275–277], the GHZ state fidelity ($\mathcal{F} > 0.5$) constitutes an accessible witness for N -partite entanglement [13]. For these reasons, GHZ state creation can serve as an important benchmark to characterize the quality of any given quantum hardware. Such states have been previously generated using systems of nuclear spins [278, 279], individually controlled optical photons [280–282], trapped ions [13, 283, 101], and superconducting quantum circuits [284, 103, 285]. Large-scale superposition states have also been generated in systems of microwave photons [286] and atomic ensembles without individual particle addressing [273].

In this Report we demonstrate the preparation of N -particle GHZ states

$$|\text{GHZ}_N\rangle = \frac{1}{\sqrt{2}} (|0101\cdots\rangle + |1010\cdots\rangle) \quad (13.1)$$

in a one dimensional array of individually trapped neutral ^{87}Rb atoms, where the qubits are encoded in an atomic ground state $|0\rangle$ and in a Rydberg state $|1\rangle$. Our entangling operation relies on the strong van-der-Waals interaction between atoms in states $|1\rangle$ and on engineering the energy spectrum of the quantum many-body system to allow for a robust quantum evolution from an initial product state to a GHZ state. The basic ingredients for the manipulation of atomic states, both for generating and characterizing GHZ states, are illustrated in Fig. 13.1. All the atoms are homogeneously coupled to a Rydberg state $|1\rangle$ via a two-photon transition with an effective coupling strength $\Omega(t)$ and detuning $\Delta(t)$ [117, 157]. In addition, we use addressing beams to introduce local energy shifts δ_i on specific sites i along the array

(Fig. 13.1A). The resulting many-body Hamiltonian is

$$\frac{H}{\hbar} = \frac{\Omega(t)}{2} \sum_{i=1}^N \sigma_x^{(i)} - \sum_{i=1}^N \Delta_i(t) n_i + \sum_{i < j} \frac{V}{|i-j|^6} n_i n_j \quad (13.2)$$

where $\sigma_x^{(i)} = |0\rangle\langle 1|_i + |1\rangle\langle 0|_i$ is the qubit flip operator, $\Delta_i(t) = \Delta(t) + \delta_i$ is the local effective detuning set by the Rydberg laser and the local light shift, $n_i = |1\rangle\langle 1|_i$ is the number of Rydberg excitations on site i , and V is the interaction strength of two Rydberg atoms on neighboring sites. The separation between adjacent sites is chosen such that the nearest-neighbor interaction $V = 2\pi \cdot 24 \text{ MHz} \gg \Omega$ results in the Rydberg blockade [88, 110, 111], forbidding the simultaneous excitation of adjacent atoms into the state $|1\rangle$.

13.2 ENTANGLEMENT PROTOCOL

To prepare GHZ states, we utilize arrays with an even number N of atoms. For large negative detuning Δ of the Rydberg laser, the many-body ground state of the Hamiltonian (2) is $|G_N\rangle = |0\rangle^{\otimes N}$. For large uniform positive detuning $\Delta_i = \Delta$, the ground state manifold consists of $N/2+1$ nearly degenerate classical configurations with $N/2$ Rydberg excitations. These include in particular the two target antiferromagnetic configurations $|A_N\rangle = |0101\cdots 01\rangle$ and $|\overline{A}_N\rangle = |1010\cdots 10\rangle$ [102], as well as other states with nearly identical energy (up to a weak second-nearest neighbor interaction), with both edges excited, such as $|10010\cdots 01\rangle$. To isolate a coherent superposition of states $|A_N\rangle$ and $|\overline{A}_N\rangle$, we introduce local light shifts δ_e using off-resonant laser beams at 840 nm, generated by an acousto-optic deflector (AOD), which energetically penalize the excitation of edge atoms (Fig. 13.1A), and effectively eliminate the contribution of undesired components. In this case, the ground state for positive detuning is given by the GHZ state (1) and there exists, in principle, an adiabatic pathway that trans-

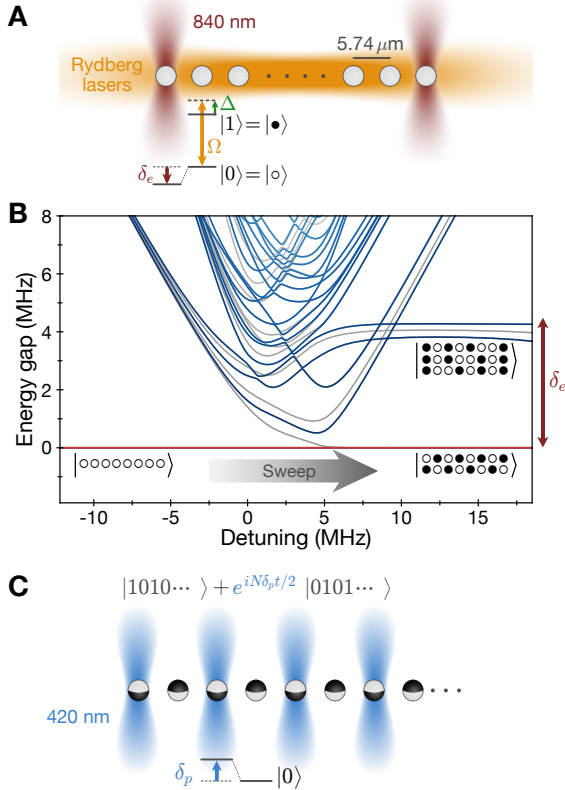


Figure 13.1: Experimental scheme and entanglement generation procedure. **A**, ^{87}Rb atoms initially in a ground state $|0\rangle = |5S_{1/2}, F = 2, m_F = -2\rangle$ are coupled to a Rydberg state $|1\rangle = |70S_{1/2}, m_J = -1/2\rangle$ by a light field with a coupling strength $\Omega/(2\pi) \leq 5 \text{ MHz}$ and a variable detuning Δ . Local addressing beams at 840 nm target the edge atoms, reducing the energy of $|0\rangle$ at those sites by a light shift δ_e . **B**, Many-body energy gap spectrum of $N = 8$ atoms, including energy shifts on the edge atoms. For positive detuning, the states with one ground state atom on the edges are favored over states with a Rydberg atom on both edges. An adiabatic pathway connects the state $|G_N\rangle = |000\dots\rangle$ with the two GHZ components. Gray lines in the spectrum are energies associated with antisymmetric states, which are not coupled to the initial state by Hamiltonian (2). **C**, Method to control the phase ϕ of GHZ states. Every other site of the array is illuminated with a local addressing beam at 420 nm, which imposes a negative differential light shift δ_p on the $|0\rangle$ - $|1\rangle$ transition. The offset in state $|0101\dots\rangle$ relative to $|1010\dots\rangle$ leads to an evolving dynamical phase.

forms the state $|G_N\rangle$ into $|\text{GHZ}_N\rangle$ by adiabatically increasing $\Delta(t)$ from negative to positive values (Fig. 13.1B).

In practice, the time necessary to adiabatically prepare such a GHZ state grows with system size and becomes prohibitively long for large N owing to small energy gaps in the many-body spectrum. To address this limitation, we employ optimal control methods to find laser pulses that maximize the GHZ state preparation fidelity while minimizing the amount of time necessary. Our specific implementation, the Remote dressed Chopped-Random Basis algorithm (RedCRAB) [287, 288], yields optimal shapes of the laser intensity and detuning for the given experimental conditions (Appendix J). For $N \leq 8$ atoms, we perform this optimization using $\delta_e/(2\pi) \approx -4.5$ MHz light shifts on the edge atoms. For larger systems of $N > 8$, we found the preparation to be more robust by increasing the edge light shifts to $\delta_e/(2\pi) \approx -6$ MHz and adding $\delta_{4,N-3}/(2\pi) \approx -1.5$ MHz light shifts on the third site from both edges.

Our experiments are based on the optical tweezer platform and experimental procedure that have been described previously [157]. Following the initialization of a defect-free N -atom array, the traps are switched off while the atoms are illuminated with the Rydberg and local light shift beams. The internal state of the atoms is subsequently measured by imaging state $|0\rangle$ atoms recaptured in the traps, while Rydberg atoms are repelled by the trapping light [53]. Fig. 13.2 demonstrates the result of such experiments for a 20-atom array. After applying the optimized pulse shown in Fig. 13.2B, we measure the probability of observing different patterns $p_n = \langle n | \rho | n \rangle$ in the computational basis, where ρ is the density operator of the prepared state. Fig. 13.2A shows the measured probability to observe each of the 2^{20} possible patterns in a 20-atom array. The states $|A_{20}\rangle$ and $|\bar{A}_{20}\rangle$ clearly stand out (blue bars) with a combined probability of 0.585(14) and almost equal probability of observing each one.

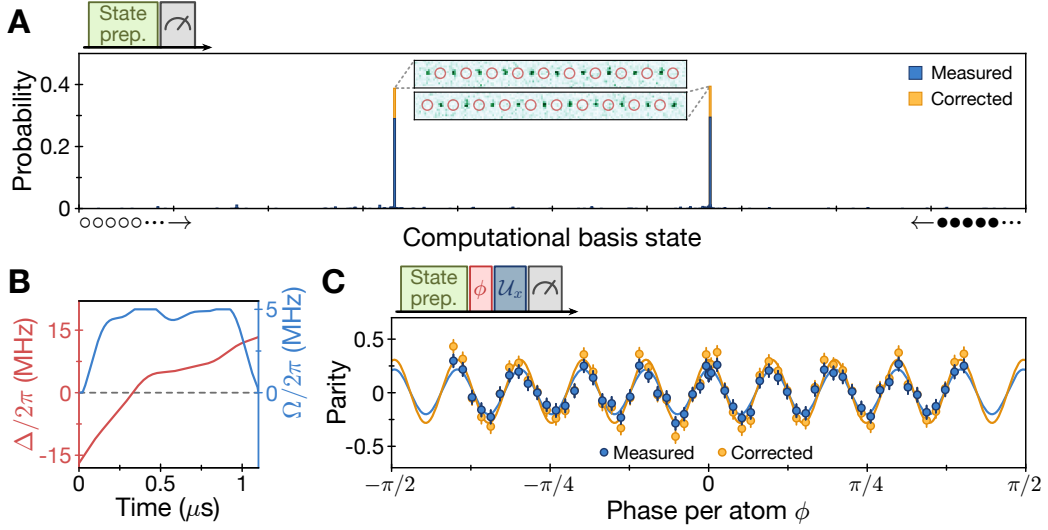


Figure 13.2: Production of a 20-atom GHZ state. **A**, Probability of observing different patterns, showing a large population of the two target patterns out of $2^{20} = 1,048,576$ possible states. Shown here are the directly measured (blue bars) and the corrected values (orange bars) for the two target states after taking into account measured detection errors. Insets show fluorescence images of the two target patterns, where red circles mark empty sites corresponding to atoms in state $|1\rangle$. **B**, Optimal control pulse used for state preparation. **C**, Parity oscillations produced by acquiring a phase ϕ between the GHZ components. We apply a staggered field with an energy shift of $\delta_p/(2\pi) = \pm 3.8$ MHz on all sites, followed by an operation \mathcal{U}_x such that subsequent parity measurements are sensitive to ϕ (Appendix J). From the population measurement and the oscillation amplitude, we obtain a lower bound on the 20-atom GHZ fidelity of $\mathcal{F} \geq 0.542(18)$. Error bars denote 68% confidence intervals.

13.3 GHZ STATES WITH UP TO 20 ATOMS

To characterize the experimentally prepared state ρ , we evaluate the GHZ state fidelity

$$\mathcal{F} = \langle \text{GHZ}_N | \rho | \text{GHZ}_N \rangle = \frac{1}{2} \left(p_{A_N} + p_{\bar{A}_N} + c_N + c_N^* \right) \quad (13.3)$$

where p_{A_N} and $p_{\bar{A}_N}$ are the populations in the target components and $c_N = \langle \bar{A}_N | \rho | A_N \rangle$ is the off-diagonal matrix element, which can be measured by utilizing the maximal sensitivity of the GHZ state to a staggered magnetic field. Specifically, evolving the systems with the Hamiltonian $H_p = \hbar\delta_p/2 \sum_{i=1}^N (-1)^i \sigma_z^{(i)}$, the amplitude c_N acquires a phase ϕ at a rate of $\dot{\phi} = N\delta_p$. Measuring an observable that oscillates at this frequency provides a lower bound

on the coherence $|c_N|$ through the oscillation contrast [104] (Appendix J). In our experiments, the staggered field is implemented by applying off-resonant focused beams of equal intensity at 420 nm, generated by another AOD, to every other site of the array (Fig. 13.1C), resulting in a local energy shift δ_p (Appendix J). Subsequently, we drive the atoms resonantly, applying a unitary operation \mathcal{U}_x in order to change the measurement basis (Appendix J), such that a measurement of the parity $\mathcal{P} = \prod_i \sigma_z^{(i)}$ becomes sensitive to the phase of c_N . Fig. 13.2C shows the measured parity as a function of the phase accumulated on each atom in the array, demonstrating the coherence of the created state.

To extract the entanglement fidelity for large atomic states, we carefully characterized our detection process used to identify atoms in $|0\rangle$ and $|1\rangle$, since it has a small but finite error. We have independently determined the probability to misidentify the state of a particle to be $p(1|0) = 0.0063(1)$, and $p(0|1) = 0.0227(42)$ (Appendix J). Using these numbers, we extract a corrected probability of preparing states $|A_{20}\rangle$ and $|\bar{A}_{20}\rangle$ to be 0.782(32) (orange bars in Fig. 13.2A) and a corrected amplitude of oscillation of 0.301(18) (orange points in Fig. 13.2C). In the population measurement, we independently confirmed that the 14 most commonly observed incorrect patterns are fully consistent with the correct target states with a single detection error. From these measurements we extract a lower bound for the 20-atom GHZ state fidelity of $\mathcal{F} \geq 0.542(18)$, certifying genuine 20-partite entanglement.

This protocol was applied for multiple system sizes of $4 \leq N \leq 20$, using $1.1\mu\text{s}$ control pulses optimized for each N individually. Consistent with expected GHZ dynamics (Fig. 13.1C and [283]), the frequency of the measured parity oscillations grows linearly with N (Fig. 13.3A). Extracting the GHZ fidelity from these measurements shows that we surpass the threshold of $\mathcal{F} = 0.5$ for all studied system sizes (Fig. 13.3B). We further characterized the lifetime of the created GHZ state by measuring the parity signal after a variable delay (Fig. 13.3C). These

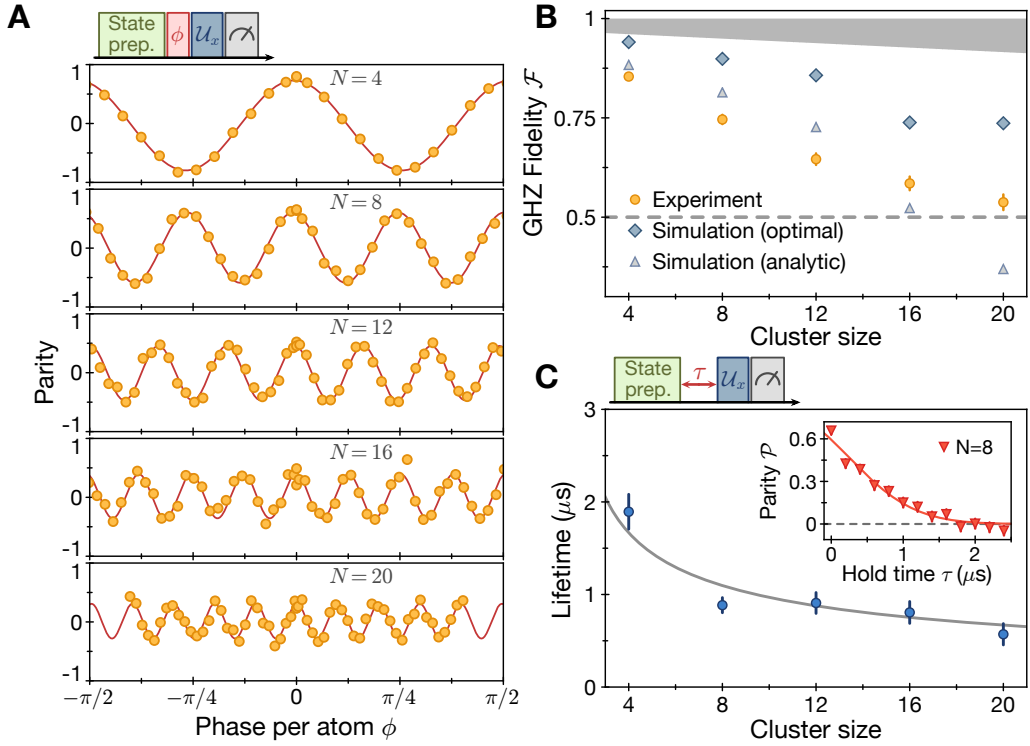


Figure 13.3: Quantifying entanglement for different system sizes. **A**, Parity oscillations measured on different system sizes. We apply a staggered field with a shift of $\delta_p/(2\pi) = \pm 3.8$ MHz on all sites and observe a scaling of the phase accumulation rate proportional to the system size N . **B**, Measured GHZ fidelity for different system sizes (Orange circles). Blue diamonds show the result of simulations that account for dephasing during state preparation, decay from off-resonant photon scattering and imperfect detection of coherence through parity oscillations (Appendix J). Pale blue triangles show identical simulations for analytic pulses of duration $T = 1.1$ μs with a linear detuning sweep and $\Omega(t) = \Omega_{\max}[1 - \cos^{12}(\pi t/T)]$, which were used as an initial guess for the RedCRAB optimization. The gray shaded area marks a region not measurable with our parity observable, see text and Appendix J for details. **C**, Lifetime of the GHZ state coherence. For all system sizes N , we measure the state parity after a variable delay following the GHZ state preparation, which decays to zero (inset). We fit the individual parity data to the tail of a Gaussian decay curve, as we assume the dephasing has started during state preparation, i.e. before $\tau = 0$. The gray line shows a theoretical prediction with no free parameters accounting for known dephasing mechanisms in our system.

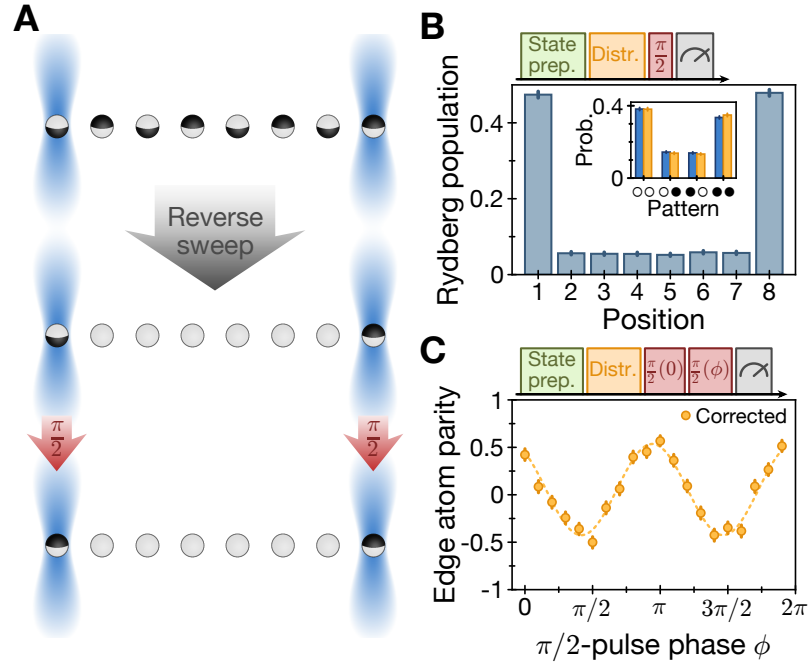


Figure 13.4: Demonstration of entanglement distribution. **A**, Experimental protocol for $N = 8$. Edge atoms are addressed by light shift beams and a reverse sweep of the Rydberg laser detuning is performed to disentangle the bulk of the array, leaving a Bell state $|\Psi^+\rangle \propto |1\cdots 0\rangle + |0\cdots 1\rangle$ on the edge. A $\pi/2$ pulse resonant only with the edge atoms is applied to convert the state $|\Psi^+\rangle$ to $|\Phi^+\rangle \propto |0\cdots 0\rangle + |1\cdots 1\rangle$. **B**, Measured Rydberg populations on each site after entanglement distribution, where the probability for a single Rydberg excitation is shared among the two edges. Inset: Probabilities for different patterns on the edge atoms, which are consistent with the Bell state $|\Phi^+\rangle$. Blue bars indicate measured values, while orange bars include corrections for detection errors. **C**, Measurement of the Bell state coherence. GHZ entanglement is distributed to the edges, a $\pi/2$ pulse is applied at laser phase $\phi = 0$, followed by a second $\pi/2$ pulse at varying phase ϕ . The amplitude of the parity oscillation provides a lower bound on the coherence of the Bell state, yielding a fidelity of $\mathcal{F} \geq 0.605(13)$.

observations are most consistent with Gaussian decay, while characteristic lifetimes are reduced relatively slowly for increasing system sizes, indicating the presence of a non-Markovian environment [274, 101].

13.4 ENTANGLEMENT DISTRIBUTION

As an application of our entanglement manipulation technique, we demonstrate its use for entanglement distribution between distant atoms. Specifically, we consider the preparation of Bell states between atoms at the two opposite edges of the array. Our approach is based

on first creating the GHZ state using the above procedure, followed by an operation that disentangles all but two target atoms. The latter is realized by shifting the transition frequencies of the two target edge atoms using two strong, blue-detuned addressing beams at 420 nm. Subsequently, we perform a reverse detuning sweep of the Rydberg laser that effectively disentangles all atoms except those at the edges. The resulting state corresponds to a coherent superposition of two pinned excitations that can be converted into a Bell state $|\Phi^+\rangle = (|00\rangle + |11\rangle)/\sqrt{2}$ by applying a resonant $\pi/2$ pulse on the edge atoms (Fig. 13.4A).

To demonstrate this protocol experimentally, we prepare a GHZ-state of 8 atoms, and turn on the detuned 420 nm addressing beams on the edge atoms resulting in a shift of $\delta_{1,8}/(2\pi) = 6$ MHz. We then use an optimized Rydberg laser pulse to distribute the entanglement, and observe the patterns $|00000000\rangle$ and $|10000001\rangle$ with a total probability of 0.729(9) after accounting for detection errors (Fig. 13.4B). We verify the coherence of the remote Bell pair by applying an additional $\pi/2$ pulse with a variable laser phase, and observe parity oscillations with an amplitude of 0.481(24) (Fig. 13.4C). Combining these results, we obtain the edge atom Bell state fidelity of 0.605(13).

13.5 DISCUSSION

Turning to the discussion of our experimental observations, we note that the optimal control provides a substantial improvement over naive analytic pulses (Fig. 13.3B), while bringing our protocol close to the speed set by a more conventional protocol of building up entanglement through a series of two-qubit operations (Appendix J). In contrast, a simple linear detuning sweep only allows for the creation of GHZ states for $N \leq 16$ within a fixed $1.1 \mu\text{s}$ window (Fig. 13.3B), even under ideal conditions. Our analysis reveals that the reason for this improvement stems from diabatic excitations and de-excitations in the many-body spectrum,

related to the recently proposed mechanisms for quantum optimization speedup [197, 198] (Appendix J).

The measured entanglement fidelity is partially limited by imperfect qubit rotations used for parity measurements. Specifically, the qubit rotation operation \mathcal{U}_x in our experiment is induced by an interacting Hamiltonian, which complicates this step. The resulting evolution can be understood in terms of quantum many-body scars [157, 189], which gives rise to coherent qubit rotations, even in the presence of strong interactions. The deviations from an ideal parity measurement arises from the Rydberg blockade constraint and long-range interactions (Appendix J). These grow with the system size, resulting in finite fidelities even for a perfect initial GHZ state (gray shaded area in Fig. 13.3B). Our quoted fidelity values do not include the correction for this imperfection and represent the lower bound on the actual GHZ state fidelities.

The entanglement generation, manipulation and lifetime are further limited by several sources of decoherence. The finite temperature of the atoms leads to random Doppler shifts on every site as well as position fluctuations that influence interaction energies. These thermal dephasing mechanisms lead to a Gaussian decay of the GHZ state coherence, which decreases with the system size as $1/\sqrt{N}$, in good agreement with our observations (Fig. 13.3B). Additionally, off-resonant laser scattering introduces a small rate of decoherence on each site in the array. We find that numerical simulations of the state preparation accounting for these imperfections predict a higher GHZ fidelity than that obtained experimentally (Fig. 13.3B and Appendix J). We can attribute this discrepancy to several additional sources of errors. Laser phase noise likely contributes to the finite fidelity of the state preparation. Drifts in the beam positions of the Rydberg lasers can lead to changing light shifts, giving rise to uncontrolled detunings, while drifts in the addressing beam positions can lead to an imbalance in the local en-

ergy shifts and thereby in the populations of the two GHZ components, limiting the maximum possible coherence. This analysis highlights the utility of GHZ states for uncovering sources of errors. We emphasize that all of these known error sources can be mitigated via technical improvements (Appendix J).

13.6 OUTLOOK

Our experiments demonstrate a new promising approach for the deterministic creation and manipulation of large-scale entangled states, enabling the certification of genuine N -partite entanglement in system sizes up to $N = 20$, the largest GHZ state demonstrated to date. These results show the utility of this approach for benchmarking quantum hardware, demonstrating that Rydberg atom arrays constitute a competitive platform for quantum information science and engineering. Specifically, the entanglement generation and distribution could be potentially utilized for applications ranging from quantum metrology and quantum networking to quantum error correction and quantum computation. Our method can be extended by mapping the Rydberg qubit states used here to ground-state hyperfine sublevels, such that the entangled atoms can remain trapped and maintain their quantum coherence over very long times [289]. This could enable the sophisticated manipulation of entanglement and realization of deep quantum circuits for applications such as quantum optimization [197, 198].

14

Parallel implementation of high-fidelity multi-qubit gates with neutral atoms

Trapped neutral atoms are attractive building blocks for large scale quantum information systems. They can be readily manipulated in large numbers while maintaining excellent quantum coherence, as has been demonstrated in remarkable quantum simulation and precision measurement experiments [173, 290]. Single atom initialization, addressing, and readout have been demonstrated in a variety of optical trapping platforms, and single-qubit gates have been implemented with exquisite fidelity [93, 291, 292]. Multi-qubit entangling gates with neutral atoms can be implemented by driving atoms to highly excited Rydberg states, which

exhibit strong and long-range interactions [29]. Protocols for entangling atoms using Rydberg interactions have been explored theoretically and experimentally over the last decade [88, 27, 110, 111, 256, 257, 289], but despite major advances, progress in this field has been limited by relatively low fidelities associated with ground-Rydberg state coherent control [112]. Recent advances in Rydberg atom control [53, 293, 182] offer new opportunities for realization of entangling gates, combining high-fidelity performance and parallelization.

In this Letter, we introduce a new method for realizing multi-qubit entangling gates between individual neutral atoms trapped in optical tweezers. In our approach, qubits are encoded in long-lived hyperfine states $|0\rangle$ and $|1\rangle$ which can be coherently manipulated individually or globally to perform single-qubit gates. Our two-qubit gate, the controlled-phase gate, is implemented with a novel protocol consisting of just two global laser pulses which drive nearby atoms within the Rydberg blockade regime [88]. We benchmark this gate by preparing Bell states of two atoms with a fidelity $\mathcal{F} \geq 95.0(2)\%$, averaged across five pairs of atoms. After accounting for state preparation and measurement errors, we extract the entanglement operation fidelity to be $\mathcal{F}^c \geq 97.4(3)\%$, competitive with other leading platforms capable of simultaneous manipulation of ten or more qubits [294–297]. We additionally demonstrate a proof-of-principle implementation of the three-qubit Toffoli gate, wherein two atoms simultaneously constrain a third atom through the Rydberg blockade, highlighting the potential use of Rydberg interactions for efficient multi-qubit operations [89, 112].

14.1 ATOM ARRAYS WITH HYPERFINE CONTROL AND RYDBERG COUPLING

In our experiments, individual atoms are trapped in optical tweezers and sorted by a real-time feedback procedure into groups of two or three, organized in a one-dimensional array [24–26].

We encode qubits in the hyperfine ground states of these atoms, with $|0\rangle = |5S_{1/2}, F =$

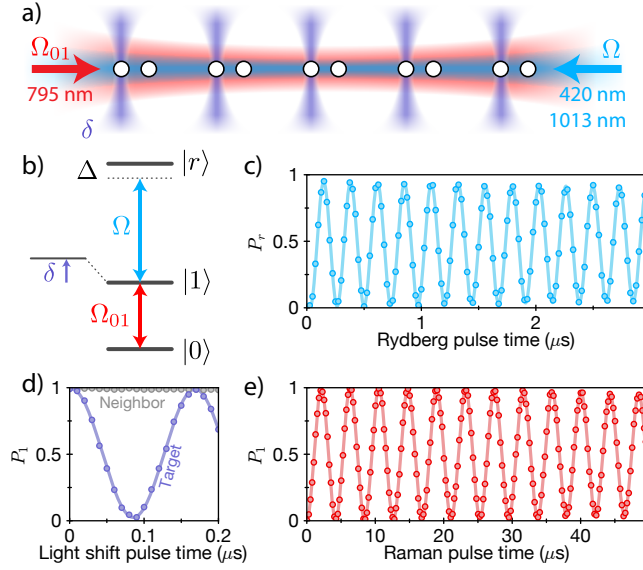


Figure 14.1: Control of individual qubits in atom arrays. a) Atoms arranged in pairs are globally driven with a 795 nm Raman laser (shown in red) which couples the hyperfine qubit levels. Local 420 nm beams (purple) are focused onto individual sites, resulting in a light shift δ used for individual addressing. Additionally, atoms are globally excited by a bichromatic Rydberg laser (shown in blue) containing 420 nm and 1013 nm light from the $|1\rangle$ qubit state to $|r\rangle$. b) Relevant atomic levels. The qubit states are $|0\rangle = |5S_{1/2}, F = 1, m_F = 0\rangle$ and $|1\rangle = |5S_{1/2}, F = 2, m_F = 0\rangle$. The qubit state $|1\rangle$ is coupled to the Rydberg state $|r\rangle = |70S_{1/2}, m_J = -1/2\rangle$ with detuning Δ and Rydberg Rabi frequency Ω . c) Rydberg Rabi oscillations from $|1\rangle$ to $|r\rangle$. Only one atom in each pair is prepared in state $|1\rangle$ to avoid interactions. Atoms in $|r\rangle$ are directly detected by loss from tweezers [182]. d) Local phase shifts as measured in a Ramsey sequence, averaged across the five atom pairs. The purple curve belongs to the addressed atom and shows high-contrast oscillations; the gray curve shows the non-addressed atom, which sees limited $< 2\%$ crosstalk. e) Rabi oscillations from $|0\rangle$ to $|1\rangle$ driven by Raman lasers. Error bars in all figures denote 68% confidence intervals and in most cases are smaller than the markers.

$|1, m_F = 0\rangle$ and $|1\rangle = |5S_{1/2}, F = 2, m_F = 0\rangle$. In each experiment we initialize all qubits in $|0\rangle$ through a Raman-assisted optical pumping procedure (Chapter 4). Single-qubit coherent control is achieved through a combination of a global laser field which homogeneously drives all qubits, as well as local addressing lasers which apply AC Stark shifts on individual qubits (Fig. 14.1a,b). The global drive field is generated by a 795 nm laser, tuned near the $5S_{1/2}$ to $5P_{1/2}$ transition. This laser is intensity modulated to produce sidebands which drive the qubits through a two-photon Raman transition with an effective Rabi frequency $\Omega_{01} \approx 2\pi \times 250$ kHz (Fig. 14.1e) [54] (Chapter 4 and Appendix K). The local addressing beams are generated by an acousto-optic deflector which splits a single 420 nm laser, tuned near the $5S_{1/2}$ to $6P_{3/2}$ transition, into several beams focused onto individual atoms (Fig. 14.1a,d) [182]. We describe these two couplings as global $X(\theta)$ qubit rotations and local $Z(\theta)$ rotations. After each sequence, we measure the individual qubit states by pushing atoms in $|1\rangle$ out of the traps with a resonant laser pulse, followed by a site-resolved fluorescence image of the remaining atoms (Appendix K).

We perform multi-qubit gates by exciting atoms from the qubit state $|1\rangle$ to the Rydberg state $|r\rangle = |70S_{1/2}, m_J = -1/2\rangle$. All atoms are homogeneously coupled from $|1\rangle$ to $|r\rangle$ through a two-photon process with effective Rabi frequency $\Omega \approx 2\pi \times 3.5$ MHz (Fig. 14.1c and Appendix K). Within a given cluster of atoms, the Rydberg interaction between nearest neighbors is $2\pi \times 24$ MHz $\gg \Omega$; neighboring atoms therefore evolve according to the Rydberg blockade in which they cannot be simultaneously excited to the Rydberg state [88].

14.2 A FAST, SYMMETRIC PROTOCOL FOR THE CONTROLLED-PHASE GATE

To entangle atoms in such arrays, we introduce a new protocol for the two-qubit controlled-phase (CZ) gate that relies only on global excitation of atoms within the Rydberg blockade

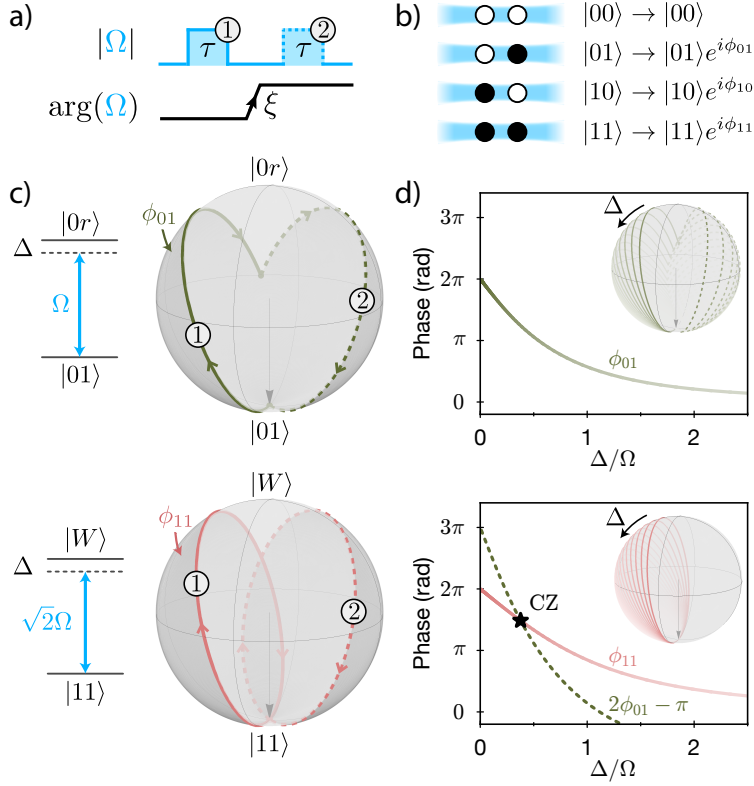


Figure 14.2: Controlled-phase (CZ) gate protocol. a) Two global Rydberg pulses of length τ and detuning Δ drive Bloch sphere rotations around two different axes due to a laser phase change ξ between pulses. b) As a result of the evolution, each basis state returns to itself with an accumulated dynamical phase. $|00\rangle$ is uncoupled and therefore accumulates no phase. $|01\rangle$ and $|10\rangle$ are equivalent by symmetry ($\phi_{01} = \phi_{10}$), while $|11\rangle$ accumulates phase ϕ_{11} . The CZ gate is realized for $\phi_{11} = 2\phi_{01} - \pi$. c) The dynamics of the $|01\rangle$ and $|11\rangle$ states can be understood in terms of two-level systems with the same detuning Δ but different effective Rabi frequencies. The pulse length τ is chosen such that the $|11\rangle$ system undergoes a complete detuned Rabi cycle during the first pulse, while the $|01\rangle$ system undergoes an incomplete oscillation. The laser phase ξ is chosen such that the second pulse drives around a different axis to close the trajectory for the $|01\rangle$ system, while driving a second complete cycle for the $|11\rangle$ system. d) The dynamical phases ϕ_{01} and ϕ_{11} are determined by the shaded area enclosed by the Bloch sphere trajectory and vary from 2π to 0 as a function of Δ , corresponding to increasingly shallow trajectories. Insets show family of trajectories for different detunings. Choosing $\Delta \approx 0.377\Omega$ realizes the CZ gate.

regime. The desired unitary operation CZ maps the computational basis states as follows:

$$\begin{aligned}
|00\rangle &\rightarrow |00\rangle \\
|01\rangle &\rightarrow |01\rangle e^{i\phi} \\
|10\rangle &\rightarrow |10\rangle e^{i\phi} \\
|11\rangle &\rightarrow |11\rangle e^{i(2\phi-\pi)}
\end{aligned} \tag{14.1}$$

This map is equivalent to the canonical form of the controlled-phase gate $\mathcal{CZ} = 2|00\rangle\langle 00| - \mathbb{1}$ up to a single-qubit phase ϕ . To realize this gate, we use two global Rydberg laser pulses of the same length τ and detuning Δ which couple $|1\rangle$ to $|r\rangle$, with the laser phase of the second pulse shifted by ξ (Fig. 14.2).

The gate can be understood by considering the behavior of the four computational basis states. The $|00\rangle$ state is uncoupled by the laser field and therefore does not evolve. The dynamics of $|01\rangle$ (and $|10\rangle$) are given by the coupling of the single atom on the $|1\rangle \leftrightarrow |r\rangle$ transition, forming a two-level system with Rabi frequency Ω and detuning Δ (Fig. 14.2c, top). The $|11\rangle$ state evolves within the Rydberg blockade regime as a two-level system due to the collective coupling from $|11\rangle \leftrightarrow |W\rangle = \frac{1}{\sqrt{2}}(|1r\rangle + |r1\rangle)$, with enhanced Rabi frequency $\sqrt{2}\Omega$ and the same detuning Δ (Fig. 14.2c, bottom). For a chosen detuning Δ , we select the pulse length τ such that the first laser pulse completes a full cycle of a detuned Rabi oscillation for the $|11\rangle$ system. The same pulse drives an incomplete Rabi oscillation on the $|01\rangle$ system. A subsequent phase jump $\Omega \rightarrow \Omega e^{i\xi}$ rotates the orientation of the drive field around the Z axis by an angle ξ such that a second pulse of length τ completes the oscillation and returns the state to $|01\rangle$, while driving a second complete detuned oscillation on the $|11\rangle$ configuration. By the end of the second pulse, both $|01\rangle$ and $|11\rangle$ return to their initial positions on the Bloch sphere but

with accumulated dynamical phases ϕ_{01} and ϕ_{11} , which depend on the geometric surface area of the Bloch sphere enclosed by the Δ -dependent trajectories. As shown in Fig. 14.2d, for a specific choice of laser detuning ($\Delta \approx 0.377\Omega$), $2\phi_{01} - \pi = \phi_{11}$, realizing the CZ gate 14.1. Remarkably, this gate protocol is faster (total time $2\tau \approx 2.732\pi/\Omega$) than the traditional approach [88] of sequential local pulses (total time $4\pi/\Omega$), and offers the additional advantage of requiring only global coupling of both qubits.

14.3 PARALLEL IMPLEMENTATION OF CZ GATE

We demonstrate the parallel operation of the CZ gate on five separate pairs of atoms by using it to create Bell states of the form $|\Phi^+\rangle = \frac{1}{\sqrt{2}}(|00\rangle + |11\rangle)$. We initialize all atomic qubits in $|0\rangle$, then apply a global $X(\pi/2)$ Raman pulse to prepare each atom in $|-\rangle_y = \frac{1}{\sqrt{2}}(|0\rangle - i|1\rangle)$. The CZ gate protocol, consisting of the two Rydberg laser pulses, is then applied over a total time of $0.4 \mu\text{s}$, during which the optical tweezers are turned off to avoid anti-trapping of the Rydberg state. The pulse sequence realizes map 14.1, along with an additional phase rotation on each qubit due to the light shift of the Rydberg lasers on the hyperfine qubit states. We embed the CZ implementation in an echo sequence to cancel the effect of the light shift, and we add an additional short light shift to eliminate the single-particle phase ϕ (Appendix K). Altogether, this realizes a unitary that combines the canonical CZ gate with a global $X(\pi)$ gate (enclosed region in Fig. 14.3a,d). A final $X(\pi/4)$ rotation produces the Bell state $|\Phi^+\rangle$ (Fig. 14.3a and Appendix K).

We characterize the experimentally produced state ρ by evaluating its fidelity with respect to the target Bell state $\mathcal{F} = \langle \Phi^+ | \rho | \Phi^+ \rangle$. The fidelity is the sum of two terms, the first of which is the Bell state populations, given by the probability of observing $|00\rangle$ or $|11\rangle$ (Fig. 14.3b). The second term is the coherence between $|00\rangle$ and $|11\rangle$, measured by applying a global $Z(\theta)$

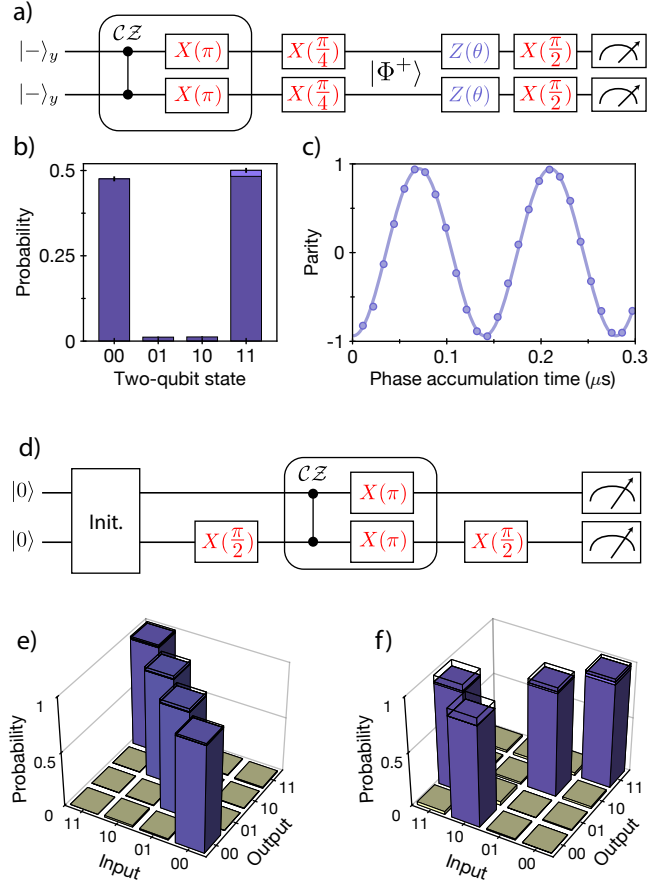


Figure 14.3: Bell state preparation and CNOT gate. a) Quantum circuit used to prepare and probe the $|\Phi^+\rangle$ state. b) Measured populations of the Bell states. Raw measurements associating $|0\rangle$ with atom presence and $|1\rangle$ with atom absence yields 97.6(2)% in the target states. Separate measurements of leakage out of the qubit subspace indicate a small contribution (light shaded region) to these probabilities; subtracting this contribution, the measured population is $\geq 95.8(3)\%$. c) The parity oscillation with respect to accumulated phase θ has a measured amplitude of 94.2(4)%. The resulting lower bound on Bell state fidelity is $\mathcal{F} \geq 95.0(2)\%$ (raw measurements yield $\mathcal{F}^{\text{raw}} = 95.9(2)\%$). Correction for SPAM errors results in $\mathcal{F}^c \geq 97.4(3)\%$. d) The CNOT gate is constructed from our native \mathcal{CZ} gate with the addition of local hyperfine qubit rotations. e) The four computational basis states are prepared with average fidelity 96.8(2)%. f) We apply the CNOT sequence to the four computational basis states and measure the truth table fidelity to be $\mathcal{F}_{\text{CNOT}} \geq 94.1(2)\%$. Corrected for SPAM errors, the fidelity is $\mathcal{F}_{\text{CNOT}}^c \geq 96.5(3)\%$. Wireframes on purple bars show ideal outcomes; solid bars show the raw measurement; the light-shaded top portions of the bars bound the contribution from qubit leakage. Only the darker lower region is counted towards fidelities.

rotation followed by a global $X(\pi/2)$ rotation and observing parity oscillations (Fig. 14.3a,c) [13]. When evaluating the contributions to the fidelity, we account for atom population left in the Rydberg state after the operation and for background losses. Both of these correspond to leakage out of the qubit subspace and can lead to overestimation of the $|1\rangle$ populations and Bell state fidelities in the raw measurements. Using separate measurements of atoms in both hyperfine qubit states (Appendix K), we determine a conservative upper bound on these leakage errors and subtract this contribution (shown in light shaded regions of bar plots in Figs. 14.3 and 14.4, see Appendix K). The resulting lower bound on the Bell state fidelity is $\mathcal{F} \geq 95.0(2)\%$.

The measured Bell state fidelity includes errors in state preparation and measurement (SPAM), as well as errors in the two-qubit entangling gate. To characterize the entangling gate specifically, we evaluate the error contributions from SPAM (1.2(1)% per atom) and compute a SPAM-corrected fidelity $\mathcal{F}^c \geq 97.4(3)\%$ (Appendix K). The majority of the remaining error is due to finite atomic temperature and laser scattering during Rydberg dynamics (Appendix K). We separately characterize our native \mathcal{CZ} gate by converting it to a controlled-NOT (CNOT) gate via local rotations (Fig. 14.3d). We measure the action of the CNOT gate on each computational basis state to obtain its truth table fidelity $\mathcal{F}_{\text{CNOT}}^c \geq 96.5(3)\%$, corrected for SPAM errors (Fig. 14.3e,f and Appendix K).

14.4 EXTENSIONS TO THREE-QUBIT CCZ (AND TOFFOLI) GATE

Finally, we extend our control of multiple atomic qubits to implement the three-qubit controlled-controlled-phase (CCZ) gate. This logic operation can be decomposed into five two-qubit gates [298–300]. Instead, we realize this multiple-control gate directly by preparing three atoms in the nearest-neighbor blockade regime such that both outer atoms constrain the be-

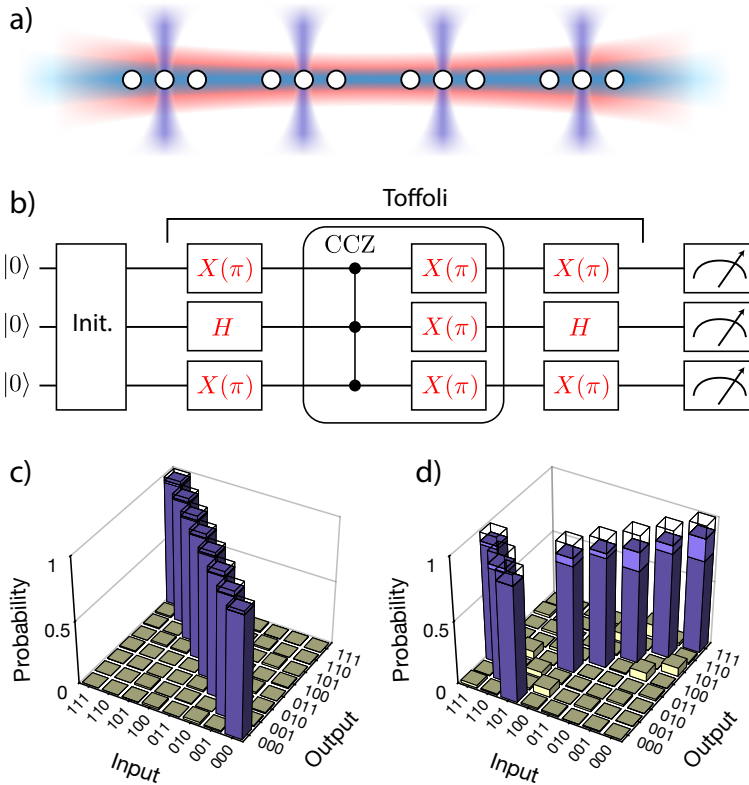


Figure 14.4: Realization of three-qubit Toffoli gate. a) The Toffoli gate is implemented in parallel on four triplets of atomic qubits using the same lasers as for two-qubit gates. b) Quantum circuit for constructing the Toffoli gate from local rotations and a globally implemented CCZ gate. c) Eight computational basis states are prepared with average fidelity $95.3(3)\%$. d) Measured truth table, with fidelity $\mathcal{F}_{\text{Toff}} \geq 83.7(3)\%$. Corrected for SPAM errors, the fidelity is $\mathcal{F}_{\text{Toff}}^c \geq 87.0(4)\%$. Wireframes on purple bars show ideal outcomes; solid bars show the raw measurement; the light-shaded top portions of the bars bound the contribution from qubit leakage. Only the darker lower region is counted towards fidelities.

havior of the middle atom. The complicated three-atom dynamics makes it challenging to analytically construct global laser pulses that realize a CCZ gate in this configuration. We therefore use numerical optimization to construct a global amplitude and frequency modulated laser pulse which approximately implements the CCZ gate (Appendix K). The laser pulse is optimized through the remote dressed chopped random basis (RedCRAB) optimal control algorithm [287, 288].

We implement the CCZ gate in parallel on four triplets of atomic qubits (Fig. 14.4a). The three atoms in each triplet are arranged such that nearest neighbors are blockaded by the strong $2\pi \times 24$ MHz interaction, as in the two-qubit experiments. The edge atoms interact with each other weakly ($2\pi \times 0.4$ MHz). As with the two-qubit gate, we embed the CCZ gate in an echo sequence to cancel light shifts, such that our gate implements CCZ along with a global $X(\pi)$ rotation. To characterize the performance of this three-qubit gate, we convert it into a Toffoli gate by applying a local Hadamard on the middle atom before and after the CCZ gate (along with edge $X(\pi)$ pulses, to simplify implementation, described in Appendix K) (Fig. 14.4b). We apply the Toffoli gate to each computational basis state to measure the truth table fidelity $\mathcal{F}_{\text{Toff}}^c \geq 87.0(4)\%$, corrected for SPAM errors (Fig. 14.4c,d and Appendix K). We additionally perform “limited tomography”, consisting of truth table measurements in a rotated basis, to verify the phases of the Toffoli unitary in a more experimentally accessible manner than full process tomography [300]. The limited tomography fidelity is $\mathcal{F}_{\text{LT}}^c \geq 86.2(6)\%$ (Appendix K).

14.5 OUTLOOK

These results can be directly improved and extended along several directions. The fidelity of Rydberg coupling is primarily limited by finite atomic temperature and off-resonant laser scat-

tering, which can be addressed by sideband cooling of atoms within optical tweezers [95, 43] and by higher power lasers. The background atomic loss and state preparation can be improved using higher quality vacuum systems [301] and more sophisticated state preparation techniques [292]. Finally, atomic qubit readout can be improved using recently demonstrated non-destructive readout protocols [292, 302, 303] to give stronger constraints on the atomic populations.

While in this work we have performed parallel gate implementation on spatially separated clusters of atoms, the same approach can be extended to non-local coupling within contiguous atom arrays using local addressing with an additional off-resonant laser system. Specifically, subsets of the array could be simultaneously illuminated to create light shifts that bring them into resonance with a global resonant Rydberg excitation laser (Appendix K). Furthermore, with more atoms arranged in the blockade volume, the controlled-phase gate demonstrated here can be extended to higher multi-qubit gates with global coupling (Appendix K). The dipolar interaction between S and P Rydberg states [304] could also be used to achieve improved gate connectivity between qubits. A combination of the present results with recently demonstrated trapping and rearrangement of individual neutral atoms in 2D and 3D [25, 30, 166] will be well-suited for the implementation of deep quantum circuits or variational quantum optimization with hundreds of qubits [167]. In addition, such a platform could be utilized to explore efficient methods for error correction and fault-tolerant operation to eventually enable scalable quantum processing.

Part IV

Conclusion

15

Conclusion

15.1 SUMMARY

This thesis describes several efforts to advance the scalability and control of neutral atom systems for quantum science. Central to these efforts were the novel methods for atom-by-atom assembly of defect-free atomic arrays, both in one and two dimensions. New techniques for excitation to Rydberg states additionally enabled state-of-the-art coherence, increasing the scope of quantum simulation and quantum information experiments that are feasible. Moreover, new methods for controlling the hyperfine degrees of freedom have enabled experiments which for the first time show high-fidelity multi-qubit quantum logic operations for neutral atoms.

Beyond the experimental advances, several conceptual advances in understanding of the Rydberg many-body Hamiltonian paved the way for new applications towards the study of many-body physics as well as novel protocols for engineering quantum entanglement. Quasi-adiabatic dynamical control of the Rydberg excitation field has enabled the study of a wide variety of quantum many-body phases which result from the competition between Rydberg interactions and the excitation drive. In simple lattices, the resulting states involve classical Ising-type ordering, and offer a clean benchmark for performance. In more sophisticated lattices, such as those featuring frustration, rich quantum phases featuring topological ordering and long-range entanglement emerge. Moreover, techniques in which quantum states are quasi-adiabatically prepared and then rapidly quenched have enabled the study of non-equilibrium dynamics. In the context of quenching Ising-type ordered states, these quenches resulted in the discovery of surprisingly slow thermalization which is now associated with the notion of quantum many-body scars. These quenches additionally offer a new approach for characterizing coherence and long-range order in entangled systems, such as in GHZ states and quantum spin liquid states. The dynamical control of the Rydberg excitation laser, along with new local controls involving local addressing, have additionally resulted in new protocols for engineering many-body GHZ-type entanglement, as well as new fast protocols for implementing universal quantum logical gates.

15.2 EXTENDING EXPERIMENTAL CAPABILITIES

15.2.1 SYSTEM SIZE

The current apparatus can create up to ~ 1000 optical tweezers, and thus supports experiments with up to ~ 500 atoms. A higher power trapping laser, along with improved higher-

NA objectives, could create arrays of 10,000 tweezers. While our existing two-dimensional sorting procedure could be applied with these larger arrays, an important ingredient is an upgraded vacuum system which features long trap lifetimes to mitigate background losses during rearrangement. Finally, recently demonstrated techniques for enhanced loading of tweezers (reaching loading probabilities of ~ 0.9) [85, 86] would facilitate yet larger atomic arrays, as well as more efficient sorting.

15.2.2 RYDBERG AND HYPERFINE COHERENCE

The coherence of the Rydberg excitation scheme is generally limited by two effects: firstly, the two-photon excitation scheme intrinsically induces spontaneous emission from the intermediate state. The rate of spontaneous emission can be reduced by increasing the power in our Rydberg lasers and increasing the detuning from the intermediate state. In practice, we are limited by the availability of laser power at the upper 1013 nm transition, and for this thesis we used the highest power (10 W) system that was available. However, this is an area of active industry development, and systems with up to 100 W may become available over the next several years. The second key coherence limitation for Rydberg coupling is the Doppler-sensitivity of the transition, which results in fluctuations in the effective laser detuning due to the thermal fluctuations of the atoms. Techniques for improved cooling of the atoms, such as Raman sideband cooling and Lambda-enhanced gray molasses, could strongly suppress Doppler dephasing on the Rydberg transition.

Coherence of hyperfine qubits, on the other hand, is limited by effects associated with the optical tweezers themselves. The differential light shift of the tweezers on the qubit transition, combined with thermal fluctuations of the atoms, result in Ramsey dephasing on the 1 ms timescale, although dynamical decoupling extends the coherence to the longer timescale of sev-

eral hundred milliseconds, limited by off-resonant scattering from the optical tweezers. Both of these effects will be suppressed by using higher power optical tweezers which are further detuned from the atomic transition, although this is a tradeoff that reduces the number of available optical tweezers.

For both Rydberg laser excitation as well as Raman driving of hyperfine qubits, a general challenge is to stabilize laser pulse amplitudes. These experiments generally have laser pulse intensity fluctuations at the scale of $0.1 - 1\%$, which is generally sufficient for quasi-adiabatic control or for low depth circuits. Improved pulse stability will however be an important step towards the implementation of more sophisticated quantum circuits. New experimental techniques for monitoring and stabilizing laser power may be necessary; alternatively, protocols with frequent re-calibration of Rabi frequencies may suffice to compensate for slow drifts of the experimental apparatus [305].

15.2.3 LOCAL ADDRESSING

The experiments in this thesis rely primarily on global laser driving of entire atomic arrays. However, local control over Rydberg couplings, as well as local control over hyperfine qubits, is a promising avenue which will enable broad new classes of experiments. For certain specific applications, it is sufficient to program a static arrangement of local addressing beams, such as the one-dimensional array experiments in which local addressing was used to create GHZ states and probe entanglement. New static two-dimensional local addressing beams could be generated by spatial light modulators and could be readily integrated with the experimental system. More challenging, however, is full dynamical control over each local addressing beam individually, especially on the nanosecond timescale necessary for calibrated Rydberg pulses. New optical systems based on arrays of individually controlled modulators are the subject of

active development in several research groups, and integration with Rydberg atom arrays will likely require collaborative development of these tools.

15.2.4 DYNAMIC SHUTTLING OF HYPERFINE QUBITS

Hyperfine qubits preserve coherence for hundreds of milliseconds in the optical tweezers. This timescale is several orders of magnitude larger than the timescale for performing Rydberg-based quantum gates, or Raman single-qubit gates. These long coherence times also could enable protocols in which atoms are dynamically moved while preserving their coherence [83, 306]. Since Rydberg based interactions are geometry-dependent, moving atoms would open up new prospects for experiments in which the interaction connectivity of the atoms is dynamically reconfigurable. Experimentally, these schemes would rely only on tools which are already in place for atom sorting in the existing apparatus, and could be explored in the near term.

15.3 OUTLOOK

A central focus of modern quantum science and technology is to build quantum devices which are beyond the reaches of classical simulability, as part of the so-called NISQ (noisy, intermediate scale quantum) era [20]. Since theoretical and numerical tools are intrinsically limited for analyzing large quantum systems, laboratory devices will play a crucial role in understanding the capabilities of such near-term quantum systems. With hundreds of individually controlled atoms, neutral atom arrays constitute a powerful NISQ-era test bed for a wide range of studies. Quantum simulations of exotic Hamiltonians allow for the explorations of novel quantum phases, including topological phases which may be utilized for robust quantum computation. Combinatorial optimization problems can be mapped to the Rydberg Hamiltonian

[167], enabling new tests and comparisons of protocols for finding high-quality solutions, including those based on quasi-adiabatic passage or on pulse protocols such as the quantum approximate optimization algorithm [150, 197, 198]. New approaches for quantum information processing based on dynamically reconfigurable arrays will enable the testing of sophisticated quantum circuits.

New experimental advances may also extend optical tweezer arrays with new opportunities. Trapping of more exotic two-electron atoms provides a distinct and powerful toolset for quantum simulation and quantum processing, as well as strong applications to quantum metrology [38, 35, 36]. Arrays of multiple atomic species may enable new approaches for higher-fidelity control or quantum error correction protocols. Alternatively, arrays of individual molecules offer a different approach towards quantum simulation, based on direct dipolar interactions between ground state molecules [39, 37]. With several new research groups exploring these many directions, this field will continue to grow and mature rapidly.

Part V

Appendices

A

Optical Setups

A.1 MOT LASER SETUP

The MOT laser setup, shown in Fig. A.1, consists of two 780 nm lasers: the MOT laser, which drives transitions from the $F = 2$ ground state to $5P_{3/2}$, and the repumper laser, which drives transitions from the $F = 1$ ground state. The repumper laser is locked to a saturated absorption spectroscopy signal from a Rubidium vapor cell on the crossover line between $F = 1 \rightarrow F' = 1$ and $F = 1 \rightarrow F' = 2$. The beam is enlarged prior to entering the vapor cell to increase the signal; alternatively, the vapor cell could be heated to increase the signal. The repumper laser is modulated by an AOM, and split into several beam paths: the MOT beams,

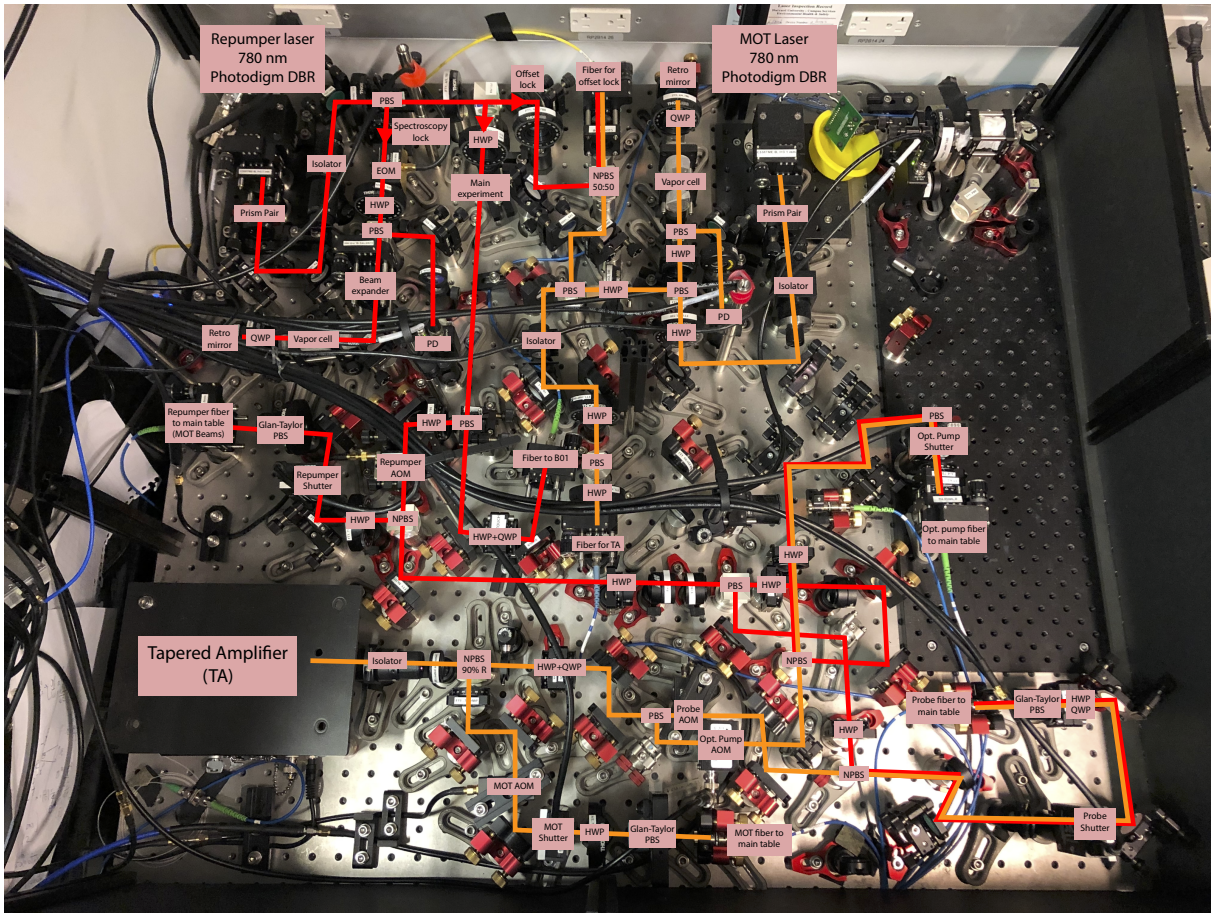


Figure A.1: MOT laser setup. This is the laser setup for the 780 nm lasers which are used for laser cooling and imaging. DBR=Distributed Bragg Reflector; PBS = Polarizing beamsplitter; NPBS=Non-polarizing beamsplitter; HWP=Half-wave plate; QWP=Quarter-wave plate; PD=Photodetector; TA=Tapered amplifier; AOM=Acousto-optic modulator.

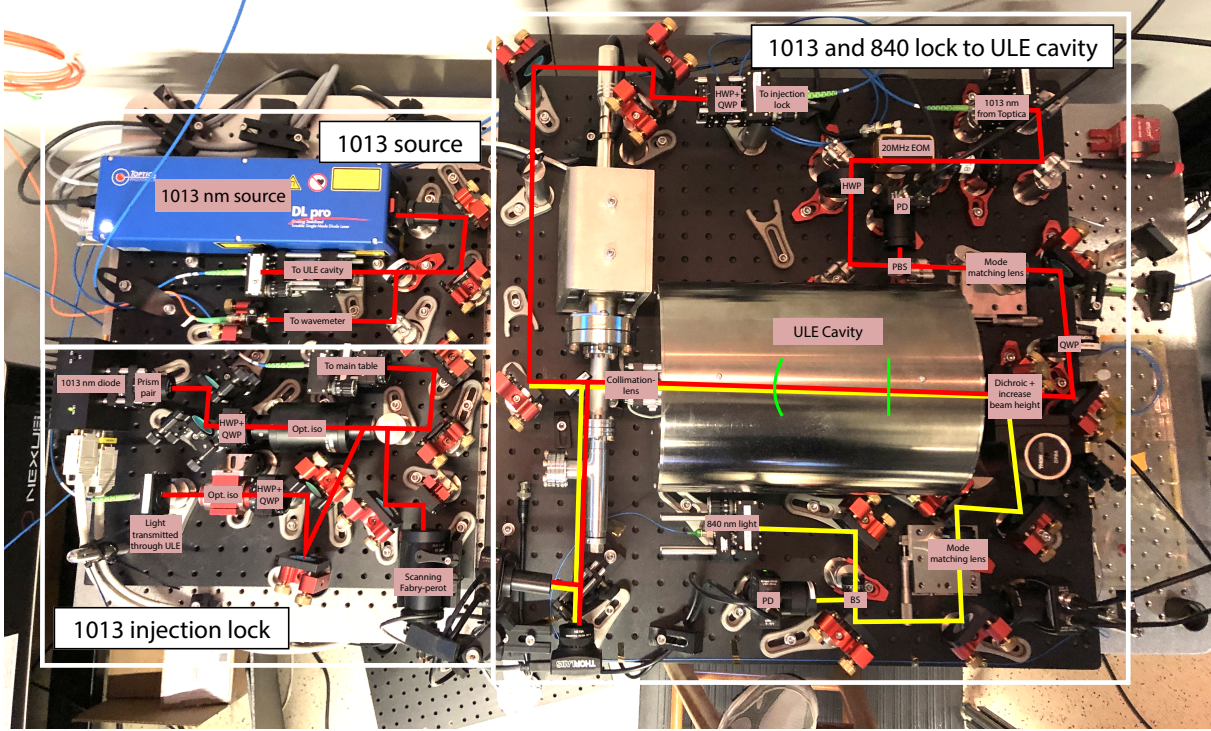


Figure A.2: Rydberg laser setup. This is the locking setup for the two-color Rydberg laser system. The 1013 nm laser is sourced from a Toptica DL pro (upper left). The light is locked to the ultra-low expansion (ULE) cavity (right section). The transmitted light is used to injection lock a laser diode (lower left). The 840 nm light (which is doubled to produce 420 nm light) is also locked to the ULE cavity. Both the 1013 nm and 840 nm lasers are locked to the ULE cavity by a Pound-Drever-Hall (PDH) lock. The 1013 nm is phase modulated by an EOM (shown) to produce the PDH sidebands. The 840 nm is phase modulated by a fiber modulator (not shown), which produces a variable frequency sideband (up to \sim GHz scale) which is locked to the cavity to allow for a tunable offset from the cavity mode. This fiber modulator also produces the PDH sidebands for the 840 nm light. The ULE cavity has a free spectral range of 1.5 GHz. ULE=Ultra low expansion; PBS = Polarizing beamsplitter; BS=Non-polarizing beamsplitter; HWP=Half-wave plate; QWP=Quarter-wave plate; PD=Photodetector.

the probe beams, and the optical pumping axis.

The MOT laser is characterized on saturated absorption spectroscopy in a vapor cell, but it is frequency-stabilized by a \sim 6.8 GHz offset lock to the repumper laser. The laser is amplified using a tapered amplifier (TA) and similarly split into separate pathways for the MOT beams, probe beams, and optical pumping axis; each pathway has a separate AOM.

A.2 RYDBERG LASER SETUP

The Rydberg laser setup is shown in Fig. A.2. The 1013 nm laser source is a Toptica DL Pro (upper left), while the 840 nm laser source for the 420 nm light is a Ti:Sapphire laser from M Squared (not shown). The two lasers are merged with dichroics and locked to the same ultra-low expansion (ULE) cavity. The 1013 nm light which is transmitted through the cavity is used to injection lock a separate laser diode (lower left of figure) to amplify the low-noise light, and this output is then coupled into a fiber amplifier (not shown). Since the transmitted light through the ULE cavity is used to source the injection lock, the injection locked laser is always parked exactly at a cavity resonance. It is therefore easy to change the 1013 nm frequency by a multiple of the 1.5 GHz free spectral range of the cavity. Finer frequency tuning of the 1013 nm is accomplished using acousto-optic modulators (AOMs).

Since the 840 nm laser is intrinsically low noise, we do not use the cavity to filter the laser, but only as a frequency reference. To make the frequency lock flexible, we generate tunable sidebands on the 840 nm light using a fiber phase modulator, and lock one of these sidebands to the ULE cavity. This allows arbitrary frequency tuning of the 840 nm light relative to any ULE cavity mode.

B

Supplementary information for Chapter 4

B.1 METHODS FOR CONVERTING PHASE MODULATION TO AMPLITUDE MODULATION

To evaluate the various methods for converting phase modulation to amplitude modulation, we consider two main parameters for each approach: (1) T , the fraction of optical power that is transmitted through the conversion system, and (2) η^{AM} , the amplitude modulation efficiency of the resulting light. The Raman Rabi frequency scales according to $\Omega_{\text{eff}} \propto T\eta^{AM}/\Delta$, where Δ is the detuning from the intermediate excited state. At the same time, the rate of optical scattering depends on the average optical power on the atoms, according to $\Gamma_{sc} \propto T/\Delta^2$.

We combine these two parameters into a single metric which best characterizes the coherence

Method	Transmission $T(\beta)$	Amp. Mod. Eff. $\eta^{AM}(\beta)$	Coherence metric $C(\beta) = T(\eta^{AM})^2$
Filter out carrier	$1 - J_0(\beta)^2$	$\frac{2J_0(\beta)J_2(\beta)}{1-J_0(\beta)^2}$	$\frac{(2J_0(\beta)J_2(\beta))^2}{1-J_0(\beta)^2}$
Filter with M.-Z. interf.	$\frac{1}{2}(1 + J_0(2\beta))$	$\frac{J_2(2\beta)}{1+J_0(2\beta)}$	$\frac{(J_2(2\beta))^2}{2(1+J_0(2\beta))}$
M.-Z. Modulator (half-trans.)	$1/2$	$J_1(\beta)$	$(J_1(\beta))^2/2$
M.-Z. Modulator (min-trans.)	$(1 - J_0(\beta))/2$	$\frac{J_2(\beta)}{1-J_0(\beta)}$	$\frac{(J_2(\beta))^2}{2(1-J_0(\beta))}$
Dispersive element (coeff. α)	1	$J_1(2\beta \sin \alpha)$	$(J_1(2\beta \sin \alpha))^2$
Two frequency components	-	$1/2$	-
N uniform sidebands	-	$\frac{N-1}{N}$	-
N optimal sidebands	-	$\cos(\frac{\pi}{N+1})$	-

Table B.1: Comparison of methods for converting phase modulation to amplitude modulation.

For each method, as a function of the phase modulation depth β , we calculate the transmission through the conversion system $T(\beta)$, the amplitude modulation efficiency $\eta^{AM}(\beta)$, and the coherence metric $C(\beta) = T(\eta^{AM})^2$. For reference, we also present the amplitude modulation efficiency for an idealized model of exactly two frequency components, of N uniform sidebands, and of N sidebands with optimal amplitudes.

Method	Optimal phase mod. β^* (rad)	Max. coherence $C(\beta^*)$
Filter out carrier	3.574	0.144
Filter with M.-Z. interf.	1.664	0.174
M.-Z. Modulator (half-trans.)	1.841	0.169
M.-Z. Modulator (min-trans.)	2.718	0.097
Dispersive element (coeff. α)	1.336 ($\alpha = 0.76$ rad)	0.339

Table B.2: Optimal conversion of phase modulation to amplitude modulation. For each of the above methods, we calculate the phase modulation depth β^* which optimizes the coherence metric, and present the optimized values. The dispersive element approach achieves the highest coherence metric, both due to the high transmission through the system as well as the high amplitude modulation efficiency.

ence properties of each approach. Specifically, we assume a fixed amount of available optical power, and we choose the laser detuning Δ such that the resulting Raman Rabi frequency Ω_{eff} is fixed. To achieve this, we set $\Delta \propto T\eta^{AM}$. For this setting, the optical scattering scales as $\Gamma_{sc} \propto 1/T(\eta^{AM})^2$. The ratio of Raman Rabi frequency to scattering rate is therefore given by $\Omega_{\text{eff}}/\Gamma_{sc} \propto T(\eta^{AM})^2$, which we define as the coherence metric C . The comparison of approaches is summarized in Table B.1.

To calculate T and η^{AM} for each approach, we begin by considering a phase modulated laser, with (normalized) field:

$$\Omega(t) = \sum_{n=-\infty}^{\infty} J_n(\beta) e^{in\omega t} \quad (\text{B.1})$$

The total power is $\sum_n |J_n(\beta)|^2 = 1$. As we evaluate T and η^{AM} by considering the filtering of various sidebands, we remarkably find that these values can be expressed as simple combinations of Bessel functions through several Bessel function identities (derived in Appendix L).

B.1.1 FILTER OUT CARRIER COMPONENT

In this approach, the phase modulation frequency $\omega = \omega_q/2$, such that second-neighboring frequency components contribute to the Raman drive. After filtering out the carrier, the resulting optical power is

$$T = 1 - |J_0(\beta)|^2 \quad (\text{B.2})$$

The amplitude modulation efficiency is

$$\eta^{AM} = \left| \left(\sum_n J_n(\beta) J_{n+2}(\beta) \right) - J_0(\beta) (J_{-2}(\beta) + J_2(\beta)) \right| / T \quad (\text{B.3})$$

$$= \frac{2J_0(\beta)J_2(\beta)}{1 - |J_0(\beta)|^2} \quad (\text{B.4})$$

The first expression sums up all pairs of frequency components separated with $\Delta n = 2$, and then subtracts the contributions from $n = 0$ with $n = \pm 2$. The sum over all pairs is identically 0, and due to evenness of Bessel functions, $J_{-2}(\beta) = J_2(\beta)$. Complex conjugation in the amplitude modulation efficiency is ignored since the Bessel functions are real valued.

B.1.2 FILTER WITH MACH-ZEHNDER INTERFEROMETER

Here we again consider phase modulation with frequency $\omega = \omega_q/2$. Passing the laser through a Mach-Zehnder interferometer with a properly chosen path-length difference between arms can result in filtering of all even index or all odd index components in the laser. The optical power after filtering out all odd sidebands (a more favorable configuration) is

$$T = \sum_{n \text{ even}} J_n(\beta)^2 = \frac{1}{2}(1 + J_0(2\beta)) \quad (\text{B.5})$$

due to a Bessel function identity (see Appendix L).

The amplitude modulation efficiency in this configuration is also greatly simplified due to a Bessel function identity:

$$\eta^{AM} = \frac{1}{T} \sum_{n \text{ even}} J_n(\beta)J_{n+2}(\beta) = \frac{1}{T} \left(\frac{1}{2} J_2(2\beta) \right) \quad (\text{B.6})$$

$$= \frac{J_2(2\beta)}{1 + J_0(2\beta)} \quad (\text{B.7})$$

B.1.3 MACH-ZEHNDER MODULATION

A Mach-Zehnder modulator is an interferometer in which phase modulation occurs in one arm of the interferometer. If the two pathways are balanced in power, the power transmitted in

one output mode is given by the relative phase between the two paths:

$$I(\phi) = \sin^2(\phi/2) = \frac{1}{2}(1 - \cos(\phi)) \quad (\text{B.8})$$

To modulate the output intensity at the qubit frequency ω_q , the relative phase can either be biased to the half-transmission point and then be modulated at ω_q , according to $\phi = \pi/2 + \beta \sin(\omega_q t)$, or it can be biased to the minimum transmission point and then modulated at $\omega_q/2$, with $\phi = \beta \sin(\omega_q t/2)$. These approaches result in different electric field components in the output light, but to analyze the Raman performance, we need only analyze the laser intensity.

We begin with the half-transmission configuration. In this case,

$$I(t) = \frac{1}{2} (1 + \sin(\beta \sin(\omega_q t))) \quad (\text{B.9})$$

Using a version of the Jacobi-Anger expansion, the right hand side can be expanded:

$$I(t) = \frac{1}{2} \left(1 - i \sum_{n \text{ odd}} J_n(\beta) e^{in\omega_q t} \right) \quad (\text{B.10})$$

The average optical power is given by the time-independent term:

$$T = 1/2 \quad (\text{B.11})$$

This is as expected, since we modulate symmetrically around the half-transmission point.

The amplitude modulation efficiency is given by the coefficient of the $e^{i\omega_q t}$ term, normalized

by T :

$$\eta^{AM} = \frac{1}{T} \frac{J_1(\beta)}{2} = J_1(\beta) \quad (\text{B.12})$$

Turning instead to the minimum transmission case, we calculate the time-dependent output intensity (where the modulation frequency is $\omega_q/2$):

$$I(t) = \frac{1}{2}(1 - \cos(\beta \sin(\omega_q t/2))) \quad (\text{B.13})$$

Again using Jacobi-Anger:

$$I(t) = \frac{1}{2} \left(1 - \sum_{n \text{ even}} J_n(\beta) e^{in\omega_q t/2} \right) \quad (\text{B.14})$$

We now read off the average optical power by setting all time dependent terms to zero:

$$T = \frac{1}{2}(1 - J_0(\beta)) \quad (\text{B.15})$$

As with the half-transmission case, the amplitude modulation efficiency is the coefficient of the $e^{i\omega_q t}$ term, here corresponding to $n = 2$, normalized by T :

$$\eta^{AM} = \frac{1}{T} \frac{J_2(\beta)}{2} = \frac{J_2(\beta)}{1 - J_0(\beta)} \quad (\text{B.16})$$

B.1.4 DISPERSIVE ELEMENTS

After reflecting from a dispersive element with uniform dispersion (GDD is independent of frequency), the normalized field is described by:

$$\Omega(t) = \sum_{n=-\infty}^{\infty} J_n(\beta) e^{in\omega t} e^{i\alpha n^2} \quad (\text{B.17})$$

The intensity is then given by:

$$|\Omega(t)|^2 = \sum_{k=-\infty}^{\infty} e^{ik\omega t} \sum_{n=-\infty}^{\infty} J_n(\beta) J_{n+k}(\beta) e^{i\alpha[(n+k)^2 - n^2]} \quad (\text{B.18})$$

Assuming the phase modulation frequency is a subharmonic of ω_q , with $\omega = \omega_q/k$, then we have the following amplitude modulation efficiency (of order k):

$$\eta_k^{AM} = \left| \sum_{n=-\infty}^{\infty} J_n(\beta) J_{n+k}(\beta) e^{2i\alpha nk} \right| \quad (\text{B.19})$$

Here we use the Bessel function identity (see Appendix L) to simplify:

$$\eta_k^{AM} = J_k(2\beta \sin(\alpha k)) \quad (\text{B.20})$$

This conclusion is quite amazing. We can immediately evaluate the upper bound on efficiency for any possible choice of β and dispersive parameter α , because the result is simply bounded by the maximum value of $J_k(z)$. Moreover, we see that modulating directly at $\omega = \omega_q$ (taking $k = 1$) is optimal, since $J_1(z)$ has a larger maximum than any higher order Bessel function – but we also see that this configuration requires the largest dispersive parameter α to achieve this maximum, due to the $\sin(\alpha k)$ coefficient within the Bessel function.

B.2 DISPERSIVE OPTICAL ELEMENTS

The group delay dispersion of an optical element is defined as:

$$\text{GDD} = \frac{\partial^2 \varphi}{\partial \omega^2} \quad (\text{B.21})$$

where $\varphi(\omega)$ is the optical phase shift (in radians) accumulated by a frequency component with angular frequency ω after the action of the element. GDD is typically measured in units of fs^2 , although many optical elements such as fibers have their dispersive properties described in terms of their group velocity dispersion (GVD), which is GDD per unit length (typical units are ps/nm/km).

Normal materials have dispersion which acts over a broad wavelength range, which plays an important role in ultrafast optics with broadband lasers, where dispersion results in pulse broadening. However, we are interested here in strong dispersion on the scale of $\sim 10 \text{ GHz}$ in the near infrared. In particular, as described in Chapter 4, we want optical elements with group delay dispersion of $8 \times 10^8 \text{ fs}^2$ to be able to optimally convert phase modulation to amplitude modulation.

Typical optical fibers at 795 nm have GVD of -120 ps/nm/km , or $4 \times 10^4 \text{ fs}^2/\text{meter}$, with attenuation 4 dB/km . To achieve the target GDD, we would require a 20 km fiber, with a resulting 80 dB laser attenuation. Some photonic crystal fibers have been designed to have significantly larger GVD, but with much higher attenuation.

In the ultrafast optics community, after sending short pulses through a long fiber, they reverse the pulse broadening by reflecting the broadened pulse from a chirped Bragg mirror. The highest available chirped Bragg mirrors offer $GDD \sim 1300 \text{ fs}^2$ per reflection. To achieve our target GDD would require $\sim 600,000$ reflections from such a mirror.

The volumetric chirped Bragg grating (CBG) that we use offers the enormous GDD = 4×10^8 fs² from a single pass. After reflecting twice from the CBG, we double the GDD to the target level, and conveniently also recombine spatial modes of all spectral components in the laser. One caveat is that the CBG has a narrow bandwidth of ~ 50 GHz, which requires angle-tuning to match to the bandwidth of the phase modulated laser. This could also limit reflectivity for very large phase modulation depth which creates many sidebands, but for $\beta \lesssim \pi$ this does not pose an issue. Another factor is that the CBG does not in fact have uniform GDD over its bandwidth, which further requires angle tuning to position the laser bandwidth at an optimal point within the CBG bandwidth.

C

Supplementary information for Chapter 6

C.1 EXPERIMENTAL SEQUENCE

C.1.1 TRAP LOADING

The experimental sequence begins by laser cooling thermal ^{87}Rb atoms in a magneto-optical trap (MOT) around the traps for 100 ms (Fig. C.1A). We use a gradient field of 9.7 G/cm, and three intersecting retroreflected beams that are 17 MHz red detuned of the free space $F = 2 \rightarrow F' = 3$ transition, overlapped with repumper beams resonant with the free space $F = 1 \rightarrow F' = 2$ transition. One of these beams is perpendicular to the optical table, and the other two are parallel to it (intersecting at an angle of $\approx 120^\circ$ due to the geometric restriction imposed

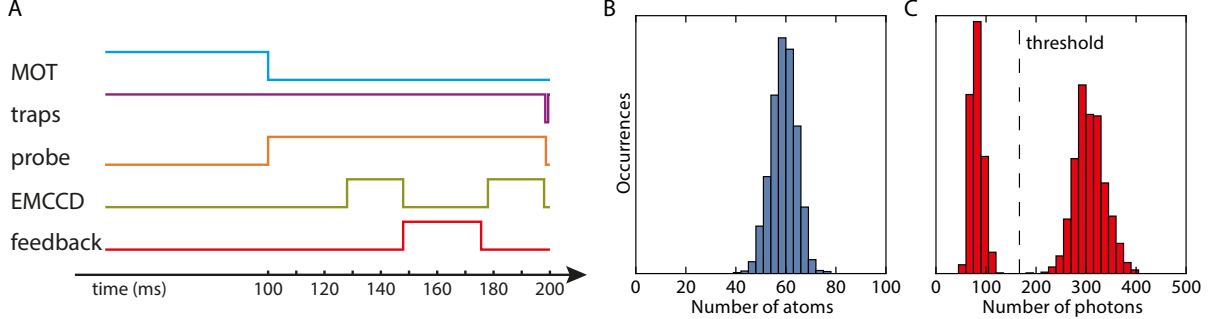


Figure C.1: Experimental sequence and atomic signal. **A)** Pulse diagram of the experimental sequence. **B)** Distribution of number of initially loaded atoms. **C)** Sample fluorescence count distribution for a single trap during 20 ms of exposure.

by the high resolution objectives). All three beams have a diameter of ≈ 1.5 cm, and carry ≈ 1.5 mW of cooling light and ≈ 0.4 mW of repumping light each. To reduce the necessary time to load the MOT, we shine UV light from a diode at 365 nm directly on the region of the glass cell within which the MOT is loaded [42].

After 100 ms, the magnetic field gradient and the MOT beams are turned off to allow the MOT to dissipate over 28 ms. At the same time we turn on a set of probe beams which are 20 MHz red-detuned from the bare atom $F = 2 \rightarrow F' = 3$ transition. The probe beams have the same geometric configuration as the MOT beams, but they have ≈ 50 times less power, and a diameter of ≈ 1 mm, which largely reduces background light due to stray reflections during imaging. The probe beams further cool the atoms through polarization-gradient cooling, and are left on for the remainder of the sequence.

The result of this process is the probabilistic loading of atoms into the traps. For the data presented in Fig. 6.3 of Chapter 6, we loaded on average 59 ± 5 atoms (Fig. C.1B).

C.1.2 IMAGING

The EMCCD camera (Andor iXON3) is triggered 128 ms after the beginning of the experimental sequence and acquires an image over the following 20 ms. Cooling light from the probe

beams is scattered by the atoms and collected on the EMCCD, forming an image of the atoms in the array. Based on the collected photon statistics for each trap, we can set clear thresholds to determine the presence of an atom in a trap (see Fig. C.1C). Furthermore, the bimodal nature of the photon statistics is an indication that the traps are occupied by either 0 or 1 atom.

C.1.3 FEEDBACK

Once the EMCCD has finished acquiring the signal, the image file is transferred over the following 10 ms to a computer which determines trap occupations, using pre-calibrated regions of interest and threshold counts for each trap, in sub-ms time. Using this information, the computer finds the correct pre-calculated waveform to displace each occupied trap during 3 ms from its initial position to its final position, and then adds up all of them into a multi-tone frequency-sweep waveform. This computation takes \approx 0.2 ms for each trap to be displaced. Once the waveform is ready, it is sent to the AOD to perform the trap displacement, and then it goes back to producing the original set of 100 traps. It is important to note that the rearrangement waveform is only calculated for loaded traps, which means that all empty traps are turned off for the duration of the rearrangement but are restored immediately afterwards, so that the trap array returns after rearrangement to its original configuration. After rearrangement, there is a \approx 7 ms buffer time before taking another 20 ms exposure image with the EMCCD. The entire process, consisting of image acquisition, transfer, analysis, waveform generation, rearrangement, and buffer, takes a total of 50 ms.

Currently, the profile of the frequency sweeps is calculated to be piece-wise quadratic in time, over a duration of 3 ms. For shorter transport times we observe an increase in the number of atoms lost during rearrangement. For the experiments reported in Chapter 6, atom losses are only slightly increased compared to the expected lifetime in static traps (see Fig. C.2).

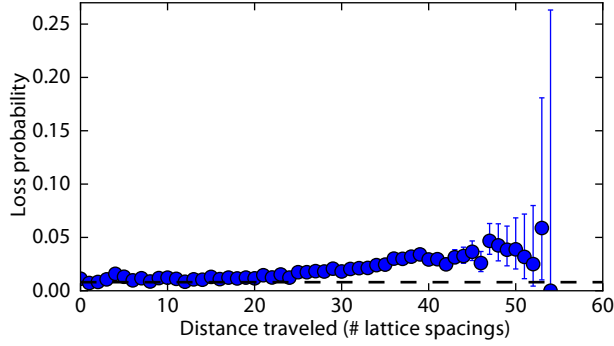


Figure C.2: Rearrangement losses. Losses as a function of total distance traveled by the atom during rearrangement for the dataset presented in Fig. 6.3 of Chapter 6. The dashed line represents the expected loss for a stationary trap with 6.2 s lifetime.

These losses depend on the distance that the atoms move, and it is possible that they could be reduced by changing the length or the profile of the frequency sweep to minimize acceleration and jerk during the trajectory. However, the fidelity of our rearrangement would not be significantly improved by minimizing these losses (see Fig. 6.3B of Chapter 6).

C.2 EXPERIMENTAL METHODS

C.2.1 GENERATING 100 TRAPS

When driving the AOD with a single radio frequency (RF) tone, a portion of the input beam is deflected by an angle θ that depends on the frequency ω of the tone. By applying 100 different RF tones $\{\omega_1, \dots, \omega_{100}\}$, we generate 100 beams with output angles $\{\theta_1, \dots, \theta_{100}\}$, where $\theta_i = \theta(\omega_i)$. The waveform that we send into the AOD is initially calculated by a computer that samples the desired waveform in the time-domain with a sampling rate of 100 MHz. We stream these waveform samples to a Software Defined Radio (SDR) (Ettus Research, model USRP X310, daughterboard UBX 160) which performs digital-analog conversion, low-pass filtering, and subsequent analog IQ upconversion by a frequency of $\omega_{\text{up}} = 74$ MHz, and outputs an analog waveform, which we then amplify and send to the AOD. The waveform that we cal-

culate initially is given by:

$$\sum_{i=1}^{100} A_i e^{i\phi_i} e^{i(\omega_i - \omega_{\text{up}})t},$$

with A_i and ϕ_i being the real amplitude and phase, respectively, of the RF tone with frequency ω_i . Since we generate all tones in the same waveform (relative to the same local oscillator inside the SDR), the tones in our waveform have well-defined phases $\{\phi_i\}$ relative to one another. Also, since all the frequencies we use are integer multiples of 1 kHz, we calculate a 1 ms waveform which is streamed on a loop without needing to continuously generate new samples.

C.2.2 EFFECTS OF INTERMODULATION

The finite power bandwidth, along with other imperfections of our system (RF amplifier and AOD) generate a nonlinear response to the input signal. To the lowest order nonlinearity, the system acts as a mixer and generates new tones at the sum and difference of the input frequencies. For example, for two tones, $A_1 e^{i\phi_1} e^{i\omega_1 t}$, $A_2 e^{i\phi_2} e^{i\omega_2 t}$, at the input, there will be a corresponding set of tones at the output:

$$E_{1,2}^- \propto e^{i(\phi_1 - \phi_2)} e^{i(\omega_1 - \omega_2)t},$$

$$E_{1,2}^+ \propto e^{i(\phi_1 + \phi_2)} e^{i(\omega_1 + \omega_2)t}$$

These terms are far removed from the main set of desired tones $\{\omega_i\}$ and can in principle be filtered by frequency. However, they seed the next order of nonlinearity.

The next order of nonlinearity contains the mixing of these first order nonlinearities with the original tones. For example, with two tones we would now see a mixing of the $(\omega_1 - \omega_2)$ tone with the original ω_1 tone to produce a sum tone at $(2\omega_1 - \omega_2)$ and a difference tone at

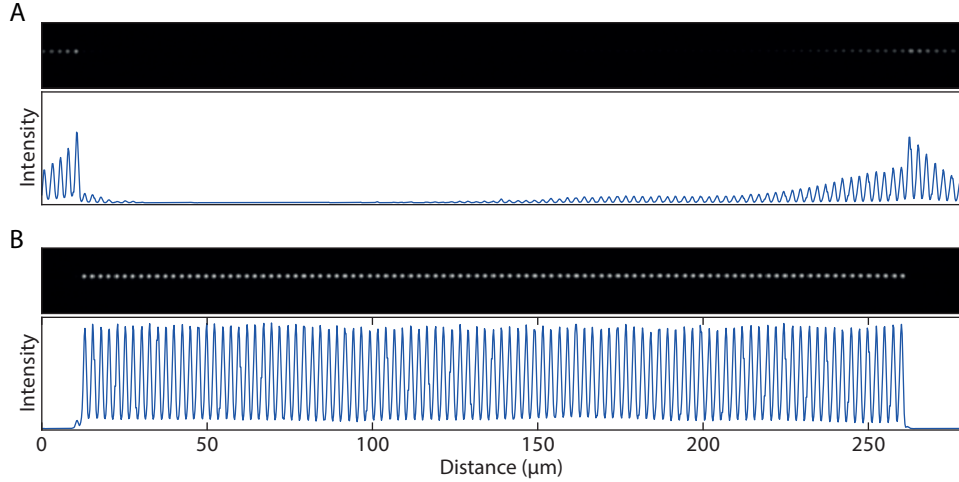


Figure C.3: Generating uniform traps. Nonlinearities inside the AOD and RF amplifier cause frequency mixing. **(A)** Setting identical phases for each input tone results in intermodulations that strongly interfere with the intended frequency tones and significantly distort the trap amplitudes. **(B)** By optimizing the phases $\{\phi_i\}$ and amplitudes $\{A_i\}$ of the RF tones we can reduce intermodulations and generate homogeneous traps.

ω_2 . Similarly, the $(\omega_1 - \omega_2)$ tone would mix with the original ω_2 tone to produce a tone at $(2\omega_2 - \omega_1)$ and ω_1 . If the phases of each input tone $\{\phi_i\}$ are not carefully selected, these intermodulations interfere destructively with the original tones, as shown in Fig. C.3A.

C.2.3 OPTIMIZING TRAP HOMOGENEITY

We address the issue of intermodulations by adjusting the phases of the different RF tones to almost completely cancel out the nonlinearities. As a first step, we generate a computer simulation of 100 tones evenly spaced in frequency and with random phases, and equal amplitudes. For each pair of traps $\{i, j\}$, we calculate the difference tone $E_{i,j}^-$. By starting with random initial phases, the difference tones nearly completely destructively interfere with one another. We then optimize each phase, one at a time, to further reduce the sum of all difference tones $\sum E_{i,j}^-$. After this, we proceed to generate the waveform to be streamed onto the SDR. The starting amplitudes for each tone are selected such that they individually produce a single deflection carrying the correct amount of optical power. The frequencies span from 74.5 MHz to

123.01 MHz in steps of 0.49 MHz.

The next step in optimization consists of imaging the focused trap array on a CCD and performing 2D Gaussian fits. We use the amplitude of these fits to feed back on the amplitude of the individual tones. Once all the fitted amplitudes are approximately uniform, we continue to the last step of optimization.

Since we are interested in the uniformity of the traps at the positions of the atoms, we measure the AC Stark shifts induced by the traps, and use these values to feed back on the amplitude of each tone. In order to extract the AC Stark shift, we shine a single laser beam onto the trapped atoms for $10\ \mu\text{s}$, and measure the loss probability introduced by this “pushout” beam as a function of detuning from the bare $F = 2 \rightarrow F' = 3$ resonance (Fig. C.4A inset). From the fits we extract the individual lightshift for each trap and use these values to perform feedback on the amplitudes. We repeat the procedure until the shifted resonances are uniform to within $\approx 2\%$ across the trap array (Fig. C.4A). At this point we have a set of optimal amplitudes $\{A_i^{opt}\}$ and phases $\{\phi_i^{opt}\}$ associated with the RF frequencies $\{\omega_i\}$ (Fig. C.3B). We interpolate between the values of $\{A_i^{opt}\}$ to define the optimal amplitude as a function of frequency $A^{opt}(\omega)$.

C.2.4 CHARACTERIZING TRAP HOMOGENEITY

To characterize the homogeneity of the final trap configuration, we perform experiments to determine the AC Stark shift and trap frequency for each trap in the array (Fig. C.4).

As outlined in the previous section, the measurement of the AC Stark shift is used to equalize the traps. We find an average shift of 17.5 MHz with a standard deviation of 0.1 MHz across the whole array.

The trap frequency (Fig. C.4B) is found through a release and recapture technique [307].

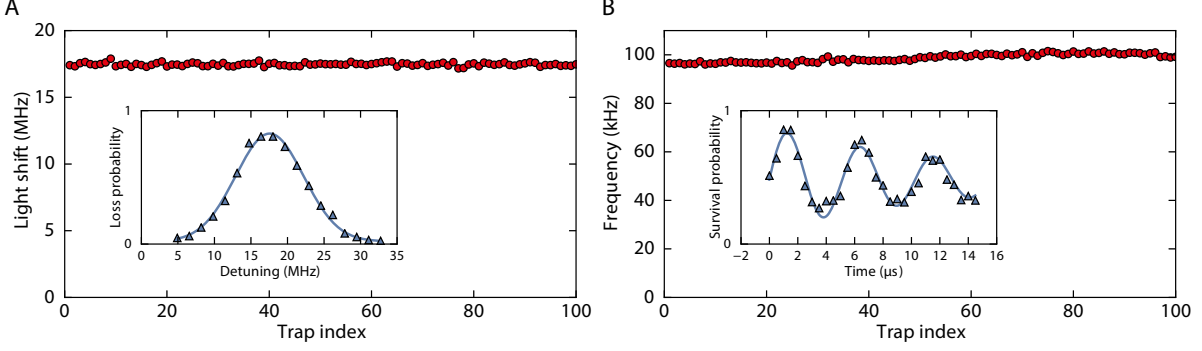


Figure C.4: Characterization of trap and atom properties. (A) The trapping light causes a lightshift on the atomic resonances that depends on the amplitude of the trap. The measured lightshifts across the array are used to optimize the RF amplitudes $\{A_i\}$. This process results in homogeneous traps with lightshifts that are uniform to within $\approx 2\%$. Inset shows the result of a “pushout” measurement (see text) on trap 26 that is used to determine the individual lightshift. (B) The trap frequencies are determined from a release and recapture measurement [307] (see inset for trap 26). The errors from the fits are smaller than the marker size for all the figures.

We obtain the radial frequency from a fit to the probability of retaining an atom as a function of hold time (Fig. C.4B inset). We find the average trap frequency to be 98.7 kHz with a standard deviation of 1.7 kHz across the array. Combining these measurements with an independent determination of the waist, we estimate a trap depth of ≈ 0.9 mK.

C.2.5 MOVING TRAPS

For most of the experimental sequence time, the traps are static. However, during short bursts we stream new waveforms to the AOD to rearrange them, and the atoms they hold. We move our traps by sweeping the frequencies $\{\omega_i(t)\}$ of the tones that correspond to the traps we wish to move, in a piecewise-quadratic fashion. This way, the atoms experience a constant acceleration a for the first half of the trajectory, and $-a$ for the second half. During the sweep, we also continuously adjust the amplitude of the RF tone to match the optimized amplitude for its current frequency: $A_i(t) = A^{opt}(\omega_i(t))$. Further, by slightly adjusting the duration of each sweep, we enforce each trap to end with the optimal phase corresponding to its new position.

Using these parameters we pre-calculate all waveforms to sweep the frequency of a tone at any given starting frequency in our array to any given final frequency, over 3 ms. This amounts to 100^2 precalculated trajectories.

C.2.6 LIFETIMES

The lifetime for each trap is found by an exponential fit to the probability of retaining an atom as a function of time. Under optimal conditions, this results in an average lifetime for the traps in our array of 11.6 s with a standard deviation of 0.5 s across the array. However, this value depends on the background pressure inside the vacuum chamber and therefore depends on the current with which we drive our dispenser atom source. For the measurements presented in Fig. 6.3 of Chapter 6, an average lifetime of 6.2 s was found from independent calibration measurements.

In these measurements, we apply continuous laser cooling throughout the hold time. We observe that without continuous cooling, the lifetime is reduced compared to these values. The retention as a function of time in this case does not follow a simple exponential decay (indicative of a heating process), and we define the time at which the retention probability crosses $1/e$ to be the lifetime. For the standard configuration in Chapter 6 (100 traps with 0.49 MHz spacing between neighboring frequencies), we find a lifetime of ≈ 0.4 s. While we have not characterized the source of the lifetime reduction in detail, we have carried out a number of measurements in different configurations to distinguish various effects:

- Generating a single trap by driving the AOD with a single frequency from a high-quality signal generator (Rohde & Schwarz SMC100A), we find a lifetime of ≈ 2 s. This indicates that there are additional heating effects, such as photon scattering from trap light or intensity noise, that are independent of the use of the SDR or the fact that we drive

the AOD with a large number of frequencies. Possible improvements include using further detuned trap light and improving our intensity stabilization. Furthermore, in a separate experiment [43], we observed that using a Titanium-Sapphire laser instead of a TA significantly improved trap lifetimes even at the same trapping wavelength.

- Generating a single trap by driving the AOD with a single frequency from the SDR, we find a lifetime of ≈ 1 s. This indicates that the RF-waveforms from the SDR could have additional phase or intensity noise. A possible source is the local oscillator used for IQ upconversion in the SDR, which could be replaced with a more phase-stable version.
- We observe the same trap lifetime of ≈ 1 s when driving the AOD with 70 frequencies at a spacing of 0.7 MHz using the SDR. This indicates that, in principle, there is no lifetime reduction associated with driving the AOD with a large number of frequencies.
- We observe a reduction of lifetime for frequency spacings smaller than ≈ 0.65 MHz. For example, we found a lifetime of ≈ 0.4 s, when setting the frequency spacing to 0.49 MHz. (This lifetime is unchanged by increasing the number of traps from 70 to 100.) We interpret this effect to be the result of interference between neighboring traps. Due to the finite spatial overlap of the tweezer light, a time-dependent modulation occurs with a frequency given by the frequency spacing between neighboring traps. When bringing traps closer together, both the spatial overlap increases and the modulation frequency approaches the parametric heating resonance at ≈ 200 kHz given by twice the radial trapping frequency.

We would like to stress that these effects only play a role after the rearrangement procedure is completed. During rearrangement, continuous laser cooling is a valid and powerful method to reduce heating effects. Additionally, the flexibility of our system makes it possible to load and

continuously cool atoms in a set of closely spaced traps, and to rearrange the filled traps to an array with larger separations, at which point cooling can be turned off. This method of rearrangement takes advantage of the large number of atoms that can be initially loaded in our set of 100 traps separated by 0.49 MHz, while eliminating the effect of interference by setting a larger final frequency separation of, for example, 0.7 MHz. Furthermore, atoms could also be transferred into a fully “static” trap array, such as an optical lattice, after rearrangement.

However, even with optimal cooling parameters, heating effects cannot be always compensated. For example, we observed a significant reduction of lifetime for frequency spacings below ≈ 0.45 MHz even with continuous laser cooling. This sets a limit on the maximum number of traps that can be generated within the bandwidth of our AOD, and therefore limits the final sizes of the atomic arrays.

C.3 PROSPECTS FOR EXTENSIONS TO 2D ARRAYS

In this section we will discuss possible extensions of our method to form uniformly filled two-dimensional (2d) arrays. We will describe two different rearrangement strategies and compare their performance given realistic parameters for loading efficiencies and lifetimes.

C.3.1 METHOD 1: ROW OR COLUMN DELETION AND REARRANGEMENT

Using a 2d AOD we could generate a 2d array of optical tweezers using two sets of RF tones, one set corresponding to rows and the other corresponding to columns. After loading atoms probabilistically into the array, it would be possible to eliminate each defect by turning off the RF frequency that generates either the row or the column containing the defect, and then transport all remaining rows and columns to form a defect-free uniform array.

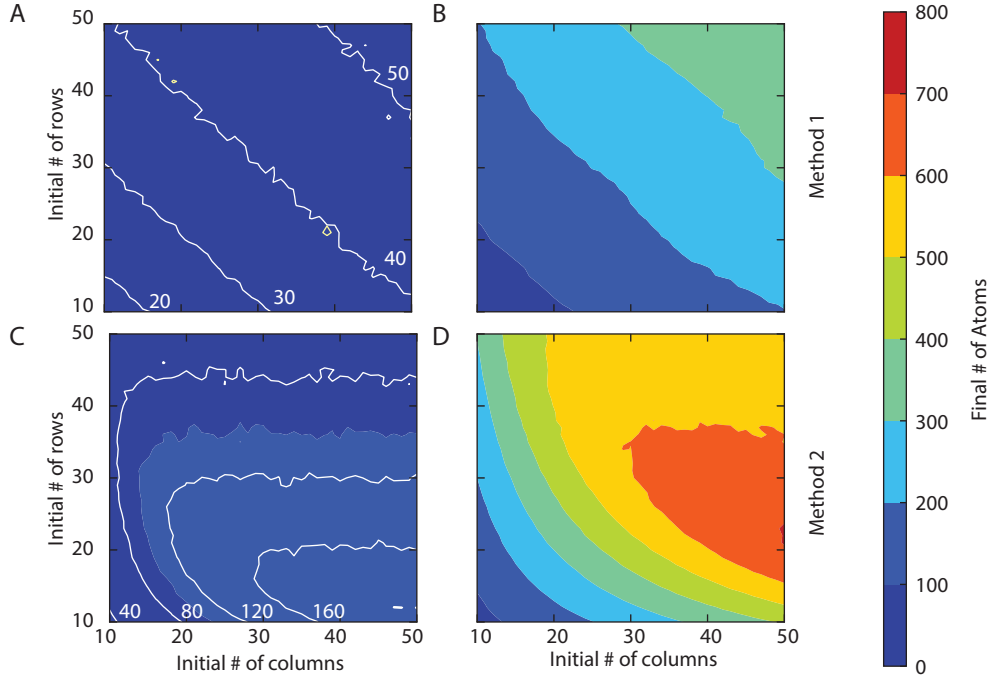


Figure C.5: Projections for 2D system sizes. Expected number of atoms in defect free rectangular arrays generated through the “Row or column deletion and rearrangement method” with 0.6 loading efficiency and 10 s lifetime (**A**), and with 0.9 loading efficiency and 60 s lifetime (**B**). Expected number of atoms in defect free rectangular arrays generated through the “Row-by-row rearrangement method” with 0.6 loading efficiency and 10 s lifetime (**C**), and with 0.9 loading efficiency and 60 s lifetime (**D**).

C.3.2 METHOD 2: ROW-BY-ROW REARRANGEMENT

A different approach is to generate a static two-dimensional array of traps using techniques such as optical lattices or spatial-light modulators. In a first step, atoms would be probabilistically loaded into this static array. After loading, we could use an independent AOD to generate a linear array of traps, deeper than the ones forming the static array and overlapping precisely with one row of static traps. By rearranging the linear array, we could transfer the atoms to their final locations in the static configuration, where they would remain after turning off the traps used for transport. Doing this for each row would make it possible to fill an entire region of the static 2d array.

C.3.3 EXPECTED PERFORMANCE AND SCALABILITY

The final size of the array will depend on the initial loading efficiency, while the probability to have a defect-free array after rearrangement will depend on the atom lifetimes in the traps, and the total feedback time. This time consists of several blocks: image taking, image transfer, waveform calculation, and trap movement. We can take an image in 20 ms. The time it takes to transfer the image from the camera to the computer takes a minimum of 9 ms and each row of atoms adds 0.8 ms to the transfer time. Analyzing the image to determine the location of the atoms and necessary frequency sweeps can be done in sub-ms time. Generating the waveform takes \approx 0.2 ms for each sweep necessary. This time scales as the final number of atoms ($O(N)$) for method 2, and with the final number of rows and columns ($O(N^{1/2})$) for method 1. Finally, the rearrangement itself takes 3 ms for each set of frequency sweeps: for method 1 there are two sweeps, and for method 2 the number of sweeps equals the number of rows.

Figure C.5 shows the result of a Monte Carlo simulation for the expected number of atoms in a defect-free rectangular array using two sets of parameters, and both rearrangement methods described above. Given our current loading efficiency of 0.6 and vacuum-limited lifetime of \approx 10 s, we can expect more than 160 atoms in the final defect-free configuration (Fig. C.5A, C). However, if we were to upgrade our vacuum setup to increase the lifetime from 10 s to 60 s, and we increased the loading efficiency to 0.9 using currently available techniques [85–87], we could expect more than 600 atoms in defect-free configurations (Fig. C.5B, D). These numbers were calculated by simulating a sequence that performed repeated rearrangement until no more defects appeared, and every point on the plot is the average of 500 simulations.

D

Supplementary information for Chapter 7

D.1 TRAPPING SETUP AND EXPERIMENTAL SEQUENCE

Our setup consists of a linear array of up to 101 evenly spaced optical tweezers. The tweezers are generated by feeding a multi-tone RF signal into an acousto-optic deflector (AA Opto-Electronic model DTSX-400-800.850), generating multiple deflections in the first diffraction order, and focusing them into the vacuum chamber using a 0.5 NA objective (Mitutoyo G Plan Apo 50X). The beams have a wavelength of 808 nm and a waist of $\sim 0.9 \mu\text{m}$, forming traps of depth $\sim 1 \text{ mK}$.

A diagram of the experimental sequence is shown in Fig. D.1a. The traps are loaded from

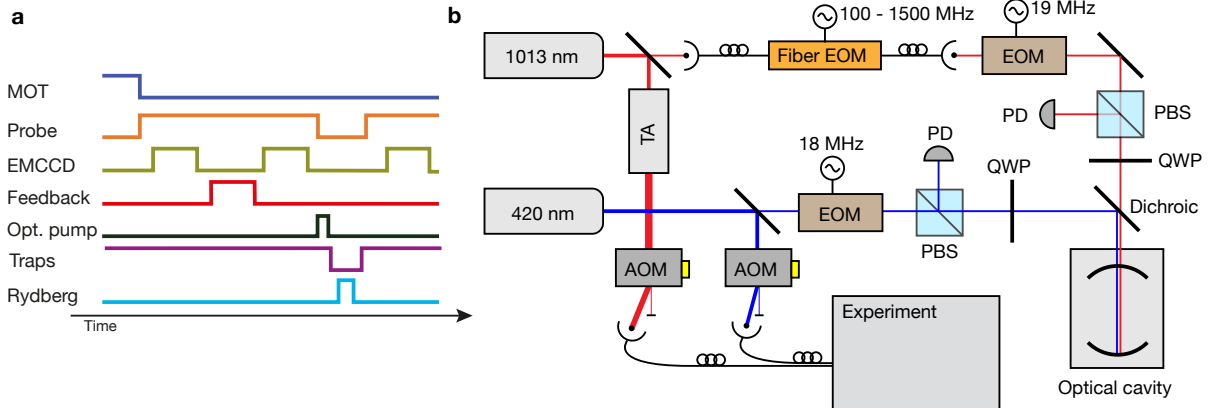


Figure D.1: Experimental sequence and Rydberg laser setup. **a**, The tweezer array is initially loaded from a MOT. A single-site resolved fluorescence image taken with an electron-multiplied-CCD camera (EM-CCD) is used to identify the loaded traps. Using this information, a feedback protocol rearranges the loaded atoms into a preprogrammed configuration, which is verified by the second EMCCD image. After that, all atoms are optically pumped into the $|F = 2, m_F = -2\rangle$ state, the tweezers are turned off, and the Rydberg lasers are pulsed. After the traps are turned back on, a third EMCCD image is taken to detect Rydberg excitations with single-site resolution. **b**, Schematic representation of the Rydberg laser setup, which is used to stabilize two external cavity diode lasers to a reference optical cavity with a fast Pound-Drever-Hall lock. Key: TA=Tapered amplifier, AOM = Acousto-optic modulator, EOM = Electro-optic modulator, PD = Photodetector, PBS = Polarizing beam splitter, QWP = Quarter wave plate.

a magneto-optical trap (MOT), leading to individual tweezer single-atom loading probabilities of ~ 0.6 . A fluorescence image of the array is taken, and the empty traps are turned off, while the filled traps are rearranged to bring the atoms into their preprogrammed positions [24]. Following the rearrangement procedure, another image of the array is taken to preselect on instances in which the initial configuration is defect-free. After taking the second image, we apply a magnetic field of ~ 1.5 G along the axis of the array, and then we optically pump all atoms into the $|F = 2, m_F = -2\rangle$ state using a σ^- -polarized beam resonant to the $|5S_{1/2}, F = 2\rangle \rightarrow |5P_{3/2}, F = 2\rangle$ transition. We then turn off the traps, pulse the Rydberg lasers on a timescale of a few microseconds, and then turn the traps back on to recapture the atoms that are in the ground state $|g\rangle$ while pushing away the atoms in the Rydberg state $|r\rangle$, and finally take a third image. Because of their long lifetime, most of the Rydberg atoms escape from the trapping region before they decay back to the ground state. This provides a convenient way to detect them as missing atoms on the third image (with finite detection fidelity discussed in

section 1.3). The entire experimental sequence, from MOT formation to the third image, takes ~ 250 ms.

D.2 RYDBERG LASERS SETUP

To introduce interactions within the array, we couple the atomic ground state $|g\rangle = |5S_{1/2}, F = 2, m_F = -2\rangle$ to a target Rydberg state $|r\rangle = |70S_{1/2}, m_J = -1/2\rangle$. The van der Waals interaction between two ^{87}Rb $70S$ atoms follows a $1/R^6$ power law and is on the order of 1 MHz at $10\ \mu\text{m}$ [47], making it the dominant energy scale in our system for up to several lattice sites.

The coupling between states $|g\rangle$ and $|r\rangle$ is induced by a two-photon transition, with $|6P_{3/2}\rangle$ as the intermediate level. We drive the transition between $|g\rangle$ and $|6P_{3/2}\rangle$ with a blue 420 nm laser (MOGLabs cateye diode laser CEL002) and the transition between $|6P_{3/2}\rangle$ and $|r\rangle$ with an IR 1013 nm laser injecting a tapered amplifier (MOGLabs CEL002 and MOA002). The detuning δ of the blue laser from the $|g\rangle \leftrightarrow |6P_{3/2}\rangle$ transition is chosen to be much larger than the single-photon Rabi frequencies (typically $\delta \sim 2\pi \times 560$ MHz $\gg \Omega_B, \Omega_R \sim 2\pi \times 60, 36$ MHz, where Ω_B and Ω_R are the single-photon Rabi frequencies for the blue and red lasers, respectively), such that the dynamics can be safely reduced to a two-level transition $|g\rangle \leftrightarrow |r\rangle$ driven by an effective Rabi frequency $\Omega = \Omega_B \Omega_R / (2\delta) \sim 2\pi \times 2$ MHz (Fig. D.2a).

The blue and IR beams are applied counter-propagating to one another along the axis of the array. An external magnetic field is additionally applied, and the beams are circularly polarized such that blue laser drives the σ^- transition between $|g\rangle$ and $|e\rangle = |6P_{3/2}, F = 3, m_F = -3\rangle$, while the red laser drives the σ^+ transition between $|e\rangle$ and $|r\rangle$. Such a stretched configuration minimizes the probability to excite unwanted states such as $|70S_{1/2}, m_J = +1/2\rangle$. The two beams are focused to waists of $20\ \mu\text{m}$ (blue) and $30\ \mu\text{m}$ (IR) at the position of the atoms, in order to get high intensity while still being able to homogeneously couple all atoms in the

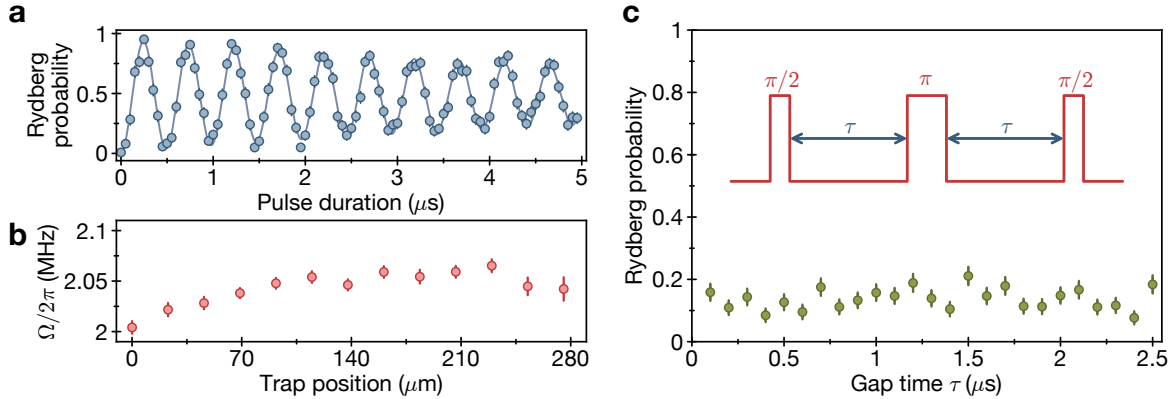


Figure D.2: Typical Rabi oscillation, homogeneity and coherence for non-interacting atoms ($a = 23 \mu\text{m}$, $\Omega \gg V_{i,i+1} \simeq 5 \text{ kHz}$). **a**, Rabi oscillations. We observe a typical decay time of $\sim 6 \mu\text{s}$, which is mainly limited by intensity fluctuations from shot to shot. **b**, The fitted Rabi frequency for each atom across the array (spatial extent $\sim 300 \mu\text{m}$) is homogeneous to within $< 3\%$. Error bars denote 68% confidence intervals. **c**, Measurement of the population in the Rydberg state after a spin echo pulse sequence drawn above. We find no decay of coherence over typical measurement periods of several microseconds, thereby ruling out fast sources of decoherence.

array (see section Coherence Limitations).

The Rydberg lasers interact with the atoms during one experimental cycle for a few μs . In order to maintain laser coherence, the linewidth must be significantly smaller than a few tens of kHz. To achieve this, we use a fast Pound-Drever-Hall scheme to lock our Rydberg lasers to an ultra-low-expansion reference cavity (ATF-6010-4 from Stable Laser Systems, with a finesse of ≥ 4000 at both 420 nm and 1013 nm). The optical setup used for this purpose is sketched on Fig. D.1b. A fraction of the beam from the blue laser first goes through a phase modulator (Newport 4005) driven by a 18 MHz sinusoidal signal, before being coupled to a longitudinal mode of the reference cavity. The reflected beam from the cavity is sent on a fast photodetector (Thorlabs PDA8A), whose signal is demodulated and low-pass filtered to create an error signal which is fed into a high-bandwidth servo controller (Vescent D2-125). The feedback signal from the servo controller is applied to the current of the laser diode using a dedicated fast input port on the laser headboard. The measured overall bandwidth of the lock is on the order of 1 MHz. The other part of the blue laser beam goes through an acousto-optic modulator

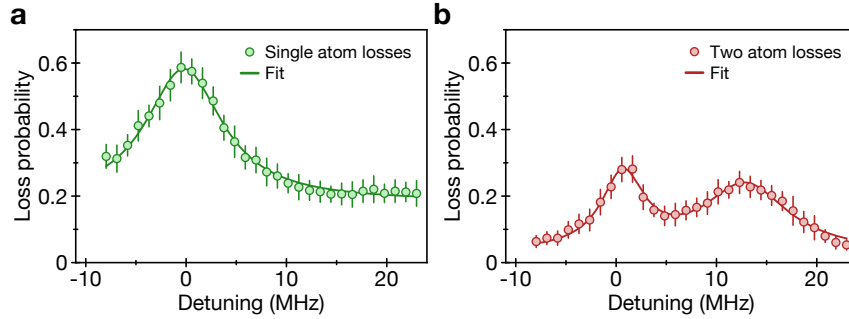


Figure D.3: Spectroscopic measurement of Rydberg interactions. Spectroscopy on pairs of atoms separated by $\sim 5.74 \mu\text{m}$. **a**, For single atom losses, we observe a single peak at $\Delta = 0$ corresponding to the two-photon coupling from $|g, g\rangle$ to $|W\rangle$. **b**, For two atom losses, we observe an additional peak at $\Delta = 2\pi \times 12.2 \text{ MHz}$. This corresponds to the four-photon coupling from $|g, g\rangle$ to $|r, r\rangle$ through the intermediate state $|W\rangle$, detuned by Δ . The interaction energy is then given by $V = 2\Delta$. Note that this four-photon resonance is broadened due to random atom positions within the optical tweezers that result in fluctuations in interaction strengths from shot to shot of the experiment. Solid lines are fits to a single Lorentzian (single atom losses) and the sum of two Lorentzians (two atom losses).

(IntraAction ATM-1002DA23), whose first diffraction order is used to excite atoms, providing frequency and amplitude control for the Rydberg pulses.

A similar scheme is implemented for the 1013 nm laser, with the notable difference that the beam used for the frequency lock first goes through a high-bandwidth ($> 5 \text{ GHz}$) fiber-based electro-optic modulator (EOM, EOSpace PM-0S5-05-PFA-PFA-1010/1030). Rather than the carrier, we use a first-order sideband from the EOM for the lock, which makes it possible to tune the frequency of the red laser over a full free-spectral range of the reference cavity (1.5 GHz) by tuning the driving frequency of the high-bandwidth EOM. Following [308] and [309], we estimate that the contribution to the laser linewidth of the noise within the servo loop relative to the cavity is less than 500 Hz.

D.3 MEASURING INTERACTION STRENGTHS

We experimentally measure the $70S \rightarrow 70S$ van der Waals interactions between atom pairs separated by $5.74 \mu\text{m}$ (identical to the spacing used for observing the Z_2 ordered phase) to

confirm our estimate of interaction strengths and to provide independent (and more precise) estimation of the exact atom spacing (Fig. D.3). At this spacing we expect the interaction V to be on the order of $2\pi \times 20$ MHz. We apply our two laser fields (420 nm and 1013 nm) to couple each atom to the Rydberg state, with two-photon detuning Δ . For $\Delta = 0$, we observe resonant coupling from $|g, g\rangle$ to $|W\rangle = \frac{1}{\sqrt{2}}(|g, r\rangle + |r, g\rangle)$ as expected for the blockaded regime in which $\Omega = 2\pi \times 2$ MHz $\ll V$. However, there is an additional resonance at $\Delta = V/2$ in which we drive a four-photon process from $|g, g\rangle$ to $|r, r\rangle$ through the off-resonant intermediate state $|W\rangle$. By spectroscopy, we determine this 4-photon resonance to be at $\Delta \sim 2\pi \times 12.2$ MHz, from which we calculate $V = 2\Delta = 2\pi \times 24.4$ MHz. This is consistent with independent measurements of our trap spacing of ~ 5.7 μm , from which we additionally calibrate the spacing used in other arrangements (3.57 μm for Z_3 order and 2.87 μm for Z_4 order). Other methods have also been used to more accurately determine interaction strengths, such as those demonstrated in Fig. 3.7 of Chapter 3.

D.4 TIMING LIMITS IMPOSED BY TURNING OFF TRAPS

Atoms can be unintentionally lost due to motion away from the trapping region during the Rydberg pulse when the traps are off. This process depends on atomic temperature and how long we turn off the traps. In particular, with our measured temperature of 12 μK (Fig. 2.8 in Chapter 2), the loss due to atomic motion for trap-off times of < 4 μs is only $\lesssim 0.1\%$. For longer trap-off times, we see loss of up to 2% at 6 μs or 9% at 10 μs . To cap this infidelity at 3%, all experiments described in Chapter 7 operate with trap-off times of ≤ 7 μs .

D.5 STATE DETECTION FIDELITY

Each atom is identified as being in $|g\rangle$ (or $|r\rangle$) at the end of the Rydberg pulse by whether it is (or is not) present in the third fluorescence image. Detection infidelity arises from accidental loss of atoms in $|g\rangle$ or accidental recapture of atoms in $|r\rangle$. For an atom in state $|g\rangle$, detection fidelity is set by the finite trap lifetime (which causes baseline loss of 1%) and motion due to turning the traps off ($\leq 3\%$ for all experiments shown, see section on Timing Limits). In particular, for the 7-atom data shown in Figure 7.3 in Chapter 7 and the 51-atom data shown in Figure 7.4 and 7.5, we measured ground state detection fidelities of 98% and 99%, respectively.

For an atom in state $|r\rangle$, the optical tweezer yields an anti-trapping potential, but there is a finite probability that the atom will decay back to the ground state and be recaptured by the tweezer before it can escape the trapping region. We quantify this probability by measuring Rabi oscillations between $|g\rangle$ and $|r\rangle$ (Fig. D.2) and extracting the maximum amplitude of the oscillation signal. After accounting for the loss of ground state atoms as an offset to the signal, we obtain a typical effective detection fidelity of 93% for the $|70S_{1/2}\rangle$ Rydberg state. Furthermore, we observe a reduced detection fidelity at lower-lying Rydberg states, which is consistent with the dependence of the Rydberg lifetime on the principal quantum number [48].

D.6 CORRECTING FOR FINITE DETECTION FIDELITY

The number of domain walls is a metric for the quality of preparing the desired crystal state. Boundary conditions make it favorable to excite the atoms at the edges. Therefore, we define a domain wall as any instance where two neighboring atoms are found in the same state or an atom at the edge of the array is found in state $|g\rangle$. In systems composed of an odd number of

particles, this definition sets the parity of domain walls to be even.

The appearance of domain walls can arise from non-adiabaticity across the phase transition, as well as scattering from the intermediate $6P$ state, imperfect optical pumping, atom loss, and other processes (see section on Coherence Limitations). However, the observed number of domain walls is artificially increased owing to detection infidelity; any atom within a crystal domain that is misidentified increases the number of measured domain walls by two. For this reason, we use a maximum-likelihood routine to estimate the parent distribution, which is the distribution of domain walls in the prepared state that best predicts the measured distribution. We use two methods to correct for detection infidelity, depending on whether we are interested only in the probability to generate the many-body ground state, or in the full probability distribution of the number of domain walls.

D.7 CORRECTING DETECTION INFIDELITY: MANY-BODY GROUND STATE PREPARATION

Having prepared the many-body ground state, the probability to correctly observe it depends on the measurement fidelity for atoms in the electronic ground state f_g , the measurement fidelity for atoms in the Rydberg state f_r , and the size of the system N . Assuming a perfect crystal state in the Z_2 phase, the total number of atoms in the Rydberg state is $n_r = (N + 1)/2$, while the number of atoms in the ground state is $n_g = (N - 1)/2$. The probability to measure the perfect state is then $p_m = f_r^{n_r} \times f_g^{n_g}$. Therefore, if we observe the ground state with probability p_{exp} , the probability of actually preparing this state is inferred to be p_{exp}/p_m . The blue data points in Fig. 7.4a in Chapter 7 are calculated this way.

D.8 CORRECTING DETECTION INFIDELITY: MAXIMUM LIKELIHOOD STATE RECONSTRUCTION

In order to correct for detection fidelity in the entire distribution of domain walls, we use a maximum-likelihood protocol. For this purpose, we assume that the density of domain walls is low, such that the probability of preparing two overlapping domain walls, meaning three consecutive atoms in the same state, is negligibly small. Under this assumption, misidentifying an atom within a domain wall shifts its location, but does not change the total number. However, misidentification of an atom within a crystal domain increases the number of domain walls by two. For any prepared state with a number of domain walls n_i , we can calculate the probability to measure n_f domain walls, $p(n_f|n_i)$. We can construct a matrix M , which transforms an initial probability distribution in number of domain walls, $\mathbf{W}_i = (p(n_i = 0), p(n_i = 2), \dots)$, into the expected observed distribution $\mathbf{W}_f = M\mathbf{W}_i$, where $M_{kl} = p(n_f = k|n_i = l)$. Given an experimentally observed distribution of domain walls, \mathbf{W}_o , and a test initial distribution \mathbf{W}'_i , we can calculate the difference vector between them $\mathbf{D}' = \mathbf{W}_o - \mathbf{W}'_f = \mathbf{W}_o - M\mathbf{W}'_i$.

Using \mathbf{D}' and the confidence intervals of the measured data (σ), we define a cost function

$$C(\mathbf{W}_o, \mathbf{W}'_i) = \sum_k \left(\frac{D'_k}{\sigma_k} \right)^2, \quad (\text{D.1})$$

where σ represents the 68% confidence intervals obtained via an approximate parametric bootstrap method [310], and the sum is taken over the elements of the vectors. We can find the most likely parent distribution, \mathbf{W}_i , by minimizing the cost function over the different possible \mathbf{W}'_i , under the constraint that every element is between 0 and 1, and the sum of the elements is 1. For this purpose, we use a Sequential Least Square Programming routine. To reduce biases, we use a random vector as a starting point of the minimization procedure. We

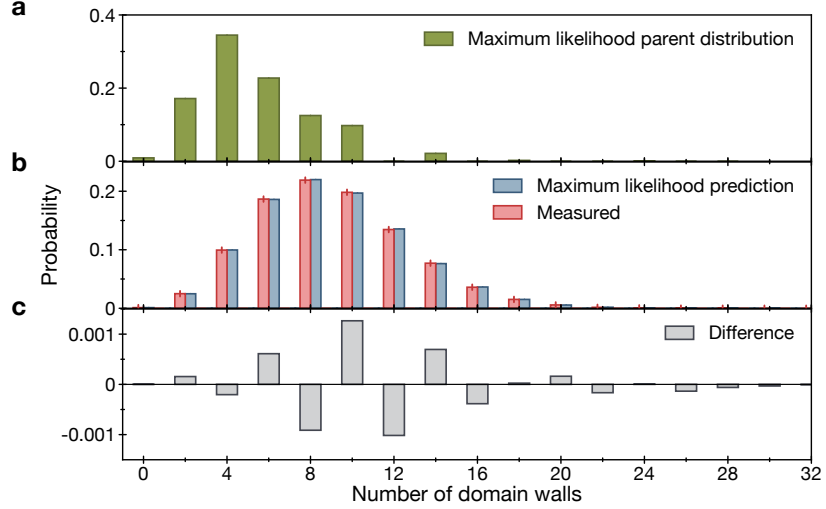


Figure D.4: State reconstruction. **a**, Reconstructed parent distribution. **b**, Comparison of measured domain wall distribution (red) and predicted observation given the parent distribution in **a** (blue). **c**, Difference between the two distributions in **b**.

checked that repeating the procedure several times with different initial vectors converged to the same parent distribution, and that the distribution of domain walls predicted by this parent distribution was in excellent agreement with the measured distribution. The result of such a procedure on the dataset used for Fig. 7.5c of Chapter 7 is shown in Fig. D.4.

D.9 ADIABATIC PULSE OPTIMIZATION

In order to prepare the ordered phases, we use frequency chirped pulses by varying the two-photon detuning Δ across the bare $|g\rangle \leftrightarrow |r\rangle$ resonance, corresponding to $\Delta = 0$. To perform these sweeps, we drive a high-modulation-bandwidth voltage-controlled oscillator (VCO, Mini-Circuits ZX95-850W-S+) according to either cubic or tangent functional forms:

$$V(t)_{\text{cubic}} = a(t - t_0)^3 + b(t - t_0) + c \Big|_{\Delta_{\min} \leq \Delta \leq \Delta_{\max}} \quad (\text{D.2})$$

$$V(t)_{\text{tangent}} = a \tan(b(t - t_0)) + c \Big|_{\Delta_{\min} \leq \Delta \leq \Delta_{\max}} \quad (\text{D.3})$$

with programmable parameters a, b, c . The output from this VCO is mixed (Mini-Circuits ZFM-2-S+) with a 750 MHz source to generate the difference frequency, which is used to drive the AOM in the 420 nm light path. The detuning Δ is set to truncate at minimum and maximum values Δ_{\min} and Δ_{\max} , respectively. The tangent adiabatic sweep has been used for datasets with 51 atoms shown on Figures 7.4 and 7.5 of Chapter 7 due to improved performance, whereas the cubic form has been used for all smaller system sizes and for the data on crystal dynamics shown on Figure 7.6 of Chapter 7.

At the end of the sweep, the number of domain walls in the crystal provides a metric for the quality of the crystal preparation. All parameters in (D.2) or (D.3) are iteratively optimized as to minimize the domain wall number, i.e. maximize the crystal preparation fidelity. The optimization starts with the offset c , followed by the b parameter, then the maximum and minimum detunings $\Delta_{\min/\max}$, and finally the a parameter. Repeated optimization of these parameters often leads to better crystal preparation fidelities [311].

After passing through the AOM, the 420 nm light is coupled into a fiber. The coupling is optimized for the VCO frequency at which the light is resonant with the $|g\rangle$ to $|r\rangle$ transition (f_{opt}), and decreases as the VCO frequency deviates from f_{opt} . The power throughout all frequency sweeps is $\geq 75\%$ of the power at f_{opt} .

D.10 COHERENCE LIMITATIONS

When sweeping into the crystalline phase, the control parameter $\Delta(t)$ must be varied slowly enough that the adiabaticity criterion is sufficiently met. However, for long pulses, additional

technical errors may become limiting. Here, we summarize some key limitations:

- **State preparation fidelity:** For all analyzed data, we preselect on defect-free atom arrays. Preparation fidelity is therefore given by the probability that each atom in the array is still present for the Rydberg pulse, and that it is prepared in the correct magnetic sublevel: $|5S_{1/2}, F = 2, m_F = -2\rangle$. Including both factors, we estimate that atoms are present and in the correct magnetic sublevel with fidelity $f > 98\%$. For experiments with 51 atoms, this leads to $\lesssim 1$ atom incorrectly prepared.
- **Spontaneous emission:** The $70S$ Rydberg state has an estimated lifetime of $150 \mu\text{s}$ (including blackbody radiation at 300 K) [48]. Additionally, for the typical intermediate detuning $\Delta \approx 2\pi \times 560 \text{ MHz}$ and single photon IR and blue Rabi frequencies of $(\Omega_R, \Omega_B) \approx 2\pi \times (36, 60) \text{ MHz}$, spontaneous emission from the intermediate state occurs on a time scale of $40 \mu\text{s}$ for the ground state, and introduces a combined effective lifetime of $50 \mu\text{s}$ for the Rydberg state. This leads to an average scattering rate of $2\pi \times 3.6 \text{ kHz}$.
- **Rabi frequency homogeneity:** We aim to align our beams to globally address all trapped atoms with a uniform Rabi frequency $|\Omega_i| = \Omega$. Experimentally, we achieve homogeneity up to differences $\lesssim 3\%$ (Fig. D.2b).
- **Intensity fluctuations:** Primarily because of pointing instability, the global Rabi frequency fluctuates by small amounts from shot to shot of the experiment. In order to reduce slow drifts of the beams, we use a 1:1.25 telescope to image on a camera their position on the plane of the atoms and feedback to stabilize their position to a target every 500 repetitions (~ 2 minutes).
- **Rydberg laser noise:** The coherence properties of the Rydberg lasers over typical

experimental times are probed by measurements on single, non-interacting atoms. In particular, spin echo measurements between $|g\rangle$ and $|r\rangle$ show no visible decay of coherence over $5\ \mu\text{s}$ (Fig. D.2c). This measurement, along with the measured noise contribution from the laser lock $< 0.5\ \text{kHz}$ (see section on Rydberg lasers setup), indicates that the laser linewidths are sufficiently narrow. Additional phase noise is introduced by the laser lock around the lock bandwidth of about $1\ \text{MHz}$. This phase noise may cause weak additional decoherence on the adiabatic sweep experiments shown in Chapter 7.

- **Finite atomic temperature:** Our finite atomic temperature of $\sim 12\ \mu\text{K}$ introduces both random Doppler shifts (of order $2\pi \times 50\ \text{kHz}$), as well as fluctuations in the atomic positions ($\sim 120\ \text{nm}$ radially, $\sim 600\ \text{nm}$ longitudinally) for each atom in each cycle of the experiment. The Doppler shift is very small in magnitude compared to the single atom Rabi frequency Ω . The position fluctuations can introduce noticeable fluctuations in the interaction energy between a pair of atoms from shot to shot. As an example, at our chosen lattice spacing of $5.9\ \mu\text{m}$, we calculate an interaction energy of $2\pi \times 24\ \text{MHz}$. However, if the distance fluctuates by values on the order of $\sqrt{2} \times 120\ \text{nm} \approx 170\ \text{nm}$, then the actual interaction energy can range from $21\ \text{MHz}$ to $29\ \text{MHz}$. The longitudinal position fluctuations add in quadrature, so they contribute less to fluctuations in distance.
- **Electric and magnetic fields:** We have observed that the Rydberg resonance can drift over time, especially for states with high principal quantum number n , which we attribute to uncontrolled fluctuations in the electric field. We can reduce these fluctuations by shining UV light at $365\ \text{nm}$ on the glass cell in between experimental sequences and during the MOT loading period, which stabilizes the charge environment on the

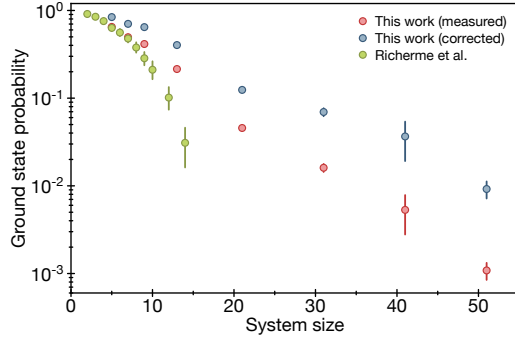


Figure D.5: Ground state preparation probability comparison. Comparison of the ground state preparation probability obtained in this work (measured, red circles; corrected for detection infidelity, blue circles) with the most complete prior observations of a Z_2 -symmetry breaking transition in a system of trapped ions [125]. We emphasize that the interaction Hamiltonians for the two systems are not identical due to the finite interaction range. In particular, the long range interactions tend to frustrate adiabatic transitions into Z_2 ordered states in [125] and, to lesser extent, in the present work.

glass cell surface. While the fluctuations for states $n \geq 100$ are still significant, they

become negligible (< 100 kHz) for our chosen state $n = 70$.

The energy shifts of the initial state $|g\rangle$ and final state $|r\rangle$ with magnetic fields are identical. Differential shifts of the intermediate state are very small compared to the detunings of the two laser beams from the $6P_{3/2}$ state. Therefore, we do not expect magnetic fields to play any significant role in fluctuations between experimental runs.

We note that the use of deterministically prepared arrays allows us to efficiently optimize the coherence properties. For example, for collective Rabi oscillations of fully blockaded groups of up to three atoms, we observe an improvement in the product $\Omega\tau_d$ of about an order of magnitude compared to previous work [117], where τ_d is the decay time of Rabi oscillations. In addition, the relatively high fidelity in the preparation of Z_2 ordered states with 51 atoms (Fig. D.5) indicates a significant amount of coherence preserved over the entire evolution. These considerations indicate that the present approach is promising for near-term coherent experiments with large scale systems [312].

D.11 COMPARISON WITH A CLASSICAL THERMAL STATE

To gain some insight into the states obtained from our preparation protocol (Fig. 7.3a in Chapter 7), we provide a quantitative comparison between experimentally measured quantities and those computed from a thermal ensemble. In particular, we note that deep in the ordered phase $\Delta/\Omega \gg 1$, the coherent coupling of the ground state to the Rydberg state can be neglected owing to strong energetic suppression, and that the effective Hamiltonian becomes diagonal in the measurement basis. This allows us to calculate all properties of a thermal state even for systems of 51 atoms by explicitly computing the partition function via the transfer matrix method [313]. Also, we may consider the interactions only up to next-nearest neighbors as the coupling strengths for longer distances are weak compared to the maximum timescale accessible in our experiments. To this end, we consider the Hamiltonian

$$\mathcal{H}_{\text{cl}} = -\Delta \sum_{i=1}^N n_i + \sum_{i=1}^{N-1} V_1 n_i n_{i+1} + \sum_{i=1}^{N-2} V_2 n_i n_{i+2}.$$

The eigenstates of this Hamiltonian are simply 2^N classical configurations, where each atom is in either $|g\rangle$ or $|r\rangle$. We label these configurations by a length- N vector $\mathbf{i} = (i_1, i_2, \dots, i_N)$ ($i_n \in \{g, r\}$), and denote their energy by $E_{\mathbf{i}}$. In a thermal ensemble $\rho = \exp(-\beta \mathcal{H}_{\text{cl}})/Z$ with $Z \equiv \text{tr}[\exp(-\beta \mathcal{H}_{\text{cl}})]$ and inverse temperature β , the probability to find a particular configuration \mathbf{i} is given by $p_{\mathbf{i}} = \exp(-\beta E_{\mathbf{i}})/Z$. Since $E_{\mathbf{i}}$ can be written as a sum of local terms involving only interactions up to a range 2, the partition sum can be evaluated using a standard transfer matrix of size 4×4 . Moreover, using this approach, we can evaluate all measurable quantities for the thermal ensemble such as the average number of domain walls $\langle D \rangle = \text{tr}\{D\rho\}$, where D is an operator counting the number of domain walls, i.e. $D = \sum_{i=1}^{N-1} (n_i n_{i+1} + (1 - n_i)(1 - n_{i+1})) + (1 - n_1) + (1 - n_N)$, the correlation function $g^{(2)}(d) = 1/(N - d) \sum_{i=1}^{N-d} g_{i,i+d}^{(2)}$, and even the full counting statistics for the domain wall

distribution in the state ρ . In particular, the probability to measure exactly n domain walls

$p_n = \text{tr}\{P_n\rho\}$ can be computed from a Fourier transform of the Kronecker delta function

$$P_n \equiv \delta_{D,n} = \frac{1}{N+2} \sum_{k=0}^{N+1} \exp[i \frac{2\pi}{N+2} k(n - D)] \text{ with } n = 0, 1, 2, \dots, N+1.$$

One can directly include the effect of imperfect detections in this formalism. To that end, we denote the expectation value of an observable O as

$$\langle\langle O \rangle\rangle = \sum_{\mathbf{i}, \mathbf{j}} O_{\mathbf{i}} \Lambda_{\mathbf{i}, \mathbf{j}} p_{\mathbf{j}}, \quad (\text{D.4})$$

where $O_{\mathbf{i}}$ is the value of the observable in state \mathbf{i} , and $\Lambda_{\mathbf{i}, \mathbf{j}}$ is the probability to detect state \mathbf{i} when the system is in state \mathbf{j} , accounting for finite detection fidelity. Assuming detection errors occur independently from one another, we have $\Lambda_{\mathbf{i}, \mathbf{j}} = \prod_n \lambda_{i_n, j_n}$ where $\lambda_{g,g} = f_g$ is the probability to correctly detect an atom in the ground state, $\lambda_{r,r} = f_r$ is the probability to correctly detect an atom in the Rydberg state, and $\lambda_{r,g} = 1 - \lambda_{g,g}$, and $\lambda_{g,r} = 1 - \lambda_{r,r}$. Equation (D.4) can be evaluated using a 16×16 transfer matrix for any observables of interest.

In order to get a quantitative comparison with our experiments, we determine the inverse temperature β in such a way that the average number of domain walls $\langle\langle D \rangle\rangle$, including the effect of imperfect detections, matches the experimentally determined value, i.e. $\langle\langle D \rangle\rangle = 9.01(2)$. For $\Delta = 2\pi \times 14 \text{ MHz}$, $V_1 = 2\pi \times 24 \text{ MHz}$ and $V_2 = 2\pi \times 0.38 \text{ MHz}$ this leads to $\beta = 3.44(1)/\Delta$ or equivalently to the entropy per atom of $s/k_B = 0.286(1)$ (Fig. D.6a,b). Since β characterizes the thermal state completely, we can extract the corresponding domain wall distribution (Fig. D.6c) and the correlation function (Fig. D.6d) as described above. We find that the correlation length in the corresponding thermal state is $\xi_{\text{th}} = 4.48(3)$, which is significantly longer than the measured correlation length $\xi = 3.03(6)$, from which we deduce that the experimentally prepared state is not thermal.

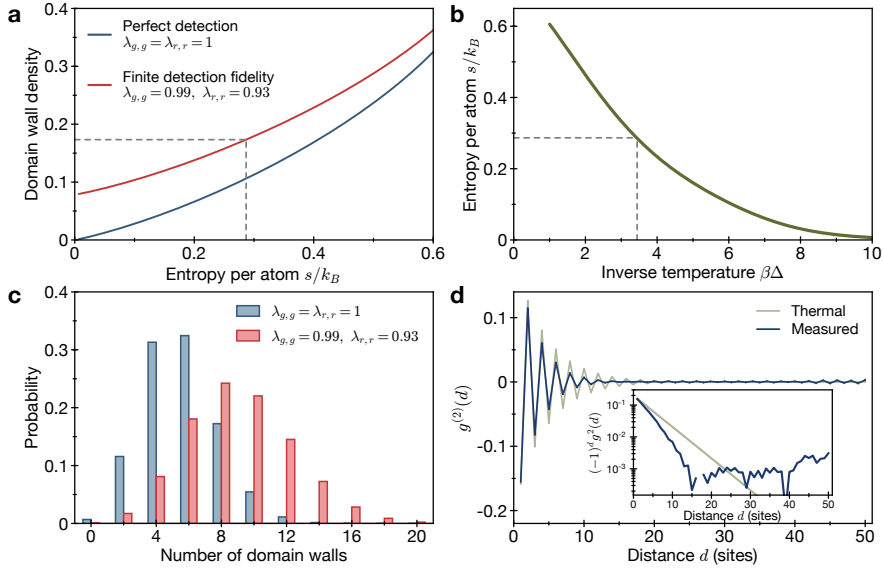


Figure D.6: Comparison to thermal state. **a**, Domain wall density for thermal states at different entropy per atom. The lower line corresponds to the actual number of domain walls in a system of the corresponding temperature, the upper line gives the domain wall density one would measure at this temperature, given the finite detection fidelity. The horizontal dashed line denotes the experimentally measured domain wall density, from which we can infer a corresponding entropy per atom and equivalently, temperature, in a thermal ensemble. **b**, Entropy per atoms for a thermal state at given inverse temperature $\beta = 1/(k_B T)$ in a 51-atom array. **c**, Expected distribution of the number of domain walls for the thermal ensemble at $\beta = 3.44/\Delta$, with (red) and without (blue) taking into account finite detection fidelity. **d**, Experimentally measured correlation function $g^{(2)}(d)$ and correlation function corresponding to a thermal ensemble at $\beta = 3.44/\Delta$. The inset shows the rectified correlation function on a logarithmic scale, indicating that the measured correlation function decays exponentially, but with a different correlation length than one obtains from a thermal state with the measured number of domain walls.

D.12 DYNAMICS AFTER SUDDEN QUENCH: MATRIX PRODUCT STATE ANSATZ

To understand the dynamics of the Z_2 Rydberg crystal following the quench of the detuning to $\Delta = 0$, we first consider a simplified model, where interactions beyond nearest neighbor are neglected. In addition, we replace the nearest neighbor interactions with hard constraints that two neighboring atoms cannot be excited at the same time; such an approximation is well controlled in the limit of $V_{i,i+1} \gg \Omega$, as in the case of our experiments, for a time exponentially long in $V_{i,i+1}/\Omega$ [129]. In this limit, the Hamiltonian can then be approximated by

$$\mathcal{H}_c = \sum_i P_g^{i-1} \left(\frac{\Omega}{2} \sigma_x^i - \Delta P_r^i \right) P_g^{i+1}, \quad (\text{D.5})$$

where $P_g^i = |g_i\rangle\langle g_i|$, $P_r^i = |r_i\rangle\langle r_i|$. We identify $P_g^{i=0} = P_g^{i=N+1} = 1$ at the boundaries.

Within this approximation, the relevant Hilbert space consists only of states with no neighboring atoms in the Rydberg state, i.e. $P_r^i P_r^{i+1} = 0$. The dimension of this constrained Hilbert space is still exponentially large and grows as $\sim \phi^N$, where $\phi = 1.618\dots$ is the golden ratio.

In the simplest approximation, one can treat the array of atoms as a collection of independent dimers, $|\Psi(t)\rangle = \bigotimes_i |\phi(t)\rangle_{2i-1,2i}$, where for each pair of atoms only three states are allowed due to the blockade constraint, $|r,g\rangle$, $|g,g\rangle$ and $|g,r\rangle$. The dynamics of each pair with initial state $|\phi(0)\rangle = |r,g\rangle$ is then given by $|\phi(t)\rangle = \frac{1}{2}(1+\cos(\Omega t/\sqrt{2}))|r,g\rangle + \frac{i}{\sqrt{2}}\sin(\Omega t/\sqrt{2})|g,g\rangle + \frac{1}{2}(1-\cos(\Omega t/\sqrt{2}))|g,r\rangle$. This dimer model predicts that each atom flips its state with respect to its initial configuration after a time $\tau = \sqrt{2}\pi/\Omega$. The corresponding oscillations between two complementary crystal configurations are thus a factor $\sqrt{2}$ slower than an independent spin model would predict, which is qualitatively consistent with the experimental observations. We note that this dimerized ansatz does not satisfy the constraint $P_r^i P_r^{i+1} = 0$ between two neighboring dimers, which is an artifact originating from the artificial partitioning of the array

into non-interacting dimers.

To go beyond this approximation, we consider an ansatz for the many-body wavefunction that treats each atom on an equal footing. The simplest such wavefunction that also allows for non-trivial entanglement between the atoms can be written as a matrix product state (MPS) with bond dimension 2 [314]. In particular we consider a manifold of states of the form $|\Psi(\{\theta_n\})\rangle = \sum_{\{i_n\}} v_L A(\theta_1)^{i_1} A(\theta_2)^{i_2} \cdots A(\theta_N)^{i_N} v_R |i_1, i_2, \dots, i_N\rangle$ with matrices

$$A(\theta_n)^g = \begin{pmatrix} \cos(\theta_n) & 0 \\ 1 & 0 \end{pmatrix} \quad A(\theta_n)^r = \begin{pmatrix} 0 & i \sin(\theta_n) \\ 0 & 0 \end{pmatrix}, \quad (\text{D.6})$$

and boundary vectors $v_L = \begin{pmatrix} 1 & 1 \end{pmatrix}$ and $v_R = \begin{pmatrix} 1 & 0 \end{pmatrix}^\top$. Here, the indices $i_n \in \{g, r\}$ enumerate the state of the n -th atom. This manifold satisfies the constraint that no two neighboring atoms are simultaneously excited. The many-body state within this subspace is completely specified by the N parameters $\theta_n \in [0, 2\pi]$. In particular, it allows to represent the initial crystal state, $\theta_{2n-1} = \pi/2$ for atoms on odd sites and $\theta_{2n} = 0$ for atoms on even sites, as well as its inverted version, $\theta_{2n-1} = 0$ for odd and $\theta_{2n} = \pi/2$ for even sites, respectively. Using the time-dependent variational principle [315], we derive equations of motion for the wave function within this manifold. For an infinite system with a staggered initial state $\theta_{n+2} = \theta_n$, such as the Z_2 ordered state, the wave function is at all times described by two parameters $\theta_a = \theta_{2n-1}$ and $\theta_b = \theta_{2n}$ for even and odd sites. The corresponding non-linear, coupled equations of motion read

$$\dot{\theta}_a = -\frac{1}{2} \sec(\theta_b) (\sin(\theta_a) \cos^2(\theta_a) \sin(\theta_b) + \cos^2(\theta_b)) \quad (\text{D.7})$$

$$\dot{\theta}_b = -\frac{1}{2} \sec(\theta_a) (\sin(\theta_b) \cos^2(\theta_b) \sin(\theta_a) + \cos^2(\theta_a)). \quad (\text{D.8})$$

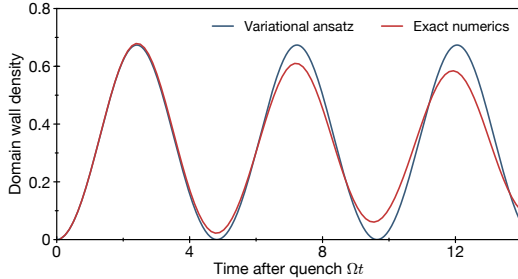


Figure D.7: Oscillations of domain wall density: Using a variational matrix product state ansatz. Dynamics of the domain wall density in the bulk of the array under the constrained Hamiltonian \mathcal{H}_c at $\Delta = 0$. The blue line shows the evolution of the domain wall density obtained from integrating the variational equation of motion eq. (D.7) with initial conditions $\theta_a = \pi/2$, $\theta_b = 0$, i.e. the crystalline initial state. The red line shows the exact dynamics of the domain wall density at the center of a system of 25 atoms initially in the crystalline state under the constrained Hamiltonian \mathcal{H}_c .

A numerical solution of these variational equations for the crystalline initial state predicts a periodic motion with a frequency of $\approx \Omega/1.51$ (Fig. D.7), where the many-body wavefunction oscillate between two staggered configurations.

D.13 DECAY OF THE OSCILLATIONS AND GROWTH OF ENTANGLEMENT AFTER QUANTUM QUENCH

In order to obtain more insight into the dynamics of our system beyond these variational models, we use exact numerical simulations to integrate the many-body Schrödinger equation. In particular, we focus on the decay of oscillations and the growth of entanglement entropy in our system. Due to the exponentially growing Hilbert space, this method is limited to relatively small system sizes. We make use of the constrained size of the Hilbert space (blockade of nearest neighboring excitations of Rydberg states), and propagate the state vector of up to 25 spins using a Krylov subspace projection method. In Fig. D.8 a we show the dynamics of the domain wall density under the time evolution of the constrained Hamiltonian \mathcal{H}_c with $\Omega = 2\pi \times 2$ MHz and $\Delta = 0$. We consider two different initial states: the disordered state where each atom is initially prepared in the ground state $|g\rangle$, and the perfect crystalline state

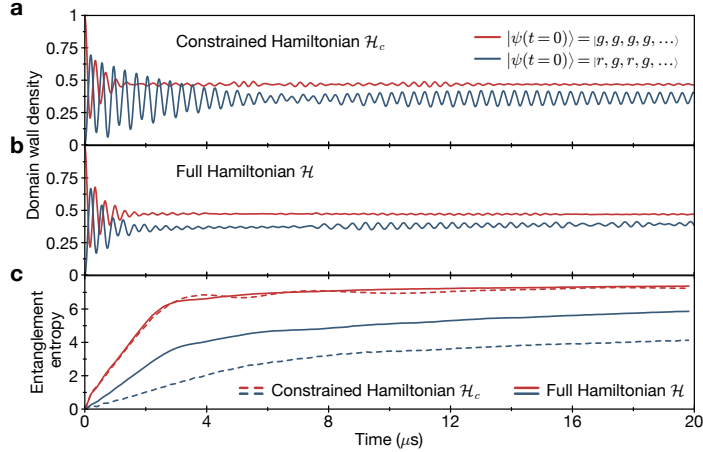


Figure D.8: Decay of oscillations after a quench and entropy growth. **a**, Dynamics of the domain wall density under the constrained Hamiltonian \mathcal{H}_c for different initial states. The red line shows the domain wall density for a system of 25 atoms initially prepared in the electronic ground state. In this case, the domain wall density quickly relaxes to a steady value corresponding to thermalization. In contrast, the blue line shows the dynamics if the system is initialized in the Z_2 ordered state. The domain wall density oscillates over several periods and even for very long times does not fully relax to a steady value. **b**, Same as in **a** but taking into account the full $1/R^6$ interactions. While the dynamics for an initial state $|g\rangle^{\otimes N}$ is very similar to the one obtained in the constrained case, for the crystalline initial state the decay of the oscillations is faster than in the constrained model. **c**, Growth of entanglement entropy in a bipartite splitting of the 25 atom array for the different cases displayed in **a** and **b**. The entropy is defined as the von Neumann Entropy of the reduced state of the first 13 atoms of the array. The dashed lines correspond to dynamics under the constrained Hamiltonian, neglecting the $1/R^6$ tail, while the solid lines take the full interactions into account. Red lines correspond to the initial state $|g\rangle^{\otimes N}$, while blue lines correspond to crystalline initial states. In all panes we chose $\Omega = 2\pi \times 2$ MHz, and where applicable, interaction parameters such that the nearest neighbor interaction evaluates to $V_{i,i+1} = 2\pi \times 25.6$ MHz.

$|r, g, r, g, \dots\rangle$. We note that in both cases the energy density corresponds to that of an infinite temperature thermal ensemble in the constrained subspace with respect to \mathcal{H}_c .

For the disordered initial state, the domain wall density quickly relaxes to a steady state value. In contrast, if the system is initialized in the perfect crystalline state, the domain wall density oscillates for long times and decays at a rate much slower than the oscillation period. We confirmed numerically that this initial decay time is independent of the system size. We further note that for every system size accessible in our numerical method, the domain wall density does not relax to a steady value even at very long times, but continues to oscillate with a reduced amplitude. Moreover, while the disordered initial state relaxes to an average domain wall density consistent with a thermal state of infinite temperature corresponding to the energy density of the initial state, this is clearly not the case for the crystalline initial state. This qualitatively distinct behavior for two different initial states is also reflected in the growth of entanglement entropy after the quench, shown in Fig. D.8c (dashed lines). While in both cases the entanglement entropy grows initially linearly, the rate of growth is significantly lower for the crystalline initial state. Moreover, unlike the case of disordered initial state where the entanglement entropy quickly saturates to its maximum value (limited by the finite system size and the constrained Hilbert space), for the crystalline initial state, the entanglement entropy does not seem to approach the same value.

To understand the influence of the $1/R^6$ -decaying interactions, we show the corresponding dynamics and entanglement growth in Fig. D.8b,c (solid lines). Numerically, we treat the strong nearest neighbor interactions perturbatively – by adiabatic eliminations of simultaneous excitation of neighboring Rydberg states – while the weak interactions beyond nearest neighbors are treated exactly. For the disordered initial state, we find that the dynamics of domain wall density and the entanglement growth remain similar to the previous case, where

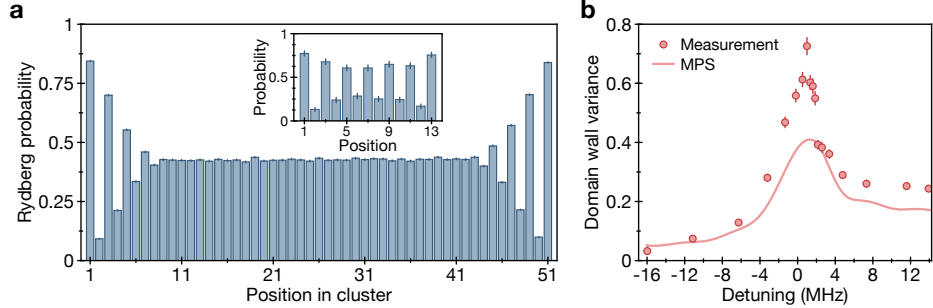


Figure D.9: State preparation with 51 atom clusters. **a**, Average position-dependent Rydberg probability in a 51 atom cluster after the adiabatic sweep. Error bars denote 68% CI. The Z_2 order is visible at the system edges, while the presence of domain walls leads to an apparently featureless bulk throughout the system center. Inset: Comparison with average Rydberg probabilities in a 13 atom chain, where the Z_2 order is visible throughout the system but the small system size prevents the study of bulk properties. **b**, Variance of the domain wall distribution during Z_2 state preparation. Points and error bars represent measured values. The solid red line corresponds to a full numerical simulation of the dynamics using a matrix product state ansatz (see text and Fig. 7.5 of Chapter 7).

long range interactions are neglected; in this case, the thermalization time is barely affected.

In contrast, for the crystalline initial state, the oscillations decay significantly faster once next-to-nearest neighbor interactions are included. We thus attribute the thermalization in this case to interactions beyond the nearest neighbor blockade constraint. From the growth of the entanglement entropy, we see that the crystalline initial state still thermalizes slower than the disordered initial state.

D.14 NUMERICAL TIME EVOLUTION VIA MATRIX PRODUCT STATE ALGORITHM

The numerical data presented in Fig. 7.5b and Fig. 7.6b in Chapter 7 are obtained by simulating the evolution of the 51 atom array during the sweep across the phase transition as well as the subsequent sudden quench using a matrix product state algorithm with bond dimension $D = 256$. We simulate the entire preparation protocol to generate the Rydberg crystal (Fig. 7.5b in the Chapter 7), and use the resulting state as an initial state for the time evolution after the sudden quench. To this end, we use a time-evolving block decimation (TEBD) algorithm [316, 317], with a Suzuki-Trotter splitting of the Hamiltonian to update the state.

The time step used in this Trotterization is $\Omega\Delta t = 0.004$. We take into account only nearest neighbor and next-nearest neighbor interactions and neglect small interactions for atoms that are separated by 3 or more sites (as discussed also in Sec. 4). We account for finite detection fidelities that are determined independently, but otherwise do not include any incoherent mechanisms. Remarkably, for local quantities, such as the domain wall density, this fully coherent simulation agrees well with the experimentally measured values. For higher-order correlation functions, such as the variance of the domain wall number, the fully coherent simulation and the experiment agree only qualitatively (Fig. D.9). The quantitative difference is likely due to either limitations of the MPS simulations or various incoherent processes present in the experiment.

E

Supplementary information for Chapter 8

E.1 RYDBERG ARRAY PREPARATION

The experiment utilizes an acousto-optic deflector to generate multiple optical tweezers, which are loaded probabilistically from a cold gas of ^{87}Rb atoms in a magneto-optical trap. Each tweezer can be loaded with up to a single atom. Once the cloud is dispersed, a fluorescence image, similar to the ones shown in Fig. 8.2a of Chapter 8, is taken to identify loaded traps. The traps are then rearranged to generate a defect-free regular array of 51 atoms, evenly separated by a distance a [24].

We define our spin Hamiltonian according to two pseudospin-1/2 states. The first is a ground-

state hyperfine sublevel, $|g\rangle = |5S_{1/2}, F = 2, m_F = -2\rangle$. The second is the interacting Rydberg state $|r\rangle = |70S, J = 1/2, m_J = -1/2\rangle$. These two states are coupled by a two-photon process via the intermediate state $|e\rangle = |6P_{3/2}, F = 3, m_F = -3\rangle$. The two lasers operate at wavelengths 420 nm for the lower transition and 1013 nm for the upper transition.

The 420 nm laser is a frequency-doubled Titanium-Sapphire laser (SolsTiS 4000 PSX F by M Squared), locked to an optical reference cavity (ATF-6010-4 from Stable Laser Systems). The 1013 nm laser is an external cavity diode laser (CEL002 by MOGLabs) that is locked to the same reference cavity. The transmitted light through the cavity is used to injection lock another 1013 nm laser diode, which is then amplified by a tapered amplifier [293]. Both beams are focused along the array axis (aligned with the quantization axis) to drive σ^- and σ^+ transitions for the 420 nm and 1013 nm beams, respectively.

E.2 PULSE GENERATION

We modulate the 420 nm Rydberg laser with an AOM driven by an arbitrary waveform generator (AWG, M4i.6631-x8 by Spectrum Instrumentation). For each experiment, we program a waveform with varying amplitudes, frequencies and phases in the time domain into the AWG, which is then transmitted to the AOM through a high-power RF amplifier (ZHL-1-2W+ by Mini-Circuits).

The nonlinear AOM response to changes in amplitude and frequency poses a technical challenge. The deflection efficiency is not proportional to the waveform amplitude, and large changes in the waveform frequency lead to variations in the deflection efficiency. These effects lead to distortions in the pulse shape. We apply feed-forward corrections to the amplitude to both match the output intensity to the desired waveform amplitude, as well as to compensate for the variations with frequency.

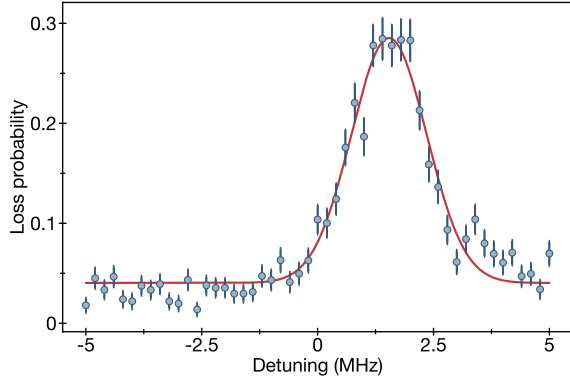


Figure E.1: Determination of initial detuning Δ_0 . At a fixed laser detuning, we linearly ramp Ω on and then off over $1 \mu\text{s}$ each. We identify the negative detuning closest to resonance for which we are fully adiabatic, such that the excitation probability at the end of the pulse returns to the minimum. From this typical measurement, taken at $R_B/a = 1.59$, we set $\Delta_0 = -2.5 \text{ MHz}$. Error bars denote 68% confidence intervals.

E.3 PULSE PARAMETERS

All pulses begin by turning on the value of Ω linearly over $1 \mu\text{s}$ at a fixed initial detuning Δ_0 .

We select our initial detuning to be as close to the critical point as possible subject to the constraint that the initial turn-on is still fully adiabatic. We identify this detuning experimentally by ramping Ω on and then off for various fixed detunings. In the adiabatic case, all the atoms should return to $|g\rangle$. We therefore select the detuning closest to resonance that still shows no excess excitation at the end of the pulse. For a typical measurement in the \mathbb{Z}_2 regime, we select $\Delta_0 = -2.5 \text{ MHz}$ (Fig. E.1).

The final detunings of the sweeps are chosen in most cases to cross the tip of the corresponding phase boundary. In some cases in which the interaction strength is on the border between two phases, we do not fully cross over the boundary (Fig. E.2a).

The power-law scaling behavior of the correlation length can be limited owing to strong nonadiabaticity far away from the critical point, where the behavior of the system is susceptible to the microscopic details and should deviate from universal theories, limiting how fast a sweep across the phase transition can be. At the same time, slow sweeps are more suscep-

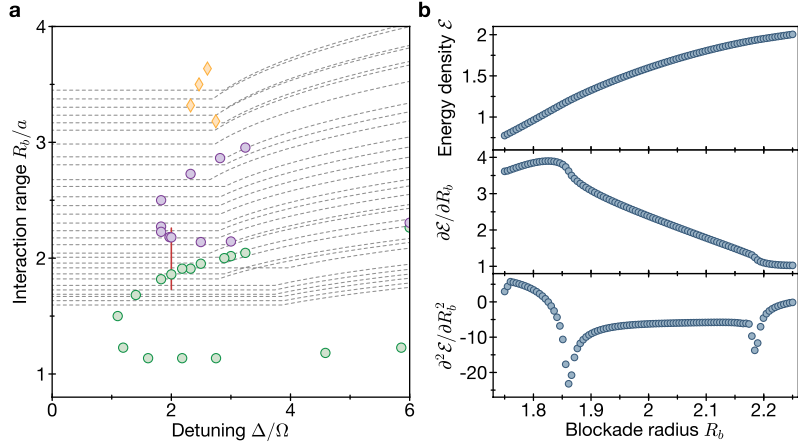


Figure E.2: Numerically extracted phase diagram with trajectories for QKZM measurements. **a**, Green (purple) markers indicate the phase boundary points between disordered and \mathbb{Z}_2 -(\mathbb{Z}_3)-ordered phases. Yellow diamonds indicate the boundaries of the disordered phase (as approached from increasing Δ with fixed Ω and R_b/a). We have not verified if these transitions are directly from disordered to \mathbb{Z}_4 -ordered phases, or involve incommensurate phases. Each gray dashed line corresponds to the trajectory across phase space used to probe for scaling behavior of correlation length growth. The horizontal section of each trace corresponds to the detuning sweep at a constant Rabi frequency, while the curved sections correspond to pulse turn-off at a fixed value of the detuning. The total duration of the detuning sweep is varied to control the rate of transition across the phase boundaries, but the time to turn the field off is not. **b**, Numerically obtained energy densities ϵ along the red solid line indicated in **(a)**. The second order derivatives of ϵ shows clear cusps at two critical points.

tible to decoherence, both because of the longer pulse time window, and because the system remains closer to the ground state near the critical point and the growing quantum correlations are increasingly sensitive to environmental noise. To determine the range of rates for which QKZM scaling can be observed, we perform a sweep into each of the ordered phases at a wide range of sweep speeds s . We fit the correlation lengths for each parameter, discarding all the instances where the correlation length is smaller than the size of the blockade radius, to a model that accounts for incoherent processes as a saturation in the final size of the correlation length, namely:

$$\xi(s) = \begin{cases} \xi_0(s_0/s)^\mu & : s \leq s_c, \\ \xi_0(s_0/s_c)^\mu & : s > s_c. \end{cases} \quad (\text{E.1})$$

From this fit, we set $s_{\min} > s_c$ and find s_{\max} such that $\xi(s_{\max}) > R_B$. An example of

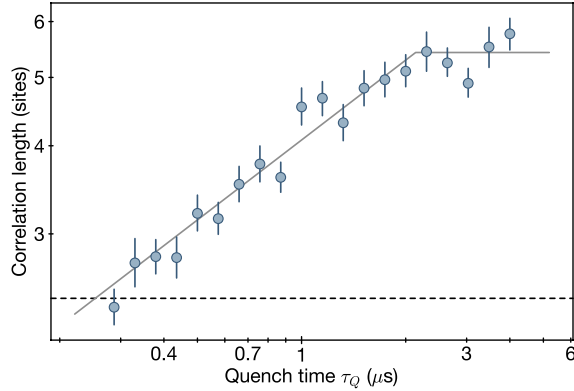


Figure E.3: Scaling window. Determination of the window of rates where scaling is valid for the transition into the \mathbb{Z}_3 -ordered phase. The black solid lines represent the result of the fitted model which grows as a power law until it saturates. The dashed horizontal line marks the size of the blockade radius. The values of all the rates used in the experiment are larger than the value at which the dashed and solid lines intersect, and smaller than the point where the model saturates. The error bars denote the uncertainty of the power-law fit.

this can be seen in Fig. E.3. In this way, we determine the sweep parameters for the different values of the interaction strength (see Fig. E.1).

E.4 NUMERICAL COMPUTATION OF THE PHASE DIAGRAM

The quantum critical points along the phase boundary on the phase diagram presented in Chapter 8 were obtained using both finite- and infinite-system density-matrix renormalization group (DMRG) algorithms [246, 318–322]. The filled colored regions are not the result of numerical simulations, and only show approximately the expected shape of the phases. In this section, we describe the details of the DMRG calculations.

For the infinite-system DMRG (iDMRG), we generally follow the method summarized in Ref. [323], where translationally invariant matrix product states (iMPS) are used as variational ansatze for ground-state wavefunctions. Our Hamiltonian with long-range interactions is encoded using matrix product operator representations, where $1/r^6$ decaying interactions

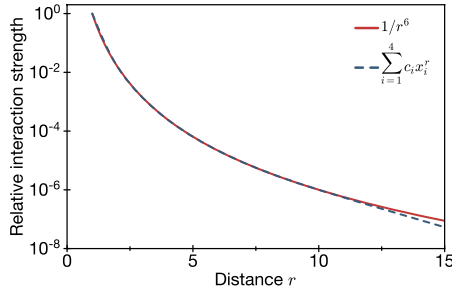


Figure E.4: Interaction potential approximation. Comparison between the exact power-law decay $1/r^6$ and its approximation using a linear combination of four exponentials. The two functions agree with each other until their relative strength decreases to 10^{-6} .

are approximated by a linear combination of four exponentials

$$\frac{1}{r^6} \approx \sum_{i=1}^4 c_i x_i^r, \quad (\text{E.2})$$

with $(c_1, c_2, c_3, c_4) = (170.55, 1.29, 0.0252, 0.000279)$ and $(x_1, x_2, x_3, x_4) = (0.00519, 0.0835, 0.279, 0.565)$ [324]. The resultant function provides an excellent approximation with relative error less than 10^{-5} (Fig. E.4). This accuracy implies that even with the strongest interaction strength probed in our experiments ($R_b \approx 3.5$), the maximum correction, $V_0 \left| 1/r^6 - \sum_{i=1}^4 c_i x_i^r \right| \lesssim (2\pi) \times 36 \text{ kHz}$, is much weaker than the smallest energy scale that can be probed within our experimental timescales.

Our phase diagram involves quantum phases that spontaneously break spatial translation symmetry. Hence, it is important that the number of spins in a translationally invariant unit cell of our iMPS ansatz must be compatible with the broken spatial symmetry. We use 2 or 6 spins as a unit cell in order to probe phase transitions from disordered to \mathbb{Z}_2 -ordered or \mathbb{Z}_3 -ordered phases, respectively. Incommensurate phases or onset of spatial symmetry breaking that is not compatible with the number of spins per unit cell can be identified by oscillatory behavior of wavefunction overlaps or energy densities over iterations.

In order to obtain the ground-state wavefunction, we iteratively optimize iMPS tensors until the (local) overlap between wavefunctions from two consecutive optimization steps approaches unity up to a small error ϵ . As convergence criteria, we require that either $\epsilon \leq 10^{-8}$ or ϵ is limited by truncation errors arising from finite bond dimension D [323]. We use a wide range of bond dimensions up to $D = 200$, depending on the quantity of interest to be computed and on the convergence of wavefunctions. For example, computing the ground state energy density is relatively insensitive to bond dimensions, while extracting correlation lengths near the critical point requires a substantially larger D .

We thus extract the phase boundaries from the energy density. Specifically, we use iDMRG to extract the ground-state energy density \mathcal{E} along a line in the parameter space, $(R_b/a, \Delta/\Omega)$, and compute its second derivative along the line. When crossing a quantum phase transition, the second-order derivative of the energy density exhibits a sharp feature. For example, Fig. E.2b shows the numerically computed energy densities per unit cell (6 spins) as a function of $R_b/a \in [1.75, 2.25]$ for a fixed $\Delta/\Omega = 2$ with $D = 10$. We find clear cusps at $R_b/a \approx 1.86$ and 2.18 , corresponding to critical points from \mathbb{Z}_2 -ordered to disordered and to \mathbb{Z}_3 -ordered phases. Similar procedures along different lines lead to the phase diagram in Fig. E.2a and in Fig. 8.1c of Chapter 8.

These phase boundaries are also reproduced using finite-system DMRG [325, 326] with a bond dimension up to $D = 60$ for a chain of $L = 51$ atoms and open boundary conditions. The first three energy levels are individually targeted, which, in turn, gives us access to the energy gap. The closing of the gap outlines well-defined lobes in the phase diagram, the boundaries of which overlap well with the points extracted previously with iDMRG (see Fig. E.5).

A few remarks are in order. First, it has been previously discussed that the \mathbb{Z}_3 -ordered phase may be interfacing incommensurate phases [120]. However, we do not find any evidence

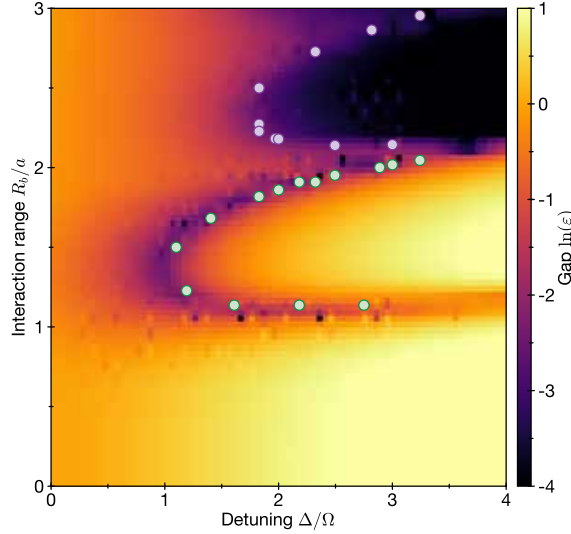


Figure E.5: Energy gap. Calculated gap between ground and first excited state using density-matrix renormalization group (DMRG) calculations. Green (purple) circles indicate the extracted quantum critical points separating the disordered from the $\mathbb{Z}_2(\mathbb{Z}_3)$ -ordered phase.

of incommensurate phases between \mathbb{Z}_2 and \mathbb{Z}_3 phases up to $\Delta/\Omega = 12$ within our numerical precision. The nature of the direct transition from disordered to \mathbb{Z}_3 -ordered phases is discussed in Refs. [160–162]. Second, we have not explicitly identified the phase transition between disordered to \mathbb{Z}_4 -ordered phases. This is because our choices of a unit cell (two or six spins) are not compatible with \mathbb{Z}_4 -ordered wavefunctions. Instead, the boundary of the disordered phase for $R_b/a > 3$ (yellow diamonds in Fig. E.2a) has been extracted from the convergence of the iDMRG algorithm; as Δ/Ω increases with a fixed R_b/a , the yellow diamonds in Fig. E.2a indicate the points at which the iDMRG algorithm ceases to converge, and instead exhibits oscillatory behaviors. Our method does not distinguish whether this is due to the onset of the \mathbb{Z}_4 -ordered phase or a gapless incommensurate phase.

E.5 CORRELATION LENGTH EXTRACTION AND SCALING

From the fluorescence pictures obtained at the end of an experimental sequence, we calculate the two-dimensional Rydberg density-density correlation map:

$$G(i, j) = \langle n_i n_j \rangle - \langle n_i \rangle \langle n_j \rangle. \quad (\text{E.3})$$

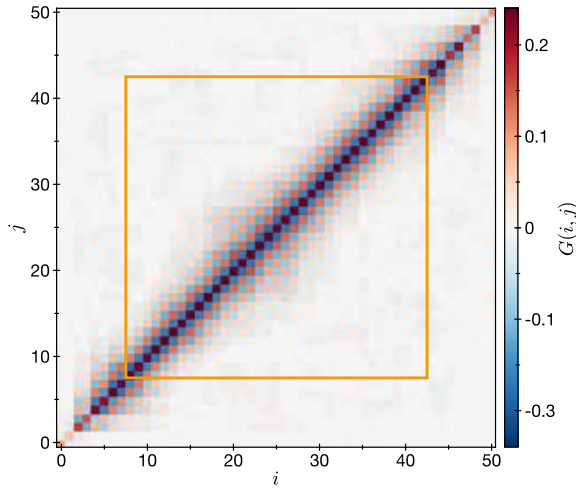


Figure E.6: Rydberg density-density correlations. Full density-density correlation map for sites i and j after a slow sweep into the \mathbb{Z}_2 -ordered phase. The orange square outline marks the bulk region used for analysis.

To minimize boundary effects, we disregard 8 sites from each edge. From the remaining bulk correlations, we average out this map over diagonal lines of constant $|i - j|$ to obtain the Rydberg density-density correlation described in Eq. (8.2) of Chapter 8 (Fig. E.6). The uncertainties for the values of $G(r)$ are found via a jackknife analysis.

Two different approaches are used to extract a characteristic length from such correlations. For transitions into \mathbb{Z}_N -ordered states (Fig. 8.4), we perform a least squares fit to the data with the model function:

$$\hat{G}(r) = Ae^{-r/\xi} \hat{G}_N(r)_{\text{gs}}, \quad (\text{E.4})$$

where A is the amplitude at $r = 0$, ξ is the correlation length, and $\hat{G}_N(r)_{\text{gs}}$ is the ideal correlation function at integer values of r for the corresponding \mathbb{Z}_N -ordered state, with a peak every N sites:

$$\begin{aligned}\hat{G}_2(r)_{\text{gs}} &= \cos(2\pi r/2) \\ \hat{G}_3(r)_{\text{gs}} &= \cos(2\pi r/3) \\ \hat{G}_4(r)_{\text{gs}} &= \cos(2\pi r/4) + 1/2 \cos(2\pi r/2).\end{aligned}\tag{E.5}$$

The range of distances used for all fits is $0 < r \leq 20$, where the cutoff at 20 sites is used to avoid any potential finite-size effects of the system.

In addition to the procedure described above, for \mathbb{Z}_2 -ordered states it is possible to extract a correlation length by fitting an exponential decay to the modulus of the correlation function, as is done in Fig. 8.2 of Chapter 8. This method allows for the determination of the correlation length in a way that is less susceptible to systematic effects arising from inversions of the alternating pattern, as observed in Fig. 8.3a. However, this method cannot be applied to \mathbb{Z}_N -ordered states for $N > 2$, necessitating the use of a more general approach, such as the function $\hat{G}(r)$ defined above. While the scaling exponents extracted using both of these methods for the \mathbb{Z}_2 -ordered state data are consistent within error bars, $\hat{G}(r)$ is used to obtain all exponents in Fig. 8.4c of Chapter 8.

To extract the most likely scaling exponent μ at a given interaction, we fit a power law

$$\xi = \xi_0 (s/s_0)^{-\mu},\tag{E.6}$$

where s is the detuning sweep rate.

E.6 \mathbb{Z}_N DOMAIN DENSITY

In the fluorescence images obtained at the end of each experimental sequence, we identify the loss of an atom to a Rydberg excitation. In this way, we can directly count the number of instances of two lost atoms separated by N sites, where every site in between contains an atom. To extract the data for Fig. 8.4b, we disregard the first 8 sites from the edges and count the instances in which both ends of the N atom chain are within the bulk, f_N . The relative probability for two lost atoms separated by N sites is given by:

$$p_N = \frac{N \times f_N}{\sum_{i>0}(i \times f_i)}. \quad (\text{E.7})$$

Unlike $G(r)$, p_N is susceptible to detection infidelity [157, 293].

E.7 LENGTH RESCALING OF CORRELATION FUNCTIONS

In Fig. 8.3 of Chapter 8, we use the normalized measured density-density correlation functions, $\frac{1}{A_i} G(r)_i$, and rescale the length r by the QKZM length scaling exponent found via the scaling analysis of correlation length, $r \rightarrow (s/s_0)^\mu r$.

E.8 FINITE-TIME SCALING

The length scaling exponent, μ , found experimentally sets constraints to the possible combinations of the critical exponents z and ν at a given interaction strength. In order to estimate, or qualitatively test, the possible values of z and ν , given the constraints set by μ , we make use of the fact that in the critical region, all system properties scale in a universal way. The QKZM predicts a universal scaling of time with a scaling exponent of $z\nu/(1+z\nu)$, in addition

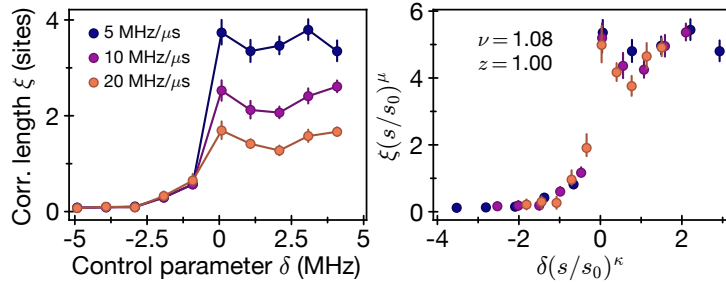


Figure E.7: Finite-size scaling across QPT into \mathbb{Z}_2 -ordered phase. **a**, Experimentally measured growth of the correlation length across the phase transition for different sweep speeds. The error bars denote the uncertainty of the power-law fit. **b**, Verification of critical exponents across the QPT into \mathbb{Z}_2 -ordered phase by rescaling the control parameter and spatial correlations. Using the experimentally extracted value of the QKZM length scaling exponent, $\mu = 0.52$, and setting the dynamical critical exponent to the Ising prediction, $z = 1$, it is observed that the data in **a** falls along a smooth function.

to the scaling of length with $\mu = \nu/(1 + z\nu)$ [327]. In the experiment, the control parameter used to cross the quantum phase transition is $\delta = \Delta - \Delta_c$, where Δ_c is the value of the detuning at the critical point and can be estimated through numerical simulations (see section on numerical computation of the phase diagram). Near the critical point, the control parameter varies in time as $\delta(t) = st$, leading to a universal scaling of $\delta(s) = \delta_0(s_0/s)^\kappa$, where $\kappa = -1/(1 + z\nu)$. Using the data shown in Chapter 8 for the correlation length growth across the transition into the \mathbb{Z}_2 -ordered phase, we can apply the transformation $\xi \rightarrow \xi(s/s_0)^\mu$ and $\delta \rightarrow \delta(s/s_0)^\kappa$, to observe how well the data collapse to a universal shape. Fig. E.7 shows that these data are consistent with having critical exponents $z = 1 \simeq \nu$, as is expected for the Ising universality class.

E.9 NUMERICAL SIMULATION OF KIBBLE-ZUREK DYNAMICS

We numerically model the dynamics of the system using matrix product states and employ a variant of a time evolving block decimation (TEBD) algorithm to propagate the state. We use a state update that allows us to exactly include the effect of interaction between atoms that

are separated by less than $\ell = 7$ sites. Interactions beyond this range are neglected. To this end, we use a Trotterization for the unitary that propagates the system from a time t_k to a time $t_{k+1} = t_k + \Delta t$ as

$$U(t_k \rightarrow t_{k+1}) \approx \prod_{p=1}^{N-\ell} \exp(-ih_p(t_k)\Delta t), \quad (\text{E.8})$$

where

$$\begin{aligned} h_p(t_k) = & \frac{1}{\ell} \sum_{j=0}^{\ell-1} \left(\frac{\Omega(t_k)}{2} \sigma_{p+j}^x - \Delta(t_k) n_{p+j} \right) \\ & + \sum_{i=0}^{\ell-2} \sum_{j=i+1}^{\ell-1} \frac{1}{\ell - (j-i)} V_{i,j} n_{p+i} n_{p+j} \end{aligned} \quad (\text{E.9})$$

for $1 < p < N - \ell$, and h_1 and $h_{N-\ell}$ are similar, but with appropriately adjusted coefficients.

We simulate the evolution according to the same pulse shape as applied in the experiment, with a time step of $\Delta t = 0.15$ ns and a bond dimension of 128. A comparison between the numerically simulated dynamics and the experimental results for different interaction strengths is shown in Fig. 8.4. As described section E.5, deviations of the individual correlation functions from an exponentially decaying period-N density wave lead to systematic effects that dominate the uncertainty in the determination of the values presented in Fig. 8.4b of Chapter 8. The comparison between experimental and numerical results is susceptible to multiple effects, including finite-size effects [328], accuracy of the approximate numerical methods used, experimental imperfections, and data fitting, which contribute to the observed discrepancy.

E.10 CHIRAL CLOCK MODELS

QPTs in the Rydberg Hamiltonian, Eq. (8.1) of Chapter 8, involving \mathbb{Z}_n ($n \geq 3$) translational symmetry breaking along one spatial direction are expected to be in the universality class of the extensively-studied \mathbb{Z}_n *chiral* clock models [329, 148, 147, 330, 163, 331, 332]. To eluci-

date this connection, let us focus on $n = 3$ and consider the case when $V_1 \gg |\Omega|, |\Delta|$, that is, nearest-neighbor interactions are strong enough to effectively preclude two neighboring atoms from simultaneously being in the Rydberg state. Since the van der Waals interactions decay rapidly as $V_x = C_6/x^6$, we neglect couplings beyond the third-nearest neighbor by approximating $V_x \approx 0$ for $x \geq 3$, leading to a truncated model of the form:

$$H_{\text{Ryd}} = \sum_{i=1}^N \frac{\Omega}{2} (|g_i\rangle\langle r_i| + |r_i\rangle\langle g_i|) - \Delta n_i + V_2 n_i n_{i+2}, \quad (\text{E.10})$$

supplemented with the constraint $n_i n_{i+1} = 0$.

The Hamiltonian (E.10) can be mapped to a system of hard-core bosons, where no more than one boson can occupy a single site. This follows upon identifying the state where the atom at site i is in the internal state $|r\rangle$ ($|g\rangle$) with the presence (absence) of a boson. Defining the bosonic annihilation and number operators, b_i and $n_i = b_i^\dagger b_i$, respectively, we obtain

$$H_b = \sum_{i=1}^N \frac{\Omega}{2} (b_i^\dagger + b_i) - \Delta n_i + V_2 n_i n_{i+2}, \quad (\text{E.11})$$

together with $n_i n_{i+1} = 0$. This model (often referred to as the $U - V$ model) was shown by Refs. [121, 120] to exhibit a phase transition in the universality class of the three-state chiral clock model (CCM), over a set of parameters.

The \mathbb{Z}_n CCM is a simple extension of the transverse-field Ising model in which each spin is promoted to have $n > 2$ states. However, instead of extending the symmetry from \mathbb{Z}_2 to \mathbb{S}_n , which would result in the n -state Potts model [333], the interactions are constructed to be invariant under \mathbb{Z}_n transformations. With $n = 3$, the three-state CCM is defined by the

Hamiltonian [331, 332]

$$H_{\text{CCM}} = -f \sum_{j=1}^N \tau_j^\dagger e^{-i\phi} - J \sum_{j=1}^{N-1} \sigma_j^\dagger \sigma_{j+1} e^{-i\theta} + \text{h.c.} \quad (\text{E.12})$$

acting on a one-dimensional chain of N spins. The three-state spin operators τ_i and σ_i , which can be represented as

$$\tau = \begin{pmatrix} 1 & 0 & 0 \\ 0 & \omega & 0 \\ 0 & 0 & \omega^2 \end{pmatrix}, \quad \sigma = \begin{pmatrix} 0 & 1 & 0 \\ 0 & 0 & 1 \\ 1 & 0 & 0 \end{pmatrix}, \quad (\text{E.13})$$

act locally on the site i , and each satisfy

$$\tau^3 = \sigma^3 = \mathbb{1}; \quad \sigma \tau = \omega \tau \sigma; \quad \omega \equiv \exp(2\pi i/3). \quad (\text{E.14})$$

Here, ϕ and θ define two chiral interaction phases: for describing spatially ordered phases, we need $\phi = 0$, whereupon time-reversal and spatial-parity are both symmetries of the Hamiltonian but a purely spatial chirality is still present. Note that H_{Ryd} does not break time-reversal symmetry, necessitating the choice of $\phi = 0$ in the quantum clock model (E.12). However, with both ϕ and θ nonzero, time-reversal and spatial-parity (inversion) symmetries are individually broken, but their product is preserved.

As depicted in Fig. 8.4a, a generic state in the Hilbert space of the \mathbb{Z}_3 CCM can be mapped to one of three states of a clock according to the eigenvalue $1, \omega$, or ω^2 of the operator σ at each site. Consequently, there can be two domain walls in the system that differ in their energies, depending upon whether the clock rotates clockwise or counterclockwise upon crossing the wall. With $\phi = 0$ and $\theta \neq 0$, these have different energies, $2J \sin(\pi/6 - \theta)$ and $2J \sin(\pi/6 + \theta)$, and are thus inequivalent, leading to a chirality in the system that is absent for $\phi = \theta = 0$.

On setting both $\phi = \theta = 0$, H_{CCM} reduces to the Hamiltonian for the three-state Potts model which possesses a larger symmetry, \mathbb{S}_3 ; the concomitant order–disorder phase transition has critical exponents $z = 1$, $\nu = 5/6$ [334, 335, 333], and accordingly $\mu \approx 0.45$. Note that these exponents are fundamentally distinct from those of the \mathbb{Z}_3 CCM, namely, $z \approx 1.33$, $\nu \approx 0.71$, yielding $\mu \approx 0.37$. The Rydberg Hamiltonian described in Chapter 8 contains a point along the phase boundary for which the condition of $\phi = \theta = 0$ is fulfilled, and with fine tuned pulses it may be possible to explore the critical properties of the three-state Potts model.

For $n = 4$, the transitions of both the Potts and the achiral clock model are in the Ashkin-Teller universality class [336, 337]. The critical exponents of the four-state Potts model are $z = 1$, $\nu = 2/3$ (implying $\mu = 0.40$), whereas the four-state *achiral* clock model is equivalent to two uncoupled Ising systems with $z = 1$, $\nu = 1$. With a nonzero chirality, however, it is believed that there is no direct transition from the ordered to the disordered phase in the four-state CCM as an intermediate gapless incommensurate phase always intervenes [148, 163, 338].

R_B/a	Δ_0	Δ_f	s_{\min}	s_{\max}
1.58	-2.5	7.5	3.5	15.2
1.62	-2.5	7.5	3.5	15.2
1.65	-2.5	7.5	3.5	15.2
1.69	-2.5	7.5	3.5	15.2
1.72	-2.5	7.5	3.5	15.2
1.76	-2.5	7.5	3.5	15.2
1.81	-2.5	5.5	4.6	19.7
1.85	-2.3	5.7	4.6	19.7
1.89	-2.4	7.6	3.5	15.2
1.94	-2.3	5.7	4.6	19.7
1.99	-2.3	5.7	4.6	19.7
2.04	-2.7	5.3	4.6	19.7
2.1	-2.3	5.7	4.6	19.7
2.16	-2.5	5.5	4.6	19.7
2.22	-2.5	5.5	4.6	19.7
2.28	-2.3	5.7	4.6	19.7
2.35	-2.5	5.5	4.6	19.7
2.43	-2.6	5.4	4.6	19.7
2.5	-2.5	5.5	4.6	19.7
2.59	-2.4	5.6	4.6	19.7
2.68	-2.7	5.3	4.6	19.7
2.77	-2.4	5.6	4.6	19.7
2.88	-2.1	5.9	4.6	19.7
2.99	-2.5	5.5	4.6	19.7
3.11	-2.5	5.5	4.6	19.7
3.17	-2.2	5.8	4.6	19.7
3.24	-2.5	5.5	4.6	19.7
3.31	-2.1	5.9	4.6	19.7
3.38	-2.6	5.4	4.6	19.7
3.45	-2.2	5.8	4.6	19.7

Table E.1: Pulse parameters for QKZM sweeps. For different blockade radii R_B/a , we list the initial and final detunings Δ_0 and Δ_f of the sweeps, and the minimum and maximum sweep speeds, s_{\min} and s_{\max} , applied.

F

Supplementary information for Chapter 9

F.1 2D ATOM REARRANGEMENT

Atoms are rearranged using an additional set of dynamically moving tweezers, which are overlaid on top of the SLM tweezer array. These movable tweezers are generated by a separate 809-nm laser source (DBR from Photodigm and tapered amplifier from MOGLabs), and are steered with a pair of independently-controlled crossed acousto-optic deflectors (AODs) (AA Opto Electronic DTSX-400). Both AODs are driven by an arbitrary waveform which is generated in real time using our home-built waveform generation software and an arbitrary waveform generator (AWG) (M4i.6631-x8 by Spectrum Instrumentation). Dynamically changing

the RF frequency allows for continuous steering of beam positions, and multi-frequency waveforms allow for multiple moving tweezers to be created in parallel [24].

While many 2D sorting protocols have been described previously [25, 339, 340, 32, 184], we implement a novel protocol which is designed to leverage parallel movement of multiple atoms simultaneously. More specifically, we create a row of moving traps which scans upwards along the SLM tweezer array to move one atom within each column up in parallel. This is accomplished by scanning a single frequency component on the vertical AOD to move from the bottom to the top of the SLM array, during which individual frequency components are turned on and off within the horizontal AOD to create and remove tweezers at the corresponding columns. This protocol is designed for SLM tweezer arrays in which traps are grouped into columns and rows. While this does constrain the possible geometries, most lattice geometries of interest can still be defined on a subset of points along fixed columns and rows.

F.2 REARRANGEMENT ALGORITHM

Here we detail the rearrangement algorithm, which is illustrated in Figure F.1. It operates on an underlying rectangular grid of rows and columns, where the SLM traps correspond to vertices of the grid. We pre-program a set of ‘target traps’ that we aim to fill.

Pre-sorting: We begin by ensuring that each column contains a sufficient number of atoms to fill the target traps in that column. In each experimental cycle, due to the random loading throughout the array, some columns may contain excess atoms while other columns may lack a sufficient number of atoms. Accordingly, we apply a ‘pre-sorting’ procedure in which we move atoms between columns. To fill a deficient column j , we take atoms from whichever side of j has a larger surplus. We identify which atoms to take by finding the nearest atoms from the surplus side which are in rows for which column j has an empty trap. We then per-

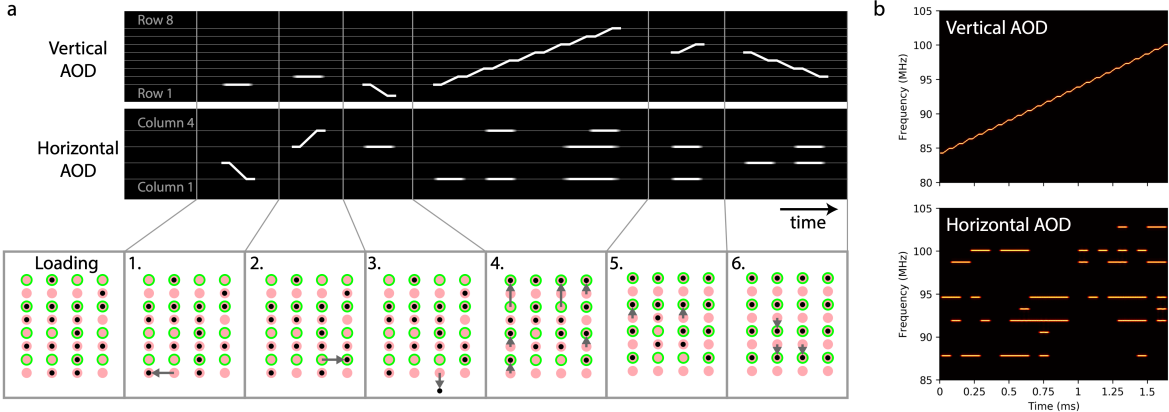


Figure F.1: Rearrangement protocol. **a.** Sample sequence of individual rearrangement steps. There are two pre-sorting moves (1, 2). Move (3) is the single ejection move. Moves (4-6) consist of parallel vertical sorting within each column, including both upward and downwards move. The upper panel illustrates the frequency spectrum of the waveform in the vertical and horizontal AODs during these moves, with the underlying grid corresponding to the calibrated frequencies which map to SLM array rows and columns. **b.** Spectrograms representing the horizontal and vertical AOD waveforms over the duration of a single vertical frequency scan during a realistic rearrangement procedure for a 26×13 array. The heat-maps show frequency spectra of the AOD waveforms over small time intervals during the scan.

form parallel horizontal sorting to move these atoms into the empty traps of j (not all surplus atoms need to be from the same source column).

If the one-side surplus is insufficient to fill column j , then we move as many surplus atoms as possible from this one side and leave j deficient. We then proceed to the next deficient column, and cycle through until all columns have sufficient atoms. In typical randomly loaded arrays, this process takes a small number of atom moves compared to the total number of moves needed for sorting. This specific algorithm can fail to properly distribute atoms between columns due to lack of available atoms, but these failures are rare and do not limit the experimental capabilities.

Ejection: After pre-sorting, we eject excess atoms in parallel by scanning the vertical AOD frequency downward, beginning at a row in which we want to pick up an atom, and ending below the bottom row of the array. In each downward scan, we eject a single atom from each column containing excess atoms; we repeat this process until all excess atoms are ejected.

Parallel sorting within columns: After pre-sorting and ejection, each column has the correct number of atoms to fill all of its target traps by moving atoms up/down within the column. We now proceed to shuffle the i^{th} -highest loaded atoms to the i^{th} -highest target traps. As the atoms cannot move through each other, in a single vertical scan atoms are moved as close as possible to their target locations, reaching their targets unless they are blocked by another atom. We repeat upward/downward scans until all atoms reach their target locations.

F.3 REARRANGEMENT PARAMETERS AND RESULTS

When using moving tweezers to pick up and drop off atoms in the SLM traps, the moving tweezers ramp on/off over 15 μs while positioned to overlap with the corresponding SLM trap. The moving tweezers are approximately twice as deep as the static traps, and move atoms between SLM traps with a speed of 75 $\mu\text{m}/\text{ms}$. Typical rearrangement protocols take a total of 50-100 ms to implement in practice, depending on the size of the target array and the random initial loading. Alignment of the AOD traps onto the SLM array is pre-calibrated by measuring both trap arrays on a monitor CMOS camera and tuning the AOD frequencies to match positions with traps from the SLM array.

A single round of rearrangement results in typical filling fractions of $\sim 98.5\%$ across all target traps in the system. This is limited primarily by the finite vacuum-limited lifetime ($\sim 10 \text{ s}$) and the duration of the rearrangement procedure. To increase filling fractions, we perform a second round of rearrangement (having skipped ejection in the first round to keep excess atoms for the second round). Since the second round of rearrangement only needs to correct for a small number of defects, it requires far fewer moves and can be performed more quickly, resulting in less background loss. With this approach, we achieve filling fractions of $\sim 99.2\%$ over more than 200 sites, with a total experimental cycle time of 400 ms.

F.4 RYDBERG LASER SYSTEM

Our Rydberg laser system is an upgraded version of a previous setup [182]. The 420-nm laser is a frequency-doubled Ti:Sapphire laser (M Squared, 15-W pump). We stabilize the laser frequency by locking the fundamental to an upgraded ultra-low expansion (ULE) reference cavity (notched cylinder design from Stable Laser Systems), with finesse $\mathcal{F} = 30,000$ at 840 nm. The 1013-nm laser source is an external-cavity diode laser (Toptica DL Pro), which is locked to the same reference cavity ($\mathcal{F} = 50,000$ at 1013 nm). To suppress high-frequency phase noise from this diode laser, we use the transmitted light through the cavity, which is filtered by the narrow cavity transmission spectrum (30 kHz linewidth) [293]. This filtered light is used to injection-lock another laser diode, whose output is subsequently amplified to 10 W by a fiber amplifier (Azur Light Systems).

Using beam shaping optics to homogeneously illuminate the atom array with both Rydberg lasers, we achieve single-photon Rabi frequencies of $(\Omega_{420}, \Omega_{1013}) = 2\pi \times (160, 50)$ MHz. We operate with an intermediate state detuning $\delta = 2\pi \times 1$ GHz, resulting in two-photon Rabi frequency $\Omega = \Omega_{420}\Omega_{1013}/2\delta \sim 2\pi \times 4$ MHz. Small inhomogeneities in the Rydberg beams result in Rabi frequency variations of $\sim 2\%$ RMS and $\sim 6\%$ peak-to-peak across the array. With these conditions, we estimate an off-resonant scattering rate of $1/(20 \mu\text{s})$ for atoms in $|g\rangle$ and $1/(150 \mu\text{s})$ for atoms in $|r\rangle$ at peak power.

F.5 RYDBERG PULSES

After initializing our atoms in the ground state $|g\rangle$, the tweezer traps are turned off for a short time ($<5 \mu\text{s}$) during which we apply a Rydberg pulse. The pulse consists of a time-dependent Rabi frequency $\Omega(t)$, time-dependent detuning $\Delta(t)$, and a relative instantaneous phase $\phi(t)$.

This is implemented by controlling the amplitude, frequency, and phase of the 420-nm laser using a tandem AOM system, similar to what is described previously [182].

F.5.1 QUASI-ADIABATIC SWEEPS

To prepare many-body ground states with high fidelity, we use an optimized quasi-adiabatic pulse shape (Fig. 9.2a). The coupling $\Omega(t)$ is initially ramped up linearly at large fixed negative detuning, held constant during the detuning sweep $\Delta(t)$, and finally ramped down linearly at large fixed positive detuning. The detuning sweep $\Delta(t)$ consists of a cubic spline interpolation between five points: initial detuning, final detuning, an inflection point where the slope reaches a minimum, and two additional points that define the duration of the slow part of the sweep. The sweep used for finding perfect checkerboard ground state probabilities (Fig. 9.2e) was obtained by optimizing the parameters of the spline cubic sweep to maximize the correlation length on a 12×12 (144 atoms) array. The sweep used in detection of the star and striated phases was optimized based on maximizing their respective order parameters. In particular, the inflection point was chosen to be near the position of the minimum gap in these sweeps in order to maximize adiabaticity.

F.5.2 LINEAR SWEEPS

To probe the phase transition into the checkerboard phase (Fig. 9.3), we use variable-endpoint linear detuning sweeps in which Ω is abruptly turned off after reaching the endpoint. This ensures that projective readout happens immediately after the end of the linear sweep instead of allowing time for further dynamics, and is essential for keeping the system within the quantum Kibble-Zurek regime. Linear sweeps are done from $\Delta = -16$ to 14 MHz ($\Delta/\Omega = -3.7$ to 3.3) at sweep rates $s = 15, 21, 30, 42, 60, 85$, and 120 MHz/ μ s. Data for locating the

quantum critical point (Fig. F.4a) is taken from the slowest of these sweeps ($s = 15 \text{ MHz}/\mu\text{s}$) to remain as close as possible to the ground state. For mapping out the 2D phase diagram (Fig. 9.4), we use the same variable-endpoint linear sweeps at fixed sweep rate $s = 12 \text{ MHz}/\mu\text{s}$, except that Ω is ramped down over 200 ns after reaching the endpoint.

F.6 STATE DETECTION

At the end of the Rydberg pulse, we detect the state of atoms by whether or not they are recaptured in our optical tweezers. Atoms in $|g\rangle$ are recaptured and detected with fidelity 99%, limited by the finite temperature of the atoms and collisions with background gas particles in the vacuum chamber.

Atoms excited to the Rydberg state are detected as a loss signal due to the repulsive potential of the optical tweezers on $|r\rangle$. However, the finite Rydberg state lifetime[48] ($\sim 80 \mu\text{s}$ for $70\text{S}_{1/2}$) leads to a probability of $\sim 15\%$ for $|r\rangle$ atoms to decay to $|g\rangle$ and be recaptured by the optical tweezers. In our previous work [182], we increased tweezer trap depths immediately following the Rydberg pulse to enhance the loss signal for atoms in $|r\rangle$. In 2D, this approach is less effective because atoms which drift away from their initial traps can still be recaptured in a large 3D trapping structure created by out-of-plane interference of tweezers.

Following an approach similar to what has been previously demonstrated [34], we increase the Rydberg detection fidelity using a strong microwave (MW) pulse to enhance the loss of atoms in $|r\rangle$ while leaving atoms in $|g\rangle$ unaffected. The MW source (Stanford Research Systems SG384) is frequency-tripled to 6.9 GHz and amplified to 3 W (Minicircuits, ZVE-3W-183+). The MW pulse, containing both 6.9 GHz and harmonics, is applied on the atoms using a microwave horn for 100 ns. When applying a Rydberg π -pulse immediately followed by the MW pulse, we observe loss probabilities of 98.6(4)%. Since this measurement includes both

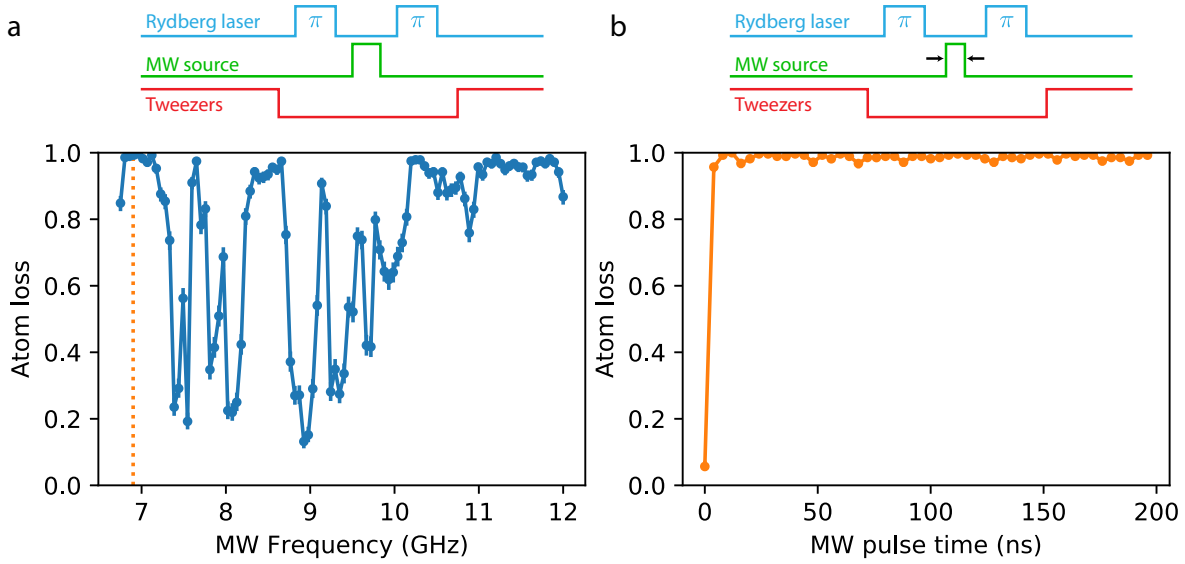


Figure F.2: Characterizing microwave-enhanced Rydberg detection fidelity. The effect of strong microwave (MW) pulses on Rydberg atoms is measured by preparing atoms in $|g\rangle$, exciting to $|r\rangle$ with a Rydberg π -pulse, and then applying the MW pulse before de-exciting residual Rydberg atoms with a final Rydberg π -pulse. (The entire sequence occurs while tweezers are briefly turned off.) **a.** Broad resonances are observed with varying microwave frequency, corresponding to transitions from $|r\rangle = |70S\rangle$ to other Rydberg states. Note that the transition to $|69P\rangle$ and $|70P\rangle$ are in the range of 10 – 12 GHz, and over this entire range there is strong transfer out of $|r\rangle$. Other resonances might be due to multi-photon effects. **b.** With fixed 6.9-GHz MW frequency and varying pulse time, there is a rapid transfer out of the Rydberg state on the timescale of several nanoseconds. Over short time-scales, there may be coherent oscillations which return population back to $|r\rangle$, so a 100 ns pulse is used for enhancement of loss signal of $|r\rangle$ in the experiment.

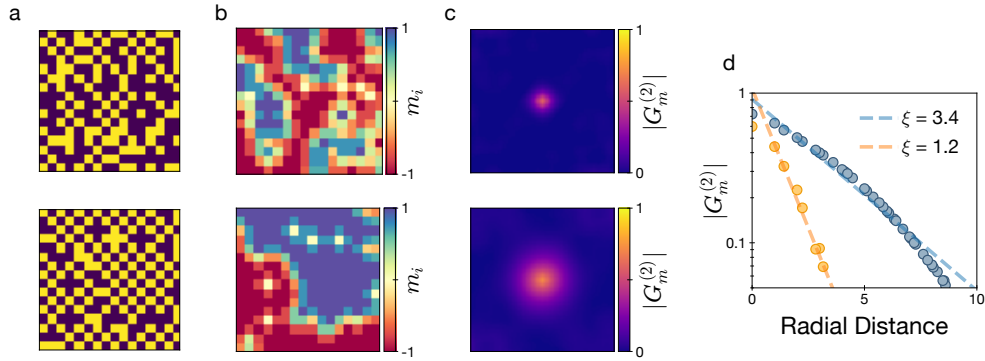


Figure F.3: Coarse-grained local staggered magnetization. **a.** Examples of Rydberg populations n_i after a faster (top) and slower (bottom) linear sweep. **b.** Corresponding coarse-grained local staggered magnetizations m_i clearly show larger extents of antiferromagnetically ordered domains (dark blue or dark red) for the slower sweep (bottom) compared to for the faster sweep (top), as expected from the Kibble-Zurek mechanism. **c.** Isotropic correlation functions $G_m^{(2)}$ for the corresponding coarse-grained local staggered magnetizations after a faster (top) or a slower (bottom). **d.** As a function of radial distance, correlations $G_m^{(2)}$ decay exponentially with a length scale corresponding to the correlation length ξ . The two decay curves correspond to faster (orange) and slower (blue) sweeps.

error in the π -pulse as well as detection errors, we apply a second Rydberg π -pulse after the MW pulse, which transfers most of the remaining ground state population into the Rydberg state. In this configuration, we observe 99.1(4)% loss probability, which is our best estimate for our Rydberg detection fidelity (Fig. F.2). We find that the loss signal is enhanced by the presence of both MW fundamental and harmonic frequencies.

F.7 COARSE-GRAINED LOCAL STAGGERED MAGNETIZATION

We define the coarse-grained local staggered magnetization for a site i with column and row indices a and b , respectively, as:

$$m_i = \frac{(-1)^{a+b}}{N_i} \sum_{\langle j,i \rangle} (n_i - n_j)$$

where j is summed over nearest neighbors of site i and N_i is the number of such nearest neighbors (4 in the bulk, 3 along the edges, or 2 on the corners). The value of m_i ranges from -1

to 1, with the extremal values corresponding to the two possible perfect antiferromagnetic orderings locally on site i and its nearest neighbors (Fig. F.3a,b). The two-site correlation function for m_i can then be defined as an average over experiment repetitions $G_m^{(2)}(k, l) = \frac{1}{N_{(k,l)}} \sum_{i,j} (\langle m_i m_j \rangle - \langle m_i \rangle \langle m_j \rangle)$, where the sum is over all pairs of sites i, j separated by a relative lattice distance of $\mathbf{x} = (k, l)$ sites and normalized by the number of such pairs $N_{(k,l)}$ (Fig. F.3c). We obtain the correlation length ξ by fitting an exponential decay to the radially averaged $G_m^{(2)}(k, l)$ (Fig. F.3d). The coarse-grained local staggered magnetization m_i is defined such that the corresponding $G_m^{(2)}(k, l)$ is isotropic (Fig. F.3c), which makes for natural radial averaging. This radial average captures correlations across the entire array better than purely horizontal or vertical correlation lengths ξ_H and ξ_V , which are more sensitive to edge effects.

F.8 DETERMINATION OF THE QUANTUM CRITICAL POINT

To accurately determine the location of the quantum critical point Δ_c for the transition into the checkerboard phase, we measure mean Rydberg excitation $\langle n \rangle$ vs. detuning Δ for a slow linear sweep with sweep rate $s = 15 \text{ MHz}/\mu\text{s}$ (Fig. F.4a). To smoothen the measured curve, we fit a polynomial for $\langle n \rangle$ vs. Δ and take its numerical derivative to identify the peak of the susceptibility χ as the critical point[126] (Fig. F.4b).

Small oscillations in $\langle n \rangle$ result from the linear sweep not being perfectly adiabatic. To minimize the effect of this on our fitting, we use the lowest-degree polynomial (cubic) whose derivative has a peak, and choose a fit window in which the reduced chi-squared metric indicates a good fit. Several fit windows around $\Delta/\Omega = 0$ to 2 give good cubic fits, and we average results from each of these windows to obtain $\Delta_c/\Omega = 1.12(4)$.

We also numerically extract the critical point for a system with numerically-tractable dimensions of 10×10 . Using the density-matrix renormalization group (DMRG) algorithm, we

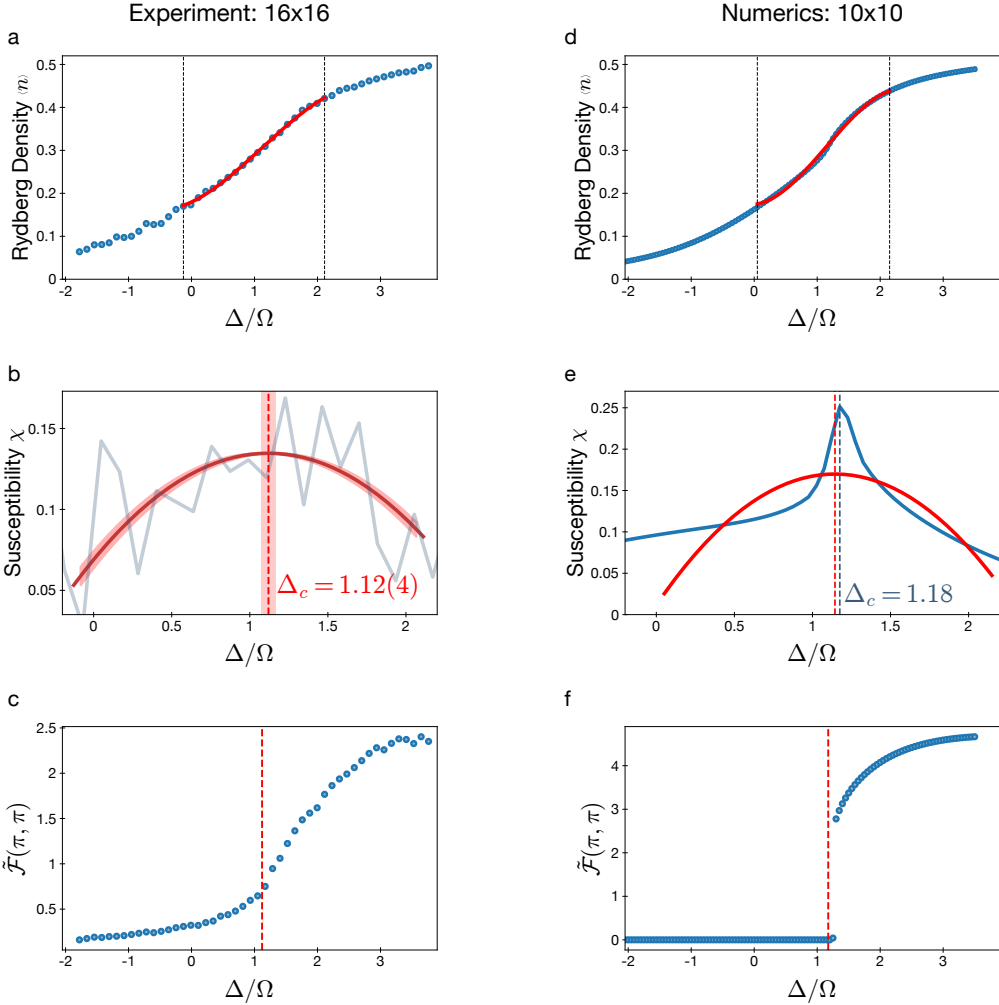


Figure F.4: Extracting the quantum critical point. **a.** The mean Rydberg excitation density $\langle n \rangle$ vs. detuning Δ/Ω on a 16×16 array. The data is fitted within a window (dashed lines) to a cubic polynomial (red curve) as a means of smoothening the data. **b.** The peak in the numerical derivative of the fitted data (red curve) corresponds to the critical point $\Delta_c/\Omega = 1.12(4)$ (red shaded regions show uncertainty ranges, obtained from varying fit windows). In contrast, the point-by-point slope of the data (gray) is too noisy to be useful. **c.** Order parameter $\tilde{\mathcal{F}}(\pi, \pi)$ for the checkerboard phase vs. Δ/Ω measured on a 16×16 array with the value of the critical point from **b.** superimposed (red line), showing the clear growth of the order parameter after the critical point. **d.** DMRG simulations of $\langle n \rangle$ vs. Δ/Ω on a 10×10 array. For comparison against the experimental fitting procedure, the data from numerics is also fitted to a cubic polynomial within the indicated window (dashed lines). **e.** The point-by-point slope of the numerical data (blue curve) has a peak at $\Delta_c/\Omega = 1.18$ (blue dashed line), in good agreement with the results (red dashed line) from both the numerical derivative of the cubic fit on the same data (red curve) and the result of the experiment. **f.** DMRG simulation of $\tilde{\mathcal{F}}(\pi, \pi)$ vs. Δ/Ω , with the exact quantum critical point from numerics shown (red line).

evaluate $\langle n \rangle$ as a function of detuning Δ , and then take the derivative to obtain a peak of the susceptibility at $\Delta_c/\Omega = 1.18$ (Fig. F.4c,d). To corroborate the validity of our experimental fitting procedure, we also fit cubic polynomials to the DMRG data and find that the extracted critical point is close to the exact numerical value (Fig. F.4d). This numerical estimate of the critical point for a 10×10 array is consistent with the experimental result on a larger 16×16 array. Moreover, our experiments on arrays of different sizes show that Δ_c/Ω does not vary significantly between 12×12 , 14×14 , and 16×16 arrays (Fig. F.5b).

F.9 DATA COLLAPSE FOR UNIVERSAL SCALING

Optimizing the universal collapse of rescaled correlation length $\tilde{\xi}$ vs. rescaled detuning $\tilde{\Delta}$ requires defining a measure of the distance between rescaled curves for different sweep rates s_i . Given $\tilde{\xi}_j^{(i)}$ and $\tilde{\Delta}_j^{(i)}$, where the index i corresponds to sweep rate s_i and j labels sequential data points along a given curve, we define a distance [341]

$$D = \sqrt{\frac{1}{N} \sum_i \sum_{i' \neq i} \sum_j \left| \tilde{\xi}_j^{(i')} - f^{(i)}(\tilde{\Delta}_j^{(i')}) \right|^2}. \quad (\text{F.1})$$

The function $f^{(i)}(\tilde{\Delta})$ is the linear interpolation of $\tilde{\xi}_j^{(i)}$ vs. $\tilde{\Delta}_j^{(i)}$, while N is the total number of terms in the three nested sums. The sum over j only includes points that fall within the domain of overlap of all data sets, avoiding the problem of linear interpolation beyond the domain of any single data set. Defined in this way, the collapse distance D measures all possible permutations of how far each rescaled correlation growth curve is from curves corresponding to other sweep rates.

Applied to our experimental data, D is a function of both the location of the critical point Δ_c and the critical exponent ν (Fig. F.5a). Using the independently measured $\Delta_c/\Omega = 1.12(4)$,

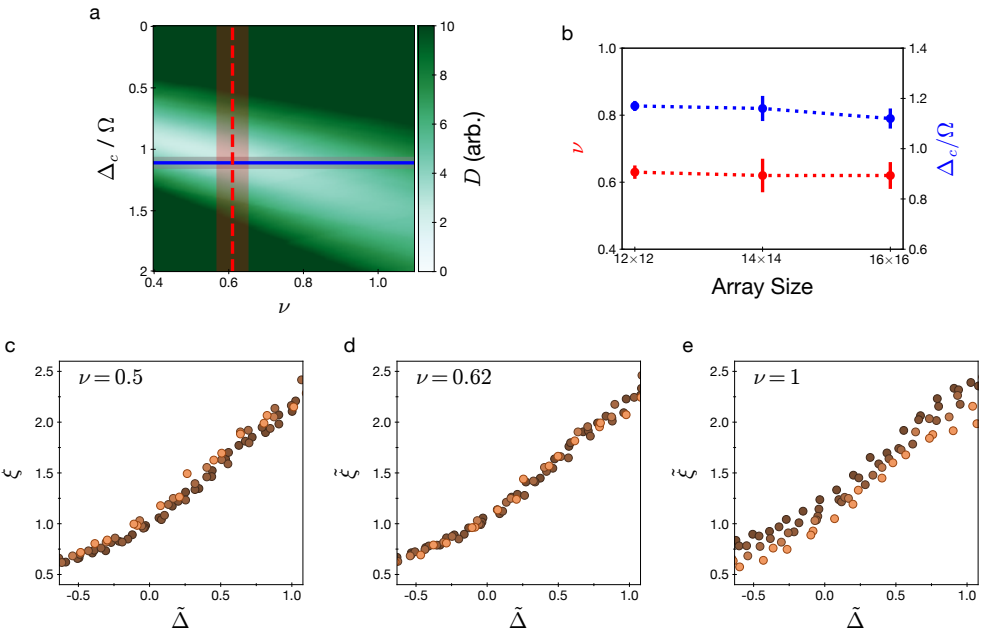


Figure F.5: Optimization of data collapse. **a.** Distance D between rescaled correlation length $\tilde{\xi}$ vs. $\tilde{\Delta}$ curves depends on both the location of the quantum critical point location Δ_c/Ω and on the correlation length critical exponent ν . The independently determined Δ_c/Ω (blue line, with uncertainty range in gray) and the experimentally extracted value of ν (dashed red line, with uncertainty range corresponding to the red shaded region) are marked on the plot. **b.** Our determination of ν (red) from data collapse around the independently determined Δ_c/Ω (blue) is consistent across arrays of different sizes. **c-e.** Data collapse is clearly better at the experimentally determined value ($\nu = 0.62$) as compared to the mean-field ($\nu = 0.5$) or the (1+1)D ($\nu = 1$) values. The horizontal extent of the data corresponds to the region of overlap of all rescaled data sets.

we obtain $\nu = 0.62(4)$ for optimal data collapse, and illustrate in particular the better collapse for this value than for other values of ν (Fig. F.5c-e). The quoted uncertainty is dominated by the corresponding uncertainty of the extracted Δ_c/Ω , rather than by the precision of finding the minimum of D for a given Δ_c/Ω . Our experiments give consistent values of Δ_c/Ω and ν for systems of size 12×12 , 14×14 , and 16×16 (Fig. F.5b).

F.10 ORDER PARAMETERS FOR MANY-BODY PHASES

We construct order parameters to identify each phase using the Fourier transform to quantify the amplitude of the observed density-wave ordering. We define the symmetrized Fourier transform $\tilde{\mathcal{F}}(k_1, k_2) = \langle \mathcal{F}(k_1, k_2) + \mathcal{F}(k_2, k_1) \rangle / 2$ to take into account the C_4 rotation symmetry between possible ground-state orderings for some phases. For the star phase, the Fourier amplitude $\tilde{\mathcal{F}}(\pi, \pi/2)$ is a good order parameter because ordering at $\mathbf{k} = (\pi, \pi/2)$ is unique to this phase. The striated phase, on the other hand, shares its Fourier peaks at $\mathbf{k} = (\pi, 0)$ and $(0, \pi)$ with the star phase, and its peak at $\mathbf{k} = (\pi, \pi)$ with the checkerboard phase; hence, none of these peaks alone can serve as an order parameter. We therefore construct an order parameter for the striated phase to be $\tilde{\mathcal{F}}(0, \pi) - \tilde{\mathcal{F}}(\pi/2, \pi)$, which is nonzero in the striated phase and zero in both checkerboard and star. Similarly, the checkerboard shares its $\mathbf{k} = (\pi, \pi)$ peak with the striated phase, so we construct $\tilde{\mathcal{F}}(\pi, \pi) - \tilde{\mathcal{F}}(0, \pi)$ as an order parameter which is zero in the striated phase and nonzero only in checkerboard.

F.11 NUMERICAL SIMULATIONS OF THE 2D PHASE DIAGRAM

We numerically compute the many-body ground states at different points in the $(\Delta/\Omega, R_b/a)$ phase diagram using the density-matrix renormalization group (DMRG) algorithm [246, 318], which operates in the space of the so-called matrix product state (MPS) ansätze. While origi-

nally developed for one-dimensional systems, DMRG can also be extended to two dimensions by representing the 2D system as a winding 1D lattice [342], albeit with long-range interactions. A major limitation to two-dimensional DMRG is that the number of states required to faithfully represent the ground-state wavefunction has to be increased exponentially with the width of the system in order to maintain a constant accuracy. For our calculations, we employ a maximum bond dimension of 1600, which allows us to accurately simulate 10×10 square arrays [186]. We also impose open boundary conditions in both directions and truncate the van der Waals interactions so as to retain up to third-nearest-neighbor couplings. The numerical convergence criterion is set by the truncation error, and the system is regarded to be well-converged to its true ground state once this error drops below a threshold of 10^{-7} . In practice, this was typically found to be achieved after $\mathcal{O}(10^2)$ successive sweeps.

Since the dimensions of the systems studied in Figure 9.4, (13×13) (experimentally) and 9×9 (numerically), are both of the form $(4n + 1) \times (4n + 1)$, the two phase diagrams are expected to be similar. In particular, both these system sizes are compatible with the commensurate ordering patterns of the crystalline phases observed in this work, and can host all three phases (at the appropriate R_b/a) with the same boundary conditions. Likewise, for extraction of the QCP, we use a 10×10 array as it is the largest numerically accessible square lattice comparable to the 16×16 array used in our study of the quantum phase transition.

F.12 MEAN-FIELD WAVEFUNCTION FOR THE STRIATED PHASE

To understand the origin of the striated phase, it is instructive to start from a simplified model in which we assume that nearest-neighbor sites are perfectly blockaded. Since we always work in a regime where $R_b/a > 1$, this model should also capture the essential physics of the full Rydberg Hamiltonian.

In the classical limit of $\Omega = 0$, the perfect checkerboard state has an energy per site of $-\Delta/2 + V(\sqrt{2}a) + V(2a)$, with $V(x)$ being the interaction between sites at a distance x , whereas the corresponding energy for the star-ordered state is $-\Delta/4$ (neglecting interactions for $x > 2a$). Accordingly, there is a phase transition between the checkerboard and star phases when $\Delta = 4[V(\sqrt{2}a) + V(2a)]$. On the other hand, for the same density of Rydberg excitations, the striated phase has a classical energy per site of $-\Delta/4 + V(2a)/2$, which is always greater than that of the star phase; hence, striated ordering never appears in the classical limit.

At finite Ω , however, the striated phase emerges due to a competition between the third-nearest-neighbor interactions and the second-order energy shift upon dressing a ground state atom off-resonantly with the Rydberg state. We can thus model the ground state of the striated phase as a product state, where (approximately) $1/2$ of the atoms are in the ground state, $1/4$ of the atoms are in the Rydberg state, and the remaining $1/4$ are in the ground state with a weak coherent admixture of the Rydberg state. A general mean-field ansatz for a many-body wavefunction of this form is given by

$$|\Psi_{\text{STR}}(a_1, a_2)\rangle = \bigotimes_{\mathbf{i} \in A_1} (\cos a_1 |g\rangle_{\mathbf{i}} + \sin a_1 |r\rangle_{\mathbf{i}}) \quad (\text{F.2})$$

$$\bigotimes_{\mathbf{i} \in A_2} (\cos a_2 |g\rangle_{\mathbf{i}} + \sin a_2 |r\rangle_{\mathbf{i}}) \bigotimes_{\mathbf{j} \in B} |g\rangle_{\mathbf{j}},$$

where A_1 and A_2 represent the two sublattices of the (bipartite) A sublattice, and $a_{1,2}$ are variational parameters. If $a_1 = a_2$, then our trial wavefunction simply represents a checkerboard state, but if $a_1 \neq a_2$, this state is *not* of the checkerboard type, and leads to the striated phase.

Based on this ansatz, we can now explicitly see how the striated phase may become energetically favorable in the presence of a nonzero Ω . Consider the atoms on the partially excited

sublattice to be in the superposition $|g\rangle + [\Omega/\{4V(\sqrt{2}a) - \Delta\}]|r\rangle$; this describes the state of the atoms on the $(1, 1)$ sublattice in the notation of Fig. 9.5. The net energy per site of the system is then

$$-\frac{\Delta}{4} + \frac{V(2a)}{2} - \frac{\Omega^2}{4(4V(\sqrt{2}a) - \Delta)} + \frac{\Omega^2 V(\sqrt{2}a)}{2(4V(\sqrt{2}a) - \Delta)^2}$$

where the third and fourth terms are the second-order energy shift and mean-field interaction shift, respectively. From this expression, we observe that if the energy gained from the dressing (these last two terms) is larger than $V(2a)/2$, then the striated phase prevails over the star phase.

F.13 DYNAMICAL PROBE OF THE STRIATED PHASE

We prepare striated ordering using an optimized cubic spline sweep along $R_b/a = 1.47$, ending at $\Delta/\Omega = 2.35$. Immediately after this sweep, the system is quenched to detuning Δ_q and relative laser phase ϕ_q . We quench at a lower Rabi frequency $\Omega_q = \Omega/4 \approx 2\pi \times 1$ MHz to improve the resolution of this interaction spectroscopy. For the chosen lattice spacing, the interaction energy between diagonal excitations is $2\pi \times 5.3$ MHz. The reference phase for the atoms $\phi = 0$ is set by the instantaneous phase of the Rydberg coupling laser at the end of the sweep into striated ordering. In the Bloch sphere picture, $\phi = 0$ corresponds to the $+x$ axis, so the wavefunctions on $(0,0)$ and $(1,1)$ sublattices correspond to vectors pointing mostly up or mostly down with a small projection of each along the $+x$ axis. In the same Bloch sphere picture, quenching at $\phi_q = \pi/2$ or $-\pi/2$ corresponds to rotations around the $+y$ or $-y$ axes (Fig. 9.5a).

To resolve the local response of the system, we use high-order correlators which are extracted from single-shot site-resolved readout. In particular, we define an operator $\hat{O}_i^{(d)}$ on the

eight atoms surrounding site i . This operator projects the neighboring atoms into configurations in which all four nearest atoms are in $|g\rangle$ and exactly d of the diagonal neighbors are in $|r\rangle$. Specifically, the operator $\hat{\mathcal{O}}_i^{(d)}$ decomposes into a projector \hat{A}_i on the four nearest neighboring atoms and $\hat{B}_i^{(d)}$ on the four diagonal neighbors, according to $\hat{\mathcal{O}}_i^{(d)} = \hat{A}_i \hat{B}_i^{(d)}$. Defining $\bar{n}_i = |g\rangle_i \langle g|$ and $n_i = |r\rangle_i \langle r|$, the nearest neighbor projector is written as $\hat{A}_i = \prod_{\langle j,i \rangle} \bar{n}_j$, where $\langle . \rangle$ denotes nearest neighbors. The projector $\hat{B}_i^{(d)}$ sums over all configurations of the diagonal neighbors (indexed k_1, k_2, k_3, k_4) with d excitations:

$$\hat{B}_i^{(4)} = n_{k_1} n_{k_2} n_{k_3} n_{k_4} \quad (\text{F.3})$$

$$\hat{B}_i^{(3)} = \bar{n}_{k_1} n_{k_2} n_{k_3} n_{k_4} + n_{k_1} \bar{n}_{k_2} n_{k_3} n_{k_4} + \dots \quad (\text{F.4})$$

$$\hat{B}_i^{(2)} = \bar{n}_{k_1} \bar{n}_{k_2} n_{k_3} n_{k_4} + \bar{n}_{k_1} n_{k_2} \bar{n}_{k_3} n_{k_4} + \dots \quad (\text{F.5})$$

These operators are used to construct the conditional Rydberg density

$$P^{(d)} = \frac{\sum_i \langle n_i \hat{\mathcal{O}}_i^{(d)} \rangle}{\sum_i \langle \hat{\mathcal{O}}_i^{(d)} \rangle}$$

which measures the probability of Rydberg excitation on site i surrounded by neighboring-atom configurations for which $\hat{\mathcal{O}}_i^{(d)} = 1$.

To quantify coherences, we measure these conditional probabilities on their corresponding resonances, after a fixed quench with variable quench phase ϕ_q . For a single particle driven by the Hamiltonian $H = \Omega(\cos \phi_q \sigma_x + \sin \phi_q \sigma_y)/2 + \Delta \sigma_z/2$ for time τ , the resulting Heisenberg evolution is given by $\sigma'_z = U^\dagger \sigma_z U$, where $U = e^{-iH\tau}$. The resulting operator can be expressed

as

$$\sigma'_z = \tilde{\Omega} \sin 2\alpha (-\sigma_x \sin \phi_q + \sigma_y \cos \phi_q) \quad (\text{F.6})$$

$$+ 2\tilde{\Delta}\tilde{\Omega} \sin^2 \alpha (\sigma_x \cos \phi_q + \sigma_y \sin \phi_q) \quad (\text{F.7})$$

$$+ (\cos^2 \alpha - (1 - 2\tilde{\Delta}^2) \sin^2 \alpha) \sigma_z \quad (\text{F.8})$$

where $\tilde{\Delta} = \Delta/\sqrt{\Delta^2 + \Omega^2}$, $\tilde{\Omega} = \Omega/\sqrt{\Delta^2 + \Omega^2}$, and $\alpha = \frac{1}{2}\tau\sqrt{\Delta^2 + \Omega^2}$.

We fit the conditional probabilities $P^{(0)}$ and $P^{(4)}$ as a function of ϕ_q (Fig. 9.5d,e), taking Δ as the effective detuning from interaction-shifted resonance, and measuring $\langle \sigma'_z \rangle$ as a function of ϕ_q to extract the Bloch vector components $\langle \sigma_x \rangle$, $\langle \sigma_y \rangle$, $\langle \sigma_z \rangle$ on the two respective sublattices. For the (1,1) sublattice response, we model the evolution averaged over random detunings, due to $\sim 15\%$ fluctuations of the interaction shifts associated with thermal fluctuations in atomic positions, which broaden and weaken the spectroscopic response. For both sublattices we also include fluctuations in the calibrated pulse area ($\sim 10\%$ due to low power used). The extracted fit values are $\sigma_{x,y,z}^{(0,0)} = -0.82(6), 0.25(2), -0.32(4)$, and $\sigma_{x,y,z}^{(1,1)} = -0.46(4), 0.01(1), 0.91(5)$.

G

Supplementary information for Chapter 10

G.1 EXPERIMENTAL SETUP AND DETAILS

We initialize a sorted array of atoms in a desired geometry and optically pump the atoms into the stretched state $|5S_{1/2}, F = 2, m_F = -2\rangle$. The atoms are then illuminated by two Rydberg laser beams at 1013 nm and 420 nm, with single-photon Rabi frequencies of $\Omega_{1013}/(2\pi) \approx 50$ MHz and $\Omega_{420}/(2\pi) \approx 160$ MHz and a detuning from the $6P_{3/2}$ intermediate state of $\delta/(2\pi) \approx 1$ GHz. Using an arbitrary waveform generator (AWG) connected to an acousto-optic modulator (AOM), we control the intensity, frequency, and phase of the 420-nm light arbitrarily. We apply the 420-nm light such that the two-photon detuning Δ starts at a large

negative value, and sweep to large positive values using a cubic time profile. For each geometry, we optimize the sweep parameters to maximize the state preparation fidelity, as measured by the contrast between Rydberg populations on sublattices A and B . See [31] for a detailed, up-to-date characterization of our experimental apparatus and adiabatic state preparation in two-dimensional arrays.

G.2 THERMALIZATION MECHANISMS AND FIXED-DETUNING QUENCHES

G.2.1 DERIVATION OF EFFECTIVE HAMILTONIAN

The Rydberg blockade mechanism arises in the limit of strong nearest-neighbor interactions, $V_0 \gg \Omega$, such that the many-body Hilbert space is split into disconnected sectors distinguished by the total number of nearest-neighbor excitations [129]. In this section we employ Schrieffer-Wolff (SW) perturbation theory to derive an effective Hamiltonian in the sector of zero nearest-neighbor excitations starting from the Rydberg Hamiltonian, defined in Eq. (10.1) in Chapter 10. The effective Hamiltonian is obtained from an expansion in the small parameter Ω/V_0 up to second order. We describe the main steps of the expansion, applicable in any lattice geometry. The subleading terms in the effective Hamiltonian provide important insights into the physical processes that facilitate thermalization of the system at short timescales and will be used in Section G.2.3 to justify the expression for the empirical decay rate of scars defined in Eq. (10.2) of Chapter 10.

The first step of the SW transformation consists of the splitting of the full Hamiltonian into the dominant part (H_0) and the perturbation (Q) so that $H = H_0 + Q$. We consider the limit where the nearest-neighbor interaction strength V_0 is the dominant energy scale compared to Rabi frequency Ω , detuning Δ , and longer-range interactions. This naturally leads to the

following splitting:

$$H_0 = V_0 \sum_{\langle ij \rangle} n_i n_j, \quad Q = \frac{\Omega}{2} \sum_i \sigma_i^x - \Delta \sum_i n_i + \frac{V_0}{2} \sum_{i,j > \text{NN}} \frac{n_i n_j}{(d_{ij}/a)^6}, \quad (\text{G.1})$$

where d_{ij}/a is the distance between sites i and j normalized by the nearest-neighbor spacing a , and the last term sums over all sites i, j with $d_{ij}/a > 1$ (i.e. beyond nearest neighbors), with the factor of $1/2$ accounting for double-counting of pairs.

The unperturbed Hamiltonian H_0 effectively counts the total number of nearest-neighbor excitations in the system. We further split the perturbation Q into the sum of generalized ladder operators T_m , defined so that $[H_0, T_m] = m V_0 T_m$, with m being an integer. Physically, this commutation rule implies that the operator T_m increases energy by $m V_0$ when applied to an eigenstate of H_0 . For the Rydberg Hamiltonian, the integer m identifies the number of nearest-neighbor excitations that are either created, if $m > 0$, or annihilated, if $m < 0$, by the application of T_m to an eigenstate of H_0 . The detuning as well as the longer range interactions commute with the dominant term in the Hamiltonian H_0 and therefore, contribute only to the T_0 operator,

$$T_0 = \frac{\Omega}{2} \sum_i \mathcal{P}_i^{D,0} \sigma_i^x - \Delta \sum_i n_i + \frac{V_0}{2} \sum_{i,j > \text{NN}} \frac{n_i n_j}{(d_{ij}/a)^6}. \quad (\text{G.2})$$

The remaining ladder operators $T_{m \neq 0}$ originate from the action of the $(\Omega/2)\sigma^x$ term,

$$T_m = \frac{\Omega}{2} \sum_i \mathcal{P}_i^{D,m} \sigma_i^+ \quad \text{for } m = 1, \dots, D \quad \text{with} \quad T_{-m} = T_m^\dagger, \quad (\text{G.3})$$

where D is the number of nearest neighbors for the given lattice and calligraphic operators $\mathcal{P}_i^{D,m}$ are defined as projectors onto the subspace where m nearest neighbors of site i are si-

multaneously excited. If the Rydberg atom at site i is flipped in this subspace, the energy of the state measured with respect to H_0 will change proportionally to the number of excited nearest neighbors m , as desired.

The SW transformation of order l is a rotation of the Hamiltonian, $H^{(l)} = \mathcal{U}_l^\dagger H \mathcal{U}_l$ that eliminates all off-diagonal (in the unperturbed eigenbasis) operators up to $O(\Omega^{l+1}/V_0^l)$. The generator of the SW transformation at order $l = 1$ can be written as $\mathcal{U}_1 = \exp(-\sum_{m \neq 0} \frac{T_m}{m V_0})$. Higher-order generators have a more complicated form, containing nested commutators of the generalized ladder operators. The rotated Hamiltonians $H^{(l)}$ are truncated at $O(\Omega^{l+1}/V_0^l)$ and therefore, the equalities below are defined up to the truncation order. The first-order Hamiltonian is,

$$H^{(1)} = H_0 + T_0 = V_0 \sum_{\langle ij \rangle} n_i n_j + \frac{\Omega}{2} \sum_i \mathcal{P}_i^{D,0} \sigma_i^x - \Delta \sum_i n_i + \frac{V_0}{2} \sum_{i,j > \text{NN}} \frac{n_i n_j}{(d_{ij}/a)^6}. \quad (\text{G.4})$$

The first term $H_0 = V_0 \sum_{\langle ij \rangle} n_i n_j$ contributes a constant that is equal to zero, as we restrict to the so-called ‘Rydberg-blockaded’ Hilbert space in which no two neighboring sites are simultaneously excited. The Hamiltonian (G.4) is an effective Hamiltonian in the Rydberg-blockaded Hilbert space. In particular, the projector $\mathcal{P}_{i,j}^{D,0}$ that dresses the spin-flip operator σ_i^x ensures that Rydberg excitations obey the blockade condition, leading to the presence of a kinetic constraint in the dynamics. Equation (G.4) is equivalent to the “PXP-model” [131, 189] but in the presence of detuning and long-range interactions.

To probe additional thermalization processes that stem from virtual excitations that violate Rydberg blockade, we consider the effective Hamiltonian with terms up to second order,

$$H^{(2)} = H^{(1)} + \sum_{m=1}^D \frac{[T_m, T_{-m}]}{m V_0} = H^{(1)} + \frac{\Omega^2}{4V_0} \left(\sum_i \sum_{m=1}^D \frac{1}{m} \mathcal{P}_i^{D,m} \sigma_i^z - \sum_{\langle ij \rangle} \mathcal{P}_{i,j}^{D,0} (\sigma_i^+ \sigma_j^- + \text{H.c.}) \right). \quad (\text{G.5})$$

Where the first term in parenthesis corresponds to multi-site interactions and the second term describes kinetically constrained hopping of Rydberg excitations between nearest-neighbor sites i, j provided that all neighbors of these two sites are in the $|g\rangle$ state.

Collecting all terms together we obtain the final expression for the effective Hamiltonian:

$$H^{(2)} = \frac{\Omega}{2} \sum_i \mathcal{P}_i^{D,0} \sigma_i^x - \Delta \sum_i n_i + \frac{V_0}{2} \sum_{i,j > \text{NN}} \frac{n_i n_j}{(d_{ij}/a)^6} + \frac{\Omega^2}{4V_0} \left(\sum_i \sum_{m=1}^D \frac{1}{m} \mathcal{P}_i^{D,m} \sigma_i^z - \sum_{\langle ij \rangle} \mathcal{P}_{i,j}^{D,0} (\sigma_i^+ \sigma_j^- + \text{H.c.}) \right). \quad (\text{G.6})$$

Previous theoretical studies have predominantly focused on the long-lived oscillations from $|\text{AF}\rangle$ -type initial states in the pure PXP-model that is given by the first term in $H^{(2)}$. The presence of quantum many-body scars in this Hamiltonian, discussed in one-dimensional chains [189] and generic bipartite two-dimensional lattices [214, 343], leads to long intrinsic decay timescales of the oscillations of local observables. It is thus reasonable to assume that the decay rates seen in experiments (and numerics of the full Rydberg Hamiltonian) are caused by the remaining terms in Eq. (G.5) that describe deviations from the PXP model, as such deformations are observed to generally increase thermalization rates [189, 213]. The derivation of the second-order Hamiltonian $H^{(2)}$ for the Rydberg-blockaded Hilbert space demonstrates that the following microscopic mechanisms dominate deviations from the PXP-model: (i) detuning that is controlled experimentally by the parameter Δ , (ii) longer-range interactions that have overall magnitude scaling with V_0 , but strongly depend on the geometry of the lattice, and (iii) higher-order corrections that scale as $\Omega^2/4V_0$. These terms will be used in Section G.2.3 to justify the phenomenological model for thermalization rate used in Chapter 10 (see also Eq. (G.10)).

G.2.2 OPTIMAL FIXED GLOBAL DETUNING FOR SUPPRESSING LONG-RANGE INTERACTIONS

In this section we show that there is an astute choice of detuning Δ_q such that the detrimental effect of long-range interaction terms is partially mitigated. As discussed in the previous section and in Chapter 10, we find empirically for fixed-detuning quenches that deviations from the pure PXP Hamiltonian limit the lifetime of the scars we observe. This motivates the rationale for quenching to small positive values of Δ_q as opposed to $\Delta_q = 0$, as the long-range interactions are always positive and so can be partially compensated by a fixed detuning. Mathematically, the optimal value of detuning can be deduced from rewriting the second and third terms in Eq. (G.6) via the spin operator $S_i^z = (1/2)\sigma_i^z$ such that $n_i = S_i^z + 1/2$, giving

$$-\Delta \sum_i n_i + \frac{V_0}{2} \sum_{i,j>\text{NN}} \frac{n_i n_j}{(d_{ij}/a)^6} = \frac{1}{2} \sum_{i,j>\text{NN}} V_{ij} S_i^z S_j^z + \sum_i S_i^z \left(-\Delta + \frac{1}{2} \sum_{i,j>\text{NN}} V_{ij} \right), \quad (\text{G.7})$$

where d_{ij}/a is the distance between sites i and j normalized by the nearest-neighbor spacing a . We observe that terms proportional to S_i^z cancel when

$$\Delta = \Delta_{q,\text{opt}} = \frac{1}{2} \sum_{i,j>\text{NN}} V_{ij} = \frac{V_0}{2} \sum_{i,j>\text{NN}} \frac{1}{(d_{ij}/a)^6}, \quad (\text{G.8})$$

resulting in

$$H^{(2)} \Big|_{\Delta=\Delta_{q,\text{opt}}} = \frac{\Omega}{2} \sum_i \sigma_i^x \prod_{i,j=\text{NN}} P_j + \frac{1}{2} \sum_{i,j>\text{NN}} V_{ij} S_i^z S_j^z + \frac{\Omega^2}{4V_0} \sum_i [\text{Many-body terms}]. \quad (\text{G.9})$$

with the [Many-body terms] described in Eq. G.6. This Hamiltonian is qualitatively similar to that in Eq. (G.6), but with smaller long-range interactions $S_i^z S_j^z$ instead of the native $n_i n_j$ interactions, due to the adopted choice of $\Delta_{q,\text{opt}}$. The long-range interactions are dominated by the contribution from next-nearest-neighbor (NNN) atoms (as $V_{ij} \propto 1/d_{ij}^6$), and due to the bipartite nature of the lattices studied here, the NNN of the i^{th} atom belong to the same sublattice as the i^{th} atom and thus have the same population evolution in time. For these reasons, the mean-field contribution from long-range interactions of the form $\sum_{i,j>\text{NN}} V_{ij} S_i^z S_j^z$ is roughly 1/4 the mean-field contribution of $\sum_{i,j>\text{NN}} V_{ij} n_i n_j$, and thereby reduces the deviation from the pure PXP Hamiltonian.

We emphasize that calculating the optimal value $\Delta_{q,\text{opt}}$ according to Eq. (G.8) requires only knowledge of V_0 and d_{ij}/a . For example, the sum in Eq. G.8 gives $\Delta_{q,\text{opt}}/V_0 \approx 0.153, 0.33, 0.0173$ for a honeycomb lattice, a square lattice, and a one-dimensional chain respectively. For lattices where different sublattice sites are not equivalent, e.g. Lieb and decorated honeycomb lattices, we calculate $\Delta_{q,\text{opt}}$ for both sublattices and take the average.

In Fig. G.1 we plot experimental measurements of scar decay rate $1/\tau$ under quenches to different fixed detunings Δ_0 on a 162-atom honeycomb lattice. We find that the smallest decay rate is achieved at $\Delta \approx 0.13 V_0$, close to the value of $\Delta_{q,\text{opt}} \approx 0.153 V_0$ for the honeycomb lattice calculated from Eq. (G.8).

G.2.3 INDEPENDENT MEASUREMENT OF DECAY MECHANISMS

In this section we explain the expression used to describe scar decay mechanisms, and then independently corroborate the phenomenological parameters α and β from the plane fit using different experimental measurements.

In Chapter 10 we used the following phenomenological expression to describe the decay rate

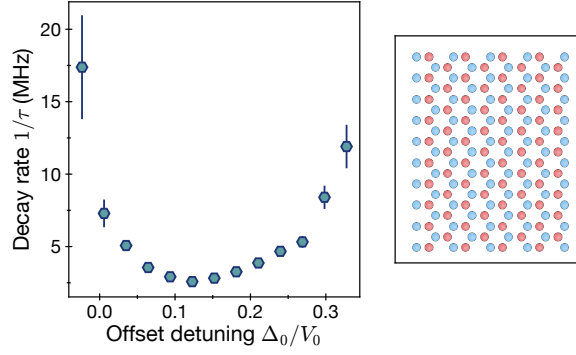


Figure G.1: Optimal fixed detuning during a fixed-detuning quench. Quenching from antiferromagnetic state $|\text{AF}_1\rangle$ to various fixed detunings Δ_0 on a 162-atom honeycomb lattice with $V_0/2\pi = 17.1$ MHz and $\Omega/2\pi = 4.3$ MHz. The optimal fixed detuning on the honeycomb lattice is calculated to be $\Delta_{q,\text{opt}} = 1/2 \sum_{i,j > \text{NN}} V_{ij} \approx 0.153 V_0$. An optimum is experimentally observed here close to $\Delta_0 \approx 0.13 V_0$, consistent with expectations from Eq. (G.8).

of collective oscillations:

$$\frac{1}{\tau} = \alpha \left(\frac{1}{2\pi} \sum_{\text{NN}} \frac{\Omega^2}{4V_0} \right) + \beta \left(\frac{1}{2\pi} \sum_{\text{NNN}} V_{ij} \right) + \frac{1}{\tau_0}, \quad (\text{G.10})$$

where α , β , and τ_0 are determined from the fit to the data. Physically this expression encodes the interplay of two different mechanisms that govern the behavior of $1/\tau$ and can be understood from the effective Hamiltonian (G.6) derived in Sec. G.2.1. The leading term in the effective Hamiltonian (G.6), the PXP model, leads to long-lived oscillations with significantly longer decay time than observed for the full Rydberg Hamiltonian, both in 1D [189, 211] and 2D [343]. After fixing the detuning to $\Delta_{q,\text{opt}}$ we arrive at the effective Hamiltonian in Eq. (G.9), describing the PXP model perturbed by the presence of (a) hopping processes of Rydberg excitations via virtual processes that involve violation of Rydberg blockade, thus being suppressed as Ω^2/V_0 at large V_0 and (b) longer-range interactions that scale as V_0 , dominated by next-nearest-neighbors (NNN). Assuming that these two terms act as independent decay mechanisms, one expects two separate contributions to the decay rate that are functions of Ω^2/V_0 and V_0 respectively, reflected by the phenomenological expression (G.10).

In order to independently measure the coefficient α , we measure the scar lifetime for different values of Rabi frequency Ω , while keeping V_0 fixed in a 9-atom chain, thereby only changing the $\Omega^2/(4V_0)$ term. We observe a linear dependence up to the point where $\Omega/V_0 \approx 0.5$, beyond which we see a strong increase of the decay rate, as the Rydberg blockade breaks down and higher-order perturbations in Ω/V_0 become significant. To independently determine the value of β , we measure the scar lifetime for zigzag-shaped chains of atoms, keeping the NN spacing constant while changing the NNN spacing (Fig. G.2B), thereby only changing the NNN interaction term.

The two independent procedures described above result in values $\alpha = 0.79(15)$ and $\beta = 0.58(7)$, which are consistent with the values extracted from the two-dimensional fit in Fig. 10.2 ($\alpha = 0.72(12)$, $\beta = 0.58(5)$) from Chapter 10. We also perform numerical simulations of the quenches in Fig. G.2 to corroborate our observations and explore imperfections of our phenomenological model. Numerical simulations of the decay rate (plotted in Fig. G.2A) agree well with the experimental data in the intermediate range of Ω . However, the fine-grained theoretical curve in Fig. G.2B reveals a significant curvature for low NNN interactions, deviating from the naive linear prediction and suggesting that the phenomenological expression (G.10) is an oversimplification and that the effective β can depend on the probed range of interaction strength. We further speculate that these oversimplifications could be more dramatic in two-dimensional lattices, where e.g. the square lattice only has a small range of V_0 which balances the contributions from imperfect blockade and NNN interactions. Future work could explore deviations from Eq. G.10 and perhaps devise clever ways to suppress these decay channels.

For Fig. 10.2 in Chapter 10, we also include data on lattices (Lieb, decorated honeycomb, edge-imbalanced decorated honeycomb) whose different sublattices have different imperfect blockade and NNN corrections. In these geometries, for the x - and y -axis values on the plane

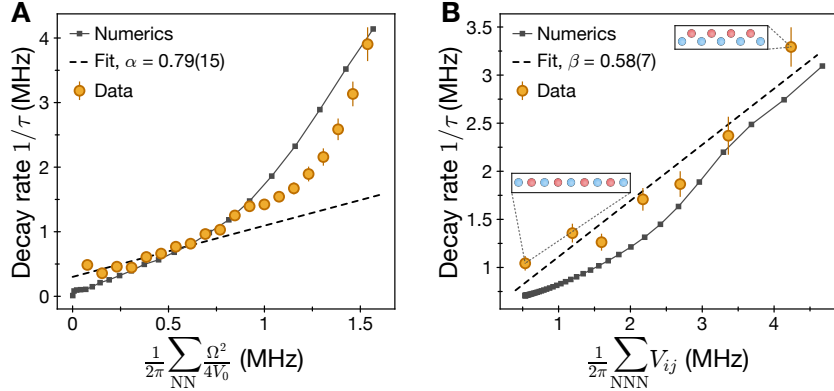


Figure G.2: Independent measurement of decay parameters α and β . **(A)** Measured decay rate as a function of coupling to blockade-violating states $\sim \Omega^2/(4V_0)$, obtained by measuring at different Rabi frequencies Ω during the quench on one-dimensional 9-atom chains with a fixed $V_0/(2\pi) = 5.9$ MHz. The linear fit (dashed line) is performed on the first 8 points, which correspond to $\Omega/V_0 < 0.5$. **(B)** Measured decay rate as a function of next-to-nearest-neighbor interactions. We prepare 9-atom chains with a variable staggering angle between neighboring sites, keeping the nearest-neighbor interaction constant at $V_0/(2\pi) = 17.1$ MHz (insets). All error bars are given by fit uncertainties. The values for α and β are consistent with the fit in Fig. 10.2 of Chapter 10 within error bars.

fit, we calculate which sublattice has the faster decay rate as given by Eq. G.10, and use those values of NN imperfect blockade and NNN interactions as the x and y values in the plot.

G.3 EXPERIMENTAL DATA ON ENHANCEMENT OF SCARS BY PERIODIC DRIVING

G.3.1 DEFINITION OF SUBHARMONIC WEIGHT

In this section we describe the Fourier transform and normalization procedures for calculating $S(\omega)$. We use the in-phase component of the Fourier transform, and because the sublattice population imbalance $\mathcal{I}(t) = \langle n \rangle_A - \langle n \rangle_B$ oscillates about a small, finite offset, we subtract the time-averaged imbalance $\bar{\mathcal{I}}$, giving

$$\tilde{S}(\omega) = \frac{2}{T} \int_0^T dt [\mathcal{I}(t) - \bar{\mathcal{I}}] \cos(\omega t), \quad (\text{G.11})$$

where T is the longest measured quench time. Akin to the definition in [216], we then normal-

ize by the total integrated intensity, giving

$$|S(\omega)|^2 = \frac{|\tilde{S}(\omega)|^2}{2 \int_0^\infty |\tilde{S}(\omega')|^2 d\omega' (T/2\pi)}. \quad (\text{G.12})$$

Finally, since we take a Fourier transform over a finite window T , to ensure the subharmonic weight is consistently defined and properly normalized, we then calculate $|S(\omega)|^2$ for a perfect subharmonic response $\mathcal{I}(t) = \cos[(\omega_m/2)t]$ and normalize such that $|S(\omega_m/2)|^2 = 1$ for this perfect subharmonic response. These normalizations yield the $|S(\omega)|^2$ that we plot throughout this work. In this way, the subharmonic weight $|S(\omega_m/2)|^2$ has a maximum of 1 which is achieved for a perfect cosine response in-phase with the drive. The intensity of the complex Fourier transform yields the same qualitative result but is broader by a factor of ≈ 2 in the frequency domain due to the finite width of time window T used in Fourier transformation.

G.3.2 ROBUSTNESS OF SUBHARMONIC RESPONSE AS A FUNCTION OF SYSTEM SIZE

In this section we describe the behavior of the subharmonic response as a function of the system size. A key signature of time-crystalline behavior is that the subharmonic response becomes more rigid as the system size increases [209, 344].

Figure G.3 plots $|S(\omega)|^2$ as a function of modulation frequency ω_m for one-dimensional chains of 3 - 17 atoms. For the 3-atom chain, a discernible subharmonic response is not observed. For the 5-atom chain, a subharmonic response is observed with $\omega_m \approx 2 \times$ the natural oscillation frequency, but at larger or smaller ω_m the response splits into two separate peaks. For the 7-atom chain, the subharmonic response persists over a wider region of ω_m and with larger peak amplitude, but at sufficiently large or small ω_m the response again splits into two peaks. Finally, for chains with 9 atoms and beyond, a stable subharmonic response is ob-

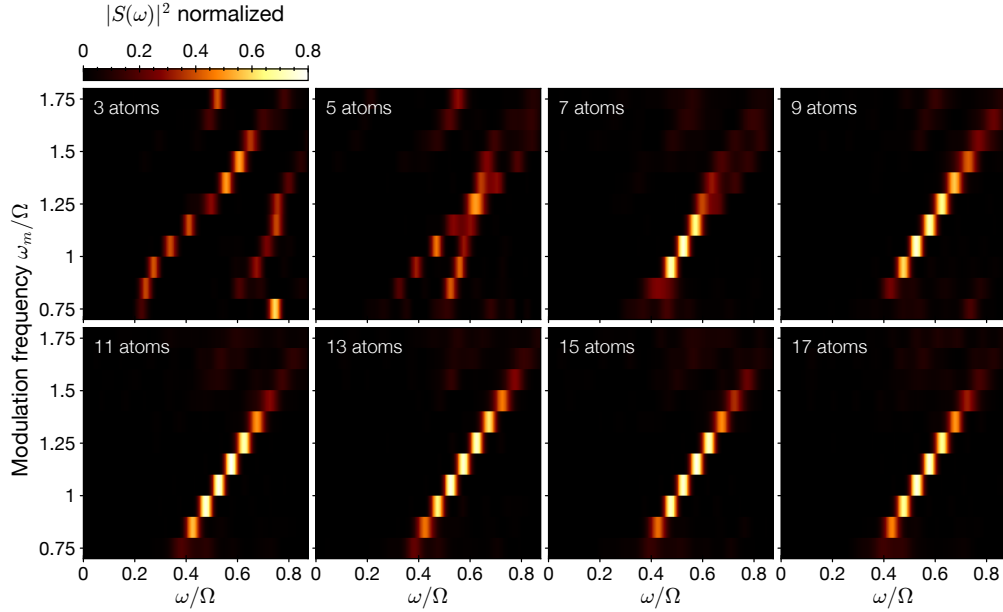


Figure G.3: System-size dependence of the subharmonic response. Fourier transform intensity $|S(\omega)|^2$ of $\langle n \rangle_A - \langle n \rangle_B$ traces for a chain of varying system size. A prominent subharmonic feature emerges and becomes more robust as the number of atoms in the chain increases, signifying that the subharmonic response is a many-body effect. All data here is a chain with $V_0/2\pi = 51$ MHz, and with drive parameters $\Delta_m = \Delta_0 = 0.55 \Omega$.

served, with large response amplitude and no discernible splitting of the central peak.

To summarize these results quantitatively, in Fig. 10.4D of Chapter 10 we plot the subharmonic rigidity, which evaluates the robustness of the subharmonic response over a range of modulation frequencies and is defined as $\sum_{\omega_m} |S_{\omega_m}(\omega = \omega_m/2)|^2$ for $\omega_m = 0.75, 0.85, \dots, 1.75 \Omega$. We attribute the small decrease in rigidity for the larger chains to a reduction in fidelity of the state preparation into one of the classical $|\text{AF}\rangle$ orderings. In addition to the chain data presented here, in Chapter 10 we also plot the measured subharmonic rigidity for a honeycomb lattice with sizes ranging from 9 to 200 atoms.

G.3.3 SIGNATURES OF A 4TH SUBHARMONIC RESPONSE

In this section we report signatures of a 4th subharmonic response. Figure G.4A plots $\langle n \rangle_A - \langle n \rangle_B$ in the presence of two different drives with modulation frequencies of $\omega_m = 1.83 \Omega$ and

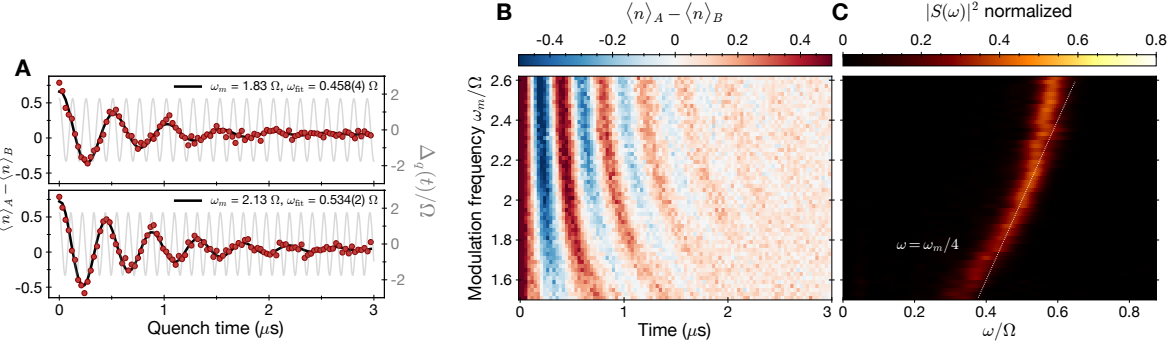


Figure G.4: Signatures of a 4th subharmonic response. (A) $\langle n \rangle_A - \langle n \rangle_B$ in the presence of two different drives with modulation frequencies of $\omega_m = 1.83 \Omega$ and 2.13Ω , resulting in responses at a 4th subharmonic of $\omega_{\text{fit}} = 0.458(4) \Omega$ and $0.534(2) \Omega$, respectively. Data is on a 9-atom chain with $V_0/2\pi = 32$ MHz and drive parameters $\Delta_m = 1.75 \Omega$ and $\Delta_0 = 0$, which is a different drive parameter regime than those used in investigating a 2nd subharmonic response. (B) $\langle n \rangle_A - \langle n \rangle_B$ data for modulation frequencies from 1.51Ω to 2.61Ω with same parameters as A. (C) Fourier transform intensity $|S(\omega)|^2$ of data in B, showing signatures of a 4th subharmonic response (dotted white line) while seemingly not as robust as the 2nd subharmonic response focused on in this work.

2.13Ω , resulting in responses at a 4th subharmonic of $\omega_{\text{fit}} = 0.458(4) \Omega$ and $0.534(2) \Omega$, respectively. Here, the quantum state synchronously returns to itself every four drive periods of $\Delta_q(t)$, as seen by comparing $\langle n \rangle_A - \langle n \rangle_B$ with the $\Delta_q(t)$ profile (gray curve).

In Fig. G.4B we then explore this 4th subharmonic response by plotting the time dynamics $\langle n \rangle_A - \langle n \rangle_B$ for modulation frequencies from 1.51Ω to 2.61Ω , and in Fig. G.4C plot its associated Fourier transform intensity $|S(\omega)|^2$. In panel C we observe signatures of a 4th subharmonic response persisting from modulation frequencies ω_m of approximately 1.8Ω to 2.2Ω , seemingly less robust than the 2nd subharmonic response that is the main focus of this work. A stronger 4th subharmonic response may exist in other drive parameter regimes or lattice configurations (we did not search widely).

G.3.4 DEPENDENCE OF SUBHARMONIC RESPONSE ON THE INITIAL STATE

In this section we demonstrate the strong dependence of the quantum dynamics on the choice of initial state, for quenches to both fixed detunings and time-dependent detunings. Such

markedly different behavior and thermalization time for different initial states can be viewed as a key signature of quantum scarring.

First we present our measurement results for quenches with a static, optimal positive detuning. We plot the sublattice populations over time for an initially prepared $|AF\rangle$ state (also referred to as $|\mathbb{Z}_2\rangle$ in one dimension [189]) and an initially prepared $|ggg\dots\rangle$ state, for a decimated honeycomb (Fig. G.5) and for a one-dimensional chain (Fig. G.6). In both the two-dimensional and one-dimensional systems, the sublattice populations of the $|ggg\dots\rangle$ state quickly equilibrate, whereas the $|AF\rangle$ state exhibits long-lived, periodic many-body revivals. These observations experimentally confirm the initial-state dependence characteristic of quantum scarring in one and two dimensions.

In Fig. G.6A we explore the relationship between the parametric drive and quantum scarring by plotting the response of the $|AF\rangle$ and $|ggg\dots\rangle$ states with and without a drive. For the $|AF\rangle$ state, the drive prolongs the sublattice oscillations and locks their oscillation frequency to half the drive frequency. In contrast, the sublattice populations of the $|ggg\dots\rangle$ state still quickly equilibrate under the drive and exhibit small oscillations at the drive frequency (harmonic response). In Figure G.6B we explore these distinct responses over a range of modulation frequencies by plotting the Fourier transform intensity of the sublattice dynamics. In Fig. 10.4B of Chapter 10 and other figures we plot $|S(\omega)|^2 = |S_{A-B}(\omega)|^2$, but this quantity is not informative for the $|ggg\dots\rangle$ state as it approaches zero in the thermodynamic limit. Accordingly, in Fig. G.6B we plot the average Fourier transform intensity of the individual sublattices, $(|S_A(\omega)|^2 + |S_B(\omega)|^2)/2$, for both the initial $|AF\rangle$ state and $|ggg\dots\rangle$ state. We find the $|AF\rangle$ initial state exhibits a strong subharmonic response and also a weak harmonic response (which disappears for $|S_{A-B}(\omega)|^2$), whereas the $|ggg\dots\rangle$ initial state shows a harmonic response but no detectable subharmonic response. These observations suggest that the

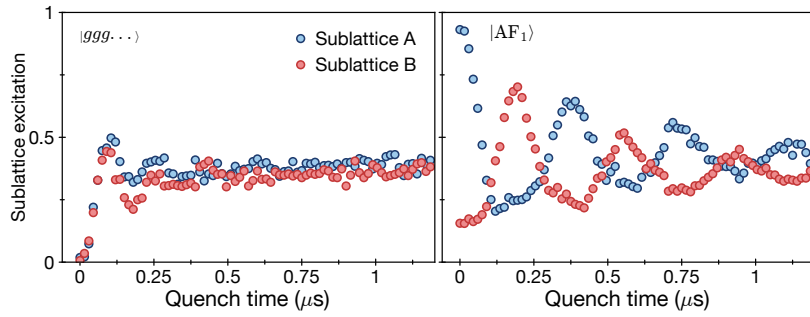


Figure G.5: Initial-state dependence on dynamics. Plotted here are fixed detuning quenches in a two-dimensional lattice (54-atom decorated honeycomb with $V_0/2\pi = 9.1$ MHz and $\Omega/2\pi = 4.2$ MHz). With a $|ggg\dots\rangle$ initial state (left) the sublattice populations quickly equilibrate. With an $|\text{AF}_1\rangle$ initial state (right) the sublattice populations oscillate and equilibrate at a significantly slower rate, whose rate is dominated by imperfect blockade and NNN interactions as explored in Chapter 10.

subharmonic stabilization observed here is intertwined with the scarring behavior itself, and is distinct from conventional time crystals by this dramatic initial-state dependence even for short times / small systems.

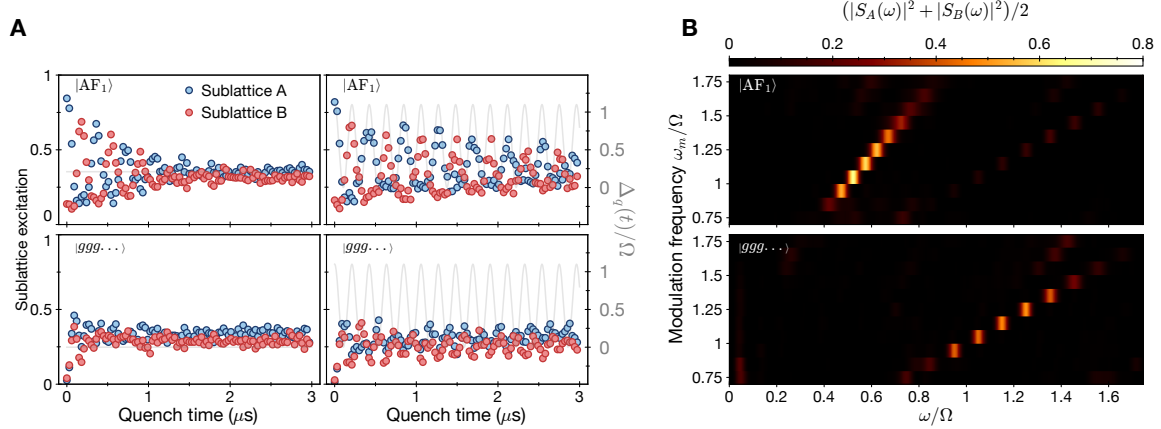


Figure G.6: Response to drive for different initial states. (A) (Left panels) Fixed detuning quench for $|\text{AF}\rangle$ (top) and $|\text{ggg}\dots\rangle$ (bottom) initial states, showing an initial-state dependence to the ensuing dynamics and equilibration time. (Right panels) Time-dependent quench for $|\text{AF}\rangle$ (top) and $|\text{ggg}\dots\rangle$ (bottom) initial states. The $|\text{AF}\rangle$ state scars are prolonged and the individual sublattice response is synchronously locked to half the drive frequency, whereas the sublattice populations of the $|\text{ggg}\dots\rangle$ state show small oscillations at the drive frequency (harmonic response). (B) Fourier transform intensity of the individual sublattices $|S_A(\omega)|^2$ and $|S_B(\omega)|^2$, averaged together. The $|\text{AF}\rangle$ initial state (top) shows a strong subharmonic response and also a weak harmonic response (which disappears for $|S_{A-B}(\omega)|^2$ as plotted in Fig. 10.4B of Chapter 10). The $|\text{ggg}\dots\rangle$ initial state (bottom) shows a harmonic response but no detectable signatures of a subharmonic response.

G.3.5 SUBHARMONIC RESPONSE WITH SQUARE PULSE MODULATION

In this section we demonstrate the robustness of the scar enhancement with respect to the pulse shape, here specifically for square pulses of $\Delta(t)$, as shown in Figure G.7A. Figure G.7B plots the dynamics of $\langle n \rangle_A - \langle n \rangle_B$ with a fixed detuning $\Delta_q = \Delta_{q,\text{opt}} = 0.5 \Omega$ (top) and a time-dependent detuning $\Delta_q(t) = \Delta_0 + \Delta_m (2\Theta[\cos(\omega_m t)] - 1)$ (bottom), where Θ is the Heaviside Theta Function. As with the cosine drive, the square pulse modulation increases the scar lifetime by a factor of five, from $\tau_{\text{fixed}} = 0.33(2) \mu\text{s}$ to $\tau_{\text{drive}} = 1.72(11) \mu\text{s}$, and changes the oscillation frequency to be half the drive frequency of $\omega_m = 1.24 \Omega$. In Figure G.7C we plot the fitted oscillation frequency and change in lifetime from driving as a function of the drive frequency, again finding a robust subharmonic locking to $\omega_m/2$ and accompanying lifetime increase, for a one-dimensional chain and a honeycomb lattice. Note that the chain in Fig. G.7C has $V_0/2\pi = 120 \text{ MHz}$, different than the $V_0/2\pi = 51 \text{ MHz}$ used in Fig. 10.3C of Chapter 10 and resulting in the different change in driven lifetime. We do not find a significant difference between the behavior of the system to cosine vs square driving, and focus on cosine driving throughout this work for consistency.

G.3.6 RATIONALE AND ROBUSTNESS FOR CHOICE OF DRIVE PARAMETERS Δ_m AND Δ_0

In this section we discuss the choice of modulation amplitude Δ_m and offset Δ_0 . Largely, these values were chosen empirically, in what was observed (experimentally and numerically) to be a robust phase space.

Similar to the discussion in Section G.4.3, preliminary hypotheses suggested that the driven stability arises in part from having extremal values of $\Delta(t)$ at times when the antiferromagnetic $|\text{AF}\rangle$ states arise, stabilizing these states as they have maximal excitation number in

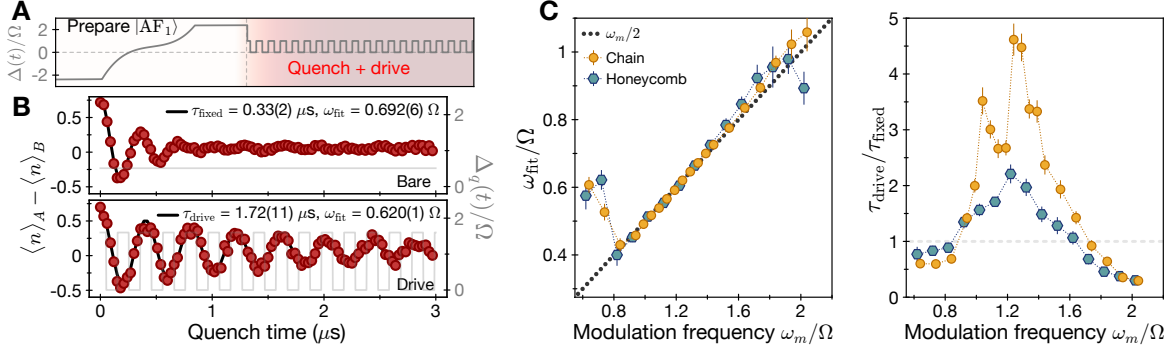


Figure G.7: Subharmonic locking with square pulse modulation. (A) Pulse sequence with square pulse drive. (B) Scar dynamics during a quench to a fixed optimal detuning (bare), and a time-dependent detuning (drive) with modulation frequency $\omega_m = 1.24 \Omega$. The drive increases the scar lifetime and changes its frequency to $\omega_m/2$. (C) Scar lifetime and response frequency as a function of ω_m , showing a lifetime increase and subharmonic locking.

the blockaded subspace. Our naive hypothesis was further that we desire a cosine profile that gives $\Delta(t) \approx 0$ at times between the revival of the $|AF\rangle$ states, in order to not disrupt the scar evolution. To satisfy these conditions, we chose values of roughly $\Delta_m = \Delta_0$ and then further optimized empirically, which seemed to be close to an optimum in the various lattices and V_0 we measured experimentally. For the idealized PXP Hamiltonian, we find that $\omega_m = 1.33 \Omega$ and $\Delta_m = 2\Delta_0 = \Omega$ appears to give oscillations which persist to hundreds of cycles. We speculate that good values for the full Rydberg Hamiltonian near $\Delta_m = \Delta_0$ instead of $\Delta_m = 2\Delta_0$ could be a consequence of the static field of the long-range interactions, requiring a larger Δ_0 to impose a static offset akin to $\Delta_{q,\text{opt}}$. We further speculate that there is an interplay between the time-dependent component of the detuning with the time-dependent component of the long-range interactions.

In Fig. G.8 we plot the $\langle n \rangle_A - \langle n \rangle_B$ dynamics and associated Fourier transform for a one-dimensional chain as a function of modulation amplitude Δ_m , at fixed offset $\Delta_0 = 0.5 \Omega$. We observe a robust subharmonic response across a wide range of Δ_m , with an optimal $\Delta_m \approx 0.7 \Omega$.

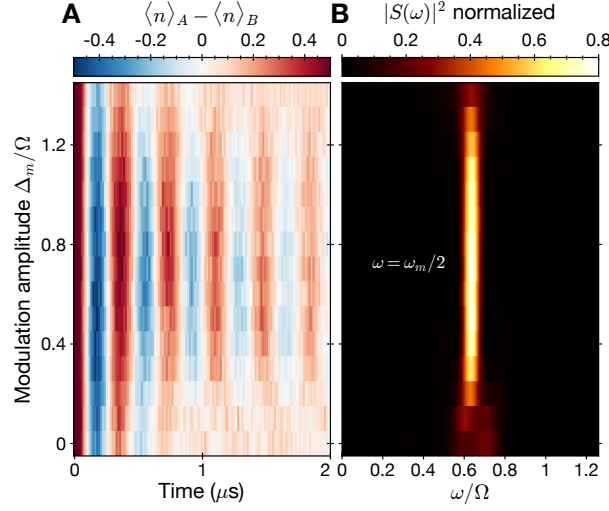


Figure G.8: Subharmonic stabilization as a function of modulation amplitude Δ_m . **(A)** Dynamics of sublattice population difference after quench as a function of modulation frequency, measured on a 9-atom chain with nearest-neighbor interaction strength $V_0/2\pi = 120$ MHz = $28 \Omega/2\pi$, detuning offset $\Delta_0 = 0.5 \Omega$, and modulation frequency $\omega_m = 1.28 \Omega$. The Δ_0 we choose here is commensurate with the optimal fixed-detuning quench $\Delta_{q,\text{opt}}$ on this lattice, so the $\Delta_m = 0$ line corresponds to data for optimal undriven scars on this lattice. **(B)** Fourier transform intensity $|S(\omega)|^2$ of data in **A**. Upon applying drive amplitude $\Delta_m \approx 0.3 \Omega$, the scar lifetime dramatically increases and exhibits a rigid subharmonic response at $\omega = \omega_m/2 = 0.64 \Omega$, independent of drive amplitude, before degrading at drive amplitude $\Delta_m \approx 1.3 \Omega$.

G.4 THEORETICAL INVESTIGATIONS OF DRIVEN SCARS

G.4.1 GROWTH OF ENTANGLEMENT ENTROPY UNDER DRIVE

The numerical data shown in Fig. G.9 demonstrates the effects of the drive to the growth of bipartite entanglement entropy in the Rydberg atom chain, and therefore, provides a direct probe of the thermalization rate of the system. In Fig. G.9A we compare the growth of entropy in quenches with no detuning, optimal static detuning, and dynamical detuning, for a 50-atom chain with open boundaries. We observe that the growth of entropy in the case of the dynamical detuning is much slower compared to the cases of static and zero detuning, illustrating the qualitative difference between the driven and static systems. The large system size ensures that the entropy dynamics are not affected by finite size effects for the time period shown. The simulation is performed by applying the time-dependent variational principle

on matrix product states [315, 345]. The time step of the simulation is $dt = 0.002$, the truncation error is $\epsilon_T = 5 \cdot 10^{-9}$ and the integration is performed using a fourth-order method. The long-range interactions are truncated for distances longer than four sites.

Figure G.9B shows the dependence of bipartite entanglement entropy growth on the frequency of the drive for a 24-atom chain with open boundaries. The calculation is performed using second-order Trotterized time evolution with time step $dt = 0.001$ applied to the full wave function. The slope of the entropy growth achieves a minimum value at $\omega_m \approx 1.225 \Omega$, similar to the optimal ω_m observed experimentally in Fig. 10.3C of Chapter 10 for the 9-atom chain.

G.4.2 STABILIZATION OF PURE PXP

Figure G.10 demonstrates that the dynamics of the idealized PXP model,

$$H_{\text{PXP}}(t) = \sum_i \left(\frac{\Omega}{2} P_{i-1} \sigma_i^x P_{i+1} - \Delta(t) n_i \right), \quad (\text{G.13})$$

are also stabilized by the cosine drive. We use a Krylov method to evolve a 22-atom chain with periodic boundary conditions in the blockaded Hilbert space. Both the slow growth of bipartite entanglement entropy and the slow decay of sublattice excitation revivals provide evidence for a suppression of thermalization mechanisms in the driven system. This result also illustrates that the effect of time-dependent detuning cannot be simply attributed to the cancellation of the long-range interactions as the drive is able to further suppress thermalization of the idealized PXP model.

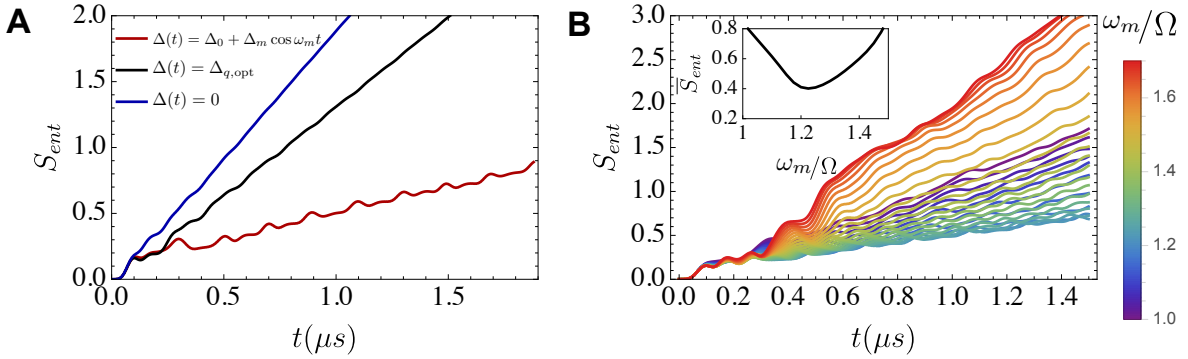


Figure G.9: Entanglement entropy dynamics of the Rydberg chain for a half-chain bipartition. The parameters of the system are $V_0/2\pi = 51$ MHz, $\Omega/2\pi = 4.2$ MHz. The time-dependent detuning amplitudes are $\Delta_0 = 0.55\Omega$, $\Delta_m = 0.55\Omega$. (A) Comparison of entanglement dynamics with harmonic detuning, optimal time-independent detuning $\Delta_{q,\text{opt}}$, and zero detuning reveals more than two-fold decrease in rate of entanglement growth due to presence of the drive. Data is shown for a 50-atom chain. The detuning parameters are $\Delta_{q,\text{opt}} = 0.0173 V_0$ and $\omega_m = 1.2 \Omega$. (B) Dependence of entanglement growth on the frequency of the drive for a 24-atom chain reveals an optimal modulation frequency that corresponds to the slowest rate of entanglement spreading. Inset: Time averaged entropy $\bar{S}_{\text{ent}} = \frac{1}{T} \int_0^T dt S_{\text{ent}}$ for $T = 1.5 \mu\text{s}$ shows a clear minimum around $\omega_m/\Omega \approx 1.225$.

G.4.3 ANALYSIS OF PULSED MODEL

Here we detail the pulsed model of scar stabilization presented in Chapter 10, corresponding to a simplified model (we assume infinitely sharp detuning pulses and idealized PXP interactions) that qualitatively reproduces key experimental observations of extended lifetime and subharmonic locking from scar states, as well as strong initial-state dependence of the phenomenon. We note that the combined concepts of pulsed Floquet driving and Rydberg atoms has been explored theoretically, although in regimes distant from the work here [346, 220, 347, 348].

The pulsed model is given by the Hamiltonian

$$H(t) = H_{\text{PXP}} + \theta N \sum_{n \in \mathbb{Z}} \delta(t - n\tau^-), \quad (\text{G.14})$$

which consists of τ -periodic delta-function ‘kicks’ of the detuning $N = \sum_i n_i$ with amplitude θ , on top of the PXP Hamiltonian. This can be thought of as an idealized, limiting case of

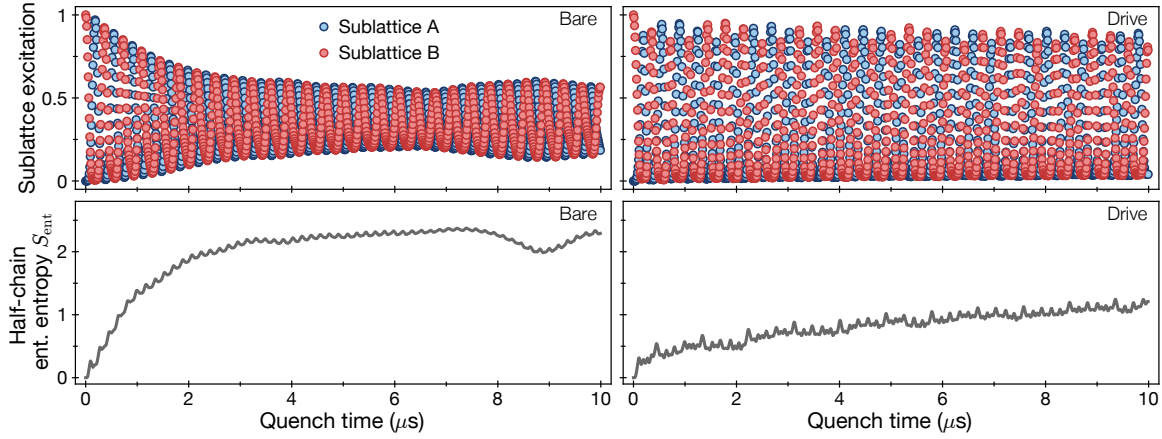


Figure G.10: Stabilization of pure PXP model under drive (numerics). (Top) Sublattice excitation probability for undriven (left) and driven (right) PXP model. (Bottom) Entanglement entropy across midway bipartition for undriven (left) and driven (right) PXP model. Numerics are calculated for a 22-atom chain with periodic boundary conditions and the timescale is set by $\Omega/2\pi = 4.2$ MHz. “Bare” is a conventional quench to $\Delta = 0$ and “Drive” is a quench to $\Delta = \Delta_0 + \Delta_m \cos(\omega_m t)$, with drive parameters $\Delta_0 = 0.5 \Omega$, $\Delta_m = 1.0 \Omega$, and $\omega_m = 1.33 \Omega$. These plots show that the cosine drive allows to delay the onset of thermalization even for the “idealized” PXP model, which describes perfect nearest-neighbor blockade ($V_0 = \infty$) with no long-range interactions.

the experimental driving where the detuning is applied instantaneously once per period. This time-dependent Hamiltonian generates the Floquet unitary

$$U_F(\theta, \tau) = e^{-i\theta N} e^{-i\tau H_{\text{PXP}}}, \quad (\text{G.15})$$

which comprises of two parts: evolution under H_{PXP} for time τ , and then an application of N for an angle θ . For a fine-tuned evolution time $\tau_c \approx 0.755 \times 2\pi \Omega^{-1}$ the first step $e^{-i\tau_c H_{\text{PXP}}}$ acts like an approximate spin-flip between the $|\text{AF}_1\rangle$ and $|\text{AF}_2\rangle$ product states, but otherwise generically serves to generate entanglement for initial states.

The Floquet unitary, parameterized by (θ, τ) , harbors a special point $\theta = \pi$. There the drive reverses dynamics generated by H_{PXP} perfectly after two driving periods. Specifically, the PXP Hamiltonian has a particle-hole symmetry under $e^{-i\pi N}$, i.e. $e^{-i\pi N} H_{\text{PXP}} e^{i\pi N} =$

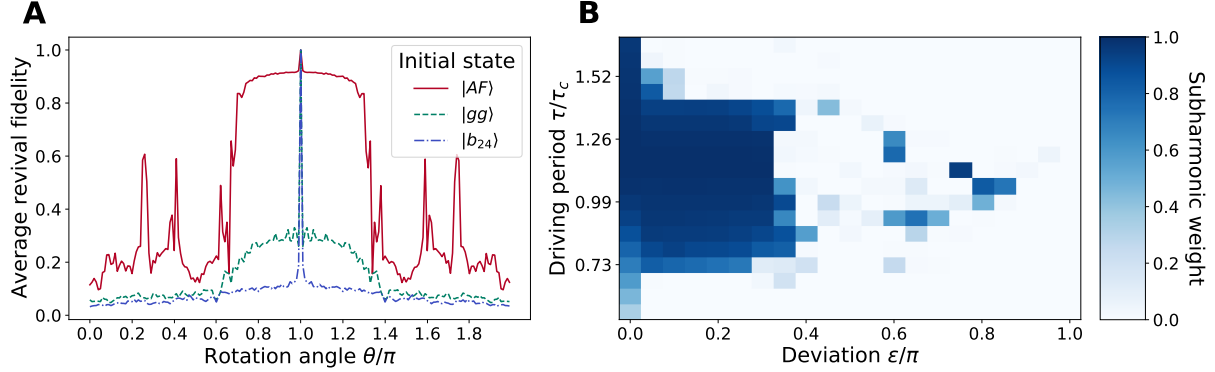


Figure G.11: State-dependent subharmonic revivals in the pulsed drive model. **(A)** Many-body revivals under Floquet unitary U_F for $\tau = \tau_c$ and varying $\varepsilon = \pi - \theta$ for a $L = 14$ chain with periodic boundary conditions. Revivals were calculated by taking the average of $|\langle \text{AF} | U_F(\pi + \varepsilon, \tau)^{2n} | \text{AF} \rangle|^2$ for $n = 1, 2, \dots, 100$. **(B)** Here, we depict the dependence of subharmonic weight on the rotation angle τ under H_{PXP} and the deviation ε from the perfect echo point $\theta = \pi$, calculated for $N = 400$ driving periods. We see oscillations persist to larger ε for τ near τ_c .

$-H_{\text{PXP}}$ (because $\sigma_i^z \sigma_i^x \sigma_i^z = -\sigma_i^x$). As such, the application of PXP during the first driving period is exactly undone during the second driving period, i.e. $U_F^2 = \mathbb{I}$. This is essentially a many-body echo, and produces perfect subharmonic revivals for all initial states for any value of τ . However, we find that away from the $\theta = \pi$ point where such an echo is no longer perfect, the $|\text{AF}_1\rangle$ and $|\text{AF}_2\rangle$ states nevertheless still exhibit substantial many-body revivals for a wide range of deviations $\varepsilon = \theta - \pi$, at fixed $\tau = \tau_c$. Indeed as can be seen in (Fig. G.11), there is a plateau of stability for θ near π for which the oscillations from the $|\text{AF}_1\rangle$ states persist beyond 100s of Floquet periods.

The pulsed model also displays subharmonic locking, notably for the $|\text{AF}\rangle$ initial states but not others like $|\text{ggg}\cdots\rangle$ (Fig. G.11B). To probe the dependence on τ and ε , we compute the weight of subharmonic response in the power spectrum of $\langle n(t) \rangle_A - \langle n(t) \rangle_B$, defined in Chapter 10 and references [216, 215]. Numerical results show that robust oscillations for $|\text{AF}\rangle$ persist until very late times (100-1000s of Floquet periods), for a wide range of τ near τ_c .

To explain the origin of this wide window of stability, we rewrite the Floquet unitary as

$$U_F(\theta, \tau) = e^{-i\varepsilon N} X = e^{-i\varepsilon \sum_{\langle ij \rangle} \sigma_i^z \sigma_j^z} X,$$

$$X \equiv e^{-i\pi N} e^{-i\tau H_{\text{PXP}}}.$$
(G.16)

Here, we make two important conceptual observations. First, the operator X is the Floquet unitary at the special point $\theta = \pi$, and as such it squares to one, i.e. $X^2 = \mathbb{I}$. Second, we notice that since we operate within the blockaded subspace, $\sum_{\langle ij \rangle} n_i n_j = 0$, we can rewrite $\sum_i n_i = \sum_{\langle ij \rangle} \sigma_i^z \sigma_j^z + \text{const.}$, justifying the second equality up to an irrelevant global phase. This Floquet unitary is of the form studied in the context of discrete time crystals (DTC) where conventionally X is a global spin-flip $\prod_i \sigma_i^x$ [209, 208, 349]. Importantly, however, X in our case is not a product of simple on-site operators but instead generates entangled dynamics.

However, X 's action implements an approximate global spin flip between the product states $|\text{AF}_1\rangle$ and $|\text{AF}_2\rangle$ when $\tau = \tau_c$, as a result of the special quantum scarring properties that H_{PXP} possesses. Furthermore, N serves to stabilize these states, as they are contained within the two dimensional blockaded ground state manifold of $\varepsilon \sum_{\langle ij \rangle} \sigma_i^z \sigma_j^z$ which is separated from the rest of the spectrum by a constant gap ε . Thus, loosely speaking, these two product states simply oscillate between one another (at stroboscopic times). The robustness of the subharmonic response across a wide parameter range is likely a result of the gap, which protects the oscillations against additional generic small perturbations to the drive (as long as they still respect the time-translation symmetry, i.e. the drive is still Floquet in nature) [344, 218]. Note that such analysis does not carry over to other initial product states, and so we do not expect robust many-body revivals from them.

The pulsed model also provides an avenue by which to understand the microstate plot in Fig. 10.3D in Chapter 10, which focuses on a 1D chain as we similarly do so below. The plot shows that driving induces stable oscillations between two states which have large populations in the antiferromagnetic states, but also acquires a significant amplitude in other microstates. Empirically, we observe that these additional microstates tend to have large values of N , and are hence microstates that have smallest energy difference from the $|AF\rangle$ states as measured by $\varepsilon \sum_{\langle ij \rangle} \sigma_i^z \sigma_j^z$. The pulsed model also predicts this behavior (Fig. G.12).

The interesting behavior of the pulsed model presented above warrants future, more detailed theoretical analysis. We emphasize however that many open questions remain, including: the role of significant next-nearest-neighbor interactions, the observed frequency range of locking (Fig. 10.4B of Chapter 10), the multi-peak structure seen in the driven lifetime of the edge-imbalanced decorated honeycomb (Fig. 10.3C of Chapter 10), and the 4th subharmonic response (Section G.3.3). Furthermore, although the pulsed model reproduces key phenomenological aspects, the precise connection between the pulsed driving and continuous driving implemented experimentally is left for future work.

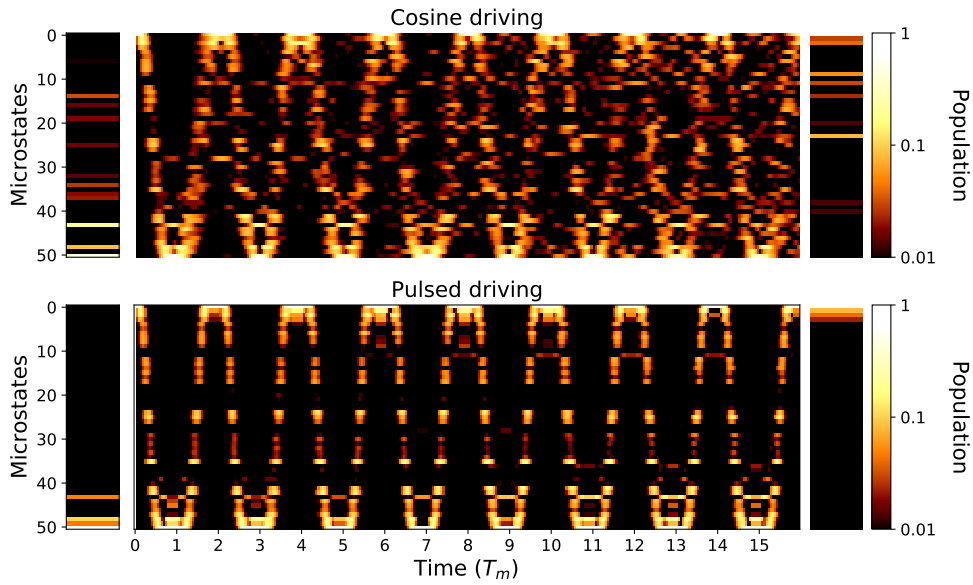


Figure G.12: Numerical simulations of microstate population dynamics. We plot the microstate distribution for (top) cosine driving ($\Delta_0 = \Delta_m = 0.55\Omega$) and (bottom) pulsed driving ($\varepsilon = 0.5$) at driving frequency $\omega_m = 1.15\Omega$ for the 1D $L = 9$ chain. The states are ordered by their Hamming distance from the $|\text{AF}_1\rangle$ state. The right and left columns depict a decomposition into microstates of the two symmetric and anti-symmetric superpositions of the two Floquet eigenstates with largest overlap with $|\text{AF}_1\rangle$, $|\text{AF}_2\rangle$ states respectively. Dynamics (center column) appear to be largely explained by these two eigenstates, as can be seen from the agreement between microstate populations at stroboscopic times. We note that the microstates populated at stroboscopic times, for both the simulations involving cosine and pulsed driving, are in qualitative agreement with those observed for the experimental protocol, as shown in Fig. 10.4D of Chapter 10.

G.5 TABULATION OF SYSTEM AND DRIVE PARAMETERS USED IN CHAPTER 10

Figure	Lattice	Geometry parameters	Quench / drive parameters
			$\Omega/2\pi = 4.2 \text{ MHz}$
Fig. 10.1B,C	Honeycomb	85 atoms, $V_0/2\pi = 9.1 \text{ MHz}$	$\Delta_0 = \Delta_{q,\text{opt}} = 0.15 V_0$
Fig. 10.2	Chain	9 atoms, $V_0 = \text{varied}$	$\Delta_0 = \Delta_{q,\text{opt}} = 0.017 V_0$
Fig. 10.2	Square	49 atoms, $V_0 = \text{varied}$	$\Delta_0 = \Delta_{q,\text{opt}} = 0.33 V_0$
Fig. 10.2	Honeycomb	85 atoms, $V_0 = \text{varied}$	$\Delta_0 = \Delta_{q,\text{opt}} = 0.15 V_0$
Fig. 10.2	Lieb	129 atoms, $V_0/2\pi = 9.1 \text{ MHz}$	$\Delta_0 = \Delta_{q,\text{opt}} = 0.20 V_0$
Fig. 10.2	Dec. hon. ^a	54 atoms, $V_0 = \text{varied}$	$\Delta_0 = \Delta_{q,\text{opt}} = 0.10 V_0$
Fig. 10.2	EIDH ^b	66 atoms, $V_0 = \text{varied}$	$\Delta_0 = \Delta_{q,\text{opt}} = 0.10 V_0$
Fig. 10.3B	Chain bare	9 atoms, $V_0/2\pi = 120 \text{ MHz}$	$\Delta_0 = \Delta_{q,\text{opt}} = 0.50 \Omega$
Fig. 10.3B	Chain drive	Same as bare	$\omega_m = 1.24 \Omega, \Delta_0 = 0.85 \Omega, \Delta_m = 0.98 \Omega$
Fig. 10.3C	Chain	9 atoms, $V_0/2\pi = 51 \text{ MHz}$	$\omega_m = \text{varied}, \Delta_0 = 0.55 \Omega, \Delta_m = 0.55 \Omega$
Fig. 10.3C	Honeycomb	41 atoms, $V_0/2\pi = 24 \text{ MHz}$	$\omega_m = \text{varied}, \Delta_0 = 0.87 \Omega, \Delta_m = 0.87 \Omega$
Fig. 10.3C	EIDH ^b	66 atoms, $V_0/2\pi = 29 \text{ MHz}$	$\omega_m = \text{varied}, \Delta_0 = 0.78 \Omega, \Delta_m = 0.98 \Omega$
Fig. 10.3D	Chain bare	9 atoms, $V_0/2\pi = 51 \text{ MHz}$	$\Delta_0 = \Delta_{q,\text{opt}} = 0.21 \Omega$
Fig. 10.3D	Chain drive	Same as bare	$\omega_m = 1.15 \Omega, \Delta_0 = 0.55 \Omega, \Delta_m = 0.55 \Omega$
Fig. 10.3E	Chain bare	16 atoms, $V_0/2\pi = 51 \text{ MHz}$	$\Delta_0 = \Delta_{q,\text{opt}} = 0.21 \Omega$
Fig. 10.3E	Chain drive	Same as bare	$\omega_m = 1.20 \Omega, \Delta_0 = 0.55 \Omega, \Delta_m = 0.55 \Omega$
Fig. 10.4A,B	Chain	9 atoms, $V_0/2\pi = 51 \text{ MHz}$	$\omega_m = \text{varied}, \Delta_0 = 0.55 \Omega, \Delta_m = 0.55 \Omega$
Fig. 10.4C	Chain	9 atoms, $V_0/2\pi = \text{varied}$	$\omega_m = \text{varied}, \Delta_0 = 0.55 \Omega, \Delta_m = 0.55 \Omega$
Fig. 10.4C	Honeycomb	41 atoms, $V_0/2\pi = \text{varied}$	$\omega_m = \text{varied}, \Delta_0 = 0.87 \Omega, \Delta_m = 0.87 \Omega$
Fig. 10.4D	Chain	3 - 17 atoms, $V_0/2\pi = 51 \text{ MHz}$	$\omega_m = \text{varied}, \Delta_0 = 0.55 \Omega, \Delta_m = 0.55 \Omega$
Fig. 10.4D	Honeycomb	9 - 200 atoms, $V_0/2\pi = 17 \text{ MHz}$	$\omega_m = \text{varied}, \Delta_0 = 0.87 \Omega, \Delta_m = 0.87 \Omega$

Table G.1: Tabulation of system and drive parameters used in Chapter 10. ^aDec. hon. stands for decorated honeycomb. ^bEIDH stands for edge-imbalanced decorated honeycomb. Varied indicates that this parameter is varied in the plot.

G.6 TABULATION OF 51-DIMENSIONAL HILBERT SPACE FROM FIGURE 10.3D

Index	Microstate	Index	Microstate	Index	Microstate
1	1 0 1 0 1 0 1 0 1	18	0 0 1 0 1 0 0 0 0	35	0 0 1 0 0 1 0 0 0
2	1 0 0 0 1 0 1 0 1	19	0 0 0 1 0 0 1 0 1	36	0 0 0 0 0 0 0 0 0
3	1 0 1 0 1 0 1 0 0	20	0 1 0 0 1 0 0 0 1	37	0 0 1 0 0 1 0 1 0
4	1 0 1 0 0 0 1 0 1	21	0 1 0 0 0 0 1 0 1	38	0 1 0 1 0 0 0 0 1
5	0 0 1 0 1 0 0 0 1	22	0 1 0 0 1 0 1 0 0	39	1 0 0 1 0 1 0 0 0
6	1 0 0 0 0 0 1 0 1	23	0 0 1 0 0 1 0 0 1	40	1 0 0 1 0 0 0 1 0
7	0 0 1 0 1 0 1 0 0	24	1 0 0 0 0 1 0 0 1	41	0 1 0 0 1 0 0 1 0
8	1 0 0 0 1 0 0 0 1	25	0 0 0 0 1 0 0 0 0	42	0 0 0 0 0 0 0 1 0
9	1 0 1 0 0 0 1 0 0	26	1 0 0 0 0 0 0 0 0	43	0 0 0 1 0 0 0 0 0
10	0 0 0 0 1 0 1 0 1	27	0 0 0 0 0 0 1 0 0	44	0 1 0 1 0 1 0 0 1
11	0 1 0 0 1 0 1 0 1	28	1 0 1 0 0 1 0 1 0	45	0 0 0 0 0 1 0 1 0
12	1 0 1 0 0 1 0 0 1	29	1 0 0 1 0 1 0 0 1	46	0 1 0 0 0 0 0 1 0
13	1 0 0 0 0 0 0 0 1	30	0 0 0 0 1 0 0 1 0	47	0 1 0 0 0 1 0 0 0
14	1 0 0 0 0 0 1 0 0	31	0 1 0 0 0 0 0 0 1	48	0 0 0 1 0 1 0 0 0
15	1 0 0 0 1 0 0 0 0	32	1 0 0 1 0 0 0 0 0	49	0 1 0 0 0 1 0 1 0
16	0 0 1 0 0 0 1 0 0	33	0 0 1 0 0 0 0 1 0	50	0 1 0 1 0 1 0 0 0
17	0 0 0 0 0 0 1 0 1	34	1 0 0 0 0 1 0 0 0	51	0 1 0 1 0 1 0 1 0

Table G.2: Tabulation of microstates in Fig. 10.3D. For the 9-atom chain, the 2^9 -dimensional Hilbert space is first reduced to 89 states by discarding states that violate the Rydberg blockade constraint, giving rise to the so-called “constrained Hilbert space”. The Hilbert space dimension is then further reduced from 89 to 51 by grouping left-right symmetric pairs of microstates. Finally, the microstates are ordered by $n_A - n_B$, or equivalently by Hamming distance from $|\text{AF}_1\rangle$, and within a given cluster of $n_A - n_B$, states are then ordered by $n_A + n_B$ (although this ordering is still not completely unique). “0” represents ground state $|g\rangle$ and “1” represents Rydberg state $|r\rangle$.

H

Supplementary information for Chapter 11

H.1 EXPERIMENTAL SYSTEM

Our experiments make use of the second generation of the atom array setup, described previously in [31]. In our experiments, atoms are excited to Rydberg states using a two-photon excitation scheme, consisting of a 420 nm laser from the ground state $5S_{1/2}$ to the intermediate state $6P_{3/2}$, and a 1013 nm laser from the intermediate state to the Rydberg state $70S_{1/2}$.

Details of both laser systems are presented in Chapter 3.

In the present work, we tune the lasers to have a detuning of $\delta = 2\pi \times -450$ MHz from the intermediate $6P_{3/2}$ state, where the 420 nm laser is red-detuned from the intermediate

state. The 1013 nm laser is always applied at maximum optical power (~ 3 W total on the atoms), and results in a single-photon Rabi frequency $\Omega_{1013} = 2\pi \times 50$ MHz. The 420 nm laser power varies depending on the protocol. During the quasi-adiabatic preparation of the dimer phase, we apply the 420 nm light at low power, which reduces the two-photon Rabi frequency and therefore increases the blockade radius to the target $R_b/a = 2.4$. This low power setting consists of a total of ~ 0.5 mW on the atoms, with a single-photon Rabi frequency $\Omega_{420} = 2\pi \times 25$ MHz. During the quasi-adiabatic preparation, we therefore have a two-photon Rabi frequency of $\Omega = \Omega_{420}\Omega_{1013}/2\delta = 2\pi \times 1.4$ MHz (details of $\Omega(t)$ and $\Delta(t)$ used for state preparation are reported in Fig. H.1). Under these conditions, we estimate the rate of off-resonant scattering from $|g\rangle$ due to the 420 nm laser to be $\sim 1/(150 \mu\text{s})$, and the decay rate of $|r\rangle$ to be $1/(80 \mu\text{s})$ (including radiative decay, blackbody stimulated transitions, and off-resonant scattering from the 1013 nm laser). State detection fidelity for both ground state and Rydberg atoms is 99% [31].

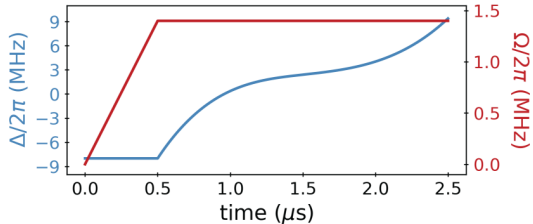


Figure H.1: Quasi-adiabatic state preparation. $\Omega(t)$ and $\Delta(t)$ used for state preparation. To probe the phase diagram at different Δ , we stop the cubic sweep at different endpoints and correspondingly turn off Ω .

To measure the X operator, following the dimer phase preparation, we apply short quenches at significantly higher blue power. This high power setting consists of a maximum power of ~ 100 mW on the atoms, corresponding to a single-photon Rabi frequency $\Omega_{420} = 2\pi \times 360$ MHz. The corresponding two-photon Rabi frequency is $\Omega = 2\pi \times 20$ MHz, and $R_b/a = 1.53$. In this configuration, the 420 nm laser introduces a substantially larger light shift on the Ryd-

berg transition of $2\pi \times 36$ MHz. To avoid systematic offsets in the effective detuning from resonance, we separately calibrate the resonance condition at both low power and high power. The 420 nm laser amplitude is controlled using a double-pass AOM with a rise time of ~ 10 ns. In the ideal model for the quench, the optimal quench time would be $\tau = 4\pi/(3\Omega\sqrt{3}) = 19$ ns for the high-power Rabi frequency. However, the 10 ns rise time extends the necessary quench time to the experimentally optimized ~ 30 ns. We note that during the rise time, the laser power is increasing to its maximum value, leading to deviations from the ideal model for the quench; this may contribute to a reduction in the measured value of X -string parities.

Throughout this work, measurements of Z and X parities are averaged over identical loops, including reflection and rotation symmetries, across the system. However, loops which touch the edge of the system are excluded to avoid boundary effects. Error bars are calculated as the standard error of the mean as $\sigma(P)/\sqrt{R}$, where R is the number of repetitions and $\sigma(P)$ is the standard deviation of the parity P , which is the average over all identical loops for each repetition.

H.2 BASIS ROTATION FOR X AND Z PARITY LOOPS

The basis rotation used to measure X parity loops is applied with a reduced blockade radius which, in the ideal limit, removes interactions between separate triangles while maintaining a hard blockade constraint on Rydberg excitations within single triangles. The rotation can therefore be understood by its action on individual fully-blockaded triangles. The Hilbert space for each triangle is four-dimensional, allowing for either zero Rydberg excitations, or one Rydberg excitation on any of the three links. Taking $\triangle, \triangle_{\text{red}}, \triangle_{\text{green}}, \triangle_{\text{blue}}$ as the basis states, the Hamiltonian for the quench in the limit of perfect intra-triangle blockade is described by the following matrix:

$$H = \frac{\Omega}{2} \begin{pmatrix} 0 & -i & -i & -i \\ i & 0 & 0 & 0 \\ i & 0 & 0 & 0 \\ i & 0 & 0 & 0 \end{pmatrix} \quad (\text{H.1})$$

The basis rotation shown in Fig. 11.3C of Chapter 11, which relates X and Z parity under evolution through this quench Hamiltonian (H.1), was proven in Ref. [193] by direct computation. Here we provide an alternative derivation. Firstly, we note that the Z operator acting on the upper two edges of a triangle () and the X operator acting on the lower edge of a triangle (), defined in Figs. 11.2 and 11.3 of Chapter 11, are given by:

$$\triangle_{\text{red}} = \begin{pmatrix} 1 & 0 & 0 & 0 \\ 0 & 1 & 0 & 0 \\ 0 & 0 & -1 & 0 \\ 0 & 0 & 0 & -1 \end{pmatrix} \quad (\text{H.2})$$

$$\triangle_{\text{blue}} = \begin{pmatrix} 0 & -1 & 0 & 0 \\ -1 & 0 & 0 & 0 \\ 0 & 0 & 0 & 1 \\ 0 & 0 & 1 & 0 \end{pmatrix} \quad (\text{H.3})$$

The X and Z parity operators can be mutually diagonalized by changing to an appropriate symmetrized basis:

Basis state		
$ 0\rangle = \triangle + \triangle_{\text{red}}$	+1	-1
$ 1\rangle = \triangle_{\text{red}} + \triangle$	-1	+1
$ 2\rangle = \triangle - \triangle_{\text{red}}$	+1	+1
$ 3\rangle = \triangle_{\text{red}} - \triangle$	-1	-1

In this basis, the quench Hamiltonian (H.1) is expressed as:

$$H = \frac{\Omega}{2} \begin{pmatrix} 0 & i & -i & 0 \\ -i & 0 & -i & 0 \\ i & i & 0 & 0 \\ 0 & 0 & 0 & 0 \end{pmatrix} \quad (\text{H.4})$$

This Hamiltonian generates cyclic permutations among the basis states $|0\rangle$, $|1\rangle$, and $|2\rangle$, while leaving $|3\rangle$ invariant. The permutation $|0\rangle \rightarrow |1\rangle \rightarrow |2\rangle \rightarrow |0\rangle$ maps the  eigenvalue to the  eigenvalue for each initial state. Moreover, the invariant state $|3\rangle$ has both  =  = -1 , so it automatically satisfies the target eigenvalue mapping. Thus, after an appropriate evolution time corresponding to a single cyclic permutation ($\tau = \frac{4\pi}{3\sqrt{3}\Omega}$), all  eigenvalues have been mapped to  eigenvalues, which is diagonal in the measurement basis. Formally, this can be expressed as:

$$\triangle_{\text{wavy}} = e^{iH\tau} \triangle_{\text{red}} e^{-iH\tau} \quad (\text{H.5})$$

We further note that this relationship holds also for parity operators defined on other sides of the triangle, e.g.,  = $e^{iH\tau} \triangle_{\text{red}} e^{-iH\tau}$. Large X parity strings or loops can be decomposed in terms of their action on individual triangles, and since the basis rotation acts on each triangle individually, this extends the mapping from X strings to corresponding dual Z strings in the rotated basis, as illustrated in Fig. H.2.

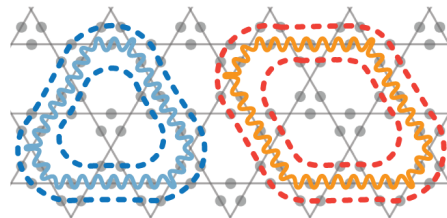


Figure H.2: Dual Z and X loops. Examples of dual Z loops (dashed lines) to closed X loops (solid wiggly lines).

H.3 SUPPLEMENTAL EXPERIMENTAL DATA

H.3.1 MEAN RYDBERG DENSITY AND BOUNDARY EFFECTS

After preparing the dimer phase for $\Delta/\Omega \sim 4$, we observe a Rydberg excitation density in the bulk of $\langle n \rangle \sim 1/4$. The sites close to the boundary of the system, however, are dominated by edge effects. In Fig. H.3, we show the Rydberg excitation density site-by-site, and demonstrate that the edge effects only permeate two to three layers into the bulk before the $\langle n \rangle \sim 1/4$ plateau is reached. In arrays with a topological defect, the hole forms an inner boundary and similarly induces edge effects (Fig. H.3C,D). These observations allow us to determine the minimum system sizes that may be used such that the physics of the system is not dominated by boundary effects, resulting in our choice of the 219-atom arrays used in this work.

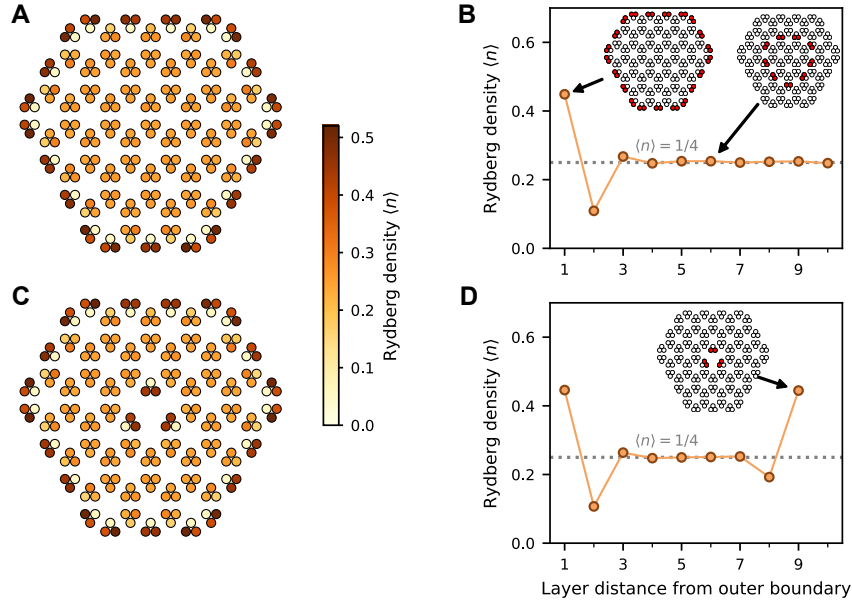


Figure H.3: Site-by-site mean Rydberg density. We measure the mean Rydberg excitation density $\langle n \rangle$ site-by-site in the dimer phase with $\Delta/\Omega = 4$ for both full arrays (**A**) as well as arrays with a hole (**C**). (**B,D**) We then plot the corresponding mean density layer-by-layer as a cross-section from the edge into the bulk, showing that within the outer two to three layers, the bulk settles into the $\langle n \rangle \sim 1/4$ phase.

H.3.2 LACK OF SPATIAL ORDER WITHIN SPIN-LIQUID PHASE

The lack of spatial order in the spin-liquid phase is a key feature that separates this phase from possible nearby solid phases. At the simplest level, spatial order can be assessed by looking at individual projective measurements of the atomic states in the ensemble. We show three examples of such snapshots in Fig. H.4, where the measured states of individual atoms are represented as small circles on the links of the kagome lattice, filled or unfilled indicating a Rydberg state or a ground state, respectively. In the mapping to a monomer-dimer model, we can alternatively consider the vertices of the kagome lattice in terms of how many adjacent Rydberg excitations (dimers) are present. In practice, vertices can have zero attached dimers (so-called monomers), a single attached dimer (corresponding to an ideal dimer covering), or more attached dimers (violating the long-range blockade constraint). In Fig. H.4, we additionally color each vertex according to the number of such attached dimers. The widespread abundance of vertices connected to a single dimer (Fig. 11.1E and snapshots from Fig. H.4) signifies occupation of the dimer phase.

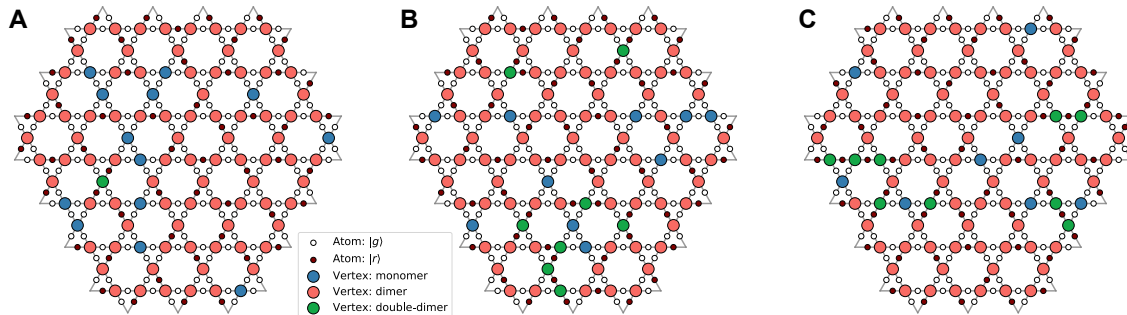


Figure H.4: Snapshots in the dimer phase. Three sample experimental realizations within the dimer phase at $\Delta/\Omega = 4.3$. The binarized atom readout is shown by small circles on the links of the kagome lattice, with open circles denoting $|g\rangle$ and filled circles denoting $|r\rangle$. Vertices of the kagome lattice (large circles) are colored according to the number of adjacent atoms in $|r\rangle$ to visually accentuate which parts of the system are properly covered with dimers.

Moreover, spatial correlations can be used to look for solid-type spatial order (Fig. H.5).

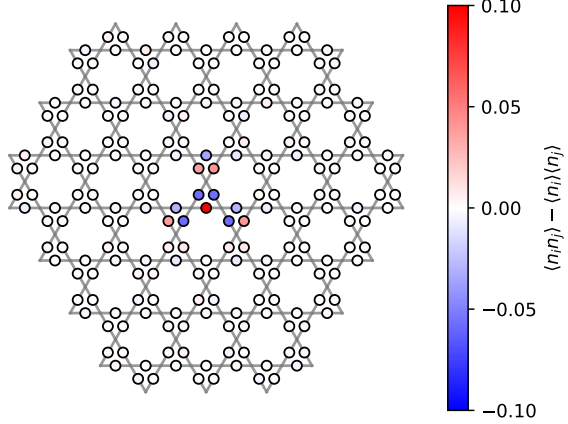


Figure H.5: Density correlations between individual Rydberg excitations. We directly measure the Rydberg density-density correlator $\langle n_i n_j \rangle - \langle n_i \rangle \langle n_j \rangle$ between a central atom and all other atoms in the system. We observe anticorrelations between the central atom and the other two atoms in the same triangle, as well as with atoms in the adjacent triangles, given by the choice of blockade radius R_b . Longer range correlations vanish. This data was taken at $\Delta/\Omega = 4.3$.

We measure Rydberg density-density correlations on the atomic array and find non-vanishing correlations for atoms within a single triangle or between adjacent triangles, with vanishing correlations over longer distances. This observation confirms the lack of spatial order in the dimer phase we prepare.

H.3.3 PHASE DEPENDENCE OF QUENCH

The quench which induces the basis rotation for measuring X parity is implemented by rapidly switching the laser detuning to $\Delta_q = 0$ following the preparation of the dimer phase, and simultaneously changing the phase of the laser field by $\pi/2$. This choice of phase approximately maximizes the X parity signal, as measured by applying the same quench duration but with variable phase (Fig. H.6A).

The phase change can be understood by interpreting it as evolution under $\sum_i n_i$ for time ϕ , followed by a fixed-phase quench. Since the quench ultimately measures coherences between different components of the wavefunction, this phase change only matters insofar as it changes the relative phases between components. We note here that coherences between perfect dimer

coverings will be unchanged by the phase change, since all perfect dimer coverings have the same number of Rydberg excitations. A wavefunction which is the superposition of all perfect dimer coverings, then, would be insensitive to the choice of phase for the quench. However, in our system there is a finite density of both monomers and vertices with two attached dimers. An X loop crossing through a monomer creates a double-dimer at that vertex, and these types of component pairs are additionally included in our X parity measurements. Since the coupled states with a monomer and a double-dimer have different numbers of Rydberg excitations, these coherences *are* phase-sensitive. Comparing the measured X parity for $\phi = \pi/2$ and $\phi = 0$ as we scan across the phase diagram (Fig. H.6B), we find that the first has larger amplitude and extends more strongly into the trivial phase, consistent with the expectation from theoretical calculations [193].

H.3.4 Z PARITY MEASUREMENTS WITH IMPROVED STATE PREPARATION

All data shown in Chapter 11 is taken with intermediate detuning $\delta = 2\pi \times -450$ MHz (see Sec. H.1) for the two-photon Rydberg excitation. This choice is to enable our largest dynamic range of Rabi frequencies, which is crucial for being able to perform state preparation at low Ω and then apply the quench at large Ω with reduced blockade radius. Larger intermediate

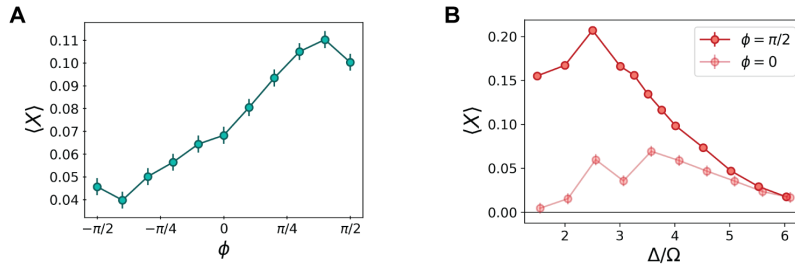


Figure H.6: Phase dependence of quench. (A) After preparing the dimer phase at $\Delta/\Omega = 4$, we quench for the pre-calibrated time τ with a variable quench phase and measure the resulting X loop parity around a single hexagon. (B) For fixed quench phase $\phi = \pi/2$ or $\phi = 0$, we measure the X parity after the pre-calibrated quench time as a function of the final detuning of the cubic sweep. The data for $\phi = \pi/2$ is reproduced from Fig. 11.3F of Chapter 11.

detuning would require performing state preparation at an even lower initial Rabi frequency, where we observe worse results. However, the small intermediate detuning introduces stronger decoherence due to increased spontaneous emission from the intermediate state. To supplement these results, we additionally perform state-preparation and measure Z parity at an increased intermediate detuning of $\delta = 2\pi \times 1$ GHz. To further optimize this state preparation, we use a larger Rabi frequency $\Omega = 2\pi \times 1.7$ MHz and a smaller lattice spacing $a = 3.7$ μ m, which should improve adiabaticity during the preparation. In this configuration, we indeed observe larger Z loop parities (Fig. H.7), but we cannot measure corresponding X loop parities. This highlights that the large dynamical range required for the measurement of the X operator is one of the main technical challenges of this experimental work. At the same time, it shows that with more available laser power for Rydberg excitation, the quality of state preparation can be improved by working at this increased intermediate detuning and higher Rabi frequencies (and with smaller lattice spacings to achieve the same blockade radius).

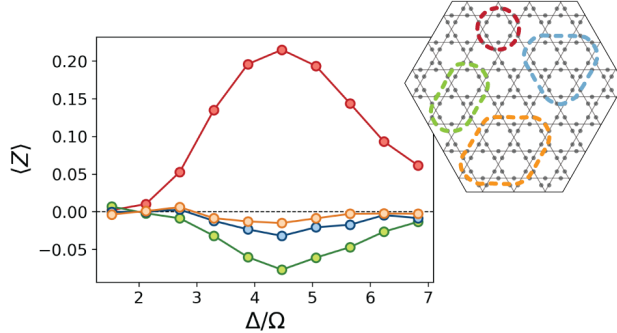


Figure H.7: Z loop parity with improved state preparation. We measure Z on closed loops with a larger intermediate state detuning for the two-photon Rydberg excitation to reduce spontaneous emission rates, and with a larger Rabi frequency during the state preparation. We observe larger parities than in the comparable Fig. 11.2 of Chapter 11.

H.3.5 CORRELATIONS BETWEEN PARITY LOOPS

String operators are used in this work to assess long-range topological order. However, the large loops which are studied can be decomposed into the product of smaller loops around sub-regions: for example, X loops can be decomposed into the product of enclosed hexagons. To demonstrate that the parity measured on large loops is indeed indicative of long-range order, rather than emerging from the ordering of each hexagon individually, we extract correlations between the separate parity loops which comprise larger loops.

We first study parity loops which enclose adjacent hexagons of the kagome lattice. The minimal such X parity loop is exactly equal to the product of the parity around the two enclosed hexagons. The connected correlator of the parity around these two inner hexagons is

$$G_X^{(2)} = \langle \text{Diagram}_1 \text{Diagram}_2 \rangle - \langle \text{Diagram}_1 \rangle \langle \text{Diagram}_2 \rangle \quad (\text{H.6})$$

Similarly, Z loops which enclose two hexagons decompose into the product of Z parity around the two hexagons, multiplied additionally by the parity around the central interior vertex (which should always be -1 in a dimer covering). We define the analogous two-hexagon connected correlator for Z as

$$G_Z^{(2)} = \langle \text{Diagram}_1 \text{Diagram}_2 \rangle - \langle \text{Diagram}_1 \rangle \langle \text{Diagram}_2 \rangle \quad (\text{H.7})$$

Higher-order connected correlations between three adjacent hexagons which form a triangle further highlight nonlocal correlations in this system. We define the connected three-point

correlator [350] which subtracts away contributions from underlying two-point correlations as

$$G_X^{(3)} = \langle \text{hexagon}_1 \text{hexagon}_2 \text{hexagon}_3 \rangle - G_{X,12}^{(2)} \langle \text{hexagon}_3 \rangle - G_{X,23}^{(2)} \langle \text{hexagon}_1 \rangle - G_{X,31}^{(2)} \langle \text{hexagon}_2 \rangle - \langle \text{hexagon}_1 \rangle \langle \text{hexagon}_2 \rangle \langle \text{hexagon}_3 \rangle \quad (\text{H.8})$$

where $G_{X,ij}^{(2)}$ is the connected correlator for hexagons i,j . Third order connected correlators for Z parity are analogously defined.

As shown in Fig. H.8, we observe nonzero two-hexagon and three-hexagon connected correlations within the dimer phase region, indicating that the parity measured on double-hexagon and triple-hexagon loops does not emerge from independently determined parity around each interior subregion, but instead emerges due to nontrivial correlations over longer length scales.

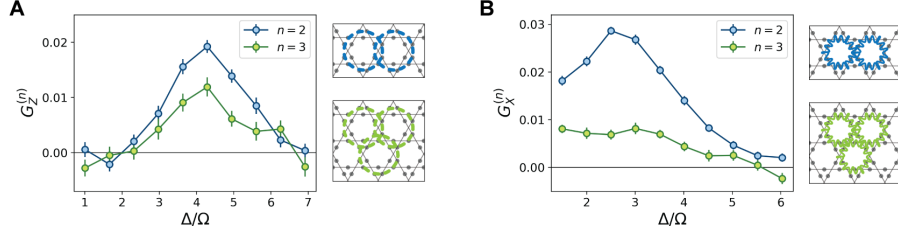


Figure H.8: Correlations between parity loops. We measure two-point and three-point connected correlations between parity around adjacent hexagons. **(A)** Z parity correlations between loops which enclose pairs and triplets of adjacent hexagons. **(B)** X parity correlations between pairs and triplets of adjacent hexagons.

H.3.6 QUASIPARTICLE EXCITATIONS

Within the dimer-monomer model, quasiparticle excitations of two types are created by the application of open X and Z strings: these are the electric (e) and magnetic (m) anyons, respectively. Open X strings create monomers (or double-dimers) at their endpoints, and thus e -anyons are identified as defects in the dimer covering. Open Z strings on the other hand impart a relative phase between various dimer configurations, corresponding to m -anyons. To un-

derstand m -anyons, we first note that all dimer coverings in the QSL superposition are related to one another by the application of properly chosen closed X loops (first row of Fig. H.9). An open Z string applied to the QSL state, then, results in different dimer coverings acquiring \pm phase factors according to the number of dimers crossed by the string. Whenever two dimer configurations are related by a closed X loop which encloses one of the endpoints of the Z string, they acquire opposite signs (Fig. H.9). After the application of the open Z string, then, $\langle X \rangle$ is inverted for any closed loop around one endpoint of the Z string, analogous to how $\langle Z \rangle$ around the endpoint of an open X string (a defect) is inverted. Since open Z strings terminate in the hexagons of the kagome lattice, we associate the resulting magnetic (m) anyons as living on these hexagons, and the X parity around hexagons therefore detects the presence of m -anyon excitations.

In Fig. H.10 we report the Z and X loop parities rescaled with area and perimeter law for different values of Δ in the relevant range of detunings. We observe that the excellent perimeter law scaling of X reported in Fig. 11.4I of Chapter 11 extends over the entire range of Δ . For Z instead we find that the initial approximate area law scaling converges towards a perimeter law for large loops.

We can shed light on the scaling behavior observed in the experiment by comparing it with the expected scaling from theory. Let us first note that the generic equilibrium expectation

$$\begin{aligned} |\psi_{QSL}\rangle &= \left| \text{dimer configuration } 1 \right\rangle + \left| \text{dimer configuration } 2 \right\rangle + \left| \text{dimer configuration } 3 \right\rangle + \dots \\ Z_o |\psi_{QSL}\rangle &= \left| \text{dimer configuration } 1' \right\rangle + \left| \text{dimer configuration } 2' \right\rangle + \dots = - \left| \text{dimer configuration } 1'' \right\rangle + \left| \text{dimer configuration } 2'' \right\rangle - \left| \text{dimer configuration } 3'' \right\rangle + \dots \end{aligned}$$

Figure H.9: Magnetic anyons. The dimer states contained in $|\psi_{QSL}\rangle$ are connected to each other by the application of X on closed loops. When an open Z string acts on the superposition, the dimer states connected by an open loop that encloses one end of the string (X_1) acquire opposite signs. The m -anyons generated at the endpoints of the string are then detected by X loops that enclose one of them, e.g. $\langle X_1 \rangle = -1$, while $\langle X_2 \rangle = +1$ is unperturbed.

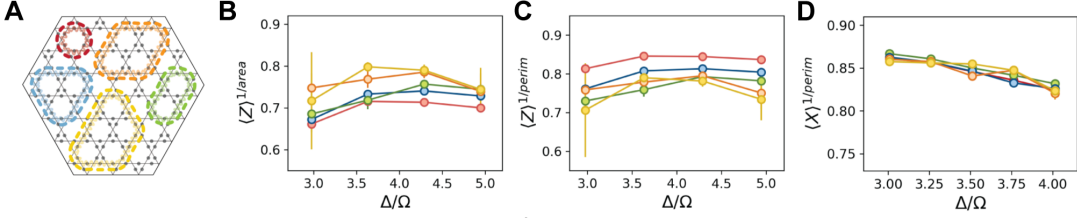


Figure H.10: Scaling of Z and X parities with the loop size. We calculate the rescaled parities $\langle Z \rangle^{1/\text{area}}$ (**B**), $\langle Z \rangle^{1/\text{perim}}$ (**C**) and $\langle X \rangle^{1/\text{perim}}$ (**D**) for the different loop sizes in (**A**). While for the X operator we observe a very good perimeter law scaling on the entire range of detunings, for Z we observe an approximate area law scaling for small loop sizes that finally converges towards a perimeter law scaling.

for both string operators is a perimeter law scaling [245]. This can be seen as a consequence of the mutual statistics of e - and m -anyons: since there will be virtual fluctuations of both anyons, these will induce correlations* for anyons of the other type, leading to a perimeter law. This generic expectation of a perimeter law is well-known in the (lattice) gauge theory community, and can be related to the phenomenon of string breaking [351]. Experimentally, we observe a perimeter law for X -loops and an (approximate) area law for Z -loops (with substantial deviations for larger loop sizes). This can be understood by noting that we enter the QSL-like state from the trivial phase, which can be interpreted as a condensate of e -anyons (i.e., both closed and open X -strings give nonzero correlations): the perimeter law for closed X strings is thus already present in the trivial phase and naturally persists into the QSL-like state (while correlations for the *open* X -strings vanish). In contrast, the Z -correlations are absent in the trivial phase proximate to the QSL: these are only developed at the quantum critical point, and since we sweep through this at a finite rate, the Z -loop correlations are only developed over a characteristic length scale, implying an area law. Numerically, we indeed confirm that Z -loop correlations are significantly enhanced upon increasing preparation time (see Sec. H.4),

*To clarify this further, we note that the monomers (and double-dimers) visible in the experimental snapshots need not to directly correspond to physical excitations, since the ground state will have so-called ‘virtual’ fluctuations when it is not in an idealized fixed-point state. These can be interpreted as correlated e -anyons. In contrast, in an ideal \mathbb{Z}_2 spin liquid, *physical* e -anyons will be uncorrelated—since this is a defining property of the deconfined phase where e -anyons move independently at sufficiently large distances.

consistent with our observations in Fig. H.7. We note that this imperfect generation of Z -loop correlations can be equivalently interpreted as generating a density of e -anyon excitations. Dynamically inducing the onset of a QSL and possible meta-stable states are rich phenomena which deserve further detailed study.

H.3.7 ADDITIONAL DATA FOR ARRAYS WITH NONTRIVIAL TOPOLOGY

The distinction between two distinct topological sectors can be better understood by looking at the transition graphs between pairs of dimer states [352]. These are built by superimposing two dimer coverings and removing the overlapping dimers (Fig. H.11). The dimer states belong to opposite topological sectors if the remaining dimers form a closed loop around the hole, indicating the set of non-local moves required to transform one into the other.

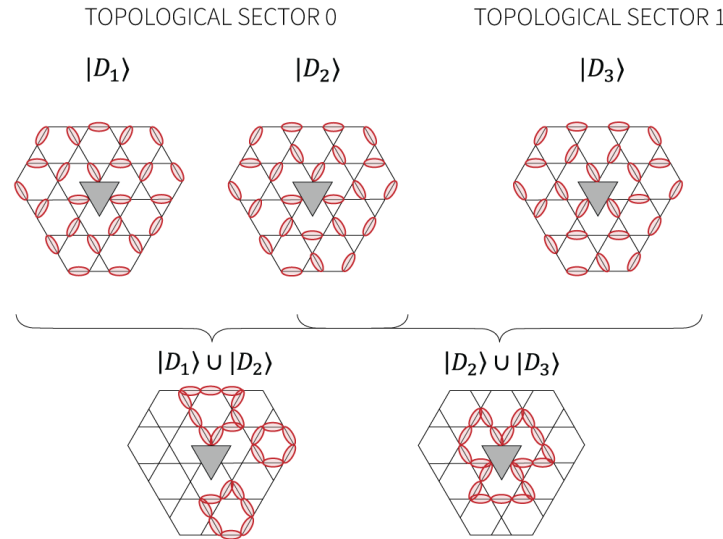


Figure H.11: Distinction between topological sectors. To determine if the three dimer coverings $|D_1\rangle, |D_2\rangle$ and $|D_3\rangle$ belong to the same or opposite topological sectors, we build the transitions graphs $|D_1\rangle \cup |D_2\rangle$ and $|D_2\rangle \cup |D_3\rangle$. In the latter we see that the dimers form a closed loop around the hole, highlighting that the two states belong to opposite sectors.

To demonstrate that the removal of three atoms at the center of the array creates an actual

inner boundary, we measure the Z and X operators on strings with both endpoints on the inner or outer boundaries (Fig. H.12). In the relevant range of detunings ($3.3 \lesssim \Delta/\Omega \lesssim 4.5$) we measure a finite $\langle Z \rangle$ and a vanishing $\langle X \rangle$ in both cases, indicating that the central hole also generates an effective boundary. This also confirms that the boundaries that are naturally created in our system are of the m -type, i.e. m -anyons localize on it (hence the finite $\langle Z \rangle$) [193].

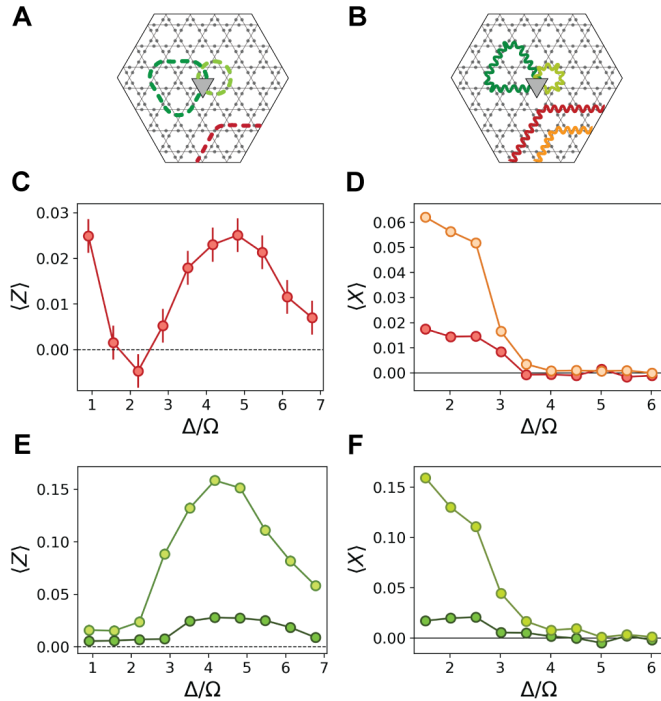


Figure H.12: Boundary-to-boundary string operators. We measure the Z (A) and X (B) operators on open strings connecting two points on the outer (C,D) or inner (E,F) boundaries of the array. Observing the same features for both, we confirm that the small central hole does indeed create an effective inner boundary.

H.4 NUMERICAL STUDIES

Below, we report on numerical studies of the Rydberg atom array. We first discuss the zero temperature equilibrium phase diagram, established using density-matrix-renormalization-group (DMRG). Next, we directly simulate the quasi-adiabatic sweep, using both exact diag-

onalization and dynamical DMRG calculations. To minimize boundary effects due to limitations of numerically accessible system sizes, these calculations are performed on a torus (exact diagonalization) or on an infinite cylinder (DMRG).

H.4.1 GROUND STATE PHASE DIAGRAM

To a first approximation, the Hamiltonian in Chapter 11 can be described by an effective ‘PXP’ model [189]

$$H_{\text{PXP}} = \sum_i \left(\frac{\Omega}{2} P \sigma_i^x P - \Delta n_i \right). \quad (\text{H.9})$$

Here, P is a projector onto $|g\rangle$ for all sites within the blockade radius R_b of the site i . This model approximates the the Rydberg Hamiltonian by treating all pairwise interaction energies as either infinite, if within the blockade radius, or zero if beyond. For $R_b = 2.4a$ (as in Chapter 11), this corresponds to blockading the first three interaction distances. In Ref. [193], it was shown that this ‘blockade model’ hosts a \mathbb{Z}_2 spin liquid for $1.5 \lesssim \Delta/\Omega \lesssim 2$.

To include the full van der Waals interactions, we incorporate $V(r) = \Omega(R_b/r)^6$ in the microscopic model within a truncation distance R_{trunc} (beyond which $V(r) = 0$), with $R_b = 2.4a$. On a technical note, we replace the very strong nearest-neighbor repulsion $V(a)/\Omega = (R_b/a)^6 \approx 191$ by $V(a) = +\infty$ by working in an effectively constrained model where any triangle can host at most one dimer. The DMRG [246, 318] simulations on cylinder geometries [342] were performed using the Tensor Network Python (TeNPy) package developed by Johannes Hauschild and Frank Pollmann [247]. A bond dimension $\chi = 1000$ was sufficient to guarantee convergence for the systems and parameters considered.

For intermediate truncation distances, we find a spin liquid in the ground state phase diagram. In particular, taking $R_{\text{trunc}} = \sqrt{7}a \approx 2.65a$, we include four nearest neighbor interactions (i.e., one more than the blockade model): every site is coupled to 10 other sites. The re-

sulting phase diagram is shown in Fig. H.13(A–C). This is obtained using the DMRG method applied to an infinitely-long cylinder XC-8 (see Ref. [193] for details about cylinder geometries of the kagome lattice). The presence of a spin liquid is determined based on the behavior of the string observables, as in the experiment. Moreover, we observe topologically degenerate ground states on the cylinder [193].

However, we find that the spin liquid is destabilized upon including even longer range interactions: for $R_{\text{trunc}} = \sqrt{7}a$ we find a spin liquid for $3.4 \lesssim \Delta/\Omega \lesssim 3.62$, for $R_{\text{trunc}} = 4a$ we find that this has shrunken down to $3.45 \lesssim \Delta/\Omega \lesssim 3.52$, and for $R_{\text{trunc}} = 6a$ there is no intervening spin liquid. Fig. H.13(D–F) shows a direct first order transition at $\Delta/\Omega \approx 3.47$ from the trivial phase to a valence bond solid (VBS). These results are summarized in Fig. H.14. We note that these conclusions are strictly valid for the Hamiltonian in eq. (11.1) of Chapter 11 and might be affected by additional terms, associated, e.g., with multi-body Rydberg interactions. Moreover, other modified ruby lattice geometries still support a ground state

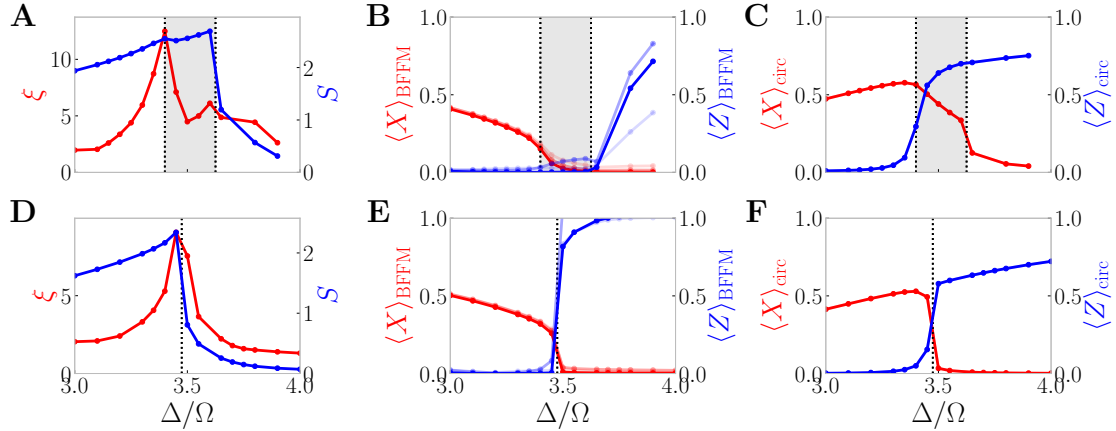


Figure H.13: Ground state phase diagram of the link-kagome model for two truncation distances. All data is for the van der Waals model with blockade radius $R_b = 2.4a$ on an XC-8 cylinder. (A–C) For truncation distance $R_{\text{trunc}} = \sqrt{7}a$, we observe a spin liquid (gray shaded area) in between the trivial phase and valence bond solid (VBS). In particular, it is characterized by a large entanglement plateau (S is the entanglement entropy upon bipartitioning the cylinder and ξ is the correlation length), vanishing of the BFFM string order parameters (darker lines correspond to larger strings) and nonzero loop variables ($\langle Z \rangle_{\text{circ}}$ and $\langle X \rangle_{\text{circ}}$) around the circumference—the signs of the latter label topologically degenerate ground states, as explained in Ref. [193]. (D–F) By increasing the truncation distance to $R_{\text{trunc}} = 6a$, the intermediate spin liquid has vanished: there is now a direct first order transition from the trivial phase to a VBS.

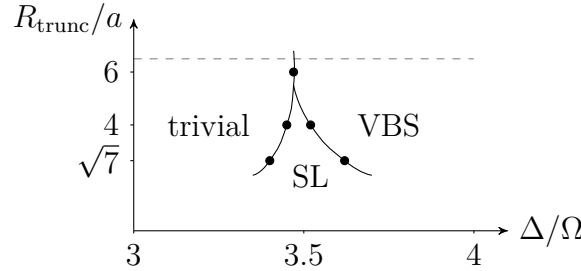


Figure H.14: Ground state phase diagram of the link-kagome model. Upon including all $V(r) \sim 1/r^6$ interactions (represented by the gray dashed line), we find that there is a direct phase transition from the trivial disordered phase to a crystalline-symmetry-breaking valence bond solid (VBS). However, the model is very close to a spin liquid phase: in fact, if we truncate the interactions to a distance R_{trunc} , we see that a \mathbb{Z}_2 spin liquid can arise in the ground state phase diagram (black dots denote phase transitions obtained via DMRG on the XC-8 cylinder). It is conceivable that dynamical state preparation is not sensitive to the longer-range couplings which destabilize the spin liquid; indeed, in Fig. H.16 we confirm that finite-time state preparation gives a state with properties characteristic of a spin liquid.

spin liquid phase even in the presence of these long range interactions [193]. At the same time, we find that quasi-adiabatic state preparation used in the experiment is far more robust to these effects. In particular, as we will now show, such state preparation avoids the first order transition to the VBS and instead results in a state reflecting correlations characteristic of a quantum spin liquid.

H.4.2 NUMERICAL SIMULATIONS OF DYNAMICAL STATE PREPARATION

The detuning ramps, $\Delta(t)$, which are employed to generate various states, are motivated by the adiabatic principle. For sufficiently slow ramps, the system follows the instantaneous ground state adiabatically [353]. In practice, finite coherence times limit the maximum evolution times, and require faster-than-adiabatic sweeps. This is expected to induce non-adiabatic processes, in particular close to the critical point, where the finite size gap is minimal [127, 146, 145].

To develop an understanding for the quantum many-body states that are generated in such quasi-adiabatic sweeps, we numerically solve the corresponding Schrödinger equation to ob-

tain the wavefunction $|\psi(t)\rangle = U(t)|\psi(0)\rangle$. We first discuss results from exact numerics on small system sizes of 36 atoms on a torus with 3×2 unit cells, using the simplified PXP-model (eq. (H.9)). Fig. H.15A shows the excitation spectrum of the instantaneous Hamiltonian throughout the sweep. Even though the system size is relatively small, the spectrum distinguishes a disordered region with a unique ground state at $\Delta/\Omega \lesssim 1.5$, and a region whose ground state physics is governed by the dimer covering configurations at $\Delta/\Omega \gtrsim 1.5$. Note that the small system size does not allow to distinguish a spin liquid phase from a VBS phase in this second regime. The color of each individual instantaneous energy eigenvalue in Fig. H.15A reflects the population of the wavefunction in the corresponding instantaneous eigenstate, $|\langle E_n | \psi(t) \rangle|^2$. We observe that non-adiabatic processes lead to finite population in states with energy $\sim \Delta$ outside the dimer covering subspace. This corresponds to the creation of pairs of monomers, consistent with the experimentally observed generation of a finite density of e -anyons. For the sweep profile shown in the inset, the total population in the dimer

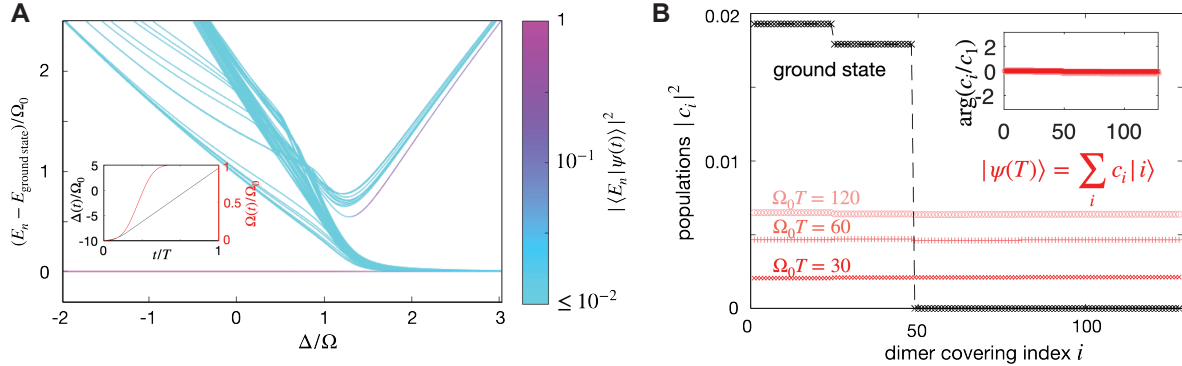


Figure H.15: Dynamical state preparation in PXP model. (A) Lowest instantaneous eigenstates of the Hamiltonian in (H.9) for 36 atoms on a torus. Colors indicate the populations of the state generated in the real time quench dynamics with Hamiltonian parameters given in the inset (data is shown for total sweep time $T = 60/\Omega_0$). (B) Decomposition of the ground state and the dynamically generated state at the end of the parameter sweep ($\Delta/\Omega_0 = 5$) over all dimer covering configurations for various sweep durations T . The total population in the dimer covering sector is $\sum_{i \in \mathcal{D}} |c_i|^2 = 0.27, 0.60, 0.82$ for $\Omega_0 T = 30, 60, 120$, respectively. For the ground state at $\Delta/\Omega = 5$ the population in the dimer covering sector is 0.89. The inset shows the phase of each amplitude. For comparison, the experimental state preparation occurs over $\Omega_0 T = 18$.

covering subspace, \mathcal{D} , at the end of the sweep is $\sum_{i \in \mathcal{D}} |\langle i | \psi(T) \rangle|^2 \approx 0.27, 0.60, 0.82$ for total sweep times $\Omega_0 T = 30, 60, 120$ respectively, showing that the defect density can be controlled and reduced by decreasing the sweep rate. In Fig. H.15B, we resolve the state $|\psi(t)\rangle$ within \mathcal{D} at the end of the detuning sweep. At this point, the instantaneous ground state consists of a superposition of a subset of dimer covering configurations, akin to a VBS state. Nevertheless, the projection of the dynamically prepared state $|\psi(t)\rangle$ onto \mathcal{D} consists of a superposition of all dimer coverings with nearly equal modulus and phase. This indicates that the system cannot resolve the slow dynamics within the dimer covering subspace during these finite-time sweeps, and instead “freezes” into a state that shares the essential features of the spin liquid state. This is consistent with our experimental observation of QSL characteristics in the dy-

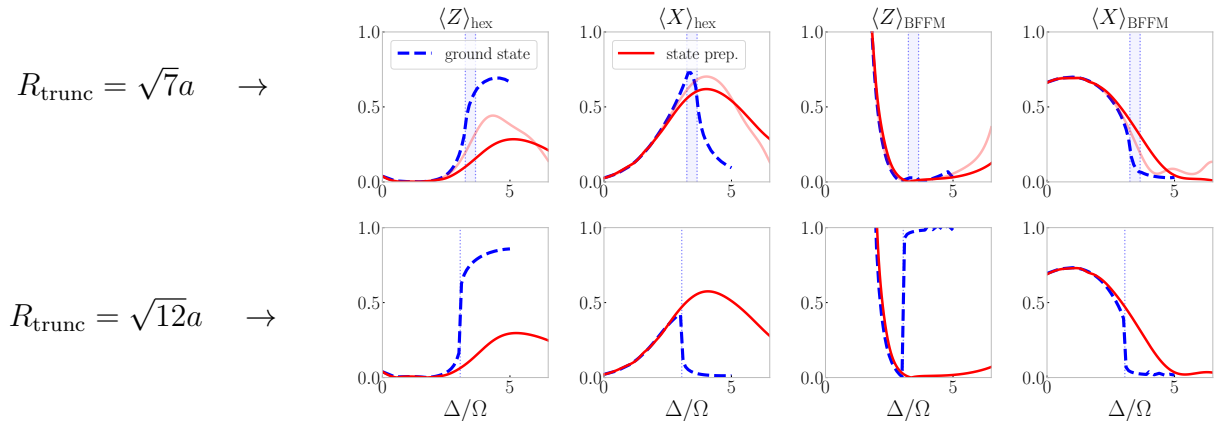


Figure H.16: Dynamical state preparation in the van der Waals model. Results are for the XC-4 cylinder for $R_b = 2.4a$. The two rows correspond to two different truncation distances, as shown. For each panel, we show both the ground state result (blue dashed, obtained by DMRG) as well as the dynamical state preparation using the protocol in Fig. H.1 (red solid, obtained by time-dependent DMRG; lighter solid line is for a sweep at half the speed). For the shorter truncation distance, the ground state hosts a spin liquid (blue shaded region). The diagonal loop around a hexagon is denoted by $\langle Z \rangle_{\text{hex}}$; the off-diagonal loop by $\langle X \rangle_{\text{hex}}$. The BFFM order parameters are evaluated for the open strings that correspond to half of these closed loops. Despite being short strings, due to the small system size, they already show a clear signature of a spin liquid where they both approximately vanish. Note that the ground state data for $R_{\text{trunc}} = \sqrt{7}a$ has a vanishing $\langle Z \rangle_{\text{BFFM}}$, even in the VBS phase: this is a finite-size artefact where the VBS phase consists of local resonances around the circumference. As a check, we also directly calculated the two-point correlator $\langle n_i n_j \rangle - \langle n_i \rangle \langle n_j \rangle$, which clearly shows the VBS order in the ground state, yet these correlations vanish in the time-evolved states (not shown). We conclude that dynamic state preparation is not sensitive to R_{trunc} , and the resulting state has properties which are similar to those of the ground state spin liquid (at $R_{\text{trunc}} = \sqrt{7}a$) albeit smeared out over a larger region.

namically prepared states over a relatively large parameter range, without any signatures of a VBS.

To further corroborate this picture, we also performed dynamical DMRG calculations for state preparation in the realistic model with van der Waals ($1/r^6$) interactions using the matrix product operator-based approach developed in Ref. [248]. We consider the infinitely-long XC-4 cylinder. As for the XC-8 results reported above, there is an intermediate spin liquid between the trivial phase and VBS phase for small truncation distance $R_{\text{trunc}} = \sqrt{7}a$: this ground state data is shown as the dashed blue lines in the top row of Fig. H.16 (the shaded region highlights the intermediate spin liquid). For larger truncation distance $R_{\text{trunc}} = \sqrt{12}a$, the spin liquid is replaced by a direct first order phase transition (blue dashed lines in bottom row of Fig. H.16). The dynamical state preparation data is shown as a solid red line: dark solid lines corresponds to the same protocol as the experimental data (see Fig. H.1); light solid line is twice as slow as the experiment.

The results in Fig. H.16 imply a few salient points. Firstly, as far as dynamical state preparation is concerned, the results for the two truncation distances are very similar: the state preparation seems insensitive to longer-range interactions destroying the intermediate spin liquid in the ground state. Secondly, in both cases, the properties of the time-evolved state are qualitatively very similar to those of the ground state for $R_{\text{trunc}} = \sqrt{7}a$ in the spin liquid regime. The two main differences are: (a) the spin liquid-like state is spread out over a larger region and shifted to the right (minimum of the BFFM order parameters is achieved near $\Delta/\Omega \approx 5$), and (b) the observables are slightly suppressed compared to their equilibrium values. With regard to the latter, we observe that the state which was prepared twice as slowly (light red line) gives improved results, in agreement with experimental observations, Fig. H.7. This is consistent with the picture that already emerged from the dynamical simu-

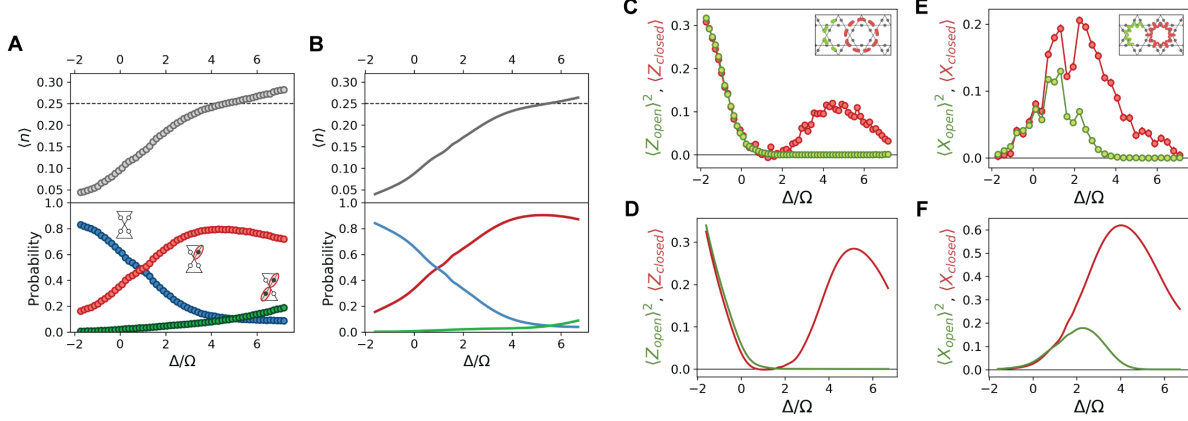


Figure H.17: Comparison between experimental results and numerical simulations of dynamical state preparation. The experimental data (**A,C,E**) is reproduced from Figs. 11.1 and 11.4 of Chapter 11, while in (**B,D,F**) we show the results of the time-dependent DMRG simulations for $R_{trunc} = \sqrt{7}a$, performed on the infinitely-long cylinder with a seven-atom-long circumference (XC-4).

lations for the PXP model in Fig. H.15: even if the ground state is not a spin liquid due to a first order transition to a VBS phase, the dynamically prepared state effectively exhibits spin liquid-like properties, presumably due to the freezing-out of m -anyons (which would need to condense to form the VBS phase). Figure H.17 demonstrates that the results of these dynamical simulations, despite different system sizes and geometry used, are in a good qualitative agreement with experimental observations.

I

Supplementary information for Chapter 12

I.1 STATE INITIALIZATION

We measure our state preparation fidelity by microwave spectroscopy. At our given magnetic field of 1.5 G, the transition frequencies from individual Zeeman sublevels of the ^{87}Rb $|F = 2\rangle$ ground state to the sublevels of the $|F = 1\rangle$ ground state are resolvable. We compare the microwave spectrum after coarse pumping into all sublevels of $|F = 2\rangle$ to the spectrum after pumping specifically into $|F = 2, m_F = -2\rangle$, as shown in Section 2.8. In the latter measurement, peaks corresponding to initial population in magnetic sublevels other than $|m_F = -2\rangle$ are nearly completely eliminated. We bound their remaining size to produce our estimate that

the initial state preparation has fidelity $> 99.5\%$. To reach this fidelity, we aligned the optical pumping laser to the magnetic field with reasonable care but without special fine tuning. However, we took great care to optimize the polarization purity to drive only σ^- transitions on the $|F = 2\rangle \rightarrow |F' = 2\rangle D_2$ transition. We performed this optimization by directly measuring the atom signal while tuning the polarization.

I.2 CHARACTERIZING STATE DETECTION FIDELITY

The Rydberg pulse that couples the ground state $|g\rangle$ to the Rydberg state $|r\rangle$ is applied within a time window τ during which the optical tweezers are briefly turned off. Atoms that are left in $|g\rangle$ at the end of the pulse are recaptured by the optical tweezers, whereas those left in $|r\rangle$ are repelled by the tweezers and lost. We characterize this detection scheme by the ground state detection fidelity f_g (the probability for an atom left in $|g\rangle$ to be recaptured) and f_r (the probability for an atom left in $|r\rangle$ to be lost).

The ground state detection fidelity f_g for a given sequence in which the tweezers are turned off for time τ is estimated by leaving the Rydberg lasers off and measuring the loss probability due to just the trap-off period. For short trap-off times $\tau < 4 \mu\text{s}$, the loss probability is $< 1\%$ so that $f_g > 0.99$. Longer trap-off times reduce this fidelity.

The Rydberg detection fidelity f_r is characterized by the assumption that our single atom Rabi oscillation contrast is limited only by detection fidelity and finite coherence. This assumption is reasonable due to independent measurements which confirm our state preparation fidelity to be $> 99.5\%$. From our fitted Rabi oscillations, we extract the amplitude at time $t = 0$ to estimate the maximum possible loss signal which is typically $96(1)\%$. We associate the remaining 4% with detection error, such that the Rydberg detection fidelity is $f_r = 0.96(1)$. This is consistent with careful analysis of the loss mechanism described in [53].

I.3 RYDBERG LASER ALIGNMENT ONTO ATOMS

We ensure consistent, centered alignment of each Rydberg excitation laser by picking off a small portion of the beam as it is coming to a focus and redirecting it onto a reference CCD camera (see Fig. 12.1b). We first identify the location on the CCD camera that corresponds to optimal alignment onto the atoms. This is done by systematically displacing the beam to several different positions, and at each position measuring the intensity on the atoms through a measurement of the light shift on the microwave transition from $|5S_{1/2}, F = 2, m_F = -2\rangle$ to $|5S_{1/2}, F = 1, m_F = -1\rangle$. We fit these measurements, along with their corresponding positions on the CCD, to extract the optimal position. This procedure takes 5 minutes. We then keep the beam aligned onto this position on the camera by feeding back to a computer controlled mirror located one focal length before the final focusing lens. This realignment takes < 5 seconds and is performed every 2 minutes. This alignment procedure is used on both beams.

I.4 STABILIZING THE ELECTRIC FIELD ENVIRONMENT WITH AN ULTRAVIOLET LED

We observe drifts in the resonance frequency of the transition to the Rydberg 70S state on the scale of several MHz. We attribute these drifts to fluctuations in the electric field induced by charges on the surface of the glass cell which is 8 mm away from the atoms. We find experimentally that shining 365 nm ultraviolet light on the glass cell stabilizes the Rydberg resonance frequency. The most stable configuration is reached by applying the UV light for most of the experimental sequence; it is turned off only for a short window encompassing the Rydberg pulses. With this configuration, we can bound electric-field induced fluctuations on the Rydberg resonance to < 50 kHz.

I.5 SINGLE-ATOM PHASE GATE

We implement our single-atom phase gate with an independent 809 nm laser that is focused onto a single atom and shifts the energy of the atomic ground state $|g\rangle$ by $2\pi \times 5$ MHz. The laser is focused to a waist of $4 \mu\text{m}$ through a microscope objective positioned opposite to the primary microscope objective which produces the optical tweezers. The phase shift beam path is aligned counter-propagating to the path of the optical tweezer that traps the addressed atom.

The beam waist was chosen to be large enough such that the atomic light shift was insensitive to small temperature-induced position fluctuations of the atom. At the same time, the waist was chosen to be small enough to enable negligible crosstalk ($< 2\%$) between two atoms separated by $5.7 \mu\text{m}$.

I.6 NUMERICAL MODEL FOR SINGLE ATOMS

The numerical model is implemented using the Python package QuTiP [354]. It includes the following three effects:

1. A static but random Doppler shift in each iteration of the experiment. At $10 \mu\text{K}$, in a counter-propagating beam configuration with wavelengths 420 nm and 1013 nm, the random Doppler shift follows a Gaussian distribution of width $2\pi \times 43.5$ kHz.
2. Off-resonant scattering from the intermediate state $|e\rangle = |6P_{3/2}, F = 3, m_F = -3\rangle$, to which both $|g\rangle$ and $|r\rangle$ are off-resonantly coupled by the 420 nm and 1013 nm lasers, respectively. The single-atom Rabi frequencies are $(\Omega_B, \Omega_R) \simeq 2\pi \times (54, 40)$ MHz, and the intermediate detuning is $\Delta \simeq 2\pi \times 540$ MHz.

We experimentally probe the decay channels of $|e\rangle$ by preparing atoms in $|g\rangle$ and then applying only the 420 nm light for varying amounts of time. After the 420 nm light is applied at the usual power and detuning, we perform microwave spectroscopy between the $|F = 1\rangle$ and $|F = 2\rangle$ ground state manifolds to determine the final atomic populations. We estimate that population leaves the Zeeman sublevel $|g\rangle = |5S_{1/2}, F = 2, m_F = -2\rangle$ with a $1/e$ timescale of $\sim 150 \mu\text{s}$. We further estimate that population enters the $|F = 1\rangle$ manifold on a timescale of $\sim 600 \mu\text{s}$.

The optical scattering rate induced by the blue laser at the known detuning and power, along with the known $6P_{3/2}$ lifetime of 115 ns, leads to an estimated scattering timescale of $45 \mu\text{s}$, which is significantly faster than the timescale at which population leaves $|g\rangle$. The dominant decay channel from $|e\rangle$, then, is back into $|g\rangle$.

We therefore make the simplification in the numerical model that scattering events from $|e\rangle$ return population to $|g\rangle$. This process is modeled by Lindblad operators $\sqrt{\gamma_B}|g\rangle\langle g|$ and $\sqrt{\gamma_R}|g\rangle\langle r|$, corresponding to scattering events from the ground state $|g\rangle$ or the Rydberg state $|r\rangle$. The simulated timescales are $\gamma_B = 1/(45 \mu\text{s})$ and $\gamma_R = 1/(80 \mu\text{s})$.

3. Finite lifetime of the Rydberg state $|r\rangle$. The total effective lifetime of $146 \mu\text{s}$ is composed of two decay channels: (1) blackbody stimulated transitions at 300 K to neighboring Rydberg states at a timescale of $230 \mu\text{s}$ and (2) radiative decay of the Rydberg state to low principal quantum number levels at a timescale of $410 \mu\text{s}$ [48].

The simplified numerical model treats blackbody stimulated transitions as decay events into a new Rydberg state $|r'\rangle$ which is dark to the laser field. Additionally, the model accounts for radiative decay into a dark ground state $|g'\rangle$.

The numerical results are additionally rescaled to account for the independently calibrated

detection fidelities.

I.7 DEFINITION OF $|W\rangle$ STATE

For experiments with two interacting atoms (as described in Figures 12.3 and 12.4 of Chapter 12), the two atoms are coupled homogeneously by the same laser field to the Rydberg state. Strictly speaking, the Hamiltonian is given by

$$\mathcal{H} = \frac{\hbar}{2} \sum_{i=1,2} \left[\Omega e^{ikx_i} |r_i\rangle \langle g_i| + h.c \right] + U |rr\rangle \langle rr|$$

The parameter Ω (taken to be real) is fixed by the laser intensities (which we assume here to be stable), and the parameter k is fixed by the combined wavevector of the two counter-propagating lasers. The parameters x_i describe the position of the two atoms along the array axis. In the Rydberg blockade regime where $U/\hbar \gg \Omega$, we project out the doubly excited state $|rr\rangle$ such that the only allowed levels are $|gg\rangle$, $|gr\rangle$, and $|rg\rangle$. We therefore rewrite the Hamiltonian as

$$\mathcal{H} = \frac{\hbar\Omega}{2} \left(e^{ikx_1} |rg\rangle \langle gg| + e^{ikx_2} |gr\rangle \langle gg| + h.c \right) \quad (\text{I.1})$$

$$= \frac{\hbar\sqrt{2}\Omega}{2} (|W\rangle \langle gg| + |gg\rangle \langle W|) \quad (\text{I.2})$$

where we have defined

$$|W\rangle = \frac{1}{\sqrt{2}} \left(e^{ikx_1} |rg\rangle + e^{ikx_2} |gr\rangle \right) \quad (\text{I.3})$$

In Chapter 12, we work in the rotating frame in which the excited state $|r\rangle$ incorporates these position-dependent phase factors. Strictly speaking, however, the definition of $|W\rangle$ de-

pends on the position of the atoms.

At the finite atomic temperature of $10 \mu\text{K}$, the atomic position along the array has a random Gaussian distribution of width $\sim 200 \text{ nm}$. The relative phase $e^{ik(x_2-x_1)}$ may therefore reach appreciable values. We choose to not include these factors in our calculation of entangled state fidelity since they are fixed relative to the excitation laser system and do not emerge in measurements. Moreover, additional pulses that map Rydberg excitations down to other ground states may effectively erase these phase factors [268].

I.8 EXTRACTING OFF-DIAGONAL MATRIX ELEMENTS OF DENSITY OPERATOR

We consider an initial two-atom state ρ_0 that has the same measured populations as $|W\rangle = \frac{1}{\sqrt{2}}(|gr\rangle + |rg\rangle)$ but unknown off-diagonal elements. Then ρ_0 can in general be expressed as

$$\rho_0 = \frac{1}{2}(|gr\rangle\langle gr| + |rg\rangle\langle rg|) + (\alpha|gr\rangle\langle rg| + h.c.) \quad (\text{I.4})$$

with off-diagonal coherence $|\alpha| \leq 1/2$. We aim to measure α , and in doing so to measure the entanglement fidelity of the two-atom system.

We consider the following protocol to determine α . First, we apply a local phase shift operation that acts only on the left atom. This is achieved by a tightly focused laser which introduces a light shift on the ground state of the left atom. In the presence of this laser, $|gr\rangle$ is shifted by δ whereas $|rg\rangle$ is unshifted. After time t , the two states have accumulated dynamical phases $|gr\rangle \rightarrow e^{i\delta t}|gr\rangle$ and $|rg\rangle \rightarrow |rg\rangle$.

This operation transforms the density matrix from ρ_0 to ρ_ϕ where

$$\rho_\phi = \frac{1}{2}(|gr\rangle\langle gr| + |rg\rangle\langle rg|) + (\alpha e^{i\delta t}|gr\rangle\langle rg| + h.c.) \quad (\text{I.5})$$

Note that if the state ρ_0 is a statistical mixture of $|gr\rangle$ and $|rg\rangle$ (that is, $\alpha = 0$), this phase shift operation does not change the density matrix.

We can rewrite ρ_ϕ from eq. (I.5) in the basis of the symmetric state $|W\rangle = \frac{1}{\sqrt{2}}(|gr\rangle + |rg\rangle)$ and the orthogonal state $|D\rangle = \frac{1}{\sqrt{2}}(|gr\rangle - |rg\rangle)$:

$$\rho_\phi = \left(\frac{1}{2} + \alpha \cos(\delta t) \right) |W\rangle \langle W| + \left(\frac{1}{2} - \alpha \cos(\delta t) \right) |D\rangle \langle D| + [(-i\alpha \sin(\delta t)) |W\rangle \langle D| + h.c.] \quad (\text{I.6})$$

Finally, a global resonant π -pulse at the enhanced Rabi frequency $\sqrt{2}\Omega$ maps $|W\rangle \rightarrow |gg\rangle$.

The probability to end in $|gg\rangle$ is therefore the probability to be in $|W\rangle$ after the phase shift operation. Therefore

$$P_{gg}(t) = \frac{1}{2} + \alpha \cos(\delta t) = 2\alpha \cos^2(\delta t/2) + \left(\frac{1}{2} - \alpha \right) \quad (\text{I.7})$$

The amplitude of the oscillation of $P_{gg}(t)$ as a function of t therefore provides a direct measurement of α .

While this derivation holds only for an initial density matrix of the form given in eq. (I.4), a more general result can be found by considering the unitaries associated with the local phase shift, $Z_\phi^{(1)}$, and the π -pulse, X_π^W . In the basis $|gg\rangle, |gr\rangle, |rg\rangle, |rr\rangle$, the operators are given by:

$$Z_\phi^{(1)} = \begin{pmatrix} e^{i\delta t} & 0 & 0 & 0 \\ 0 & e^{i\delta t} & 0 & 0 \\ 0 & 0 & 1 & 0 \\ 0 & 0 & 0 & 1 \end{pmatrix} \quad X_\pi^W = \begin{pmatrix} 0 & \frac{i}{\sqrt{2}} & \frac{i}{\sqrt{2}} & 0 \\ \frac{i}{\sqrt{2}} & \frac{1}{2} & -\frac{1}{2} & 0 \\ \frac{i}{\sqrt{2}} & -\frac{1}{2} & \frac{1}{2} & 0 \\ 0 & 0 & 0 & 1 \end{pmatrix} \quad (\text{I.8})$$

For an arbitrary initial density matrix ρ , the final density matrix is $\rho' = U\rho U^\dagger$ where U is

the combined unitary $U = X_\pi^W Z_\phi^{(1)}$. The final probability to measure $|gg\rangle$ is then

$$P_{gg}(t) = \rho'_{gg,gg} = \frac{1}{2} (\rho_{gr,rg} e^{i\delta t} + \rho_{rg,gr} e^{-i\delta t}) + C \quad (\text{I.9})$$

where the constant C is independent of the phase accumulation time t . Since $\rho_{gr,rg} = \rho_{rg,gr}^* = \alpha e^{i\theta}$ for some real amplitude α and angle θ , we have

$$P_{gg}(t) = \alpha \cos(\delta t + \theta) + C \quad (\text{I.10})$$

We therefore see that for any initial density matrix, the amplitude of the oscillation of $P_{gg}(t)$ as a function of t gives a direct measurement of the off-diagonal coherence between $|gr\rangle$ and $|rg\rangle$.

I.9 PROSPECTS FOR NEAR-TERM IMPROVED COHERENCE AND READOUT

We consider near-term achievable coherence based on a realistic improved laser system with 10 times the power on each transition while maintaining low phase noise. This will increase our single-photon Rabi frequencies to $\Omega_B = 2\pi \times 171$ MHz ($\Omega_R = 2\pi \times 126$ MHz). Balancing off-resonant scattering with the finite lifetime of the Rydberg state, we estimate that an optimal intermediate detuning in this configuration will be $\Delta = 2\pi \times 3.6$ GHz, resulting in a two-photon Rabi frequency of $\Omega = 2\pi \times 3$ MHz with a combined coherence time of 92 μ s. In the absence of intensity fluctuations, this would result in $\Omega\tau = 276$, or equivalently a π -pulse fidelity of 0.998. In the same configuration, two atoms within the Rydberg blockade can be excited to the $|W\rangle$ state at the enhanced Rabi frequency in 118 ns with a fidelity of 0.999 (up to the breakdown of the blockade which can be reduced below 0.001 for reasonable separations between atoms).

For improving readout, we consider an approach involving the rapid mapping of Rydberg states to a secondary long-lived ground state. Without invoking a second Rydberg laser system, this mapping could be achieved by a coherent transfer from $|g\rangle$ to a second ground state $|g'\rangle$ followed by a π -pulse to map $|r\rangle$ to $|g\rangle$. The first pulse can be performed by a Raman laser system in $< 0.5 \mu\text{s}$ (a π -pulse at 1 MHz, which has previously been achieved [54]), and the second pulse can be performed in $0.17 \mu\text{s}$ (a π -pulse at 3 MHz). Combined, the mapping can be performed with fidelity better than 0.99. Finally, state readout within the ground state manifold can be routinely accomplished with fidelity > 0.995 by pushing out $|F = 2\rangle$ atoms with cycling light on the $|F = 2\rangle \rightarrow |F' = 3\rangle$ transition.

J

Supplementary information for Chapter 13

J.1 EXPERIMENTAL SETUP

The Rydberg excitations are enabled by a two-color laser system at 420 nm and 1013 nm wavelength. The 420 nm light is derived from a frequency-doubled titanium sapphire laser (M Squared SolsTiS 4000 PSX F) locked to an ultrastable reference cavity (by Stable Laser Systems). The 1013 nm light is obtained from a high-power fiber amplifier (ALS-IR-1015-10-A-SP by Azur Light Systems). The seed light is derived from a Fabry-Pérot laser diode injection locked to an external cavity diode laser (CEL002 by MOGLabs) stabilized to the same reference cavity and filtered by the cavity transmission [293]. The detuning of both Rydberg lasers

to the intermediate state $|6P_{3/2}, F = 3, m_F = -3\rangle$ is approximately $2\pi \times 2$ GHz. The individual Rabi frequencies of the two Rydberg lasers are $\Omega_{420}/(2\pi) \approx 174$ MHz and $\Omega_{1013}/(2\pi) \approx 115$ MHz. This gives a two-photon Rabi frequency of $\Omega = \Omega_{420}\Omega_{1013}/(2\Delta) \approx 2\pi \times 5$ MHz. We define the local phases of each atom's states $|0\rangle$ and $|1\rangle$ in the reference frame associated with the local phases of Rydberg excitation lasers, such that the two GHZ components have a relative phase $\phi = 0$ after state preparation.

To drive the optimal control pulses, we modulate the 420 nm Rydberg laser with an acousto-optic modulator (AOM) driven by an arbitrary waveform generator (AWG, M4i.6631-x8 by Spectrum). We correct the nonlinear response of the AOM to the drive amplitude by a feed-forward approach to obtain the target output intensity pattern. Furthermore, the AOM efficiency changes with changing frequency, which we compensate by feeding forward onto the waveform amplitude to suppress the intensity variations with frequency. In addition, the light shift on the Rydberg transition from the 420 nm laser can be as large as $2\pi \times 4$ MHz. While the pulse intensity changes, this light shift changes, modifying the detuning profile. We therefore correct the frequency profile as a function of the pulse intensity to compensate this shift. These steps ensure that the experimentally applied pulse is a faithful representation of the desired profile.

The local addressing beam patterns are generated by two AODs (DTSX400-800 by AA Opto-electronic), each driven by multiple frequencies obtained from an arbitrary waveform generator (M4i.6631-x8 by Spectrum).

J.2 OPTIMAL CONTROL

Optimal control was originally developed as a tool to harness chemical reactions to obtain the largest amount of desired products with given resources, and then introduced in quantum

information processing as a standard way of designing quantum protocols and quantum devices [355–358] as well as in manipulating quantum many-body systems to exploit complex phenomena [359–367, 288]. Quantum optimal control theory identifies the optimal shape of a time-dependent control pulse to drive a quantum many-body system to accomplish given task, e.g. state preparation or quantum gate implementation. The quality of the transformation is certified by a Figure of Merit (FoM) that can be calculated or measured, e.g. the fidelity of the final state with respect to the target one, the final occupation, or the energy.

In this work, the optimization is achieved through RedCRAB, the remote version of the dressed Chopped RAndom Basis (dCRAB) optimal control via a cloud server [359, 366, 288]. Within the optimization, control fields such as the Rabi coupling $\Omega(t)$ are adjusted as $\Omega(t) = \Omega_0(t) + f(t)$, where $\Omega_0(t)$ is an initial guess function obtained from physical intuition or existing suboptimal solutions. The correcting function $f(t)$ is expanded by randomized basis functions. In this work, we chose a truncated Fourier basis. Thus, $f(t) = \Gamma(t) \sum_{k=1}^{n_c} [A_k \sin(\omega_k t) + B_k \cos(\omega_k t)]$, where $\omega_k = 2\pi(k + r_k)/\tau$ are randomized Fourier frequencies with $r_k \in [-0.5, 0.5]$, τ is the final time, and $\Gamma(t)$ is a fixed scaling function to keep the values at initial and final times unchanged, i.e., $\Gamma(0) = \Gamma(\tau) = 0$. The optimization task is then translated into a search for the optimal combination of $\{A_k, B_k\}$ with a given r_k to maximize the fidelity between the target state and the time evolved state at τ . It can be solved by iteratively updating $\{A_k, B_k\}$ using a standard Nelder-Mead algorithm [368]. In the basic version of the CRAB algorithm, all r_k are fixed and the local control landscape is explored for all n_c frequencies simultaneously. This leads to a restriction in the number of frequencies that can be efficiently optimised. Using the dressed CRAB (dCRAB) algorithm, only one Fourier frequency ω_k is optimised at a time. We then move on to ω_{k+1} after a certain number of iterations of the CRAB routine. This enables the method to include an arbitrarily large number of Fourier compo-

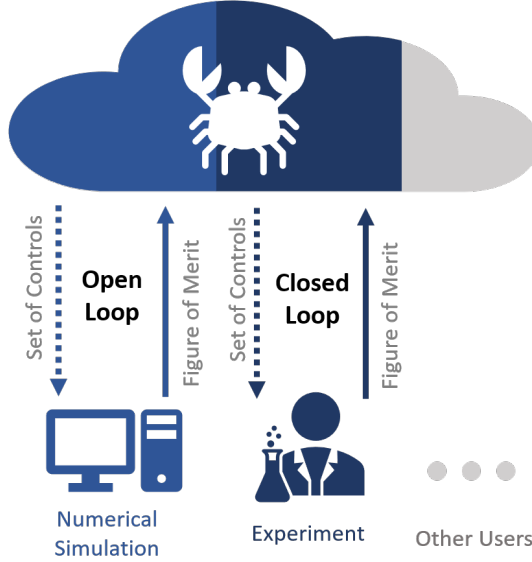


Figure J.1: RedCRAB optimization loop. The remote dCRAB server generates and transmits a trial set of controls to the user, who evaluates the corresponding performance in terms of a FoM and sends the feedback information to the server, concluding one iteration loop. In the next loop, the server tends to generate an improved set of controls based on previous feedback information. The optimization continues until it converges. The FoM evaluation can be achieved either by numerical calculation (open-loop optimization) or experimental measurement (closed-loop optimization).

nents and deriving the solutions without – whenever no other constraints are present – being trapped by local optima [287].

In the RedCRAB optimization, the server generates and transmits a trial set of controls to the client user, who will then evaluate the corresponding FoM and communicates the feedback information to the server finishing one iteration loop (Fig. J.1). The optimization continues iteratively and the optimal set of controls, as well as the corresponding FoM are derived. In the RedCRAB optimization, the user can either evaluate the FoM by numerical calculation, namely open-loop optimization, or by experimental measurement, which is called closed-loop optimization. In this work, open-loop optimization was carried out only. The resulting controls could later serve as the initial guess for a future closed-loop optimization. This last step would ensure that the resulting controls are robust, since all unknown or not modelled experi-

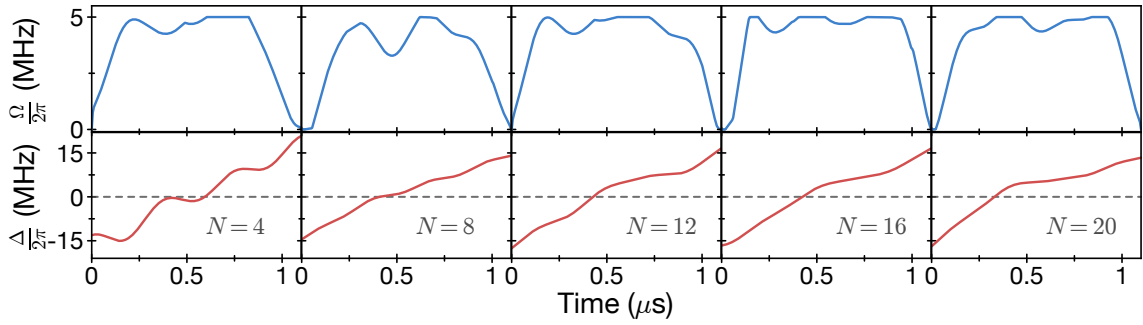


Figure J.2: Optimal control pulse diagrams. Shown are the Rabi frequency (top) and detuning profiles (bottom) for the different system sizes investigated here.

mental defects and perturbations would automatically be corrected for.

For the open-loop optimization of the pulse, we constrained the preparation time to $1.1\ \mu\text{s}$ and allowed the detuning $\Delta/(2\pi)$ to vary between $-20\ \text{MHz}$ and $20\ \text{MHz}$, while $\Omega/(2\pi)$ could vary between $0 - 5\ \text{MHz}$. The resulting pulses are shown in Fig. J.2. While shorter pulses can work sufficiently well for smaller system sizes, we use an equal pulse duration for all N for better comparability. We find that the optimized pulses for larger systems appear smoother than for smaller system sizes, where the pulses bear less resemblance to an adiabatic protocol. However, the adiabaticity does not improve for larger system sizes, owing to the shrinking energy gaps.

J.3 OPTIMAL CONTROL DYNAMICS

To gain insight into the timescales required to prepare a GHZ state in our setup, we can compare our optimal control protocol with a minimal quantum circuit consisting of a series of two-qubit gates that would achieve the same task. In this circuit, a Bell pair is created in the first layer $p = 1$ in the middle of the array using the Rydberg blockade, which for our maximal coupling strength of $\Omega/(2\pi) = 5\ \text{MHz}$ takes $100\ \text{ns}/\sqrt{2}$. The entanglement can be spread to

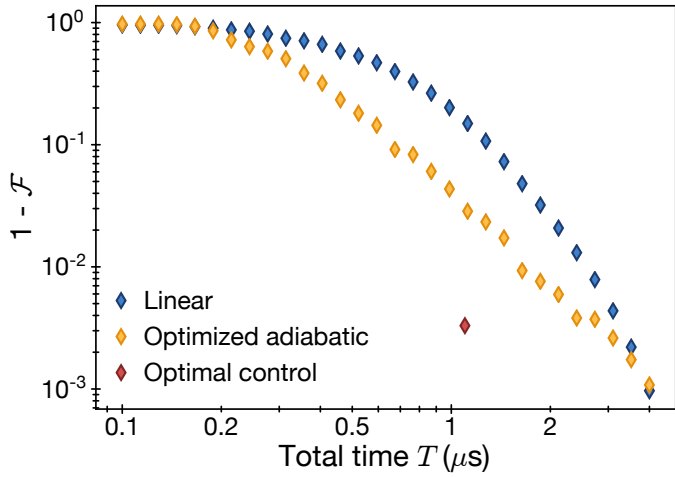


Figure J.3: Comparison of ramping profile fidelities. Comparison of linear ramps (blue) to optimized adiabatic ramps (orange) for $N = 12$ as a function of the total ramp time T . The optimal control pulse used in the experiment takes $T = 1.1 \mu s$ and achieves a higher fidelity than either the linear ramp or the optimized adiabatic ramp.

the two atoms adjacent to this Bell pair by simultaneously applying a pair of local π pulses of 100 ns to those sites, corresponding to controlled rotations. A sequence of such gate layers $p = 2, \dots, 10$, including operations on qubit pairs and the free evolution of other qubits, leads to the same GHZ state we prepare. This gate sequence requires approximately 1 μs , which is within 10% of the total evolution time required in our optimal control sequence, which builds up the entanglement in parallel. Furthermore, the fidelity of each layer of such a circuit effectively acting on all $N = 20$ qubits needs to be higher than 0.94 to achieve the 20-qubit GHZ fidelity demonstrated in this work.

It is interesting to compare this required evolution time with a parameter ramp that tries to adiabatically connect the initial state to the GHZ state. To this end, we parametrize the detuning and Rabi frequency as $\Delta(s) = (1 - s)\Delta_0 + s\Delta_1$ and $\Omega(s) = \Omega_{\max}[1 - \cos^{12}(\pi s)]$ respectively. A naïve (unoptimized) linear ramp of the detuning corresponds to choosing $s = t/T$. Alternatively, one can adjust the local ramp speed to minimize diabatic transitions, for

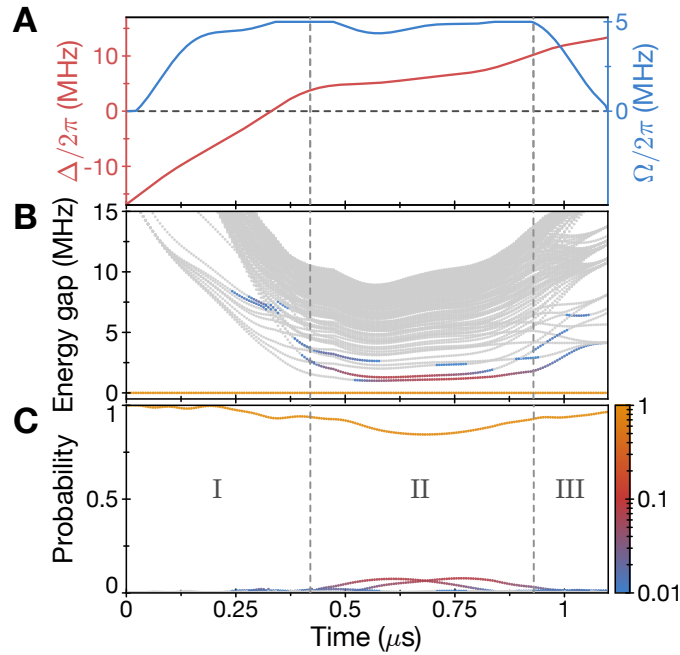


Figure J.4: Dynamics of an optimized 20-atom GHZ state preparation. **A**, Optimized control parameters $\Omega(t)$ and $\Delta(t)$ for $N = 20$ atoms. **B**, Energy eigenvalues of instantaneous eigenstates of the Hamiltonian relative to the ground state energy. The population in each energy eigenstate is color coded on a logarithmic scale. Light gray points correspond to populations smaller than 0.01. **C**, Probability in each instantaneous eigenstate as the initial state evolves under the time-dependent Hamiltonian. The probability is dominated by the ground state and a few excited states. The time evolution is computed by exact numerical integration of Schrödinger's equation, and 100 lowest energy eigenstates are obtained by using Krylov subspace method algorithms. For computational efficiency, we only consider the even parity sector of the Hamiltonian with no more than three nearest neighboring Rydberg excitations owing to the Rydberg blockade.

example by choosing $s(t)$ minimizing

$$D = \left(\frac{ds}{dt} \right)^2 \sum_{n>0} \frac{|\langle E_n(s) | \partial_s H(s) | E_0(s) \rangle|^2}{(E_n(s) - E_0(s))^2}$$

during a ramp of duration T . Here $|E_n(s)\rangle$ are the instantaneous eigenstates of the Hamiltonian $H(s)$ specified by the parameters $\Omega(s)$ and $\Delta(s)$, with $|E_0(s)\rangle$ denoting the instantaneous ground state. In Figure J.3, we show the results of numerical simulations using both the linear sweep and a sweep that minimizes the strength of diabatic processes quantified by D . Both sweep profiles require larger total evolution time T than the optimal control pulse to reach similar fidelities.

To understand the origin of the speedup through optimal control, we numerically simulate the corresponding evolution and analyze the population of the instantaneous energy eigenstates (Fig. J.4). The optimal control dynamics can be divided into three different regions: (I) A fast initial quench, (II) a slow quench, and (III) a fast final quench. Even though the change in the Hamiltonian parameters in region (I) is rather rapid, the system remains mostly in the instantaneous ground state, with negligible populations of the excited states, since the energy gap is large. In contrast, in region (II) the parameters change slows down, reflecting the fact that the energy gap becomes minimal. Unlike the adiabatic case however, one can observe nontrivial population dynamics, with a temporary population of excited states. Importantly, the optimal control finds a path in the parameter space such that the population is mostly recaptured in the ground state at the end of region (II). Finally, in region (III) the gap is large again and the system parameters are quickly changed to correct also for higher order contributions. This suggests that it actively uses diabatic transitions that go beyond the adiabatic principle. This mechanism is related to the recently discussed speedup in the context of the quantum approximate optimization algorithm (QAOA) [197, 198].

J.4 QUANTIFYING DETECTION

The many-body dynamics involving coherent excitation to Rydberg states occurs during a few-microsecond time window in which the optical tweezers are turned off. After the coherent dynamics, the tweezers are turned back on, and atoms in the ground state $|0\rangle$ are recaptured. However, there is a small but finite chance of losing these atoms. To quantify this error, we perform the GHZ state preparation experiment while disabling the 420 nm Rydberg pulse. This keeps all atoms in state $|0\rangle$, and we measure the loss probability to find a 0.9937(1) detection fidelity.

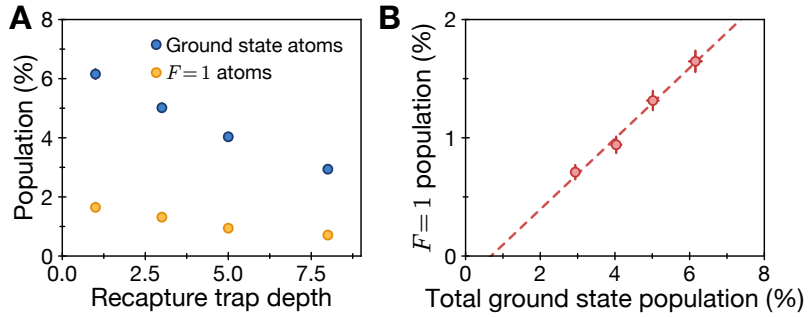


Figure J.5: Quantifying detection errors. **A**, Measurement of the recaptured Rydberg atoms in the ground state (blue points) and in the $F = 1$ ground-state manifold (orange points) as a function of the tweezer depth upon recapture. **B**, Recaptured populations in all ground state levels. The intersection with the horizontal axis gives an estimate of the atoms that were not excited to the Rydberg state, bounding the π pulse fidelity.

Atoms in state $|1\rangle$ on the other hand have a small chance of being misidentified as being in state $|0\rangle$, as these atoms can decay prematurely from the Rydberg state to the ground state and get recaptured by the tweezers. This error probability can be measured by preparing atoms at sufficiently large distances as to be non-interacting and applying a calibrated π pulse to transfer all atoms to $|1\rangle$ and measure the probability of recapturing them. However, part of this signal is given by the π pulse infidelity, i.e. a small fraction of atoms which did not get excited to $|1\rangle$ in the first place.

To quantify the π pulse fidelity, we note that a Rydberg atom that decays and is recaptured can decay either into the $F = 2$ or $F = 1$ ground states with branching ratios α and β , respectively ($\alpha + \beta = 1$). Our initial optical pumping of atoms into $|0\rangle$ has high fidelity > 0.998 , measured using microwave spectroscopy on different sublevels of the $F = 2$ manifold. Thus, the final population of $F = 1$ atoms should be given only by Rydberg atom decay/recapture events. Following a π pulse to excite all atoms to the Rydberg state, the final measured population in $F = 1$ is $p_1 = p \times \beta$, where p is the total decay and recapture probability of a Rydberg atom. Meanwhile, the final measured population in $F = 2$ is $p_2 = p \times \alpha + \epsilon$, which includes both decay events from Rydberg atoms as well as residual

population ϵ left from an imperfect π pulse. Experimentally, we separately measure the total recaptured ground state population ($p_1 + p_2$), as well as the $F = 1$ population p_1 only (by a resonant push-out of $F = 2$ atoms). We additionally can vary the overall recapture probability p by changing the depth of the tweezers that we recapture atoms in, which changes the repulsive force exerted by the optical tweezers on Rydberg atoms [53]. We measure p_1 and ($p_1 + p_2$) at four different total recapture probabilities to extract the π pulse infidelity as $\epsilon = 0.006(3)$ (Fig. J.5). From these measurements, we conclude a Rydberg detection fidelity of 0.9773(42).

Detection errors of $|0\rangle$ can be mitigated by implementing ground-state cooling in the tweezers [95, 43], which reduces the probability of loss after releasing the atoms. The detection fidelity of $|1\rangle$ can be improved by using Rydberg states with a longer radiative lifetime, actively ionizing the Rydberg atoms by electric or optical fields, or by pulling them away from the trapping region with electric field gradients.

J.5 ACCOUNTING FOR DETECTION IMPERFECTIONS

The small imperfections in state detection of single qubits leads to a prominent effect on the analysis of large systems. The probability for a single detection error is sufficiently low that multiple errors per chain are very unlikely, and we observe that the reduction in probability of observing the correct GHZ pattern is dominated by these errors, as opposed to excitations of the system (Fig. J.6A). This conclusion is further confirmed by noting that near-ideal correlations extend across the entire system (Fig. J.7).

To properly infer the obtained fidelities, we account for these imperfections using the following procedure:

Coherences: The coherences are extracted from the amplitude of parity oscillations. Each point in the parity oscillation is analyzed from the measured distribution of the number of ex-

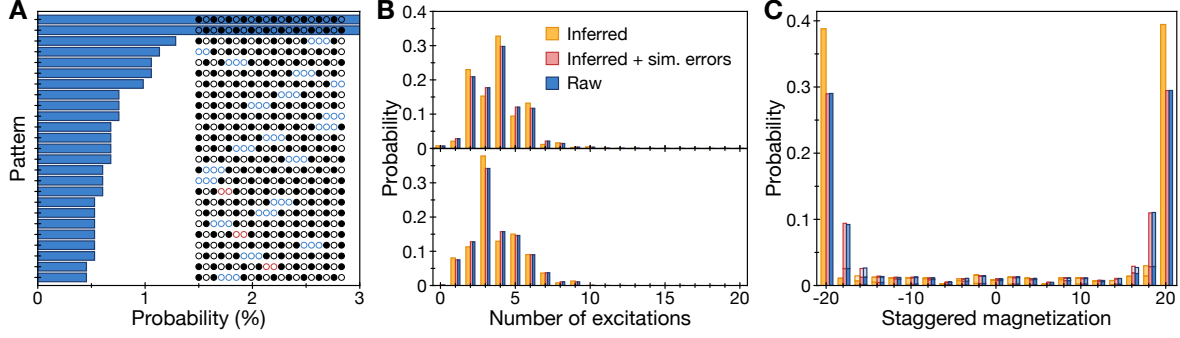


Figure J.6: Inference of parity and populations. **A**, Histogram of observed patterns after preparing a 20-atom GHZ state. Open circles denote atoms in $|0\rangle$ and filled circles denote atoms in state $|1\rangle$. Blue domains mark regions where a single detection error has likely occurred, since such patterns are energetically costly at large positive detuning of the Rydberg laser. Red domains mark true domain walls, where the antiferromagnetic order is broken. Following the correct GHZ patterns, the 14 most observed patterns are consistent with a single detection error. **B**, Distribution of number of excitations measured for two different times of the parity oscillation for a 20-atom array, with the upper (lower) plot at $\phi = 0$ ($\phi = \pi/20$) of phase accumulation per atom, showing a net positive (negative) parity. Blue bars show directly measured values, orange bars show the statistically inferred parent distribution, and red bars denote the parent distribution after adding simulated errors to compare to the raw data. **C**, Staggered magnetization M_n extracted from the measurement of GHZ populations for 20 atoms. The vertically split bars with different shading denote different occurrences of number of excitations.

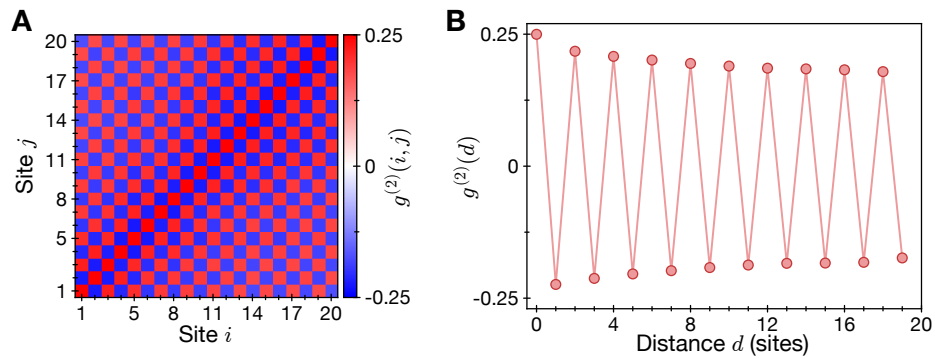


Figure J.7: Density-density correlations for a 20-atom GHZ state. **A**, We evaluate the correlation function $g^{(2)}(i,j) = \langle n_i n_j \rangle - \langle n_i \rangle \langle n_j \rangle$ and observe strong correlations of Rydberg excitations across the entire system. **B**, The density-density correlations over distance, given by $g^{(2)}(d) \propto \sum_i g^{(2)}(i, i + d)$ decay only very slowly throughout the array.

citations in the system. We encode this measured probability distribution in the vector \mathbf{W} , where W_n is the probability to observe exactly n excitations in the system ($0 \leq n \leq N$). The true probability distribution of excitation numbers, prior to the effect of detection errors, is denoted \mathbf{V} . Detection errors transform this distribution according to a matrix M , where M_{mn} encodes the probability that a state with n excitations will be detected as having m excitations. Each matrix element is calculated using combinatoric arguments from the measured detection fidelities. We determine the true distribution \mathbf{V} as the one that minimizes the cost function $|M\mathbf{V} - \mathbf{W}|^2$. (Fig. J.6B). This procedure is similar to applying the inverse matrix M^{-1} to the measured distribution \mathbf{W} , but is more robust in the presence of statistical noise on the measured distribution. Error bars on the inferred values are evaluated by random sampling of detection fidelities, given our measured values and uncertainties.

Populations: We carry out a similar procedure for the population data; however, we are interested in assessing the probability of two particular target states, which are defined not only by their number of excitations but also by their staggered magnetizations $M_n = \sum_{i=1}^N (-1)^i \langle \sigma_z^{(i)} \rangle$. Our procedure therefore operates by grouping all possible microstates according to their common staggered magnetization and number of excitations (Fig. J.6C). For N particles, there are in general $(N/2 + 1)^2$ such groups. As before, we denote the raw measured distribution with respect to these groups as \mathbf{W} . We construct a detection error matrix M that redistributes populations between groups according to the measured detection error rates. We optimize over all possible true distributions to find the inferred distribution \mathbf{V} that minimizes the cost function $|M\mathbf{V} - \mathbf{W}|^2$. Following this procedure, we sum the populations in the two groups that uniquely define the two target GHZ components with a staggered magnetization of $\pm N$, and $N/2$ excitations.

J.6 BOUNDING THE GHZ STATE COHERENCE

We expand an experimental GHZ-like density matrix in the following form

$$\rho = \alpha_1 |A_N\rangle\langle A_N| + \alpha_2 |\bar{A}_N\rangle\langle\bar{A}_N| + (\beta |A_N\rangle\langle\bar{A}_N| + \beta^* |\bar{A}_N\rangle\langle A_N|) + \rho' \quad (\text{J.1})$$

where $|A_N\rangle = |0101\dots\rangle$ and $|\bar{A}_N\rangle = |1010\dots\rangle$ are the target GHZ components, α_i characterizes the diagonal populations in these states ($0 \leq \alpha_i \leq 1$), β characterizes the off-diagonal coherence between these states ($0 \leq |\beta| \leq 1/2$), and ρ' contains all other parts of the density matrix. The GHZ fidelity of state ρ is given by:

$$\mathcal{F} = \langle \text{GHZ}_N | \rho | \text{GHZ}_N \rangle = \frac{\alpha_1 + \alpha_2}{2} + \text{Re}(\beta) \quad (\text{J.2})$$

To measure the coherence $|\beta|$, we implement a staggered magnetic field to which the target GHZ state is maximally sensitive:

$$H_{\text{st}} = \frac{\hbar\delta}{2} \sum_{i=1}^N (-1)^i \sigma_z^{(i)} \quad (\text{J.3})$$

Applying H_{st} to the system for time T results in unitary phase accumulation $U(T) = \exp(-iH_{\text{st}}T/\hbar)$. We then apply a unitary \mathcal{U} to the system and measure in the computational basis. From repeated measurements, we calculate the expectation value of the global parity operator $\mathcal{P} = \prod_i \sigma_z^{(i)}$ as a function of the phase accumulation time T . Denote the time-dependent expectation value $E(T)$, where $-1 \leq E(T) \leq 1$.

We show that if $E(T)$ has a frequency component that oscillates at a frequency of $N\delta$, then the amplitude of this frequency component sets a lower bound for $|\beta|$. Importantly, this holds

for any unitary \mathcal{U} used to detect the phase accumulation.

Proof: The expectation value $E(T)$ can be written explicitly as the expectation value of the time-evolved observable $\mathcal{P} \rightarrow U^\dagger(T)\mathcal{U}^\dagger\mathcal{P}\mathcal{U}U(T)$. In particular,

$$E(T) = \text{Tr}[\rho U^\dagger(T)\mathcal{U}^\dagger\mathcal{P}\mathcal{U}U(T)] = \sum_n \langle n | \rho U^\dagger(T)\mathcal{U}^\dagger\mathcal{P}\mathcal{U}U(T) | n \rangle \quad (\text{J.4})$$

where $|n\rangle$ labels all computational basis states. Since the phase accumulation Hamiltonian H_{st} is diagonal in the computational basis, the basis states $|n\rangle$ are eigenvectors of $U(T)$ with eigenvalues denoting the phase accumulation. Specifically,

$$H_{\text{st}}|n\rangle = \frac{\hbar\delta}{2}M_n|n\rangle \Rightarrow U(T)|n\rangle = e^{-i\delta TM_n/2}|n\rangle \quad (\text{J.5})$$

where M_n is the staggered magnetization of state $|n\rangle$ defined earlier. The staggered magnetization of the state $|A_N\rangle$ is maximal: $M_{A_N} = N$, and the staggered magnetization of $|\overline{A}_N\rangle$ is minimal: $M_{\overline{A}_N} = -N$. Note that all other computational basis states have strictly smaller staggered magnetizations. Inserting an identity operator in Eq. (4):

$$E(T) = \sum_{n,m} \langle n | \rho | m \rangle \langle m | U(T)^\dagger \mathcal{U}^\dagger \mathcal{P} \mathcal{U} U(T) | n \rangle = \sum_{n,m} e^{-i\delta T(M_n - M_m)/2} \langle n | \rho | m \rangle \langle m | \mathcal{U}^\dagger \mathcal{P} \mathcal{U} | n \rangle \quad (\text{J.6})$$

The highest frequency component comes from the states with maximally separated staggered magnetization, $|n\rangle = |A_N\rangle$ and $|m\rangle = |\overline{A}_N\rangle$. Separating out this frequency component as $F(T)$, we obtain:

$$F(T) = 2\text{Re} \left[e^{-iN\delta T} \langle A_N | \rho | \overline{A}_N \rangle \langle \overline{A}_N | \mathcal{U}^\dagger \mathcal{P} \mathcal{U} | A_N \rangle \right] = 2\text{Re} \left[\beta e^{-iN\delta T} \langle \overline{A}_N | \mathcal{U}^\dagger \mathcal{P} \mathcal{U} | A_N \rangle \right] \quad (\text{J.7})$$

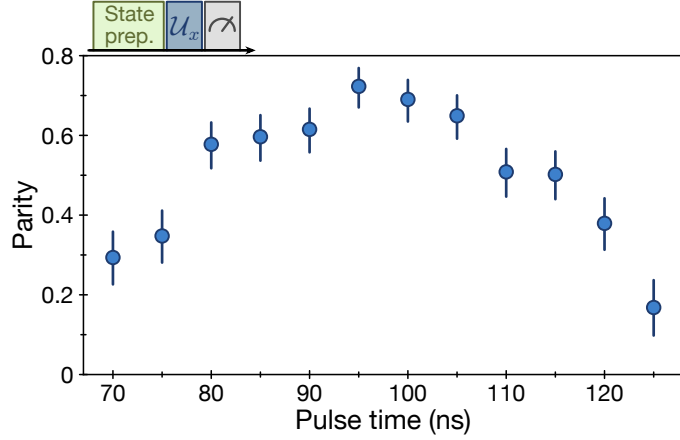


Figure J.8: Parity signal measured as a function of the time the operation \mathcal{U}_x is applied. The total time includes delays in the AOM response and the finite laser pulse rise time.

We note that the parity matrix element is bounded as $0 \leq |\langle \bar{A}_N | \mathcal{U}^\dagger \mathcal{P} \mathcal{U} | A_N \rangle| \leq 1$. Furthermore, the matrix element is real-valued and positive for the unitary \mathcal{U} considered in the experiment. Fitting $F(T)$ to an oscillation with amplitude $C \geq 0$ and phase ϕ according to $F(T) = C \cos(N\delta T - \phi)$, we produce our lower bound for the off-diagonal coherence β :

$$|\beta| \geq C/2; \quad \arg(\beta) = \phi \quad (\text{J.8})$$

J.7 PARITY DETECTION

The ideal observable to measure GHZ phase is the parity $\mathcal{P}_x = \prod_i \sigma_x^{(i)}$. However, the presence of Rydberg interactions and the Rydberg blockade prevents us from rotating all qubits such that we can measure in this basis. Instead, in this work we generate a unitary $\mathcal{U}_x = \exp\left(-i\Omega t/2 \sum_i \sigma_x^{(i)} - iH_{\text{int}}t/\hbar\right)$ by resonantly driving all atoms in the presence of these interactions given by H_{int} for a fixed, optimized time (Fig. J.8), and subsequently measure the parity $\mathcal{P} = \prod_i \sigma_z^{(i)}$ in the computational basis. The finite duration of the unitary \mathcal{U}_x incurs a small amount of additional infidelity, owing both to dephasing and an additional laser scat-

tering. However, we estimate that this effect should only lead to small losses in fidelity on the percent level.

While it is not obvious that the parity observable used here is suitable, we can understand the parity oscillations in the picture of weakly interacting spin-1 particles defined on dimers of neighboring pairs of sites. For two adjacent sites, we can define eigenstates of a spin-1 S_z operator as $|o\bullet\rangle = |-\rangle$, $|oo\rangle = |0\rangle$, and $|\bullet o\rangle = |+\rangle$. In this notation, the antiferromagnetic GHZ state we prepare is given by a ferromagnetic GHZ state in the spin-1 basis:

$$|GHZ_N\rangle = \frac{1}{\sqrt{2}} (|+++ \cdots\rangle + |--- \cdots\rangle) \quad (\text{J.9})$$

We must express all operations on the GHZ state in this new notation. In particular, the transverse field of the form $\hbar\Omega/2 \sum_i \sigma_x^{(i)}$ applied to individual atoms gets transformed to an operation $\hbar\Omega/\sqrt{2} \sum_j S_x^{(j)}$ on all dimers. Furthermore, the staggered field $\hbar\delta/2 \sum_i (-1)^i \sigma_z^{(i)}$ we apply to individual atoms to rotate the GHZ phase is equivalent to an operation of the form $\hbar\delta \sum_j S_z^{(j)}$ acting on individual dimers.

The parity operator in the single-qubit basis $\mathcal{P} = \prod_i \sigma_z^{(i)}$ can be transformed into the dimer basis as

$$\mathcal{P} = \prod_j \left(-|+\rangle\langle+|_j - |-\rangle\langle-|_j + |0\rangle\langle0|_j \right) \quad (\text{J.10})$$

by noting that the three dimer states are eigenstates of \mathcal{P} , i.e. $\mathcal{P} |\pm\rangle = -|\pm\rangle$ and $\mathcal{P} |0\rangle = |0\rangle$.

Assuming we begin from a GHZ state, applying a rotation on all dimers for a duration given by $\Omega t = \pi/\sqrt{2}$ saturates the difference in \mathcal{P} between GHZ states of opposite phase. This shows that such a protocol would be optimal if the dimer approximation were exact. However, interactions between dimers cannot be neglected. In particular, the Rydberg blockade suppresses configurations of the form $|\cdots - + \cdots\rangle$ owing to the strong nearest-neighbor interac-

tion V , and neighboring dimers of the same type such as $| \cdots \pm \pm \cdots \rangle$ have a weak interaction given by the next-to-nearest neighbor interaction strength $V_2 = V/2^6$. We can thus express the interactions in the system as

$$\frac{H_{\text{int}}}{\hbar} = \sum_{j=1}^{N/2-1} V_2 |+\rangle\langle+|_j|+\rangle\langle+|_{j+1} + V_2 |- \rangle\langle-|_j|- \rangle\langle-|_{j+1} + V |- \rangle\langle-|_j|+\rangle\langle+|_{j+1} \quad (\text{J.11})$$

An exact simulation of the dimer rotation under the interaction Hamiltonian (11) shows that both these interaction effects reduce the parity contrast by a small amount. In the recently discussed context of quantum many-body scars [157, 189, 213, 211], these effects of residual interactions lead of small deviations from a stable periodic trajectory through phase space.

J.8 STAGGERED FIELD CALIBRATION

To apply the staggered field (3), we address each of the even sites in the array with a focused off-resonant laser beam at 420 nm. However, the unitary in question requires a staggered field with opposite sign on every site. We compensate for the missing acquired phase on the sites in between the addressed ones by shifting the phase of the Rydberg laser, through a change in phase of the radio-frequency drive of the AOM. The intensity of each addressing beam is measured by applying a spin-echo sequence with an addressing pulse of variable duration to determine the light shift on the Rydberg transition. We correct for inhomogeneous intensities so that all atoms are subject to the same light shift.

We measure and calibrate the staggered field by measuring the effect of the field on each atom individually. To do so, we alternately rearrange the atoms to form different subsets of the 20-atom system that are sufficiently far apart to avoid interactions between them. In this configuration, every atom is then subject to a $\pi/2$ rotation about the x -axis, followed by the

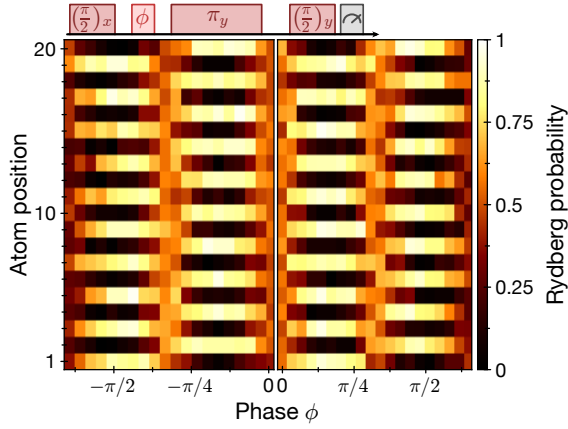


Figure J.9: Phase accumulation measured on an array of 20 sites. The left panel demonstrates application of a negative staggered field by applying local addressing beams on the odd sites in the array. The right panel shows a positive staggered field by instead applying local addressing beams on the even sites in the array. Phase is accumulated on each site at a rate of $2\pi \times 3.8$ MHz.

System size N	4	8	12	16	20
Raw populations	0.893(6)	0.797(8)	0.695(9)	0.629(12)	0.585(14)
Inferred	0.946(10)	0.892(17)	0.824(21)	0.791(29)	0.782(32)
Raw coherence	0.710(12)	0.516(11)	0.371(10)	0.282(11)	0.211(11)
Inferred	0.759(11)	0.598(16)	0.462(19)	0.373(19)	0.301(18)
Raw fidelity	0.801(7)	0.657(7)	0.533(7)	0.455(8)	0.398(9)
Inferred	0.852(7)	0.745(12)	0.643(14)	0.582(17)	0.542(18)

Table J.1: Measured GHZ data for all system sizes. Errors denote 68% confidence intervals.

staggered field for variable duration, then a $\pi/2$ rotation about the y -axis, to distinguish positive from negative phase evolution. With an additional π rotation about the y -axis, we perform a spin echo to mitigate effects of dephasing. The outcome of this protocol is shown in Fig. J.9 and demonstrates the implementation of the staggered magnetic field. By switching the local addressing beams to the opposite set of alternating sites, we switch the sign of the staggered field, enabling the measurement of both positive and negative phase accumulation.

J.9 MEASURED GHZ FIDELITIES

For each system size N , we measure the GHZ populations and the GHZ coherence by parity oscillations (Figs. 13.2 and 13.3 of Chapter 13). From the raw measurements, we infer the true GHZ fidelity using the maximum likelihood procedure discussed in Section J.5. All measured values are shown in table J.1. Error bars on raw populations represent a 68% confidence interval for the measured value. Error bars on the raw coherences are fit uncertainties from the parity oscillations. Error bars on the inferred values include propagation of the uncertainty in the estimation of the detection fidelities.

J.10 EXPERIMENTAL IMPERFECTIONS

We identify a number of experimental imperfections that to varying degrees can limit the coherent control of our atomic system.

1. **Atomic temperature:** The atom temperature of $\sim 10 \mu\text{K}$ leads to fluctuating Doppler shifts in the addressing lasers of order $\sim 2\pi \times 43 \text{ kHz}$, as well as fluctuations in atomic position that leads to variation in Rydberg interactions strengths. These fluctuations are included in the simulations shown in Fig. 13.3 of Chapter 13. These effects can be dramatically reduced by improved atomic cooling, most notably by sideband cooling within the optical tweezers to the motional ground state [95, 43].
2. **Laser scattering:** The two-photon excitation scheme to our chosen Rydberg state leads to off-resonant scattering from the intermediate state, $6P_{3/2}$. This scattering rate has a timescale of $50 - 100 \mu\text{s}$ for the two laser fields, and can be reduced by higher laser powers and further detuning from the intermediate state.

3. Rydberg state lifetime: The $70S$ Rydberg state has an estimated lifetime of $150\ \mu s$ [48], limited both by radiative decay and blackbody-stimulated transitions. This effect could be mitigated by selecting a higher Rydberg state with a longer lifetime or by cryogenic cooling of the blackbody environment.

Additional error sources that may limit our coherence properties include laser phase noise, which can be mitigated by better laser sources and stabilization schemes, and fluctuations in local addressing beam intensities and positions, which can be addressed by active feedback on the beam positions and improved thermal and mechanical stability of the setup. Simulations predict that we could go beyond the system sizes studied here. While GHZ states of $N = 24$ could be within reach with current parameters, generation of even larger GHZ states should be feasible with the additional technical improvements discussed above.

J.11 GROUND-STATE QUBIT ENCODING

The GHZ state parity could be more easily detected and manipulated if the qubits were encoded in a basis of hyperfine sublevels of the electronic ground state. In particular, one can consider two alternative qubit states $|\tilde{0}\rangle = |5S_{1/2}, F = 1, m_F = -1\rangle$ and $|\tilde{1}\rangle = |5S_{1/2}, F = 2, m_F = -2\rangle$. Rotations between these states are possible through stimulated Raman transitions or microwave driving, and the interactions are introduced by coupling $|\tilde{1}\rangle$ to a Rydberg level $|r\rangle$. This type of hyperfine encoding has been employed in multiple experiments with cold Rydberg atoms [110, 111, 289]. To prepare GHZ states in this basis, all atoms can be initialized in $|\tilde{1}\rangle$ and the system transferred to the state $|\tilde{1}r\tilde{1}r\dots\rangle + |\tilde{1}\tilde{1}r\tilde{1}\dots\rangle$ using the method described in this work. A ground-state qubit π pulse followed by a π pulse on the Rydberg transition transforms the state into $|\tilde{0}\tilde{1}\tilde{0}\tilde{1}\dots\rangle + |\tilde{1}\tilde{0}\tilde{1}\tilde{0}\dots\rangle$, enabling the long-lived storage of entanglement. Additionally, local qubit rotations can flip the state of every other site to prepare

the canonical form of the GHZ state, $|\tilde{0}\tilde{0}\tilde{0}\cdots\rangle + |\tilde{1}\tilde{1}\tilde{1}\cdots\rangle$, which can achieve entanglement-enhanced metrological sensitivity to homogeneous external fields [273]. Incorporating this type of hyperfine qubit encoding with Rydberg qubit control will be important for realizing quantum gates and deeper quantum circuits in future experiments.

K

Supplementary information for Chapter 14

We drive transitions between our qubit states using a 795 nm Raman laser which is $2\pi \times 100$ GHz red-detuned from the $5S_{1/2}$ to $5P_{1/2}$ transition. We couple the laser into a fiber-based Mach-Zehnder intensity modulator (Jenoptik AM785) which is DC biased around minimum transmission. The modulator is driven at half the qubit frequency ($\omega_{01} = 2\pi \times 6.83$ GHz), resulting in sidebands at $\pm 2\pi \times 3.42$ GHz, while the carrier and higher order sidebands are strongly suppressed. This approach is passively stable on the timescale of one day without any active feedback, in contrast with other approaches to generate sidebands through phase modulation and then separate suppression of the carrier mode with free space optical cavities or

interferometers*.

The Raman laser is aligned along the array of atoms (co-aligned with the 8.5 G bias magnetic field) and is σ^+ polarized, such that the two sidebands coherently drive π transitions between the $F = 1$ and $F = 2$ ground state manifolds with a Rabi frequency of $\Omega = 2\pi \times 250$ kHz. The Raman drive light induces a differential light shift of $2\pi \times 20$ kHz on the qubit transition; we adjust the drive frequency of the intensity modulator to correct for this light shift when we apply a Raman pulse.

K.1 OPTICAL PUMPING INTO $|0\rangle$

We optically pump atoms into $|0\rangle = |5S_{1/2}, F = 1, m_F = 0\rangle$ using a Raman-assisted pumping scheme with an 8.5 G magnetic field. The procedure is described in Section 4.7. We repeat the optical pumping cycle 70 times over a duration of 300 μ s to achieve a $|0\rangle$ preparation fidelity of 99.3(1)%.

K.2 RYDBERG LASER SYSTEM

We couple atoms from $|1\rangle = |5S_{1/2}, F = 2, m_F = 0\rangle$ to $|r\rangle = |70S_{1/2}, m_J = -1/2\rangle$ through a two-color laser system at 420 nm and 1013 nm, described in [182]. The lasers are polarized to drive σ^- and σ^+ transitions, respectively, through the intermediate state $|6P_{3/2}\rangle$. In previous experiments using $|5S_{1/2}, F = 2, m_F = -2\rangle$ as the ground state level, selection rules ensured that only a single intermediate sublevel within $|6P_{3/2}\rangle$ and only a single Rydberg state could be coupled. Additionally, the combined two-photon transition was magnetically insensitive.

Coupling from $|1\rangle = |5S_{1/2}, F = 2, m_F = 0\rangle$ to Rydberg states, as in these experiments, adds a few complications. Firstly, multiple intermediate states are coupled and both $|70S_{1/2}, m_J =$

*Note: an improved Raman driving scheme is presented in Chapter 4.

$\pm 1/2$ sublevels within the Rydberg manifold can be reached. This requires working at a higher magnetic field to spectrally separate the $m_J = \pm 1/2$ Rydberg levels. In these experiments, we work at a magnetic field of 8.5 G such that the splitting between $m_J = \pm 1/2$ is $2\pi \times 23.8$ MHz. The matrix element is also reduced in the coupling from $|1\rangle$ to $|r\rangle$ while the laser scattering rate stays the same; additionally, the transition is now magnetically sensitive. Nonetheless, this scheme benefits from high-quality qubit states $|0\rangle$ and $|1\rangle$ within the ground state manifold which can be easily coupled with a Raman laser system and which preserve coherence in optical tweezers. We note that the sensitivity to electric fields is unchanged in this scheme, but we can bound drifting or fluctuating electric fields in that the Rydberg resonance varies by < 50 kHz [293].

K.3 CONSTRUCTING QUANTUM CIRCUITS FROM NATIVE SINGLE-QUBIT GATES

All pulse sequences shown in Chapter 14 are decomposed into pre-calibrated single-qubit gates (and, where indicated, global multi-qubit gates). The two single-qubit gates are $X(\pi/4)$, implemented globally on all qubits simultaneously, and $Z(\pi)$, implemented by a light shift from a laser focused onto a single atom. In practice, the local $Z(\pi)$ gates are applied to one atom from each cluster at the same time (i.e., the left atom of each cluster or the middle of each cluster).

K.3.1 INITIALIZING COMPUTATIONAL BASIS STATES

For two qubits, we initialize all four computational basis states using global $X(\pi/2)$ pulses (consisting of two sequential $X(\pi/4)$ gates) and local $Z(\pi)$ gates on the left atom only (top qubit in each circuit). The $|00\rangle$ state requires no pulses to prepare, and the $|11\rangle$ state requires only a global $X(\pi)$ gate. We prepare $|01\rangle$ as follows:

$$|0\rangle \xrightarrow{X(\pi/2)} \xrightarrow{Z(\pi)} \xrightarrow{X(\pi/2)} |0\rangle$$

$$|0\rangle \xrightarrow{X(\pi/2)} \xrightarrow{X(\pi/2)} |1\rangle$$

and $|10\rangle$ according to

$$|0\rangle \xrightarrow{X(\pi/2)} \xrightarrow{Z(\pi)} \xrightarrow{X(3\pi/2)} |1\rangle$$

$$|0\rangle \xrightarrow{X(\pi/2)} \xrightarrow{X(3\pi/2)} |0\rangle$$

For three qubits, we initialize the eight computational basis states again using global $X(\pi/2)$ pulses and local $Z(\pi)$ pulses which can be applied to any of the three atoms. $|000\rangle$ and $|111\rangle$ can again be prepared with either no operation or with a global $X(\pi)$ gate, respectively. Other states have one atom in $|1\rangle$ and the other two in $|0\rangle$, or vice versa. We illustrate how both configurations are prepared by showing two examples. First, $|100\rangle$:

$$|0\rangle \xrightarrow{X(\pi/2)} \xrightarrow{Z(\pi)} \xrightarrow{X(3\pi/2)} |1\rangle$$

$$|0\rangle \xrightarrow{X(\pi/2)} \xrightarrow{X(3\pi/2)} |0\rangle$$

$$|0\rangle \xrightarrow{X(\pi/2)} \xrightarrow{X(3\pi/2)} |0\rangle$$

Next, we consider preparation of $|110\rangle$, which requires instead local addressing on the right-most atom.

$$|0\rangle \xrightarrow{X(\pi/2)} \xrightarrow{X(\pi/2)} |1\rangle$$

$$|0\rangle \xrightarrow{X(\pi/2)} \xrightarrow{X(\pi/2)} |1\rangle$$

$$|0\rangle \xrightarrow{X(\pi/2)} \xrightarrow{Z(\pi)} \xrightarrow{X(\pi/2)} |0\rangle$$

K.3.2 LOCAL $X(\pi/2)$ FOR CNOT GATE

To convert the \mathcal{CZ} gate to the CNOT gate, we apply a local $X(\pi/2)$ before and after the gate to the target atom. We implement this as follows:

$$\begin{array}{c} \text{---} \boxed{X(\pi/4)} \text{---} \boxed{Z(\pi)} \text{---} \boxed{X(\pi/4)} \text{---} = \text{---} \boxed{Z(\pi)} \text{---} \\ \text{---} \boxed{X(\pi/4)} \text{---} \text{---} \boxed{X(\pi/4)} \text{---} = \text{---} \boxed{X(\pi/2)} \text{---} \end{array}$$

This circuit applies a local $X(\pi/2)$ on the right atom; while it additionally applies a $Z(\pi)$ gate on the left atom, this circuit is only applied in a context in which the left atom is in a computational basis state $|0\rangle$ or $|1\rangle$, in which case the $Z(\pi)$ gate only introduces a global phase and therefore plays no role. In general, applying additional $Z(\pi)$ gates could be used to cancel the effect on the left atom, but this was not necessary for these experiments.

K.3.3 LOCAL HADAMARD FOR TOFFOLI IMPLEMENTATION

To convert the CCZ gate to a Toffoli gate, we apply a local rotation on the target (middle) qubit before and after the CCZ pulse. The simplest method to accomplish this given our native gate set is to apply a global $X(\pi/4)$, followed by a local $Z(\pi)$ on the middle qubit, and then a global $X(3\pi/4)$.

$$\begin{array}{c} \text{---} \boxed{X(\pi/4)} \text{---} \boxed{X(3\pi/4)} \text{---} \boxed{X(\pi)} \text{---} \\ \text{---} \boxed{X(\pi/4)} \text{---} \boxed{Z(\pi)} \text{---} \boxed{X(3\pi/4)} \text{---} = \text{---} \boxed{H} \text{---} \\ \text{---} \boxed{X(\pi/4)} \text{---} \boxed{X(3\pi/4)} \text{---} \boxed{X(\pi)} \text{---} \end{array}$$

On each edge qubit, the net effect is simply a $X(\pi)$ gate. On the middle qubit, this sequence constitutes a Hadamard gate (defined along a different axis than the typical defini-

tion), where

$$H = \frac{1}{\sqrt{2}} \begin{pmatrix} 1 & i \\ -i & -1 \end{pmatrix} \quad (\text{K.1})$$

K.4 DESIGN OF TWO-QUBIT CZ GATE

In this section we provide a detailed theoretical discussion of the two-qubit gate realized in the experiment. The desired unitary operation maps the computational basis states as follows:

$$\begin{aligned} |00\rangle &\rightarrow |00\rangle \\ |01\rangle &\rightarrow |01\rangle \\ |10\rangle &\rightarrow |10\rangle \\ |11\rangle &\rightarrow |11\rangle e^{i\pi} \end{aligned} \quad (\text{K.2})$$

Up to a global gauge choice (i.e. global rotation of the qubits), this is equivalent to the following gate

$$\begin{aligned} |00\rangle &\rightarrow |00\rangle \\ |01\rangle &\rightarrow |01\rangle e^{i\phi_1} \\ |10\rangle &\rightarrow |10\rangle e^{i\phi_1} \\ |11\rangle &\rightarrow |11\rangle e^{i(2\phi_1 + \pi)} \end{aligned} \quad (\text{K.3})$$

where ϕ_1 is arbitrary.

To realize such a gate we drive both atoms globally and homogeneously with a laser that couples state $|1\rangle$ to the Rydberg state $|r\rangle$. This can be achieved via a single laser field or by a two-photon process. The Hamiltonian governing the dynamics of a pair of atoms is given by

$$H = \sum_{i=1}^2 \frac{1}{2} (\Omega |1\rangle_i \langle r| + \Omega^* |r\rangle_i \langle 1|) - \Delta |r\rangle_i \langle r| + V |r\rangle_1 \langle r| \otimes |r\rangle_2 \langle r|$$

where Δ is the detuning of the excitation laser from the transition frequency between states $|1\rangle$ and $|r\rangle$, and Ω is the corresponding Rabi frequency. The interaction strength between two atoms in Rydberg states is given by V . In the following analysis we first assume that $V \gg |\Omega|, |\Delta|$, which can be realized by trapping the atoms sufficiently close to each other. This so-called Rydberg-blockade regime simplifies the following discussion, but is not crucial for the realization of the gate.

The dynamics of the system decouples into a few simple sectors:

- (i) The state $|00\rangle$ doesn't evolve.
- (ii) If one of the atoms is in $|0\rangle$, only the other system evolves. The dynamics is thus equivalent to that of a two level system (TLS) with states $|1\rangle = |a_1\rangle$ and $|r\rangle = |b_1\rangle$ and Hamiltonian

$$H_1 = \frac{1}{2}(\Omega|a_1\rangle\langle b_1| + \Omega^*|b_1\rangle\langle a_1|) - \Delta|b_1\rangle\langle b_1|.$$

- (iii) If both atoms are initially in state $|1\rangle$, then the dynamics is again equivalent to that of an effective single TLS, formed by the states $|11\rangle = |a_2\rangle$ and $\frac{1}{\sqrt{2}}(|r,1\rangle + |1,r\rangle) = |b_2\rangle$, with Hamiltonian

$$H_2 = \frac{\sqrt{2}}{2}(\Omega|a_2\rangle\langle b_2| + \Omega^*|b_2\rangle\langle a_2|) - \Delta|b_2\rangle\langle b_2|.$$

This assumes a perfect Rydberg blockade, equivalent to $V \rightarrow \infty$. We stress again that this assumption simplifies the analysis but is not necessary to realize our proposed gate.

The controlled-phase gate can be constructed from two identical global pulses of the Rydberg laser field, with equal duration τ and detuning Δ , along with a phase jump by ξ in between. Each pulse changes the state of the atoms according to the unitary $U = \exp(-iH\tau)$. The change of the laser phase between pulses, $\Omega \rightarrow \Omega e^{i\xi}$, effectively corresponds to driving the system around a different axis on the Bloch sphere.

Let us examine how the four computational basis states evolve under the action of \mathcal{U} , which describes the effect of both laser pulses combined. First we note that $\mathcal{U}|00\rangle = |00\rangle$. Thus the unitary \mathcal{U} maps the state $|00\rangle$ as expected for the CZ gate.

Next, let us consider the evolution of state $|11\rangle$. We choose the length of each pulse τ such that a system prepared in state $|11\rangle$ undergoes a complete, detuned Rabi oscillation and returns to the state $|11\rangle$ already after the first single pulse; that is, $U|11\rangle = e^{i\phi_2/2}|11\rangle$. This is guaranteed by the choice

$$\tau = 2\pi/\sqrt{\Delta^2 + 2\Omega^2}. \quad (\text{K.4})$$

The second pulse also leads to a complete, detuned Rabi cycle about a different axis, but results in the same accumulated phase. In total, we find $\mathcal{U}|11\rangle = e^{i\phi_2}|11\rangle$. The dynamical phase accumulated by this process is given by $\phi_2 = 2\pi \times 2\Delta/\sqrt{\Delta^2 + 2\Omega^2}$.

Finally, let us consider the evolution of the states $|01\rangle$ and $|10\rangle$. In each case, this is also described by a detuned Rabi oscillation. However, due to the mismatch between the effective Rabi frequencies in H_1 and H_2 , the state $|10\rangle$ ($|01\rangle$) does not return to itself after the time τ but a superposition state is created: $U|10\rangle = \cos(\alpha)|10\rangle + \sin(\beta)e^{i\gamma}|r0\rangle$, and $U|01\rangle = \cos(\alpha)|01\rangle + \sin(\beta)e^{i\gamma}|0r\rangle$. The real coefficients α , β and γ are determined by the choice of Ω , Δ and τ , and can easily be calculated (we omit explicit expressions here for compactness). Crucially, by a proper choice of the phase jump between the two pulses, ξ , one can always guarantee that the system returns to the state $|10\rangle$ ($|01\rangle$) after the second pulse. This can be calculated to be

$$e^{-i\xi} = \frac{-\sqrt{y^2 + 1} \cos\left(\frac{1}{2}s\sqrt{y^2 + 1}\right) + iy \sin\left(\frac{1}{2}s\sqrt{y^2 + 1}\right)}{\sqrt{y^2 + 1} \cos\left(\frac{1}{2}s\sqrt{y^2 + 1}\right) + iy \sin\left(\frac{1}{2}s\sqrt{y^2 + 1}\right)} \quad (\text{K.5})$$

where we use the short hand notation $y = \Delta/\Omega$ and $s = \Omega\tau$. With this choice of the phase we thus have $\mathcal{U}|10\rangle = e^{-i\phi_1}|10\rangle$ and $\mathcal{U}|01\rangle = e^{-i\phi_1}|01\rangle$. The acquired dynamical phase can be calculated using straightforward algebra, and is a function of Δ/Ω , $\tau\Omega$ and ξ . Since we fixed τ in equation (K.4), and ξ in (K.5), ϕ_1 is actually solely determined by the dimensionless quantity Δ/Ω . Note that also ϕ_2 is only a function of Δ/Ω . However, the functional dependence is different, and we can find a choice for Δ/Ω such that $e^{i\phi_2} = e^{i(2\phi_1+\pi)}$ (see Fig. 14.2 of Chapter 14). With this choice, we obtain exactly the gate given in (K.3) which is equivalent to the controlled-phase gate (K.2) (up to trivial single qubit rotations). For completeness we give the corresponding numerical values of the relevant parameters:

$$\Delta/\Omega = 0.377371 \quad (\text{K.6})$$

$$\xi = 3.90242 \quad (\text{K.7})$$

$$\Omega\tau = 4.29268 \quad (\text{K.8})$$

Finally, we note that this construction can be generalized to multi-qubit controlled phase gates in fully blockaded systems with more than two atoms.

K.4.1 ACCOUNTING FOR IMPERFECT BLOCKADE

The above analysis is based on the perfect blockade mechanism. Finite blockade interactions (and other experimental imperfections, such as coupling to other Rydberg states) can be accounted for, and lead only to an effective renormalization of the parameters given in (K.6). To see this, note that a finite value of V only affects the dynamics if the system is initially in the state $|11\rangle$. Instead of being restricted to the two states $|a_2\rangle = |11\rangle$ and $|b_2\rangle = |1r\rangle + |r1\rangle$, a

third state $|c_2\rangle = |rr\rangle$ has to be considered, and H_2 is replaced by

$$H_2 = \frac{\sqrt{2}}{2} (\Omega|a_2\rangle\langle b_2| + \Omega|b_2\rangle\langle c_2| + \Omega^*|c_2\rangle\langle b_2| + \Omega^*|b_2\rangle\langle a_2|) - \Delta|b_2\rangle\langle b_2| + (V - 2\Delta)|c_2\rangle\langle c_2|. \quad (\text{K.9})$$

For $V \gg |\Delta|, |\Omega|$, the effect for finite blockade simply reduces to the two-level system $\{|a_2\rangle, |b_2\rangle\}$ where Δ is renormalized by an amount $\Omega^2/(2V)$. Even for small $V > 0$ and a given Δ , we can always choose Ω and τ such that the system initialized in the state $|a_2\rangle$ returns after the first pulse. Thus finite blockade simply replaces the complete Rabi oscillation in the fully blockaded regime, by a slightly more complicated, but still closed path in a two-dimensional Hilbert space. The analysis of the dynamics of the other computational basis states is unaffected by the finite value of V . It is thus straightforward to ensure that a system initially in the state $|10\rangle$ returns to $|10\rangle$ for each choice of V and Δ . This allows one to use Δ as a control knob for the relative dynamical phases acquired by $|11\rangle$ and $|10\rangle$, and thus realize a CZ gate.

K.5 EXPERIMENTAL CALIBRATION OF CZ GATE

The CZ gate requires two laser pulses with a relative phase shift between them. The detuning of the two pulses Δ is determined relative to the experimentally calibrated Rydberg resonance by numerical calculations. The pulse time and the phase jump between pulses both require experimental calibration due to perturbations in timing and phase associated with an AOM-based control system. The pulse time τ is calibrated first by preparing both atoms in the qubit pair in $|1\rangle$ and driving at detuning Δ to the Rydberg state. We observe detuned Rabi oscillations to the symmetrically excited state $|W\rangle = \frac{1}{\sqrt{2}}(|1r\rangle + |r1\rangle)$ and extract the pulse time at which the population returns fully to $|11\rangle$.

After fixing τ , we prepare only single isolated atoms in $|1\rangle$ and we drive two pulses of length τ with a variable relative phase. By identifying the phase for which the single atom returns fully to $|1\rangle$ by the end of the sequence, we fix the relative phase ξ .

Finally, we calibrate the global phase shift necessary to convert the CZ gate (with single-particle phase ϕ) into the canonical form:

$$\mathcal{CZ} = \begin{pmatrix} 1 & 0 & 0 & 0 \\ 0 & -1 & 0 & 0 \\ 0 & 0 & -1 & 0 \\ 0 & 0 & 0 & -1 \end{pmatrix} \quad (\text{K.10})$$

We implement this phase correction by applying the global 420 nm laser for a fixed time in the absence of the 1013 nm Rydberg light; this avoids any resonant Rydberg excitation and instead only adds a phase shift. To calibrate the phase correction, we apply the Bell state sequence in which we attempt to prepare the Bell state $|\Phi^+\rangle$ and then we apply an additional $X(\pi/2)$ rotation to both qubits. If our phase correction is optimal, we should prepare the state $|\Psi^+\rangle$, which we can measure in populations. We vary the global phase correction to maximize the measured populations in $|\Psi^+\rangle$ at the end of this sequence.

K.6 PREPARATION OF BELL STATE USING \mathcal{CZ} GATE AND $\pi/4$ PULSE

Our global implementation of the \mathcal{CZ} gate enables the preparation of Bell states with no local addressing. The protocol is most naturally understood by describing the two-qubit system in the Bell basis:

$$|\Psi^\pm\rangle = \frac{1}{\sqrt{2}}(|01\rangle \pm |10\rangle) \quad (\text{K.11})$$

$$|\Phi^\pm\rangle = \frac{1}{\sqrt{2}}(|00\rangle \pm |11\rangle) \quad (\text{K.12})$$

We prepare the system in $|00\rangle$, and after a global $X(\pi/2)$ pulse, we prepare the state

$$|\psi_1\rangle = \frac{1}{2}(|00\rangle - i|01\rangle - i|10\rangle - |11\rangle) \quad (\text{K.13})$$

The controlled-phase gate creates the state

$$|\psi_2\rangle = \mathcal{CZ}|\psi_1\rangle = \frac{1}{2}(|00\rangle + i|01\rangle + i|10\rangle + |11\rangle) \quad (\text{K.14})$$

$$= \frac{1}{\sqrt{2}}(|\Phi^+\rangle + i|\Psi^+\rangle) \quad (\text{K.15})$$

The states $|\Phi^+\rangle$ and $|\Psi^+\rangle$ are both within the triplet manifold of the two qubits and are coupled resonantly by a global drive field to form an effective two level system with twice the single-particle Rabi frequency. A $\pi/2$ pulse within this effective two-level system corresponds to a $\pi/4$ pulse at the single-particle Rabi frequency, and maps:

$$|\psi_2\rangle = \frac{1}{\sqrt{2}}(|\Phi^+\rangle + i|\Psi^+\rangle) \rightarrow |\psi_3\rangle = |\Phi^+\rangle \quad (\text{K.16})$$

K.7 IMPLEMENTATION OF CCZ GATE

We implement the controlled-controlled-phase (CCZ) gate in the regime in which nearest neighbors are constrained by the Rydberg blockade, but next-nearest neighbors have only weak interactions. In light of this, the CCZ gate that we aim to implement is motivated by the fact that both edge atoms can simultaneously blockade the middle (target) atom. In particular, we consider the following scheme to implement CCZ that involves local excitation to Rydberg states:

1. Apply a π pulse on both edge atoms, transferring all of their population in $|1\rangle$ to $|r\rangle$.

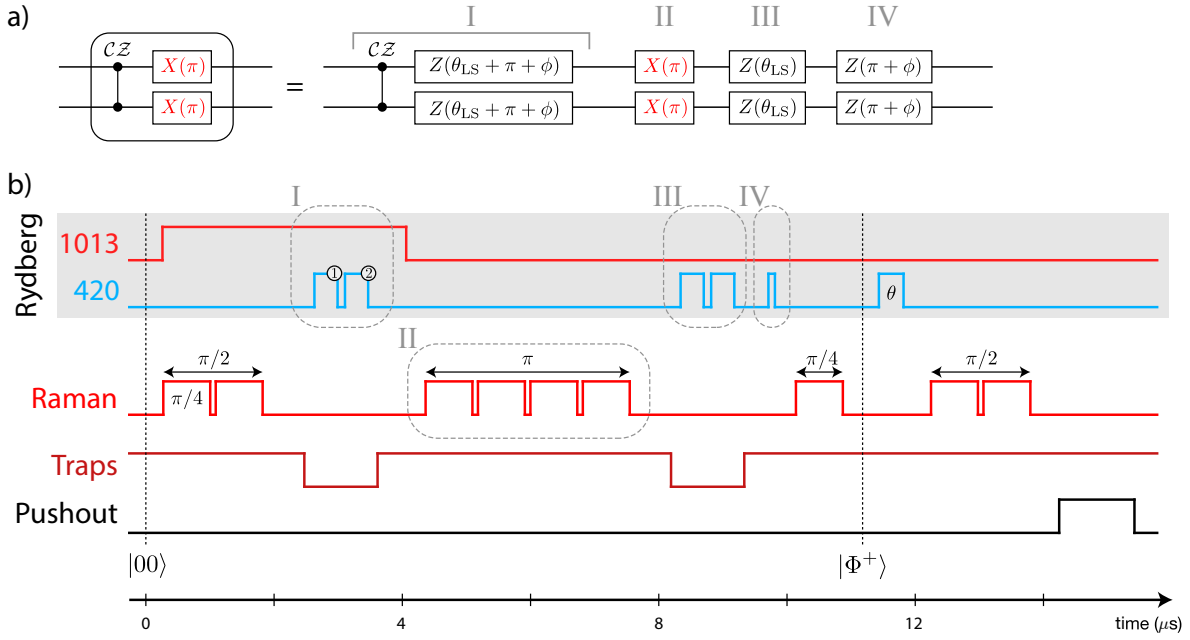


Figure K.1: Detailed pulse sequences. a) The implementation of the controlled-phase gate in the enclosed region (left hand side, as in Fig. 14.3 of Chapter 14), is shown in more explicit detail on the right hand side. The direct implementation of the $\mathcal{C}\mathcal{Z}$ gate (region I) includes an extra phase shift on both qubits. This is corrected by a hyperfine qubit $X(\pi)$ echo pulse (II), followed by the appropriate phase shifts (III and IV). b) The full pulse sequence for preparing Bell states begins with both atoms in $|0\rangle$ and a global $X(\pi/2)$ pulse (produced by two $\pi/4$ Raman pulses) to put both atoms in $|\downarrow\rangle_y$. Then, while the 1013 nm laser is on, the 420 nm laser is applied in two pulses (with a relative phase between the pulses) to enact the CZ gate, along with global phase shifts coming from the light shift of the 420 nm laser. A global $X(\pi)$ pulse flips the qubit states, at which point the same 420 nm pulses are applied but now in the absence of 1013 nm light. This negates the effect of light shifts in the first portion of the CZ gate implementation. Then, an additional short pulse of the 420 nm laser adds an additional phase correction to turn the CZ gate into the canonical $\mathcal{C}\mathcal{Z}$ gate. A subsequent global $X(\pi/4)$ pulse prepares the two atoms in the Bell state $|\Phi^+\rangle$. A final 420 nm laser pulse can be used to add dynamical phase to this Bell state, which can be detected by a subsequent global $X(\pi/2)$ for measuring parity oscillations. Finally, we push out atoms in $|1\rangle$ to detect populations.

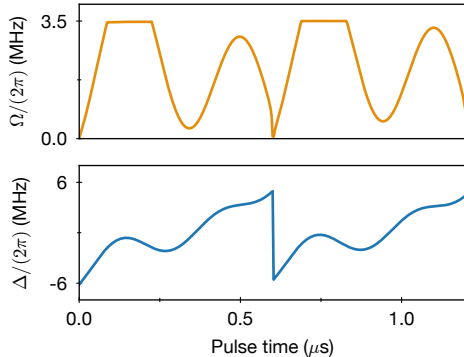


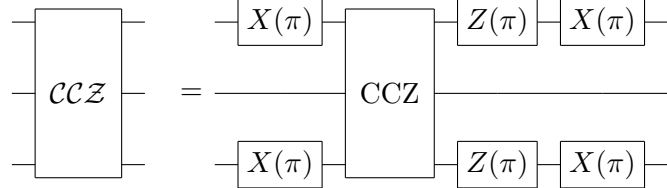
Figure K.2: Optimal control pulse for CCZ implementation. Time variation of Rydberg Rabi frequency and detuning to approximately implement the CCZ gate with numerically simulated fidelity 97.6%.

2. Apply a 2π pulse on the center atom, exciting from $|1\rangle$ to $|r\rangle$ and back to $|1\rangle$, accumulating a π phase shift only if neither edge atom is blockading this central atom and the atom is in $|1\rangle$.
3. Apply another π pulse on the edge atoms to return any population from $|r\rangle$ to $|1\rangle$.

Such a protocol realizes the following unitary:

$$\text{CCZ} = \begin{pmatrix} 1 & 0 & 0 & 0 & 0 & 0 & 0 & 0 \\ 0 & -1 & 0 & 0 & 0 & 0 & 0 & 0 \\ 0 & 0 & -1 & 0 & 0 & 0 & 0 & 0 \\ 0 & 0 & 0 & -1 & 0 & 0 & 0 & 0 \\ 0 & 0 & 0 & 0 & -1 & 0 & 0 & 0 \\ 0 & 0 & 0 & 0 & 0 & 0 & 1 & 0 \\ 0 & 0 & 0 & 0 & 0 & 0 & 0 & -1 \\ 0 & 0 & 0 & 0 & 0 & 0 & 0 & 1 \end{pmatrix} \quad (\text{K.17})$$

This unitary is equivalent to the canonical controlled-controlled-phase gate, denoted $\mathcal{CCZ} = \mathbb{1} - 2|111\rangle\langle 111|$ up to local rotations:



In the absence of local excitation to Rydberg states, we find that global Rydberg coupling can still approximately realize this unitary. Since different input configurations evolve according to dynamics of few-level systems with different coupling frequencies, it is challenging to design a single analytic global pulse to control all input configurations properly. For example, the $|001\rangle$ state couples to $|00r\rangle$ as a two-level system with Rabi frequency Ω . The $|011\rangle$ state couples to $\frac{1}{\sqrt{2}}(|01r\rangle + |0r1\rangle)$ with Rabi frequency $\sqrt{2}\Omega$. The $|111\rangle$ state couples both to $|1r1\rangle$ with Rabi frequency Ω , and also couples to $\frac{1}{\sqrt{2}}(|r11\rangle + |11r\rangle)$ with Rabi frequency $\sqrt{2}\Omega$ (which then couples to $|r1r\rangle$). The systems are further complicated by the finite next-nearest neighbor interactions.

bor interaction between edge atoms.

To find a global pulse that works on all input configurations, we use the RedCRAB optimal control algorithm [287, 288] to optimize an amplitude and frequency profile for the coupling field. The optimized pulse, shown in Fig. K.2, has duration of $1.2 \mu\text{s}$ and achieves a numerically simulated gate fidelity of 97.6%.

Future experimental implementations with colder atoms could achieve higher gate fidelities by designing gate timings to intentionally cancel the effect of the unwanted phase accumulation between next-nearest neighbors. Alternatively, few-qubit gates could be implemented with all atoms in the fully blockaded regime by bringing atoms closer together or by exciting to higher Rydberg states.

K.8 ECHO PROCEDURE FOR CZ AND CCZ

The Rydberg pulse which implements the CZ or the CCZ gate includes both a 1013 nm laser field and a 420 nm laser field, the latter of which adds a differential light shift to the qubit levels of $\sim 2\pi \times 3 \text{ MHz}$. To correct for the phase accumulated due to this light shift, after the CZ gate we apply a qubit $X(\pi)$ rotation on all atoms and then apply the same 420 nm pulse used for the CZ gate, but this time in the absence of 1013 nm light. The single particle phase ϕ (eq. (14.1) of Chapter 14) inherent in the design of the CZ protocol is separately corrected by an additional short pulse of the 420 nm laser. The full detailed pulse sequence is shown in Fig. K.1.

K.9 STATE READOUT THROUGH ATOM LOSS

Our primary technique for state readout is to apply a resonant laser pulse that heats atoms in $|1\rangle$ (in $F = 2$, more generally) out of the tweezers, after which we take a fluorescence im-

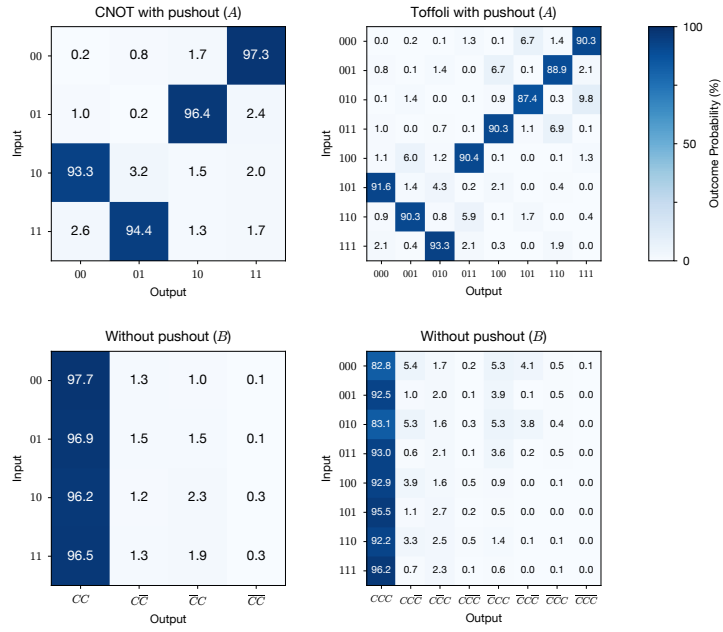


Figure K.3: Here we show full measurement statistics for the CNOT and Toffoli truth tables. In both situations, for each input computational basis state, we measure the probability distribution (shown in percentage points) of different output configurations both with and without the pushout pulse which removes $|1\rangle$ population, corresponding to the A matrix and B matrix, respectively. The output distribution of the A matrix is mainly associated with qubit levels $|0\rangle$ and $|1\rangle$ according to whether the atom is present or absent. However, this approach overestimates population in $|1\rangle$ since leftover population in the Rydberg state and losses due to other processes lead to the same measurement outcome as $|1\rangle$. To distinguish this effect, we measure without the pushout pulse (bottom row) to assess how much population is left in the computational subspace (C), rather than lost into the Rydberg state and therefore out of the computational subspace (\bar{C}). Comparing these two measurements provides a lower bound on the true atomic populations in the $|0\rangle$ and $|1\rangle$ qubit states.

age of remaining atoms in $|0\rangle$. This method correctly identifies atoms in $|0\rangle$, but can mistake atoms that were lost through background loss processes or by residual Rydberg excitation for atoms in $|1\rangle$, leading to an overestimation of the population in $|1\rangle$. For any measurements involving Rydberg excitation, we therefore collect measurement statistics both with and without the pushout pulse, which provides an upper bound on how much leakage out of the qubit subspace occurred, and therefore also gives a lower bound on the true population in $|1\rangle$.

We illustrate this procedure in the context of two-qubit experiments. Let us denote the two types of measurements as A (in which we apply the pushout of $|1\rangle$ atoms) and B (in which we

disable the pushout). For each measurement procedure, we obtain statistics of observing the four two-qubit states, consisting of ‘lost’ or ‘present’ for each qubit. The A vector associates these as $|0\rangle$ and $|1\rangle$, so A_{ij} (for $i, j \in \{0, 1\}$) denotes the probability of identifying the left and right atom in 0, 1 through the simple loss/presence analysis. However, the atoms can be not only in the qubit states 0, 1 but they can also be lost from the trap or in the Rydberg state, which in both cases will be detected as ‘lost’. Let us denote C as the computational subspace containing $|0\rangle$ and $|1\rangle$, and denote \bar{C} as anything outside this subspace (including Rydberg population or loss). The B vector measures whether the atoms are in C (either $|0\rangle$ or $|1\rangle$), or not (\bar{C}), so is denoted B_{ij} where $i, j \in \{C, \bar{C}\}$.

Both A_{ij} and B_{ij} can be explicitly expressed in terms of the underlying atomic populations $p_{\alpha\beta}$, where $\alpha, \beta \in \{0, 1, \bar{C}\}$, as follows;

$$A_{00} = p_{00} \quad (\text{K.18})$$

$$A_{01} = p_{01} + p_{0\bar{C}} \quad (\text{K.19})$$

$$A_{10} = p_{10} + p_{\bar{C}0} \quad (\text{K.20})$$

$$A_{11} = p_{11} + p_{1\bar{C}} + p_{\bar{C}1} + p_{\bar{C}\bar{C}} \quad (\text{K.21})$$

$$B_{CC} = p_{00} + p_{01} + p_{10} + p_{11} \quad (\text{K.22})$$

$$B_{C\bar{C}} = p_{0\bar{C}} + p_{1\bar{C}} \quad (\text{K.23})$$

$$B_{\bar{C}C} = p_{\bar{C}0} + p_{\bar{C}1} \quad (\text{K.24})$$

$$B_{\bar{C}\bar{C}} = p_{\bar{C}\bar{C}} \quad (\text{K.25})$$

Measuring A_{ij} and B_{ij} , we can now solve for the atomic populations of interest: $p_{00}, p_{01}, p_{10}, p_{11}$.

$$p_{00} = A_{00} \quad (\text{K.26})$$

$$p_{01} = A_{01} - B_{C\bar{C}} + p_{1\bar{C}} \quad (\text{K.27})$$

$$p_{10} = A_{10} - B_{\bar{C}C} + p_{\bar{C}1} \quad (\text{K.28})$$

$$p_{11} = A_{11} - B_{CC} - B_{C\bar{C}} - B_{\bar{C}C} + (p_{0\bar{C}} + p_{\bar{C}0}) \quad (\text{K.29})$$

Since all probabilities are non-negative and $B_{C\bar{C}} + B_{\bar{C}C} + B_{\bar{C}\bar{C}} = 1 - B_{CC}$, we have our lower bounds for the true populations:

$$p_{00} = A_{00} \quad (\text{K.30})$$

$$p_{01} \geq A_{01} - B_{C\bar{C}} \quad (\text{K.31})$$

$$p_{10} \geq A_{10} - B_{\bar{C}C} \quad (\text{K.32})$$

$$p_{11} \geq A_{11} - (1 - B_{CC}) \quad (\text{K.33})$$

This is the analysis carried out for the Bell state populations, the CNOT truth table, and the Toffoli truth table (extended to three qubits). For the truth tables, the analysis is carried out for each measurement configuration (corresponding to a different input computational basis state) separately, shown as the rows in the matrices of Fig. K.3.

K.10 CORRECTING FOR STATE PREPARATION AND MEASUREMENT ERRORS

We consider the problem of correcting a measured fidelity for state preparation and measurement (SPAM) errors. We denote P as the probability to correctly initialize and measure all qubits; generally, $P = (1 - \epsilon)^N$ for single-particle SPAM error rate of ϵ . The measured fidelity is related to the ‘corrected fidelity’ according to:

$$\mathcal{F} = P \times \mathcal{F}^c + (1 - P) \times \mathcal{F}^{\text{false}} \quad (\text{K.34})$$

Here $\mathcal{F}^{\text{false}}$ denotes the false contribution to the measured fidelity signal in cases in which SPAM errors occur. The main subtlety in performing this correction is properly evaluating the potential false contribution $\mathcal{F}^{\text{false}}$.

Experimentally, the SPAM error is $\epsilon = 1.2(1)\%$ per qubit, consisting of two effects: first, the optical pumping into $|0\rangle$ has an error probability of $0.7(1)\%$, constituting a state preparation

error. Second, there is a small chance that an atom can be lost due to a background collision either before or after the Bell state circuit is performed. Loss before the circuit contributes as a state preparation error; loss after the circuit but prior to the readout fluorescence image contributes as a measurement error. The total background loss contribution is 0.5(1)% error per atom.

K.10.1 BELL STATE FIDELITY

The total probability that no errors occur on either of two qubits is $P = 97.6(2)\%$. Equation (K.34) holds for both the population measurement and the parity oscillation measurement separately. The population measurement explicitly only counts lower bounds on the population of atoms within the qubit subspace (Section K.9). Therefore, in cases where an atom is lost there is no false contribution to the measured fidelity. However, our measured fidelity does not distinguish between atoms pumped into magnetic sublevels outside of the qubit subspace. We estimate that in cases when one of the two atoms are prepared in an incorrect magnetic sublevel (1.4(2)% probability), there can be a false contribution of $\mathcal{F}^{\text{false}} = 1 - \cos^2(7\pi/8) \approx 15\%$ (calculated by evaluating the quantum circuit in Fig. 14.3a of Chapter 14 with one atom not participating). The lower bound on the measured probabilities $p_{00} + p_{11} \geq 95.8(3)\%$ therefore set a lower bound on the corrected populations: $p_{00}^c + p_{11}^c \geq 97.9(4)\%$.

On the other hand, the parity oscillation amplitude receives no false contribution from cases when an atom is prepared in the wrong sublevel or is lost, because this error is independent of the accumulated phase and therefore does not oscillate as a function of the phase accumulation time. The false contribution is therefore $\mathcal{F}^{\text{false}} = 0$. In this case, the coherence C (given by the amplitude of the parity oscillation) is related to the corrected coherence by $C = P \times C^c$. Since $C = 94.2(4)\%$, we obtain a corrected coherence of $C^c = 96.5(4)\%$. The

total SPAM-corrected Bell state fidelity, then, is $\mathcal{F}^c = \frac{1}{2}(p_{00}^c + p_{11}^c + C^c) \geq 97.2(3)\%$.

K.10.2 CNOT TRUTH TABLE

We measure the truth table by performing the CNOT gate on each computational basis state. The basis states are prepared with finite fidelity, as measured and shown in Fig. 14.3e of Chapter 14. For each basis state, we wish to assess how the finite output fidelity in the target state compares to the finite initialization fidelity to determine how well the gate performs on this input state. We establish a probability P_{ij} of no SPAM error occurring for each measurement setting (where ij denotes the setting in which we initialize the computational basis state $|ij\rangle$). Additionally, we measure a lower bound on the output probability in the target state, \mathcal{F}_{ij} .

We now consider false contributions to the measured fidelity. When an error involving atom loss occurs, there is no false contribution to fidelity since fidelity only measures atom population within the qubit subspace. Alternatively, in cases when the wrong computational basis state is prepared, then $\mathcal{F}^{\text{false}}$ is bounded above by the largest unwanted element of the truth table, or $< 4\%$. The total false contribution therefore is $(1 - P) \times \mathcal{F}^{\text{false}} < (3\%) \times (4\%) \lesssim 0.1\%$. This contribution is below our measurement resolution and we do not account for it. The corrected fidelity is therefore just given by $\mathcal{F}_{ij}^c = \mathcal{F}_{ij}^{\text{meas}} / P_{ij}$. The average corrected truth table fidelity, given by the average of \mathcal{F}_{ij}^c , is therefore $\mathcal{F}_{\text{CNOT}}^c \geq 96.5\%$ (see Table K.1).

K.10.3 TOFFOLI TRUTH TABLE

We perform the same analysis to evaluate the corrected Toffoli truth table fidelity as for the CNOT truth table. The average corrected truth table fidelity is $\mathcal{F}_{\text{Toff}}^c \geq 87.0\%$ (see Table K.1).

	Raw outcomes	Lower bound	Corrected
Bell state populations	97.6%	95.8%	97.9%
Bell state coherences	94.2%	94.2%	96.5%
Bell state fidelity	95.9%	95.0%	97.2%
CNOT: Input 00	97.3%	95.0%	96.5%
01	96.4%	94.9%	97.9%
10	93.3%	93.3%	96.3%
11	94.4%	93.1%	95.4%
CNOT Truth table	95.4%	94.1%	96.5%
Toffoli: Input 000	90.3%	73.1%	75.1%
001	88.9%	82.6%	86.2%
010	87.4%	73.0%	76.0%
011	90.3%	86.7%	90.0%
100	90.4%	84.3%	87.4%
101	91.6%	91.6%	95.7%
110	90.3%	87.0%	90.5%
111	93.3%	91.0%	95.0%
Toffoli Truth table	90.3%	83.7%	87.0%

Table K.1: Summary of measurement results. Raw outcomes correspond to simple assignment of atom presence to qubit state 0 or 1. The lower bound comes from subtracting a conservative upper bound estimate on how much leakage out of the qubit subspace there may be, as determined by a separate measurement in which we do not push out $|1\rangle$ atoms. The corrected column shows the fidelities corrected for SPAM errors.

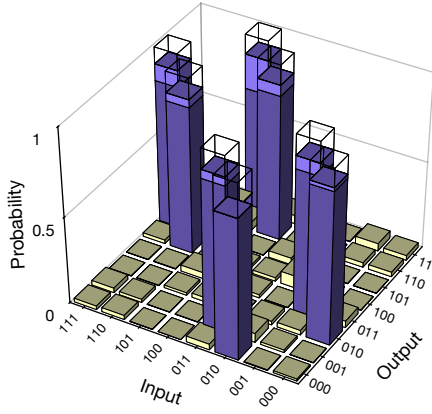
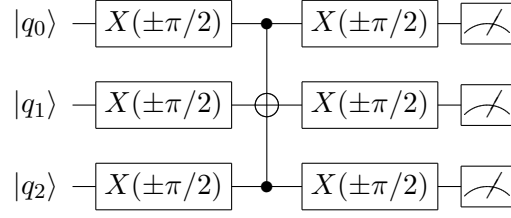


Figure K.4: Limited tomography of Toffoli gate. The raw target probabilities average to 88.0(3)%. Since four of the measurement configurations are precisely global $X(\pi)$ gates applied to the other four input states, we can compare these output distributions to properly account for leftover Rydberg population, similar to the procedure discussed in Section K.9. We establish the limited tomography fidelity is therefore $\mathcal{F} \geq 81.5(5)\%$. Corrected for SPAM errors, the fidelity is $\geq 86.2(6)\%$.

K.11 LIMITED TOMOGRAPHY OF TOFFOLI GATE

The truth table of the Toffoli gate provides a representation of the magnitude of the matrix elements of the gate expressed in the logical basis. However, the measured populations carry no information about the relative phases between the different entries. Performing a similar procedure as the truth table but rotating the Toffoli gate to act on the X -basis instead of the Z -basis makes it possible to recover some information about these phases. A restricted version of such a procedure has been used before as a way to characterize the fidelity of the Toffoli gate [300], and has been dubbed “Limited Tomography”. The procedure consists of initializing all the computational basis states in the Z -basis, and then applying an $X(\pm\pi/2)$ rotation to all qubits before and after a Toffoli gate. The sign is chosen to be $X(+\pi/2)$ when the target qubit is initialized in $|0\rangle$ and $X(-\pi/2)$ when the target qubit is initialized in $|1\rangle$.



Conditioning the sign of the rotation on the state of the target qubit enforces that the target qubit is always in the same state $|+\rangle_y$ prior to the action of the Toffoli gate itself.

The Toffoli gate implemented in our system, which includes an echo pulse that acts as a global $X(\pi)$ gate (see Fig. 14.4 of Chapter 14), is described ideally by the unitary matrix:

$$T_{\text{Ideal}} = \begin{pmatrix} 0 & 0 & 0 & 0 & 0 & i & 0 & 0 \\ 0 & 0 & 0 & 0 & 0 & 0 & 1 & 0 \\ 0 & 0 & 0 & 0 & 0 & 0 & 0 & -i \\ 0 & 0 & 0 & 0 & 1 & 0 & 0 & 0 \\ 0 & 0 & 0 & 1 & 0 & 0 & 0 & 0 \\ 0 & 0 & -1 & 0 & 0 & 0 & 0 & 0 \\ 0 & 1 & 0 & 0 & 0 & 0 & 0 & 0 \\ -1 & 0 & 0 & 0 & 0 & 0 & 0 & 0 \end{pmatrix}, \quad (\text{K.35})$$

Performing the limited tomography procedure on this unitary should result in the following output truth table:

$$\text{Lim}[T_{\text{Ideal}}] = \begin{bmatrix} 0 & 0 & 1 & 0 & 0 & 0 & 0 & 0 \\ 0 & 0 & 0 & 1 & 0 & 0 & 0 & 0 \\ 1 & 0 & 0 & 0 & 0 & 0 & 0 & 0 \\ 0 & 1 & 0 & 0 & 0 & 0 & 0 & 0 \\ 0 & 0 & 0 & 0 & 0 & 0 & 1 & 0 \\ 0 & 0 & 0 & 0 & 0 & 0 & 0 & 1 \\ 0 & 0 & 0 & 0 & 1 & 0 & 0 & 0 \\ 0 & 0 & 0 & 0 & 0 & 1 & 0 & 0 \end{bmatrix}, \quad (\text{K.36})$$

where each row shows the target output probabilities for a given input state. However, if the Toffoli gate is allowed to deviate from the ideal unitary by arbitrary phases ϕ_j according to

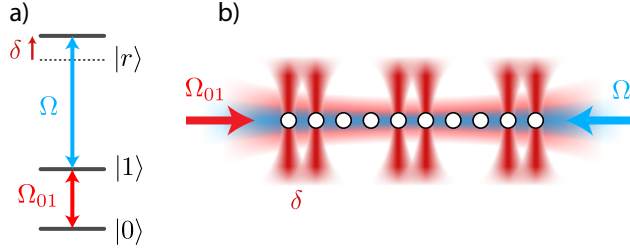


Figure K.5: Parallel gate implementation in a contiguous chain of atoms. (a) Local addressing lasers can shift the frequency of the Rydberg transition from $|1\rangle$ to $|r\rangle$ by δ without changing the $|0\rangle \leftrightarrow |1\rangle$ frequency. (b) The local addressing lasers are focused onto a subset of qubits on which we aim to perform parallel multi-qubit gates. The global Rydberg coupling laser is tuned to the light-shifted resonance, so that only the locally addressed atoms are coupled to the Rydberg state for gate implementation.

$$T_\phi = \begin{pmatrix} 0 & 0 & 0 & 0 & 0 & ie^{i\phi_1} & 0 & 0 \\ 0 & 0 & 0 & 0 & 0 & 0 & e^{i\phi_2} & 0 \\ 0 & 0 & 0 & 0 & 0 & 0 & 0 & -ie^{i\phi_3} \\ 0 & 0 & 0 & 0 & e^{i\phi_4} & 0 & 0 & 0 \\ 0 & 0 & 0 & e^{i\phi_5} & 0 & 0 & 0 & 0 \\ 0 & 0 & -e^{i\phi_6} & 0 & 0 & 0 & 0 & 0 \\ 0 & e^{i\phi_7} & 0 & 0 & 0 & 0 & 0 & 0 \\ -e^{i\phi_8} & 0 & 0 & 0 & 0 & 0 & 0 & 0 \end{pmatrix}, \quad (\text{K.37})$$

then the limited tomography truth table reflects this phase deviation. In particular, each truth table matrix element in which the limited tomography should produce unity will instead result in a peak probability of $|\frac{1}{8} \sum_j e^{i\phi_j}|^2$. The average fidelity of the limited tomography truth table therefore reflects how close the phases on the Toffoli unitary are to their ideal values, and can only reach unity if each phase is correct. Our measured limited tomography truth table is shown in Fig. K.4.

It is worth noting that the limited tomography protocol only makes use of four of the eight X -basis input states, as seen by the fact that the target qubit is always initialized in $|+\rangle$. This makes four out of the eight measurements equivalent to the other four up to a global $X(\pi)$ rotation at the end. Comparing these two sets of measurements gives a constraint on the probability of leakage out of the qubit subspace, similarly to the approach described in Section K.9.

K.12 PARALLEL GATE IMPLEMENTATION IN A CONTIGUOUS ARRAY

The experiments performed here involve parallel multi-qubit gate implementation on separated pairs of atoms, where the inter-pair interaction is negligible. However, one can extend this protocol to parallel gate implementation in a contiguous chain of atoms, as illustrated in Fig. K.5. We consider an additional local addressing laser system which can address an arbitrary subset of atoms, using for example an acousto-optic deflector. Specifically, one can select a wavelength for this laser such that the imparted light shift affects the $|0\rangle$ and $|1\rangle$ states equally, but differently from the Rydberg state $|r\rangle$. In such a case, the light shift from this new local addressing laser does not apply any qubit manipulations, but instead simply shifts the effective Rydberg resonance. Near-infrared wavelengths tuned far from any ground state optical transition ($\lambda \gtrsim 820$ nm) are suitable for Rubidium.

With such a system, we could illuminate all pairs of adjacent atoms on which we intend to perform two-qubit gates, and then by tuning the Rydberg laser to the light-shifted resonance we would perform the multi-qubit gate on all pairs in parallel. The only constraint is that there must be sufficient space between addressed pairs such that the interaction (cross-talk) between them is negligible in a particular layer of gate implementation.

L

Bessel function identities

In this chapter, we derive several Bessel function identities which are relevant for the evaluation of various protocols for converting phase modulation to amplitude modulation for Raman laser driving.

L.1 DESTRUCTIVE INTERFERENCE OF PURE PHASE MODULATION

The Bessel function identities that describe destructive interference in Raman driving with a phase modulated laser can be easily derived from the Jacobi-Anger expansion:

$$e^{i\beta \sin \omega t} = \sum_{n=-\infty}^{\infty} J_n(\beta) e^{in\omega t} \quad (\text{L.1})$$

Taking the magnitude squared of both sides, we find:

$$1 = \sum_{m,n} J_n(\beta) J_m(\beta) e^{i(m-n)\omega t} \quad (\text{L.2})$$

Regrouping the sum in terms of indices n and $k = m - n$, we find:

$$1 = \sum_{k=-\infty}^{\infty} e^{ik\omega t} \left[\sum_{n=-\infty}^{\infty} J_n(\beta) J_{n+k}(\beta) \right] \quad (\text{L.3})$$

Since the left hand side is time independent, the coefficients of the time dependent terms $e^{ik\omega t}$ must vanish for any $k \neq 0$:

$$\sum_{n=-\infty}^{\infty} J_n(\beta) J_{n+k}(\beta) = 0 \quad (\text{L.4})$$

Since these sums represent amplitude modulation at frequency $k\omega$, this tautologically says that pure phase modulation has no amplitude modulation.

L.2 QUADRATIC PHASE SHIFTS

Claim:

$$J_k(2z \sin \phi) = (-i)^k e^{ik\phi} \sum_{n=-\infty}^{\infty} J_n(z) J_{n+k}(z) e^{2in\phi} \quad (\text{L.5})$$

Proof: We begin using the Jacobi-Anger expansion, treating $\beta = 2z \sin \phi$ as the modulation depth.

$$e^{i(2z \sin \phi)(\sin \theta)} = \sum_{n=-\infty}^{\infty} J_n(2z \sin \phi) e^{in\theta} \quad (\text{L.6})$$

Alternatively, instead of expanding the left hand side using Jacobi-Anger, we could also multiply the two sine functions, recalling the trigonometric identity:

$$\sin(x)\sin(y) = \frac{1}{2} (\cos(x-y) - \cos(x+y)). \quad (\text{L.7})$$

Plugging this in, we obtain:

$$e^{i(2z\sin\phi)(\sin\theta)} = \left(e^{iz\cos(\phi-\theta)}\right) \left(e^{-iz\cos(\phi+\theta)}\right) \quad (\text{L.8})$$

We are now graced with the opportunity to apply the Jacobi-Anger expansion twice, once for each term on the right-hand side. Setting this expression equal to the right-hand side of equation (L.6), we obtain:

$$\left(\sum_{n=-\infty}^{\infty} i^n J_n(z) e^{in(\phi-\theta)}\right) \left(\sum_{m=-\infty}^{\infty} i^m J_m(-z) e^{im(\phi+\theta)}\right) = \sum_{k=-\infty}^{\infty} J_k(2z\sin\phi) e^{ik\theta} \quad (\text{L.9})$$

Expanding the left hand side as a sum over indices n, m :

$$\sum_{n,m} i^{n+m} J_n(z) J_m(-z) e^{i(n+m)\phi} e^{i(m-n)\theta} = \sum_{k=-\infty}^{\infty} J_k(2z\sin\phi) e^{ik\theta} \quad (\text{L.10})$$

We will now rewrite the left hand side with a change in indexing, using n and $k' \equiv m - n$, and regroup terms to pull the k' sum to be the outer sum:

$$\sum_{k'=-\infty}^{\infty} e^{ik'\theta} \left[i^{k'} e^{ik'\phi} \sum_{n=-\infty}^{\infty} i^{2n} J_n(z) J_{n+k'}(-z) e^{2in\phi} \right] = \sum_{k=-\infty}^{\infty} [J_k(2z\sin\phi)] e^{ik\theta} \quad (\text{L.11})$$

Recalling that $J_{n+k}(-z) = (-1)^{n+k} J_{n+k}(z)$, and using that $i^{2n} = (-1)^n$, we simplify:

$$\sum_{k'=-\infty}^{\infty} e^{ik'\theta} \left[(-i)^{k'} e^{ik'\phi} \sum_{n=-\infty}^{\infty} J_n(z) J_{n+k'}(z) e^{2in\phi} \right] = \sum_{k=-\infty}^{\infty} [J_k(2z \sin \phi)] e^{ik\theta} \quad (\text{L.12})$$

In both sides of the equation, we have an outer sum over k (or k'), with orthogonal functions $e^{ik\theta}$. We therefore must require that the coefficients are all equal for corresponding $k = k'$. Rewriting the equality between coefficients:

$$J_k(2z \sin \phi) = (-i)^k e^{ik\phi} \sum_{n=-\infty}^{\infty} J_n(z) J_{n+k}(z) e^{2in\phi} \quad (\text{L.13})$$

L.3 EVEN SIDEBANDS

We can now use (L.13) to prove identities regarding a field with only the even sidebands. We first consider the total power in a beam with only the even-index sidebands:

Claim:

$$T \equiv \sum_{n \text{ even}} J_n(\beta)^2 = \frac{1}{2} (1 + J_0(2\beta)) \quad (\text{L.14})$$

Proof: We find that the sum over even sidebands is quite similar to a sum over *all* sidebands, but with a minus sign on the odd sidebands. To see this,

$$\sum_{n=-\infty}^{\infty} (-1)^n J_n(\beta)^2 = \sum_{n \text{ even}} J_n(\beta)^2 - \sum_{n \text{ odd}} J_n(\beta)^2 \quad (\text{L.15})$$

Recalling that the sum of the power in all sidebands must be unity, we know that

$$\sum_{n \text{ odd}} J_n(\beta)^2 = 1 - \sum_{n \text{ even}} J_n(\beta)^2 \quad (\text{L.16})$$

Plugging this into equation (L.15), we have:

$$\sum_{n=-\infty}^{\infty} (-1)^n J_n(\beta)^2 = -1 + 2 \sum_{n \text{ even}} J_n(\beta)^2 \quad (\text{L.17})$$

$$= -1 + 2T \quad (\text{L.18})$$

The left hand side now happens to be in a very similar form to the right hand side of equation (L.13). In particular, we now write (L.13) with $k = 0, \phi = \pi/2$, and $z = \beta$:

$$J_0(2\beta) = \sum_{n=-\infty}^{\infty} (-1)^n J_n(\beta)^2 \quad (\text{L.19})$$

Inserting this result into eq. (L.18), we solve for T :

$$T = \frac{1}{2} (1 + J_0(2\beta))$$

(L.20)

Claim: Now we can apply a similar technique to prove another identity related to the situation of even sidebands:

$$\sum_{n \text{ even}} J_n(\beta) J_{n+2}(\beta) = \frac{1}{2} J_2(2\beta) \quad (\text{L.21})$$

Proof: We begin by directly applying the quadratic dispersion identity (L.13) with $k = 2, \phi = \pi/2$, and $z = \beta$:

$$J_2(2\beta) = \sum_{n=-\infty}^{\infty} (-1)^n J_n(\beta) J_{n+2}(\beta) \quad (\text{L.22})$$

Again separating in terms of even and odd terms:

$$J_2(2\beta) = \sum_{n \text{ even}} J_n(\beta) J_{n+2}(\beta) - \sum_{n \text{ odd}} J_n(\beta) J_{n+2}(\beta) \quad (\text{L.23})$$

Recalling that the sum over all pairs of sidebands is identically 0, we know that

$$\sum_{n \text{ odd}} J_n(\beta) J_{n+2}(\beta) = - \sum_{n \text{ even}} J_n(\beta) J_{n+2}(\beta) \quad (\text{L.24})$$

We now plug this result in and find:

$$\boxed{\sum_{n \text{ even}} J_n(\beta) J_{n+2}(\beta) = \frac{1}{2} J_2(2\beta)} \quad (\text{L.25})$$

Bibliography

- [1] A. Einstein, B. Podolsky, and N. Rosen, “Can Quantum-Mechanical Description of Physical Reality Be Considered Complete?” *Physical Review* **47**, 777 (1935).
- [2] E. Schrödinger, “Die gegenwärtige Situation in der Quantenmechanik,” *Die Naturwissenschaften* **23**, 807 (1935).
- [3] E. Schrödinger, “Are There Quantum Jumps? Part I,” *The British Journal for the Philosophy of Science* **3**, 109 (1952).
- [4] G. A. Morris and R. Freeman, “Enhancement of nuclear magnetic resonance signals by polarization transfer,” *Journal of the American Chemical Society* **101**, 760 (1979).
- [5] A. Aspect, J. Dalibard, and G. Roger, “Experimental Test of Bell’s Inequalities Using Time- Varying Analyzers,” *Physical Review Letters* **49**, 1804 (1982).
- [6] J. C. Bergquist, R. G. Hulet, W. M. Itano, and D. J. Wineland, “Observation of Quantum Jumps in a Single Atom,” *Physical Review Letters* **57**, 1699 (1986).
- [7] M. H. Anderson, J. R. Ensher, M. R. Matthews, C. E. Wieman, and E. A. Cornell, “Observation of Bose-Einstein Condensation in a Dilute Atomic Vapor,” *Science* **269**, 198 (1995).
- [8] K. B. Davis, M. O. Mewes, M. R. Andrews, N. J. van Druten, D. S. Durfee, D. M. Kurn, and W. Ketterle, “Bose-Einstein Condensation in a Gas of Sodium Atoms,” *Physical Review Letters* **75**, 3969 (1995).
- [9] C. Monroe, D. M. Meekhof, B. E. King, W. M. Itano, and D. J. Wineland, “Demonstration of a Fundamental Quantum Logic Gate,” *Physical Review Letters* **75**, 4714 (1995).
- [10] M. Brune, F. Schmidt-Kaler, A. Maali, J. Dreyer, E. Hagley, J. M. Raimond, and S. Haroche, “Quantum Rabi Oscillation: A Direct Test of Field Quantization in a Cavity,” *Physical Review Letters* **76**, 1800 (1996).
- [11] E. Hagley, X. Maître, G. Nogues, C. Wunderlich, M. Brune, J. M. Raimond, and S. Haroche, “Generation of Einstein-Podolsky-Rosen Pairs of Atoms,” *Physical Review Letters* **79**, 1 (1997).
- [12] D. G. Cory, M. D. Price, and T. F. Havel, “Nuclear magnetic resonance spectroscopy: An experimentally accessible paradigm for quantum computing,” *Physica D: Nonlinear Phenomena* **120**, 82 (1998).

- [13] C. A. Sackett, D. Kielpinski, B. E. King, C. Langer, V. Meyer, C. J. Myatt, M. Rowe, Q. A. Turchette, W. M. Itano, D. J. Wineland, and C. Monroe, “Experimental entanglement of four particles,” *Nature* **404**, 256 (2000).
- [14] R. P. Feynman, “Simulating physics with computers,” *International Journal of Theoretical Physics* **21**, 467 (1982).
- [15] I. Bloch, J. Dalibard, and S. Nascimbène, “Quantum simulations with ultracold quantum gases,” *Nature Physics* **8**, 267 (2012).
- [16] C. Monroe, W. Campbell, L.-M. Duan, Z.-X. Gong, A. Gorshkov, P. Hess, R. Islam, K. Kim, N. Linke, G. Pagano, P. Richerme, C. Senko, and N. Yao, “Programmable quantum simulations of spin systems with trapped ions,” *Reviews of Modern Physics* **93**, 025001 (2021).
- [17] A. Browaeys and T. Lahaye, “Many-body physics with individually controlled Rydberg atoms,” *Nature Physics* **16**, 132 (2020).
- [18] P. Shor, in *Proceedings 35th Annual Symposium on Foundations of Computer Science* (IEEE Comput. Soc. Press, Santa Fe, NM, USA, 1994) pp. 124–134.
- [19] L. K. Grover, in *Proceedings of the twenty-eighth annual ACM symposium on Theory of computing - STOC '96* (ACM Press, Philadelphia, Pennsylvania, United States, 1996) pp. 212–219.
- [20] J. Preskill, “Quantum Computing in the NISQ era and beyond,” *Quantum* **2**, 79 (2018).
- [21] F. Arute, K. Arya, R. Babbush, D. Bacon, J. C. Bardin, R. Barends, R. Biswas, S. Boixo, F. G. S. L. Brando, D. A. Buell, B. Burkett, Y. Chen, Z. Chen, B. Chiaro, R. Collins, W. Courtney, A. Dunsworth, E. Farhi, B. Foxen, A. Fowler, C. Gidney, M. Giustina, R. Graff, K. Guerin, S. Habegger, M. P. Harrigan, M. J. Hartmann, A. Ho, M. Hoffmann, T. Huang, T. S. Humble, S. V. Isakov, E. Jeffrey, Z. Jiang, D. Kafri, K. Kechedzhi, J. Kelly, P. V. Klimov, S. Knysh, A. Korotkov, F. Kostritsa, D. Landhuis, M. Lindmark, E. Lucero, D. Lyakh, S. Mandrà, J. R. McClean, M. McEwen, A. Megrant, X. Mi, K. Michelsen, M. Mohseni, J. Mutus, O. Naaman, M. Neeley, C. Neill, M. Y. Niu, E. Ostby, A. Petukhov, J. C. Platt, C. Quintana, E. G. Rieffel, P. Roushan, N. C. Rubin, D. Sank, K. J. Satzinger, V. Smelyanskiy, K. J. Sung, M. D. Trevithick, A. Vainsencher, B. Villalonga, T. White, Z. J. Yao, P. Yeh, A. Zalcman, H. Neven, and J. M. Martinis, “Quantum supremacy using a programmable superconducting processor,” *Nature* **574**, 505 (2019).
- [22] H.-S. Zhong, H. Wang, Y.-H. Deng, M.-C. Chen, L.-C. Peng, Y.-H. Luo, J. Qin, D. Wu, X. Ding, Y. Hu, P. Hu, X.-Y. Yang, W.-J. Zhang, H. Li, Y. Li, X. Jiang, L. Gan, G. Yang, L. You, Z. Wang, L. Li, N.-L. Liu, C.-Y. Lu, and J.-W. Pan, “Quantum computational advantage using photons,” *Science* **370**, 1460 (2020).

- [23] N. Schlosser, G. Reymond, I. Protsenko, and P. Grangier, “Sub-poissonian loading of single atoms in a microscopic dipole trap,” *Nature* **411**, 1024 (2001).
- [24] M. Endres, H. Bernien, A. Keesling, H. Levine, E. R. Anschuetz, A. Krajenbrink, C. Senko, V. Vuletic, M. Greiner, and M. D. Lukin, “Atom-by-atom assembly of defect-free one-dimensional cold atom arrays,” *Science* **354**, 1024 (2016).
- [25] D. Barredo, S. de Léséleuc, V. Lienhard, T. Lahaye, and A. Browaeys, “An atom-by-atom assembler of defect-free arbitrary two-dimensional atomic arrays,” *Science* **354**, 1021 (2016).
- [26] H. Kim, W. Lee, H.-g. Lee, H. Jo, Y. Song, and J. Ahn, “In situ single-atom array synthesis using dynamic holographic optical tweezers,” *Nature Communications* **7**, 13317 (2016).
- [27] M. Saffman, T. G. Walker, and K. Mølmer, “Quantum information with Rydberg atoms,” *Reviews of Modern Physics* **82**, 2313 (2010).
- [28] R. Löw, H. Weimer, J. Nipper, J. B. Balewski, B. Butscher, H. P. Büchler, and T. Pfau, “An experimental and theoretical guide to strongly interacting Rydberg gases,” *Journal of Physics B: Atomic, Molecular and Optical Physics* **45**, 113001 (2012).
- [29] A. Browaeys, D. Barredo, and T. Lahaye, “Experimental investigations of dipole–dipole interactions between a few Rydberg atoms,” *Journal of Physics B: Atomic, Molecular and Optical Physics* **49**, 152001 (2016).
- [30] D. Barredo, V. Lienhard, S. de Léséleuc, T. Lahaye, and A. Browaeys, “Synthetic three-dimensional atomic structures assembled atom by atom,” *Nature* **561**, 79 (2018).
- [31] S. Ebadi, T. T. Wang, H. Levine, A. Keesling, G. Semeghini, A. Omran, D. Bluvstein, R. Samajdar, H. Pichler, W. W. Ho, S. Choi, S. Sachdev, M. Greiner, V. Vuletic, and M. D. Lukin, “Quantum Phases of Matter on a 256-Atom Programmable Quantum Simulator,” *arXiv:2012.12281* (2020).
- [32] D. Ohl de Mello, D. Schäffner, J. Werkmann, T. Preuschhoff, L. Kohfahl, M. Schlosser, and G. Birkl, “Defect-Free Assembly of 2D Clusters of More Than 100 Single-Atom Quantum Systems,” *Physical Review Letters* **122**, 203601 (2019).
- [33] H. Levine, A. Keesling, G. Semeghini, A. Omran, T. T. Wang, S. Ebadi, H. Bernien, M. Greiner, V. Vuletić, H. Pichler, and M. D. Lukin, “Parallel Implementation of High-Fidelity Multiqubit Gates with Neutral Atoms,” *Physical Review Letters* **123**, 170503 (2019).
- [34] T. Graham, M. Kwon, B. Grinkemeyer, Z. Marra, X. Jiang, M. Lichtman, Y. Sun, M. Ebert, and M. Saffman, “Rydberg-Mediated Entanglement in a Two-Dimensional Neutral Atom Qubit Array,” *Physical Review Letters* **123**, 230501 (2019).

- [35] I. S. Madjarov, J. P. Covey, A. L. Shaw, J. Choi, A. Kale, A. Cooper, H. Pichler, V. Schkolnik, J. R. Williams, and M. Endres, “High-fidelity entanglement and detection of alkaline-earth Rydberg atoms,” *Nature Physics* **16**, 857 (2020).
- [36] A. W. Young, W. J. Eckner, W. R. Milner, D. Kedar, M. A. Norcia, E. Oelker, N. Schine, J. Ye, and A. M. Kaufman, “Half-minute-scale atomic coherence and high relative stability in a tweezer clock,” *Nature* **588**, 408 (2020).
- [37] L. Anderegg, L. W. Cheuk, Y. Bao, S. Burchesky, W. Ketterle, K.-K. Ni, and J. M. Doyle, “An optical tweezer array of ultracold molecules,” *Science* **365**, 1156 (2019).
- [38] S. Saskin, J. Wilson, B. Grinkemeyer, and J. Thompson, “Narrow-Line Cooling and Imaging of Ytterbium Atoms in an Optical Tweezer Array,” *Physical Review Letters* **122**, 143002 (2019).
- [39] L. R. Liu, J. D. Hood, Y. Yu, J. T. Zhang, N. R. Hutzler, T. Rosenband, and K.-K. Ni, “Building one molecule from a reservoir of two atoms,” *Science* **360**, 900 (2018).
- [40] P. Anderson, “Resonating valence bonds: A new kind of insulator?” *Materials Research Bulletin* **8**, 153 (1973).
- [41] D. Kim, A. Keesling, A. Omran, H. Levine, H. Bernien, M. Greiner, M. D. Lukin, and D. R. Englund, “Large-scale uniform optical focus array generation with a phase spatial light modulator,” *Optics Letters* **44**, 3178 (2019).
- [42] C. Klempert, T. van Zoest, T. Henninger, O. Topic, E. Rasel, W. Ertmer, and J. Arlt, “Ultraviolet light-induced atom desorption for large rubidium and potassium magneto-optical traps,” *Physical Review A* **73**, 013410 (2006).
- [43] J. D. Thompson, T. G. Tiecke, A. S. Zibrov, V. Vuletić, and M. D. Lukin, “Coherence and Raman Sideband Cooling of a Single Atom in an Optical Tweezer,” *Physical Review Letters* **110**, 133001 (2013).
- [44] N. Belmehri, L. Förster, W. Alt, A. Widera, D. Meschede, and A. Alberti, “Microwave control of atomic motional states in a spin-dependent optical lattice,” *Journal of Physics B: Atomic, Molecular and Optical Physics* **46**, 104006 (2013).
- [45] C. Tuchendler, A. M. Lance, A. Browaeys, Y. R. P. Sortais, and P. Grangier, “Energy distribution and cooling of a single atom in an optical tweezer,” *Physical Review A* **78**, 033425 (2008).
- [46] M. Mack, F. Karlewski, H. Hattermann, S. Höckh, F. Jessen, D. Cano, and J. Fortágh, “Measurement of absolute transition frequencies of Rb 87 to nS and nD Rydberg states by means of electromagnetically induced transparency,” *Physical Review A* **83**, 052515 (2011).

- [47] K. Singer, J. Stanojevic, M. Weidemüller, and R. Côté, “Long-range interactions between alkali Rydberg atom pairs correlated to the ns–ns, np–np and nd–nd asymptotes,” *J. Phys. B* **38** (2005).
- [48] I. I. Beterov, I. I. Ryabtsev, D. B. Tretyakov, and V. M. Entin, “Quasiclassical calculations of blackbody-radiation-induced depopulation rates and effective lifetimes of Rydberg nS, nP, and nD alkali-metal atoms with $n < 80$,” *Phys. Rev. A* **79** (2009).
- [49] S. de Léséleuc, S. Weber, V. Lienhard, D. Barredo, H. P. Büchler, T. Lahaye, and A. Browaeys, “Accurate Mapping of Multilevel Rydberg Atoms on Interacting Spin- 1 / 2 Particles for the Quantum Simulation of Ising Models,” *Physical Review Letters* **120**, 113602 (2018).
- [50] D. Steck, A., “Rubidium 87 D Line Data,” Available online at <http://steck.us/alkalidata> (revision 2.2.1, 21 November 2019).
- [51] D. Bowman, T. L. Harte, V. Chardonnet, C. De Groot, S. J. Denny, G. Le Goc, M. Anderson, P. Ireland, D. Cassettari, and G. D. Bruce, “High-fidelity phase and amplitude control of phase-only computer generated holograms using conjugate gradient minimisation,” *Optics Express* **25**, 11692 (2017).
- [52] P. Zupancic, P. M. Preiss, R. Ma, A. Lukin, M. Eric Tai, M. Rispoli, R. Islam, and M. Greiner, “Ultra-precise holographic beam shaping for microscopic quantum control,” *Optics Express* **24**, 13881 (2016).
- [53] S. de Léséleuc, D. Barredo, V. Lienhard, A. Browaeys, and T. Lahaye, “Analysis of imperfections in the coherent optical excitation of single atoms to Rydberg states,” *Physical Review A* **97**, 053803 (2018).
- [54] D. D. Yavuz, P. B. Kulatunga, E. Urban, T. A. Johnson, N. Proite, T. Henage, T. G. Walker, and M. Saffman, “Fast Ground State Manipulation of Neutral Atoms in Microscopic Optical Traps,” *Physical Review Letters* **96**, 063001 (2006).
- [55] M. P. A. Jones, J. Beugnon, A. Gaëtan, J. Zhang, G. Messin, A. Browaeys, and P. Grangier, “Fast quantum state control of a single trapped neutral atom,” *Physical Review A* **75**, 040301 (2007).
- [56] D. Hayes, D. N. Matsukevich, P. Maunz, D. Hucul, Q. Quraishi, S. Olmschenk, W. Campbell, J. Mizrahi, C. Senko, and C. Monroe, “Entanglement of Atomic Qubits using an Optical Frequency Comb,” *Physical Review Letters* **104**, 140501 (2010).
- [57] R. Islam, W. C. Campbell, T. Choi, S. M. Clark, C. W. S. Conover, S. Debnath, E. E. Edwards, B. Fields, D. Hayes, D. Hucul, I. V. Inlek, K. G. Johnson, S. Korenblit, A. Lee, K. W. Lee, T. A. Manning, D. N. Matsukevich, J. Mizrahi, Q. Quraishi,

- C. Senko, J. Smith, and C. Monroe, “Beat note stabilization of mode-locked lasers for quantum information processing,” *Optics Letters* **39**, 3238 (2014).
- [58] J. Mizrahi, B. Neyenhuis, K. Johnson, W. C. Campbell, C. Senko, D. Hayes, and C. Monroe, “Quantum Control of Qubits and Atomic Motion Using Ultrafast Laser Pulses,” *Applied Physics B* **114**, 45 (2014).
- [59] C. Cohen-Tannoudji and J. Dupont-Roc, “Experimental Study of Zeeman Light Shifts in Weak Magnetic Fields,” *Physical Review A* **5**, 968 (1972).
- [60] F. L. Kien, P. Schneeweiss, and A. Rauschenbeutel, “Dynamical polarizability of atoms in arbitrary light fields: general theory and application to cesium,” *The European Physical Journal D* **67**, 92 (2013).
- [61] L. Glebov, V. Smirnov, E. Rotari, I. Cohanoschi, L. Glebova, O. Smolski, J. Lumeau, C. Lantigua, and A. Glebov, “Volume-chirped Bragg gratings: monolithic components for stretching and compression of ultrashort laser pulses,” *Optical Engineering* **53**, 051514 (2014).
- [62] T. Gullion, D. B. Baker, and M. S. Conradi, “New, compensated Carr-Purcell sequences,” *Journal of Magnetic Resonance (1969)* **89**, 479 (1990).
- [63] S. Kuhr, W. Alt, D. Schrader, I. Dotsenko, Y. Miroshnychenko, A. Rauschenbeutel, and D. Meschede, “Analysis of dephasing mechanisms in a standing-wave dipole trap,” *Physical Review A* **72**, 023406 (2005).
- [64] R. Ozeri, W. M. Itano, R. B. Blakestad, J. Britton, J. Chiaverini, J. D. Jost, C. Langer, D. Leibfried, R. Reichle, S. Seidelin, J. H. Wesenberg, and D. J. Wineland, “Errors in trapped-ion quantum gates due to spontaneous photon scattering,” *Physical Review A* **75**, 042329 (2007).
- [65] R. Ozeri, C. Langer, J. Jost, B. DeMarco, A. Ben-Kish, B. Blakestad, J. Britton, J. Chiaverini, W. Itano, D. Hume, D. Leibfried, T. Rosenband, P. Schmidt, and D. Wineland, “Hyperfine Coherence in the Presence of Spontaneous Photon Scattering,” *Physical Review Letters* **95**, 030403 (2005).
- [66] N. Schwegler, *Towards Low-Latency Parallel Readout of Multiple Trapped Ions*, Ph.D. thesis, ETH Zürich (2018).
- [67] S. Haroche, “Controlling photons in a box and exploring the quantum to classical boundary,” *Annalen der Physik* **525**, 753 (2013).
- [68] D. J. Wineland, “Nobel Lecture: Superposition, entanglement, and raising Schrödinger’s cat,” *Reviews of Modern Physics* **85**, 1103 (2013).

- [69] C. Monroe and J. Kim, “Scaling the Ion Trap Quantum Processor,” *Science* **339**, 1164 (2013).
- [70] M. H. Devoret and R. J. Schoelkopf, “Superconducting Circuits for Quantum Information: An Outlook,” *Science* **339**, 1169 (2013).
- [71] W. S. Bakr, A. Peng, M. E. Tai, R. Ma, J. Simon, J. I. Gillen, S. Folling, L. Pollet, and M. Greiner, “Probing the Superfluid-to-Mott Insulator Transition at the Single-Atom Level,” *Science* **329**, 547 (2010).
- [72] J. F. Sherson, C. Weitenberg, M. Endres, M. Cheneau, I. Bloch, and S. Kuhr, “Single-atom-resolved fluorescence imaging of an atomic Mott insulator,” *Nature* **467**, 68 (2010).
- [73] C. Weitenberg, M. Endres, J. F. Sherson, M. Cheneau, P. Schauß, T. Fukuhara, I. Bloch, and S. Kuhr, “Single-spin addressing in an atomic Mott insulator,” *Nature* **471**, 319 (2011).
- [74] D. S. Weiss, J. Vala, A. V. Thapliyal, S. Myrgren, U. Vazirani, and K. B. Whaley, “Another way to approach zero entropy for a finite system of atoms,” *Physical Review A* **70**, 040302 (2004).
- [75] J. Vala, A. V. Thapliyal, S. Myrgren, U. Vazirani, D. S. Weiss, and K. B. Whaley, “Perfect pattern formation of neutral atoms in an addressable optical lattice,” *Physical Review A* **71**, 032324 (2005).
- [76] M. Weber, J. Volz, K. Saucke, C. Kurtsiefer, and H. Weinfurter, “Analysis of a single-atom dipole trap,” *Physical Review A* **73**, 043406 (2006).
- [77] K. D. Nelson, X. Li, and D. S. Weiss, “Imaging single atoms in a three-dimensional array,” *Nature Physics* **3**, 556 (2007).
- [78] M. J. Piotrowicz, M. Lichtman, K. Maller, G. Li, S. Zhang, L. Isenhower, and M. Saffman, “Two-dimensional lattice of blue-detuned atom traps using a projected Gaussian beam array,” *Physical Review A* **88**, 013420 (2013).
- [79] F. Nogrette, H. Labuhn, S. Ravets, D. Barredo, L. Béguin, A. Vernier, T. Lahaye, and A. Browaeys, “Single-Atom Trapping in Holographic 2D Arrays of Microtraps with Arbitrary Geometries,” *Physical Review X* **4**, 021034 (2014).
- [80] A. M. Kaufman, B. J. Lester, C. M. Reynolds, M. L. Wall, M. Foss-Feig, K. R. A. Hazzard, A. M. Rey, and C. A. Regal, “Two-particle quantum interference in tunnel-coupled optical tweezers,” *Science* **345**, 306 (2014).
- [81] A. M. Kaufman, B. J. Lester, M. Foss-Feig, M. L. Wall, A. M. Rey, and C. A. Regal, “Entangling two transportable neutral atoms via local spin exchange,” *Nature* **527**, 208 (2015).

- [82] Y. Miroshnychenko, W. Alt, I. Dotsenko, L. Förster, M. Khudaverdyan, D. Meschede, D. Schrader, and A. Rauschenbeutel, “An atom-sorting machine,” *Nature* **442**, 151 (2006).
- [83] J. Beugnon, C. Tuchendler, H. Marion, A. Gaëtan, Y. Miroshnychenko, Y. R. P. Sor-tais, A. M. Lance, M. P. A. Jones, G. Messin, A. Browaeys, and P. Grangier, “Two-dimensional transport and transfer of a single atomic qubit in optical tweezers,” *Nature Physics* **3**, 696 (2007).
- [84] M. Schlosser, J. Kruse, C. Gierl, S. Teichmann, S. Tichelmann, and G. Birkl, “Fast transport, atom sample splitting and single-atom qubit supply in two-dimensional arrays of optical microtraps,” *New Journal of Physics* **14**, 123034 (2012).
- [85] T. Grünzweig, A. Hilliard, M. McGovern, and M. F. Andersen, “Near-deterministic preparation of a single atom in an optical microtrap,” *Nature Physics* **6**, 951 (2010).
- [86] B. J. Lester, N. Luick, A. M. Kaufman, C. M. Reynolds, and C. A. Regal, “Rapid Production of Uniformly Filled Arrays of Neutral Atoms,” *Physical Review Letters* **115**, 073003 (2015).
- [87] Y. H. Fung and M. F. Andersen, “Efficient collisional blockade loading of a single atom into a tight microtrap,” *New Journal of Physics* **17**, 073011 (2015).
- [88] D. Jaksch, J. I. Cirac, P. Zoller, S. L. Rolston, R. Côté, and M. D. Lukin, “Fast Quantum Gates for Neutral Atoms,” *Physical Review Letters* **85**, 2208 (2000).
- [89] H. Weimer, M. Müller, I. Lesanovsky, P. Zoller, and H. P. Büchler, “A Rydberg quantum simulator,” *Nature Physics* **6**, 382 (2010).
- [90] J. D. Thompson, T. G. Tiecke, N. P. de Leon, J. Feist, A. V. Akimov, M. Gullans, A. S. Zibrov, V. Vuletić, and M. D. Lukin, “Coupling a Single Trapped Atom to a Nanoscale Optical Cavity,” *Science* **340**, 1202 (2013).
- [91] A. Goban, C.-L. Hung, S.-P. Yu, J. Hood, J. Muniz, J. Lee, M. Martin, A. McClung, K. Choi, D. Chang, O. Painter, and H. Kimble, “Atom–light interactions in photonic crystals,” *Nature Communications* **5**, 3808 (2014).
- [92] S. Murmann, F. Deuretzbacher, G. Zürn, J. Bjerlin, S. Reimann, L. Santos, T. Lompe, and S. Jochim, “Antiferromagnetic Heisenberg Spin Chain of a Few Cold Atoms in a One-Dimensional Trap,” *Physical Review Letters* **115**, 215301 (2015).
- [93] T. Xia, M. Lichtman, K. Maller, A. Carr, M. Piotrowicz, L. Isenhower, and M. Saffman, “Randomized Benchmarking of Single-Qubit Gates in a 2D Array of Neutral-Atom Qubits,” *Physical Review Letters* **114**, 100503 (2015).

- [94] Y. Wang, X. Zhang, T. A. Corcovilos, A. Kumar, and D. S. Weiss, “Coherent Addressing of Individual Neutral Atoms in a 3D Optical Lattice,” *Physical Review Letters* **115**, 043003 (2015).
- [95] A. M. Kaufman, B. J. Lester, and C. A. Regal, “Cooling a Single Atom in an Optical Tweezer to Its Quantum Ground State,” *Physical Review X* **2**, 041014 (2012).
- [96] P. Kómár, T. Topcu, E. Kessler, A. Derevianko, V. Vuletić, J. Ye, and M. Lukin, “Quantum Network of Atom Clocks: A Possible Implementation with Neutral Atoms,” *Physical Review Letters* **117**, 060506 (2016).
- [97] J. F. Barry, D. J. McCarron, E. B. Norrgard, M. H. Steinecker, and D. DeMille, “Magneto-optical trapping of a diatomic molecule,” *Nature* **512**, 286 (2014).
- [98] N. R. Hutzler, L. R. Liu, Y. Yu, and K.-K. Ni, “Eliminating light shifts for single atom trapping,” *New Journal of Physics* **19**, 023007 (2017).
- [99] T. D. Ladd, F. Jelezko, R. Laflamme, Y. Nakamura, C. Monroe, and J. L. O’Brien, “Quantum computers,” *Nature* **464**, 45 (2010).
- [100] D. D. Awschalom, L. C. Bassett, A. S. Dzurak, E. L. Hu, and J. R. Petta, “Quantum spintronics: engineering and manipulating atom-like spins in semiconductors,” *Science* **339** (2013).
- [101] T. Monz, P. Schindler, J. T. Barreiro, M. Chwalla, D. Nigg, W. A. Coish, M. Harlander, W. Hänsel, M. Hennrich, and R. Blatt, “14-Qubit Entanglement: Creation and Coherence,” *Physical Review Letters* **106**, 130506 (2011).
- [102] R. Islam, C. Senko, W. C. Campbell, S. Korenblit, J. Smith, A. Lee, E. E. Edwards, C.-C. J. Wang, J. K. Freericks, and C. Monroe, “Emergence and Frustration of Magnetism with Variable-Range Interactions in a Quantum Simulator,” *Science* **340**, 583 (2013).
- [103] C. Song, K. Xu, W. Liu, C.-p. Yang, S.-B. Zheng, H. Deng, Q. Xie, K. Huang, Q. Guo, L. Zhang, P. Zhang, D. Xu, D. Zheng, X. Zhu, H. Wang, Y.-A. Chen, C.-Y. Lu, S. Han, and J.-W. Pan, “10-Qubit Entanglement and Parallel Logic Operations with a Superconducting Circuit,” *Physical Review Letters* **119**, 180511 (2017).
- [104] M. Gärttner, J. G. Bohnet, A. Safavi-Naini, M. L. Wall, J. J. Bollinger, and A. M. Rey, “Measuring out-of-time-order correlations and multiple quantum spectra in a trapped-ion quantum magnet,” *Nature Physics* **13**, 781 (2017).
- [105] S. Kuhr, “Quantum-gas microscopes: a new tool for cold-atom quantum simulators,” *National Science Review* **3**, 170 (2016).

- [106] S. Trotzky, Y.-A. Chen, A. Flesch, I. P. McCulloch, U. Schollwöck, J. Eisert, and I. Bloch, “Probing the relaxation towards equilibrium in an isolated strongly correlated one-dimensional Bose gas,” *Nature Physics* **8**, 325 (2012).
- [107] A. Mazurenko, C. S. Chiu, G. Ji, M. F. Parsons, M. Kanász-Nagy, R. Schmidt, F. Grusdt, E. Demler, D. Greif, and M. Greiner, “A cold-atom Fermi–Hubbard anti-ferromagnet,” *Nature* **545**, 462 (2017).
- [108] T. F. Ronnow, Z. Wang, J. Job, S. Boixo, S. V. Isakov, D. Wecker, J. M. Martinis, D. A. Lidar, and M. Troyer, “Defining and detecting quantum speedup,” *Science* **345**, 420 (2014).
- [109] P. L. McMahon, A. Marandi, Y. Haribara, R. Hamerly, C. Langrock, S. Tamate, T. Inagaki, H. Takesue, S. Utsunomiya, K. Aihara, R. L. Byer, M. M. Fejer, H. Mabuchi, and Y. Yamamoto, “A fully programmable 100-spin coherent Ising machine with all-to-all connections,” *Science* **354**, 614 (2016).
- [110] T. Wilk, A. Gaëtan, C. Evellin, J. Wolters, Y. Miroshnychenko, P. Grangier, and A. Browaeys, “Entanglement of Two Individual Neutral Atoms Using Rydberg Blockade,” *Physical Review Letters* **104**, 010502 (2010).
- [111] L. Isenhower, E. Urban, X. L. Zhang, A. T. Gill, T. Henage, T. A. Johnson, T. G. Walker, and M. Saffman, “Demonstration of a Neutral Atom Controlled-NOT Quantum Gate,” *Physical Review Letters* **104**, 010503 (2010).
- [112] M. Saffman, “Quantum computing with atomic qubits and Rydberg interactions: progress and challenges,” *Journal of Physics B: Atomic, Molecular and Optical Physics* **49**, 202001 (2016).
- [113] J. D. Pritchard, D. Maxwell, A. Gauguet, K. J. Weatherill, M. P. A. Jones, and C. S. Adams, “Cooperative Atom-Light Interaction in a Blockaded Rydberg Ensemble,” *Physical Review Letters* **105**, 193603 (2010).
- [114] P. Schauß, M. Cheneau, M. Endres, T. Fukuhara, S. Hild, A. Omran, T. Pohl, C. Gross, S. Kuhr, and I. Bloch, “Observation of spatially ordered structures in a two-dimensional Rydberg gas,” *Nature* **491**, 87 (2012).
- [115] P. Schauss, J. Zeiher, T. Fukuhara, S. Hild, M. Cheneau, T. Macri, T. Pohl, I. Bloch, and C. Gross, “Crystallization in Ising quantum magnets,” *Science* **347**, 1455 (2015).
- [116] J. Zeiher, J.-y. Choi, A. Rubio-Abadal, T. Pohl, R. van Bijnen, I. Bloch, and C. Gross, “Coherent Many-Body Spin Dynamics in a Long-Range Interacting Ising Chain,” *Physical Review X* **7**, 041063 (2017).

- [117] H. Labuhn, D. Barredo, S. Ravets, S. de Léséleuc, T. Macrì, T. Lahaye, and A. Browaeys, “Tunable two-dimensional arrays of single Rydberg atoms for realizing quantum Ising models,” *Nature* **534**, 667 (2016).
- [118] Y. O. Dudin, L. Li, F. Bariani, and A. Kuzmich, “Observation of coherent many-body Rabi oscillations,” *Nature Physics* **8**, 790 (2012).
- [119] J. Zeiher, P. Schauß, S. Hild, T. Macrì, I. Bloch, and C. Gross, “Microscopic Characterization of Scalable Coherent Rydberg Superatoms,” *Physical Review X* **5**, 031015 (2015).
- [120] P. Fendley, K. Sengupta, and S. Sachdev, “Competing density-wave orders in a one-dimensional hard-boson model,” *Physical Review B* **69**, 075106 (2004).
- [121] S. Sachdev, K. Sengupta, and S. M. Girvin, “Mott insulators in strong electric fields,” *Physical Review B* **66**, 075128 (2002).
- [122] J. Schachenmayer, I. Lesanovsky, A. Micheli, and A. J. Daley, “Dynamical crystal creation with polar molecules or Rydberg atoms in optical lattices,” *New Journal of Physics* **12**, 103044 (2010).
- [123] T. Pohl, E. Demler, and M. D. Lukin, “Dynamical Crystallization in the Dipole Blockade of Ultracold Atoms,” *Physical Review Letters* **104**, 043002 (2010).
- [124] D. Petrosyan, K. Mølmer, and M. Fleischhauer, “On the adiabatic preparation of spatially-ordered Rydberg excitations of atoms in a one-dimensional optical lattice by laser frequency sweeps,” *Journal of Physics B: Atomic, Molecular and Optical Physics* **49**, 084003 (2016).
- [125] P. Richerme, C. Senko, J. Smith, A. Lee, S. Korenblit, and C. Monroe, “Experimental performance of a quantum simulator: Optimizing adiabatic evolution and identifying many-body ground states,” *Physical Review A* **88**, 012334 (2013).
- [126] S. Sachdev, *Quantum phase transitions*, second edition ed. (Cambridge University Press, Cambridge; New York, 2011).
- [127] W. H. Zurek, U. Dorner, and P. Zoller, “Dynamics of a Quantum Phase Transition,” *Physical Review Letters* **95**, 105701 (2005).
- [128] L. D’Alessio, Y. Kafri, A. Polkovnikov, and M. Rigol, “From quantum chaos and eigenstate thermalization to statistical mechanics and thermodynamics,” *Advances in Physics* **65**, 239 (2016).
- [129] D. Abanin, W. De Roeck, W. W. Ho, and F. Huveneers, “A Rigorous Theory of Many-Body Prethermalization for Periodically Driven and Closed Quantum Systems,” *Communications in Mathematical Physics* **354**, 809 (2017).

- [130] A. Feiguin, S. Trebst, A. W. W. Ludwig, M. Troyer, A. Kitaev, Z. Wang, and M. H. Freedman, “Interacting Anyons in Topological Quantum Liquids: The Golden Chain,” *Physical Review Letters* **98**, 160409 (2007).
- [131] I. Lesanovsky and H. Katsura, “Interacting Fibonacci anyons in a Rydberg gas,” *Physical Review A* **86**, 041601 (2012).
- [132] R. Moessner and K. S. Raman, in *Introduction to Frustrated Magnetism*, edited by C. Lacroix, P. Mendels, and F. Mila, 437-479 (Springer, 2011).
- [133] H. Pichler, G. Zhu, A. Seif, P. Zoller, and M. Hafezi, “Measurement protocol for the entanglement spectrum of cold atoms,” *Phys. Rev. X* **6** (2016).
- [134] M. Schiulaz, A. Silva, and M. Müller, “Dynamics in many-body localized quantum systems without disorder,” *Physical Review B* **91**, 184202 (2015).
- [135] B. Swingle, G. Bentsen, M. Schleier-Smith, and P. Hayden, “Measuring the scrambling of quantum information,” *Physical Review A* **94**, 040302 (2016).
- [136] A. Chandran, M. D. Schulz, and F. J. Burnell, “The eigenstate thermalization hypothesis in constrained Hilbert spaces: A case study in non-Abelian anyon chains,” *Physical Review B* **94**, 235122 (2016).
- [137] D. A. Huse and M. E. Fisher, “Commensurate melting, domain walls, and dislocations,” *Physical Review B* **29**, 239 (1984).
- [138] W. Lechner, P. Hauke, and P. Zoller, “A quantum annealing architecture with all-to-all connectivity from local interactions,” *Science Advances* **1**, e1500838 (2015).
- [139] E. Farhi and A. W. Harrow, “Quantum Supremacy through the Quantum Approximate Optimization Algorithm,” *arXiv:1602.07674* (2019).
- [140] T. W. B. Kibble, “Topology of cosmic domains and strings,” *Journal of Physics A: Mathematical and General* **9**, 1387 (1976).
- [141] W. H. Zurek, “Cosmological experiments in superfluid helium?” *Nature* **317**, 505 (1985).
- [142] A. del Campo and W. H. Zurek, “Universality of phase transition dynamics: Topological defects from symmetry breaking,” *International Journal of Modern Physics A* **29**, 1430018 (2014).
- [143] N. Navon, A. L. Gaunt, R. P. Smith, and Z. Hadzibabic, “Critical dynamics of spontaneous symmetry breaking in a homogeneous Bose gas,” *Science* **347**, 167 (2015).
- [144] A. Polkovnikov, K. Sengupta, A. Silva, and M. Vengalattore, “Nonequilibrium dynamics of closed interacting quantum systems,” *Reviews of Modern Physics* **83**, 863 (2011).

- [145] A. Polkovnikov, “Universal adiabatic dynamics in the vicinity of a quantum critical point,” *Physical Review B* **72**, 161201 (2005).
- [146] J. Dziarmaga, “Dynamics of a Quantum Phase Transition: Exact Solution of the Quantum Ising Model,” *Physical Review Letters* **95**, 245701 (2005).
- [147] D. A. Huse and M. E. Fisher, “Domain Walls and the Melting of Commensurate Surface Phases,” *Physical Review Letters* **49**, 793 (1982).
- [148] S. Ostlund, “Incommensurate and commensurate phases in asymmetric clock models,” *Physical Review B* **24**, 398 (1981).
- [149] L. Tagliacozzo, A. Celi, P. Orland, M. W. Mitchell, and M. Lewenstein, “Simulation of non-Abelian gauge theories with optical lattices,” *Nature Communications* **4**, 2615 (2013).
- [150] E. Farhi, J. Goldstone, S. Gutmann, and M. Sipser, “Quantum Computation by Adiabatic Evolution,” *arXiv:quant-ph/0001106* (2000).
- [151] B. Gardas, J. Dziarmaga, W. H. Zurek, and M. Zwolak, “Defects in Quantum Computers,” *Scientific Reports* **8**, 4539 (2018).
- [152] M. Anquez, B. Robbins, H. Bharath, M. Boguslawski, T. Hoang, and M. Chapman, “Quantum Kibble-Zurek Mechanism in a Spin-1 Bose-Einstein Condensate,” *Physical Review Letters* **116**, 155301 (2016).
- [153] L. W. Clark, L. Feng, and C. Chin, “Universal space-time scaling symmetry in the dynamics of bosons across a quantum phase transition,” *Science* **354**, 606 (2016).
- [154] M. Endres, T. Fukuhara, D. Pekker, M. Cheneau, P. Schau , C. Gross, E. Demler, S. Kuhr, and I. Bloch, “The ‘Higgs’ amplitude mode at the two-dimensional superfluid/Mott insulator transition,” *Nature* **487**, 454 (2012).
- [155] D. Chen, M. White, C. Borries, and B. DeMarco, “Quantum Quench of an Atomic Mott Insulator,” *Physical Review Letters* **106**, 235304 (2011).
- [156] S. Braun, M. Friesdorf, S. S. Hodgman, M. Schreiber, J. P. Ronzheimer, A. Riera, M. del Rey, I. Bloch, J. Eisert, and U. Schneider, “Emergence of coherence and the dynamics of quantum phase transitions,” *Proceedings of the National Academy of Sciences* **112**, 3641 (2015).
- [157] H. Bernien, S. Schwartz, A. Keesling, H. Levine, A. Omran, H. Pichler, S. Choi, A. S. Zibrov, M. Endres, M. Greiner, V. Vuletić, and M. D. Lukin, “Probing many-body dynamics on a 51-atom quantum simulator,” *Nature* **551**, 579 (2017).

- [158] M. Kolodrubetz, B. K. Clark, and D. A. Huse, “Nonequilibrium Dynamic Critical Scaling of the Quantum Ising Chain,” *Physical Review Letters* **109**, 015701 (2012).
- [159] R. W. Cherng and L. S. Levitov, “Entropy and correlation functions of a driven quantum spin chain,” *Physical Review A* **73**, 043614 (2006).
- [160] R. Samajdar, S. Choi, H. Pichler, M. D. Lukin, and S. Sachdev, “Numerical study of the chiral Z 3 quantum phase transition in one spatial dimension,” *Physical Review A* **98**, 023614 (2018).
- [161] S. Whitsitt, R. Samajdar, and S. Sachdev, “Quantum field theory for the chiral clock transition in one spatial dimension,” *Physical Review B* **98**, 205118 (2018).
- [162] N. Chepiga and F. Mila, “Floating Phase versus Chiral Transition in a 1D Hard-Boson Model,” *Physical Review Letters* **122**, 017205 (2019).
- [163] F. D. M. Haldane, P. Bak, and T. Bohr, “Phase diagrams of surface structures from Bethe-ansatz solutions of the quantum sine-Gordon model,” *Physical Review B* **28**, 2743 (1983).
- [164] A. Dutta, G. Aeppli, B. K. Chakrabarti, U. Divakaran, T. F. Rosenbaum, and D. Sen, *Quantum Phase Transitions in Transverse Field Spin Models: From Statistical Physics to Quantum Information* (Cambridge University Press, Cambridge, 2015).
- [165] R. Moessner, S. L. Sondhi, and E. Fradkin, “Short-ranged resonating valence bond physics, quantum dimer models, and Ising gauge theories,” *Physical Review B* **65**, 024504 (2001).
- [166] A. Kumar, T.-Y. Wu, F. Giraldo, and D. S. Weiss, “Sorting ultracold atoms in a three-dimensional optical lattice in a realization of Maxwell’s demon,” *Nature* **561**, 83 (2018).
- [167] H. Pichler, S.-T. Wang, L. Zhou, S. Choi, and M. D. Lukin, “Quantum Optimization for Maximum Independent Set Using Rydberg Atom Arrays,” *arXiv:1808.10816* (2018).
- [168] J. Zhang, G. Pagano, P. W. Hess, A. Kyprianidis, P. Becker, H. Kaplan, A. V. Gorshkov, Z.-X. Gong, and C. Monroe, “Observation of a many-body dynamical phase transition with a 53-qubit quantum simulator,” *Nature* **551**, 601 (2017).
- [169] G. Pagano, A. Bapat, P. Becker, K. S. Collins, A. De, P. W. Hess, H. B. Kaplan, A. Kyprianidis, W. L. Tan, C. Baldwin, L. T. Brady, A. Deshpande, F. Liu, S. Jordan, A. V. Gorshkov, and C. Monroe, “Quantum approximate optimization of the long-range Ising model with a trapped-ion quantum simulator,” *Proceedings of the National Academy of Sciences* **117**, 25396 (2020).

- [170] N. Friis, O. Marty, C. Maier, C. Hempel, M. Holzäpfel, P. Jurcevic, M. B. Plenio, M. Huber, C. Roos, R. Blatt, and B. Lanyon, “Observation of Entangled States of a Fully Controlled 20-Qubit System,” *Physical Review X* **8**, 021012 (2018).
- [171] I. Aleiner, F. Arute, K. Arya, J. Atalaya, R. Babbush, J. C. Bardin, R. Barends, A. Bengtsson, S. Boixo, A. Bourassa, M. Broughton, B. B. Buckley, D. A. Buell, B. Burkett, N. Bushnell, Y. Chen, Z. Chen, B. Chiaro, R. Collins, W. Courtney, S. Demura, A. R. Derk, A. Dunsworth, D. Eppens, C. Erickson, E. Farhi, A. G. Fowler, B. Foxen, C. Gidney, M. Giustina, J. A. Gross, M. P. Harrigan, S. D. Harrington, J. Hilton, A. Ho, S. Hong, T. Huang, W. J. Huggins, L. B. Ioffe, S. V. Isakov, E. Jeffrey, Z. Jiang, C. Jones, D. Kafri, K. Kechedzhi, J. Kelly, S. Kim, P. V. Klimov, A. N. Korotkov, F. Kostritsa, D. Landhuis, P. Laptev, E. Lucero, O. Martin, J. R. McClean, T. McCourt, M. McEwen, A. Megrant, X. Mi, K. C. Miao, M. Mohseni, W. Mruczkiewicz, J. Mutus, O. Naaman, M. Neeley, C. Neill, H. Neven, M. Newman, M. Y. Niu, T. E. O’Brien, A. Opremcak, E. Ostby, B. Pató, A. Petukhov, C. Quintana, N. Redd, P. Roushan, N. C. Rubin, D. Sank, K. J. Satzinger, V. Shvarts, V. Smelyanskiy, D. Strain, M. Szalay, M. D. Trevithick, B. Villalonga, T. White, Z. J. Yao, P. Yeh, and A. Zalcman, “Accurately computing electronic properties of materials using eigenenergies,” *arXiv:2012.00921* (2020).
- [172] C. S. Wang, J. C. Curtis, B. J. Lester, Y. Zhang, Y. Y. Gao, J. Freeze, V. S. Batista, P. H. Vaccaro, I. L. Chuang, L. Frunzio, L. Jiang, S. Girvin, and R. J. Schoelkopf, “Efficient Multiphoton Sampling of Molecular Vibronic Spectra on a Superconducting Bosonic Processor,” *Physical Review X* **10**, 021060 (2020).
- [173] C. Gross and I. Bloch, “Quantum simulations with ultracold atoms in optical lattices,” *Science* **357**, 995 (2017).
- [174] J.-y. Choi, S. Hild, J. Zeiher, P. Schauss, A. Rubio-Abadal, T. Yefsah, V. Khemani, D. A. Huse, I. Bloch, and C. Gross, “Exploring the many-body localization transition in two dimensions,” *Science* **352**, 1547 (2016).
- [175] R. Harris, Y. Sato, A. J. Berkley, M. Reis, F. Altomare, M. H. Amin, K. Boothby, P. Bunyk, C. Deng, C. Enderud, S. Huang, E. Hoskinson, M. W. Johnson, E. Ladizinsky, N. Ladizinsky, T. Lanting, R. Li, T. Medina, R. Molavi, R. Neufeld, T. Oh, I. Pavlov, I. Perminov, G. Poulin-Lamarre, C. Rich, A. Smirnov, L. Swenson, N. Tsai, M. Volkmann, J. Whittaker, and J. Yao, “Phase transitions in a programmable quantum spin glass simulator,” *Science* **361**, 162 (2018).
- [176] M. Morgado and S. Whitlock, “Quantum simulation and computing with Rydberg-interacting qubits,” *AVS Quantum Science* **3**, 023501 (2021).

- [177] V. Lienhard, S. de Léséleuc, D. Barredo, T. Lahaye, A. Browaeys, M. Schuler, L.-P. Henry, and A. M. Läuchli, “Observing the Space- and Time-Dependent Growth of Correlations in Dynamically Tuned Synthetic Ising Models with Antiferromagnetic Interactions,” *Physical Review X* **8**, 021070 (2018).
- [178] E. Guardado-Sánchez, P. T. Brown, D. Mitra, T. Devakul, D. A. Huse, P. Schauß, and W. S. Bakr, “Probing the Quench Dynamics of Antiferromagnetic Correlations in a 2D Quantum Ising Spin System,” *Physical Review X* **8**, 021069 (2018).
- [179] H. Kim, Y. Park, K. Kim, H.-S. Sim, and J. Ahn, “Detailed Balance of Thermalization Dynamics in Rydberg-Atom Quantum Simulators,” *Physical Review Letters* **120**, 180502 (2018).
- [180] S. de Léséleuc, V. Lienhard, P. Scholl, D. Barredo, S. Weber, N. Lang, H. P. Büchler, T. Lahaye, and A. Browaeys, “Observation of a symmetry-protected topological phase of interacting bosons with Rydberg atoms,” *Science* **365**, 775 (2019).
- [181] A. Keesling, A. Omran, H. Levine, H. Bernien, H. Pichler, S. Choi, R. Samajdar, S. Schwartz, P. Silvi, S. Sachdev, P. Zoller, M. Endres, M. Greiner, V. Vuletić, and M. D. Lukin, “Quantum Kibble–Zurek mechanism and critical dynamics on a programmable Rydberg simulator,” *Nature* **568**, 207 (2019).
- [182] A. Omran, H. Levine, A. Keesling, G. Semeghini, T. T. Wang, S. Ebadi, H. Bernien, A. S. Zibrov, H. Pichler, S. Choi, J. Cui, M. Rossignolo, P. Rembold, S. Montangero, T. Calarco, M. Endres, M. Greiner, V. Vuletić, and M. D. Lukin, “Generation and manipulation of Schrödinger cat states in Rydberg atom arrays,” *Science* **365**, 570 (2019).
- [183] I. S. Madjarov, A. Cooper, A. L. Shaw, J. P. Covey, V. Schkolnik, T. H. Yoon, J. R. Williams, and M. Endres, “An Atomic-Array Optical Clock with Single-Atom Readout,” *Physical Review X* **9**, 041052 (2019).
- [184] K.-N. Schymik, V. Lienhard, D. Barredo, P. Scholl, H. Williams, A. Browaeys, and T. Lahaye, “Enhanced atom-by-atom assembly of arbitrary tweezer arrays,” *Physical Review A* **102**, 063107 (2020).
- [185] M. D. Lukin, M. Fleischhauer, R. Cote, L. M. Duan, D. Jaksch, J. I. Cirac, and P. Zoller, “Dipole Blockade and Quantum Information Processing in Mesoscopic Atomic Ensembles,” *Physical Review Letters* **87**, 037901 (2001).
- [186] R. Samajdar, W. W. Ho, H. Pichler, M. D. Lukin, and S. Sachdev, “Complex Density Wave Orders and Quantum Phase Transitions in a Model of Square-Lattice Rydberg Atom Arrays,” *Physical Review Letters* **124**, 103601 (2020).

- [187] T. Felser, S. Notarnicola, and S. Montangero, “Efficient Tensor Network *Ansatz* for High-Dimensional Quantum Many-Body Problems,” *Physical Review Letters* **126**, 170603 (2021).
- [188] H.-Y. Huang, R. Kueng, and J. Preskill, “Predicting many properties of a quantum system from very few measurements,” *Nature Physics* **16**, 1050 (2020).
- [189] C. J. Turner, A. A. Michailidis, D. A. Abanin, M. Serbyn, and Z. Papić, “Weak ergodicity breaking from quantum many-body scars,” *Nature Physics* **14**, 745 (2018).
- [190] F. M. Surace, P. P. Mazza, G. Giudici, A. Lerose, A. Gambassi, and M. Dalmonte, “Lattice Gauge Theories and String Dynamics in Rydberg Atom Quantum Simulators,” *Physical Review X* **10**, 021041 (2020).
- [191] D. Bluvstein, A. Omran, H. Levine, A. Keesling, G. Semeghini, S. Ebadi, T. T. Wang, A. A. Michailidis, N. Maskara, W. W. Ho, S. Choi, M. Serbyn, M. Greiner, V. Vuletić, and M. D. Lukin, “Controlling quantum many-body dynamics in driven Rydberg atom arrays,” *Science* **371**, 1355 (2021).
- [192] R. Samajdar, W. W. Ho, H. Pichler, M. D. Lukin, and S. Sachdev, “Quantum phases of Rydberg atoms on a kagome lattice,” *Proceedings of the National Academy of Sciences* **118**, e2015785118 (2021).
- [193] R. Verresen, M. Lukin, D., and A. Vishwanath, “Prediction of Toric Code Topological Order from Rydberg Blockade,” *arXiv:2011.12310* (2020).
- [194] M. C. Bañuls, R. Blatt, J. Catani, A. Celi, J. I. Cirac, M. Dalmonte, L. Fallani, K. Jansen, M. Lewenstein, S. Montangero, C. A. Muschik, B. Reznik, E. Rico, L. Tagliacozzo, K. Van Acoleyen, F. Verstraete, U.-J. Wiese, M. Wingate, J. Zakrzewski, and P. Zoller, “Simulating lattice gauge theories within quantum technologies,” *The European Physical Journal D* **74**, 165 (2020).
- [195] S. Notarnicola, M. Collura, and S. Montangero, “Real-time-dynamics quantum simulation of (1 + 1)-dimensional lattice QED with Rydberg atoms,” *Physical Review Research* **2**, 013288 (2020).
- [196] J. M. Auger, S. Bergamini, and D. E. Browne, “Blueprint for fault-tolerant quantum computation with Rydberg atoms,” *Physical Review A* **96**, 052320 (2017).
- [197] E. Farhi, J. Goldstone, and S. Gutmann, “A Quantum Approximate Optimization Algorithm,” *arXiv:1411.4028* (2014).
- [198] L. Zhou, S.-T. Wang, S. Choi, H. Pichler, and M. D. Lukin, “Quantum Approximate Optimization Algorithm: Performance, Mechanism, and Implementation on Near-Term Devices,” *Physical Review X* **10**, 021067 (2020).

- [199] D. S. Wild, D. Sels, H. Pichler, C. Zanoci, and M. D. Lukin, “Quantum Sampling Algorithms for Near-Term Devices,” *arXiv:2005.14059* (2020).
- [200] J. Maldacena, S. H. Shenker, and D. Stanford, “A bound on chaos,” *Journal of High Energy Physics* **2016**, 106 (2016).
- [201] M. Srednicki, “Chaos and quantum thermalization,” *Physical Review E* **50**, 888 (1994).
- [202] M. Rigol, V. Dunjko, and M. Olshanii, “Thermalization and its mechanism for generic isolated quantum systems,” *Nature* **452**, 854 (2008).
- [203] A. M. Kaufman, M. E. Tai, A. Lukin, M. Rispoli, R. Schittko, P. M. Preiss, and M. Greiner, “Quantum thermalization through entanglement in an isolated many-body system,” *Science* **353**, 794 (2016).
- [204] M. Schreiber, S. S. Hodgman, P. Bordia, H. P. Luschen, M. H. Fischer, R. Vosk, E. Altman, U. Schneider, and I. Bloch, “Observation of many-body localization of interacting fermions in a quasirandom optical lattice,” *Science* **349**, 842 (2015).
- [205] T. Langen, S. Erne, R. Geiger, B. Rauer, T. Schweigler, M. Kuhnert, W. Rohringer, I. E. Mazets, T. Gasenzer, and J. Schmiedmayer, “Experimental observation of a generalized Gibbs ensemble,” *Science* **348**, 207 (2015).
- [206] R. Nandkishore and D. A. Huse, “Many-Body Localization and Thermalization in Quantum Statistical Mechanics,” *Annual Review of Condensed Matter Physics* **6**, 15 (2015).
- [207] E. J. Heller, “Bound-State Eigenfunctions of Classically Chaotic Hamiltonian Systems: Scars of Periodic Orbits,” *Physical Review Letters* **53**, 1515 (1984).
- [208] V. Khemani, A. Lazarides, R. Moessner, and S. Sondhi, “Phase Structure of Driven Quantum Systems,” *Physical Review Letters* **116**, 250401 (2016).
- [209] D. V. Else, B. Bauer, and C. Nayak, “Floquet Time Crystals,” *Physical Review Letters* **117**, 090402 (2016).
- [210] E. Urban, T. A. Johnson, T. Henage, L. Isenhower, D. D. Yavuz, T. G. Walker, and M. Saffman, “Observation of Rydberg blockade between two atoms,” *Nature Physics* **5**, 110 (2009).
- [211] W. W. Ho, S. Choi, H. Pichler, and M. D. Lukin, “Periodic Orbits, Entanglement, and Quantum Many-Body Scars in Constrained Models: Matrix Product State Approach,” *Physical Review Letters* **122**, 040603 (2019).
- [212] C.-J. Lin and O. I. Motrunich, “Exact Quantum Many-Body Scar States in the Rydberg-Blockaded Atom Chain,” *Physical Review Letters* **122**, 173401 (2019).

- [213] V. Khemani, C. R. Laumann, and A. Chandran, “Signatures of integrability in the dynamics of Rydberg-blockaded chains,” *Physical Review B* **99**, 161101 (2019).
- [214] A. A. Michailidis, C. J. Turner, Z. Papić, D. A. Abanin, and M. Serbyn, “Stabilizing two-dimensional quantum scars by deformation and synchronization,” *Physical Review Research* **2**, 022065 (2020).
- [215] J. Zhang, P. W. Hess, A. Kyprianidis, P. Becker, A. Lee, J. Smith, G. Pagano, I.-D. Potirniche, A. C. Potter, A. Vishwanath, N. Y. Yao, and C. Monroe, “Observation of a discrete time crystal,” *Nature* **543**, 217 (2017).
- [216] S. Choi, J. Choi, R. Landig, G. Kucsko, H. Zhou, J. Isoya, F. Jelezko, S. Onoda, H. Sumiya, V. Khemani, C. von Keyserlingk, N. Y. Yao, E. Demler, and M. D. Lukin, “Observation of discrete time-crystalline order in a disordered dipolar many-body system,” *Nature* **543**, 221 (2017).
- [217] N. Y. Yao, C. Nayak, L. Balents, and M. P. Zaletel, “Classical discrete time crystals,” *Nature Physics* **16**, 438 (2020).
- [218] D. V. Else, B. Bauer, and C. Nayak, “Prethermal Phases of Matter Protected by Time-Translation Symmetry,” *Physical Review X* **7**, 011026 (2017).
- [219] P. Ponte, A. Chandran, Z. Papić, and D. A. Abanin, “Periodically driven ergodic and many-body localized quantum systems,” *Annals of Physics* **353**, 196 (2015).
- [220] B. Mukherjee, A. Sen, D. Sen, and K. Sengupta, “Dynamics of the vacuum state in a periodically driven Rydberg chain,” *Physical Review B* **102**, 075123 (2020).
- [221] V. Giovannetti, “Quantum-Enhanced Measurements: Beating the Standard Quantum Limit,” *Science* **306**, 1330 (2004).
- [222] X.-G. Wen, “Colloquium : Zoo of quantum-topological phases of matter,” *Reviews of Modern Physics* **89**, 041004 (2017).
- [223] S. Sachdev, “Topological order, emergent gauge fields, and Fermi surface reconstruction,” *Reports on Progress in Physics* **82**, 014001 (2019).
- [224] A. Kitaev, “Fault-tolerant quantum computation by anyons,” *Annals of Physics* **303**, 2 (2003).
- [225] C. Nayak, S. H. Simon, A. Stern, M. Freedman, and S. Das Sarma, “Non-Abelian anyons and topological quantum computation,” *Reviews of Modern Physics* **80**, 1083 (2008).
- [226] L. Savary and L. Balents, “Quantum spin liquids: a review,” *Reports on Progress in Physics* **80**, 016502 (2017).

- [227] D. S. Rokhsar and S. A. Kivelson, “Superconductivity and the Quantum Hard-Core Dimer Gas,” *Physical Review Letters* **61**, 2376 (1988).
- [228] N. Read and S. Sachdev, “Large- N expansion for frustrated quantum antiferromagnets,” *Physical Review Letters* **66**, 1773 (1991).
- [229] S. Sachdev, “Kagome’- and triangular-lattice Heisenberg antiferromagnets: Ordering from quantum fluctuations and quantum-disordered ground states with unconfined bosonic spinons,” *Physical Review B* **45**, 12377 (1992).
- [230] R. Moessner and S. L. Sondhi, “Resonating Valence Bond Phase in the Triangular Lattice Quantum Dimer Model,” *Physical Review Letters* **86**, 1881 (2001).
- [231] G. Misguich, D. Serban, and V. Pasquier, “Quantum Dimer Model on the Kagome Lattice: Solvable Dimer-Liquid and Ising Gauge Theory,” *Physical Review Letters* **89**, 137202 (2002).
- [232] B. I. Halperin and J. K. Jain, *Fractional Quantum Hall Effects: New Developments* (WORLD SCIENTIFIC, 2020).
- [233] T.-H. Han, J. S. Helton, S. Chu, D. G. Nocera, J. A. Rodriguez-Rivera, C. Broholm, and Y. S. Lee, “Fractionalized excitations in the spin-liquid state of a kagome-lattice antiferromagnet,” *Nature* **492**, 406 (2012).
- [234] M. Fu, T. Imai, T.-H. Han, and Y. S. Lee, “Evidence for a gapped spin-liquid ground state in a kagome Heisenberg antiferromagnet,” *Science* **350**, 655 (2015).
- [235] M. Hermele, V. Gurarie, and A. M. Rey, “Mott Insulators of Ultracold Fermionic Alkaline Earth Atoms: Underconstrained Magnetism and Chiral Spin Liquid,” *Physical Review Letters* **103**, 135301 (2009).
- [236] N. Y. Yao, A. V. Gorshkov, C. R. Laumann, A. M. Läuchli, J. Ye, and M. D. Lukin, “Realizing Fractional Chern Insulators in Dipolar Spin Systems,” *Physical Review Letters* **110**, 185302 (2013).
- [237] A. Glaetzle, M. Dalmonte, R. Nath, I. Rousochatzakis, R. Moessner, and P. Zoller, “Quantum Spin-Ice and Dimer Models with Rydberg Atoms,” *Physical Review X* **4**, 041037 (2014).
- [238] A. Celi, B. Vermersch, O. Viyuela, H. Pichler, M. D. Lukin, and P. Zoller, “Emerging Two-Dimensional Gauge Theories in Rydberg Configurable Arrays,” *Physical Review X* **10**, 021057 (2020).
- [239] C. Song, D. Xu, P. Zhang, J. Wang, Q. Guo, W. Liu, K. Xu, H. Deng, K. Huang, D. Zheng, S.-B. Zheng, H. Wang, X. Zhu, C.-Y. Lu, and J.-W. Pan, “Demonstration

of Topological Robustness of Anyonic Braiding Statistics with a Superconducting Quantum Circuit,” *Physical Review Letters* **121**, 030502 (2018).

- [240] C. K. Andersen, A. Remm, S. Lazar, S. Krinner, N. Lacroix, G. J. Norris, M. Gabureac, C. Eichler, and A. Wallraff, “Repeated quantum error detection in a surface code,” *Nature Physics* **16**, 875 (2020).
- [241] S. Zhou, D. Green, E. D. Dahl, and C. Chamon, “Experimental Realization of Spin Liquids in a Programmable Quantum Device,” *arXiv:2009.07853* (2020).
- [242] P. Scholl, M. Schuler, H. J. Williams, A. A. Eberharter, D. Barredo, K.-N. Schymik, V. Lienhard, L.-P. Henry, T. C. Lang, T. Lahaye, A. M. Läuchli, and A. Browaeys, “Programmable quantum simulation of 2D antiferromagnets with hundreds of Rydberg atoms,” *arXiv:2012.12268* (2020).
- [243] J. Bricmont and J. Frölich, “An order parameter distinguishing between different phases of lattice gauge theories with matter fields,” *Physics Letters B* **122**, 73 (1983).
- [244] K. Fredenhagen and M. Marcu, “Charged states in Z2 gauge theories,” *Communications in Mathematical Physics* **92**, 81 (1983).
- [245] K. Gregor, D. A. Huse, R. Moessner, and S. L. Sondhi, “Diagnosing deconfinement and topological order,” *New Journal of Physics* **13**, 025009 (2011).
- [246] S. R. White, “Density matrix formulation for quantum renormalization groups,” *Physical Review Letters* **69**, 2863 (1992).
- [247] J. Hauschild and F. Pollmann, “Efficient numerical simulations with Tensor Networks: Tensor Network Python (TeNPy),” *SciPost Physics Lecture Notes* , 5 (2018).
- [248] M. P. Zaletel, R. S. K. Mong, C. Karrasch, J. E. Moore, and F. Pollmann, “Time-evolving a matrix product state with long-ranged interactions,” *Physical Review B* **91**, 165112 (2015).
- [249] M. B. Hastings and X.-G. Wen, “Quasiadiabatic continuation of quantum states: The stability of topological ground-state degeneracy and emergent gauge invariance,” *Physical Review B* **72**, 045141 (2005).
- [250] I. Cong, S. Choi, and M. D. Lukin, “Quantum convolutional neural networks,” *Nature Physics* **15**, 1273 (2019).
- [251] E. Dennis, A. Kitaev, A. Landahl, and J. Preskill, “Topological quantum memory,” *Journal of Mathematical Physics* **43**, 4452 (2002).
- [252] L. Tagliacozzo, A. Celi, A. Zamora, and M. Lewenstein, “Optical Abelian lattice gauge theories,” *Annals of Physics* **330**, 160 (2013).

- [253] A. Kitaev, “Anyons in an exactly solved model and beyond,” *Annals of Physics* **321**, 2 (2006).
- [254] D. S. Weiss and M. Saffman, “Quantum computing with neutral atoms,” *Physics Today* **70**, 44 (2017).
- [255] K. M. Maller, M. T. Lichtman, T. Xia, Y. Sun, M. J. Piotrowicz, A. W. Carr, L. Isenhower, and M. Saffman, “Rydberg-blockade controlled-not gate and entanglement in a two-dimensional array of neutral-atom qubits,” *Physical Review A* **92**, 022336 (2015).
- [256] Y.-Y. Jau, A. M. Hankin, T. Keating, I. H. Deutsch, and G. W. Biedermann, “Entangling atomic spins with a Rydberg-dressed spin-flip blockade,” *Nature Physics* **12**, 71 (2016).
- [257] Y. Zeng, P. Xu, X. He, Y. Liu, M. Liu, J. Wang, D. Papoulař, G. Shlyapnikov, and M. Zhan, “Entangling Two Individual Atoms of Different Isotopes via Rydberg Blockade,” *Physical Review Letters* **119**, 160502 (2017).
- [258] J. Zeiher, R. van Bijnen, P. Schauß, S. Hild, J.-y. Choi, T. Pohl, I. Bloch, and C. Gross, “Many-body interferometry of a Rydberg-dressed spin lattice,” *Nature Physics* **12**, 1095 (2016).
- [259] K. Singer, M. Reetz-Lamour, T. Amthor, L. G. Marcassa, and M. Weidemüller, “Suppression of Excitation and Spectral Broadening Induced by Interactions in a Cold Gas of Rydberg Atoms,” *Physical Review Letters* **93**, 163001 (2004).
- [260] R. Heidemann, U. Raitzsch, V. Bendkowsky, B. Butscher, R. Löw, L. Santos, and T. Pfau, “Evidence for Coherent Collective Rydberg Excitation in the Strong Blockade Regime,” *Physical Review Letters* **99**, 163601 (2007).
- [261] T. M. Weber, M. Höning, T. Niederprüm, T. Manthey, O. Thomas, V. Guarnera, M. Fleischhauer, G. Barontini, and H. Ott, “Mesoscopic Rydberg-blockaded ensembles in the superatom regime and beyond,” *Nature Physics* **11**, 157 (2015).
- [262] O. Firstenberg, C. S. Adams, and S. Hofferberth, “Nonlinear quantum optics mediated by Rydberg interactions,” *Journal of Physics B: Atomic, Molecular and Optical Physics* **49**, 152003 (2016).
- [263] N. Akerman, N. Navon, S. Kotler, Y. Glickman, and R. Ozeri, “Universal gate-set for trapped-ion qubits using a narrow linewidth diode laser,” *New Journal of Physics* **17**, 113060 (2015).
- [264] L. Gerster, *Spectral filtering and laser diode injection for multi-qubit trapped ion gates*, Ph.D. thesis, ETH Zurich (2015).

- [265] M. J. Martin, *Quantum Metrology and Many-Body Physics: Pushing the Frontier of the Optical Lattice Clock*, Ph.D. thesis, JILA (2013).
- [266] J. Hald and V. Ruseva, “Efficient suppression of diode-laser phase noise by optical filtering,” *Journal of the Optical Society of America B* **22**, 2338 (2005).
- [267] T. Nazarova, C. Lisdat, F. Riehle, and U. Sterr, “Low-frequency-noise diode laser for atom interferometry,” *Journal of the Optical Society of America B* **25**, 1632 (2008).
- [268] H. Labuhn, S. Ravets, D. Barredo, L. Béguin, F. Nogrette, T. Lahaye, and A. Browaeys, “Single-atom addressing in microtraps for quantum-state engineering using Rydberg atoms,” *Physical Review A* **90**, 023415 (2014).
- [269] D. Kielpinski, V. Meyer, M. A. Rowe, C. A. Sackett, W. M. Itano, C. Monroe, and D. J. Wineland, “A Decoherence-Free Quantum Memory Using Trapped Ions,” *Science* **291**, 1013 (2001).
- [270] C. F. Roos, G. P. T. Lancaster, M. Riebe, H. Häffner, W. Hänsel, S. Gulde, C. Becher, J. Eschner, F. Schmidt-Kaler, and R. Blatt, “Bell States of Atoms with Ultralong Lifetimes and Their Tomographic State Analysis,” *Physical Review Letters* **92**, 220402 (2004).
- [271] L. S. Theis, F. Motzoi, F. K. Wilhelm, and M. Saffman, “High-fidelity Rydberg-blockade entangling gate using shaped, analytic pulses,” *Physical Review A* **94**, 032306 (2016).
- [272] D. M. Greenberger, M. A. Horne, and A. Zeilinger, in *Bell’s Theorem, Quantum Theory and Conceptions of the Universe.*, edited by M. Kafatos (Springer Netherlands, Dordrecht, 1989) pp. 69–72.
- [273] L. Pezzè, A. Smerzi, M. K. Oberthaler, R. Schmied, and P. Treutlein, “Quantum metrology with nonclassical states of atomic ensembles,” *Reviews of Modern Physics* **90**, 035005 (2018).
- [274] M. A. Nielsen and I. L. Chuang, *Quantum computation and quantum information*, 10th ed. (Cambridge University Press, Cambridge ; New York, 2010).
- [275] L. Amico, R. Fazio, A. Osterloh, and V. Vedral, “Entanglement in many-body systems,” *Reviews of Modern Physics* **80**, 517 (2008).
- [276] O. Gühne and G. Tóth, “Entanglement detection,” *Physics Reports* **474**, 1 (2009).
- [277] R. Islam, R. Ma, P. M. Preiss, M. Eric Tai, A. Lukin, M. Rispoli, and M. Greiner, “Measuring entanglement entropy in a quantum many-body system,” *Nature* **528**, 77 (2015).

- [278] R. Laflamme, E. Knill, W. H. Zurek, P. Catasti, and S. V. S. Mariappan, “NMR Greenberger–Horne–Zeilinger states,” *Philosophical Transactions of the Royal Society of London. Series A: Mathematical, Physical and Engineering Sciences* **356**, 1941 (1998).
- [279] P. Neumann, N. Mizuochi, F. Rempp, P. Hemmer, H. Watanabe, S. Yamasaki, V. Jacques, T. Gaebel, F. Jelezko, and J. Wrachtrup, “Multipartite Entanglement Among Single Spins in Diamond,” *Science* **320**, 1326 (2008).
- [280] D. Bouwmeester, J.-W. Pan, M. Daniell, H. Weinfurter, and A. Zeilinger, “Observation of Three-Photon Greenberger-Horne-Zeilinger Entanglement,” *Physical Review Letters* **82**, 1345 (1999).
- [281] J.-W. Pan, M. Daniell, S. Gasparoni, G. Weihs, and A. Zeilinger, “Experimental Demonstration of Four-Photon Entanglement and High-Fidelity Teleportation,” *Physical Review Letters* **86**, 4435 (2001).
- [282] X.-L. Wang, Y.-H. Luo, H.-L. Huang, M.-C. Chen, Z.-E. Su, C. Liu, C. Chen, W. Li, Y.-Q. Fang, X. Jiang, J. Zhang, L. Li, N.-L. Liu, C.-Y. Lu, and J.-W. Pan, “18-Qubit Entanglement with Six Photons’ Three Degrees of Freedom,” *Physical Review Letters* **120**, 260502 (2018).
- [283] D. Leibfried, E. Knill, S. Seidelin, J. Britton, R. B. Blakestad, J. Chiaverini, D. B. Hume, W. M. Itano, J. D. Jost, C. Langer, R. Ozeri, R. Reichle, and D. J. Wineland, “Creation of a six-atom ‘Schrödinger cat’ state,” *Nature* **438**, 639 (2005).
- [284] L. DiCarlo, M. D. Reed, L. Sun, B. R. Johnson, J. M. Chow, J. M. Gambetta, L. Frunzio, S. M. Girvin, M. H. Devoret, and R. J. Schoelkopf, “Preparation and measurement of three-qubit entanglement in a superconducting circuit,” *Nature* **467**, 574 (2010).
- [285] C. Song, K. Xu, H. Li, Y.-R. Zhang, X. Zhang, W. Liu, Q. Guo, Z. Wang, W. Ren, J. Hao, H. Feng, H. Fan, D. Zheng, D.-W. Wang, H. Wang, and S.-Y. Zhu, “Generation of multicomponent atomic Schrödinger cat states of up to 20 qubits,” *Science* **365**, 574 (2019).
- [286] B. Vlastakis, G. Kirchmair, Z. Leghtas, S. E. Nigg, L. Frunzio, S. M. Girvin, M. Mirrahimi, M. H. Devoret, and R. J. Schoelkopf, “Deterministically Encoding Quantum Information Using 100-Photon Schrodinger Cat States,” *Science* **342**, 607 (2013).
- [287] N. Rach, M. M. Müller, T. Calarco, and S. Montangero, “Dressing the chopped-random-basis optimization: A bandwidth-limited access to the trap-free landscape,” *Physical Review A* **92**, 062343 (2015).
- [288] R. Heck, O. Vuculescu, J. J. Sørensen, J. Zoller, M. G. Andreasen, M. G. Bason, P. Ejlertsen, O. Elíasson, P. Haikka, J. S. Laustsen, L. L. Nielsen, A. Mao, R. Müller,

- M. Napolitano, M. K. Pedersen, A. R. Thorsen, C. Bergenholz, T. Calarco, S. Montangero, and J. F. Sherson, “Remote optimization of an ultracold atoms experiment by experts and citizen scientists,” *Proceedings of the National Academy of Sciences* **115**, E11231 (2018).
- [289] C. J. Picken, R. Legaie, K. McDonnell, and J. D. Pritchard, “Entanglement of neutral-atom qubits with long ground-Rydberg coherence times,” *Quantum Science and Technology* **4**, 015011 (2018).
- [290] X. Zhang and J. Ye, “Precision measurement and frequency metrology with ultracold atoms,” *National Science Review* **3**, 189 (2016).
- [291] Y. Wang, A. Kumar, T.-Y. Wu, and D. S. Weiss, “Single-qubit gates based on targeted phase shifts in a 3D neutral atom array,” *Science* **352**, 1562 (2016).
- [292] T.-Y. Wu, A. Kumar, F. Giraldo, and D. S. Weiss, “Stern–Gerlach detection of neutral-atom qubits in a state-dependent optical lattice,” *Nature Physics* **15**, 538 (2019).
- [293] H. Levine, A. Keesling, A. Omran, H. Bernien, S. Schwartz, A. S. Zibrov, M. Endres, M. Greiner, V. Vuletić, and M. D. Lukin, “High-Fidelity Control and Entanglement of Rydberg-Atom Qubits,” *Physical Review Letters* **121**, 123603 (2018).
- [294] K. Wright, K. M. Beck, S. Debnath, J. M. Amini, Y. Nam, N. Grzesiak, J.-S. Chen, N. C. Pisenti, M. Chmielewski, C. Collins, K. M. Hudek, J. Mizrahi, J. D. Wong-Campos, S. Allen, J. Apisdorf, P. Solomon, M. Williams, A. M. Ducore, A. Blinov, S. M. Kreikemeier, V. Chaplin, M. Keesan, C. Monroe, and J. Kim, “Benchmarking an 11-qubit quantum computer,” *Nature Communications* **10**, 5464 (2019).
- [295] A. Erhard, J. J. Wallman, L. Postler, M. Meth, R. Stricker, E. A. Martinez, P. Schindler, T. Monz, J. Emerson, and R. Blatt, “Characterizing large-scale quantum computers via cycle benchmarking,” *Nature Communications* **10**, 5347 (2019).
- [296] M. Gong, M.-C. Chen, Y. Zheng, S. Wang, C. Zha, H. Deng, Z. Yan, H. Rong, Y. Wu, S. Li, F. Chen, Y. Zhao, F. Liang, J. Lin, Y. Xu, C. Guo, L. Sun, A. D. Castellano, H. Wang, C. Peng, C.-Y. Lu, X. Zhu, and J.-W. Pan, “Genuine 12-Qubit Entanglement on a Superconducting Quantum Processor,” *Physical Review Letters* **122**, 110501 (2019).
- [297] K. X. Wei, I. Lauer, S. Srinivasan, N. Sundaresan, D. T. McClure, D. Toyli, D. C. McKay, J. M. Gambetta, and S. Sheldon, “Verifying multipartite entangled Greenberger-Horne-Zeilinger states via multiple quantum coherences,” *Physical Review A* **101**, 032343 (2020).
- [298] A. Barenco, C. H. Bennett, R. Cleve, D. P. DiVincenzo, N. Margolus, P. Shor, T. Sleator, J. A. Smolin, and H. Weinfurter, “Elementary gates for quantum computation,” *Physical Review A* **52**, 3457 (1995).

- [299] A. Fedorov, L. Steffen, M. Baur, M. P. da Silva, and A. Wallraff, “Implementation of a Toffoli gate with superconducting circuits,” *Nature* **481**, 170 (2012).
- [300] C. Figgatt, D. Maslov, K. A. Landsman, N. M. Linke, S. Debnath, and C. Monroe, “Complete 3-Qubit Grover search on a programmable quantum computer,” *Nature Communications* **8**, 1918 (2017).
- [301] J. P. Covey, I. S. Madjarov, A. Cooper, and M. Endres, “2000-Times Repeated Imaging of Strontium Atoms in Clock-Magic Tweezer Arrays,” *Physical Review Letters* **122**, 173201 (2019).
- [302] M. Martinez-Dorantes, W. Alt, J. Gallego, S. Ghosh, L. Ratschbacher, Y. Völzke, and D. Meschede, “Fast Nondestructive Parallel Readout of Neutral Atom Registers in Optical Potentials,” *Physical Review Letters* **119**, 180503 (2017).
- [303] M. Kwon, M. F. Ebert, T. G. Walker, and M. Saffman, “Parallel Low-Loss Measurement of Multiple Atomic Qubits,” *Physical Review Letters* **119**, 180504 (2017).
- [304] S. de Léséleuc, D. Barredo, V. Lienhard, A. Browaeys, and T. Lahaye, “Optical Control of the Resonant Dipole-Dipole Interaction between Rydberg Atoms,” *Physical Review Letters* **119**, 053202 (2017).
- [305] J. Choi, A. L. Shaw, I. S. Madjarov, X. Xie, J. P. Covey, J. S. Cotler, D. K. Mark, H.-Y. Huang, A. Kale, H. Pichler, F. G. S. L. Brandão, S. Choi, and M. Endres, “Emergent Randomness and Benchmarking from Many-Body Quantum Chaos,” *arXiv:2103.03535* (2021).
- [306] A. Lengwenus, J. Kruse, M. Schlosser, S. Tichelmann, and G. Birkl, “Coherent Transport of Atomic Quantum States in a Scalable Shift Register,” *Physical Review Letters* **105**, 170502 (2010).
- [307] Y. R. P. Sortais, H. Marion, C. Tuchendler, A. M. Lance, M. Lamare, P. Fournet, C. Armellin, R. Mercier, G. Messin, A. Browaeys, and P. Grangier, “Diffraction-limited optics for single-atom manipulation,” *Physical Review A* **75**, 013406 (2007).
- [308] J. L. Hall and M. Zhu, in *Laser manipulation of atoms and ions*, edited by E. Arimondo, W. D. Phillips, and F. Strumia, pp. 671–702, (Elsevier, 1993).
- [309] R. W. Fox, C. W. Oates, and L. W. Hollberg, in *Cavity-Enhanced Spectroscopies*, edited by R. van Zee and J. Looney, pp. 1–46, (Elsevier, 2003).
- [310] J. Glaz and C. P. Sison, “Simultaneous confidence intervals for multinomial proportions,” *Journal of Statistical Planning and Inference* **82**, 251 (1999).

- [311] J. Johansson, P. Nation, and F. Nori, “QuTiP: An open-source Python framework for the dynamics of open quantum systems,” *Computer Physics Communications* **183**, 1760 (2012).
- [312] S. Boixo, S. V. Isakov, V. N. Smelyanskiy, R. Babbush, N. Ding, Z. Jiang, M. J. Bremner, J. M. Martinis, and H. Neven, “Characterizing quantum supremacy in near-term devices,” *Nature Physics* **14**, 595 (2018).
- [313] R. J. Baxter, *Exactly solved models in statistical mechanics*, (Courier Corporation, 2007).
- [314] U. Schollwöck, “The density-matrix renormalization group: a short introduction,” *Philosophical Transactions of the Royal Society A: Mathematical, Physical and Engineering Sciences* **369**, 2643 (2011).
- [315] J. Haegeman, J. I. Cirac, T. J. Osborne, I. Pižorn, H. Verschelde, and F. Verstraete, “Time-Dependent Variational Principle for Quantum Lattices,” *Physical Review Letters* **107**, 070601 (2011).
- [316] G. Vidal, “Efficient Simulation of One-Dimensional Quantum Many-Body Systems,” *Physical Review Letters* **93**, 040502 (2004).
- [317] A. J. Daley, C. Kollath, U. Schollwöck, and G. Vidal, “Time-dependent density-matrix renormalization-group using adaptive effective Hilbert spaces,” *Journal of Statistical Mechanics: Theory and Experiment* **2004**, P04005 (2004).
- [318] S. R. White, “Density-matrix algorithms for quantum renormalization groups,” *Physical Review B* **48**, 10345 (1993).
- [319] S. Östlund and S. Rommer, “Thermodynamic Limit of Density Matrix Renormalization,” *Physical Review Letters* **75**, 3537 (1995).
- [320] S. Rommer and S. Östlund, “Class of ansatz wave functions for one-dimensional spin systems and their relation to the density matrix renormalization group,” *Physical Review B* **55**, 2164 (1997).
- [321] J. Dukelsky, M. A. Martín-Delgado, T. Nishino, and G. Sierra, “Equivalence of the variational matrix product method and the density matrix renormalization group applied to spin chains,” *Europhysics Letters (EPL)* **43**, 457 (1998).
- [322] I. Peschel, M. Kaulke, X. Wang, and K. Hallberg, eds., *Density-matrix renormalization: a new numerical method in physics: lectures of a seminar and workshop held at the Max-Planck-Institut für Physik komplexer Systeme, Dresden, Germany, August 24th to September 18th, 1998* (Springer, Berlin, 1999).

- [323] I. P. McCulloch, “Infinite size density matrix renormalization group, revisited,” *arXiv:0804.2509* (2008).
- [324] B. Pirvu, V. Murg, J. I. Cirac, and F. Verstraete, “Matrix product operator representations,” *New Journal of Physics* **12**, 025012 (2010).
- [325] U. Schollwöck, “The density-matrix renormalization group,” *Reviews of Modern Physics* **77**, 259 (2005).
- [326] U. Schollwöck, “The density-matrix renormalization group in the age of matrix product states,” *Annals of Physics* **326**, 96 (2011).
- [327] M. Gerster, B. Haggenmiller, F. Tschirsich, P. Silvi, and S. Montangero, “Dynamical Ginzburg criterion for the quantum-classical crossover of the Kibble-Zurek mechanism,” *Physical Review B* **100**, 024311 (2019).
- [328] D. Jaschke, K. Maeda, J. D. Whalen, M. L. Wall, and L. D. Carr, “Critical phenomena and Kibble–Zurek scaling in the long-range quantum Ising chain,” *New Journal of Physics* **19**, 033032 (2017).
- [329] D. A. Huse, “Simple three-state model with infinitely many phases,” *Physical Review B* **24**, 5180 (1981).
- [330] D. A. Huse, A. M. Szpilka, and M. E. Fisher, “Melting and wetting transitions in the three-state chiral clock model,” *Physica A: Statistical Mechanics and its Applications* **121**, 363 (1983).
- [331] P. Fendley, “Parafermionic edge zero modes in Z_n -invariant spin chains,” *Journal of Statistical Mechanics: Theory and Experiment* **2012**, P11020 (2012).
- [332] Y. Zhuang, H. J. Changlani, N. M. Tubman, and T. L. Hughes, “Phase diagram of the Z_3 parafermionic chain with chiral interactions,” *Physical Review B* **92**, 035154 (2015).
- [333] F. Y. Wu, “The Potts model,” *Reviews of Modern Physics* **54**, 235 (1982).
- [334] S. Alexander, “Lattice gas transition of He on Grafoil. A continuous transition with cubic terms,” *Physics Letters A* **54**, 353 (1975).
- [335] R. J. Baxter, “Hard hexagons: exact solution,” *Journal of Physics A: Mathematical and General* **13**, L61 (1980).
- [336] J. V. José, L. P. Kadanoff, S. Kirkpatrick, and D. R. Nelson, “Renormalization, vortices, and symmetry-breaking perturbations in the two-dimensional planar model,” *Physical Review B* **16**, 1217 (1977).
- [337] L. P. Kadanoff, “Connections between the Critical Behavior of the Planar Model and That of the Eight-Vertex Model,” *Physical Review Letters* **39**, 903 (1977).

- [338] J. Yeomans, “ANNNI and clock models,” *Physica B+C* **127**, 187 (1984).
- [339] W. Lee, H. Kim, and J. Ahn, “Defect-free atomic array formation using the Hungarian matching algorithm,” *Physical Review A* **95**, 053424 (2017).
- [340] C. Sheng, J. Hou, X. He, P. Xu, K. Wang, J. Zhuang, X. Li, M. Liu, J. Wang, and M. Zhan, “Efficient preparation of two-dimensional defect-free atom arrays with nearest-fewest sorting-atom moves,” *Physical Review Research* **3**, 023008 (2021).
- [341] S. M. Bhattacharjee and F. Seno, “A measure of data collapse for scaling,” *Journal of Physics A: Mathematical and General* **34**, 6375 (2001).
- [342] E. Stoudenmire and S. R. White, “Studying Two-Dimensional Systems with the Density Matrix Renormalization Group,” *Annual Review of Condensed Matter Physics* **3**, 111 (2012).
- [343] A. Michailidis, C. Turner, Z. Papić, D. Abanin, and M. Serbyn, “Slow Quantum Thermalization and Many-Body Revivals from Mixed Phase Space,” *Physical Review X* **10**, 011055 (2020).
- [344] C. W. von Keyserlingk, V. Khemani, and S. L. Sondhi, “Absolute stability and spatiotemporal long-range order in Floquet systems,” *Physical Review B* **94**, 085112 (2016).
- [345] J. Haegeman, C. Lubich, I. Oseledets, B. Vandereycken, and F. Verstraete, “Unifying time evolution and optimization with matrix product states,” *Physical Review B* **94**, 165116 (2016).
- [346] C.-h. Fan, D. Rossini, H.-X. Zhang, J.-H. Wu, M. Artoni, and G. C. La Rocca, “Discrete time crystal in a finite chain of Rydberg atoms without disorder,” *Physical Review A* **101**, 013417 (2020).
- [347] B. Mukherjee, S. Nandy, A. Sen, D. Sen, and K. Sengupta, “Collapse and revival of quantum many-body scars via Floquet engineering,” *Physical Review B* **101**, 245107 (2020).
- [348] K. Mizuta, K. Takasan, and N. Kawakami, “Exact Floquet quantum many-body scars under Rydberg blockade,” *Physical Review Research* **2**, 033284 (2020).
- [349] D. V. Else, W. W. Ho, and P. T. Dumitrescu, “Long-Lived Interacting Phases of Matter Protected by Multiple Time-Translation Symmetries in Quasiperiodically Driven Systems,” *Physical Review X* **10**, 021032 (2020).
- [350] M. Rispoli, A. Lukin, R. Schittko, S. Kim, M. E. Tai, J. Léonard, and M. Greiner, “Quantum critical behaviour at the many-body localization transition,” *Nature* **573**, 385 (2019).

- [351] E. Fradkin and S. H. Shenker, “Phase diagrams of lattice gauge theories with Higgs fields,” *Physical Review D* **19**, 3682 (1979).
- [352] B. Sutherland, “Systems with resonating-valence-bond ground states: Correlations and excitations,” *Physical Review B* **37**, 3786 (1988).
- [353] T. Kato, “On the Adiabatic Theorem of Quantum Mechanics,” *Journal of the Physical Society of Japan* **5**, 435 (1950).
- [354] J. Johansson, P. Nation, and F. Nori, “QuTiP 2: A Python framework for the dynamics of open quantum systems,” *Computer Physics Communications* **184**, 1234 (2013).
- [355] S. Montangero, T. Calarco, and R. Fazio, “Robust Optimal Quantum Gates for Josephson Charge Qubits,” *Physical Review Letters* **99**, 170501 (2007).
- [356] C. Brif, R. Chakrabarti, and H. Rabitz, “Control of quantum phenomena: past, present and future,” *New Journal of Physics* **12**, 075008 (2010).
- [357] J. Cui and F. Mintert, “Robust control of long-distance entanglement in disordered spin chains,” *New Journal of Physics* **17**, 093014 (2015).
- [358] C. P. Koch, “Controlling open quantum systems: tools, achievements, and limitations,” *Journal of Physics: Condensed Matter* **28**, 213001 (2016).
- [359] P. Doria, T. Calarco, and S. Montangero, “Optimal Control Technique for Many-Body Quantum Dynamics,” *Physical Review Letters* **106**, 190501 (2011).
- [360] S. J. Glaser, U. Boscain, T. Calarco, C. P. Koch, W. Köckenberger, R. Kosloff, I. Kuprov, B. Luy, S. Schirmer, T. Schulte-Herbrüggen, D. Sugny, and F. K. Wilhelm, “Training Schrödinger’s cat: quantum optimal control: Strategic report on current status, visions and goals for research in Europe,” *The European Physical Journal D* **69**, 279 (2015).
- [361] I. Brouzos, A. I. Streltsov, A. Negretti, R. S. Said, T. Caneva, S. Montangero, and T. Calarco, “Quantum speed limit and optimal control of many-boson dynamics,” *Physical Review A* **92**, 062110 (2015).
- [362] S. Lloyd and S. Montangero, “Information Theoretical Analysis of Quantum Optimal Control,” *Physical Review Letters* **113**, 010502 (2014).
- [363] S. van Frank, M. Bonneau, J. Schmiedmayer, S. Hild, C. Gross, M. Cheneau, I. Bloch, T. Pichler, A. Negretti, T. Calarco, and S. Montangero, “Optimal control of complex atomic quantum systems,” *Scientific Reports* **6**, 34187 (2016).
- [364] M. M. Müller, A. Kölle, R. Löw, T. Pfau, T. Calarco, and S. Montangero, “Room-temperature Rydberg single-photon source,” *Physical Review A* **87**, 053412 (2013).

- [365] T. Caneva, M. Murphy, T. Calarco, R. Fazio, S. Montangero, V. Giovannetti, and G. E. Santoro, “Optimal Control at the Quantum Speed Limit,” *Physical Review Letters* **103**, 240501 (2009).
- [366] T. Caneva, T. Calarco, R. Fazio, G. E. Santoro, and S. Montangero, “Speeding up critical system dynamics through optimized evolution,” *Physical Review A* **84**, 012312 (2011).
- [367] J. Cui, Rick van Bijnen, T. Pohl, S. Montangero, and T. Calarco, “Optimal control of Rydberg lattice gases,” *Quantum Science and Technology* **2**, 035006 (2017).
- [368] J. A. Nelder and R. Mead, “A Simplex Method for Function Minimization,” *The Computer Journal* **7**, 308 (1965)